THE BACTERIAL CELL: COUPLING BETWEEN GROWTH, NUCLEOID REPLICATION, CELL DIVISION, AND SHAPE, VOLUME 2

EDITED BY: Ariel Amir, Jaan Männik, Conrad L. Woldringh and Arieh Zaritsky
PUBLISHED IN: Frontiers in Microbiology

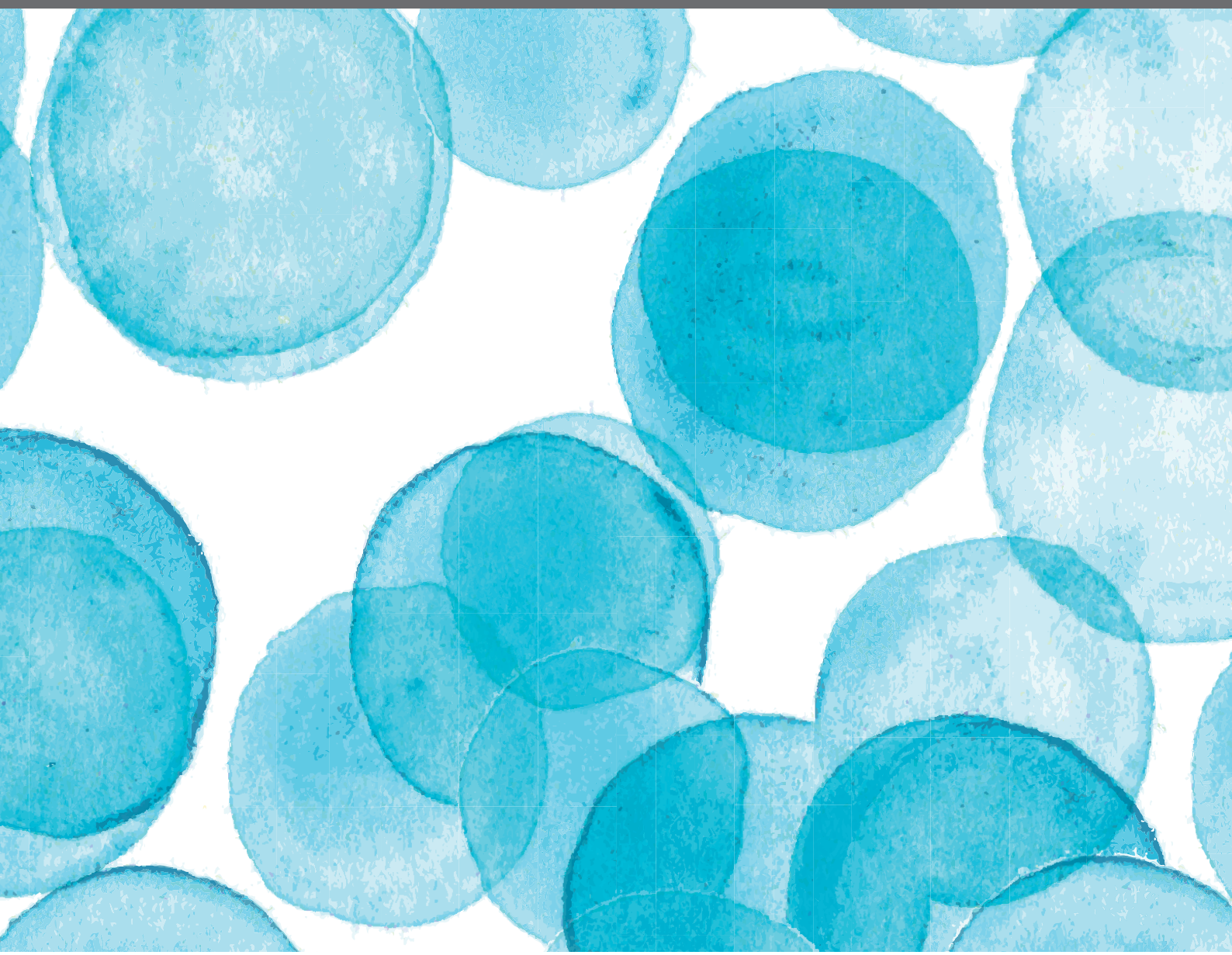

frontiers Research Topics

ISSN 1664-8714
ISBN 978-2-88963-156-8
DOI 10.3389/978-2-88963-156-8

About Frontiers

Frontiers is more than just an open-access publisher of scholarly articles: it is a pioneering approach to the world of academia, radically improving the way scholarly research is managed. The grand vision of Frontiers is a world where all people have an equal opportunity to seek, share and generate knowledge. Frontiers provides immediate and permanent online open access to all its publications, but this alone is not enough to realize our grand goals.

Frontiers Journal Series

The Frontiers Journal Series is a multi-tier and interdisciplinary set of open-access, online journals, promising a paradigm shift from the current review, selection and dissemination processes in academic publishing. All Frontiers journals are driven by researchers for researchers; therefore, they constitute a service to the scholarly community. At the same time, the Frontiers Journal Series operates on a revolutionary invention, the tiered publishing system, initially addressing specific communities of scholars, and gradually climbing up to broader public understanding, thus serving the interests of the lay society, too.

Dedication to Quality

Each Frontiers article is a landmark of the highest quality, thanks to genuinely collaborative interactions between authors and review editors, who include some of the world's best academicians. Research must be certified by peers before entering a stream of knowledge that may eventually reach the public - and shape society; therefore, Frontiers only applies the most rigorous and unbiased reviews.
Frontiers revolutionizes research publishing by freely delivering the most outstanding research, evaluated with no bias from both the academic and social point of view. By applying the most advanced information technologies, Frontiers is catapulting scholarly publishing into a new generation.

What are Frontiers Research Topics?

Frontiers Research Topics are very popular trademarks of the Frontiers Journals Series: they are collections of at least ten articles, all centered on a particular subject. With their unique mix of varied contributions from Original Research to Review Articles, Frontiers Research Topics unify the most influential researchers, the latest key findings and historical advances in a hot research area! Find out more on how to host your own Frontiers Research Topic or contribute to one as an author by contacting the Frontiers Editorial Office: researchtopics@frontiersin.org

THE BACTERIAL CELL: COUPLING BETWEEN GROWTH, NUCLEOID REPLICATION, CELL DIVISION, AND SHAPE, VOLUME 2

Topic Editors:
Ariel Amir, Harvard University, United States
Jaan Männik, University of Tennessee, Knoxville, United States
Conrad L. Woldringh, University of Amsterdam, the Netherlands
Arieh Zaritsky, Ben-Gurion University of the Negev, Israel

The 1st volume of our Research Topic "The Bacterial Cell: Coupling between Growth, Nucleoid Replication, Cell Division and Shape" was published as an eBook in May 2016 (see: http://journal.frontiersin.org/researchtopic/2905/the-bacterial-cell-coupling-between-growth-nucleoid-replication-cell-division-and-shape). As a sign of growing interest to the topic, two workshops followed the same year: "Stochasticity in the Cell Cycle" in Jerusalem (Israel) by the Hebrew University's Institute of Advanced Studies and EMBO's "Cell Size Regulation" in Joachimsthal (Germany). From the time of launching the first edition, several new groups have entered the field, and many established groups have made significant advances using state-of-the-art microscopy and microfluidics. Combining these approaches with the techniques pioneered by quantitative microbiologists decades ago, these approaches have provided remarkable amounts of numerical data. Most of these data needed yet to be put into a broader theoretical perspective. Moreover, the molecular mechanisms governing coordination and progression of the main bacterial cell cycle processes have remained largely unknown. These outstanding fundamental questions and the growing interest to the field motivated us to launch the next volume titled "The Bacterial Cell: Coupling between Growth, Nucleoid Replication, Cell Division, and Shape, Volume 2" shortly after completion of the first edition in October 2016.

The issue contains 17 contributions from a diverse array of scientists whose field of study spans microbiology, biochemistry, genetics, experimental and theoretical biophysics. The specific questions addressed in the issue include: What triggers initiation of chromosome replication? How is cell division coordinated with replication both spatially and temporally? How is cell size controlled and linked to the rate of mass growth? What role plays physical organization of the chromosomes in their segregation and in regulation of cell division?

The publications covering these questions are divided into three topical areas: 1) Cell Cycle Regulation, 2) Growth and Division, and 3) Nucleoid Structure and Replication.

New ideas and techniques put forward in these articles bring us closer to understand these fundamental cellular processes, but the quest to resolve them is far from being complete. Plans for the next edition are under way along with further meetings and

workshops, e.g., an EMBO Workshop on Bacterial cell biophysics: DNA replication, growth, division, size and shape in Ein Gedi (Israel), May 2020. We hope that via such interdisciplinary exchange of ideas we will come closer to answering the above-mentioned complex and multifaceted questions.

Citation: Amir, A., Männik, J., Woldringh, C. L., Zaritsky, A., eds. (2019). The Bacterial Cell: Coupling between Growth, Nucleoid Replication, Cell Division, and Shape, Volume 2. Lausanne: Frontiers Media. doi: 10.3389/978-2-88963-156-8

Table of Contents

CHAPTER 3
NUCLEOID AND REPLICATION

frontiers in Microbiology

EDITORIAL
published: 04 September 2019
doi: 10.3389/fmicb.2019.02056

Editorial: The Bacterial Cell: Coupling between Growth, Nucleoid Replication, Cell Division, and Shape Volume 2

Ariel Amir[1], *Jaan Männik*[2]*, *Conrad L. Woldringh*[3] *and Arieh Zaritsky*[4]

[1] School of Engineering and Applied Sciences, Harvard University, Cambridge, MA, United States, [2] Department of Physics and Astronomy, University of Tennessee, Knoxville, Knoxville, TN, United States, [3] Bacterial Cell Biology, Faculty of Science, Swammerdam Institute for Life Sciences, University of Amsterdam, Amsterdam, Netherlands, [4] Faculty of Natural Sciences, Ben-Gurion University of the Negev, Be'er Sheva, Israel

Keywords: cell cycle, nucleoid, divisome, cell division, cell envelope, cell shape, chromosome replication

Editorial on the Research Topic

The Bacterial Cell: Coupling between Growth, Nucleoid Replication, Cell Division, and Shape Volume 2

The bacterial cell cycle has been under intense investigation for many decades, yet many of the most fundamental questions remain wide open. DNA replication, cell division, protein synthesis, and cell envelope production are believed to be all coupled, but the causal relations between these different processes, and even which process is downstream of which, are not always known. Moreover, it is not clear to what degree the cellular "architecture" governing this coupled, complex system is conserved across different bacteria, or even within one bacterial species across different growth conditions!

Many investigations in biology focus on a small subset of proteins/other cellular components and explore how they function upon genetic or external perturbations. To study the bacterial cell cycle it is beneficial, even obligatory, to also consider the relations between various processes that *a priori* could have been thought of as completely uncoupled from each other, as for instance are transcriptional activity and nucleoid compaction. This may be the reason why this problem has been a "tough egg to crack" and why many basic questions remain unclear to date.

Recent advances in microscopy and microfluidics technologies have enabled to gather large amounts of single-cell data. Combined with mathematical modeling and statistical analyses these datasets are beginning to reveal novel and unexpected couplings between cell cycle processes. Such approaches reinvigorated the field recently and led to some exciting results, which altogether have motivated this Edition.

The contributions to this volume are divided to three Chapters: (1) Coupling between Major Cellular Processes, (2) Cell Growth and Division, and (3) Bacterial Nucleoid and Initiation of Replication. The following briefly summarizes the contributions to these three topics in that order.

The first Chapter starts with the work of Kleckner et al. that addresses the coupling between cell division and chromosome replication in *Escherichia coli*. The early studies by Cooper and Helmstetter from the 1960's have been consistent with such a coupling, where the former is downstream the latter, both being downstream of a third cellular series of processes. Here Kleckner et al. postulate a different order of couplings by extending their previous "licensing" hypothesis (referred to as a "progression permission" now). "Permission" comprises both cell growth (mass accumulation) and divisome assembly combined with placement of the terminus domain at mid-cell, which is proposed to cause a global change in nucleoid organization. Progress

OPEN ACCESS

Edited by:
Biswarup Mukhopadhyay, Virginia Tech, United States

Reviewed by:
Peter Graumann, University of Marburg, Germany

***Correspondence:**
Jaan Männik
JMannik@utk.edu

Specialty section:
This article was submitted to Microbial Physiology and Metabolism, a section of the journal Frontiers in Microbiology

Received: *01 July 2019*
Accepted: *20 August 2019*
Published: *04 September 2019*

Citation:
Amir A, Männik J, Woldringh CL and Zaritsky A (2019) Editorial: The Bacterial Cell: Coupling between Growth, Nucleoid Replication, Cell Division, and Shape Volume 2. Front. Microbiol. 10:2056. doi: 10.3389/fmicb.2019.02056

of this "permission" implements two parallel downstream events: replication initiation and septum closure, that occur in a comparable way in both slow and fast growth conditions.

Logsdon and Aldridge review growth and size control in mycobacteria and conclude that division is tightly linked to DNA replication, albeit in a different way than the Cooper-Helmstetter model, whereby a constant volume (rather than constant time) is added from initiation of DNA replication to division. Within the "parallel adder" model proposed, two independent volume integrators are operating simultaneously, one controlling cell division and the other initiation of DNA replication. To further complicate matters, in mycobacteria such as *M. smegmatis* division is asymmetric, and one has to distinguish between "accelerator" and "alternator" cells—each possessing a different volume increment.

Another "theme" relevant for several contributions regards the role of variability between genetically identical cells and its utility in studying cell cycle-related problems. Grilli et al. demonstrate how growth can be characterized phenomenologically by utilizing natural fluctuations (i.e., stochasticity). Correlations between key cell cycle variables are used as an additional method of characterizing phenotypes; systematic analysis of correlations between cell size and generation time in *E. coli*, for instance, constrains the landscape of possible molecular mechanisms, the details of which are yet to be understood.

In contrast, Govindarajan et al. show how isogenic cells may utilize variability to increase the population's fitness: clustering of EI, a protein important for sugar uptake and metabolism, occurs stochastically and leads to phenotypic diversity. Furthermore, it differs between growing and non-growing cells. The enhanced clustering in non-growing conditions is suggested to confer a fitness advantage, as the EI clusters provide a reservoir to be utilized at times of need.

Gangwe Nana et al. also study phenotypic variability in *E. coli*, in this case arising from asymmetric partitioning of a cellular resource between two daughter cells. The authors use Secondary Mass Spectrometry imaging to infer growth rates and observe that distribution of their ^{15}N label is not homogenous in the cells but asymmetric between the cell halves. They propose that growth rate diversity relates to asymmetric partitioning of cellular resources during division, hypothesizing that inheritance of DNA strands between daughters is responsible for this asymmetry. According to the hypothesis the two parental strands of DNA are expected to be physically associated with different proteins conveying to them a different survival strategy.

Even if universal principles governing cell cycle regulation do exist in bacteria, they must operate on a specific cellular machinery, which differs from species to species. Key components of this machinery are divisome and elongasome complexes responsible for cell division and elongation, respectively. These cellular components are discussed in the second Chapter. Three review papers by van Teeseling et al., den Blaauwen, Caspi and Dekker highlight both the diversity of these machineries in different microorganisms as well as common themes. Much of the research so far has focused on a limited number of model organisms, in particular *E. coli*. Its close relative, *Thiosymbion,* divides *parallel* to the long axes of the cell, unlike the conventional model system. den Blaauwen hypothesizes that mutations in two key coordinating proteins of divisome and elangosome, FtsZ, and MreB respectively, may allow reorienting the cell division plane. Interestingly, this mode of lateral growth and longitudinal division challenges current ideas about DNA segregation and nucleoid movement.

van Teeseling et al. tackle the question of what leads to bacterial morphological diversity. While the key architecture for peptidoglycan synthesis is largely conserved in most cells, many additions to this architecture allow diversification of the morphologies leading to adaptation of the cells to their particular ecological niche. These additions, which in some cases are important for their virulence, may be useful targets for narrow band antibiotics.

Caspi and Dekker expand the topic of cell division to archaea and overview the Cdv system. They argue that although Cdv is similar to the eukaryotic ESCRT system, it is functionally different. Along the lines of common and diverging features, Flores et al. show that the placement of division in *Agrobacterium tumefaciens* depends on the widespread Min system but also on other molecular systems; the origin of which is yet to be determined.

A common theme in bacterial cell division is that septal closure needs to overcome high turgor pressure. What cellular process or structure provides the force for constriction is not clear yet. Osawa and Erickson hypothesize that among other factors excess membrane synthesis during division may force it to bleb inwards and such membrane deformation may create sufficient force to pinch the cell at its middle. Interestingly, Kumar et al., who present new experimental data on Z-ring dynamics in *E. coli*, observe that the radius of FtsZ protofilament decreases faster than the cell envelope radius. Could the difference in these two rates be explained by excess inner membrane added to the septal region as hypothesized by Osawa and Erickson?

Microfluidic techniques have become important tools in studies of growth and division. It has generally been taken for granted that bacteria grow in such devices similarly to classical liquid cultures. This has been examined by Yang et al. who show that growth rate and cell sizes in these devices are sensitively dependent on length and cross-sectional dimensions of the channels. The main growth-limiting factor in these devices is assigned to mechanical friction forces rather than nutrient limitation in the narrow channels.

A key component of cellular "architecture" mentioned above is the nucleoid, the structure and replication of which are discussed in the third Chapter of this volume. Applying Structural Illumination Microscopy, Martin et al. show that upon deletion of ribosomal RNA operons, nucleolus-like compartments are no longer formed on the nucleoid border and the nucleoid expands. They propose that long-range interactions between transcription foci may play a role in DNA compaction. Katayama et al. discuss the structural features of the *oriC* region and the regulatory cycle of DnaA-ATP, whereas Rao et al. demonstrate the influence of DnaA-ATP binding to mutated recognition sites on the timing of replication-initiation. These and other aspects of the orisome assembly have been integrated by Hansen and Atlung in their discussion of the Initiator Titration Model. Their model also shows how baby cells of

different sizes that result from asymmetric divisions will initiate at different times, but will have about the same size (but not the same age) at the next initiation. The same model can also explain the larger amount of DNA in large newborn cells at fast growth as measured by Huls et al. These authors furthermore find that the larger siblings that initiate earlier segregate their nucleoids faster thus allowing them to divide earlier at a shorter length as dictated by the adder principle. In this view both initiation of replication and the processes leading to cell division are coupled to growth rate, as also emphasized by Kleckner et al.

AUTHOR CONTRIBUTIONS

All authors listed have made a substantial, direct and intellectual contribution to the work, and approved it for publication.

FUNDING

The work was supported in part by US-Israel BSF research grant 2017004 (JM and AZ), National Institutes of Health award under R01GM127413, NSF CAREER MCB-1252890 (JM), and NSF CAREER 1752024 (AA).

Conflict of Interest Statement: The authors declare that the research was conducted in the absence of any commercial or financial relationships that could be construed as a potential conflict of interest.

frontiers in Microbiology

HYPOTHESIS AND THEORY
published: 09 July 2018
doi: 10.3389/fmicb.2018.01469

Coordination of Growth, Chromosome Replication/Segregation, and Cell Division in *E. coli*

Nancy E. Kleckner[1]*, *Katerina Chatzi*[1], *Martin A. White*[1], *Jay K. Fisher*[2] *and Mathieu Stouf*[1]

[1] *Department of Molecular and Cellular Biology Harvard University, Cambridge, MA, United States,* [2] *Redbud Labs, Durham, NC, United States*

Bacterial cells growing in steady state maintain a 1:1:1 relationship between an appropriate mass increase, a round of DNA replication plus sister chromosome segregation, and cell division. This is accomplished without the cell cycle engine found in eukaryotic cells. We propose here a formal logic, and an accompanying mechanism, for how such coordination could be provided in *E. coli.* Completion of chromosomal and divisome-related events would lead, interactively, to a "progression control complex" (PCC) which provides integrated physical coupling between sister terminus regions and the nascent septum. When a cell has both (i) achieved a sufficient mass increase, and (ii) the PCC has developed, a conformational change in the PCC occurs. This change results in "progression permission," which triggers both onset of cell division and release of terminus regions. Release of the terminus region, in turn, directly enables a next round of replication initiation via physical changes transmitted through the nucleoid. Division and initiation are then implemented, each at its own rate and timing, according to conditions present. Importantly: (i) the limiting step for progression permission may be either completion of the growth requirement or the chromosome/divisome processes required for assembly of the PCC; and, (ii) the outcome of the proposed process is granting of permission to progress, not determination of the absolute or relative timings of downstream events. This basic logic, and the accompanying mechanism, can explain coordination of events in both slow and fast growth conditions; can accommodate diverse variations and perturbations of cellular events; and is compatible with existing mathematical descriptions of the *E. coli* cell cycle. Also, while our proposition is specifically designed to provide 1:1:1 coordination among basic events on a "per-cell cycle" basis, it is a small step to further envision permission progression is also the target of basic growth rate control. In such a case, the rate of mass accumulation (or its equivalent) would determine the length of the interval between successive permission events and, thus, successive cell divisions and successive replication initiations.

Keywords: *E. coli*, cell cycle coordination, bacteria, chromosome, cell division, DNA replication, licensing

OPEN ACCESS

Edited by:
Arieh Zaritsky,
Ben-Gurion University of the Negev, Israel

Reviewed by:
Kirsten Skarstad,
Oslo University Hospital, Norway
Marco Cosentino Lagomarsino,
UMR7238 Biologie Computationnelle et Quantitative (CQB), France

***Correspondence:**
Nancy E. Kleckner
kleckner@fas.harvard.edu

Specialty section:
This article was submitted to Microbial Physiology and Metabolism, a section of the journal Frontiers in Microbiology

Received: *21 February 2018*
Accepted: *12 June 2018*
Published: *09 July 2018*

Citation:
Kleckner NE, Chatzi K, White MA, Fisher JK and Stouf M (2018) Coordination of Growth, Chromosome Replication/Segregation, and Cell Division in E. coli. Front. Microbiol. 9:1469. doi: 10.3389/fmicb.2018.01469

INTRODUCTION AND OVERVIEW

All cells growing in steady state must ensure a 1:1:1 relationship among doublings of cell mass, rounds of chromosome duplication/segregation and cell divisions. In eukaryotic cells, this relationship is ensured by operation of the cell cycle engine, in interplay with affected molecular events (Siddiqui et al., 2013). How this relationship is ensured in prokaryotes, e.g., *E. coli*, is unclear but widely discussed. Notably, *E. coli* can grow with both linear and overlapping chromosome/division cycles, with wide variations in the durations of component processes in different situations and, in any given situation, among different individual cells. The need for a coherent coordination process seems especially important in light of this dramatic variability on both the population and single cell levels. Here we propose that a process exists specifically to ensure the necessary 1:1:1 coordination and we propose both a formal logic and a specific mechanism for such coordination. Furthermore, we suggest that the proposed process could serve not only for coordination, but also as the mechanism by which occurrence of cell division [and an accompanying round of initiation(s)] is linked to cell growth conditions.

In brief: (**Figure 1A**), when the cell has satisfied requirements both for growth (mass accumulation or its correlate) and for completion of chromosome replication/segregation and divisome development (which are functionally related processes; below), chromosomal events and septum closure are coordinately permitted to progress, resulting in, respectively, replication initiation and cell division. After progression permission has been granted, the two downstream outcomes will be implemented. This formal logic will function regardless of which of the two required input events is rate-limiting. During implementation, the absolute and relative timings of the two downstream outputs will be influenced by the rates of individual component events. We show below that this logic can function analogously in slow and fast growth regimes; that it is robust to variations in the rates cellular events; and that it can gracefully accommodate growth rate transitions.

A key feature of the proposed mechanism for this process is a progression control complex (PCC) (**Figure 1A**). This PCC would form by interaction of sister terminus domains with the developing mid-cell divisome, dependent on proteins known to interactively mediate chromosome/divisome interplay (**Figure 1B**). Once formed, the PCC would inhibit onset of a next round of replication initiation and onset of cell division. Concomitantly, growth-related events are occurring.

In some situations (e.g., slow growth conditions), completion of the growth requirement will be rate-limiting irrespective of chromosome/divisome events, with PCC-mediated inhibition remaining in play until the growth requirement is met. In other situations (e.g., fast growth conditions), the chromosome/divisome events involved in PCC development seem to be rate limiting. In these conditions, it is less clear when and how the sensing of growth status occurs and thus this input may be independent of PCC development or feed directly into PCC development itself (or potentially both) (**Figure 1A** legend). In any of these cases, however, progression permission would occur as soon as PCC development is complete.

In all growth conditions, once both the growth and chromosome/divisiome requirements have been met, the PCC would undergo a conformational change that concomitantly: (i) triggers onset of septum closure (and thus cell division); and (ii) releases the terminus domain from divisome components (and thereby allowing a next round of replication initiation to occur whenever other requirements and required components are present). This conformational change in the

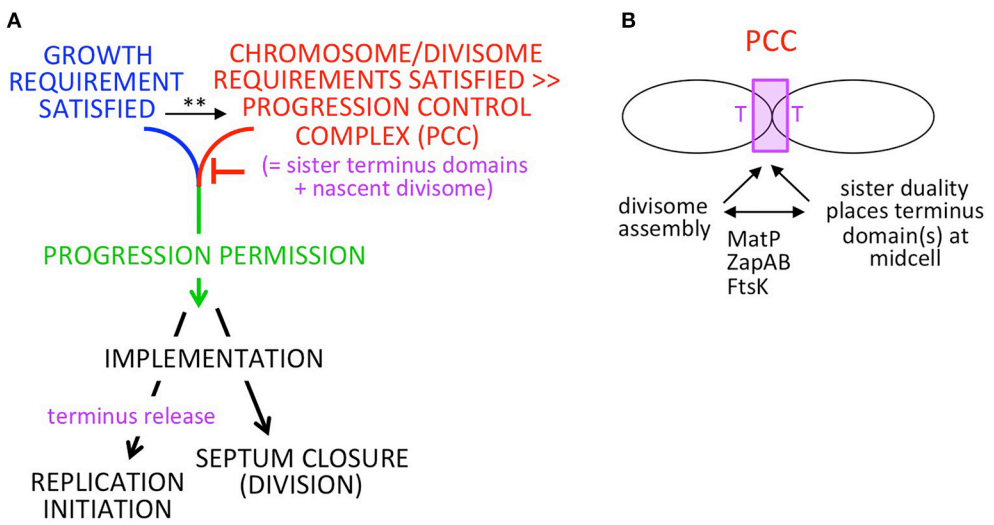

FIGURE 1 | Progression permission model. **(A)** General logic for 1:1:1 coordination of cell growth, replication initiation and cell division. Note: in slow growth conditions, PCC development clearly precedes satisfaction of the growth requirement such that the two features operate in parallel. In fast growth conditions, it is less clear whether the growth input is independent of PCC development and/or feeds into development of the PCC. This ambiguity is indicated by the (**); see text. **(B)** Development of the proposed PPC by integration of chromosome and divisome inputs.

PCC would comprise "progression permission" (**Figure 1A** green).

We further suggest that the PCC transition that triggers resultant division/initiation could be the event by which cells sense and respond to growth condition, with PCC transition events occurring more or less frequently under faster or slower growth conditions.

We also note that, as described below, the mechanism described for these effects involves not only direct physical interaction among relevant components but a physical mechanism for constraining and permitting replication initiation that involves transmission of information throughout the nucleoid. Such a process would be an attractive way to achieve coordination (and control) in the absence of a eukaryotic-like cell cycle engine.

FORMAL LOGIC

E. coli grows in two different regimes, termed "slow" and "fast" growth (e.g., Helmstetter et al., 1968; Wallden et al., 2016).

One approach to describing these regimes is provided by the formulation of Cooper and Helmstetter, who divided the cell division cycle into two components - the "C-period," which comprises bulk DNA replication, and the "D-period" which comprises the period between the end of bulk DNA

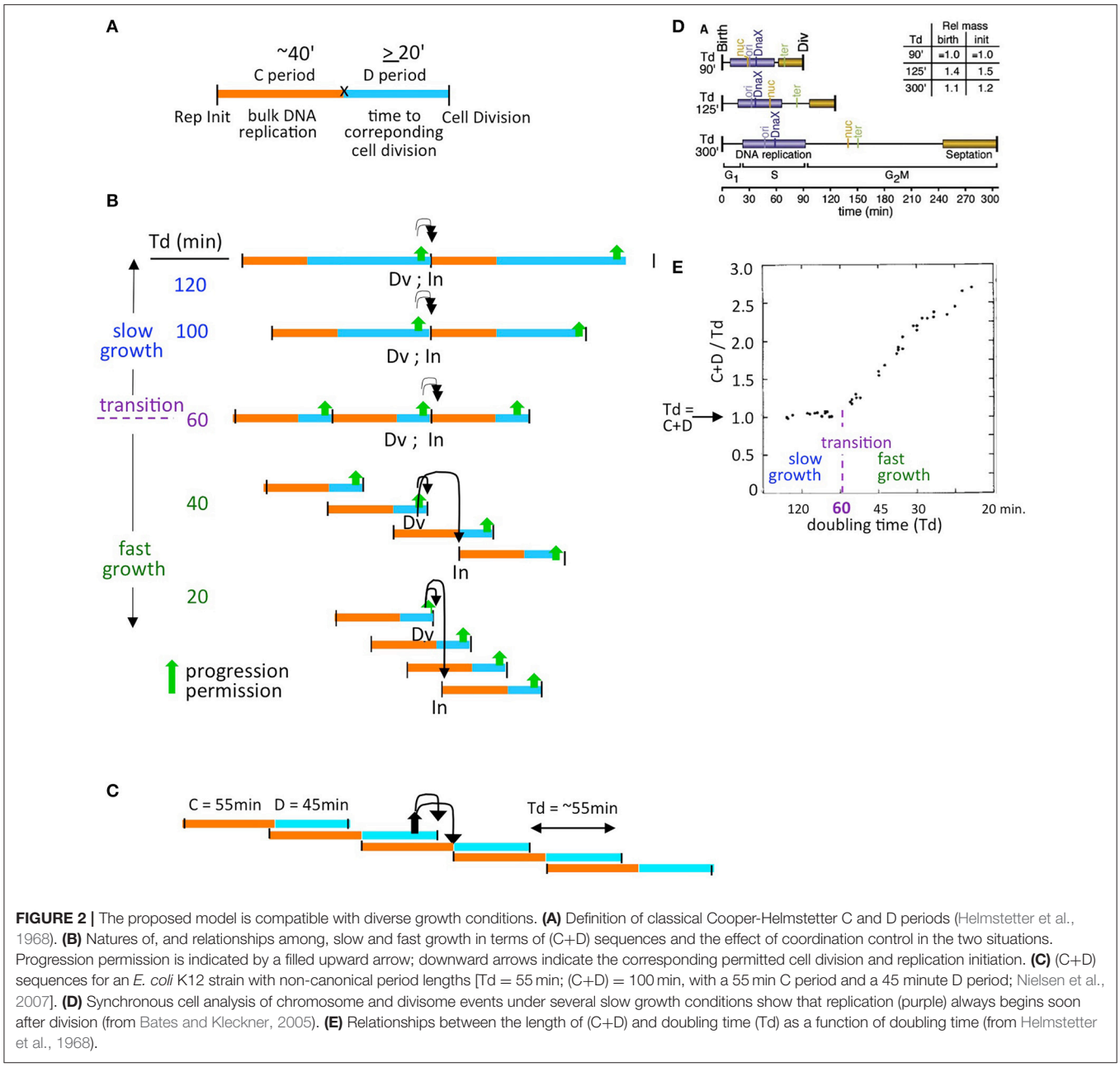

FIGURE 2 | The proposed model is compatible with diverse growth conditions. **(A)** Definition of classical Cooper-Helmstetter C and D periods (Helmstetter et al., 1968). **(B)** Natures of, and relationships among, slow and fast growth in terms of (C+D) sequences and the effect of coordination control in the two situations. Progression permission is indicated by a filled upward arrow; downward arrows indicate the corresponding permitted cell division and replication initiation. **(C)** (C+D) sequences for an *E. coli* K12 strain with non-canonical period lengths [Td = 55 min; (C+D) = 100 min, with a 55 min C period and a 45 minute D period; Nielsen et al., 2007]. **(D)** Synchronous cell analysis of chromosome and divisome events under several slow growth conditions show that replication (purple) always begins soon after division (from Bates and Kleckner, 2005). **(E)** Relationships between the length of (C+D) and doubling time (Td) as a function of doubling time (from Helmstetter et al., 1968).

replication and the corresponding division, at which the sisters generated during replication segregate to daughter (sister) cells (Helmstetter et al., 1968; **Figure 2A**).

Cooper and Helmstetter's classical studies used strain B/r, where the C period is roughly constant at ∼40 min under diverse conditions.

- In "slow growth" conditions, C and D periods follow one another in sequence, with a constant C-period followed by an appropriately long D-period. At progressively shorter doubling times, the D-period becomes progressively shorter (**Figure 2B** top).
- At a certain doubling time (classically ∼60 min, implying a D-period of ∼20 min) a minimum length of the D-period is reached (**Figure 2B** middle). This condition marks the transition between slow and fast growth. The basis for this minimum D-period is not established; however a strong possibility is that a certain minimum time is required for completion of sister terminus separation (e.g., dimer reduction and decatenation) and for the actual act of septum formation via closure of the Z-ring, which are two closely interrelated processes.
- Thereafter, in the "fast growth" regime, cells can double more often than every 60 min, but now do so via partially overlapping (C+D) periods, with such periods occurring at intervals corresponding to the mass doubling time (**Figure 2B** bottom).

The same rules pertain analogously in *E. coli* K12, which exhibits a diversity of C and D period lengths under different conditions (e.g., **Figure 2C**).

Experimentally, it is observed that, in slow growth conditions, each cell division is closely accompanied by a next round of replication initiation (e.g., Bates and Kleckner, 2005; **Figure 2D**), with the two events occurring in either order according to the situation. Close coupling of division and initiation is also a necessary consequence of the Cooper-Helmstetter formalism because, in slow growth conditions, (C+D) periods follow sequentially one upon the other (**Figure 2A**). Correspondingly, in these conditions, (C+D) is the same as the doubling time ((C+D)/Td = 1; Helmstetter et al., 1968; **Figure 2E**).

This sequence of events seen in slow growth conditions gives the impression that, following a division, the chromosome cycle is initiated and completed, and then the cell waits until it becomes large enough, at which time it divides. Put another way: it seem as if the timing of division (and an accompanying replication initiation) is limited by cell growth (although for an alternative, see Logsdon et al., 2017).

In contrast, in fast growth conditions, where (C+D) has reached its minimum value and the cell has been forced into overlapping (C+D) periods, it seems as if chromosome/divisome events are limiting.

Both situations are all accommodated by the formal logic of progression permission control described above (**Figures 1A**, **2B,C**). A cell must satisfy both its growth requirement and its chromosome/divisome requirements in order to progress to the next round of cell division and replication initiation.

In Cooper-Helmstetter terminology, we thus envision that each particular (C+D) sequence sets up a PCC. Then, once the two requirements of growth and PCC formation are satisfied, progression permission would occur. This event will always enable occurrence of the division that defines the end of the initiating (C+D) sequence and will also enable occurrence of a next round of replication initiation (which may then occur sooner or later according to the conditions). In slow growth, this sequence of events leads to one division and an accompanying replication initiation on each of the single sister chromosomes in each daughter cell (**Figure 2B**).

In fast growth, this leads to a division and a round of replication initiations that occur on all origins present in the two daughter cells at that particular time (**Figure 2B**), in accord with the fact that all of the cell's origins fire synchronously under fast growth conditions (Skarstad et al., 1986).

This basic logic pertains to diverse "wild type" growth conditions regardless of the exact lengths of the C and D periods, which are known to vary widely among different *E. coli* strains and conditions (e.g., Nielsen et al., 2007; **Figure 2C**; below).

Mechanism: Insights From Slow Growth

The notion of a growth-sensitive progression permission process, and the above-proposed mechanism for such a process, have emerged from detailed analysis of events in slow growth conditions.

We previously observed, under such conditions, not only that division and replication initiation are closely coupled in time (above) but also that the process of division is accompanied by a change in the disposition of the nucleoid which, in turn, precedes initiation of DNA replication. Importantly, cell division and this nucleoid transition occur independently of one another. This feature suggests that the two events could be parallel downstream outcomes of a common upstream event. Given that accumulation of sufficient cell mass triggers onset of division (above), these findings give rise to the simple notion that accumulation of sufficient cell mass triggers two coordinate events: (i) onset of septation; and (ii) a change in nucleoid state which, in turn, makes possible replication initiation. (For comments on this previously-proposed idea and its subsequent misinterpretations, see footnote[1]).

[1]The "progression permission" proposal outlined above is an extension of our previously described "licensing hypothesis". The validity of that hypothesis has sometimes been questioned. However, all such statements of which we are aware are all based on fundamental misunderstanding of the basic idea. Since the same misunderstandings would pertain to the hypothesis described here, we address them directly. Two misunderstandings are most common. (1) The hypothesis is stated to be wrong because it does not accommodate effects on replication initiation timing due to changes in DnaA concentration. This is incorrect because "licensing" is, by its nature, a "permission-granting" process. It does *not* determine the timing of replication, which instead is determined during the implementation step, downstream of "licensing", by the concentrations of DnaA-ATP, IHF, supercoiling and likely additional factors. The same considerations apply to cell division. To eliminate this confusion, we have subdivided the proposed steps into "progression permission" and "implementation". (2) The hypothesis has been deemed invalid because replication initiation can occur in an *ftsZ* mutant, where division does not occur. This is incorrect for two reasons. (a) Cell division and licensing (progression permission) for replication initiation do not occur in series in a dependent relationship; instead, they are parallel downstream outcomes. (b)

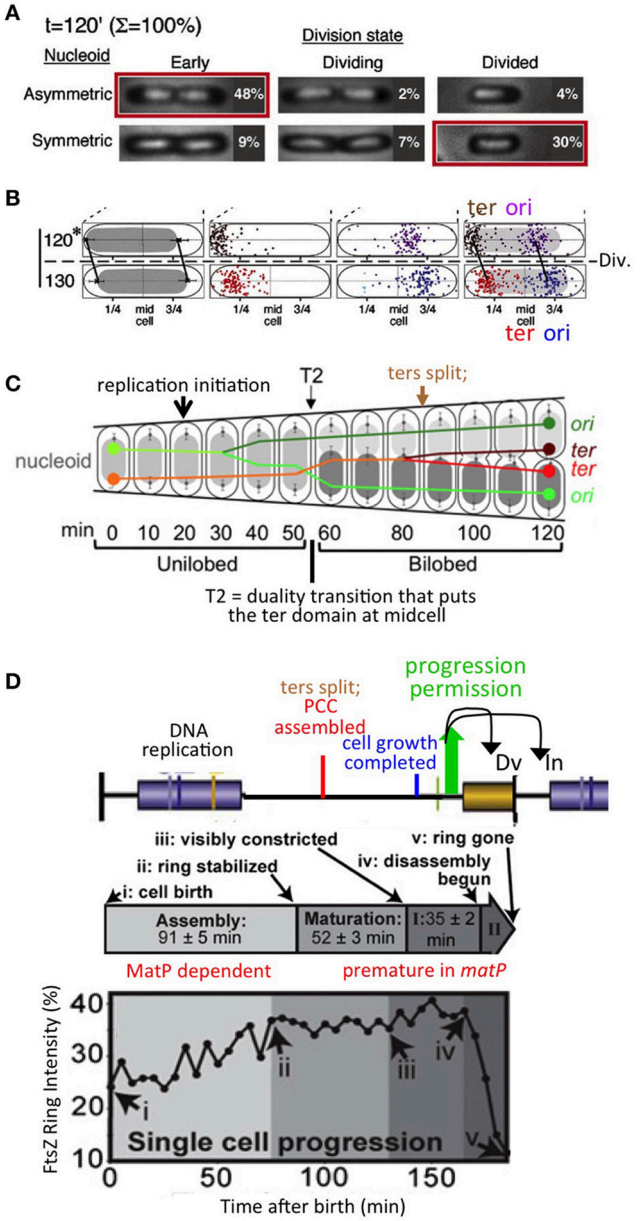

FIGURE 3 | Chromosomal and divisome events under slow growth conditions. **(A)**. Cell division is accompanied by a change in nucleoid disposition, from sister nucleoids closely juxtaposed to mid-cell via their terminus regions to each nucleoid centrally positioned within its (future or existing) sister (daughter) cells. Note that septum closure and the nucleoid transition can occur in either order, implying that they are independent events. **(B)** The nucleoid transition in **(A)** involves a whole body movement of the nucleoid, with origin and terminus regions remaining in the same relative positions. **(A,B)** are from Bates and Kleckner (2005). **(C)** Sequence of chromosomal events including replication initiation; a prominent transition to nucleoid duality, accompanied by an exchange of places of one sister (marked by its origin) and the mother material (marked by its terminus), and ensuing terminus dynamics including splitting and transit of one terminus across midcell (from Joshi et al., 2011 based on data in Bates and Kleckner, 2005). **(D)**. Divisome (FtsZ) assembly dynamics defined under slow growth conditions (from Coltharp et al., 2016) (middle and bottom) as compared to chromosomal events predicted by interpolation of data from similar conditions (**Figure 1D**) and the proposed progression permission/PCC model (**Figures 1A,B**).

The specific observations that led to this idea are as follows (Bates and Kleckner, 2005; **Figures 3A,B**). Prior to onset of septation, sister nucleoids are closely juxtaposed to midcell via their terminus regions, and thus asymmetrically positioned within their respective emerging cells. Then, two events occur concomitantly: (i) the septum closes, thus implementing cell division; and (ii) the nucleoid is released from midcell, after which it comes to occupy a more central location within the cell (**Figure 3A**). This change in nucleoid position occurs without any change in the positions of the origin and terminus within the nucleoid, and thus appears to comprise a "whole body" movement of the nucleoid (**Figure 3B**). Importantly, since completion of septation and nucleoid release can occur in either order (**Figure 3A**), these two events are independent and thus could be parallel downstream outcomes of an earlier event (above). Moreover, following nucleoid release, the origin moves toward the middle of the cell, while the terminus region also moves inward, after which replication initiates (**Figure 3C**). Thus, release of the nucleoid from midcell could potentially permit initiation of replication.

This latter idea has the additional implication that establishment of tethering of the nucleoid to midcell poses a block to initiation, with initiation then permitted by release from that tethering. To explain how release of tethering might have this effect, we further suggested that the signals for blocking, and then permitting, replication initiation would involve propagation of a change in state through the nucleoid itself. The possibility of such an effect was raised originally by the finding, in this same study, that release of key sister linkages, now known to be mediated by long-lasting inter-sister "snaps," results in a global reorganization of the nucleoid (Bates and Kleckner, 2005; Joshi et al., 2011; **Figure 3C**). This possibility was further supported by the discovery that the nucleoid is a physically coherent object, which appears to be intrinsically stiff (Wiggins et al., 2010; Hadizadeh Yazdi et al., 2012; Fisher et al., 2013), and which undergoes coherent motions along its entire length and width, on ∼20 and ∼2 min time scales (Fisher et al., 2013).

Subsequently, the tether/release idea was tested directly by Bates and colleagues, who examined the consequences of artificially tethering the nucleoid to the edge of the cell (Magnan et al., 2015). That study found that artificial tethering causes a block to replication initiation, but without blocking completion of ongoing replication, and moreover that this effect is accompanied by a global loss of negative supercoiling, which presumably explains the initiation block. These are exactly the types of effects originally envisioned.

From this and other information, we can now suggest a more complete mechanism for a regulatory process as outlined above (**Figures 1A,B**). Ultimately, a central feature is physical

In order for replication initiation to be "licensed", it must first be impeded; this impediment was proposed then (as above) to involve association with the cell septum; and thus, when there is no cell septum, there will be no association and thus no impediment. Therefore, the phenotype of an *ftsZ* mutant as predicted by our hypothesis is that the chromosome cycle will run free, on its own intrinsic "clock", which is what is observed. The presentation above makes more explicit the assumptions upon which the ideas are based.

association between replicated sister terminus domains and the nascent mid-cell septum which emerges in a mutually interdependent process, giving the proposed PCC (**Figure 1B**). When requisite cellular events are completed, the PCC would undergo a conformational change that coordinately triggers onset of septation (and thus cell division) and release of the terminus domain (which, in turn, permits replication initiation). The conformational change in the PCC would comprise "progression permission." Progression permission would then be followed by implementation of the two downstream outcomes, which occur on their own respective clocks, dependent on relevant conditions and factors. For example, it can be expected that alterations in initiation factors (e.g., Boye et al., 1996; Ryan et al., 2004; Kasho et al., 2014, 2017; Sakiyama et al., 2017; DnaA, IHF and supercoiling) may delay or accelerate the timing of replication initiation by effects on implementation, downstream of progression permission. The same considerations apply to cell division, which (like initiation) is sensitive to growth conditions (Coltharp et al., 2016). These effects can explain, for example, why initiation and division can occur in either order in slow growth conditions (above) and why the relative times of initiation and division are predicted to vary under different fast growth regimes (**Figures 2B,C**). Conversely, observation of such differences has no bearing on the validity of the proposed logic and mechanism (see Footnote[1]).

The existence of the proposed terminus domain/nascent divisome PCC is further supported by the following observations.

(1) A key event described for slowly-growing cells is a global transition that places the terminus domain in the vicinity of mid-cell. In brief, sisters initially emerge to the same side of unreplicated mother material. At a certain point, a global transition occurs in which one sister (and its origin) changes places with the mother material, placing the terminus domain in the vicinity of midcell, after which it undergoes further changes, e.g., splitting and movement of one terminus to the opposite side of midcell, which presumptively reflect capture of the terminus domain by the divisome (Bates and Kleckner, 2005; **Figure 3C**). These events are completed well before division, more or less in the middle of the "D-period" (**Figure 3C**). We show below that an analogous effect occurs in fast growth conditions.

(2) Analysis of septum-formation in slowly growing cells (Coltharp et al., 2016) shows that the amount of FtsZ at mid-cell increases, stabilizes and remains at a high level for a significant period of time until onset of septation. The time at which stabilization occurs is more or less in the middle of the "D-period," i.e., in the same time window that terminus domain events are being completed (**Figure 3D**).

(3) Functionally, the terminus domain is required for normal development of the septum: MatP, which is specifically devoted to terminus domain organization, is required for proper localization and development of the septum (Coltharp et al., 2016; **Figure 1B**). Absence of MatP has the same effects on mid-cell FtsZ accumulation as absence of MinC, a negative regulator of septum localization via the MinCDE system.

(4) Moreover, and of especial importance: in the absence of MatP, both sister segregation and onset of septum formation are premature (Mercier et al., 2008; Coltharp et al., 2016). The latter finding led to the conclusion that chromosome segregation (along with cell wall synthesis) are rate-limiting for division. In the present context, this finding strongly suggests, directly, that the presence of the terminus domain is important for impeding, and then allowing proper timing of, septal ring closure for cell division, as we propose.

(5) Association of the terminus region with the septum is well known to be important for proper completion of terminus-related events, including dimer reduction and decatenation (reviewed in Reyes-Lamothe et al., 2012). The terminus region and MatP interact with the developing septum via ZapAB (Männik et al., 2016; Buss et al., 2017). Moreover, FtsK is an intriguing candidate for a molecule that mediates signaling in both directions between the terminus domain and the septum, as in our proposed model. FtsK is in direct contact with both the cell septum and the chromosomal terminus region and is essential for execution of both cell division and regular chromosome segregation (reviews in Grainge, 2010; Bouet et al., 2014). Correspondingly, FtsK has already been proposed to be a mediator of coordination between final events of the chromosome cycle and cell division (Stouf et al., 2013), to contribute to nucleoid/septum localization (Bailey et al., 2014) and to sense addition of a fixed increment of cell size between divisions under fast growth conditions (Campos et al., 2014; below).

(6) Events of the chromosome cycle can proceed efficiently in the absence of cell division (e.g., in *ftsZ* and *ftsK* mutants) and also even in the absence of a cell wall (in "L-forms"; K. Chatzi, M. Stouf, and N.K. unpublished). This fact implies that a specific mechanism for coordination of chromosomal events with divisome events must be essential for regular growth and division in wild type cells. We also note that our model specifically predicts that the chromosome cycle will run free in *ftsZ/ftsK* mutants: in the absence of FtsZ/K, no PCC will form and thus neither the inhibition nor the enabling of replication initiation will occur. [We also reiterate actually that division *per se* is not required for initiation of replication in our proposed scenario (**Figure 1A**), because septum closure and terminus release (and thus initiation) are observed to be parallel, independent events (**Figure 3A**) (see Footnote[1]).

Mechanism: Extension to Fast Growth

The scenario that emerges from analysis of slow growth conditions can be mapped analogously onto chromosomal/nucleoid and divisome events that occur under fast growth conditions. In principle, each replication initiation that marks the start of a C period should set up a corresponding sister ter/septum PCC (above; **Figures 2B,C**). Furthermore, PCC assembly is presumably always completed after completion of bulk DNA replication, i.e., during the ensuing D-period, also in slow growth conditions.

As described for slow growth conditions above, key events for establishment of the PCC should be: (i) a duality transition that

places sister terminus domains at mid-cell and (ii) interaction of the terminus region specifically with the septum. Then: a conformational change in the PCC should permit both onset of septation and terminus release (and thereby replication initiation) (cartoon in **Figure 4** left, top and bottom).

Evidence that exactly the same progression occurs in fast growth conditions can be obtained by appropriate inspection of time-lapse data for doubling every ∼55 min (Youngren et al., 2014; **Figure 2C**; **Figure 4** right, top and bottom).

About-to-divide (or divided and unseparated) cells have four nucleoid units, with a set of two units located on either side of the division site, and with a pair of terminus regions located at the inner borders between each pair (**Figure 4** right, iv and viii). This configuration persists for a while after division. Thus, each daughter cell contains two now-expanding nucleoid bodies with a pair of terminus regions located between them, which position is also now midcell, and thus is the site of the next division (**Figure 4** right, i,ii and v,vi). Then, each of the two terminus markers moves away from that pre-division site to a position within its respective adjacent nucleoid (**Figure 4** right, ii to iii; vi to vii). This terminus transition has been strongly emphasized (Youngren et al., 2014). In the present context, it can be seen to be analogous to the division-associated event seen in slow growth conditions at which each sister terminus domain moves away from mid-cell to an inward position within its corresponding nucleoid (**Figure 4** left, ix to i, ii). Moreover, in fast growth, this terminus transition is again followed shortly by division and, by the predictions of defined (C+D) periods (**Figure 2C**, **Figure 4** legend), a round of replication initiations (**Figure 4** right, iv and viii).

Detailed inspection of these fast growth images further reveals that movement of each terminus to within its adjacent nucleoid unit is accompanied by acquisition of duality within that unit (**Figure 4** right, iii and vii, horizontal brackets) such that the terminus region is now located in between a pair of newly-individualized nucleoid units (**Figure 4** right, iii and vii). The combination of nucleoid duality and placement of the terminus between the resultant pair of units corresponds to the critical duality transition seen in slow growth conditions where the terminus becomes localized between sister nucleoid units as part of a global reorganization (**Figures 3C**, **4** left, iii to iv).

Thus, under fast growth conditions, just as in slow growth conditions: (i) a transition occurs in which terminus domains are initially tethered to a future septum site and then released (analogously to events at the end of the slow growth program) and (ii) a nucleoid duality transition occurs that places a single terminus domain between two developing sister nucleoids (analogously to the duality transition that occurs in the middle of the slow growth program).

When these and other events are mapped onto the fast growing cell's multiple overlapping (C+D) periods (**Figure 4** right), it emerges that: (i) the release of terminus domains from the future mid-cell division site should be the downstream outcome of a prior progression permission event (which concomitantly can be inferred to yield a round of replication initiation); and (ii) the nucleoid duality transition with accompanying inter-nucleoid unit terminus localization, should be the event that permits development of the PCC that mediates the next set of division and initiation events (**Figure 4** right). When these events are viewed in the context of a single (C+D) period, they are exactly analogously to the sequence defined for slow growth conditions (e.g., **Figure 4** left green with **Figure 4** right green).

We also note that in this fast growth condition, a particular (C+D) sequence (e.g., $C+D_N$; **Figure 4** top right green) is initiated by progression permission two sequences earlier ($C+D_{N-2}$; **Figure 4** top right orange) and permits its corresponding division and a round of initiation for two sequences later ($C+D_{N+2}$; **Figure 4** top right turquoise), thereby spanning a total of five (C+D) sequences.

The same principles also explain *E. coli* K12 data obtained under very fast growth conditions. In cells growing with a doubling time of 17 min, about-to-divide cells contain 16 origins and four termini that are organized into four nucleoid units which, upon division, give cells with 8 origins, which are organized into two nucleoid units, each with a pair of termini (M. White and D. Leach, personal communication). Strikingly, these nucleoid configurations are essentially identical to those seen in cells doubling at a 55 min doubling time (above) and thus can be gracefully explained by simply adding another round of replication initiation to each nucleoid unit. Correspondingly, application of the above-described duality > PCC formation > progression permission pattern to this situation results in exactly the appropriate outcome, with each (C+D) sequence now spanning seven additional (C+D) sequences, i.e., ($C+D_{N-3}$) to ($C+D_{N+3}$), rather than the five observed at Td = 55 min (not shown).

That is: a simple progression defined by analysis of slow growth conditions can be mapped directly onto events of fast-growing cells despite the complexity conferred by multiple overlapping (C+D) sequences.

ACCOMMODATIONS AND COMPATIBILITIES

The proposed coordination model directly accommodates natural variations in the lengths of the C and D periods (e.g., **Figure 2C** vs. **Figure 2B**).

This model also accommodates the occurrence defects or delays in upstream processes required for the PCC transition. For example, certain mutations that affect chromosome state and/or divisome state can prolong the length of the D-period, without changing growth rate or the C period (Zheng et al., 2016; Si et al., 2017). Some or all of these mutations could confer their effects by altering the time required for development of the PCC (**Figure 5A**). Similarly, mutations that directly or indirectly reduce the rate of DNA replication will also delay PCC development, while retaining proper coordination, e.g., as in strains with naturally longer C-periods. In the extreme, such an effect could also explain why, in *dnaA* mutants and an initiation-specific *dnaC* mutant, cell division is blocked or delayed/defective, respectively (Cambridge et al., 2014; D. Bates, personal communication; Kleckner laboratory unpublished). In

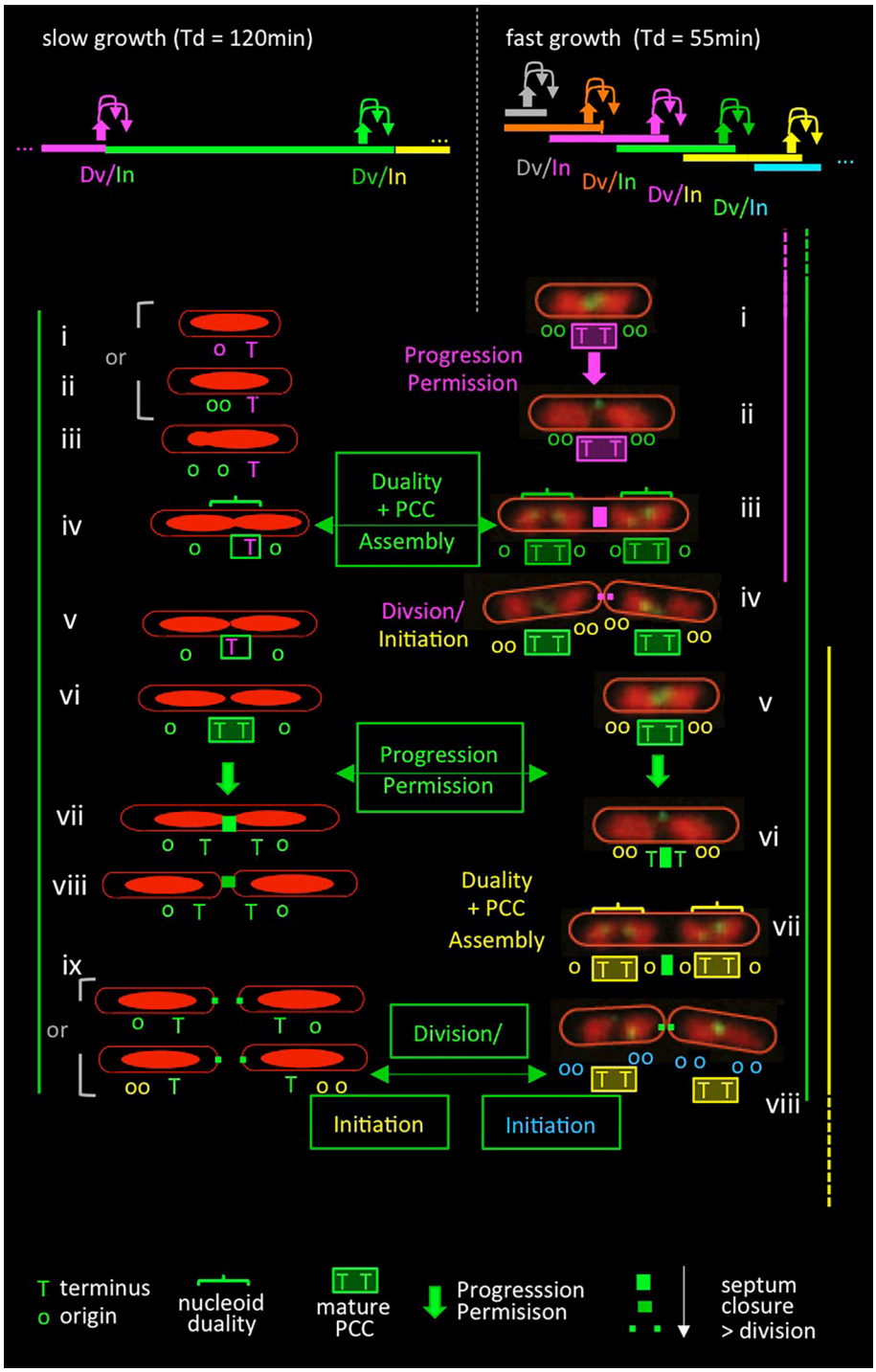

FIGURE 4 | Comparison of events in slow and fast growth conditions in the context of the progression permission model. Top: patterns of (C+D) sequences (bar) with corresponding events of coordination control including progression permission (upward filled arrows) and the corresponding permitted cell division and replication initiation events (downward arrows). Slow growth patterns correspond to conditions in **Figures 3A–C** (Bates and Kleckner, 2005); fast growth patterns correspond to conditions in **Figure 2C** (Nielsen et al., 2007). Bottom: patterns of events in slow (left) and fast (right) growth conditions. Events are color-coded in relation to the (C+D) period to which they correspond, as defined in the top panel. Bottom left side: patterns of nucleoid morphologies and terminus and origin dynamics observed experimentally in slow growth conditions [(Bates and Kleckner, 2005); **Figure 3C**] plus predicted events of the proposed progression permission process including PCC assembly, progression permission, and the ensuing permitted division and replication initiation. Note that replication begins after division in the study of Bates and Kleckner (**Figure 3**) but often begins just before division in a number of other slow growth conditions. Bottom right side: nucleoid and terminus morphologies extracted from live cell time-lapse movies of Youngren et al. (2014) and overlaid with predicted events of the proposed progression permission process as it would

(Continued)

FIGURE 4 | occur in the corresponding partially overlapping (C+D) periods. Origin numbers and dispositions predicted from "C+D" patterns (Nielsen et al., 2007) are superimposed. Events in slow and fast growth conditions are directly compared by the (C+D) sequences defined in green boxes, as described in the text. The replication initiations resulting from these sequences are shown at the bottom in green boxes, with origin colors of the corresponding (C+D) sequence. (Note that somewhat different replication timing was inferred by analysis of fluorescent foci of SSB; however, that inference failed to take into account the fact that sister replisomes tend to first cluster and then split, implying that SSB foci are not a reliable indicator of the number of replication forks. Indeed, data inspection shows that pairs of SSB foci tend to emerge at the same time as nucleoid duality, in accord with occurrence by splitting rather than as a reflection of the time of initiation).

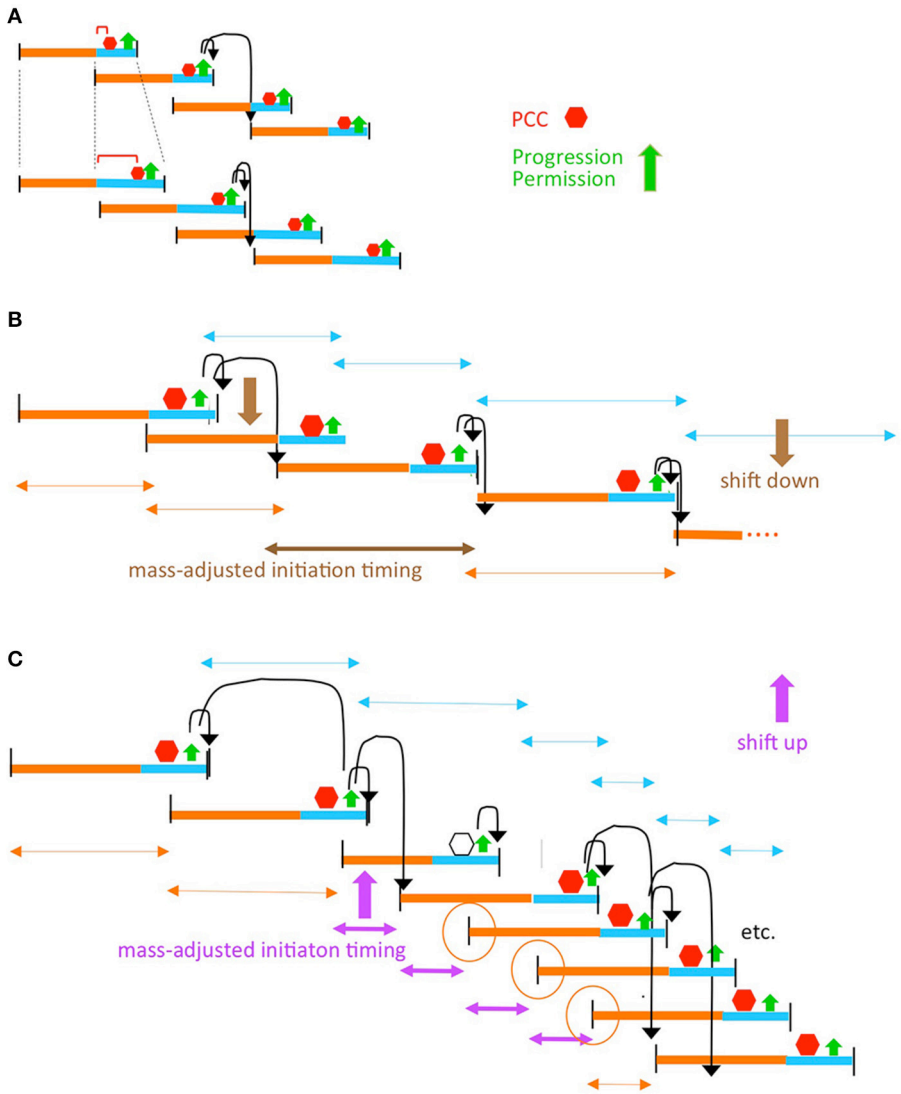

FIGURE 5 | The progression permission model can accommodate diverse situations. **(A)** Perturbations of chromosome/divisome events that delay PCC formation. **(B)** Growth rate transitions. It is well established that, in a given growth condition, replication initiation tends to occur at a particular cell mass (sometimes parameterized as the mass/origin ratio; Donachie, 1968). Thus, in some situations, a change in growth conditions can be implemented by the simple expedient of having replication initiation occur at the cell mass corresponding to the new growth rate **(B)**. However, some situations, notably a dramatic increase in growth rate, require that replication initiate before the time at which it would normally be allowed to occur by a scheduled progression permission event. In such cases, the required adjustment can be made if PCC activity is compromised in such a way that it still forms in response to onset of a (C+D) sequence, and regulates the ensuing division, but is no longer able to regulate replication initiation. As a result, initiation can run free until such time as a properly constituted PCC has again formed **(C)**. Open hexagon indicates the (C+D) period in which PCC control over replication intiation is abrogated. Orange circles denote the replication initiations that are determined independently of PCC control due to the combined effects of PCC control abrogation and timing relative to re-establishment of PCC control. This scenario corresponds to the Cooper-Helmstetter observations that ongoing C period(s) is/are completed before there is a change to a new interval between divisions [the phenomenon of "rate maintenance" Helmstetter et al., 1968]; compare orange and turquoise double-headed arrows in **(B,C)**.

other situations, events related to sensing the accumulation of cell mass might be defective, again resulting in a delay in the PCC transition, but without loss of cooordination.

The proposed coordination model can also gracefully accommodate transitions from one growth rate to another (**Figures 5B,C**). Notably, dramatic upshifts can be mediated by differential disabling of the PCC(s) ability to regulate replication initiation (**Figure 5C**).

We also note that that all of the proposed effects pertain in the context of Cooper-Helmstetter formalism, as shown above. They are therefore compatible with mathematical descriptions that utilize that formalism. Most specifically, the exact timing of replication initiation could still be determined by, or at least closely correlated with, mass-to-origin ratio ["initiation mass"; Donachie 1968].

We also note that the proposed mechanism is logically distinct from canonical "checkpoint" mechanisms (e.g., Boye and Boye and Nordström, 2003; Arjes et al., 2014), although the coordination outcome is similar.

Finally, the possibility of a PCC-mediated coordination process also raises new possibilities for the origins of cell-to-cell variability. For example, an individual cell may sometimes divide without an initiation (Ho and Amir, 2015) or, oppositely, may undergo two initiations between cell divisions rather than one (Wallden et al., 2016). Analogous cell-to-cell variability occurs in the timing of cell division. In the context of the current model, they could be explained by stochastic fluctuations in upstream component events required for permission granting; in the actual PCC transition *per se*; and/or in the execution of events during the "implementation" stage.

DOES THE PCC TRANSITION INTEGRATE CELLULAR EVENTS WITH GROWTH CONDITIONS?

The discussions above consider the issue of coordination, where assembly of the PCC and growth inputs lead to progression of the PCC in a process that acts to ensure a 1:1:1 relationship among the mass/size increase required for division, replication initiation/segregation and cell division *per se*.

However, we suggest that this process is, in fact, the mechanism that links all three processes to cell growth conditions. In faster or slower growing cells, the cohort of coordinated events must occur more or less frequently. In its formal logic, our proposal is agnostic with respect to how this frequency is determined, i.e., in how occurrence of a cohort of coordinated events is coupled to the rate of cell growth (**Figure 6**).

Correspondingly, the above proposal is fully compatible with a process in which growth conditions are sensed at the replication initiation step, with all other events occurring as a downstream consequence, and without any input from cellular parameters other than cell mass (**Figure 6** purple; Amir, 2017). Our proposal is similarly compatible with the proposition that inter-division time is sensed by properties of the cell container alone, e.g., surface to volume ratio, without considering input

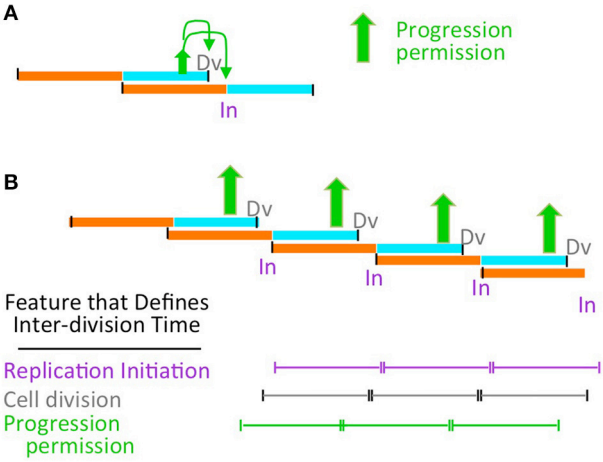

FIGURE 6 | Possible relationship of progression permission to growth rate control. **(A)** Progression permission enables division and replication initiation in a particular growth regime. **(B)** In a given balanced growth condition, all indicated events occur in a 1:1:1:1:1 relationship with a particular relative timing (on a population average level). Thus, the ultimate determinant of cell division timing (e.g., by addition of a particular amount of cell mass Ho et al., 2018) could be progression permission (this work); cell division (Harris and Theriot, 2016) or replication initiation (Amir, 2017).

from chromosomal events (**Figure 6** gray; Harris and Theriot, 2016).

On the other hand: it is straightforward to envision that interplay of growth with the PCC to give permission granting is actually the critical event that couples replication initiation and cell division to growth rate. In such a case, the rate of cell growth would determine the length of time between such transitions and, thereby, the inter-division time, with each transition resulting coordinately in both cell division and initiation of the next chromosome cycle (**Figure 6** green).

Additionally, recent studies suggest that under fast growth conditions, division is triggered by accumulation of an appropriate fixed amount of cell length (or volume/mass) (the so-called "adder" rule; review in Ho et al., 2018). Under such conditions, acquisition of this fixed amount would be the rate-limiting step for division because it would enable PCC formation (which is rate-limiting under these conditions; above). In contrast, in slow growth conditions, where accumulation of cell material is apparently limiting irrespective of PCC formation (above), acquisition of sufficient material would activate the already assembled PCC.

Two very recent reports are fully consonant with the above suggestions.

- First, recent single cell analyses raise the possibility that inputs from both growth and the chromosome cycle are integrated to determine division timing on a single cell level and to a corresponding suggestion that division is defined by an "AND" gate which takes into account inputs from both components (Micali et al., 2018a,b). However, differently from the model proposed here, where integration of different components

is upstream of initiation and division, the proposed "AND" gate integrates chromosome and divisome requirements at a later stage to actually set the timing of cell division in individual cells. We also note that the actual occurrence of cell division by our model involves not only PCC activation but the downstream events involved in implementation of septum formation, which is also sensitive to growth conditions (Coltharp et al., 2016).

- Woldringh and colleagues (Huis et al., 2018) have presented evidence that, in fast-growing cells, prominent nucleoid duality occurs earlier in larger newborn cells than in smaller newborns. At any given growth condition, larger cells accumulate mass more rapidly and thus divide sooner than smaller cells. These authors suggest that this difference in time to division is explained by the different amounts of time required for progression to duality. Modeling further suggests that the relationship between replication initiation and segregation, whose effects play out in the timing of the duality transition, can underlie variations in inter-division time under different fast growth conditions. This scenario is similar in spirit to the model presented above where (i) nucleoid duality plays a prominent role in enabling the proposed PCC development and (ii) resultant development of this chromosome-divisome complex is the rate limiting step for division in fast growth conditions.

AUTHOR CONTRIBUTIONS

NK, KC, MW, JF, MS contributed to the concepts in this paper and to the preparation of the manuscript.

FUNDING

KC, MS and research related to this manuscript were supported by a grant to NK from the N.I.H. (RO1 GM025326).

ACKNOWLEDGMENTS

We gratefully acknowledge Erik Boye and Kurt Nordstrom for their provocative suggestion that chromosomal events and the cell growth/division events comprise parallel pathways that are coordinated by checkpoint linkages (Boye and Nordström, 2003). We also acknowledge David Bates, Erik Boye, Ariel Amir, Po-Yi Ho, and Marco Cosentino Lagomarsino for stimulating discussions.

REFERENCES

Amir, A. (2017). Is cell size a spandrel? *Elife* 6:e22186. doi: 10.7554/eLife.22186

Arjes, H. A., Kriel, A., Sorto, N. A., Shaw, J. T., Wang, J. D., and Levin, P. A. (2014). Failsafe mechanisms couple division and DNA replication in bacteria. *Curr. Biol.* 24, 2149–2155. doi: 10.1016/j.cub.2014.07.055

Bailey, M. W., Bisicchia, P., Warren, B. T., Sherratt, D. J., and Männik, J. (2014). Evidence for divisome localization mechanisms independent of the Min system and SlmA in *Escherichia coli*. *PLoS Genet.* 10:e1004504. doi: 10.1371/journal.pgen.1004504

Bates, D., and Kleckner, N. (2005). Chromosome and replisome dynamics in *E. coli*: loss of sister cohesion triggers global chromosome movement and mediates chromosome segregation. *Cell* 121, 899–911. doi: 10.1016/j.cell.2005.04.013

Bouet, J. Y., Stouf, M., Lebailly, E., and Cornet, F. (2014). Mechanisms for chromosome segregation. *Curr. Opin. Microbiol.* 22, 60–65. doi: 10.1016/j.mib.2014.09.013

Boye, E., and Nordström, K. (2003). Coupling the cell cycle to cell growth. *EMBO Rep*. 4, 757–760. doi: 10.1038/sj.embor.embor895

Boye, E., Stokke, T., Kleckner, N., and Skarstad, K. (1996). Coordinating DNA replication initiation with cell growth: differential roles for DnaA and SeqA proteins. *Proc. Natl. Acad. Sci. U.S.A.* 93, 12206–11. doi: 10.1073/pnas.93.22.12206

Buss, J. A., Peters, N. T., Xiao, J., and Bernhardt, T. G. (2017). ZapA and ZapB form an FtsZ-independent structure at midcell. *Mol. Microbiol.* 104, 652–663. doi: 10.1111/mmi.13655

Cambridge, J., Blinkova, A., Magnan, D., Bates, D., and Walker, J. R. (2014). A replication-inhibited unsegregated nucleoid at mid-cell blocks Z-ring formation and cell division independently of SOS and the SlmA nucleoid occlusion protein in *Escherichia coli*. *J. Bacteriol.* 196, 36–49. doi: 10.1128/JB.01230-12

Campos, M., Surovtsev, I. V., Kato, S., Paintdakhi, A., Beltran, B., Ebmeier, S. E., et al. (2014). A constant size extension drives bacterial cell size homeostasis. *Cell* 159, 1433–1446. doi: 10.1016/j.cell.2014.11.022

Coltharp, C., Buss, J., Plumer, T. M., and Xiao, J. (2016). Defining the rate-limiting processes of bacterial cytokinesis. *Proc. Natl. Acad. Sci. U.S.A.* 113, E1044–E1053. doi: 10.1073/pnas.1514296113

Donachie, W. D. (1968). Relationship between cell size and time of initiation of DNA replication. *Nature* 219, 1077–1079. doi: 10.1038/2191077a0

Fisher, J. K., Bourniquel, A., Witz, G., Weiner, B., Prentiss, M., and Kleckner, N. (2013). Four-dimensional imaging of *E. coli* nucleoid organization and dynamics in living cells. *Cell* 153, 882–895. doi: 10.1016/j.cell.2013.04.006

Grainge, I. (2010). FtsK–a bacterial cell division checkpoint? *Mol. Microbiol.* 78, 1055–1057. doi: 10.1111/j.1365-2958.2010.07411.x

Hadizadeh Yazdi, N., Guet, C. C., Johnson, R. C., and Marko, J. F. (2012). Variation in the folding and dynamics of the *Escherichia coli* chromosome with growth conditions. *Mol. Microbiol.* 86, 1318–1333. doi: 10.1111/mmi.12071

Harris, L. K., and Theriot, J. A. (2016). Relative rates of surface and volume synthesis set bacterial cell size. *Cell* 165, 1479–1492. doi: 10.1016/j.cell.2016.05.045

Helmstetter, C., Cooper, S., Pierucci, O., and Revelas, E. (1968). On the bacterial life sequence. *Cold Spring Harb. Symp. Quant. Biol.* 33, 809–822. doi: 10.1101/SQB.1968.033.01.093

Ho, P. Y., and Amir, A. (2015). Simultaneous regulation of cell size and chromosome replication in bacteria. *Front. Microbiol.* 6:662. doi: 10.3389/fmicb.2015.00662

Ho, P. Y., Lin, J., and Amir, A. (2018). Modeling Cell Size Regulation: From Single-Cell-Level Statistics to Molecular Mechanisms and Population-Level Effects. *Annu. Rev. Biophys.* 47, 251–271. doi: 10.1146/annurev-biophys-070317-032955

Huls, P. G., Vischer, N. O. E., and Woldringh, C. L. (2018). Different Amounts of DNA in newborn cells of *Escherichia coli* preclude a role for the chromosome in size control according to the "Adder" Model. *Front. Microbiol.* 9:664. doi: 10.3389/fmicb.2018.00664

Joshi, M. C., Bourniquel, A., Fisher, J., Ho, B. T., Magnan, D., Kleckner, N., et al. (2011). *Escherichia coli* sister chromosome separation includes an abrupt global transition with concomitant release of late-splitting intersister snaps. *Proc. Natl. Acad. Sci. U.S.A.* 108, 2765–2770. doi: 10.1073/pnas.1019593108

Kasho, K., Fujimitsu, K., Matoba, T., Oshima, T., and Katayama, T. (2014). Timely binding of IHF and Fis to DARS2 regulates ATP-DnaA production and replication initiation. *Nucleic Acids Res.* 42, 13134–13149. doi: 10.1093/nar/gku1051

Kasho, K., Tanaka, H., Sakai, R., and Katayama, T. (2017). Cooperative DnaA Binding to the Negatively Supercoiled datA Locus Stimulates DnaA-ATP Hydrolysis. *J. Biol. Chem.* 292, 1251–1266. doi: 10.1074/jbc.M116.762815

Logsdon, M. M., Ho, P. Y., Papavinasasundaram, K., Richardson, K., Cokol, M., Sassetti, C. M., et al. (2017). A parallel adder coordinates mycobacterial cell-cycle progression and cell-size homeostasis in the context of asymmetric growth and organization. *Curr. Biol.* 27, 3367-3374. e7. doi: 10.1016/j.cub.2017.09.046

Magnan, D., Joshi, M. C., Barker, A. K., Visser, B. J., and Bates, D. (2015). DNA Replication Initiation Is Blocked by a Distant Chromosome-Membrane Attachment. *Curr. Biol.* 25, 2143–2149. doi: 10.1016/j.cub.2015.06.058

Männik, J., Castillo, D. E., Yang, D., Siopsis, G., and Männik, J. (2016). The role of MatP, ZapA and ZapB in chromosomal organization and dynamics in *Escherichia coli*. *Nucleic Acids Res.*. 44, 1216–1226. doi: 10.1093/nar/gkv1484

Mercier, R., Petit, M. A., Schbath, S., Robin, S., El Karoui, M., Boccard, F., et al. (2008). The MatP/matS site-specific system organizes the terminus region of the *E. coli* chromosome into a macrodomain. *Cell* 135, 475–485. doi: 10.1016/j.cell.2008.08.031

Micali, G., Grilli, J., Marchi, J., Osella, M., and Lagomarsino, M. C. (2018a). Dissecting the control mechanisms for DNA replication and cell division in *E. coli*. *bioRxiv*. [preprint]. doi: 10.1101/308155

Micali, G., Grilli, J., Marchi, J., Osella, M., and Lagomarsino, M. C. (2018b). Concurrent processes set *E. coli* cell division. *bioRxiv*. [preprint]. doi: 10.1101/301671

Nielsen, H. J., Youngren, B., Hansen, F. G., and Austin, S. (2007). Dynamics of *Escherichia coli* chromosome segregation during multifork replication. *J. Bacteriol.* 189, 8660–8666. doi: 10.1128/JB.01212-07

Reyes-Lamothe, R., Nicolas, E., and Sherratt, D. J. (2012). Chromosome replication and segregation in bacteria. *Annu. Rev. Genet.* 46, 121–43. doi: 10.1146/annurev-genet-110711-155421

Ryan, V. T., Grimwade, J. E., Camara, J. E., Crooke, E., and Leonard, A. C. (2004). *Escherichia coli* prereplication complex assembly is regulated by dynamic interplay among Fis, IHF, and DnaA. *Mol. Microbiol.* 51, 1347–1359. doi: 10.1046/j.1365-2958.2003.03906.x

Sakiyama, Y., Kasho, K., Noguchi, Y., Kawakami, H., and Katayama, T. (2017). Regulatory dynamics in the ternary DnaA complex for initiation of chromosomal replication in *Escherichia coli*. *Nucleic Acids Res.* 45, 12354–12373. doi: 10.1093/nar/gkx914

Si, F., Li, D., Cox, S. E., Sauls, J. T., Azizi, O., Sou, C., et al. (2017). Invariance of initiation mass and predictability of cell size in *Escherichia coli*. *Curr. Biol.* 27, 1278–1287. doi: 10.1016/j.cub.2017.03.022

Siddiqui, K., On, K. F., and Diffley, J. F. (2013). Regulating DNA replication in eukarya. *Cold Spring Harb. Perspect. Biol.* 5:a012930. doi: 10.1101/cshperspect.a012930

Skarstad, K., Boye, E., and Steen, H. B. (1986). Timing of initiation of chromosome replication in individual *Escherichia coli* cells. *EMBO J.* 5, 1711–1717.

Stouf, M., Meile, J. C., and Cornet, F. (2013). FtsK actively segregates sister chromosomes in *Escherichia coli*. *Proc. Natl. Acad. Sci. U.S.A.* 110, 11157–11162. doi: 10.1073/pnas.1304080110

Wallden, M., Fange, D., Lundius, E. G., Baltekin, Ö., and Elf, J. (2016). The synchronization of replication and division cycles in individual *E. coli* cells. *Cell* 166, 729–739. doi: 10.1016/j.cell.2016.06.052

Wiggins, P. A., Cheveralls, K. C., Martin, J. S., Lintner, R., and Kondev, J. (2010). Strong intranucleoid interactions organize the *Escherichia coli* chromosome into a nucleoid filament. *Proc. Natl. Acad. Sci. U.S.A.* 107, 4991–4995. doi: 10.1073/pnas.0912062107

Youngren, B., Nielsen, H. J., Jun, S., and Austin, S. (2014). The multifork *Escherichia coli* chromosome is a self-duplicating and self-segregating thermodynamic ring polymer. *Genes Dev.* 28, 71–84. doi: 10.1101/gad.231050.113

Zheng, H., Ho, P. Y., Jiang, M., Tang, B., Liu, W., Li, D., et al. (2016). Interrogating the *Escherichia coli* cell cycle by cell dimension perturbations. *Proc. Natl. Acad. Sci. U.S.A.* 113, 15000–15005. doi: 10.1073/pnas.1617932114

Conflict of Interest Statement: The authors declare that the research was conducted in the absence of any commercial or financial relationships that could be construed as a potential conflict of interest.

frontiers in Microbiology

REVIEW
published: 21 March 2018
doi: 10.3389/fmicb.2018.00514

Stable Regulation of Cell Cycle Events in Mycobacteria: Insights From Inherently Heterogeneous Bacterial Populations

*Michelle M. Logsdon[1,2] and Bree B. Aldridge[1,2,3]**

[1] Department of Molecular Biology and Microbiology, Tufts University School of Medicine, Boston, MA, United States, [2] Department of Molecular Microbiology, Sackler School of Graduate Biomedical Sciences, Tufts University, Boston, MA, United States, [3] Department of Biomedical Engineering, Tufts University School of Engineering, Medford, MA, United States

Model bacteria, such as *E. coli* and *B. subtilis*, tightly regulate cell cycle progression to achieve consistent cell size distributions and replication dynamics. Many of the hallmark features of these model bacteria, including lateral cell wall elongation and symmetric growth and division, do not occur in mycobacteria. Instead, mycobacterial growth is characterized by asymmetric polar growth and division. This innate asymmetry creates unequal birth sizes and growth rates for daughter cells with each division, generating a phenotypically heterogeneous population. Although the asymmetric growth patterns of mycobacteria lead to a larger variation in birth size than typically seen in model bacterial populations, the cell size distribution is stable over time. Here, we review the cellular mechanisms of growth, division, and cell cycle progression in mycobacteria in the face of asymmetry and inherent heterogeneity. These processes coalesce to control cell size. Although *Mycobacterium smegmatis* and *Mycobacterium bovis* Bacillus Calmette-Guérin (BCG) utilize a novel model of cell size control, they are similar to previously studied bacteria in that initiation of DNA replication is a key checkpoint for cell division. We compare the regulation of DNA replication initiation and strategies used for cell size homeostasis in mycobacteria and model bacteria. Finally, we review the importance of cellular organization and chromosome segregation relating to the physiology of mycobacteria and consider how new frameworks could be applied across the wide spectrum of bacterial diversity.

Keywords: cell size, mycobacteria, *Mycobacterium smegmatis*, BCG, chromosome organization, cell cycle, asymmetry, cell size control

OPEN ACCESS

Edited by:
Conrad L. Woldringh, University of Amsterdam, Netherlands

Reviewed by:
Alfonso Soler-Bistue, Instituto de Investigaciones Biotecnológicas (IIB-INTECH), Argentina
Babak Javid, Tsinghua University, China

****Correspondence:***
Bree B. Aldridge
bree.aldridge@tufts.edu

Specialty section:
This article was submitted to Microbial Physiology and Metabolism, a section of the journal Frontiers in Microbiology

Received: *09 January 2018*
Accepted: *06 March 2018*
Published: *21 March 2018*

Citation:
Logsdon MM and Aldridge BB (2018) Stable Regulation of Cell Cycle Events in Mycobacteria: Insights From Inherently Heterogeneous Bacterial Populations. Front. Microbiol. 9:514. doi: 10.3389/fmicb.2018.00514

INTRODUCTION

Mycobacteria are unusual compared to other well-studied bacteria. They grow slowly, are not stained by dyes traditionally used to identify and differentiate bacteria, and have remarkably thick and waxy cell walls (Jankute et al., 2015). Although they have a similar rod shaped morphology as many model bacterial species, recent attention to their basic physiology demonstrates distinct growth modes, subcellular organization, cell cycle timing, division patterns, and size control. Due to these differences, much of the knowledge of basic cell cycle and growth processes developed in well-studied bacteria cannot be directly translated to mycobacteria. These models, however, provide valuable context for studying how the basic physiology of mycobacteria fits into the spectrum of previously studied microorganisms.

Mycobacterial infection remains a major threat to global health. Tuberculosis, caused by infection with *Mycobacterium tuberculosis*, is currently responsible for more deaths than any other single infectious agent (WHO, 2017). Key to mycobacterial virulence and drug tolerance is the ability to tightly control growth. Despite the importance of *M. tuberculosis* growth patterns contributing to infection dynamics, the basic lifecycle properties of mycobacteria are just beginning to be characterized. Until recently, mycobacteria were considered too slow growing and difficult to study to serve as an informative subject for basic cell physiology investigations. Division times of mycobacterial species vary wildly, and all are much longer than the model bacterium *E. coli*, who doubles every 20 min in rich medium. On the extreme end, *Mycobacterium leprae*, the causative agent of leprosy, doubles only once every 14 days and cannot be cultured *in vitro*. *M. tuberculosis* and Bacillus Calmette-Guérin (BCG) are slow growing, culturable mycobacteria with division times of 18–24 h in rich medium. *M. tuberculosis* is an airborne infectious organism that requires a high level of containment during experiments and can only be manipulated within a biosafety level 3 facility (BL3). BCG is often used as a proxy for *M. tuberculosis* in experiments because it is a closely related slow growing mycobacterium but is not pathogenic and does not require a specialized BL3 facility for experiments. However, BCG exposure can cause false positive reactions to the PPD skin test used to monitor exposure to tuberculosis (known as seroconversion, also seen in patients who have received the BCG vaccination) (Cohn, 2001). Therefore BCG can only be manipulated within a biosafety cabinet. *Mycobacterium smegmatis,* a non-pathogenic soil bacterium with a division time of about 3 h, is a commonly used model mycobacteria because it does not cause infection or seroconversion, can be used on a standard BL2 bench top, and allows experiments to be performed on a shorter, more manageable time scale. Much of the growth and division machinery is conserved between *M. smegmatis* and *M. tuberculosis* and the use of *M. smegmatis* as a model organism has allowed the field to progress rapidly in our understanding of the distinct mechanisms of growth and division in mycobacteria (Hett and Rubin, 2008). Additionally, the availability of microfluidic technologies has made basic cell biology studies more accessible, and in the past decade it has become apparent that growth variation within isogenic populations is an intrinsic property of mycobacteria (Aldridge et al., 2012; Kieser and Rubin, 2014). To gain a better understanding of their lifecycle and persistence, it is imperative that we approach mycobacteria as unique and complex organisms.

Differences in physiology between mycobacteria and model bacteria include mechanisms of cell division and growth. A key characteristic of mycobacterial physiology is their striking pattern of asymmetric growth and division (Aldridge et al., 2012; Kieser and Rubin, 2014; Meniche et al., 2014; Manina et al., 2015; Rego et al., 2017). Mycobacteria elongate asymmetrically, preferentially from the old pole (Aldridge et al., 2012; Meniche et al., 2014; Botella et al., 2017; Rego et al., 2017). The new pole experiences a lag in growth before initiating growth partway through the cell cycle (**Figure 1A**) (Aldridge et al., 2012; Botella et al., 2017). The mechanisms controlling initiation or "licensing" of new pole growth are not well understood. In *M. smegmatis* the new pole grows at a slower rate from licensing to division than the old pole, while in *M. tuberculosis*, the rate of new pole growth catches up to the rate of old pole growth preceding division (Botella et al., 2017). Due to differential growth characteristics in cell poles preceding division, sister cells inheriting the mother's old pole have different polar growth characteristics than sister cells inheriting the new pole (Aldridge et al., 2012; Kieser and Rubin, 2014). The "accelerator" sister cell inherits the mother's old pole and is larger and faster growing while the "alternator" sister inherits the mother's new pole and is smaller and slower growing (**Figure 1A**) (Aldridge et al., 2012). This review will address our current understanding of mycobacterial cell biology regarding the generation of asymmetry among closely related cells, impacts of asymmetry on population structure, coordination of innate asymmetry and key cell cycle events, and regulation of cell size in the face of differential growth and size characteristics in mycobacteria.

THE BASIS OF ASYMMETRY

The molecular mechanisms underlying asymmetric growth and division in mycobacteria are just beginning to be elucidated. Many growth and division factors localize in specific patterns to facilitate temporal regulation of growth from each pole. Most well studied bacteria, including *E. coli*, *B. subtilis,* and *C. crescentus* elongate laterally along the length of the cell wall using actin like protein MreB (Daniel and Errington, 2003; Takacs et al., 2010; Dominguez-Escobar et al., 2011; Garner et al., 2011; Wang et al., 2012; White and Gober, 2012; Kysela et al., 2013; Errington, 2015). Mycobacteria, on the other hand, elongate primarily from subpolar regions adjacent to cell poles where the coiled-coil protein Wag31 (also called DivIVA) serves as a scaffold for the elongation complex (Kang et al., 2008; Meniche et al., 2014). Wag31 is targeted to the cell pole through recognition of membrane curvature, where it anchors peptidoglycan, arabinogalactan, and mycolic acid synthesizing enzymes (MurG, GlfT2, and Pks13, respectively) (Meniche et al., 2014). Wag31 preferentially localizes to the old cell pole, consistent with the observation that the old pole serves as the primary site of cell elongation throughout the mycobacterial cell cycle (**Figure 1A**) (Kang et al., 2008; Meniche et al., 2014). Wag31 moves to the new pole at septation to prepare for eventual new pole elongation (**Figure 1A**) (Kang et al., 2008; Santi et al., 2013). Several of the proteins anchored by Wag31, including arabinoglactan synthesizing protein GlfT2, specifically associate with a specialized membrane domain called the pure membrane free of cell wall components (PMf) (Hayashi et al., 2016). GlfT2 is localized to growing old poles, indicating that lipid biosynthetic reactions required for cell envelope synthesis are targeted to regions of active cell growth (Hayashi et al., 2016). Wag31 interacts with the cell wall associated membrane fraction and not the PMf (Hayashi et al., 2016). It has yet to be determined how the distinct PMf and cell wall associated membrane fractions

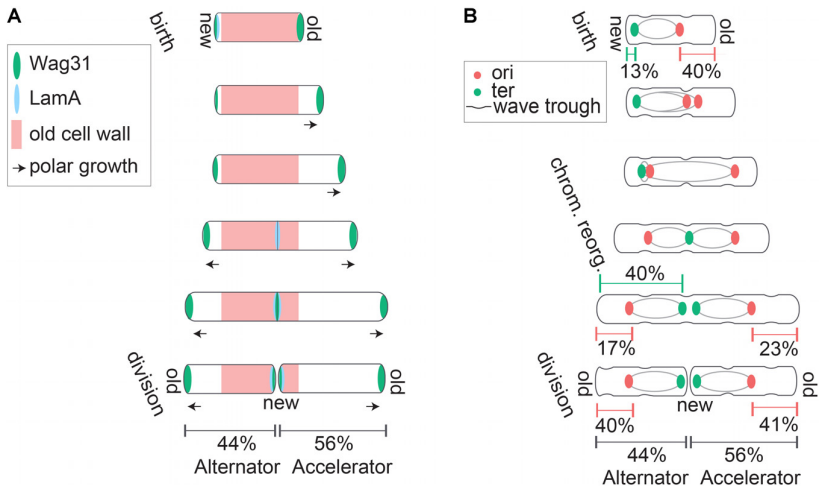

FIGURE 1 | Asymmetric polar growth and division in mycobacteria. **(A)** Mycobacteria grow primarily from subpolar regions (marked with arrows), and elongate preferentially from the old pole. Asymmetric polar growth is directed by elongation and divisome components Wag31 (green) and LamA (blue). At birth, LamA actively inhibits growth from the new pole while Wag31 localizes to the old pole and organizes the elongation complex to promote growth at the old pole. Later in the cell cycle LamA inhibition of new pole growth is relieved, while Wag31 accumulates and promotes growth from the new pole. Finally, LamA and Wag31 accumulate at the septum region where Wag31 assembles the elongation complex while LamA inhibits growth from this site that becomes the new pole after division. **(B)** Mycobacteria divide asymmetrically and organize their chromosomes asymmetrically within the cell. Asymmetric division is partially organized by surface wave troughs inherited from previous generations. Cells divide at the centermost wave trough along the cell body. At birth, the ori region of the chromosome (red) is positioned midcell, but closer to the old pole, and the ter (green) is positioned near the new pole. The chromosome reorganizes part way through the cell cycle. Ori's partition and travel to asymmetric quarter cell positions and the terminus translocates to an asymmetric midcell location that corresponds with surface wave trough and septum placement. At division, proportional chromosome localization is reestablished in daughter cells despite the differential sizes of accelerator and alternator sisters.

work together to promote cell growth. Regardless, it is clear that the localization of a metabolically active membrane domain, as well as scaffold protein Wag31, provides a means of targeting cell growth preferentially to cell poles.

Many mycobacterial growth studies employ fluorescently tagged Wag31 as an elongation and early cell division marker because of its important role in organizing cell elongation complexes (Santi et al., 2013; Meniche et al., 2014; Santi and McKinney, 2015; Botella et al., 2017). Wag31-fluorescent protein fusions form clear and bright fluorescent bands at sites of cell growth and septation. However, the function of Wag31 is very sensitive to fluorescent protein fusion and overexpression. Adding a GFP tag to the C-terminus of native Wag31 leads to aberrant localization of the Wag31-GFP band at the new pole, causing the new pole to become the primary site of growth (Meniche et al., 2014). The C-terminal tagged Wag31-GFP also caused a 40% decrease in cell elongation rate, increased cell width, and an abnormal curved shape in cells (Meniche et al., 2014). However, a merodiploid strain with an unaltered native copy of Wag31 and a fluorescent protein tagged copy of Wag31 integrated elsewhere on the chromosome localized as expected to the old pole and restored the wild type cell shape phenotype (Meniche et al., 2014).

A recent study used super-resolution microscopy and fluorescent D-amino acids (FDAAs) to stain a *M. smegmatis* reporter strain expressing an episomal mCherry tagged Wag31 (Botella et al., 2017). FDAAs are a recently developed class of reporters that are incorporated directly into growing peptidoglycan to identify specific regions of elongation along a bacterial cell (Siegrist et al., 2013; Kuru et al., 2015; Botella et al., 2017). In mycobacteria, FDAA staining was used to differentiate growth from old versus new poles. Cells expressing a fluorescently tagged Wag31 elongated more symmetrically between old and new poles compared to wild type *M. smegmatis*, which elongated preferentially from the old pole (Botella et al., 2017). Together, these bodies of work suggest that Wag31 localization and function is particularly sensitive to fluorescent protein tags, because several of the constructs utilized significantly alter cell growth and polarity (Santi et al., 2013; Meniche et al., 2014; Santi and McKinney, 2015; Botella et al., 2017). Adding a fluorescent protein to any important enzyme can alter enzyme activity, localization, and cell physiology (Landgraf et al., 2012), and this seems especially true of Wag31. A loss of cellular growth asymmetry could have major consequences for bacterial population structure and fitness; therefore we must be cautious in interpreting results from studies performed with fluorescently tagged Wag31 in mycobacteria.

Asymmetric polar growth in mycobacteria is created by a protein conserved among mycobacteria but with no homologs in other characterized bacteria. This protein, called LamA (named for Loss of Asymmetry Mutant A), is a member of the mycobacterial division complex where it actively inhibits growth at the new pole (**Figure 1A**) (Rego et al., 2017). LamA interacts with penicillin binding protein PonA1. Deletion of LamA allows Wag31 to be recruited to the new pole more rapidly, indicating that LamA works to delay assembly of the elongation complex at the new pole (Rego et al., 2017). LamA inhibition of new pole growth in WT cells allows the old pole to grow preferentially,

creating the characteristic asymmetric polar growth patterns of mycobacteria (**Figure 1A**).

Though identifying functions of proteins Wag31 and LamA provides us with a glimpse of the networks involved in regulating asymmetric growth in mycobacteria, the extent of their interactions with elongation complexes have yet to be fully elucidated. A current understanding of the processes involved in cell elongation complexes is described in an excellent review by Kieser and Rubin (2014). The enzymatic activity of a large number of proteins is required for synthesizing peptidoglycan, arabinogalactan, and mycolic acid layers in mycobacteria. Asymmetry-promoting proteins Wag31 and LamA likely interact with enzyme complexes and membrane domains involved in cell wall and cell membrane synthesis (Meniche et al., 2014; Hayashi et al., 2016). It will be interesting to understand exactly how previously identified cell elongation networks are asymmetrically regulated at each pole and how growth cues such as nutrient status may interface with these pathways.

In addition to growing asymmetrically, mycobacteria also divide asymmetrically and undergo a fast, mechanical v-snapping process of daughter cell separation (Aldridge et al., 2012; Richardson et al., 2016; Zhou et al., 2016). There is evidence to suggest that sites of asymmetric division are not just established at division, but are inherited from previous generations. Atomic force microscopy (AFM) of the mycobacterial cell surface revealed that cell surface wave troughs can determine division site selection (Eskandarian et al., 2017). Repeating surface waveform troughs are inherited over several generations and the total number of troughs scales with cell size (**Figure 1B**) (Eskandarian et al., 2017). Cells divide at the centermost trough and the other troughs are passed down to subsequent generations to be used as a future division site (**Figure 1B**) (Eskandarian et al., 2017). Furthermore, while cell wall synthetic enzymes GlfT2, MurG, and Pks13 show primary localization to subpolar regions where growth occurs, re-examination of this data indicates secondary localization peaks at quarter cell positions (Meniche et al., 2014). It has yet to be investigated if these elongation complex positions co-localize with surface wave troughs, as a potential means of using division troughs to position cell elongation complexes a generation in advance.

Wild type *M. smegmatis* cells divide at the central surface wave trough while cells deficient in chromosome partitioning can divide at off-center wave troughs, indicating a regulatory role for chromosome segregation in division site selection (Eskandarian et al., 2017). Mycobacteria lack homologues of defined nucleoid occlusion systems (Noc proteins) and minicell (Min) proteins used by other bacteria to prevent chromosome splicing during cell division (Wu and Errington, 2011; Monahan et al., 2014; Schumacher, 2017). Despite the lack of known nucleoid occlusion proteins, *M. smegmatis* cells exhibit a clear relationship between asymmetric chromosome positioning and asymmetric division placement (Eskandarian et al., 2017; Logsdon et al., 2017) (**Figure 1B**). Division occurs in the wave trough nearest the local DNA minimum even in mycobacteria deficient in chromosome segregation, demonstrating the existence of a mechanism to prevent damage to the chromosome during cell division (Eskandarian et al., 2017).

Together, these studies support the idea that chromosome dynamics contributes to asymmetric cell division in mycobacteria. The chromosome is a large, essential macromolecule that may play a key role in determining the layout of many aspects of the intracellular space (Campos and Jacobs-Wagner, 2013). Different bacterial species exhibit a variety of chromosome orientations and arrangements, reflecting the diversity of bacterial cell shapes, sizes, and growth modes. For example, in *E. coli* replication is initiated midcell and continues with two replication forks moving independently before terminating midcell (Reyes-Lamothe et al., 2008). This pattern represents an L-ori-R (left-origin-right) orientation. In *C. crescentus*, DNA replication begins near the flagellar old pole during the swarmer to stalked cell transition. The replisome migrates midcell while the newly replicated ori "flips" and travels across the cell from the stalked pole to the newly formed flagellar pole (Bowman et al., 2008). The *C. crescentus* chromosome organization pattern represents an ori-ter-ter-ori (origin-terminus-terminus-origin) orientation. Other bacteria with ori-ter-ter-ori chromosome organizations include *Pseudomonas aeruginosa*, chromosome 1 of *Vibrio cholerae*, and *Myxococcus xanthus* (Fogel and Waldor, 2005; Harms et al., 2013; Vallet-Gely and Boccard, 2013). *B. subtilis*, on the other hand, oscillates between an ori-ter-ter-ori and L-ori-R pattern, depending on cell cycle stage (Wang et al., 2014).

Chromosome organization and partitioning likely direct many cellular processes. These processes include ensuring genetic inheritance, directing cell division, regulating transcription, and targeting transcripts and their encoded proteins to their necessary location within the cell (Montero Llopis et al., 2010; Nevo-Dinur et al., 2011; Govindarajan et al., 2012; Campos and Jacobs-Wagner, 2013). For example, the order of genes along the chromosome is highly conserved in gammaproteobacteria and correlated with the temporal regulation of gene expression (Sobetzko et al., 2012). The most highly conserved aspect of global gene arrangements is distance from either the ori or ter region (Sobetzko et al., 2012). Proximity of a gene to the ori or ter region on the chromosome could contribute to temporal regulation of its expression through gene dosage, which refers to the difference in copy number of genes located near the ori versus the ter while DNA replication is ongoing (Slager and Veening, 2016). Genes in the ori region are replicated first and thus periodically have two copies while genes near the ter only have one copy until the end of replication. In *Vibrio cholerae*, the ori proximal location and expression of ribosome genes is essential for proper growth and host invasion. Moving half of the genes required for ribosome proteins to distal sites along the chromosome leads to significant defects in growth and invasion processes (Soler-Bistue et al., 2015). In mycobacteria, a notable operon positioned near the ori is called the division cell wall (dcw) cluster and contains many genes whose products are required for cell wall synthesis and division, including *ftsZ, ftsQ, ftsW, murC, murG, murD, murX, murF, murE*, and *wag31* (Kang et al., 2008). The functional implications of maintaining this growth and division operon near the ori have yet to be investigated in mycobacteria, but it stands to reason that this position could allow regulation of expression through

gene dosing and/or proper localization of important growth and division proteins.

The molecular machinery responsible for chromosome partitioning and placement within most studied bacterial cells (with the notable exception of *E. coli*) is the ParABs system (Lee and Grossman, 2006; Mierzejewska and Jagura-Burdzy, 2012; Iniesta, 2014; Lagage et al., 2016). The ParABs system in mycobacteria consists of two 16 bp centromere-like *parS* sequences located near the ori on the chromosome (Casart et al., 2008). The ParB DNA binding protein specifically recognizes and binds the *parS* sequences, and its activity is negatively regulated through Ser/Thr kinase phosphorylation (Baronian et al., 2015). ParA, a Walker ATPase, interacts with ParB and directs segrosome partitioning (Ginda et al., 2017). The movement of the ori across the cell to the new pole allows the cell to divide into daughter cells with two neatly packaged chromosomes. ParB colocalizes with the nucleoid associated protein responsible for maintaining chromosome compaction, HupB, indicating a role for HupB in ori segregation (Holowka et al., 2017). The ParABs system is also strongly integrated with aspects of the elongation and division machinery in *M. smegmatis*. Knocking out or overproducing ParA impairs cell division, resulting in filamentous and multinucleoidal cells that have failed to divide (Maloney et al., 2009). ParA interacts directly with the polar protein responsible for the organization of growth and division factories, Wag31 (Ginda et al., 2013). Therefore, studying chromosome partitioning could give us new insight into the integration of chromosome organization and cell division processes.

Several groups have characterized the chromosome organization of mycobacteria using live cell microscopy, and multiple models of chromosome subcellular organization have been proposed. Santi and McKinney (2015) used a fluorescent protein tagged ParB/Wag31 dual reporter strain to conclude that the ori is localized midcell before replication and after replication, both ori's segregate to mirror symmetric quarter cell positions to prepare for midcell localization in the two daughter cells. Chromosomal locus attB1, located at 245° on the left lobe, was found initially localized near the new pole before translocating midcell during replication. Based on the midcell position of the ori and new pole position of the left lobe, they concluded the *M. smegmatis* chromosome organization had a R-ori-L configuration, as in *E. coli*. However, the use of a fluorescent protein labeled Wag31 may have affected the growth polarity in these reporter cells (Meniche et al., 2014; Botella et al., 2017).

Recent studies using ParB (Trojanowski et al., 2015; Ginda et al., 2017) or fluorescent reporter operator system (FROS)-ori (Logsdon et al., 2017) reporters independently converged on a model in which the ori is positioned asymmetrically and closer to the new pole at birth (**Figure 1B**). A few differences between the reporters utilized and results generated should be noted. The ParB reporter consistently shows ori splitting and segregation much earlier than the FROS ori reporter (Santi and McKinney, 2015; Trojanowski et al., 2015, 2017; Ginda et al., 2017; Logsdon et al., 2017). Many cells inherited two ParB foci, indicating these origins had already undergone a second round of replication and a second segregation event before division, which was not observed using the FROS-ori reporter (Ginda et al., 2017; Logsdon et al., 2017; Trojanowski et al., 2017). In these cases, the ParB reporter displayed differing frequencies of re-splitting before division between studies ranging from 0% (Trojanowski et al., 2015), to 11% (Trojanowski et al., 2017), to 75% (Ginda et al., 2017). It is not apparent why these reporters produce different segregation dynamics, however, the asymmetric ori positioning was consistent across studies (Trojanowski et al., 2015, 2017; Ginda et al., 2017; Logsdon et al., 2017). Identification of ori positioning, along with the use of a FROS-terminus reporter, allowed for a more comprehensive investigation of subcellular chromosome localization and strongly supports an ori-ter-ter-ori chromosome orientation (Logsdon et al., 2017). Localization data show the terminus positioned near the new pole at birth followed by a rapid translocation event to the midcell partway through the cell cycle (**Figure 1B**). This asymmetric ori-ter-ter-ori chromosome positioning is not unique to mycobacteria, as it has been previously described in *Myxococcus xanthus* (Harms et al., 2013).

How do chromosome organization patterns in mycobacteria contribute to cell division? The observed ori-ter-ter-ori orientation pattern is asymmetric within the cell throughout the entire cell cycle (Ginda et al., 2017; Logsdon et al., 2017). Though the chromosome terminus translocates midcell, it is not located precisely halfway between each pole. Rather, it is slightly shifted toward the new pole, in a manner that corresponds with asymmetric septum positioning at cell division (**Figure 1B**) (Logsdon et al., 2017). In many cells, the terminus shifts midcell but remains as a single focus (even after replication has completed) until 15–30 min before cell division. Just before division, the two terminus foci move slightly apart and the septum forms directly between them.

Terminus translocation midcell could be a very early determinant of the division site. How the terminus finds this location is unclear – there are systems identified for origin localization in mycobacteria and other bacteria but not terminus localization. The terminus and inherited wave troughs may interact to target termini to the future division spot. Additionally, interactions of the terminus with members of the divisome to prevent division over chromosomes have not been characterized. Mycobacteria do not have homologs of any identified nucleoid occlusion systems but it stands to reason that they have an alternate system that only allows septum formation in the DNA deficient space between termini at division. Overall, many studies indicate that asymmetry is an integral part of mycobacterial physiology that sets this genus apart from other well studied, symmetric bacteria.

BEHAVIORAL CONSEQUENCES OF ASYMMETRY

The establishment of systematic asymmetry in mycobacterial cells likely has functional consequences on behaviors of both single cells and populations of mycobacteria. One consequence of cellular asymmetry is the creation of cellular heterogeneity,

even between presumably isogenic sister cells. Phenotypic heterogeneity creates subpopulations of mycobacteria from a single progenitor with varying size, growth, and cell cycle properties (Aldridge et al., 2012; Richardson et al., 2016). Deterministic generation of heterogeneity among populations of cells may serve as a bacterial "bet hedging" mechanism, allowing a subpopulation of cells with a particular phenotype to survive environmental stress (Kysela et al., 2013; Richardson et al., 2016). Differentiation of cell phenotypes leading to bet hedging is apparent in the model organism *C. crescentus*. Upon division, two distinct daughter cell types are generated. One daughter cell is immobile and has a polar stalk while the other has a polar flagellum used for swarming motility. The stalked daughter remains attached to its current environment, while the swarmer daughter takes a risk to swim away and colonize a new, potentially preferential environment (Kysela et al., 2013). In this way, if environmental conditions wipe out all cells at the initial site of colonization, half the cells are already searching for a viable site where they can grow and replicate.

The functional consequences of asymmetric growth and division in mycobacteria are perhaps more subtle. Differences in cell size and cell cycle stage at the time of antibiotic treatment contribute to differential antibiotic susceptibility (Aldridge et al., 2012; Richardson et al., 2016). When treated with cell wall acting antibiotics, faster growing accelerator cells are more sensitive to cycloserine and meropenem than their sister alternator cells (Aldridge et al., 2012). Additionally, *M. smegmatis* cells exhibit differential susceptibility to rifampicin treatment. Rifampicin tolerant cells are larger at birth and inherit older growth poles compared to susceptible cells (Richardson et al., 2016). Together, these studies indicate that asymmetric growth and division within a population of mycobacteria allows certain cells to survive an antibiotic stressor while others with different phenotypic characteristics perish.

The role of asymmetric growth and division in *M. tuberculosis* infection is just beginning to be investigated. Recently, Vijay et al. (2017) examined cell size distributions of 158 clinically isolated *M. tuberculosis* strains and observed that *M. tuberculosis* cell sizes are smaller and less variable after growing in rich liquid broth compared to their sizes directly from patient sputum or passaged through J774 mouse macrophages. These measurements suggest that clinical, non-laboratory adapted strains of *M. tuberculosis* may increase phenotypic heterogeneity in response to host stress conditions. Additionally, cell length and heterogeneity increased in clinically isolated multidrug resistant *M. tuberculosis* (MDR-TB) strains when exposed to the first line antibiotics rifampicin and isoniazid (Vijay et al., 2017). Cell size variability further increased in MDR-TB subjected to both macrophage infection and rifampicin treatment (Vijay et al., 2017). This increase in *M. tuberculosis* size and variability suggests a synergistic effect between drug stress and infection. Thus, phenotypic heterogeneity manifested in cell size in addition to defined genetic mutations, may shape *M. tuberculosis* drug and host tolerance during infection.

Manina et al. (2015) also investigated the effect of host and drug stress on *M. tuberculosis* phenotypic heterogeneity in defined conditions with the lab adapted Erdman strain of *M. tuberculosis*. A GFP tagged rRNA reporter was used to demonstrate increases in *M. tuberculosis* cell-to-cell heterogeneity in nutrient limited medium, stationary phase culture, macrophage infection, and mouse lung infection compared to growth in rich medium (Manina et al., 2015). Increased *M. tuberculosis* cellular variability may be a direct response to stressful environmental conditions, although the physiological and molecular response leading to phenotypic changes in *M. tuberculosis* are poorly understood. Increased phenotypic heterogeneity observed under host and drug stress could be mediated through subtle changes in patterns of *M. tuberculosis* asymmetric growth and division. These studies suggest that amplifying phenotypic heterogeneity may allow a subpopulation of *M. tuberculosis* cells to persist within a host during infection and drug treatment. If true, it is tempting to speculate that identifying and targeting particularly tolerant cell subpopulation could clear TB infection more efficiently.

Finally, molecular support for the hypothesis that phenotypic heterogeneity promotes bacterial survival comes from studies using the symmetrically growing LamA mutant. Δ*lamA M. smegmatis* and *M. tuberculosis* show less size heterogeneity than wild type cells and are killed more rapidly and uniformly by rifampicin and cell wall acting antibiotics (Rego et al., 2017). This molecular study, together with population level studies, support the hypothesis that asymmetric polar growth actively creates heterogeneity amongst bacterial cells to serve as a bulk survival mechanism, ensuring a subpopulation of *M. tuberculosis* can persist in stressful environments.

CELL CYCLE

To coordinate chromosome duplication with changes in cell size, growth rate, and variability in stressful growth conditions, mycobacteria alter the dynamics of their cell cycle. These changes are essential to adapt to a wide variety of environments and ensure faithful replication and genetic inheritance. The bacterial cell cycle is usually described as three basic phases: B period occurs after division and before DNA replication, C is the period of active DNA replication, and D occurs after DNA replication but before cell division. In *M. smegmatis*, a fraction of cells begin a new round of DNA replication before division and their daughters subsequently skip B period and continue straight into C (Santi et al., 2013; Sukumar et al., 2014; Trojanowski et al., 2015; Richardson et al., 2016; Logsdon et al., 2017). We named this occurrence the E period (Sukumar et al., 2014). Overall, *M. smegmatis* spends the majority of the cell cycle in C period replicating the chromosome while B and D period are relatively short (**Figure 2A**) (Santi et al., 2013; Sukumar et al., 2014; Logsdon et al., 2017; Trojanowski et al., 2017). E period occurs more frequently and lasts longer in cells that were large at birth (**Figure 2A**) (Logsdon et al., 2017).

A similar but distinct overlap in replication cycles was recently reported in *M. smegmatis*. Trojanowski et al. (2017) observed multifork replication in 11% of *M. smegmatis* cells growing in rich medium. Multifork replication occurs when a second (or

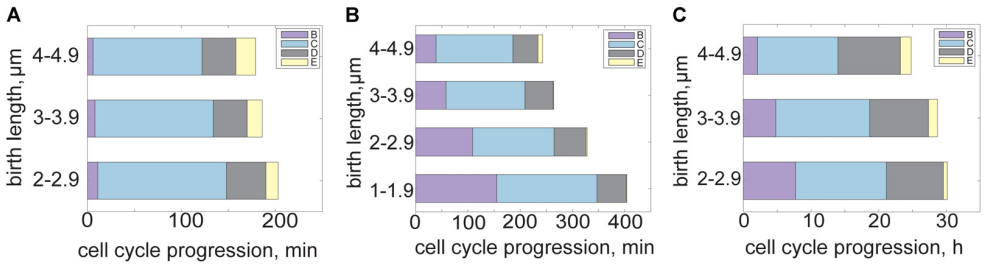

FIGURE 2 | Mycobacterial cell cycle and growth dynamics shift in fast versus slow growth conditions. **(A)** Bar plot of *M. smegmatis* cell cycle progression in rich medium. B period (pre-replication, purple) is short while C (active DNA replication, blue) encompasses most of the cell cycle. D period (post replication, gray) is relatively constant across cell birth sizes but E period (re-initiation, yellow) is associated with cells born larger. **(B)** Bar plot showing *M. smegmatis* cell cycle progression and variability across cell sizes in carbon limited medium. B period is disproportionally extended in carbon limited growth conditions, as smaller cells require more time to initiate DNA replication. E period encompasses less of the cell cycle during carbon limitation. **(C)** Bar plot showing BCG cell cycle progression across cell sizes in rich medium. Duration of B period is associated with cell size, with cells born smaller waiting longer to initiate DNA replication. C and D periods are relatively constant in the BCG cell cycle and E period is infrequent. Data from Logsdon et al. (2017).

third or fourth) round of replication begins before the first has completed (Helmstetter, 1968; Trojanowski et al., 2017). Multifork replication is typically associated with fast growing bacterial species as an adaption to fast growth conditions, in which division time is shorter than the time required to replicate the chromosome. By initiating several rounds of replication before the first has completed, daughter cells inherit an already partially replicated chromosome, preventing the rate of division from outpacing the rate of chromosome duplication. The differing observations of E period and multifork replication in mycobacteria come from studies using different fluorescent DNA replication reporters and imaging/growth conditions, making it difficult to make direct comparisons (Santi et al., 2013; Sukumar et al., 2014; Logsdon et al., 2017; Trojanowski et al., 2017). Even so, both multifork replication and E period are associated with large cells, and the frequency of both re-initiation events decreases under nutrient limitation (Logsdon et al., 2017; Trojanowski et al., 2017).

It is uncommon to observe re-initiation (E period) or multifork replication in slow growing bacteria, particularly a species with a period of DNA replication (C period) shorter than the interdivision time. Mycobacteria therefore break the paradigm in bacterial cell physiology that supposes only fast growing organisms engage in multifork replication. The effects of gene dosage on transcription are multiplied during multifork replication (ori:ter ratios are 4:1 instead of 2:1 or 1:1) and could lead to an overabundance of transcripts from genes located near the ori and set into motion any number of cellular regulatory programs (Slager and Veening, 2016). Ultimately, the effect of gene dosage and transcript abundance could create an additional layer of heterogeneity in the subpopulation of mycobacterial cells experiencing reinitiation. Because *M. smegmatis* cells engaging in multifork replication comprise only a small percent of the total population (11%) many more cells need to be studied to determine the functional utility of this behavior (Trojanowski et al., 2017). Overall, multifork replication may serve a different purpose or evolutionary advantage in slow growing mycobacteria compared to fast growing model bacteria and these cell cycle patterns require further investigation.

Several other distinct cell cycle timing changes occur in mycobacteria under nutrient limitation. Studying cells grown under carbon limitation presents a chance to examine cell cycle dynamics in environmental conditions more similar to those encountered during early infection. When grown in carbon-limited medium, the average *M. smegmatis* interdivision time increases by 2 h (Logsdon et al., 2017). Rather than slowing all periods of the cell cycle equally, B period is extended disproportionally (**Figure 2B**). The proportion of the cell cycle spent in B period is negatively correlated with cell birth size, meaning that small cells require significantly more time before initiating DNA replication than cells born large (**Figure 2B**) (Logsdon et al., 2017). However, post initiation time (C+D+E periods) remains constant and independent of cell size at birth (**Figure 2B**). The extended delay before initiation could be an adaption strategy to early infection, during which there is evidence that mycobacteria slow or halt their growth to avoid host detection (Rohde et al., 2012).

The slow growing mycobacterial species BCG is often used as a non-pathogenic model for another slow growing pathogenic mycobacteria, *M. tuberculosis*. The BCG interdivision time is longer than *M. smegmatis* (and comparable to that of *M. tuberculosis*), spanning from 15 to 20 h with a C period lasting an average of 9.4 h (**Figure 2C**) (Nair et al., 2009; Logsdon et al., 2017). The B period shows an extended duration and negative correlation with cell size at birth while the total time spent initiation to division remains constant across cell size, as in carbon limited *M. smegmatis* (**Figure 2C**) (Logsdon et al., 2017). The very long interdivision and DNA replication times in slow growing species present a long standing puzzle for mycobacteriologists (Ditse et al., 2017). A recent study of the *M. tuberculosis* DNA polymerase DnaE1 showed that the process of nucleotide incorporation is not the rate-limiting step in DNA replication or division times, because recombinant *M. tuberculosis* DnaE1 polymerase works faster *in vitro* than the *E. coli* DNA polymerase PolIIIα (Rock et al., 2015). Therefore there must be additional factors limiting the rate of DNA replication and cell cycle progression in slow growing mycobacteria that should be identified with future work. The

necessity of coordinating DNA replication with chromosome partitioning, elongation, division, and metabolic status likely plays a role in determining rates of DNA replication in slow growing mycobacteria.

During growth in nutrient-limited environments, cell cycle timing and cell sizes become more heterogeneous. The mycobacterial cell cycle (particularly in slow growing mycobacteria) may be innately asynchrononus. The length of B period varies significantly based on cell birth size, and daughter birth sizes are intrinsically unequal, thus cell cycle timing is also intrinsically unequal (Aldridge et al., 2012; Logsdon et al., 2017). This asynchrony may provide an additional level of heterogeneity to promote population survival. The cell cycle stage at the start of rifampicin treatment is a strong predictor of bacterial survival on a single cell level (Richardson et al., 2016). It is therefore intriguing that slow growing mycobacteria BCG or carbon limited *M. smegmatis* have a means of generating cells in many stages of the cell cycle within a single colony. These studies suggest that mycobacterial cell cycle dynamics could determine, on a single cell level, which bacteria will survive nutrient or antibiotic pressure. Elucidating the effect of cell cycle dynamics on bacterial stress tolerance and survival will require additional single cell experiments and analysis (Taheri-Araghi et al., 2015b). With continued study focusing on the timing of cell cycle components in individual cells, we can begin to elucidate how mycobacteria regulate their lifecycle to persist in the face of environmental stress.

CELL SIZE CONTROL

It is clear that mycobacteria must manage variability in size, growth, and cell cycle timing in the wide range of conditions potentially encountered during infection. Coordination of these essential cell processes ensures reproducibility of cell sizes in the face of environmental stress. Even under rich growth conditions, asymmetric elongation and division in mycobacteria give rise to increased variability in cell size compared to model bacteria such as *E. coli*, *B. subtilis*, and *C. crescentus*, yet the distribution of this variability is stable over time (Aldridge et al., 2012; Amir, 2014; Campos et al., 2014; Taheri-Araghi et al., 2015a). Cell size homeostasis is an important aspect of the physiology of all living cells because without a mechanism of regulation, cell sizes and physiological properties would rapidly diverge and become unsustainable. Mycobacterial populations maintain stability in cell size variation despite larger sister cells elongating faster and smaller sister cells elongating slower, indicating a strong cellular mechanism of size regulation to prevent differences in size and growth rate from compounding and diverging over time. What mechanism is used by mycobacteria to maintain control of cell sizes when their variability in cell size increases under stress?

In well-studied, model bacterial species the distribution of cell birth sizes is quite narrow. *E. coli* birth size distribution has a coefficient of variation (CV) of 12% and *C. crescentus* maintains a CV of 14%, despite being another asymmetrically dividing bacterial species (Campos et al., 2014; Iyer-Biswas et al., 2014). This tightly controlled population structure has fascinated microbiologists for decades and lead to several attempts to model the factors controlling bacterial cell division and cell size (Schaechter et al., 1958; Koch and Schaechter, 1962; Cooper and Helmstetter, 1968; Donachie, 1968). However, it was not clear how cell size control models, which are well studied in other bacteria, would translate given the physical asymmetry of mycobacteria.

Mathematical models of bacterial cell size control have been introduced beginning in the 1960s (Koch and Schaechter, 1962; Cooper and Helmstetter, 1968; Donachie, 1968; Amir, 2014; Campos et al., 2014; Ho and Amir, 2015; Taheri-Araghi et al., 2015a; Harris and Theriot, 2016; Sauls et al., 2016; Soifer et al., 2016; Wallden et al., 2016; Zheng et al., 2016; Jun et al., 2018). To date, most models of bacterial cell size control have been built on the assumption that bacteria grow exponentially at a single-cell level (Schaechter et al., 1958). However, time resolution of imaging in *M. smegmatis* is limited due to phototoxic effects, such that single cell traces cannot distinguish between linear and exponential modes of growth. Though growth data on a single-cell level have been reported as either an averaged growth rate (length/time) or an exponential growth constant (1/time) depending on the analysis type, consensus whether mycobacterial growth per cell is linear or exponential is lacking. (Aldridge et al., 2012; Santi et al., 2013; Wakamoto et al., 2013; Logsdon et al., 2017; Priestman et al., 2017). There are other advanced techniques used to definitively determine the mode of mass increase within a bacterial cell over time (Godin et al., 2010; Cermak et al., 2016), however, these have not been applied to mycobacteria.

Recent studies have taken advantage of growth measurements from many cells to compare against expected relationships between generation time and cell size of exponentially or linearly growing bacteria. Studies using bulk measurements and single cell traces with model selection are in agreement with exponential growth expectations compared to a linear growth model (Logsdon et al., 2017; Priestman et al., 2017). Interestingly, both found that the fraction of *M. smegmatis* cells with the longest interdivision times deviate from exponential growth and appear more linear (Logsdon et al., 2017; Priestman et al., 2017). It would be interesting to determine if another cellular growth mechanism in these slowly dividing cells affects apparent linear versus exponential growth. Perhaps very large cells inherited old growth poles or experienced a lag in growth and could have distinct stress responses compared to their exponentially growing counterparts (Kysela et al., 2013).

Historically, models of cell size control used measurements of size or time to relate events within the cell cycle of exponentially growing cells ("timer" or "sizer" models) (**Figures 3A,B**) (Koch and Schaechter, 1962; Robert et al., 2014; Willis and Huang, 2017). Time increments measure the minutes or hours between events, (e.g., cells grow 100 min before division), while size measurements record the absolute length at an event (e.g., cells divide once reaching 7 μm in length) (**Figures 3A,B**). Models of cell size control used one or both types of measurements simultaneously to describe bacterial cell division. Model bacteria were largely considered to follow a sizer model as timer models are very sensitive to slight differences in exponential growth

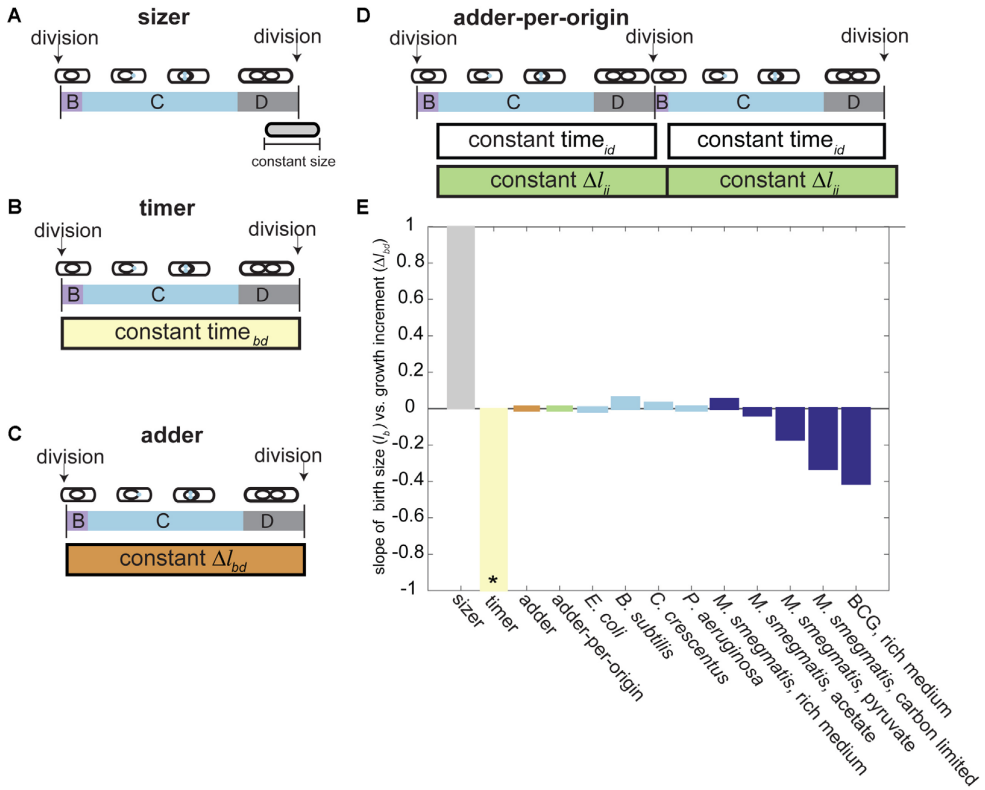

FIGURE 3 | Models of bacterial cell size control. **(A)** In the sizer model, cells divide once they reach a constant size (e.g., cells divide once reaching 7 μm in length). **(B)** In the timer model, cells divide a constant time after birth (e.g., cells divide 100 min after birth). **(C)** In the adder model, cells divide after adding a constant growth increment from birth (e.g., cells divide after adding 3 μm to their birth length). **(D)** In the adder-per-origin model, cells add a constant increment from initiation to initiation and then divide a constant time after initiation (e.g., cells divide 100 min after initiation, and grow 3 μm between initiation events). **(E)** Bar plot depicting the slope of cell birth length (Δl_b) versus birth to division adder increment (Δl_{bd}) for several size control models and bacterial populations. Model predictions for the slope of Δl_b vs. Δl_{bd} are shown on the left of the graph. The sizer model (left, gray bar) predicts a slope of 1, because cells born smaller must grow more to reach the required size for division (Koch and Schaechter, 1962; Sauls et al., 2016). The timer model (yellow bar) predicts a slope of –1. In a population of cells where growth rate is exponentially correlated with cell size, larger cells are expected to grow more than smaller cells in the same amount of time, giving a negative slope (Robert et al., 2014; Sauls et al., 2016; Willis and Huang, 2017). The adder model supposes that all cells add a constant growth increment from birth to division regardless of birth size and thus gives a slope of 0 (Taheri-Araghi et al., 2015a). The adder-per-origin model posits that all cells grow a constant length from initiation to initiation, and then divide a constant time after initiation. However, a constant adder from initiation to initiation mathematically reduces to an adder correlation from birth to division, giving a slope of zero (Amir, 2014). Light blue bars represent l_b vs. Δl_{bd} slope measurements from populations of model bacteria. *E. coli* and *B. subtilis* from Taheri-Araghi et al. (2015a), *C. crescentus* from Campos et al. (2014), *P. aeruginosa* from Deforet et al. (2015). Dark blue bars represent l_b vs. Δl_{bd} slope measurements from mycobacterial populations. *M. smegmatis* rich media, carbon limited, and BCG from Logsdon et al. (2017). *M. smegmatis* acetate and pyruvate from Priestman et al. (2017). *The timer model was shown in several studies to be incompatible with generation of stable bacterial cell size homeostasis (Trucco and Bell, 1970; Robert et al., 2014).

rates among cells and thus do not reach balanced growth and size homeostasis (Trucco and Bell, 1970; Robert et al., 2014). A key sizer model prediction is that birth size plotted against birth to division elongation is negatively correlated, because smaller cells must grow more to reach the absolute cell size for division (**Figure 3E**) (Koch and Schaechter, 1962; Sauls et al., 2016). Alternatively, a non-correlation or negative correlation between these two parameters had been interpreted as a time-based mechanism (**Figure 3E**) (Sveiczer et al., 1996; Robert et al., 2014; Willis and Huang, 2017). Therefore, when we first observed no correlation between *M. smegmatis* birth size and elongation, we concluded that mycobacteria use a time-based mechanism to control cell division (Aldridge et al., 2012).

Soon after, a new framework for understanding cell size control was introduced centered on the amount of growth rather than absolute size or elapsed time. Growth increments measure the change in length between two events (e.g., cells divide after adding 4 μm to their original length). The new model is referred to as an incremental or adder model of cell size control and postulates that every cell grows a constant length between birth and division, regardless of birth size (**Figure 3C**) (Campos et al., 2014; Taheri-Araghi et al., 2015a). With this in mind, a non-correlation between birth size and birth to division elongation (as seen in *M. smegmatis*) could be reinterpreted as arising from an adder (**Figure 3E**). Several studies adapted this model to predict that a constant change in cell length (Δl_{bd}), surface area, or volume from birth to division regulates cell size

(Amir, 2014; Campos et al., 2014; Deforet et al., 2015; Taheri-Araghi et al., 2015a; Harris and Theriot, 2016; Sauls et al., 2016; Soifer et al., 2016). In all cases, homeostasis is achieved because average birth size converges to the length of the increment added at each generation (Jun and Taheri-Araghi, 2015). Adding a constant length increment compensates for aberrant birth sizes by correcting outlier cells back to the population mean with exponential decay at each round of division (Taheri-Araghi et al., 2015a).

Thus, until recently, it was thought that mycobacteria used an adder mechanism of cell size control. Data from several labs corroborated the constant growth increment from birth to division in populations of *M. smegmatis* in rich medium (**Figure 3E**) (Aldridge et al., 2012; Santi et al., 2013; Logsdon et al., 2017; Priestman et al., 2017). Some of these data were produced several years before the mathematical framework for the adder model of cell size control was introduced, and have been retrospectively interpreted through this lens (Aldridge et al., 2012; Santi et al., 2013; Sauls et al., 2016). However, as recent work has shown, this adder behavior is not consistent across growth conditions (**Figure 3E**).

Several studies tested the growth and division of mycobacteria in sub-optimal carbon conditions because intracellular infection is thought to be carbon limited, with cholesterol serving as a key carbon source for *M. tuberculosis* during persistent infection (Pandey and Sassetti, 2008). Cell growth measurements of *M. smegmatis* cells grown with carbon restricted medium or with the cholesterol by-products acetate or pyruvate as the primary carbon source significantly deviated from expected adder correlations (**Figure 3E**). When cells are grown in acetate as a primary carbon source, accelerators continue to follow the adder principle but alternators are not consistent with an adder, showing a significantly negative correlation between birth length and growth birth to division (**Figure 3E**) (Priestman et al., 2017). Both accelerator and alternator cell populations grown in pyruvate and carbon limited medium deviate from the adder model and show a significantly negative correlation between birth length and growth birth to division (**Figure 3E**) (Logsdon et al., 2017; Priestman et al., 2017). BCG cells growing in rich medium also deviate from the adder model expectation (**Figure 3E**) (Logsdon et al., 2017). In other bacteria that follow the adder model, the constant growth correlation is maintained across many nutrient rich or poor growth media. Instead of shifting the correlation between birth length and total elongation, species like *E. coli* and *B. subtilis* change the value of the length added to cell size to allow cell sizes to adapt to nutrient poor or rich media (Taheri-Araghi et al., 2015a). Therefore, the negative correlation between birth length and birth to division growth indicates that the adder model cannot capture size control in the slow growing mycobacterium species BCG or in *M. smegmatis* growing in nutrient poor medium (**Figure 3E**). It is quite remarkable that the model mycobacterium *M. smegmatis* appeared to be an adder in standard, rich-growth conditions. This apparent (but not true) adder behavior also emphasizes the importance of mathematical modeling and nutritional perturbations in studying bacterial cell size control.

Because the correlation between birth size and growth shifts to become negative in nutrient limited growth conditions (Logsdon et al., 2017; Priestman et al., 2017), this *M. smegmatis* birth to division adder correlation in rich medium presents as an emergent property rather than the actual mechanism of size control (**Figure 3E**). To look beyond simple birth to division models of size control, many studies evaluate the relationship between cell size and intermediate cell cycle events (Cooper and Helmstetter, 1968; Donachie, 1968; Hill et al., 2012; Adiciptaningrum et al., 2015; Ho and Amir, 2015; Soifer et al., 2016; Wallden et al., 2016; Zheng et al., 2016; Banerjee et al., 2017; Osella et al., 2017). Several studies investigating the quantitative basis of cell cycle and size control showed that an initiation-to-initiation adder correlation mathematically reduces to an adder correlation from birth to division (**Figure 3E**) (Amir, 2014; Ho and Amir, 2015). On this basis, it was proposed that cell size control in bacteria is simply a consequence of a mechanism evolved to control the number of replication forks in bacteria (Amir, 2017). These observations served as the backbone of the adder-per-origin model, in which cells add a constant increment from initiation to initiation and then divide a constant time after initiation (**Figure 3D**). The adder-per-origin model has the appealing property of regulating cell size based on the growth rate and number of origins in the cell (particularly in bacteria that use multifork replication). Ori number must have an exponential dependence on growth rate, to ensure that cell growth does not outpace DNA replication (Schaechter et al., 1958; Ho and Amir, 2015). Therefore, an initiation dependent model could regulate mycobacterial cells with different growth rates (e.g., accelerator and alternator sister cells) and cells with multiple initiations per cell cycle (e.g., cells with an E period or multifork replication).

We recently developed an initiation-dependent model of cell size control that describes the specific growth and division properties in mycobacteria. These properties include asymmetric polar growth and division, shifting lengths of B and E period during slow growth, and increased variability in cell size during slow growth (Logsdon et al., 2017). The new model is named the parallel adder model because it is based on a regulatory mechanism in which cells add two constant growth increments simultaneously. One growth increment spans between two DNA replication initiation events (Δl_{ii}) while the other increment spans initiation to division (Δl_{id}) (**Figure 4A**). Together, these parallel increments allow coupled regulation of cell division and cell cycle dynamics. When directly tested against previously established models of cell size control, including adder and adder-per-origin models, the parallel adder model was significantly better fit to 13 key cell cycle and cell size measurements in *M. smegmatis* and BCG (Logsdon et al., 2017). The primary difference between initiation-to-initiation adder models in mycobacteria (parallel adder) versus previously studied *E. coli* (adder-per-origin) is that *E. coli* cell division occurs a constant time after initiation, while mycobacteria divide after a constant growth increment from initiation to division (Amir, 2014; Ho and Amir, 2015; Logsdon et al., 2017). However, in both cases initiation of DNA replication provides the key checkpoint controlling cell division and initiation in the next generation.

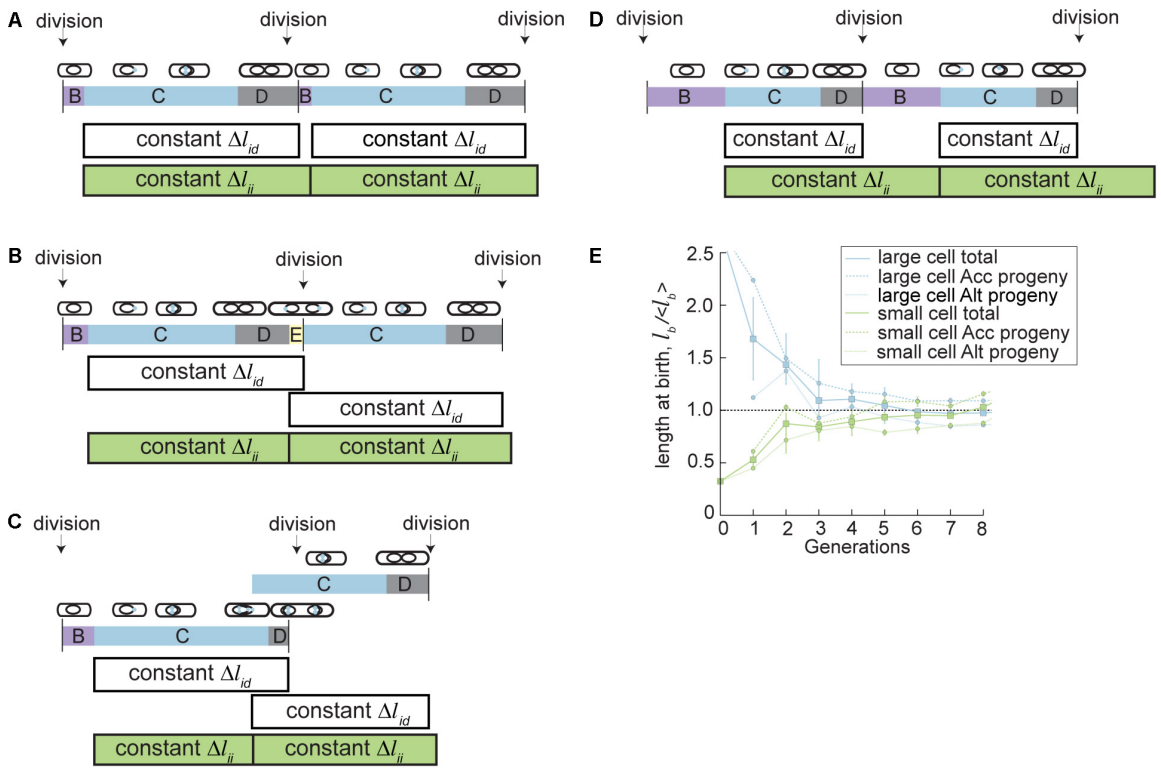

FIGURE 4 | A parallel adder model describes mycobacterial cell size control in fast and slow growth conditions. In the parallel adder model of cell size control, cells grow a constant length between two initiations (Δl_{ii}, green bars), and simultaneously grow a constant length between initiation and division (Δl_{id}, white bars). The mean of these two growth increments represents the average birth size. Initiation of DNA replication occurs at the beginning of C period (blue). **(A)** Parallel adder growth increments (Δl_{id} and Δl_{ii}) describe *M. smegmatis* cell cycle and division dynamics during fast growth. **(B)** The similar length of *M. smegmatis* parallel adder growth increments (Δl_{id} and Δl_{ii}) in fast growth conditions can cause stochastic overlaps in initiation and division, leading to reinitiation during D period, called E period (shown in yellow). The parallel adder accommodates stochastic re-initiation events including E period and allows recovery of population cell cycle dynamics. **(C)** The similar length of *M. smegmatis* parallel adder growth increments (Δl_{id} and Δl_{ii}) in fast growth conditions can cause stochastic overlaps in initiation and division, leading to reinitiation during C period, called multifork replication (shown by overlapping C periods). The parallel adder accommodates stochastic re-initiation events and allows recovery of population cell cycle dynamics. **(D)** The parallel adder model shifts relative lengths of Δl_{id} and Δl_{ii} growth increments during slow growth conditions (carbon limited *M. smegmatis* or BCG in rich medium) to accommodate differences in cell size, growth rate, and cell cycle dynamics during slow growth. However, constant Δl_{id} and Δl_{ii} increments pattern is maintained. **(E)** The parallel adder model leads to cell size convergence in accelerator and alternator subpopulations, despite innate asymmetry. Plot showing parallel adder simulations for progeny of hypothetical cells born extremely large (blue) or small (green). The average cell birth length with SEM bars over eight generations is plotted for a hypothetical cell (accelerator) born 2.53x the population average and a hypothetical cell (alternator) born 0.33x the population average. Average sizes of accelerator and alternator cell progeny from each hypothetical progenitor cell are also plotted with SEM bars over seven generations. Figure **(E)** is adapted from Logsdon et al. (2017).

Importantly, the increments of the parallel adder model shift to allow cells to optimize total size in a variety of growth environments (Logsdon et al., 2017). Parallel adder increments can adjust in total length and in relation to one another, allowing shifts in cell cycle timing and variability, most notably in B period and E period. In rich growth conditions, the Δl_{ii} and Δl_{id} growth increments are similar in length (Logsdon et al., 2017). This necessitates a shorter pre-initiation period (B period) and can often cause an overlap of initiation periods before division, meaning that the mother cell experiences E period (**Figure 4B**) or multifork replication (**Figure 4C**) and daughter cells entirely skip B. However, in BCG and carbon limited *M. smegmatis* cells, Δl_{ii} increments are much longer than Δl_{id}, leading to longer B periods and lowered frequency of both E period and multifork replication (**Figure 4D**). In this way, cell cycles are adjusted to create increased variability in timing under nutrient stress or in slow growing mycobacteria.

With a parallel adder, size convergence occurs by the same principle as other adder models, e.g., if cells add a constant length regardless of their initial size, cells smaller than average will increase in size and cells larger than average will decrease in size until they reach the population average (which is equal to the size of the growth increment added) over several generations (**Figure 4E**) (Amir, 2014; Taheri-Araghi et al., 2015a). The parallel adder regulates birth size by setting the cell length at birth equal to the average of the Δl_{ii} and Δl_{id} increments. Δl_{ii} and Δl_{id} measurements are specific for accelerator and alternator subtypes, and so accelerator and alternator cells converge to distinct average cell sizes (Logsdon et al., 2017). This creates increased variability in mycobacterial size compared to other studied bacteria, and reflects the distinct size, growth, and adder

increment properties measured in accelerator vs. alternator cells. As an example, an accelerator cell will add an accelerator specific Δl_{ii} increment as well as an accelerator specific Δl_{id} increment. Averaging the lengths of those two growth increments allows calculation of the birth size of the average accelerator progeny. Accelerator specific increments are larger than alternator specific increments, causing the average accelerator cell size to be larger than that of the larger alternator cell size (**Figure 4E**). Another well characterized asymmetrically dividing bacterial species, *C. crescentus*, exhibits an asymmetric incremental growth pattern that is opposite that of *M. smegmatis*. *C. crescentus* large (stalked) cells add a smaller increment and small (swarmer) cells add a larger increment to compensate for asymmetric birth sizes, leading to less variable birth and division sizes (Campos et al., 2014). Though *M. smegmatis* does not have this mechanism of compensating for asymmetric birth sizes, both accelerator and alternator cell types can recover from aberrant large or small birth sizes to reach homeostasis with the parallel adder model (**Figure 4E**). Therefore, the total population average can also reach homeostasis, albeit slightly more variable than most bacteria (Logsdon et al., 2017).

In the parallel adder model, initiation of DNA replication is the key checkpoint regulating cell division and size control under many conditions. Additional support for an initiation dependent model comes from a recent study identifying a novel essential component of the mycobacterial replication machinery called Rv0004. Rv0004 interacts with helicase loader DnaB and affects the interaction of DnaA and DnaB (Mann et al., 2017). When Rv0004 is depleted from cells growing in rich medium, variability in *M. smegmatis* birth size more than doubles, from a CV of 18% to a CV of 40% (Mann et al., 2017). This increased variability indicates that the process of initiation is molecularly coupled to division, as interrupting replisome assembly disrupts division and cell size regulation. It is possible though that there are additional "backup" mechanisms regulating cell division in the absence of initiation, as many of these cells still do divide, albeit with less size consistency than WT cells (Mann et al., 2017). Additional genetic or chemical inhibition of cell cycle processes will allow us to tease apart regulatory mechanisms of cell division and size control.

There are many additional and important questions regarding size control in mycobacteria to be addressed with future research. While the parallel adder describes mycobacterial growth under all conditions studied thus far (*M. smegmatis* rich growth, *M. smegmatis* carbon limitation, and BCG rich growth), it is possible that other growth conditions may reveal inconsistencies with the model and require further assessment or model modification. Additionally, it has yet to be determined whether any of the developed models of cell size control apply to *M. tuberculosis*. Cell size control models could provide an important tool for probing *M. tuberculosis* population dynamics during infection. Though correlations between cell size and antibiotic tolerance hold under controlled growth conditions, it is not known if they apply to variable and stressful conditions present in a host (Lin et al., 2014; Cadena et al., 2017; Martin et al., 2017). Cell size and cell cycle dynamics are crucial to understand during infection because of previously observed correlations with stress tolerance (Aldridge et al., 2012; Manina et al., 2015; Richardson et al., 2016; Vijay et al., 2017).

In summary, mycobacteria actively create population heterogeneity through growth, division, and cell cycle patterns. The extent of variability is partially determined by growth conditions and environmental stress experienced by mycobacterial cells. Differences in cell size within a population of mycobacteria increase under a wide variety of stressors. *M. smegmatis* and BCG coordinate basic cell cycle properties with their increased variation under stress using a unique model of cell size control. The parallel adder model accommodates inherent variation in cell cycle and growth that is likely important for population survival. Models of the cell cycle and size control could be particularly useful in predicting bacterial population dynamics during infection leading to the development of persistent subpopulations. Understanding the increase in cell-to-cell variability observed in *M. tuberculosis* cells under stress could aid in identifying and targeting the molecular pathways responsible for population heterogeneity and stress tolerance.

Despite the irregularities of mycobacteria compared to other well-studied rod shaped organisms, mycobacterial studies may provide a means of untangling many unanswered questions about bacterial physiology. Mycobacteria actively create exaggerated heterogeneity among closely related cells, allowing the resolution of bacterial population structure with a level of detail never before observed. We can assess functional differences created between (presumably) genetically identical sister cells, and easily identify phenotypic characteristics that allow survival under stress. Mycobacteria do not follow commonly observed patterns of growth, division, and size control, forcing researchers to look beyond established mechanisms developed with data from other bacteria. It became necessary to develop a novel model to account for innate asymmetry and pre-determined cell-to-cell variation observed in mycobacteria. The development of models to describe asymmetric mycobacterial cell properties may provide frameworks through which to understand other asymmetric or pole growing bacteria. In fact, when considering the diversity of bacterial cell sizes and shapes, ranging from filaments to spirochetes to cocci, and spanning sizes of 0.3–750 μm, we cannot help but wonder if mycobacteria are not so unusual after all.

AUTHOR CONTRIBUTIONS

ML and BA conceived of the review topic and structure, wrote the manuscript, and edited the manuscript.

FUNDING

This work was supported by an NIH Director's New Innovator Award 1DP2LM011952-01.

ACKNOWLEDGMENTS

We thank Ariel Amir and Po-Yi Ho for many helpful discussions on bacterial cell size control.

REFERENCES

Adiciptaningrum, A., Osella, M., Moolman, M. C., Cosentino Lagomarsino, M., and Tans, S. J. (2015). Stochasticity and homeostasis in the *E. coli* replication and division cycle. *Sci. Rep.* 5:18261. doi: 10.1038/srep18261

Aldridge, B. B., Fernandez-Suarez, M., Heller, D., Ambravaneswaran, V., Irimia, D., Toner, M., et al. (2012). Asymmetry and aging of mycobacterial cells lead to variable growth and antibiotic susceptibility. *Science* 335, 100–104. doi: 10.1126/science.1216166

Amir, A. (2014). Cell size regulation in bacteria. *Phys. Rev. Lett.* 112:208102. doi: 10.1103/PhysRevLett.112.208102

Amir, A. (2017). Is cell size a spandrel? *eLife* 6:e22186. doi: 10.7554/eLife.22186

Banerjee, S., Lo, K., Daddysman, M. K., Selewa, A., Kuntz, T., Dinner, A. R., et al. (2017). Biphasic growth dynamics control cell division in *Caulobacter crescentus*. *Nat. Microbiol.* 2:17116. doi: 10.1038/nmicrobiol.2017.116

Baronian, G., Ginda, K., Berry, L., Cohen-Gonsaud, M., Zakrzewska-Czerwinska, J., Jakimowicz, D., et al. (2015). Phosphorylation of *Mycobacterium tuberculosis* ParB participates in regulating the ParABS chromosome segregation system. *PLoS One* 10:e0119907. doi: 10.1371/journal.pone.0119907

Botella, H., Yang, G., Ouerfelli, O., Ehrt, S., Nathan, C. F., and Vaubourgeix, J. (2017). Distinct spatiotemporal dynamics of peptidoglycan synthesis between *Mycobacterium smegmatis* and *Mycobacterium tuberculosis*. *mBio* 8:e01183-17. doi: 10.1128/mBio.01183-17

Bowman, G. R., Comolli, L. R., Zhu, J., Eckart, M., Koenig, M., Downing, K. H., et al. (2008). A polymeric protein anchors the chromosomal origin/ParB complex at a bacterial cell pole. *Cell* 134, 945–955. doi: 10.1016/j.cell.2008.07.015

Cadena, A. M., Fortune, S. M., and Flynn, J. L. (2017). Heterogeneity in tuberculosis. *Nat. Rev. Immunol.* 17, 691–702. doi: 10.1038/nri.2017.69

Campos, M., and Jacobs-Wagner, C. (2013). Cellular organization of the transfer of genetic information. *Curr. Opin. Microbiol.* 16, 171–176. doi: 10.1016/j.mib.2013.01.007

Campos, M., Surovtsev, I. V., Kato, S., Paintdakhi, A., Beltran, B., Ebmeier, S. E., et al. (2014). A constant size extension drives bacterial cell size homeostasis. *Cell* 159, 1433–1446. doi: 10.1016/j.cell.2014.11.022

Casart, Y., Gamero, E., Rivera-Gutierrez, S., González-y-Merchand, J. A., and Salazar, L. (2008). *par* genes in *Mycobacterium bovis* and *Mycobacterium smegmatis* are arranged in an operon transcribed from "SigGC" promoters. *BMC Microbiol.* 8:51. doi: 10.1186/1471-2180-8-51

Cermak, N., Olcum, S., Delgado, F. F., Wasserman, S. C., Payer, K. R., A Murakami, M., et al. (2016). High-throughput measurement of single-cell growth rates using serial microfluidic mass sensor arrays. *Nat. Biotechnol.* 34, 1052–1059. doi: 10.1038/nbt.3666

Cohn, D. L. (2001). The effect of BCG vaccination on tuberculin skin testing. Does it matter? *Am. J. Respir. Crit. Care Med.* 164, 915–916. doi: 10.1164/ajrccm.164.6.2107090c

Cooper, S., and Helmstetter, C. E. (1968). Chromosome replication and the division cycle of *Escherichia coli* B/r. *J. Mol. Biol.* 31, 519–540. doi: 10.1016/0022-2836(68)90425-7

Daniel, R. A., and Errington, J. (2003). Control of cell morphogenesis in bacteria: two distinct ways to make a rod-shaped cell. *Cell* 113, 767–776. doi: 10.1016/S0092-8674(03)00421-5

Deforet, M., Van Ditmarsch, D., and Xavier, J. B. (2015). Cell-size homeostasis and the incremental rule in a bacterial pathogen. *Biophys. J.* 109, 521–528. doi: 10.1016/j.bpj.2015.07.002

Ditse, Z., Lamers, M. H., and Warner, D. F. (2017). DNA replication in *Mycobacterium tuberculosis*. *Microbiol. Spectr.* 5:TBTB2-0027-2016.

Dominguez-Escobar, J., Chastanet, A., Crevenna, A. H., Fromion, V., Wedlich-Soldner, R., and Carballido-Lopez, R. (2011). Processive movement of MreB-associated cell wall biosynthetic complexes in bacteria. *Science* 333, 225–228. doi: 10.1126/science.1203466

Donachie, W. D. (1968). Relationship between cell size and time of initiation of DNA replication. *Nature* 219, 1077–1079. doi: 10.1038/2191077a0

Errington, J. (2015). Bacterial morphogenesis and the enigmatic MreB helix. *Nat. Rev. Microbiol.* 13, 241–248. doi: 10.1038/nrmicro3398

Eskandarian, H. A., Odermatt, P. D., Ven, J. X. Y., Hannebelle, M. T. M., Nievergelt, A. P., Dhar, N., et al. (2017). Division site selection linked to inherited cell surface wave troughs in mycobacteria. *Nat. Microbiol.* 2:17094. doi: 10.1038/nmicrobiol.2017.94

Fogel, M. A., and Waldor, M. K. (2005). Distinct segregation dynamics of the two *Vibrio cholerae* chromosomes. *Mol. Microbiol.* 55, 125–136. doi: 10.1111/j.1365-2958.2004.04379.x

Garner, E. C., Bernard, R., Wang, W., Zhuang, X., Rudner, D. Z., and Mitchison, T. (2011). Coupled, circumferential motions of the cell wall synthesis machinery and MreB filaments in *B. subtilis*. *Science* 333, 222–225. doi: 10.1126/science.1203285

Ginda, K., Bezulska, M., Ziolkiewicz, M., Dziadek, J., Zakrzewska-Czerwinska, J., and Jakimowicz, D. (2013). ParA of *Mycobacterium smegmatis* co-ordinates chromosome segregation with the cell cycle and interacts with the polar growth determinant DivIVA. *Mol. Microbiol.* 87, 998–1012. doi: 10.1111/mmi.12146

Ginda, K., Santi, I., Bousbaine, D., Zakrzewska-Czerwinska, J., Jakimowicz, D., and Mckinney, J. (2017). The studies of ParA and ParB dynamics reveal asymmetry of chromosome segregation in mycobacteria. *Mol. Microbiol.* 105, 453–468. doi: 10.1111/mmi.13712

Godin, M., Delgado, F. F., Son, S., Grover, W. H., Bryan, A. K., Tzur, A., et al. (2010). Using buoyant mass to measure the growth of single cells. *Nat. Methods* 7, 387–390. doi: 10.1038/nmeth.1452

Govindarajan, S., Nevo-Dinur, K., and Amster-Choder, O. (2012). Compartmentalization and spatiotemporal organization of macromolecules in bacteria. *FEMS Microbiol. Rev.* 36, 1005–1022. doi: 10.1111/j.1574-6976.2012.00348.x

Harms, A., Treuner-Lange, A., Schumacher, D., and Sogaard-Andersen, L. (2013). Tracking of chromosome and replisome dynamics in *Myxococcus xanthus* reveals a novel chromosome arrangement. *PLoS Genet.* 9:e1003802. doi: 10.1371/journal.pgen.1003802

Harris, L. K., and Theriot, J. A. (2016). Relative rates of surface and volume synthesis set bacterial cell size. *Cell* 165, 1479–1492. doi: 10.1016/j.cell.2016.05.045

Hayashi, J. M., Luo, C. Y., Mayfield, J. A., Hsu, T., Fukuda, T., Walfield, A. L., et al. (2016). Spatially distinct and metabolically active membrane domain in mycobacteria. *Proc. Natl. Acad. Sci. U.S.A.* 113, 5400–5405. doi: 10.1073/pnas.1525165113

Helmstetter, C. E. (1968). DNA synthesis during the division cycle of rapidly growing *Escherichia coli* B/r. *J. Mol. Biol.* 31, 507–518. doi: 10.1016/0022-2836(68)90424-5

Hett, E. C., and Rubin, E. J. (2008). Bacterial growth and cell division: a mycobacterial perspective. *Microbiol. Mol. Biol. Rev.* 72, 126–156. doi: 10.1128/MMBR.00028-07

Hill, N. S., Kadoya, R., Chattoraj, D. K., and Levin, P. A. (2012). Cell size and the initiation of DNA replication in bacteria. *PLoS Genet.* 8:e1002549. doi: 10.1371/journal.pgen.1002549

Ho, P. Y., and Amir, A. (2015). Simultaneous regulation of cell size and chromosome replication in bacteria. *Front. Microbiol.* 6:662. doi: 10.3389/fmicb.2015.00662

Holowka, J., Trojanowski, D., Ginda, K., Wojtas, B., Gielniewski, B., Jakimowicz, D., et al. (2017). HupB is a bacterial nucleoid-associated protein with an indispensable eukaryotic-like tail. *mBio* 8:e01272-17. doi: 10.1128/mBio.01272-17

Iniesta, A. A. (2014). ParABS system in chromosome partitioning in the bacterium *Myxococcus xanthus*. *PLoS One* 9:e86897. doi: 10.1371/journal.pone.0086897

Iyer-Biswas, S., Wright, C. S., Henry, J. T., Lo, K., Burov, S., Lin, Y., et al. (2014). Scaling laws governing stochastic growth and division of single bacterial cells. *Proc. Natl. Acad. Sci. U.S.A.* 111, 15912–15917. doi: 10.1073/pnas.1403232111

Jankute, M., Cox, J. A., Harrison, J., and Besra, G. S. (2015). Assembly of the Mycobacterial Cell Wall. *Annu. Rev. Microbiol.* 69, 405–423. doi: 10.1146/annurev-micro-091014-104121

Jun, S., Si, F., Pugatch, R., and Scott, M. (2018). Fundamental principles in bacterial physiology - history, recent progress, and the future with focus on cell size control: a review. *Rep. Prog. Phys.* doi: 10.1088/1361-6633/aaa628 [Epub ahead of print].

Jun, S., and Taheri-Araghi, S. (2015). Cell-size maintenance: universal strategy revealed. *Trends Microbiol.* 23, 4–6. doi: 10.1016/j.tim.2014.12.001

Kang, C. M., Nyayapathy, S., Lee, J. Y., Suh, J. W., and Husson, R. N. (2008). Wag31, a homologue of the cell division protein DivIVA, regulates growth,

morphology and polar cell wall synthesis in mycobacteria. *Microbiology* 154, 725–735. doi: 10.1099/mic.0.2007/014076-0

Kieser, K. J., and Rubin, E. J. (2014). How sisters grow apart: mycobacterial growth and division. *Nat. Rev. Microbiol.* 12, 550–562. doi: 10.1038/nrmicro3299

Koch, A. L., and Schaechter, M. (1962). A model for statistics of the cell division process. *J. Gen. Microbiol.* 29, 435–454. doi: 10.1099/00221287-29-3-435

Kuru, E., Tekkam, S., Hall, E., Brun, Y. V., and Van Nieuwenhze, M. S. (2015). Synthesis of fluorescent D-amino acids and their use for probing peptidoglycan synthesis and bacterial growth in situ. *Nat. Protoc.* 10, 33–52. doi: 10.1038/nprot.2014.197

Kysela, D. T., Brown, P. J., Huang, K. C., and Brun, Y. V. (2013). Biological consequences and advantages of asymmetric bacterial growth. *Annu. Rev. Microbiol.* 67, 417–435. doi: 10.1146/annurev-micro-092412-155622

Lagage, V., Boccard, F., and Vallet-Gely, I. (2016). Regional control of chromosome segregation in *Pseudomonas aeruginosa*. *PLoS Genet.* 12:e1006428. doi: 10.1371/journal.pgen.1006428

Landgraf, D., Okumus, B., Chien, P., Baker, T. A., and Paulsson, J. (2012). Segregation of molecules at cell division reveals native protein localization. *Nat. Methods* 9, 480–482. doi: 10.1038/nmeth.1955

Lee, P. S., and Grossman, A. D. (2006). The chromosome partitioning proteins Soj (ParA) and Spo0J (ParB) contribute to accurate chromosome partitioning, separation of replicated sister origins, and regulation of replication initiation in *Bacillus subtilis*. *Mol. Microbiol.* 60, 853–869. doi: 10.1111/j.1365-2958.2006.05140.x

Lin, P. L., Ford, C. B., Coleman, M. T., Myers, A. J., Gawande, R., Ioerger, T., et al. (2014). Sterilization of granulomas is common in active and latent tuberculosis despite within-host variability in bacterial killing. *Nat. Med.* 20, 75–79. doi: 10.1038/nm.3412

Logsdon, M. M., Ho, P. Y., Papavinasasundaram, K., Richardson, K., Cokol, M., Sassetti, C. M., et al. (2017). A parallel adder coordinates mycobacterial cell-cycle progression and cell-size homeostasis in the context of asymmetric growth and organization. *Curr. Biol.* 27, 3367.e7–3374.e7. doi: 10.1016/j.cub.2017.09.046

Maloney, E., Madiraju, M., and Rajagopalan, M. (2009). Overproduction and localization of *Mycobacterium tuberculosis* ParA and ParB proteins. *Tuberculosis* 89(Suppl. 1), S65–S69. doi: 10.1016/S1472-9792(09)70015-0

Manina, G., Dhar, N., and Mckinney, J. D. (2015). Stress and host immunity amplify *Mycobacterium tuberculosis* phenotypic heterogeneity and induce nongrowing metabolically active forms. *Cell Host Microbe* 17, 32–46. doi: 10.1016/j.chom.2014.11.016

Mann, K. M., Huang, D. L., Hooppaw, A. J., Logsdon, M. M., Richardson, K., Lee, H. J., et al. (2017). Rv0004 is a new essential member of the mycobacterial DNA replication machinery. *PLoS Genet.* 13:e1007115. doi: 10.1371/journal.pgen.1007115

Martin, C. J., Cadena, A. M., Leung, V. W., Lin, P. L., Maiello, P., Hicks, N., et al. (2017). Digitally barcoding *Mycobacterium tuberculosis* reveals in vivo infection dynamics in the macaque model of tuberculosis. *mBio* 8:e00312-17 doi: 10.1128/mBio.00312-17

Meniche, X., Otten, R., Siegrist, M. S., Baer, C. E., Murphy, K. C., Bertozzi, C. R., et al. (2014). Subpolar addition of new cell wall is directed by DivIVA in mycobacteria. *Proc. Natl. Acad. Sci. U.S.A.* 111, E3243–E3251. doi: 10.1073/pnas.1402158111

Mierzejewska, J., and Jagura-Burdzy, G. (2012). Prokaryotic ParA-ParB-parS system links bacterial chromosome segregation with the cell cycle. *Plasmid* 67, 1–14. doi: 10.1016/j.plasmid.2011.08.003

Monahan, L. G., Liew, A. T., Bottomley, A. L., and Harry, E. J. (2014). Division site positioning in bacteria: one size does not fit all. *Front. Microbiol.* 5:19. doi: 10.3389/fmicb.2014.00019

Montero Llopis, P., Jackson, A. F., Sliusarenko, O., Surovtsev, I., Heinritz, J., Emonet, T., et al. (2010). Spatial organization of the flow of genetic information in bacteria. *Nature* 466, 77–81. doi: 10.1038/nature09152

Nair, N., Dziedzic, R., Greendyke, R., Muniruzzaman, S., Rajagopalan, M., and Madiraju, M. V. (2009). Synchronous replication initiation in novel *Mycobacterium tuberculosis* dnaA cold-sensitive mutants. *Mol. Microbiol.* 71, 291–304. doi: 10.1111/j.1365-2958.2008.06523.x

Nevo-Dinur, K., Nussbaum-Shochat, A., Ben-Yehuda, S., and Amster-Choder, O. (2011). Translation-independent localization of mRNA in *E. coli*. *Science* 331, 1081–1084. doi: 10.1126/science.1195691

Osella, M., Tans, S. J., and Cosentino Lagomarsino, M. (2017). Step by step, cell by cell: quantification of the bacterial cell cycle. *Trends Microbiol.* 25, 250–256. doi: 10.1016/j.tim.2016.12.005

Pandey, A. K., and Sassetti, C. M. (2008). Mycobacterial persistence requires the utilization of host cholesterol. *Proc. Natl. Acad. Sci. U.S.A.* 105, 4376–4380. doi: 10.1073/pnas.0711159105

Priestman, M., Thomas, P., Robertson, B. D., and Shahrezaei, V. (2017). Mycobacteria modify their cell size control under sub-optimal carbon sources. *Front. Cell Dev. Biol.* 5:64. doi: 10.3389/fcell.2017.00064

Rego, E. H., Audette, R. E., and Rubin, E. J. (2017). Deletion of a mycobacterial divisome factor collapses single-cell phenotypic heterogeneity. *Nature* 546, 153–157. doi: 10.1038/nature22361

Reyes-Lamothe, R., Possoz, C., Danilova, O., and Sherratt, D. J. (2008). Independent positioning and action of *Escherichia coli* replisomes in live cells. *Cell* 133, 90–102. doi: 10.1016/j.cell.2008.01.044

Richardson, K., Bennion, O. T., Tan, S. M., Hoang, A. N., Cokol, M., and Aldridge, B. B. (2016). Temporal and intrinsic factors of rifampicin tolerance in mycobacteria. *Proc. Natl. Acad. Sci. U.S.A.* 113, 8302–8307. doi: 10.1073/pnas.1600372113

Robert, L., Hoffmann, M., Krell, N., Aymerich, S., Robert, J., and Doumic, M. (2014). Division in *Escherichia coli* is triggered by a size-sensing rather than a timing mechanism. *BMC Biol.* 12:17. doi: 10.1186/1741-7007-12-17

Rock, J. M., Lang, U. F., Chase, M. R., Ford, C. B., Gerrick, E. R., Gawande, R., et al. (2015). DNA replication fidelity in *Mycobacterium tuberculosis* is mediated by an ancestral prokaryotic proofreader. *Nat. Genet.* 47, 677–681. doi: 10.1038/ng.3269

Rohde, K. H., Veiga, D. F., Caldwell, S., Balazsi, G., and Russell, D. G. (2012). Linking the transcriptional profiles and the physiological states of *Mycobacterium tuberculosis* during an extended intracellular infection. *PLoS Pathog.* 8:e1002769. doi: 10.1371/journal.ppat.1002769

Santi, I., Dhar, N., Bousbaine, D., Wakamoto, Y., and Mckinney, J. D. (2013). Single-cell dynamics of the chromosome replication and cell division cycles in mycobacteria. *Nat. Commun.* 4:2470. doi: 10.1038/ncomms3470

Santi, I., and McKinney, J. D. (2015). Chromosome organization and replisome dynamics in *Mycobacterium smegmatis*. *mBio* 6:e01999-14. doi: 10.1128/mBio.01999-14

Sauls, J. T., Li, D., and Jun, S. (2016). Adder and a coarse-grained approach to cell size homeostasis in bacteria. *Curr. Opin. Cell Biol.* 38, 38–44. doi: 10.1016/j.ceb.2016.02.004

Schaechter, M., Maaloe, O., and Kjeldgaard, N. O. (1958). Dependency on medium and temperature of cell size and chemical composition during balanced grown of *Salmonella typhimurium*. *J. Gen. Microbiol.* 19, 592–606. doi: 10.1099/00221287-19-3-592

Schumacher, M. A. (2017). Bacterial nucleoid occlusion: multiple mechanisms for preventing chromosome bisection during cell division. *Subcell. Biochem.* 84, 267–298. doi: 10.1007/978-3-319-53047-5_9

Siegrist, M. S., Whiteside, S., Jewett, J. C., Aditham, A., Cava, F., and Bertozzi, C. R. (2013). (D)-Amino acid chemical reporters reveal peptidoglycan dynamics of an intracellular pathogen. *ACS Chem. Biol.* 8, 500–505. doi: 10.1021/cb3004995

Slager, J., and Veening, J. W. (2016). Hard-wired control of bacterial processes by chromosomal gene location. *Trends Microbiol.* 24, 788–800. doi: 10.1016/j.tim.2016.06.003

Sobetzko, P., Travers, A., and Muskhelishvili, G. (2012). Gene order and chromosome dynamics coordinate spatiotemporal gene expression during the bacterial growth cycle. *Proc. Natl. Acad. Sci. U.S.A.* 109, E42–E50. doi: 10.1073/pnas.1108229109

Soifer, I., Robert, L., and Amir, A. (2016). Single-cell analysis of growth in budding yeast and bacteria reveals a common size regulation strategy. *Curr. Biol.* 26, 356–361. doi: 10.1016/j.cub.2015.11.067

Soler-Bistue, A., Mondotte, J. A., Bland, M. J., Val, M. E., Saleh, M. C., and Mazel, D. (2015). Genomic location of the major ribosomal protein gene locus determines *Vibrio cholerae* global growth and infectivity. *PLoS Genet.* 11:e1005156. doi: 10.1371/journal.pgen.1005156

Sukumar, N., Tan, S., Aldridge, B. B., and Russell, D. G. (2014). Exploitation of *Mycobacterium tuberculosis* reporter strains to probe the impact of vaccination at sites of infection. *PLoS Pathog.* 10:e1004394. doi: 10.1371/journal.ppat.1004394

Sveiczer, A., Novak, B., and Mitchison, J. M. (1996). The size control of fission yeast revisited. *J. Cell Sci.* 109(Pt 12), 2947–2957.

Taheri-Araghi, S., Bradde, S., Sauls, J. T., Hill, N. S., Levin, P. A., Paulsson, J., et al. (2015a). Cell-size control and homeostasis in bacteria. *Curr. Biol.* 25, 385–391. doi: 10.1016/j.cub.2014.12.009

Taheri-Araghi, S., Brown, S. D., Sauls, J. T., Mcintosh, D. B., and Jun, S. (2015b). Single-cell physiology. *Annu. Rev. Biophys.* 44, 123–142. doi: 10.1146/annurev-biophys-060414-034236

Takacs, C. N., Poggio, S., Charbon, G., Pucheault, M., Vollmer, W., and Jacobs-Wagner, C. (2010). MreB drives de novo rod morphogenesis in *Caulobacter crescentus* via remodeling of the cell wall. *J. Bacteriol.* 192, 1671–1684. doi: 10.1128/JB.01311-09

Trojanowski, D., Ginda, K., Pioro, M., Holowka, J., Skut, P., Jakimowicz, D., et al. (2015). Choreography of the *Mycobacterium* replication machinery during the cell cycle. *mBio* 6:e02125-14. doi: 10.1128/mBio.02125-14

Trojanowski, D., Holowka, J., Ginda, K., Jakimowicz, D., and Zakrzewska-Czerwinska, J. (2017). Multifork chromosome replication in slow-growing bacteria. *Sci. Rep.* 7:43836. doi: 10.1038/srep43836

Trucco, E., and Bell, G. I. (1970). A note on the dispersionless growth law for single cells. *Bull. Math. Biophys.* 32, 475–483. doi: 10.1007/BF02476766

Vallet-Gely, I., and Boccard, F. (2013). Chromosomal organization and segregation in *Pseudomonas aeruginosa*. *PLoS Genet.* 9:e1003492. doi: 10.1371/journal.pgen.1003492

Vijay, S., Vinh, D. N., Hai, H. T., Ha, V. T. N., Dung, V. T. M., Dinh, T. D., et al. (2017). Influence of stress and antibiotic resistance on cell-length distribution in *Mycobacterium tuberculosis* clinical isolates. *Front. Microbiol.* 8:2296. doi: 10.3389/fmicb.2017.02296

Wakamoto, Y., Dhar, N., Chait, R., Schneider, K., Signorino-Gelo, F., Leibler, S., et al. (2013). Dynamic persistence of antibiotic-stressed mycobacteria. *Science* 339, 91–95. doi: 10.1126/science.1229858

Wallden, M., Fange, D., Lundius, E. G., Baltekin, O., and Elf, J. (2016). The synchronization of replication and division cycles in individual *E. coli* cells. *Cell* 166, 729–739. doi: 10.1016/j.cell.2016.06.052

Wang, S., Furchtgott, L., Huang, K. C., and Shaevitz, J. W. (2012). Helical insertion of peptidoglycan produces chiral ordering of the bacterial cell wall. *Proc. Natl. Acad. Sci. U.S.A.* 109, E595–E604. doi: 10.1073/pnas.1117132109

Wang, X., Montero Llopis, P., and Rudner, D. Z. (2014). *Bacillus subtilis* chromosome organization oscillates between two distinct patterns. *Proc. Natl. Acad. Sci. U.S.A.* 111, 12877–12882. doi: 10.1073/pnas.1407461111

White, C. L., and Gober, J. W. (2012). MreB: pilot or passenger of cell wall synthesis? *Trends Microbiol.* 20, 74–79. doi: 10.1016/j.tim.2011.11.004

WHO (2017). *Global Tuberculosis Report 2017*. Geneva: World Health Organization.

Willis, L., and Huang, K. C. (2017). Sizing up the bacterial cell cycle. *Nat. Rev. Microbiol.* 15, 606–620. doi: 10.1038/nrmicro.2017.79

Wu, L. J., and Errington, J. (2011). Nucleoid occlusion and bacterial cell division. *Nat. Rev. Microbiol.* 10, 8–12. doi: 10.1038/nrmicro2671

Zheng, H., Ho, P. Y., Jiang, M., Tang, B., Liu, W., Li, D., et al. (2016). Interrogating the *Escherichia coli* cell cycle by cell dimension perturbations. *Proc. Natl. Acad. Sci. U.S.A.* 113, 15000–15005. doi: 10.1073/pnas.1617932114

Zhou, X., Halladin, D. K., and Theriot, J. A. (2016). Fast mechanically driven daughter cell separation is widespread in actinobacteria. *mBio* 7:e00952-16. doi: 10.1128/mBio.00952-16

Conflict of Interest Statement: The authors declare that the research was conducted in the absence of any commercial or financial relationships that could be construed as a potential conflict of interest.

frontiers in Microbiology

ORIGINAL RESEARCH
published: 30 July 2018
doi: 10.3389/fmicb.2018.01541

The Empirical Fluctuation Pattern of *E. coli* Division Control

Jacopo Grilli[1], *Clotilde Cadart*[2,3], *Gabriele Micali*[4,5], *Matteo Osella*[6,7] *and Marco Cosentino Lagomarsino*[8,9,10]*

[1] Santa Fe Institute, Santa Fe, NM, United States, [2] Centre National de la Recherche Scientifique, Institut Curie, PSL Research University, UMR 144, Paris, France, [3] Institut Pierre-Gilles de Gennes, PSL Research University, Paris, France, [4] Department of Environmental Microbiology, Eawag, Dübendorf, Switzerland, [5] Department of Environmental Systems Science, ETH Zurich, Zurich, Switzerland, [6] Physics Department, University of Turin, Turin, Italy, [7] Istituto Nazionale di Fisica Nucleare Sezione di Torino, Turin, Italy, [8] Sorbonne Université, Paris, France, [9] Centre National de la Recherche Scientifique, UMR 7238, Paris, France, [10] IFOM, FIRC Institute of Molecular Oncology, Milan, Italy

In physics, it is customary to represent the fluctuations of a stochastic system at steady state in terms of linear response to small random perturbations. Previous work has shown that the same framework describes effectively the trade-off between cell-to-cell variability and correction in the control of cell division of single *E. coli* cells. However, previous analyses were motivated by specific models and limited to a subset of the measured variables. For example, most analyses neglected the role of growth rate variability. Here, we take a comprehensive approach and consider several sets of available data from both microcolonies and microfluidic devices in different growth conditions. We evaluate all the coupling coefficients between the three main measured variables (interdivision times, cell sizes and individual-cell growth rates). The linear-response framework correctly predicts consistency relations between *a priori* independent experimental measurements, which confirms its validity. Additionally, the couplings between the cell-specific growth rate and the other variables are typically non zero. Finally, we use the framework to detect signatures of mechanisms in experimental data involving growth rate fluctuations, finding that (1) noise-generating coupling between size and growth rate is a consequence of inter-generation growth rate correlations and (2) the correlation patterns agree with a near-adder model where the added size has a dependence on the single-cell growth rate. Our findings define relevant constraints that any theoretical description should reproduce, and will help future studies aiming to falsify some of the competing models of the cell cycle existing today in the literature.

Keywords: linear response theory, single-cell growth and division, fluctuation patterns, control of cell division, models, theoretical, data interpretation, statistical

OPEN ACCESS

Edited by:
Ariel Amir,
Harvard University, United States

Reviewed by:
Hanna Salman,
University of Pittsburgh, United States
Sattar Taheri-Araghi,
California State University, Northridge, United States

***Correspondence:**
Marco Cosentino Lagomarsino
marco.cosentino-lagomarsino@ifom.eu

Specialty section:
This article was submitted to Microbial Physiology and Metabolism, a section of the journal Frontiers in Microbiology

Received: *15 March 2018*
Accepted: *20 June 2018*
Published: *30 July 2018*

Citation:
Grilli J, Cadart C, Micali G, Osella M and Cosentino Lagomarsino M (2018) The Empirical Fluctuation Pattern of E. coli *Division Control. Front. Microbiol. 9:1541. doi: 10.3389/fmicb.2018.01541*

1. INTRODUCTION

Today, dynamically tracked data of many dividing cells offer the possibility to analyze with great precision and detail the decision process leading to cell division (Osella et al., 2017). While such data are starting to be abundant, measurements of many single cells yield a complex tangle of correlation patterns between growth-related variables, which is often difficult to grasp. Consequently, new theoretical and data-analysis tools need to be developed in order to extract from such data the relevant information to understand the control of cell-cycle progression, cell division and their impact on cell proliferation.

Specifically, one can restrict the question to the control of cell size, where some general principles are emerging from empirical data. *E. coli* cells grow with a cell-specific growth rate, they are born with a cell-specific size, and they divide with a cell-specific cell-cycle time. A cell that deviates from average behavior in size or growth rate can correct by a compensatory deviation in doubling time. A "near-adder" control of cell division (Campos et al., 2014; Taheri-Araghi et al., 2015), whereby the differential size extension in a single cell cycle is independent of the initial size of the cell, is an effective principle governing cell division. Additionally, the distributions of interdivision times and cell sizes across conditions (Iyer-Biswas et al., 2014b; Kennard et al., 2016) show a clear link between average values and the variability of these variables from cell to cell, thus suggesting a "universal" shape of the size distribution. However, we still understand relatively little regarding how these simple principles emerge (Ho and Amir, 2015; Harris and Theriot, 2016; Wallden et al., 2016; Osella et al., 2017). For example, there is a debate on whether near-adder behavior could emerge from specific mechanisms or molecular circuits (Taheri-Araghi et al., 2015; Harris and Theriot, 2016), as a byproduct of chekpoint control of cell-cycle progression (Adiciptaningrum et al., 2015; Wallden et al., 2016), or as a consequence of external constraints or trade-offs (Osella et al., 2017).

Comprehensive and precise quantitative methods are necessary in both data analysis and theory to deal with the new data. Broadly, the open question is how much a mechanism can be isolated and specified with available data. The simplest theoretical framework for cell-cycle control describes the cell cycle as a discrete-time process, relating the measured variables (size, interdivision times, etc.) across generations (Amir, 2014; Campos et al., 2014; Taheri-Araghi et al., 2015; Grilli et al., 2017). We have recently shown the general existing equivalence between this simple discrete-time formalism to more detailed continuous-time models describing the division process by a division rate varying with cell state and time (Grilli et al., 2017). In the limit where deviations around the mean initial size (or interdivision time) are small (as first proposed in Amir, 2014), we have shown explicitly how the resulting "linear-response" framework describes a wide range of division control mechanisms and characterizes with remarkable precision the available experimental data. These results make the linear-response framework perfectly suitable to model cell-cycle control in *E. coli* given the available datasets.

However, studies are usually restricted to a subset of the measured variables. Most importantly, while single-cell growth rate clearly fluctuates (Wang et al., 2010), very few studies have addressed the consequences of these fluctuations on cell division control, and the studies that did started from very specific assumptions (Osella et al., 2014; Wallden et al., 2016; Logsdon et al., 2017). More specifically, previous studies adopting the linear-response framework typically neglected cell-to-cell variability in growth rates.

Here, we extend this linear-response framework to incorporate growth rate fluctuations, and we show how it can be used in general to evaluate exhaustively all the possible correlations and fluctuations in the data. We use this systematic approach to evaluate jointly all the homeostatic and noise-generating couplings measured in different experimental studies, and to connect correlation patterns with possible mechanisms underlying cell division.

2. DATA SETS

We tested our theoretical considerations and their implications on the analysis of empirical data with *E. coli* single-cell growth division data from Kiviet et al. (2014), Taheri-Araghi et al. (2015), Kennard et al. (2016), and Wallden et al. (2016). Scripts and formatted data are available with the authors. A detailed list of the growth conditions is available in the Supplementary Information of Cadart et al. (2017).

3. LINEAR-RESPONSE FRAMEWORK FOR CELL GROWTH-DIVISION FLUCTUATIONS

3.1. General Features of Fluctuations of Cell Size and Growth Rate

This section describes the main model assumptions and definitions. We assume exponential growth (Campos et al., 2014; Iyer-Biswas et al., 2014b; Osella et al., 2014; Taheri-Araghi et al., 2015) of cell size $V(t) = V(0)\exp(\alpha t)$, where α is the single-cell growth rate. A cell divides at size $V_f = V_0\exp(\alpha\tau_d)$, where V_0 is the size at birth and τ_d is the division time. We neglect the fluctuations around binary fission or the process of filamentation and recovery (Osella et al., 2014), thus cell size at division V_f is equally partitioned between the two daughter cells in our description. Given the assumption of exponential growth, it is useful to introduce the logarithmic size $q(t) = \log(V(t)/V^*)$. With this notation, the exponential growth translates into a linear relationship $q(t) = q(0) + \alpha t$. In the definition of q, we introduced a size scale V^*, which in principle can be an arbitrary scale, to make the argument of the logarithm dimensionless. A particularly useful choice is to define $V^* = \langle V_0\rangle$, so that, at least in the small noise limit, $\langle q(0)\rangle = 0$ independently of the condition (Grilli et al., 2017).

The distribution of cell size at birth gives a static picture of cell-size fluctuations. It is well accepted (Taheri-Araghi et al., 2015; Kennard et al., 2016; Grilli et al., 2017) that the distributions of size at birth (or, equivalently, at division) obtained for different strains and conditions collapse when rescaled by their average. This collapse is the consequence of the existence of a unique size-scale parameter of cell size control that varies across conditions (Kennard et al., 2016; Grilli et al., 2017). A consequence of the collapse is that the expectation of any function of the rescaled size at birth $V_0/\langle V_0\rangle$ is constant across conditions. **Figure 1** shows that the variance of $\log V_0/\langle V_0\rangle$ (which is by definition equal to σ_q^2) is constant across conditions, as predicted by the collapse of the size distribution.

Growth rates fluctuations are usually neglected. Contrarily to the well accepted collapse of the size distributions (Giometto et al., 2013; Taheri-Araghi et al., 2015; Kennard et al., 2016; Grilli et al., 2017), there is no consensus on whether the distribution of the single-cell growth rates collapse when rescaled by the average

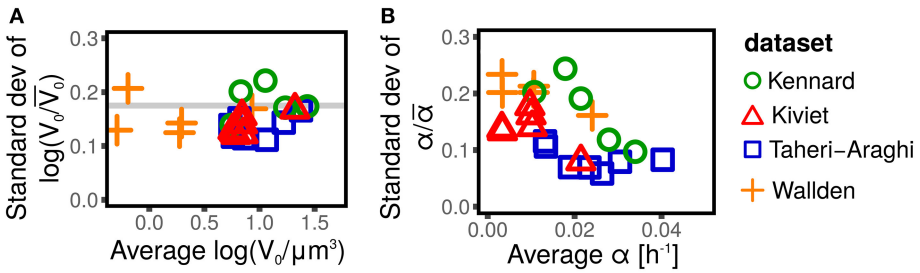

FIGURE 1 | Scaling of size fluctuations, quantified by log-initial size $\log V_0$, and single-cell growth rate α for different datasets (symbols and colors) and conditions. Each symbol represents an average over all single cells available in the dataset (defined by shape and color) for a specific strain in a specific condition. **(A)** Shows that the standard deviation of the rescaled log-initial size $\log(V_0/\langle V_0\rangle)$, is constant across conditions and experiments, and does not depend on the average log-initial size $\langle \log V_0\rangle$. This fact is a consequence of the collapse of initial size distribution (Taheri-Araghi et al., 2015; Kennard et al., 2016; Grilli et al., 2017), since the standard deviation $\log(V_0/\langle V_0\rangle)$ is a function of the coefficient of variation of the initial size only (Grilli et al., 2017). **(B)** Shows the standard deviation of the rescaled growth rate $\alpha/\langle\alpha\rangle$ (which corresponds to the coefficient of variation of α). This quantity is approximately constant for some datasets (e.g., Taheri-Araghi et al., 2015, blue squares), suggesting a collapse of the growth rate distribution (Taheri-Araghi et al., 2015), while it shows a decreasing trend in others (e.g., Kennard et al., 2016, green circles).

growth rate, with some studies reporting the collapse (Taheri-Araghi et al., 2015) and others showing the opposite (Kennard et al., 2016). **Figure 1** shows that the coefficient of variation of the growth rate appears to be constant, independently of the condition and the average growth rate (consistently with the collapse hypothesis) for some datasets (Taheri-Araghi et al., 2015), while it shows a decreasing trend for others (Kiviet et al., 2014; Kennard et al., 2016; Wallden et al., 2016). A possible explanation of these differences could lay in the growth mode of the different experiments (microcolonies in agar or polyacrylamide, wide microfluidics channels, single-file microfluidics channels, etc). Theoretical efforts to provide a rationale of growth rate distributions are available (Iyer-Biswas et al., 2014b; Pugatch, 2015; De Martino et al., 2016; De Martino et al., 2017).

Independently of the controversy about the collapse of the growth rate distributions, it is clear from **Figure 1**, that the fluctuations of the growth rates are not negligible. The coefficients of variation are in the range 0.1–0.3, which is comparable with the typical fluctuations of the sizes at birth, whose CVs are of the order of 0.2 (Amir, 2014; Grilli et al., 2017).

3.2. Linear-Response Framework in Presence of Growth Rate Fluctuations

Since the coefficient of variation of both sizes and growth rates are around 0.2, it is reasonable to assume that the size-control mechanism can be expanded around the average size and average growth rate (Amir, 2014; Grilli et al., 2017). This maps the problem into a discrete-time linear response framework. This section generalizes the usual linear response approach to include single-cell growth rates fluctuations, with the goal of disentangling how size and growth rate fluctuations are connected.

We use a discrete-time description, focusing on a single-cell at a given generation i. This cell has initial size $V_0^{(i)}$, which corresponds to a log-size at birth $q_0^{(i)}$, a growth rate $\alpha^{(i)}$ and divides at a log-size $q_f^{(i)}$ after a time $\tau_d^{(i)}$. These variables are connected by the relation

$$q_f^{(i)} = q_0^{(i)} + \alpha^{(i)}\tau_d^{(i)} \,. \tag{1}$$

We also indicate the net logarithmic multiplicative growth (sometimes referred to as elongation) by

$$G^{(i)} = \alpha^{(i)}\tau_d^{(i)} = \log(V_f^{(i)}/V_b^{(i)}) = q_f^{(i)} - q_0^{(i)} \,.$$

Here, $\alpha^{(i)}$ is a random variable with mean $\langle\alpha\rangle$ (which depends on the condition) and variance σ_α^2. We assume that individual cells maintain the same growth rate for a whole cell cycle (this approximation corresponds to how growth rate distributions are often evaluated in empirical data). The growth rates of subsequent generations are drawn from a common (Gaussian) distribution, but may be correlated across generations, with Pearson correlation coefficient ρ. An alternative approach to model growth fluctuations would consist in modeling the stochastic fluctuations of $\alpha^{(i)}$ in continuous time (Iyer-Biswas et al., 2014a,b). The more minimalistic discrete-time approach that we employ can be seen as a coarse-graining of an appropriate continuous-time model. We also note that the discrete-time modeling approach is equivalent to a continuous-time description for single-exponential growth (Grilli et al., 2017; Ho et al., 2018), but in presence of a growth rate fluctuating in continuous time, this equivalence does not hold anymore. For the small fluctuations observed in the data, the two approaches are qualitatively equivalent and likely quantitatively not distinguishable given the available statistical power.

We introduce the variable fluctuations

$$\begin{aligned} \delta G^{(i)} &:= G^{(i)} - \langle G\rangle \\ \delta\tau_d^{(i)} &:= \tau_d^{(i)} - \langle\tau\rangle \\ \delta\alpha^{(i)} &:= \alpha^{(i)} - \langle\alpha\rangle \\ \delta q_0^{(i)} &:= q_0^{(i)} - \langle q_0\rangle \,. \end{aligned} \tag{2}$$

Under the above assumptions, the evolution equations for the fluctuations of the three main variables can be written as

$$\begin{aligned}\frac{\delta G^{(i)}}{\sigma_G} &= -\lambda_{Gq}\frac{\delta q_0^{(i)}}{\sigma_q} - \lambda_{G\alpha}\frac{\delta\alpha^{(i)}}{\sigma_\alpha} + \nu_G^{(i)} \\ \frac{\delta \tau_d^{(i)}}{\sigma_\tau} &= -\lambda_{\tau q}\frac{\delta q_0^{(i)}}{\sigma_q} - \lambda_{\tau\alpha}\frac{\delta\alpha^{(i)}}{\sigma_\alpha} + \nu_\tau^{(i)}\,,\end{aligned} \tag{3}$$

where λ_{XY} are linear coupling parameters (analogous to "susceptibilities") between measured variables. Such linear couplings are central in comparing this theory to experimental data. $\nu_\tau^{(i)}$ and $\nu_G^{(i)}$ are zero-mean random variables representing cell-to-cell variability ("noise"). Previous approaches neglecting cell size fluctuations assume $\delta\alpha = 0$. In order to be solved, Equation 3 requires the specification of how the fluctuations $\delta\alpha^{(i)}$ are related to the fluctuations of logarithmic size $\delta q_0^{(i)}$. We assume that generally the individual growth rate may depend on the initial size, i.e., within a linear-response framework,

$$\frac{\delta\alpha^{(i)}}{\sigma_\alpha} = -\lambda_{\alpha q}\frac{\delta q_0^{(i)}}{\sigma_q} + \nu_\alpha^{(i)}\,. \tag{4}$$

The values of these coupling constants can be associated to specific mechanisms of size control (Amir, 2014; Grilli et al., 2017). For instance a timer corresponds to $\lambda_{\tau q} = 0$ and $\lambda_{\tau\alpha} = 0$, while a sizer mechanism implies $\lambda_{Gq}\sigma_G/\sigma_q = 1$ and $\lambda_{G\alpha} = 0$. A standard adder corresponds instead to $\lambda_{Gq}\sigma_G/\sigma_q = 1/2$ (Amir, 2014; Grilli et al., 2017).

This general framework can be used to evaluate the direct couplings between fluctuations of birth size, growth rate and division time. In particular, all the couplings λs can be evaluated from the Pearson correlations of these variables or from the slope of conditional averages. The two methods are equivalent if the slopes are estimated using least-squares method. Indeed, assuming a relationship $y = \beta * x +$ noise , and performing a linear regression, the least-square estimate of beta is $\beta = \mathrm{cov}(x, y)/\mathrm{var}(x)$. Any discrepancy of the values of the coupling parameters obtained in these two different ways should be considered as a signature of the violation of the linear-response regime (Cadart et al., 2017). For instance, by multiplying both sides of Equation (4) by $\delta q_0/\sigma_q$ and averaging over the fluctuations, it is easy to obtain (see Supplementary Information)

$$c_{\alpha q} = -\lambda_{\alpha q}\,, \tag{5}$$

where $c_{\alpha q}$ is the Pearson correlation between the growth rate α and the log-size q. Similarly, multiplying by $\delta q/\sigma_q$ Equation (3) and averaging gives

$$c_{\tau q} = -\lambda_{\tau q} - \lambda_{\tau\alpha}c_{\alpha q} = -\lambda_{\tau q} + \lambda_{\tau\alpha}\lambda_{\alpha q}\,. \tag{6}$$

Finally, multiplying the same equation by $\delta\alpha/\sigma_\alpha$ and averaging over fluctuations gives

$$c_{\tau\alpha} = -\lambda_{\tau q}c_{\alpha q} - \lambda_{\tau\alpha} = -\lambda_{\tau\alpha} + \lambda_{\tau q}\lambda_{\alpha q}\,. \tag{7}$$

A detailed comparison between the two ways to evaluate the couplings in empirical data is shown in the Supplementary Information of Cadart et al. (2017). The very small discrepancies found reinforce the ideas that the linear-response framework is effective.

The last two equations clearly show that the presence of a non-zero coupling between single-cell growth rate and birth size induces a non-trivial dependence of the correlations from all the coupling parameters. In other words, when the coupling between division time and cell size is estimated uniquely from $c_{\tau q}$ (Amir, 2014; Grilli et al., 2017), one is measuring a combination of two different effects: the direct coupling between division time and size at birth and an indirect coupling mediated by growth rate fluctuations.

Direct and indirect effects can be disentangled by solving Equations (6) and (7) to calculate $\lambda_{\tau q}$ and $\lambda_{\tau\alpha}$ in terms of measurable covariances,

$$\lambda_{\tau q} = -\frac{c_{\tau q} - c_{\alpha q}c_{\tau\alpha}}{1 - c_{\alpha q}^2}\,, \tag{8}$$

and

$$\lambda_{\tau\alpha} = -\frac{c_{\tau\alpha} - c_{\alpha q}c_{\tau q}}{1 - c_{\alpha q}^2}\,. \tag{9}$$

Figure 2 illustrates this procedure over one example dataset.

The main assumption of the above modeling framework is that all the relations between the variables are linear. Deviations from linear response are not captured, but in the data these are fairly small (see **Figure 2**). Additionally, it is difficult to evaluate precisely the non-linear behavior from data because the statistics decreases radically for large fluctuations where such non-linear trends are stronger. Given the statistical power available from existing datasets, it is typically not possible to discriminate non-linear terms from stochastic fluctuations (Grilli et al., 2017).

It has previously been noted that measured Pearson correlations between observed variables in such experiments are very sensitive to (experimental and biological) noise (Eun et al., 2018), so that it is not simple to reconstruct mechanisms from correlations. Our approach, which directly tackles this issue, has two main advantages. First, it subtracts the contributions of indirect correlations and only measures direct couplings. Second, the coupling constants are insensitive to noise, because they are defined as linear slopes of conditional averages, and therefore robust to experimental noise. This is supported by the analysis of Cadart et al. (2017) mentioned above, verifying the equivalence between theory coupling constants measured directly and their expressions in terms of covariances. Indeed, this equivalence not only supports the validity of the linear regime, but also reinforces the idea that scatter in the data (due e.g., to experimental noise) does not bias too much the coupling constants, when they are estimated from the covariances.

We also note that the choice of parameters in Equations (3) and (4) is not unique. There are several alternative (equivalent) choices of fluctuating variables, linked by the condition that $G =$

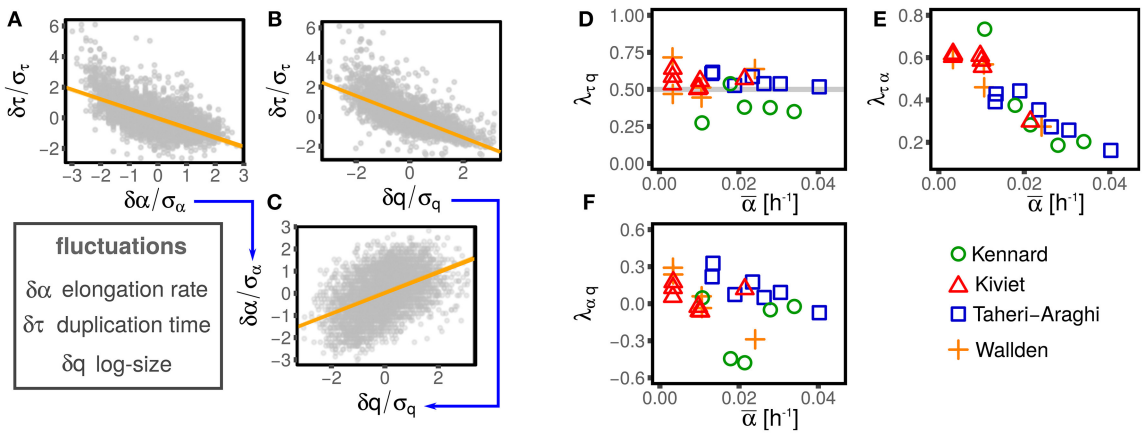

FIGURE 2 | Illustration of the linear-response framework of size control, including growth rate fluctuations. **(A,B)** Show the dependency of the interdivision time fluctuations from fluctuations of logarithmic initial size and growth rate for one dataset (Wallden et al., 2016 intermediate growth rate). Since growth rate and size fluctuations are not independent **(C)**, the slopes observed in **(A,B)** are determined by a combination of the coupling between size fluctuation and interdivision time (with strength $\lambda_{\tau q}$, see Equation 2) and the effect of growth rate fluctuation on interdivision time (with strength $\lambda_{\tau\alpha}$, see Equation 2). The method described in the text disentangles direct and indirect effect on the slopes of **(A–C)** to obtain the direct couplings between τ, α, and q, which are shown in **(D–F)**, for different datasets (symbols and colors) and conditions. Interestingly, all the possible couplings are non-zero. Current models do not describe these nontrivial correlations, which poses a challenge to future models.

$\alpha\tau$: α, τ, q; α, G, q; G, τ, q. Each triplet carries a set of linear-response coupling constants between pairs of variables that can be mapped to the ones defined above.

4. RESULTS

4.1. All the Possible Couplings Between Measured Variables Are Non-zero in Empirical Datasets

One might expect that not all the possible couplings are different from zero, supporting the simplifying assumptions made by most studies. **Figure 2** shows instead that all the independent couplings $\lambda_{\tau q}$, $\lambda_{\tau\alpha}$, and $\lambda_{\alpha q}$ are in fact not negligible.

The existence of nonzero couplings between division time and growth rate $\lambda_{\tau\alpha}$ or, equivalently, elongation and growth rate $\lambda_{G\alpha}$ (see next section and **Figure 3**) suggests that cell size control depends in a non-trivial way on growth rate fluctuations. Moreover, the existence of a coupling between growth rates and cell size (measured by the coefficient $\lambda_{\alpha q}$), affects the observed correlation between division time and size at birth $c_{\tau q}$ (see Equation 6), or, equivalently, the slope of the size-growth plot c_{Gq} (Skotheim, 2013), which is normally used to evaluate the strength of the size control. Different values of these correlations are associated with different strengths of cell size control (Skotheim, 2013; Osella et al., 2014), and, more indirectly, to different cell size control mechanisms (Amir, 2014; Grilli et al., 2017). The presence of non-zero couplings between interdivision time and growth rate and between growth rate and size effectively reduces or increases the observed strength of homeostasis, and might be a signature of the mechanisms effecting such control.

4.2. The Linear-Response Framework Allows to Define Consistency Relations

As discussed above, the framework provides equivalent alternative descriptions for the interdivision time τ or the net growth G as state variables. These two parameter settings are equivalent under the linear-control assumption. This section deals with the mapping between these parametrizations, and reports consistency tests defined by the expected relations using empirical data.

The consistency relations can be obtained from the relation $G^{(i)} = \alpha^{(i)}\tau^{(i)}$, which, under the linearization assumption reduces to (see Supplementary Information)

$$\delta G^{(i)} = \langle\tau\rangle\delta\alpha^{(i)} + \langle\alpha\rangle\delta\tau^{(i)}\,. \tag{10}$$

Using this relation together with Equation (3), one obtains (see Supplementary Information)

$$\lambda_{Gq} = \langle\alpha\rangle\lambda_{\tau q}\frac{\sigma_\tau}{\sigma_G} \tag{11}$$

and

$$\lambda_{G\alpha} = \langle\alpha\rangle\lambda_{\tau\alpha}\frac{\sigma_\tau}{\sigma_G} + \langle\tau\rangle\frac{\sigma_\alpha}{\sigma_G}\,. \tag{12}$$

An important consequence of Equation (12) is that a nonzero $\lambda_{G\alpha}$ (or $\lambda_{\tau\alpha}$) could appear even if the corresponding coupling $\lambda_{\tau\alpha}$ (or $\lambda_{G\alpha}$) was null. For instance, if the coupling $\lambda_{\tau\alpha}$ is negligible, indicating that the interdivision time is independent from the single-cell growth rate, one would still observe a nonzero $\lambda_{G\alpha}$. In fact, in that case, the division time would be independent of the growth rate and therefore, in the same amount of time, cells growing faster would grow more than slow-growing cells. Interestingly, this is not the case. Both $\lambda_{\tau\alpha}$ (see **Figure 2**) and $\lambda_{G\alpha}$

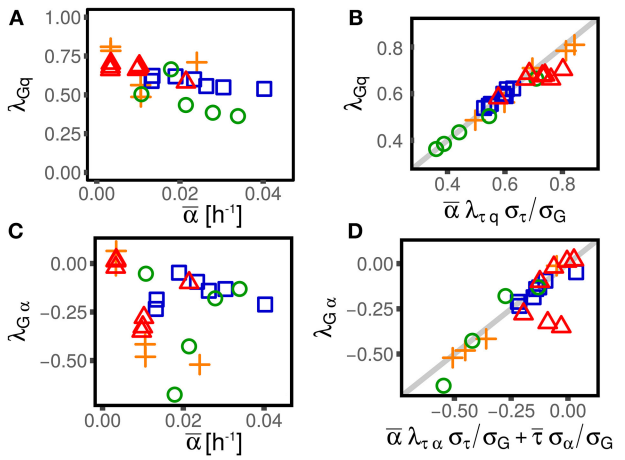

FIGURE 3 | Alternative parameterizations of cell-size control linear response are consistent across different experimental datasets and conditions (symbols and colors are the same as in **Figure 1**). One can parametrize the effect of size and growth rate fluctuations on interdivision time, or, alternatively, their effect on the final size (or the elongation *G*). **(A,C)** Show the effect of log-size fluctuation on elongation (with strength λ_{Gq}, see Equation 3) and the effect of growth rate fluctuation on interdivision time (with strength $\lambda_{G\alpha}$). The linear framework predicts consistency relations between the alternative parameterizations **(B,D)**, which are verified across datasets and conditions in the plots in the right panel.

are in fact different from zero (see **Figure 2**), suggesting that some specific mechanism must be at play in determining their value.

Figure 3 shows that these consistency relations are verified in the data. This result shows that the generalization of the linear-response framework to include growth rate fluctuations can correctly describe the data. As previously discussed, small deviations from these relations could be due to the presence of non-linearities that cannot be captured by the theoretical framework. However, non-linearities can be appreciated only in presence of large fluctuations (Grilli et al., 2017). Also note that while these deviations could be the signature of not-yet-understood biological mechanisms, they could also come from measurement, segmentation or tracking errors associated to specific experimental and image-analysis protocols.

4.3. Growth Rate Fluctuations Can Confound Standard Tests of Division Control Mechanisms, the Case of "Grower" vs. "Timer"

A standard simple analysis to understand what kind of cell division control is in place is based on size-growth plots (Skotheim, 2013) and more generally on measures of correlation between cell elongation and initial size. Since growth rate fluctuations are typically neglected, a value of $\lambda_{Gq} = 0$, i.e., no correlation between elongation and size at birth (**Figure 4A**), is usually interpreted as the signature of a "timer." However, in presence of growth rate fluctuations the value of this coupling parameter alone is not enough to pinpoint a single mechanism. In fact, $\lambda_{Gq} = 0$ can be the actual result of a timer, i.e., $\lambda_{\tau q} = 0$ which then requires that $\lambda_{\tau\alpha} = 0$ (**Figure 4B**). However, the relevant variable that is actually uncoupled to size could be the net growth (elongation) itself, rather than the doubling time and the growth rate. In this case, one has a "grower" (**Figure 4C**), for which again $\lambda_{Gq} = 0$ and $\lambda_{G\alpha} = 0$. For a grower, $\lambda_{\tau q} = 0$, but $\lambda_{\tau\alpha} = -\langle\tau\rangle\sigma_\alpha/(\langle\alpha\rangle\sigma_\tau)$. Importantly, if $\lambda_{\alpha q} \neq 0$, then the correlation between τ and q ($c_{\tau q}$) is also different from zero in a grower. This illustrative example emphasizes the importance of keeping into account growth rate fluctuations in order to correctly interpret empirical correlations patterns. It also shows how the linear-response framework proposed here can be used to delineate the correct interpretation. A more general decomposition of contribution of growth vs. timing coupling to size control is discussed in Cadart et al. (2017).

We now proceed to describe two situations where our analysis points directly to specific mechanisms contributing to the complexity of the observed correlation patterns.

4.4. Mother-Daughter Growth Rate Correlations Explain the Prevalent Negative Coupling Between Growth Rates and Cell Size Observed in Data

Since the framework describes exhaustively the measured correlations in the datasets, it can be used to explore signatures of mechanisms by which division is coupled to size. This section provides a rationale for the emergence of a non-zero coupling between single-cell growth rate and size at birth $\lambda_{\alpha q}$ observed in most datasets. In particular, we show that a negative $\lambda_{\alpha q}$ may emerge from the presence of a correlation between the growth rates across generations.

Figure 5 shows the Pearson correlation ρ between the mother and the daughter(s) growth rates in several data sets. We computed the correlation using both the daughters (when available in the dataset). Some previous studies have reported, or assumed, small mother-daughter correlations in growth rate (Wang et al., 2010; Eun et al., 2018), while others have found larger ones (Wallden et al., 2016). An important result of the present analysis is that this correlation is never negligible in the analyzed data sets and appears very conserved across conditions and experimental setup. Specifically, all the datasets considered here show a significantly positive correlation, which does not seem to depend strongly on the condition and takes values around 0.3. Variations of single-cell growth rates can be both due to an external origin (e.g., local variation of nutrients in an agar experiment) or inherent to the mechanisms of growth (e.g., from fluctuations in gene expression Iyer-Biswas et al., 2014a). In both cases, one may expect the presence of positive correlation across generations.

We can model mother-daughter correlations in growth rate as a linear constraint on the single-cell growth rates over generations

$$\delta\alpha^{(i+1)} = \rho\delta\alpha^{(i)} + \sigma_\alpha \nu_\alpha^{(i)} . \quad (13)$$

This equation substitutes Equation (4), and must be considered together with Equation 3. The question we address is whether

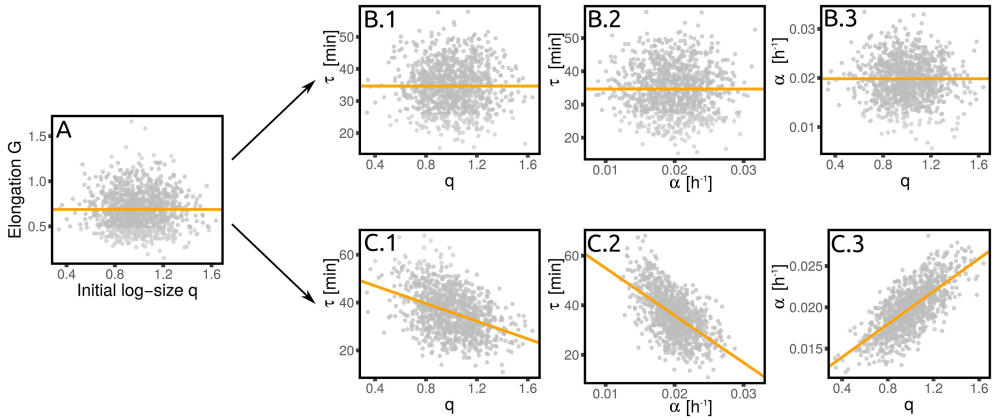

FIGURE 4 | A grower is not a timer. The absence of a correlation between elongation and initial size **(A)** does not necessarily imply a timer **(B)**, where the interdivision time is independent of the initial size. **(C)** Shows the alternative scenario (the grower), where the growth rate depends on the initial size. This correlation, together with the independence of the elongation from the growth rate, implies a dependence of the interdivision time on both initial size and growth rate. Both panels are obtained from numerical simulations of the corresponding linearized model with $\sigma_\alpha/\langle\alpha\rangle = 0.2$ and $\sigma_q^2 = 0.2$.

inter-generational correlations give rise to a non-zero coupling $\lambda_{\alpha q}$ between single-cell growth rate and size.

Since we are considering a fully linear framework, a non-zero coupling $\lambda_{\alpha q}$ can be directly mapped into a non-zero correlation between single-cell growth rate and size $c_{\alpha q}$ via Equation (5). We find that a non-zero correlation $c_{\alpha q}$ emerges in presence of a non-zero correlation of growth rate across generation and a non-zero coupling $\lambda_{G\alpha}$. In the Supplementary Information we obtain the relation

$$\lambda_{\alpha q} = -c_{\alpha q} = \rho \frac{\lambda_{G\alpha}}{1 - \rho(1 - \lambda_{Gq}\sqrt{\frac{\sigma_G^2}{\sigma_q^2}})} \sqrt{\frac{\sigma_G^2}{\sigma_q^2}} \,. \tag{14}$$

From the above equation we observe that, for positive ρ and negative $\lambda_{G\alpha}$ (the case of empirical data) only negative couplings $\lambda_{\alpha q}$ can emerge. Hence, mother-daughter growth rate correlations provide a rationale for this widespread negative coupling.

Figure 5 shows that the prediction of Equation (14) quantitatively reproduces the values of $\lambda_{\alpha q}$ for the datasets that display negative values of this coupling. On the other hand, some datasets have weakly positive couplings $\lambda_{\alpha q}$, which cannot be reproduced via this mechanism. This suggests that some other unknown mechanisms might play a role in coupling growth rates and sizes.

4.5. An Adder Model Captures the Experimental Correlation Patterns Only If Added Size Depends on Single-Cell Growth Rate

This section explores how the observed negative values for the coupling $\lambda_{G\alpha}$ emerge from a simple extension of the adder model that explicitly includes growth rate fluctuations. According to the adder model (Amir, 2014; Taheri-Araghi et al., 2015), the size at division V_f is given by

$$V_f = (V_0 + \Delta)e^{\nu} \,, \tag{15}$$

where Δ is the added size and ν is a noise term. We also know that the average size $\langle V_0\rangle$ has an exponential dependence on the average growth rate $\langle\alpha\rangle$, which is often referred to as Schaechter's law (Schaechter et al., 1958; Taheri-Araghi et al., 2015; Kennard et al., 2016; Si et al., 2017). Since for steadily dividing cells the average size at birth is equal to the added size, the exponential dependence of the average size on the average growth rate also implies that the average added size must have an exponential dependence on the average growth rate.

Equation (15) does not take into account fluctuations of the growth rate, and there are several possibilities to extend it. Schaechter's law can be seen as a constraint, as the added size averaged over fluctuations of the growth rate has to scale nearly exponentially with the average growth rate. Two possible extreme scenarios can be disentangled with the data. The first scenario assumes that in a given growth condition the added size does not depend on the fluctuation of the growth rate, i.e.,

$$\Delta = S_0 \exp(\langle\alpha\rangle T) \,. \tag{16}$$

In such case, two cells with different individual growth rates, but growing in the same condition, will add (on average) the same size. In the opposite extreme scenario, the added size depends on the single-cell growth rate, following Schaecter's law *even for small fluctuations*

$$\Delta = S_0 \exp(\alpha T) \,. \tag{17}$$

In this second scenario, cells in the same growth conditions growing at different growth rates will add on average different sizes. Conversely, cells growing under different conditions but having the same growth rate due to single-cell fluctuations will

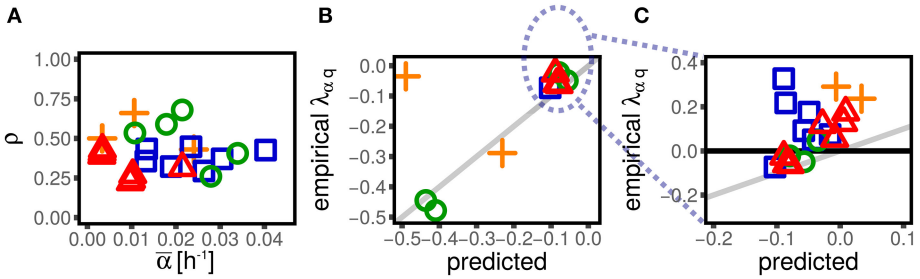

FIGURE 5 | Mother-daughter correlations in growth rate induce negative values of $\lambda_{\alpha q}$. **(A)** Shows the correlation between mother and daughter growth rate across datasets (symbols and colors, see **Figure 1**) and conditions. All the datasets display a significant positive correlation. Panel shows the value of $\lambda_{\alpha q}$ predicted from our theory assuming the empirical mother-daughter growth rate correlations (see Equation 14), compared to the empirical ones for negative values of $\lambda_{\alpha q}$. The assumed mechanism correctly predicts negative values of $\lambda_{\alpha q}$, but the prediction cannot capture the datasets with positive values of $\lambda_{\alpha q}$, which are shown in **(C)** (not visible in **B**).

add (on average) the same size. Since fluctuations of α are small, in both cases the average added size $\langle\Delta\rangle$ will scale exponentially with the average growth rate.

This question was approached in Kennard et al. (2016), but the linear-response theoretical framework gives us the tools to reformulate it more precisely. **Figure 6** shows how we proceed to test the two scenarios. For each dataset we estimated the parameter T (which can be related to the duration of the replication/segregation ("C+D") period Donachie, 1968; Zheng et al., 2016; Si et al., 2017) from $\langle\log\Delta\rangle$ averaged across cells within each condition. Note that for both Equations (16) and (17), the slope of $\langle\log\Delta\rangle$ *vs* $\langle\alpha\rangle$ is T. For each condition, one can then compare the relation between the (logarithmic) added size and the individual growth rate. Under the first scenario, the relation should show no dependency (a flat slope). Under the second scenario, one should instead expect a linear relation with slope T (where T is the mean timing from replication initiation to division, assumed to be nearly constant across conditions).

Under the assumption that fluctuations are small, one can linearize the models and compare the coupling coefficients. In the first case, one obtains $\lambda_{G\alpha} = 0$, while in the second case a non-trivial coupling arises with value

$$\lambda_{G\alpha} = \frac{\sigma_\alpha}{\sigma_G} - \frac{T}{2}. \tag{18}$$

Figure 6 compares this prediction with the empirical values of this coupling parameter measured across datasets, obtaining a remarkable agreement. It is important to stress that the parameter T, which in turn determines the value of $\lambda_{G\alpha}$, has been measured only using the dependence of average added size on the average growth rate across different conditions, without considering single-cell data. This procedure assumes that the parameters S_0 and T are constant within each dataset across different conditions (Donachie, 1968; Si et al., 2017). Variation around Schaecter's law, which could arise for many reasons (Zheng et al., 2016; Si et al., 2017), can affect the values of these parameters. Precise estimates, or measurements of T can improve the prediction of Equation (18). Moreover, the variability around

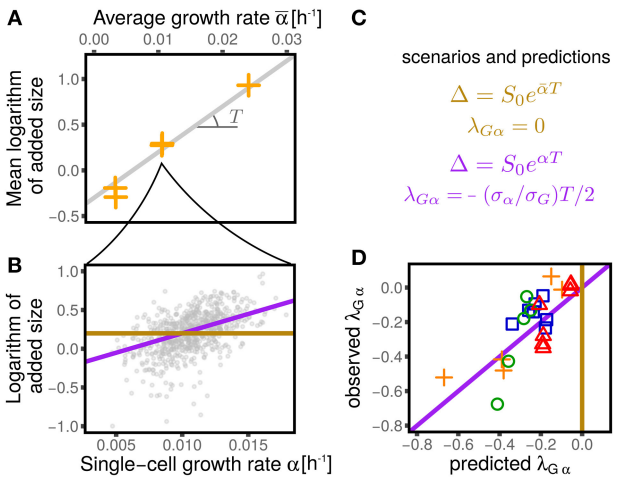

FIGURE 6 | Dependency of added size on single-cell growth rates and effect on the values of $\lambda_{G\alpha}$. **(A)** Shows that the average logarithmic added size is linear when plotted against the average growth rate (for all the conditions from Wallden et al., 2016). We consider two extreme scenarios for the logaritmic added size of individual cells: it could depend only on the average growth rate (gold line) or it could linearly grow with the single-cell growth rate (purple line), with the same slope observed in **(A)**. **(B)** Shows the results of the two scenarios for one condition (intermediate growth rate data set from Wallden et al., 2016). These two scenarios translate into two different predictions for the value of $\lambda_{G\alpha}$, which are reported in panel **(C)** and tested in panel **(D)**. The non-zero values of $\lambda_{G\alpha}$ are therefore a consequences of the dependence of the added size on the the single-cell growth rate.

the adder mechanism (visible in the values of λ_{Gq} plotted in **Figure 3**) also affects the predictions.

5. DISCUSSION AND CONCLUSIONS

With a long list of recent published studies, the current literature on cell division control remains fragmented in terms of conceptual tools and conclusions on the data (Osella et al., 2017).

This work proposes an extension of the linear-response framework to include growth rate fluctuations, and at the same time provides a comparative meta-analysis of different datasets.

As such, we hope it could be useful to the community. The results lead us to propose the linear-response model as a basic common data-analysis framework for the recent (and future) growth division data obtained on bacteria.

Analyzing the experimental data, we found two important results. First, the linear response framework including growth rate fluctuations provides a remarkably good description of the data. Couplings are in all cases only moderately nonlinear (Grilli et al., 2017), and all the predicted self-consistency relations are verified to a satisfactory degree. This carries the important lesson that models where nonlinear couplings are involved might be true, but they would be hard to test with the currently available data. Second, we show that the linear correlation patterns store a wealth of information that is not yet fully appreciated. In particular, single-cell growth rates seem to have a complex effect on cell cycle progression and cell-division control.

The study of the linear coupling parameters between growth rate and size reveals an unexpected variability across experiments. This variability depends on the growth conditions and on the measured mother-daughter correlations in growth rate. Thus, the effect of growth rate fluctuations on cell size varies from one experiment to the other and appears, in some cases, to contribute to size correction. In contrast, the near-adder correlation for the net growth G and the dependency of interdivision time on initial size are robustly observed in all datasets, although quantitatively, they also vary across conditions.

Since all these linear-response effects are clearly testable, we believe that future efforts should be funneled into explaining these patterns comprehensively. Each particular model for a size control mechanism carries a set of constraints for the linear-coupling parameters, which are easily testable in the data. Such testing involves all the measured variables and correlations. Hence, our framework provides a comprehensive and stringent tool to test proposed mechanisms.

The question of specifying the mechanisms for cell division and cell-cycle progression remains largely open, and therefore could benefit from such a systematic tool. One main limitation of current studies is that they discard relevant information and only consider a subset of correlation patterns. Conversely, linear-coupling parameters allow to control all the measured correlations at once. In this work, we provided a proof of principle that this plan of action can be effective by studying two simple examples: (i) the role of mother-daughter correlations in size control, and (ii) the role of growth rate fluctuation in determining the added size.

In particular, we find that growth rate fluctuations are not consistent with an adder model where the added size does not depend on the single-cell growth rate. This could be an important clue on the mechanism underlying the adder behavior and could help selecting one of the currently proposed models (Ho and Amir, 2015; Taheri-Araghi et al., 2015; Harris and Theriot, 2016; Wallden et al., 2016).

Finally, we address the coherence between different experimental data sets. The discrepancies we found could be due to biological factors, but also to possible sources of experimental noise and systematic errors in the data. Current experimental and data-analysis pipelines are different in both the segmentation and tracking steps. This problem is largely disregarded and in particular we know very little about possible induced biases in the measured correlations, which would lead to different conclusions on the mechanistic aspects. As end-users of the data, we propose our pipeline, i.e., comparing all measurable linear correlations as a useful testing ground for different datasets. In our analysis, we have noticed different trends depending on the experimental laboratory, and growth device, as well as outlier points where possibly the growth conditions were not steady or the analysis had problems. Interestingly, while some observations are robust, others are more erratic across datasets. Beyond this, we can just encourage the experimentalists to adopt common protocols and shared comparison pipelines in future studies. It would be sufficient to define a well defined "reference experiment" with fixed strain, growth device, and growth conditions that each data set needs to share, in order to make precise comparisons possible.

AUTHOR CONTRIBUTIONS

MCL and JG planned the study. JG, MCL, and MO developed the modeling framework, JG, CC, and GM, analyzed data. JG and MCL outlined and wrote the paper. MO, CC, and GM contributed with scientific discussion and critical reading.

ACKNOWLEDGMENTS

This work was supported by the International Human Frontier Science Program Organization, grant RGY0070/2014. We acknowledge useful discussions with A. Amir. MO is supported by the Departments of Excellence Grant awarded by the Italian Ministry of Education, University and Research (MIUR) (L. 232/2016). GM was supported by grant no. 31003A 169978 from the Swiss National Science Foundation to Martin Ackermann. JG was supported by an Omidyar Postdoctoral Fellowship at the Santa Fe Institute.

SUPPLEMENTARY MATERIAL

The Supplementary Material for this article can be found online at: https://www.frontiersin.org/articles/10.3389/fmicb.2018.01541/full#supplementary-material

REFERENCES

Adiciptaningrum, A., Osella, M., Moolman, M. C., Cosentino Lagomarsino, M., and Tans, S. J. (2015). Stochasticity and homeostasis in the e. coli replication and division cycle. *Sci. Rep.* 5:18261. doi: 10.1038/srep18261

Amir, A. (2014). Cell size regulation in bacteria. *Phys. Rev. Lett.* 112:208102. doi: 10.1103/PhysRevLett.112.208102

Cadart, C., Monnier, S., Grilli, J., Attia, R., Terriac, E., Baum, B., et al. (2017). Size control in mammalian cells involves modulation of both growth rate and cell cycle duration. *bioRxiv 152728*. doi: 10.1101/152728

Campos, M., Surovtsev, I. V., Kato, S., Paintdakhi, A., Beltran, B., Ebmeier, S. E., et al. (2014). A constant size extension drives bacterial cell size homeostasis. *Cell* 159, 1433–1446. doi: 10.1016/j.cell.2014.11.022

De Martino, D., Capuani, F., and De Martino, A. (2016). Growth against entropy in bacterial metabolism: the phenotypic trade-off behind empirical growth rate distributions in *E. coli*. *Phys. Biol.* 13:036005. doi: 10.1088/1478-3975/13/3/036005

De Martino, D., Capuani, F., and De Martino, A. (2017). Quantifying the entropic cost of cellular growth control. *Phys. Rev. E* 96:010401. doi: 10.1103/PhysRevE.96.010401

Donachie, W. D. (1968). Relationship between cell size and time of initiation of DNA replication. *Nature* 219, 1077–1079. doi: 10.1038/2191077a0

Eun, Y.-J., Ho, P.-Y., Kim, M., LaRussa, S., Robert, L., Renner, L. D., et al. (2018). Archaeal cells share common size control with bacteria despite noisier growth and division. *Nat. Microbiol.* 3, 148–154. doi: 10.1038/s41564-017-0082-6

Giometto, A., Altermatt, F., Carrara, F., Maritan, A., and Rinaldo, A. (2013). Scaling body size fluctuations. *Proc. Natl. Acad. Sci. U.S.A.* 110, 4646–4650. doi: 10.1073/pnas.1301552110

Grilli, J., Osella, M., Kennard, A. S., and Lagomarsino, M. C. (2017). Relevant parameters in models of cell division control. *Phys. Rev. E* 95:032411. doi: 10.1103/PhysRevE.95.032411

Harris, L. K., and Theriot, J. A. (2016). Relative rates of surface and volume synthesis set bacterial cell size. *Cell* 165, 1479–1492. doi: 10.1016/j.cell.2016.05.045

Ho, P.-Y., and Amir, A. (2015). Simultaneous regulation of cell size and chromosome replication in bacteria. *Front. Microbiol.* 6:662. doi: 10.3389/fmicb.2015.00662

Ho, P.-Y., Lin, J., and Amir, A. (2018). Modeling cell size regulation: from single-cell level statistics to molecular mechanisms and population level effects. *Annu. Rev. Biophys.* 47, 251–271. doi: 10.1146/annurev-biophys-070317-032955

Iyer-Biswas, S., Crooks, G. E., Scherer, N. F., and Dinner, A. R. (2014a). Universality in stochastic exponential growth. *Phys. Rev. Lett.* 113:028101. doi: 10.1103/PhysRevLett.113.028101

Iyer-Biswas, S., Wright, C. S., Henry, J. T., Lo, K., Burov, S., Lin, Y., et al. (2014b). Scaling laws governing stochastic growth and division of single bacterial cells. *Proc. Natl. Acad. Sci. U.S.A.* 111, 15912–15917. doi: 10.1073/pnas.1403232111

Kennard, A. S., Osella, M., Javer, A., Grilli, J., Nghe, P., Tans, S. J., et al. (2016). Individuality and universality in the growth-division laws of single E. coli cells. *Phys. Rev. E* 93:012408. doi: 10.1103/PhysRevE.93.012408

Kiviet, D. J., Nghe, P., Walker, N., Boulineau, S., Sunderlikova, V., and Tans, S. J. (2014). Stochasticity of metabolism and growth at the single-cell level. *Nature* 514, 376–379. doi: 10.1038/nature13582

Logsdon, M. M., Ho, P.-Y., Papavinasasundaram, K., Richardson, K., Cokol, M., Sassetti, C. M., et al. (2017). A parallel adder coordinates mycobacterial cell-cycle progression and cell-size homeostasis in the context of asymmetric growth and organization. *Curr. Biol.* 27, 3367–3374.e7. doi: 10.1016/j.cub.2017.09.046

Osella, M., Nugent, E., and Cosentino Lagomarsino, M. (2014). Concerted control of Escherichia coli cell division. *Proc. Natl. Acad. Sci. U.S.A.* 111, 3431–3435. doi: 10.1073/pnas.1313715111

Osella, M., Tans, S. J., and Cosentino Lagomarsino, M. (2017). Step by step, cell by cell: quantification of the bacterial cell cycle. *Trends Microbiol.* 25, 250–256. doi: 10.1016/j.tim.2016.12.005

Pugatch, R. (2015). Greedy scheduling of cellular self-replication leads to optimal doubling times with a log-fréchet distribution. *Proc. Natl. Acad. Sci. U.S.A.* 112, 2611–2616. doi: 10.1073/pnas.1418738112

Schaechter, M., Maaløe, O., and Kjeldgaard, N. O. (1958). Dependency on medium and temperature of cell size and chemical composition during balanced grown of salmonella typhimurium. *J. Gen. Microbiol.* 19, 592–606. doi: 10.1099/00221287-19-3-592

Si, F., Li, D., Cox, S. E., Sauls, J. T., Azizi, O., Sou, C., et al. (2017). Invariance of initiation mass and predictability of cell size in *Escherichia coli*. *Curr. Biol.* 27, 1278–1287. doi: 10.1016/j.cub.2017.03.022

Skotheim, J. M. (2013). Cell growth and cell cycle control. *Mol. Biol. Cell* 24:678. doi: 10.1091/mbc.E13-01-0002

Taheri-Araghi, S., Bradde, S., Sauls, J. T., Hill, N. S., Levin, P. A., Paulsson, J., et al. (2015). Cell-size control and homeostasis in bacteria. *Curr. Biol.* 25, 385–391. doi: 10.1016/j.cub.2014.12.009

Wallden, M., Fange, D., Lundius, E. G., Baltekin, Ö., and Elf, J. (2016). The synchronization of replication and division cycles in individual *E. coli* cells. *Cell* 166, 729–739. doi: 10.1016/j.cell.2016.06.052

Wang, P., Robert, L., Pelletier, J., Dang, W. L., Taddei, F., Wright, A., et al. (2010). Robust growth of *Escherichia coli*. *Curr. Biol.* 20, 1099–1103. doi: 10.1016/j.cub.2010.04.045

Zheng, H., Ho, P.-Y., Jiang, M., Tang, B., Liu, W., Li, D., et al. (2016). Interrogating the escherichia coli cell cycle by cell dimension perturbations. *Proc. Natl. Acad. Sci. U.S.A.* 113, 15000–15005. doi: 10.1073/pnas.1617932114

Conflict of Interest Statement: The authors declare that the research was conducted in the absence of any commercial or financial relationships that could be construed as a potential conflict of interest.

frontiers in Microbiology

ORIGINAL RESEARCH
published: 17 January 2018
doi: 10.3389/fmicb.2017.02695

Phenotypic Heterogeneity in Sugar Utilization by *E. coli* Is Generated by Stochastic Dispersal of the General PTS Protein EI from Polar Clusters

*Sutharsan Govindarajan†, Nitsan Albocher†, Tamar Szoke, Anat Nussbaum-Shochat and Orna Amster-Choder**

Department of Microbiology and Molecular Genetics, IMRIC, Faculty of Medicine, The Hebrew University of Jerusalem, Jerusalem, Israel

Although the list of proteins that localize to the bacterial cell poles is constantly growing, little is known about their temporal behavior. EI, a major protein of the phosphotransferase system (PTS) that regulates sugar uptake and metabolism in bacteria, was shown to form clusters at the *Escherichia coli* cell poles. We monitored the localization of EI clusters, as well as diffuse molecules, in space and time during the lifetime of *E. coli* cells. We show that EI distribution and cluster dynamics varies among cells in a population, and that the cluster speed inversely correlates with cluster size. In growing cells, EI is not assembled into clusters in almost 40% of the cells, and the clusters in most remaining cells dynamically relocate within the pole region or between the poles. In non-growing cells, the fraction of cells that contain EI clusters is significantly higher, and dispersal of these clusters is often observed shortly after exiting quiescence. Later, during growth, EI clusters stochastically re-form by assembly of pre-existing dispersed molecules at random time points. Using a fluorescent glucose analog, we found that EI function inversely correlates with clustering and with cluster size. Thus, activity is exerted by dispersed EI molecules, whereas the polar clusters serve as a reservoir of molecules ready to act when needed. Taken together our findings highlight the spatiotemporal distribution of EI as a novel layer of regulation that contributes to the population phenotypic heterogeneity with regard to sugar metabolism, seemingly conferring a survival benefit.

Keywords: bacterial polarity, cell poles, proteins localization, dynamic localization, PTS system, general PTS proteins, phenotypic heterogeneity

OPEN ACCESS

Edited by:
Ariel Amir,
Harvard University, United States

Reviewed by:
Simon Ringgaard,
Max Planck Society (MPG), Germany
Thomas Shimizu,
Fundamental Research on Matter Institute for Atomic and Molecular Physics (NWO), Netherlands

****Correspondence:***
Orna Amster-Choder
ornaam@ekmd.huji.ac.il

† These authors have contributed equally to this work.

Specialty section:
This article was submitted to Microbial Physiology and Metabolism, a section of the journal Frontiers in Microbiology

Received: *03 August 2017*
Accepted: *26 December 2017*
Published: *17 January 2018*

Citation:
Govindarajan S, Albocher N, Szoke T, Nussbaum-Shochat A and Amster-Choder O (2018) Phenotypic Heterogeneity in Sugar Utilization by E. coli Is Generated by Stochastic Dispersal of the General PTS Protein EI from Polar Clusters. Front. Microbiol. 8:2695. doi: 10.3389/fmicb.2017.02695

INTRODUCTION

The poles of rod-shaped bacterial cells play an important role in various molecular processes, including DNA segregation, metabolic regulation and aggregate clearance (Bowman et al., 2011; Govindarajan et al., 2012; Laloux and Jacobs-Wagner, 2014). The poles are also emerging as hubs for localization of many proteins, including sensory systems (Alley et al., 1992; Janakiraman and Goldberg, 2004; Briegel et al., 2009; Rudner and Losick, 2010; Amster-Choder, 2011). Currently, a handful of mechanisms have been suggested to underlie targeting of proteins to the poles. These include interaction with the polar anionic lipid cardiolipin, recognition of membrane domains with strong negative curvature, present in the poles and septa, and self-assembly in nucleoid-free

spaces (reviewed in Govindarajan et al., 2012; Laloux and Jacobs-Wagner, 2014; Treuner-Lange and Sogaard-Andersen, 2014).

Notably, while the list of proteins that localize to the poles is constantly growing, less is known about their dynamics within or between the poles. Several polar complexes were shown to exhibit dynamic behavior, relocating from pole to pole, from pole to mid-cell, or from lateral sites to the poles, with their spatiotemporal dynamics often linked to developmental pathways (Jensen et al., 2002). A classic example for proteins that exhibit pole-to-pole dynamics is the *Escherichia coli* MinCDE complex, which negatively regulates FtsZ polymerization at the poles and restricts Z-ring formation to mid-cell (Lutkenhaus, 2007). In *Caulobacter crescentus*, the polarity-establishing proteins PopZ and TipN were shown to relocate from one pole to the other in a cell cycle-dependent manner, such that they mark the old and new pole, respectively (Huitema et al., 2006; Lam et al., 2006; Bowman et al., 2008; Ebersbach et al., 2008). FtsZ, which assembles into a ring in mid-cell during division, was recently shown to relocate to the cell poles of non-dividing cells and re-assemble there (Yu et al., 2017). Dynamic localization from lateral sites to the poles was observed for chemoreceptor complexes in *E. coli* (Thiem and Sourjik, 2008).

The bacterial phosphotransferase (PTS) system controls hierarchical uptake and utilization of preferred carbohydrates from complex environments (Deutscher et al., 2006). Additionally, the PTS controls other pathways, including carbon catabolite repression and inducer exclusion (Deutscher et al., 2006). The spatial organization of the PTS system has been studied in our lab. We found that the control center of the PTS system, which comprises the major PTS proteins EI and HPr, localizes to the cell poles of *E. coli*. Although EI and HPr interact with each other, polar localization of each of them occurs independently of the other (Lopian et al., 2010). Moreover, activation of the PTS system was shown to affect the localization of HPr but not of EI. Our recent study, which focused on identifying the mechanism of EI localization revealed that a geometric cue is important for EI targeting (Govindarajan et al., 2013). Thus, similar to DivIVA, a *B. subtilis* negative membrane curvature sensor protein, EI localizes to regions of strong negative curvature in the membrane, which are usually present in the poles and septa (Govindarajan et al., 2013). However, unlike DivIVA, which can directly sense the membrane curvature through its membrane-binding α-helical domain (Lenarcic et al., 2009; Ramamurthi and Losick, 2009; Oliva et al., 2010), the soluble EI protein was suggested to localize to these regions via other, yet unknown, proteins that sense membrane curvature.

In this study, we employed time-lapse fluorescence microscopy in live cells to explore the temporal organization of EI in growing and quiescent *E. coli* cells. We show that polar EI clusters are often dynamic and that their dynamic range differs among cells in the population, with their speed negatively correlating with cluster size. EI dynamics is energy-dependent, since it is negatively affected by inhibition of cell metabolism. EI cluster dynamics does not depend on the type of sugar, whether it is PTS or non-PTS. However, regardless of the sugar source, EI clustering inversely correlates with its function, that is, EI has a higher capacity to be active in cells in which it is uniformly distributed, and its higher-order assembly into clusters prevents its activity. In line with this, during transition from inactive to active state of growth, EI molecules disperse out of the cluster in a significant number of cells in a population. Intriguingly, EI cluster formation is an event that is stochastic in time, which generates phenotypic heterogeneity within a population.

RESULTS

EI Clusters Exhibit Several Dynamic Localization Patterns that Are Energy Dependent

The general PTS protein EI has been shown to form clusters that localize mainly to the poles or to mid-cell (Lopian et al., 2010; Govindarajan et al., 2013). However, the temporal behavior of these clusters, as well as that of EI molecules that are not associated with clusters has not been characterized. We first set out to monitor the spatiotemporal localization of EI in actively growing cells. For this purpose, we monitored exponentially growing cells, which express EI fused to mCherry, as well as ZapA—a marker for septal location (Galli and Gerdes, 2010)—fused to GFP, both expressed from the native chromosomal loci under the control of their respective promoters, by time-lapse microscopy. First, we verified that the activity of the chromosome-encoded EI-mCherry protein is comparable to that of the wild-type protein by comparing the growth rate of the strains expressing EI-mCherry or EI in minimal medium supplemented with PTS sugars (glucose or sorbitol) or with a non-PTS sugar (lactose). The results in Figure S1 show that the growth of the two strains on all sugar sources is alike, indicating that EI-mCherry has a similar activity to EI. Next, cells expressing EI-mCherry and ZapA-GFP were grown in minimal medium supplemented with glucose till they reached $OD_{600} = 0.2$, and images were acquired every minute for 10 min Based on the presence and the spatiotemporal localization patterns exhibited by EI, we divided the cells to four groups (see **Figures 1A,B** and Movie S1): (a) Non-dynamic (non-Dyn), that is, the EI cluster was observed in one of the poles without detectable movement (9%); (b) Dynamic within one pole (Dyn-1P), that is, the EI cluster was dynamic within the zone of one pole (43%); (c) Dynamic outside the zone of one pole (Dyn-OP), that is, the EI cluster switched from one pole to another or between the pole and mid-cell (11%); (d) EI clusters were not detected (UC), but, rather, EI molecules appeared as freely diffuse in the cytoplasm (37%) (**Figures 1A,B**). Two-dimensional trajectories of the movement tracks, presented in **Figure 1C**, show that, except for cells that exhibited a non-dynamic pattern (non-Dyn), in all cells exhibiting dynamic localization patterns (Dyn-1P and Dyn-OP), EI moved in a zigzag manner, that is, in jagged lines with sharp turns.

Heat map presentation of EI-mCherry fluorescence intensity, made for representative cells at time 0, shows an inverse correlation between the EI cluster intensity and its dynamics (**Figure 1A**, last panel). Thus, the intensity of non-Dyn clusters is

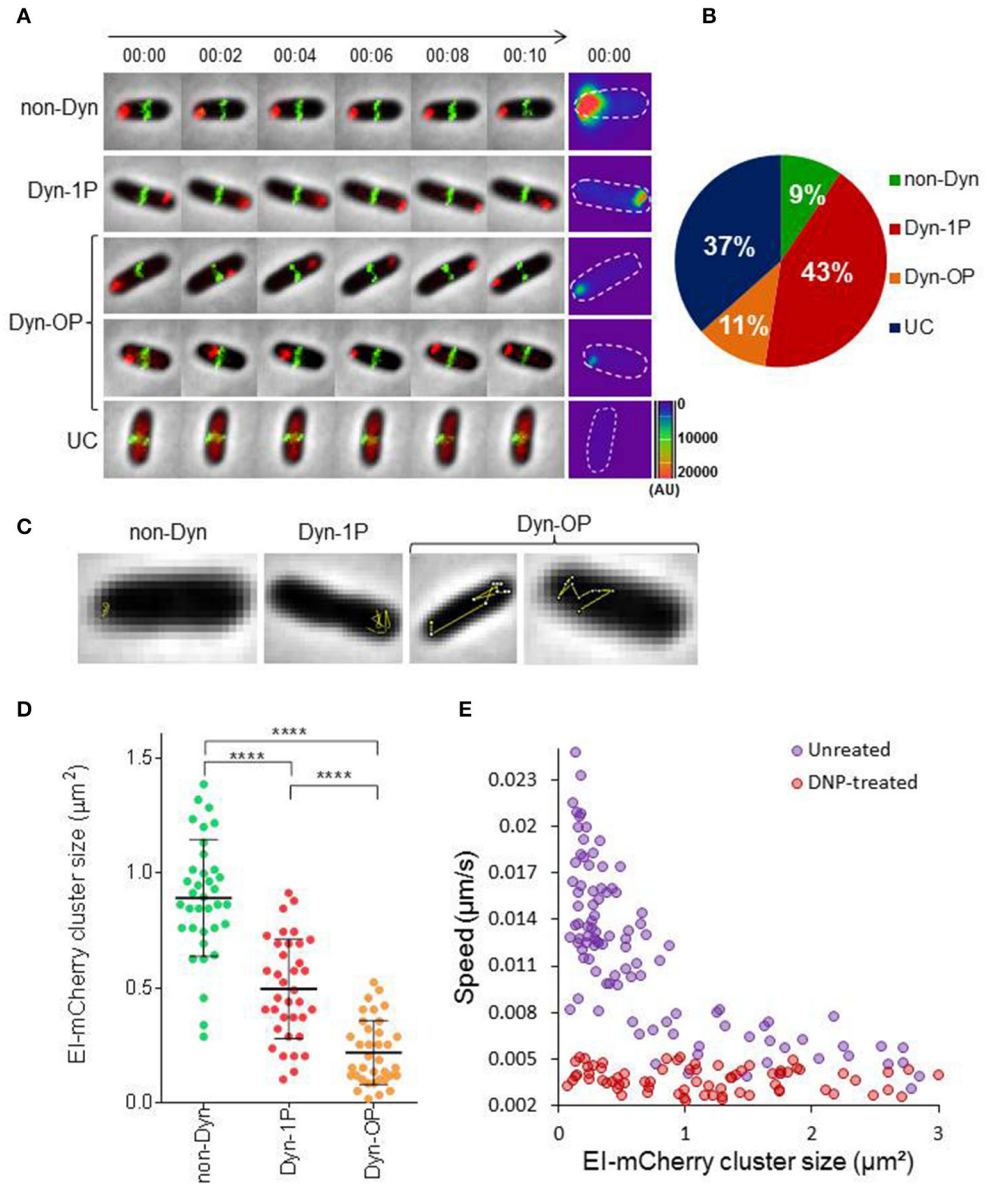

FIGURE 1 | EI is a dynamic protein whose motion is metabolism-dependent **(A)** Time-lapse microscopy images of wild-type *E. coli* cells expressing EI-mCherry and ZapA-GFP. Representative images of the four different patterns of EI dynamics are shown: (a) non-dynamic (non-Dyn), (b) dynamic within one pole (Dyn-1P), (c) dynamic between the two poles or from pole to midcell (Dyn-OP), (d) undetectable cluster (UC). The mCherry and GFP fusion proteins were observed by fluorescence microscopy and cells were observed with phase microscopy. Overlays of the fluorescence signal (GFP, green and mCherry, red) over the phase contrast images (gray) are shown. Surface intensity plots showing the fluorescent intensity (AU) of the EI-mCherry signal at time 0, which corresponds to the cellular distribution of EI-mCherry in each of the cells. The contour of each cell is outlined. **(B)** Pie chart showing the fractions of cells that exhibit the different patterns of EI dynamics, i.e., non-dynamic (non-Dyn, green), dynamic within one pole (Dyn-1P, red), dynamic from pole to midcell or from pole to pole (Dyn-OP, orange), and undetectable cluster (UC, blue), in populations grown to early log in minimal medium supplemented with glucose as carbon source. The Standard division was between 1 and 2%. **(C)** Two-dimensional trajectories of EI-mCherry cluster movement overlaid on the corresponding phase contrast (gray) images. **(D)** Distribution diagram indicating the distribution of EI-mCherry clusters area (μm^2) in cells (referred to as size) exhibiting the different patterns of EI dynamics (40 cells from each group). *P*-values were obtained by ordinary one-way ANOVA: ****p-value < 0.0001. **(E)** Scatter plot of cluster speed ($\mu m/s$) vs. EI-mCherry clusters area (μm^2), drawn for cells treated (red) or not treated (purple) with DNP. See Materials and Methods for experimental details. Spearman correlation for the untreated $\rho = -0.78$, p-value $< 10^{-8}$.

much higher compared to Dyn-1P, and the intensity of the latter is significantly higher than that of Dyn-OP. To quantitatively analyze the relationship between EI dynamics and cluster size at the population level, we plotted the area of EI-mCherry clusters (will be referred to as cluster size) for each localization pattern in the corresponding population (**Figure 1D**, $n = 120$). The results demonstrate that non-Dyn clusters have the largest area and are non-mobile, Dyn-1P clusters are smaller and they move within a

limited zone, and Dyn-OP clusters are the smallest and the most mobile. These results indicate that the dynamics of EI clusters inversely correlates with their size, that is, the bigger the cluster, the more static it is.

Next, we quantitatively analyzed the correlation between the rate of EI clusters movement and their size. To answer this question, we performed time-lapse experiments, during which we acquired images of EI-mCherry localization every 10 s for a total of 5 min. From these images, we calculated the average speed (μm/s) of individual EI-mCherry clusters and plotted it as a function of average EI-mCherry cluster size. The results (**Figure 1E**, purple circles) show that the average speed of EI cluster inversely correlates with its size (Spearman correlation $\rho = -0.78$, p-value $< 10^{-8}$), that is, clusters with smaller size moved faster than clusters with bigger size.

To figure out whether active cellular metabolism is required for EI motion, we repeated the time-lapse experiment described above with cells treated with Di-nitro phenol (DNP), an inhibitor of cell metabolism (Parry et al., 2014). The results (**Figure 1E**, red circles) show that movement of EI was restrained in DNP-treated cells, as evidenced by the dramatic reduction in cluster speed, and the lack of correlation between the speed and the cluster size.

Together, the data presented in this section suggest that the motion range and speed of EI clusters inversely correlate with their size and that this motion requires energy.

EI Clusters Are Formed Stochastically in Time by Assembly of Pre-existing Dispersed Molecules

To shed light on the process of EI cluster formation, we asked whether EI clusters form by *de novo* protein synthesis or by assembly of pre-existing molecules. We assumed that if new clusters nucleate as a result of expression burst, then the amount of EI before cluster formation would be lower than its amount after cluster formation. On the other hand, if new clusters are formed by assembly of pre-existing molecules, the amount of EI before and after cluster formation are expected to be comparable. To distinguish between these possibilities, we followed, by time-lapse microscopy, the process of EI cluster formation in 78 cells, and quantified the mean intensity (MI) and the standard deviation intensity (SDI) of the EI-mCherry fluorescent signal before and after cluster formation (**Figure 2A**). Of note, whereas the MI estimates the amount of EI-mCherry in the cell, the SDI provides information on the distribution of EI-mCherry within the cell i.e., whether or not a cluster has been formed. Moreover, Figure S2 shows that the size of EI-mCherry clusters directly correlates with cellular EI mCherry SDI (Pearson correlation $\rho = 0.83$ P-value = 7.89E-34). This implies that the cluster size and the cellular distribution of the EI-mCherry signal directly correlate and, hence, we can use the SDI of the signal as an estimate for cluster size. Thus, cells with low SDI value have diffuse EI molecules, while cells with high SDI value have highly clustered EI. As shown in **Figure 2Aa**, the mean fluorescence intensity of EI-mCherry of individual cells, before and after cluster formation, are comparable, indicating that the new clusters are assembled from pre-existing molecules. We then plotted the SDI of EI-mCherry before and after cluster formation, one against the other. The results in **Figure 2Ab** show that the SDI fluorescence intensity values of EI-mCherry after cluster formation were higher than the values before cluster formation in the majority of cells, indicating that new clusters are indeed formed in these cells.

Together, the results in **Figures 2Aa,b** imply that the new clusters are formed from pre-existing molecules. To validate this observation, we tracked the distribution and the concentration of EI-mCherry molecules in 36 individual cells, in which this protein appeared diffuse at time 0, for 60 min. To determine the cell cycle status of the cells, we also measured the area of these cells. The results presented in **Figure 2Ba** show that the growth rate was similar in all the tracked cells. Moreover, the EI-mCherry MI did not change much during cell growth, i.e., was similar in all time points (**Figure 2Bb**). However, in 14 cells, the EI-mCherry SDI abruptly increased at different time points, indicating that new clusters are formed in these cells during the time course of the experiment (**Figure 2Bc**).

The results in **Figures 2A,B** suggest that the freely diffuse EI molecules assemble rapidly and haphazardly to form higher order clusters within the cytoplasm in a manner that is independent of EI-mCherry level, which does not fluctuate. Of note, the results in **Figure 2B** were not obtained with synchronized cells. To test whether there is any linkage between cluster formation and time or cell cycle, we followed newly divided cells ($n = 80$), in which EI-mCherry molecules appeared diffuse, and monitored the time at which the clusters formed (**Figure 2Ca**). Additionally, the length of the cell, which provides information on the cell cycle status, at the time of cluster formation was also measured (**Figure 2Cb**). As shown in **Figures 2Ca,b**, the time of cluster formation and the length of the cell during cluster formation were very different in these cells, which were synchronized according to their cell cycle, indicating that new EI clusters are formed stochastically during the cell cycle. Of note, the stochasticity is deduced from the fact that we did not find any cellular parameter that is linked to EI clustering. The possibility that EI clusters are formed in response to some unknown intracellular change exist, but this putative change, in turn, is seemingly not linked to cell growth and cell cycle and shows stochasticity in time. Taken together, our results show that *E. coli* populations are heterogonous with respect to whether and when EI clusters are formed during growth.

Diffuse EI Molecules Dynamically Incorporate into Polar Clusters

After showing that diffuse EI molecules can assemble to form a new cluster, we asked whether these molecules can join a pre-formed EI cluster. To answer this question we performed Fluorescence Recovery After Photobleaching (FRAP). For this purpose, we photobleached the entire pole area, where the clusters are localized, and the recovery of fluorescence intensity at the pole was measured as a function of time and plotted relative

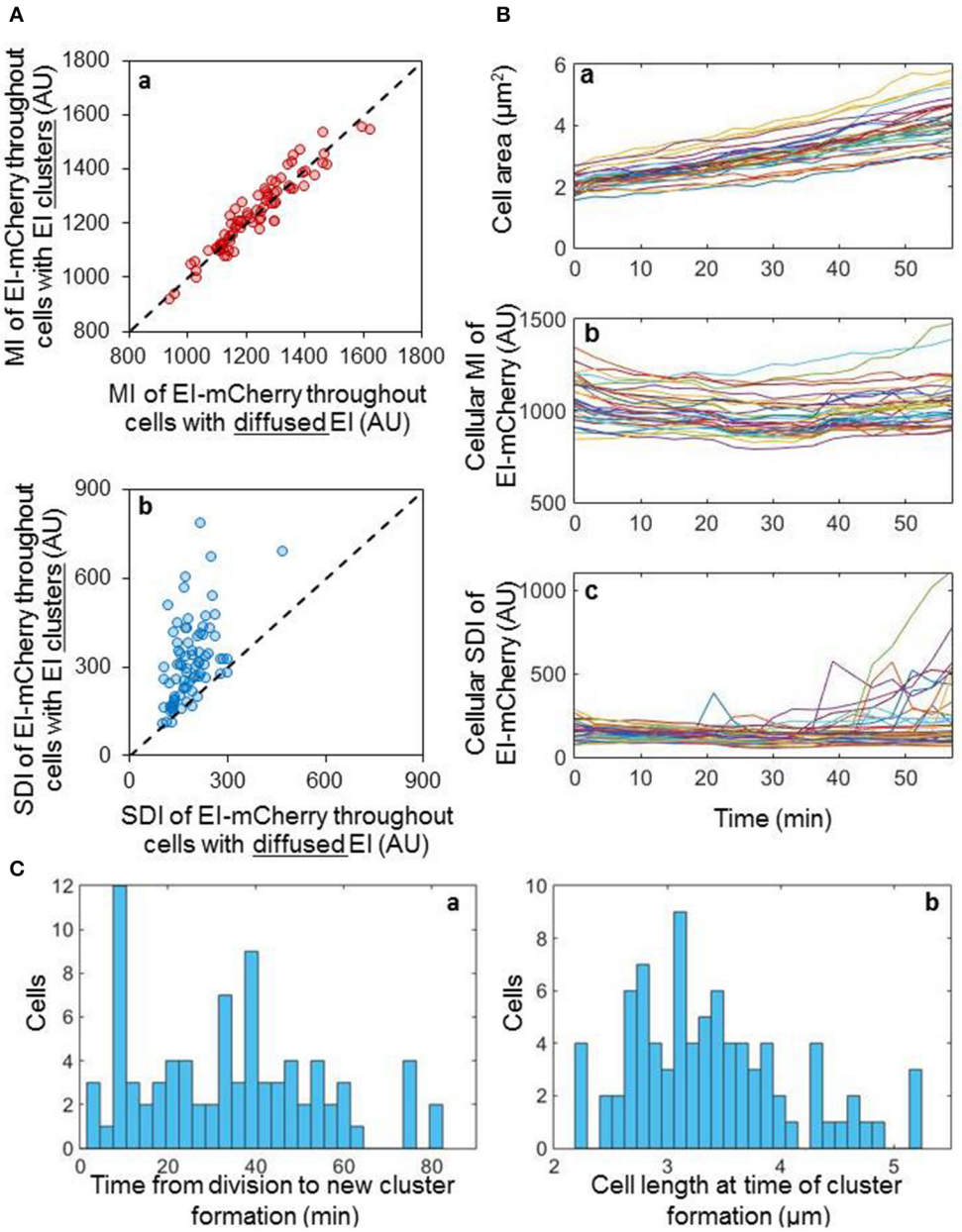

FIGURE 2 | EI clusters are formed by assembly of pre-existing dispersed molecules in a stochastic manner **(A)** Scatter plots of the cellular EI-mCherry mean intensity (MI) **(a)** or the cellular EI-mCherry standard deviation intensity (SDI) **(b)** for individual cells before cluster formation vs. after cluster formation ($n = 78$). Dashed line, $y = x$. **(B)** Line charts showing the area **(a)**, MI **(b)** and SDI **(c)** of individual cells, in which EI-mCherry appeared diffuse at time 0, over 60 min ($n = 36$). **(C)** Distribution of the time it takes a new cluster to form from the time each cell has divided **(a)** and distribution of the cell length at the time a new cluster has formed in each cell **(b)**.

to the time after bleaching. For the analysis, we chose cells with big EI clusters that were non-dynamic before photobleaching. Furthermore, in order to distinguish between recovery by assembly of pre-existing diffuse molecules and recovery by assembly of newly synthesized molecules, we performed another set of FRAP with cells spotted on an agar pad that contained the translation inhibitor chloramphenicol (CM). The results in **Figure 3A** show that nearly 6% of EI-mCherry fluorescent signal in the pole area was recovered after 600 s in untreated cells ($n = 14$), whereas the recovery of the fluorescent signal in the CM-treated cells during this time was slightly lower i.e., nearly 4% ($n = 12$). That is, about one third of the recovered EI-mCherry at the pole were *de novo* synthesized. Of note, the time it took the polar signal to appear and the pace it developed in the untreated and CM-treated samples were very similar (**Figure 3B**). These results indicate that the majority of

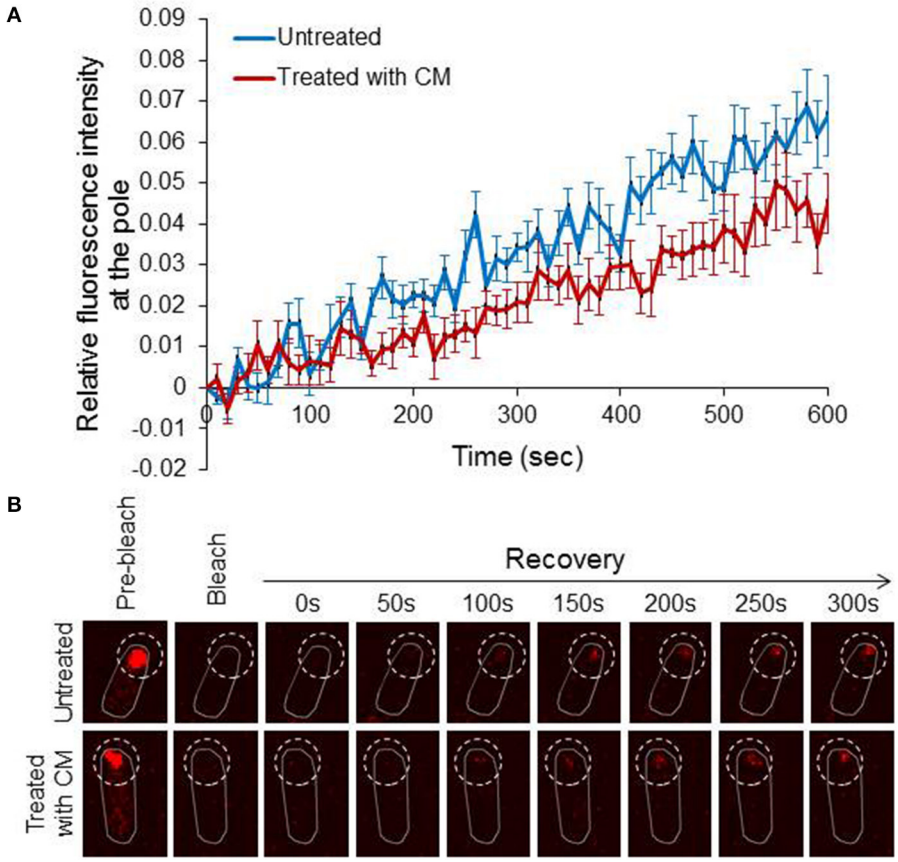

FIGURE 3 | Diffuse EI molecules dynamically incorporate into polar clusters **(A)** Line chart showing the recovery of EI-mCherry fluorescence signal in untreated cells (blue) ($n = 14$) or in chloramphenicol-treated cells (red) ($n = 12$) from the time of bleaching (time 0) over 600 s. Mean and standard error are shown. **(B)** Representative FRAP microscopy images of wild-type *E. coli* cells expressing EI-mCherry in the absence of treatment (upper panel) or in the presence of chloramphenicol (lower panel). Images at selective time points are shown. The contour of the bleached area in the fluorescent images is outlined.

molecules that assemble with the clusters are pre-existing diffuse EI-mCherry molecules, which were present outside the bleached area.

Growth Phase, but not the Carbon Source in the Growth Medium, Affects Formation of EI Clusters

To determine whether dynamic localization of EI depends on the presence of PTS sugars, we followed EI cluster dynamics in minimal medium supplemented with either glucose or sorbitol, which are PTS sugars, or with lactose, which is a non-PTS sugar, as a sole carbon source, and quantified the fraction of cells in each of the groups that exhibit the different patterns of EI dynamic localization. The results in **Figure 4A** show that EI clusters were similarly distributed between the groups when cells were grown in glucose or sorbitol containing media, and were only slightly and not significantly different in cells grown in lactose containing media. Hence, the spatiotemporal behavior of EI does not depend on the type of sugar in the growth medium and does not really change between cells grown in the presence of PTS and non-PTS sugars.

Next, we asked whether formation of EI cluster depends on the growth state of the cells. To this end, we grew EI-mCherry-expressing cells in non-PTS medium (minimal medium with lactose) or in PTS medium (minimal medium with glucose or sorbitol) and calculated the percentage of cells with EI clusters at early logarithmic (EL), mid logarithmic (ML), early stationary phase (SP), and late stationary phase (after overnight growth, ON). As shown in **Figure 4B**, in all three growth media, nearly 60% of cells in EL growth phase formed EI clusters, and this percentage increased a bit upon transition from EL to ML (65–70%) and remained similar during early SP. Conversely, the percentage of cells with EI clusters increased significantly in ON cultures (80–95%), with cells grown in lactose medium containing the highest percentage of clusters. The difference in the percentage of cells with EI clusters in ON cells is not due to an increase in the cellular amount of EI, since Western blot analysis, using α-mCherry antibodies, show that the amount of EI-mCherry present in cells at the different growth phases and in the different growth media, is largely comparable, similar to the housekeeping control protein GroEL (**Figure 4C**). Therefore, the percentage of cells with EI clusters in the population is growth phase-dependent and is the highest in quiescent cells.

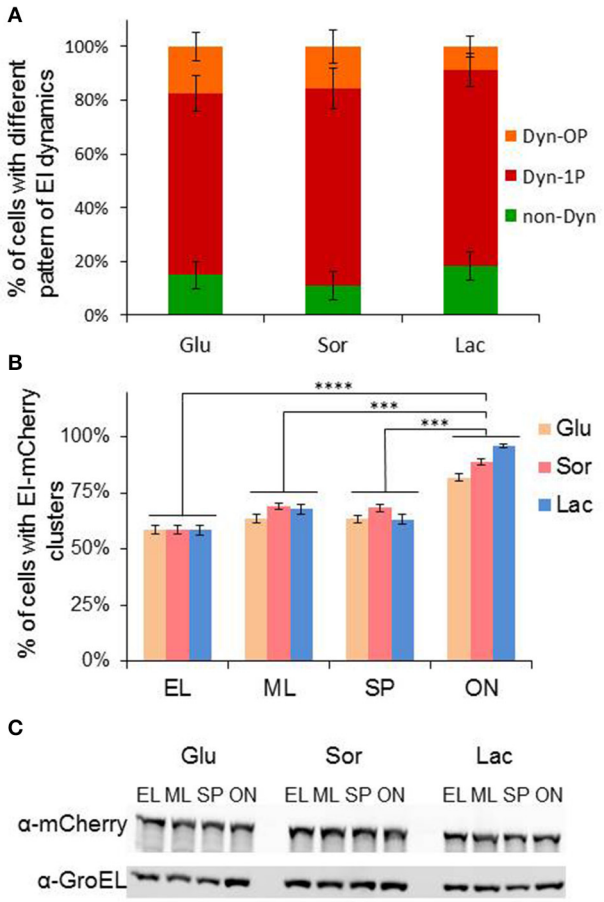

FIGURE 4 | Growth phase, but not the carbon source in the growth medium, affects formation of EI clusters**. (A)** Stacked column chart showing the fractions of cells that exhibit a certain pattern of EI dynamics, i.e., non-dynamic (non-Dyn, green), dynamic within one pole (Dyn-1P, red) and dynamic from pole to midcell or from pole to pole (Dyn-OP, orange), in populations grown to early logarithmic phase in minimal medium supplemented with glucose (Glu, $n = 328$), sorbitol (Sor, $n = 311$) or lactose (Lac, $n = 286$). Cells from three independent experiments were analyzed. Ordinary one-way ANOVA indicated no significant variations among the samples. **(B)** Column chart of the fraction of cells with detectable clusters in cultures grown on different carbon sources glucose (Glu), sorbitol (Sor) or lactose (Lac) at different growth phases: early log (EL; OD_{600} 0.2–0.25), mid-log (ML; OD_{600} 0.5–0.55), early stationary phase (SP; OD_{600} 1.00–1.1) and after overnight growth (ON). More than 400 cells were analyzed from three independent experiments. *P*-values were obtained by ordinary one-way ANOVA: ***p-value < 0.001; ****p-value $<$ 0.0001. **(C)** Western blot analysis showing the level of EI-mCherry and GroEL proteins, detected by α-mCherry and α-GroEL antibodies, respectively. Cells were grown on different carbon sources to different growth phases, as in **(B)**. Equal amount of samples were collected at specific growth phases, separated on 10% SDS polyacrylamide gel, blotted onto nitrocellulose membrane and detected by the two antibodies.

The Process of EI Cluster Dispersal Occurs after Exiting Quiescence

The finding that more ON cells contain EI clusters than growing cells (**Figure 4B**) raised the question of what happens during the transition from stationary to logarithmic phase. Do clusters disperse or a fraction of new cells are born without clusters? To address this question, we spotted diluted ON culture on an agar pad with fresh medium and observed the cells for 3 h by time-lapse microscopy. At the time that the cells were spotted on the agar pad (time 0), we monitored the distribution (SDI) of the EI-mCherry fluorescent signal in 269 cells (**Figure 5A**, left panel). Of note, as explained above, cluster size can be inferred from the SDI (Figure S2). From this time point and on, we classified the cells to cells having or not having detectable clusters at each time point till they divided (**Figure 5A**, middle panels). Together, the results in the left and middle panels of **Figure 5A** show that the population contained the following sub-populations: (i) A relatively small sub-population with no detectable clusters at time 0 (13%), which formed clusters during cell growth in the vast majority of cases. (ii) A very big sub-population of cells with relatively small clusters at time 0 (64%) that dispersed during growth and reformed (35%, see such a cell in **Figure 5B**) or did not disperse (29%) till they divided. (iii) A medium size sub-population of cells with big clusters at time 0 (23%) that remained throughout the experiment.

To negate the possibility of other factors, such as mechanical perturbations upon shifting cells from liquid media to solid media, contribute to cluster disassembly, we performed a control experiment in which ON cells were spotted on an agar pad made from overnight filtered medium ($n = 255$). In this setup, none of the EI clusters dispersed and only 4% of the cells divided during the 3 h time-lapse microscopy, suggesting that dispersal of EI clusters is specific to transition from quiescence to active growth (Figure S3).

To better understand the nature of the transition from ON to EL phase regarding EI distribution, we followed EI cluster size by tracking the SDI of 10 cells from each of the three sub-populations in **Figure 5A**. The results of this analysis are presented in Figure S4. The left panel shows the SDI at time 0, using the same scale for all sub-populations. The middle panel shows whether and when the cells had a detectable cluster at each time point till they divided. The right panel shows the SDI at each time point till division, using a different scale for each sub population. By and large, the results show a common trend for each of the first two groups. The SDI of cells in sub-population (i), which had no detectable clusters when they exited quiescence (upper panels; purple shades), remains low till cluster formation, but, upon cluster formation, the SDI doubles, suggesting that cluster formation is a rapid event, although cluster size continues to increase. In cells from sub-population (ii), which had relatively small clusters when exiting quiescence (middle panels; blue shades), there is a moderate decrease in SDI values, even in cells with clusters that remained detectable throughout the experiment, suggesting that cluster dispersal is a continuous process, rather than an abrupt event. With time, the SDI value start to increases. The SDI in cells from sub-population (iii), which had big clusters after exiting quiescence (lower panels; green shades), showed fluctuations with no consistent trend, maybe because big clusters are old and do not disperse completely, or because there is more noise in our measurements in this range. Together, these results suggest that, unlike the abrupt event of cluster formation that occurs at random time

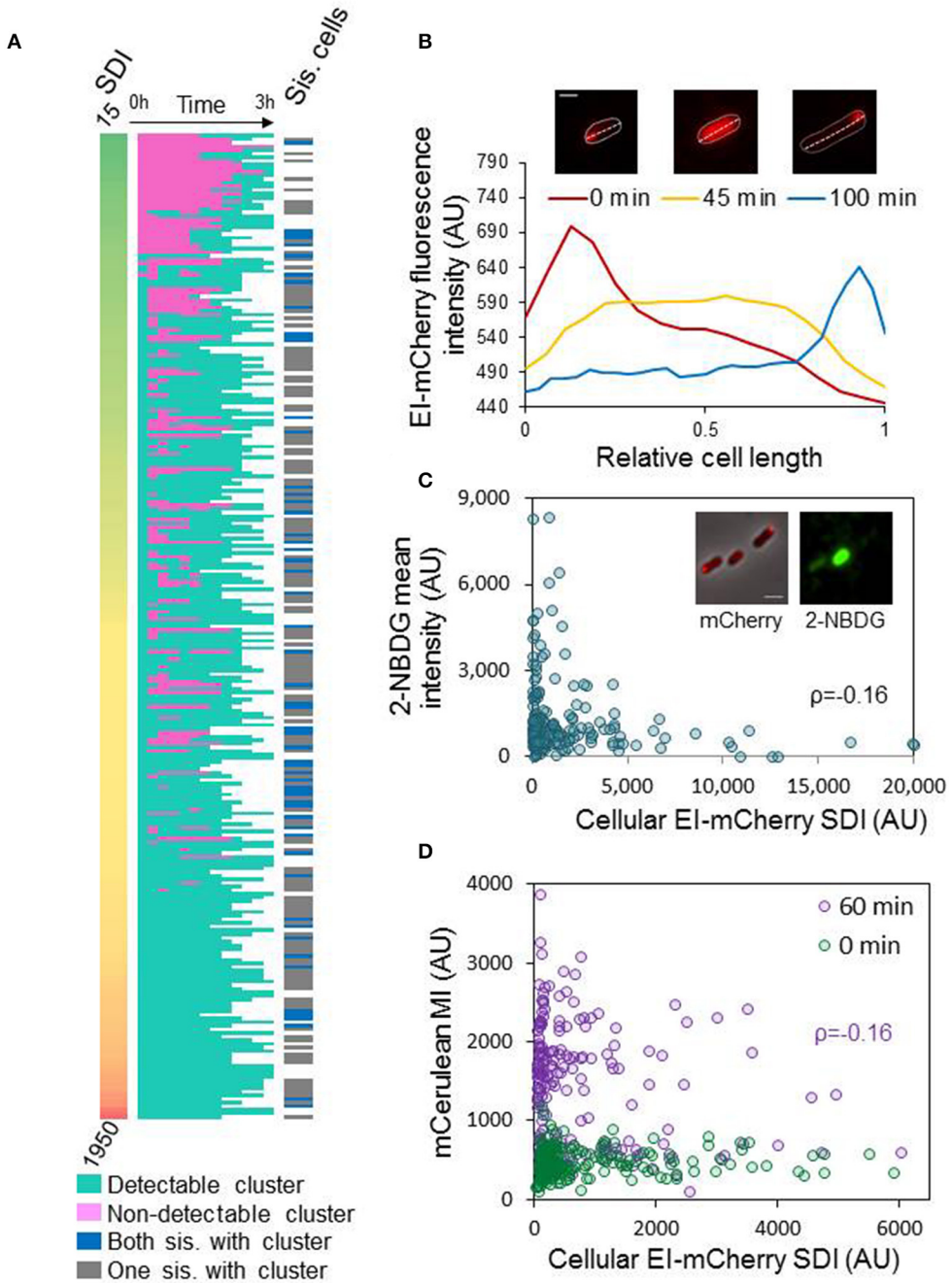

FIGURE 5 | Assembly of EI into clusters affects EI function and dynamics **(A)** Diluted ON cultures were spotted on an agar pad with fresh medium and the cells were observed at time 0, and every 15 min till they divided or for 3 h, by time-lapse microscopy. Left panels: heat map of standard deviation intensity (SDI) of EI-mCherry at time 0. Middle panels: heat map of cells with (turquoise) or without (pink) detectable EI-mCherry clusters over time, from time 0 till cell division (white, time after cell division). Right panels: Heat map of dividing cells with a cluster in each sister cell (blue) or only in one of the sister cells (gray) after 3 h; white rows denote cells that did not divide within the 3 h. **(B)** The images show a representative cell from the ON population, which has an EI-mCherry cluster at time 0 that completely disperses during growth (see image after 45 min) and later reforms (see image after 100 min). The contour of the cell is outlined. Scale bar corresponds to 1 μm. The plot shows the EI-mCherry intensity in this cell vs. the relative cell length at the different time points at which the images were taken (0, 45, and 100 min). **(C)** The images show a representative cells from the ON population, which express EI-mCherry, that were incubated with the glucose analog 2-NBDG. The mCherry fusion protein (red) and the 2-NBDG (green) were observed by fluorescence microscopy and are shown over the phase contrast images (gray) that were observed with phase microscopy. Scale bar 2 μm. The scatter plot presents the 2-NBDG mean intensity (AU) vs. the EI-mCherry SDI (AU) ($n = 194$). Pearson correlation $\rho = 0.16$; p-value $= 0.02$. **(D)** The scatter plot shows the mean intensity (MI) of mCerulean expressed from Pnag, vs. the cellular EI-mCherry SDI (AU) at the moment of transition to NAG-continuing medium (0 min; green cycles; $n = 222$) and after an hour (60 min; purple cycles; $n = 274$). Pearson correlation for the "60 min" plot $\rho = -0.16$; p-value $= 0.007$. Pearson correlation for the "0 min" plot $\rho = 0.06$; p-value $= 0.366$.

points during the cell cycle, dispersal of EI from the cluster is a gradual process, which most cells are going through when exiting quiescence, although it might not be completed, since in some cells EI molecules start to join the cluster before its complete dispersal. Therefore, the process of cluster assembly seems stochastic in time, whereas disassembly is probably due to active sensing, together generating a heterogeneous population.

Because all cells except for two had detectable EI-mCherry clusters during their lifetime, we tested the possibility that cluster formation promote division by measuring the time of cluster formation relative to the cell cycle duration. The results in Figure S5A show no linkage between cluster formation and the cell cycle stage ($n = 138$). Moreover, we did not observe a significant difference in cell cycle duration between cells which were born with or without a cluster (Figure S5B). Finally, 15% of the cells which were born without cluster divide without forming a cluster. Therefore, cluster formation does not seem to promote division. The reason that 2 cells out of 269 cells recovering from ON did not form a cluster (**Figure 5A**) is probably due to long cell cycle duration. Still, the possibility that EI cluster formation is linked to cell division can be revisited if EI mutants that do not form clusters become available.

Since most cells divided within the timespan of the experiment (3 h), we also addressed the question of what is the fraction of cells that are born without clusters. Hence, we asked if both sister cells had clusters after cell division or only one. The results in **Figure 5A** show that all cells but two had clusters before division, and that 72% of the sister-cell pairs had only one cell with a cluster (**Figure 5A**, right panel, gray) and in 28% of the cases both sister cells had a cluster (**Figure 5A**, right panel, blue) at the end of the time-lapse experiment, implying that 64% of the cells after doubling of the population had clusters. Taking into consideration that at the beginning of the experiment 87% of the cells had clusters, the percentage of clusters in the population dropped after division. Summarily, two phenomena were observed when closely following cells that emerge from stationary phase: the majority of newly added cells lack detectable clusters, suggesting that all EI molecules are dispersed and active at the beginning of growth, and EI clusters in most cells form and disperse at random times during growth, yielding a phenotypically heterogeneous population.

Clustering of EI Inversely Correlates with EI Function

The process of EI cluster dispersal and the random events of cluster formation, characterized above, are probably general rather than sugar-specific, as there were more EI clusters in ON cultures than in the EL, ML, and SP cultures, independent of the carbon source (**Figure 4B**). We hypothesized that when the carbon source in the medium is consumed and EI activity is not required, it tends to form clusters that can disperse when a fresh carbon source is supplied and EI needs to function. To explore the possible correlation between EI distribution and function, we incubated overnight cells with 2-NBDG, a fluorescent glucose analog, for 10 min. After washing the cells, images were acquired to quantify the clusters of EI-mCherry and the amount of 2-NBDG in each cell. The scatter plot of EI-mCherry SDI against 2-NBDG mean fluorescence, shown in **Figure 5C**, suggests that EI has a higher capacity to be active (higher 2-NBDG signal) in cells with lower SDI of EI-mCherry, i.e., cells in which EI-mCherry is distributed uniformly or form small clusters. These results imply that EI is less active when it is clustered in higher-order assemblies and, thus, that its function inversely correlates with clustering and with cluster size (Pearson correlation $\rho = -0.16$; p value $= 0.02$).

Since 2-NBDG is metabolized to a non-fluorescent product (Yoshioka et al., 1996), we decided to test the correlation between EI distribution and function by another approach. For this purpose, we constructed a strain that contains an EI-mCherry fusion, expressed from the native chromosomal locus, as well as mCerulean gene under the regulation of N-acetyl glucosamine (NAG) promoter (*Pnag*). To induce expression from *Pnag* promoter, phosphorylated NAG needs to be present inside the cell (Yamada and Saier, 1988; Westermayer et al., 2016). Since EI is the first protein in the phosphorylation cascade that enables uptake and phosphorylation of PTS sugars, including NAG (Yamada and Saier, 1988), expression of mCerulean implies that EI is active. The constructed strain, which was initially grown in minimal medium containing glycerol until EL phase, was resuspended in fresh minimal medium containing NAG. Fluorescent images were acquired in order to quantify the expression of EI-mCherry and mCerulean proteins, at time 0 and 60 min. The expression of mCerulean from *Pnag* (mean intensity of Pnag-mCerulean) as well as the distribution of EI-mCherry in the cell (SDI of EI-mCherry) were plotted against each other. As shown in **Figure 5D**, at time 0 min, at which point cells which were grown only in the presence of glycerol, induction of Pnag-mCerulean could not be observed. In contrast, expression of Pnag-mCerulean was clearly induced when cells were grown in the presence of NAG for 60 min. More importantly, the scatter plots in **Figure 5D** suggest that EI has a higher capacity to be active (higher mCerulean production) in cells with lower SDI of EI-mCherry i.e., those cells in which EI-mCherry is distributed uniformly or form small clusters. This suggests that EI is relatively less active when it clusters to form higher-order assemblies. Although the possibility of other factors, for example, changes in the uptake or degradation of the sugars, contributing to the observed heterogeneity cannot be completely ruled out, the results obtained with the two assays which tested EI activity in different manners, suggest that EI activity inversely correlates with clustering.

DISCUSSION

Dynamic organization of proteins in higher-order assemblies, provides a versatile and attractive mechanism for metabolic regulation. In this study, by using time-lapse microscopy as a primary tool, we demonstrate for the first time that the temporal distribution of a central metabolic enzyme, the *E. coli* general PTS protein EI, is multimodal, and that EI clustering inversely correlates with its enzymatic activity. We also show significant

repositioning of EI molecules from being in a cluster to being in a diffuse state during transition from inactive to active state of growth, highlighting the importance of EI cluster formation for future need of sugar metabolism.

Our data show that EI clusters, observed as mostly polar in snap-shots in previous studies (Lopian et al., 2010; Govindarajan et al., 2013), exhibit rapid and continuous relocation within the pole region, between the two poles or between the pole and midcell. Thus, the EI clusters spend most of the time in the poles or pole-to-be and a small fraction of their time in relocating among or within these sites, explaining their observation as merely polar in snap-shots. Still, a significant fraction of cells (nearly 11%) contain an EI cluster that remains static at one pole. The demonstration that the mobility of newly formed EI clusters is not restricted to a single pole region, whereas that of bigger clusters is restricted only to the pole region till they become non-dynamic is in line with our finding that the motion and speed of EI clusters is influenced by their size. It has recently been suggested that dynamics of macromolecular complexes within the bacterial cytoplasm inversely correlates with their size (Parry et al., 2014). Our observation of inverse correlation between the size of the EI clusters and their dynamics is in agreement with this.

We have previously shown that EI clusters are located at or near negatively curved regions, although the EI soluble protein, which cannot be anchored in the membrane, localizes to these regions via other, yet unknown, proteins that sense membrane curvature (Govindarajan et al., 2013). Of note, EI is not the first polar protein reported to form at negatively curved membrane regions and to exhibit dynamics. The membrane-anchored chemoreceptors, recently shown to also recognize negative curvature (Strahl et al., 2015), exhibit dynamic cluster positions within the polar zone, which can be more subtle (Studdert and Parkinson, 2005) or less (Thiem et al., 2007). Another protein that senses membrane curvature, but shows dynamics is MreB (Izoré and van den Ent, 2017). Together, these examples highlight the fact that capture of proteins at specific sites, including the poles, is transient, with the degree of transience depending of the nature of the interactions. In light of these findings, dynamics of a soluble protein, such as EI, despite its association with a yet unknown curvature-sensing protein, is less surprising.

EI is the first protein in the PTS system cascade, which controls preferential use of sugars, i.e., preferred use of PTS sugars over non-PTS sugar. Still, EI is important also for uptake of non-PTS sugars, since phosphorylated IIA^{glc}, which receives the phosphate from EI via HPr, is required for the activation of adenylate cyclase, whose product is required for the transcription of non-PTS catabolic operons (Deutscher et al., 2014). Indeed, we show that the nature of the sugar, whether it is PTS or non-PTS, does not affect the mobility of EI clusters. Moreover, our results suggest that EI assembly into clusters and disassembly is a mechanism to control its activity in sugar metabolism, independent of the nature of the sugar. This is deduced from the finding that the majority of cells in overnight cultures that grew in the presence of PTS or non-PTS sugars, which apparently exhausted the sugar source and are not actively growing, contained more EI clusters compared to cells in the other growth phases, suggesting that assembly of EI into clusters reflects a non-functional state. We provide a support for this hypothesis by showing that in a significant percentage of cells from overnight cultures (35%), the EI clusters break down and disperse in the cytoplasm shortly after inoculation into a fresh medium. However, at later time points within the cell cycle, new clusters are formed at random time points, in what seem like rapid and non-synchronized events. The negative relationship between EI clustering and sugar uptake is deduced from our demonstration that the intracellular level of a fluorescent glucose analog, as well as the expression of a PTS-dependent promoter inversely correlate with EI clustering. Having said that, disassembly and reassembly of EI clusters were not observed in all cells. It is possible that some cells have an existing pool of disperse active cytoplasmic EI, not detectable in our experiments, whereas EI clusters below our detection capability may exist in other cells, serving as "nucleation centers" for EI higher-order assemblies.

Taken together, our data suggests that EI molecules that are not needed at a given moment join the cluster, from which they can easily disperse when needed. The finding that 63% of the cells in exponential phase have clusters, in addition to diffuse molecules, imply that most cells have more EI than needed under the conditions tested. Since EI is involved in various processes beyond PTS sugar uptake, such as chemotaxis, catabolite repression and utilization of nutrients such as nitrogen and potassium (Lüttmann et al., 2015), our data suggest that the cells anticipate higher need of EI. Hence, the capability of EI clusters to assemble and disassemble contributes to dynamic regulation of the current and expected cellular metabolism.

Many cases of bacterial proteins, whose higher-order assembly hinder their active site or prevent a conformational change required for their activity, have been documented. One example is the CTP synthetase, whose large scale polymerization keeps a subpopulation of the protein in a conformationally restricted form, which can be readily activated (Ingerson-Mahar et al., 2010; Barry et al., 2014). Another example is MurG, an enzyme involved in peptidoglycan subunit synthesis that, when produced in excess, is sequestered to the poles in an inactive form, which, upon need, can be released to the cytoplasm in an active form (Michaelis and Gitai, 2010). More recently, FtsZ was also demonstrated to assemble at the cell poles of non-dividing cells, in the form of a quiescent body, and only upon sensing growth-supporting conditions, the pole-localized FtsZ structures disassemble to form active molecules that engage in cell division (Yu et al., 2017). In all of these cases, the proteins are not degraded when they are not required, but, rather, are kept as a dynamic storage depots, which can be used in the future. Of note, we have previously reported that cluster formation of *B. subtilis* EI occurs only upon growth in a medium supplemented with mannitol as the carbon source and not in a rich medium, such as LB, in which it appeared diffuse (Govindarajan et al., 2013). Hence, it appears that the dynamic clustering property of EI is a general phenomenon, which holds for Gram positive bacteria as well.

Populations of genetically uniform microorganisms, bacterial and yeast cells alike, were shown to exhibit phenotypic

heterogeneity with regard to fitness-determining traits (e.g., Gefen and Balaban, 2009; Holland et al., 2014; Wang et al., 2014). This phenomenon, vastly studied with respect to variability among bacterial cells in their resistance to antibiotics, is considered a population-based strategy that can be beneficial to a growing population. The mechanisms that underlie adaptation to stress by heteroresistance are not fully understood at the single cell level. Population heterogeneity was also studied with respect to metabolism, which continuously adapts to unpredictable environmental changes. Upon nutrient change, including that of carbon source, a homogeneous *E. coli* population was shown to split into a growing and a non-growing persisters, which was suggested to stem from stochastic variation in metabolic flux (Kotte et al., 2014). We show that bacterial populations are composed of phenotypic subsets with respect to cluster mobility of a major carbon metabolic enzyme, EI, which can be explained by difference in cluster size. However, the level of heterogeneity is revealed when observing single cells in the population. Thus, despite our general observation that more cells in a quiescent population contain EI clusters than in a growing population, we show that cluster formation is a stochastic event that happen at random timings in individual cells and is not tied up to cell cycle. This stochasticity gains further importance in light of our finding that cluster formation inversely correlates with enzyme activity. Recent studies have shown that biochemical processes are inherently stochastic and cause molecule abundances to fluctuate (Elowitz et al., 2002), a phenomenon that can be used to generate distinct phenotypes (Balaban et al., 2004; Losick and Desplan, 2008). Our findings provide a new organizational explanation to enzymatic heterogeneity, which can hold also for other cellular pathways. Moreover, different reported cases of phenotypic heterogeneity might be linked in nature, as suggested by the observation that uptake of sugars and amino acids increases uptake of various antibiotics (Franklin and Godfrey, 1965; Peng et al., 2015).

EXPERIMENTAL PROCEDURES

Bacterial Strains and Growth Media

Unless otherwise indicated, overnight cultures were grown in LB supplemented with appropriate antibiotics at 30°C. M9 medium, supplemented with glucose, sorbitol or lactose, were used for time-lapse microscopy experiments. For inhibition of cell metabolism, Dinitrophenol (DNP) at a concentration of 2 mM, was added to the growth medium. When appropriate, antibiotics were added at the following concentrations: kanamycin (30 μg/ml) and chloramphenicol (25 μg/ml) (Sigma-Aldrich). MG1655Φ(*ptsI*-mCherry)strain expressing EI-mCherry from the native chromosomal locus was described previously (Lopian et al., 2010). SUT201, which expresses EI-mCherry and ZapA-GFP from the chromosome, was constructed by P1 transduction of *zapA-gfp(::cat)* from HC261 (Peters et al., 2011) to MG1655Φ(*ptsI*-mCherry). NTS102, which expresses EI-mCherry, *Psrl*-mVenus and *Pnag*-mCerulean from the chromosome, was constructed by P1 transduction of MG1655Φ(*ptsI*-mCherry), linked to KanR, to T1683 (Westermayer et al., 2016).

Growth Conditions Used for Snap-Shot and Time-Lapse Imaging

Ariekacells^R coverslip cell chamber (SC15012) was used for time-lapse imaging. Overnight cultures were diluted 1:100 in fresh M9 medium and cells were allowed to grow at 30°C, unless otherwise indicated, till they reached OD_{600} of 0.2. Samples were then spotted on 1% agarose pads, prepared with the respective minimal medium and supplemented with the appropriate sugar which had been pre-equilibrated to 30°C, and imaged immediately by time-lapse microscopy. For calculating the fraction of each dynamic group, time-lapse images were acquired every 3 min for a total of 1 h. For FRAP microscopy, cells were grown in M9 glucose media as described above, and samples were spotted on 1% M9 glucose agarose pads without or with chloramphenicol (25 μg/ml). To measure the correlation of cluster speed vs. EI-mCherry cluster size, cultures grown in fresh M9 glucose medium until OD_{600} of 0.2 were spotted on 1% M9 glucose agar pad and time-lapse images were acquired every 10 s for a total of 5 min. For calculating the fraction of cells with detectable EI clusters, MG1655Φ(*ptsI*-mCherry) cells were grown overnight in M9 minimal medium supplemented with casamino acids, vitamin B1 and 0.4% sugar (glucose, sorbitol or lactose). The media was supplemented with kanamycin. Overnight cultures were diluted 1:100 in the respective fresh M9 medium and cultures were grown until specific growth phase. Snap shot were taken from the cultures at OD_{600} 0.2 to 0.25 for early log (EL), 0.5 to 0.55 for mid log (ML), 1 to 1.1 for stationary phase (SP) and after overnight growth (ON). To follow EI localization in overnight-grown cells that were inoculated into fresh medium, MG1655Φ(*ptsI*-mCherry) cells, which were grown overnight in M9 minimal media supplemented with CAA, vitamin B1, and glucose, were diluted and spotted onto 1% agar pads in the same medium, which had been pre-equilibrated to 30°C, and imaged immediately by time-lapse microscopy. To measure the correlation of 2-NBDG [(2-(N-(7-Nitrobenz-2-oxa-1,3-diazol-4-yl)Amino)-2-Deoxyglucose] uptake vs. EI-mCherry spatiotemporal organization, MG1655Φ(*ptsI*-mCherry) cells were grown overnight in M9 minimal medium supplemented with casamino acids, vitamin B1 and 0.4% glucose. Cells were pelleted, washed thrice and incubated for 10 min in M9 minimal medium supplemented with casamino acids, vitamin B1 and 10 μM 2-NBDG. After 10 min, cells were washed thrice and imaged in the microscope. To measure the correlation of *Pnag* mCerulean expression vs. EI-mCherry spatiotemporal organization, NTS102 cells were grown overnight in M63 minimal media supplemented with CCA, vitamin B1 and Glycerol (M63 glycerol) diluted 1:100 into M63 glycerol and grown till $OD_{600} = 0.3–0.35$. Cells were pelleted and resuspended in M63 supplemented with vitamin B1 and NAG. Snap shot in phase contrast, mCherry and mCerulean (CFP) channels were taken at time 0 and after 1 h.

Fluorescence Microscopy

Fluorescence microscopy was carried out as described previously (Govindarajan et al., 2013). For snap-shot imaging, 0.5 ml cells were centrifuged, washed with 1X phosphate buffered saline

(PBS) and finally resuspended in 10–100 μl of PBS. Light microscopy was performed on a Nikon Eclipse Ti-E inverted microscope equipped with Perfect Focus System (PFS), CFI PLAN Apochromat DM 100X (numeric aperture 1.45) oil Ph3 objective and ORCA Flash 4 camera (Hamamatsu photonics). Chroma filter cubes were used as follows: ET-GFP for GFP and 2-NBDG, and ET-mCherry for mCherry. Time-lapse imaging was performed with the aid of OKOLAB cage incubator. Unless otherwise indicated, cells were spotted on 1% agar pads containing M9 media supplemented with glucose, sorbitol or lactose. Agar pads were pre-equilibrated to the appropriate temperature and cells were imaged by time-lapse microscopy at the respective temperature. For each experiment, all images were collected using uniform parameters of magnification and exposure. Images were processed using NIS Elements-AR (Nikon). Two-dimensional trajectories of dynamical clusters were obtained by processing the time-lapse images using Fiji in combination with its Manual Tracking plugin (Schindelin et al., 2012). Correlations were calculated using MATLAB. Statistical tests were performed using GraphPad Prism.

For FRAP microscopy, Nikon A1R confocal microscope equipped with Apochromat 60X objective (numeric aperture 1.4) was used. Photobleaching was done over the area in which the EI cluster is localized. Recovery was measured every 10 s for a total period of 10 min. Mean fluorescence intensity was normalized to the total fluorescence intensity for each ROI after bleaching. Images were analyzed using NIS Elements AR module.

Image Analysis

Unless otherwise indicated, image analysis was done by NIS-Elements Advanced Research (AR) version 4.4 software (Nikon).

Analyzing of EI Cluster Size

Regions of interest (ROIs) were selected to mark the cluster region of the first image in each time-lapse series as following. First the details of the mCherry-acquired image were enhanced using the "Homogenization" tool. Next, binary layers were created using the "Define Threshold" tool. ROI were then drawn over the binary layers and copied onto the original mCherry image and the area of each ROI was exported. Finally, cells with marked ROI were manually sorted according to their EI dynamic pattern (non-Dyn, Dyn-1P or Dyn-OP). Scatter plot of the cluster area value for each pattern was obtained using GraphPad Prism. The statistical significance of the differences among cells with detectable clusters was determined by ordinary one-way ANOVA test using GraphPad Prism.

Calculating the Fraction of Each Dynamic Group

Time-lapse of individual cells were manually classified based on their EI dynamic pattern (non-Dyn, Dyn-1P, Dyn-OP or UC). The results of this analysis are presented as a pie chart or a stacked column chart. The statistical significance of the differences among cells with detectable clusters were determined by ordinary one-way ANOVA test using GraphPad Prism.

Measuring the Correlation between Cluster Speed and Cluster Size

EI-mCherry clusters were marked throughout each time-lapse series by binary layer by using the "Define Threshold" tool. Clusters marked by binary layer were tracked using the "Track Binaries" tool of the NIS-Elements AR "Tracking" module. The binary center was tracked from the end to the beginning without any skip. For other features, we used the default parameters of the program. Values for average cluster speed and cluster area, which were obtained from the Tracking analysis, were plotted and displayed as a scatter plot. Spearman correlation was calculated using MATLAB corr function.

Measuring the Correlation between Cluster Area and Cell SDI

First, ROIs were selected to mark the cells outline as following. Binary layers were created using the "Define Threshold" tool over the phase contrast images. ROI were then drawn over the binary layers. Next, EI-mCherry clusters were marked by binary layer by using "Define Threshold" tool. Then the binary lyres were copied onto the original mCherry images. Finally, mCherry images data were exported. The SDI of the ROIs, which were drawn over the cell outline, were plotted and correlated with the MI of the binary layers, which were drawn over the cluster, using Microsoft Excel and MATLAB corr function.

Measuring Cells Arrea EI-mCerry Concentration and Distribution

ROIs were selected to mark the cells outline throughout time-lapse series of cells with undetectable clusters as following. ROI were selected on the first phase contrast image in each time-lapse series, using the "Define New ROI" tool of the "Tracking" module. Then the tool "Track Autodetected ROIs" of the "Tracking" module was used to outline the selected cells by appropriate ROI for each time point throughout the time-lapse series. The data were exported from the mCherry-acquired image and plotted using MATLAB custom made script.

Calculating the Distribution of EI Clusters from Cell Cycle-Synchronized Population

SUT201, which expresses EI-mCherry and ZapA-GFP from the chromosome, was used. Time-lapse images were acquired every 3 min for a total period of 3 h. From these images, newly born daughter cells, in which EI clusters were not detected, were manually monitored. The time at which a clear Z-ring was observed was noted and this was considered time 0 for the newly born daughter cells. The time-lapse series of individual cells were monitored and the time at which new clusters were formed was noted. Using the NIS Elements AR module, the cell length at the time of new cluster formation was measured.

Calculating the Fraction of Cells with Detectable EI Clusters

For each growth condition, 400 or more cells from three independent experiments were manually classified as having or not having a detectable EI-mCherry cluster. The statistical significance of the differences among cells with detectable clusters were determined by ordinary one-way ANOVA test using GraphPad Prism.

Following EI Localization in Overnight-Grown Cells Inoculated into Fresh

medium: ROIs were selected to mark the cells outline of the first image in each time-lapse series as following. Binary layers were created using the "Define Threshold" tool over the phase contrast acquired images. ROI were then drawn over the binary layers. From each ROI, the value of SDI from the mCherry channel, taken at time 0, for each cell were obtained and presented as a heat map. Each cell outlined by ROI was manually monitored and noted for each time point of the time-lapse series as having or not having a detectable EI-mCherry cluster until cell division was completed. At the final time point, the sister cells were classified depending on whether both had detectable clusters or not. Finally, the cells were aligned according to their EI-mCherry SDI values.

The Relation between 2-NBDG Uptake and EI-mCherry Spatiotemporal Organization

ROIs were selected to mark the cells outline of the first image in each time-lapse series as following. Binary layers were created using the "Define Threshold" tool over the phase contrast images. ROI were then drawn over the binary layers. From each ROI, the 2-NBDG MI value and the SDI values of the mCherry signal were exported and presented as a scatter plot.

Western Blotting

Equal amount of samples were collected, washed and their proteins were separated on 10% SDS–polyacrylamide gels. Gels were subjected to Western blot analysis as described previously (Lopian et al., 2010). α-GroEL (Abcam) and α-mCherry (Abcam) were used for detection of GroEL and EI-mCherry proteins, respectively.

AUTHOR CONTRIBUTIONS

SG, NA, and OA-C contributed to the design of the study and wrote the manuscript; SG, NA, and TS contributed to data acquisition; SG, NA, TS, AN-S, and OA-C contributed to data interpretation.

ACKNOWLEDGMENTS

This research was supported by the Israel Science Foundation founded by the Israel Academy of Sciences and Humanities and the Deutsch-Israeli Project Cooperation (DIP). We thank Zakhariya Manevitch from the Core Research Facility of the Faculty of Medicine at The Hebrew University for help with FRAP microscopy. We acknowledge Thomas G. Bernhardt (Harvard Medical School) for gifts of strains. We thank members of Orna Amster-Choder's lab for fruitful discussions.

SUPPLEMENTARY MATERIAL

The Supplementary Material for this article can be found online at: https://www.frontiersin.org/articles/10.3389/fmicb.2017.02695/full#supplementary-material

REFERENCES

Alley, M. R., Maddock, J. R., and Shapiro, L. (1992). Polar localization of a bacterial chemoreceptor. *Genes Dev.* 6, 825–836. doi: 10.1101/gad.6.5.825

Amster-Choder, O. (2011). The compartmentalized vessel: the bacterial cell as a model for subcellular organization (a tale of two studies). *Cell. Logist.* 1, 77–81. doi: 10.4161/cl.1.2.16152

Balaban, N. Q., Merrin, J., Chait, R., Kowalik, L., and Leibler, S. (2004). Bacterial persistence as a phenotypic switch. *Science* 305, 1622–1625. doi: 10.1126/science.1099390

Barry, R. M., Bitbol, A.-F., Lorestani, A., Charles, E. J., Habrian, C. H., Hansen, J. M., et al. (2014). Large-scale filament formation inhibits the activity of CTP synthetase. *Elife* 3:e03638. doi: 10.7554/eLife.03638

Bowman, G. R., Comolli, L. R., Zhu, J., Eckart, M., Koenig, M., Downing, K. H., et al. (2008). A polymeric protein anchors the chromosomal origin/ParB complex at a bacterial cell pole. *Cell* 134, 945–955. doi: 10.1016/j.cell.2008.07.015

Bowman, G. R., Lyuksyutova, A. I., and Shapiro, L. (2011). Bacterial polarity. *Curr. Opin. Cell Biol.* 23, 71–77. doi: 10.1016/j.ceb.2010.10.013

Briegel, A., Ortega, D. R., Tocheva, E. I., Wuichet, K., Li, Z., Chen, S., et al. (2009). Universal architecture of bacterial chemoreceptor arrays. *Proc. Natl. Acad. Sci. U.S.A.* 106, 17181–17186. doi: 10.1073/pnas.0905181106

Deutscher, J., Aké, F. M. D., Derkaoui, M., Zébré, A. C., Cao, T. N., Bouraoui, H., et al. (2014). The bacterial phosphoenolpyruvate: carbohydrate phosphotransferase system: regulation by protein phosphorylation and phosphorylation-dependent protein-protein interactions. *Microbiol. Mol. Biol. Rev.* 78, 231–256. doi: 10.1128/MMBR.00001-14

Deutscher, J., Francke, C., and Postma, P. W. (2006). How phosphotransferase system-related protein phosphorylation regulates carbohydrate metabolism in bacteria. *Microbiol. Mol. Biol. Rev.* 70, 939–1031. doi: 10.1128/MMBR.00024-06

Ebersbach, G., Briegel, A., Jensen, G. J., and Jacobs-Wagner, C. (2008). A self-associating protein critical for chromosome attachment, division, and polar organization in caulobacter. *Cell* 134, 956–968. doi: 10.1016/j.cell.2008.07.016

Elowitz, M. B., Levine, A. J., Siggia, E. D., and Swain, P. S. (2002). Stochastic gene expression in a single cell. *Science* 297, 1183–1186. doi: 10.1126/science.1070919

Franklin, T. J., and Godfrey, A. (1965). Resistance of *Escherichia coli* to tetracyclines. *Biochem. J.* 94:54.

Galli, E., and Gerdes, K. (2010). Spatial resolution of two bacterial cell division proteins: ZapA recruits ZapB to the inner face of the Z-ring. *Mol. Microbiol.* 76, 1514–1526. doi: 10.1111/j.1365-2958.2010.07183.x

Gefen, O., and Balaban, N. Q. (2009). The importance of being persistent: heterogeneity of bacterial populations under antibiotic stress. *FEMS Microbiol. Rev.* 33, 704–717. doi: 10.1111/j.1574-6976.2008.00156.x

Govindarajan, S., Elisha, Y., Nevo-Dinur, K., and Amster-Choder, O. (2013). The general phosphotransferase system proteins localize to sites of strong negative curvature in bacterial cells. *MBio* 4:e00443–13. doi: 10.1128/mBio.00443-13

Govindarajan, S., Nevo-Dinur, K., and Amster-Choder, O. (2012). Compartmentalization and spatiotemporal organization of macromolecules in bacteria. *FEMS Microbiol. Rev.* 36, 1005–1022. doi: 10.1111/j.1574-6976.2012.00348.x

Holland, S. L., Reader, T., Dyer, P. S., and Avery, S. V. (2014). Phenotypic heterogeneity is a selected trait in natural yeast populations subject to environmental stress. *Environ. Microbiol.* 16, 1729–1740. doi: 10.1111/1462-2920.12243

Huitema, E., Pritchard, S., Matteson, D., Radhakrishnan, S. K., and Viollier, P. H. (2006). Bacterial birth scar proteins mark future flagellum assembly site. *Cell* 124, 1025–1037. doi: 10.1016/j.cell.2006.01.019

Ingerson-Mahar, M., Briegel, A., Werner, J. N., Jensen, G. J., and Gitai, Z. (2010). The metabolic enzyme CTP synthase forms cytoskeletal filaments. *Nat. Cell Biol.* 12, 739–746. doi: 10.1038/ncb2087

Izoré, T., and van den Ent, F. (2017). Bacterial Actins. *Subcell. Biochem.* 84, 245–266. doi: 10.1007/978-3-319-53047-5_8

Janakiraman, A., and Goldberg, M. B. (2004). Recent advances on the development of bacterial poles. *Trends Microbiol.* 12, 518–525. doi: 10.1016/j.tim.2004.09.003

Jensen, R. B., Wang, S. C., and Shapiro, L. (2002). Dynamic localization of proteins and DNA during a bacterial cell cycle. *Nat. Rev. Mol. Cell Biol.* 3, 167–176. doi: 10.1038/nrm758

Kotte, O., Volkmer, B., Radzikowski, J. L., and Heinemann, M. (2014). Phenotypic bistability in *Escherichia coli* 9s central carbon metabolism. *Mol. Syst. Biol.* 10:736. doi: 10.15252/msb.20135022

Laloux, G., and Jacobs-Wagner, C. (2014). How do bacteria localize proteins to the cell pole? *J. Cell Sci.* 127, 11–19.

Lam, H., Schofield, W. B., and Jacobs-Wagner, C. (2006). A landmark protein essential for establishing and perpetuating the polarity of a bacterial cell. *Cell* 124, 1011–1023. doi: 10.1016/j.cell.2005.12.040

Lenarcic, R., Halbedel, S., Shaw, M., Wu, L. J., Errington, J., Marenduzzo, D., et al. (2009). Localisation of DivIVA by targeting to negatively curved membranes. *EMBO J.* 28, 2272–2282. doi: 10.1038/emboj.2009.129

Lopian, L., Elisha, Y., Nussbaum-Shochat, A., and Amster-Choder, O. (2010). Spatial and temporal organization of the *E. coli* PTS components. *EMBO J.* 9, 3630–3645. doi: 10.1038/emboj.2010.240

Losick, R., and Desplan, C. (2008). Stochasticity and cell fate. *Science* 320, 65–68. doi: 10.1126/science.1147888

Lutkenhaus, J. (2007). Assembly dynamics of the bacterial MinCDE system and spatial regulation of the Z ring. *Annu. Rev. Biochem.* 76, 539–562. doi: 10.1146/annurev.biochem.75.103004.142652

Lüttmann, D., Göpel, Y., and Görke, B. (2015). Cross-talk between the canonical and the nitrogen-related phosphotransferase systems modulates synthesis of the KdpFABC potassium transporter in *Escherichia coli*. *J. Mol. Microbiol. Biotechnol.* 25, 168–177. doi: 10.1159/000375497

Michaelis, A. M., and Gitai, Z. (2010). Dynamic polar sequestration of excess MurG may regulate enzymatic function. *J. Bacteriol.* 192, 4597–4605. doi: 10.1128/JB.00676-10

Oliva, M. A., Halbedel, S., Freund, S. M., Dutow, P., Leonard, T. A., Veprintsev, D. B., et al. (2010). Features critical for membrane binding revealed by DivIVA crystal structure. *EMBO J.* 29, 1988–2001. doi: 10.1038/emboj.2010.99

Parry, B. R., Surovtsev, I. V., Cabeen, M. T., O'Hern, C. S., Dufresne, E. R., and Jacobs-Wagner, C. (2014). The bacterial cytoplasm has glass-like properties and is fluidized by metabolic activity. *Cell* 156, 183–194. doi: 10.1016/j.cell.2013.11.028

Peng, B., Su, Y.-B., Li, H., Han, Y., Guo, C., Tian, Y.-M., et al. (2015). Exogenous alanine and/or glucose plus kanamycin kills antibiotic-resistant bacteria. *Cell Metab.* 21, 249–261. doi: 10.1016/j.cmet.2015.01.008

Peters, N. T., Dinh, T., and Bernhardt, T. G. (2011). A fail-safe mechanism in the septal ring assembly pathway generated by the sequential recruitment of cell separation amidases and their activators. *J. Bacteriol.* 193, 4973–4983. doi: 10.1128/JB.00316-11

Ramamurthi, K. S., and Losick, R. (2009). Negative membrane curvature as a cue for subcellular localization of a bacterial protein. *Proc. Natl. Acad. Sci. U.S.A.* 106, 13541–13545. doi: 10.1073/pnas.0906851106

Rudner, D. Z., and Losick, R. (2010). Protein subcellular localization in bacteria. *Cold Spring Harb. Perspect. Biol.* 2:a000307. doi: 10.1101/cshperspect.a000307

Schindelin, J., Arganda-Carreras, I., Frise, E., Kaynig, V., Longair, M., Pietzsch, T., et al. (2012). Fiji: an open-source platform for biological-image analysis. *Nat. Methods* 9, 676–682. doi: 10.1038/nmeth.2019

Strahl, H., Ronneau, S., González, B. S., Klutsch, D., Schaffner-Barbero, C., and Hamoen, L. W. (2015). Transmembrane protein sorting driven by membrane curvature. *Nat. Commun.* 6:8728. doi: 10.1038/ncomms9728

Studdert, C. A., and Parkinson, J. S. (2005). Insights into the organization and dynamics of bacterial chemoreceptor clusters through *in vivo* crosslinking studies. *Proc. Natl. Acad. Sci. U.S.A.* 102, 15623–15628. doi: 10.1073/pnas.0506040102

Thiem, S., and Sourjik, V. (2008). Stochastic assembly of chemoreceptor clusters in *Escherichia coli*. *Mol. Microbiol.* 68, 1228–1236. doi: 10.1111/j.1365-2958.2008.06227.x

Thiem, S., Kentner, D., and Sourjik, V. (2007). Positioning of chemosensory clusters in *E. coli* and its relation to cell division. *EMBO J.* 26, 1615–1623. doi: 10.1038/sj.emboj.7601610

Treuner-Lange, A., and Søgaard-Andersen, L. (2014). Regulation of cell polarity in bacteria. *J. Cell Biol.* 206, 7–17. doi: 10.1083/jcb.201403136

Wang, X., Kang, Y., Luo, C., Zhao, T., Liu, L., Jiang, X., et al. (2014). Heteroresistance at the single-cell level: adapting to antibiotic stress through a population-based strategy and growth-controlled interphenotypic coordination. *MBio* 5:e00942–13. doi: 10.1128/mBio.00942-13

Westermayer, S. A., Fritz, G., Gutiérrez, J., Megerle, J. A., Weißl, M. P. S., Schnetz, K., et al. (2016). Single-cell characterization of metabolic switching in the sugar phosphotransferase system of *Escherichia coli*. *Mol. Microbiol.* 100, 472–485. doi: 10.1111/mmi.13329

Yamada, M., and Saier, M. H. (1988). Positive and negative regulators for glucitol (gut) operon expression in *Escherichia coli*. *J. Mol. Biol.* 203, 569–583. doi: 10.1016/0022-2836(88)90193-3

Yoshioka, K., Saito, M., Oh, K. B., Nemoto, Y., Matsuoka, H., Natsume, M., et al. (1996). Intracellular fate of 2-NBDG, a fluorescent probe for glucose uptake activity, in *Escherichia coli* cells. *Biosci. Biotechnol. Biochem.* 60, 1899–1901. doi: 10.1271/bbb.60.1899

Yu, J., Liu, Y., and Chang, Z. (2017). An organelle-like structure correlated with the quiescent state of bacterial cells. *bioRxiv*. doi: 10.1101/107466

Conflict of Interest Statement: The authors declare that the research was conducted in the absence of any commercial or financial relationships that could be construed as a potential conflict of interest.

frontiers in Microbiology

ORIGINAL RESEARCH
published: 11 May 2018
doi: 10.3389/fmicb.2018.00849

Division-Based, Growth Rate Diversity in Bacteria

Ghislain Y. Gangwe Nana[1], Camille Ripoll[2], Armelle Cabin-Flaman[3], David Gibouin[3], Anthony Delaune[3], Laurent Janniere[4†], Gerard Grancher[5], Gaelle Chagny[5], Corinne Loutelier-Bourhis[6], Esther Lentzen[7], Patrick Grysan[7], Jean-Nicolas Audinot[7] and Vic Norris[1]*

[1] *Laboratory of Microbiology Signals and Microenvironment, Department of Biology, University of Rouen, Mont Saint Aignan, France,* [2] *Department of Biology, University of Rouen, Mont Saint Aignan, France,* [3] *Groupe de Physique des Matériaux, Centre National de la Recherche Scientifique, Département de Biologie, Université de Rouen Normandie, Saint-Etienne du Rouvray, France,* [4] *Laboratoire iSSB, Evry, France,* [5] *R. Salem Laboratory of Maths, UMR 6085 Centre National de la Recherche Scientifique-University of Rouen, Saint Etienne du Rouvray, France,* [6] *UMR Centre National de la Recherche Scientifique, 6014 COBRA, University of Rouen, Mont Saint Aignan, France,* [7] *Material Research & Technology Department, Luxembourg Institute of Science and Technology, Belvaux, Luxembourg*

To investigate the nature and origins of growth rate diversity in bacteria, we grew *Escherichia coli* and *Bacillus subtilis* in liquid minimal media and, after different periods of ^{15}N-labeling, analyzed and imaged isotope distributions in individual cells with *Secondary Ion Mass Spectrometry*. We find a striking inter- and intra-cellular diversity, even in steady state growth. This is consistent with the strand-dependent, hyperstructure-based hypothesis that a major function of the cell cycle is to generate coherent, growth rate diversity via the semi-conservative pattern of inheritance of strands of DNA and associated macromolecular assemblies. We also propose quantitative, general, measures of growth rate diversity for studies of cell physiology that include antibiotic resistance.

Keywords: heterogeneity, asymmetry, bacteria, DNA segregation, cell cycle, secondary Ion mass spectrometry, NanoSIMS 50, isotope-labeling

OPEN ACCESS

Edited by:
Conrad L. Woldringh, University of Amsterdam, Netherlands

Reviewed by:
Tanneke Den Blaauwen, University of Amsterdam, Netherlands
Niculina Musat, Helmholtz-Zentrum für Umweltforschung (UFZ), Germany

***Correspondence:**
Vic Norris
victor.norris@univ-rouen.fr

†Present Address:
Laurent Janniere, Génomique Métabolique, Génoscope, Institut François Jacob, CEA, CNRS, Univ Evry, Université Paris-Saclay, Evry, France

Specialty section:
This article was submitted to Microbial Physiology and Metabolism, a section of the journal Frontiers in Microbiology

Received: *27 November 2017*
Accepted: *12 April 2018*
Published: *11 May 2018*

Citation:
Gangwe Nana GY, Ripoll C, Cabin-Flaman A, Gibouin D, Delaune A, Janniere L, Grancher G, Chagny G, Loutelier-Bourhis C, Lentzen E, Grysan P, Audinot J-N and Norris V (2018) Division-Based, Growth Rate Diversity in Bacteria. Front. Microbiol. 9:849. doi: 10.3389/fmicb.2018.00849

INTRODUCTION

Although phenotypic diversity is fundamental to the way populations of bacteria deal with the opportunities and risks presented by their environment including exposure to antibiotics (Smits et al., 2006; Maisonneuve and Gerdes, 2014), the extent of this diversity and the mechanisms responsible for generating it remain to be fully elucidated. Phenotypic diversity is reflected in the diversity of growth rates. The conclusion drawn from early, influential studies on non-differentiating bacteria growing on nutrient plates (Schaechter et al., 1962) or in liquid media (Ecker and Kokaisl, 1969) was that individual cells had the same growth rate. In recent years, however, the results from microfluidics and other studies have pointed to the radically different conclusion that individual bacteria grow in apparently the same conditions with different rates (Godin et al., 2010; Campos et al., 2014; Taheri-Araghi et al., 2015; Wallden et al., 2016). That said, there is no disagreement that major changes in the growth rate *at the level of the population* due to growth in nutritionally different media are accompanied by major changes in the size and composition of the cells (Schaechter et al., 1958).

Growth rates affect the key steps of the cell cycle (Weart et al., 2007) and, reciprocally, the cell cycle affects growth rates (Wang et al., 2010; Bowman et al., 2013; Osella et al., 2014). If

an evolutionarily useful phenotypic diversity at the level of growth rates is to be generated—for example, to allow some bacteria to escape the action of an antibiotic (Balaban et al., 2004; Kim and Wood, 2016)—each phenotype must be coherent with respect to the set of genes expressed (Norris and Amar, 2012). To achieve such coherent diversity, we have proposed that one of the parental strands of DNA can be physically associated with proteins appropriate for a survival strategy whilst the other strand can be physically associated with proteins appropriate for a growth strategy, so allowing division to generate daughters with different, coherent phenotypes (Rocha et al., 2003). To investigate growth rate diversity, we grew the model organisms *Escherichia coli* and *Bacillus subtilis* in liquid minimal media, labeled them with the rare, stable isotope, ^{15}N, and analyzed them using the sensitive, quantitative imaging technique of Secondary Ion Mass Spectrometry (SIMS) (Musat et al., 2008; Boxer et al., 2009; Petroff et al., 2011).

MATERIALS AND METHODS

Cell Culture

E. coli BL21 (B F^- *ompT lon hsdS*(rB^- mB^-) *gal dcm* λ(DE3) was grown continuously at 37°C in M9 medium containing per liter 0.1 mmol $CaCl_2$, 8.498 g Na_2HPO_4-$2H_2O$, 3 g KH_2PO_4, 1 g NH_4Cl, 2 mmol $MgSO_4$, 0.5 g NaCl, 4 g D-glucose. Twenty-five milliliters of culture was shaken at 240 r.p.m. in a 250 ml Ehrlenmeyer flask in either a Buhler incubator or a New Brunswick G76 shaker. The mass doubling time was 64 min (OD_{600}). After 15 generations at an OD_{600} that never exceeded 0.1, bacteria were inoculated, via preheated pipettes, at the dilution of 1:10 in new M9 medium with $^{15}NH_4Cl$ (98% ^{15}N, ISOTEC, USA) as the only nitrogen source (note that an OD_{600} of 0.1 corresponds to early exponential growth and, in the conditions we used, plenty of nutrients are available and the cells could have continued growing exponentially for several more generations). One milliliter samples were then taken at 2, 4, 8, 16, 32, 64, and 128 min; the OD_{600} was <0.05 after labeling for 128 min. Growth was stopped by adding 1 mL of M9 ^{14}N medium at 0°C. All subsequent manipulations were then performed at or below 4°C. To exclude the artifactual incorporation of isotopes during this cold treatment, cells were grown in ^{14}N medium and growth was stopped by adding M9 ^{15}N medium at 0°C and cells were prepared and analyzed as described below; no incorporation of ^{15}N was detected (Supplementary Figure 1). To exclude the presence of contaminant bacteria, a standard metabolic test, API, was performed, which confirmed that the bacteria were *E. coli* (not shown); moreover, the bacteria produced identical colonies on agar plates (not shown) and the mass doubling time as measured by optical density corresponded to that previously reported for this strain in the same growth conditions. Finally, if it is supposed we started with equal numbers of two different species, for example, one with a mass doubling time of 36 min and the other 72 min; after 960 min of steady-state growth—round 15 generations—the slower species would be present at a frequency of $2^{960/72}/2^{960/36}$ so around 1/10000, effectively leaving a single species growing at the faster rate.

B. subtilis 168 trpC2 (Burkholder and Giles, 1947) was grown at 40°C in Spizizen medium containing per liter 50 mmol $CaCl_2$, 14 g K_2HPO_4, 6 g KH_2PO_4, 2 g $(NH_4)_2SO_4$, 1 g $C_6H_5Na_3O_7.2H_2O$, 2 mmol $MgSO_4$, 11 mg Fe III citrate, 10 μmol $MnCl_2$, 1 μmol $FeSO_4$, 4 mg $FeCl_3$, 2g D-glucose, 100 mg tryptophan, and 1 g casein hydrolysate. 50 ml of culture were shaken at 240 r.p.m. in a 250 ml Ehrlenmeyer flask in a Buhler incubator. After a 1:50 dilution of an overnight culture, bacteria were grown for 3 h to reach exponential phase (in which the mass doubling time was measured at OD_{600} as 42 min). At the start of this exponential phase, $^{13}C_6$-D-glucose (99% ^{13}C, ISOTEC, USA) and $^{15}NH_4Cl$ (98% ^{15}N, ISOTEC, USA) were added to give final ratios of ^{13}C-D-glucose:^{12}C-D-glucose of 1 and $^{15}NH_4Cl$:$^{14}NH_4Cl$ of 1. Samples of 10 mL were then taken at 90 min and 120 min. Growth was stopped by adding 10 mL of Spizizen medium at 0°C. All subsequent manipulations were then performed at or below 4°C. Samples were centrifuged in a Sigma 3K18C at 6000 r.p.m. (8,700 g) for 10 min and the pellets were resuspended in 0.1 mol/L cacodylate plus 0.04% $MgCl_2$ (to help avoid autolysis), then centrifuged again at 6000 r.p.m. for 15 min.

Preparation of Cells

Samples were centrifuged in a Sigma 3K18C at 6000 r.p.m. (8,700g) for 10 min. Then one of two fixation methods was used. Cells were fixed either with ethanol but without formaldehyde (in the case of all Figures shown except **Figure 1I** and Supplementary Figure 2G) or with formaldehyde but without ethanol (in the case of **Figure 1I** and Supplementary Figure 2G):

Method 1: The pellets were resuspended in 0.2 mol/L cacodylate plus 0.04% $MgCl_2$ (to help avoid autolysis), then centrifuged again at 6000 r.p.m. for 15 min. The following dehydration step was performed at 4°C for both *B. subtilis* and *E. coli*. The pellet was resuspended in 25% ethanol (in 0.2 mol/L cacodylate) for 20 min, then 50% ethanol (in 0.2 mol/L cacodylate pH 7.4) for 15 min and centrifuged at 6,000 r.p.m. (8700*g*) for 10 min. The pellet was then suspended in 10 μL of 50% ethanol (in 0.2 mol/L cacodylate) and 2 μL were deposited on a silicon chip (which had previously been cleaned by sonication during successive immersions in distilled water, 96% ethanol, acetone, 3:1 H_2SO_4:H_2O_2, water, and finally 96% ethanol). The dehydrated bacteria on the chip were then baked in a vacuum at 50°C for *B. subtilis* and at 40°C for *E. coli*.

Method 2: The pellets were resuspended in 1 mL of formaldehyde 3.7% buffered with 0.2 mol/L cacodylate pH 7.4 for 30 min, then centrifuged again at 12,000*g* for 10 min at 4°C. The pellet was rinsed for 10 min in 0.2 mol/L cacodylate pH 7.4; this rinsing was then repeated once. The pellet was then suspended in 20 μL of 0.2 mol/L cacodylate and 2 μL were deposited on a silicon chip. The dehydrated bacteria on the chip were then baked in a vacuum at 50°C.

SIMS Analysis

The bacteria on the chip were analyzed using a Zeiss Scanning Electron Microscope (which showed the bacterial morphology expected with no evidence for lysis, Supplementary Figure 3) and a CAMECA NanoSIMS 50. The latter entails bombardment of the sample with a high energy primary beam of ions that

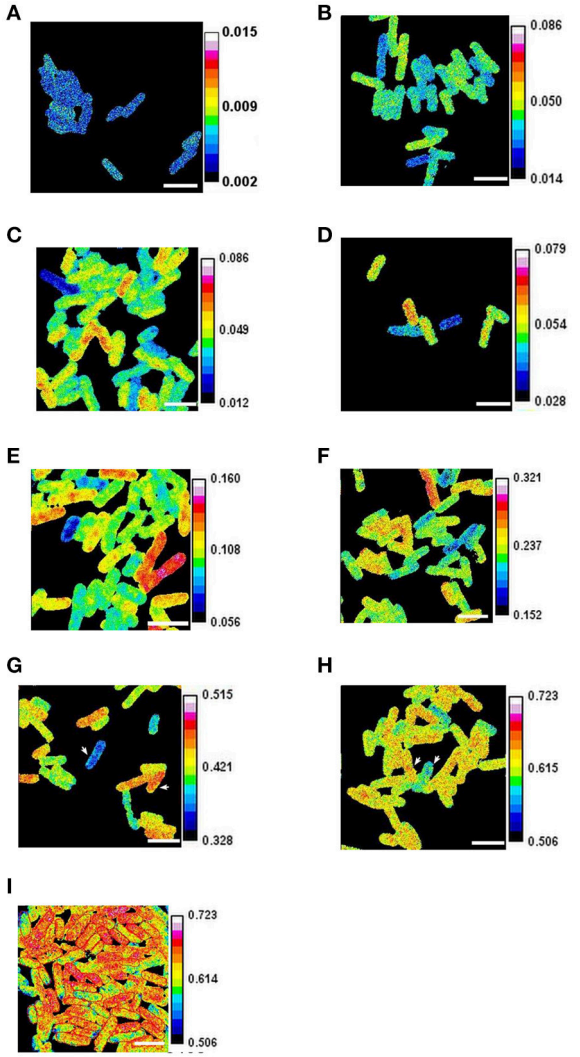

FIGURE 1 | Heterogeneous growth of *E. coli*. Cells growing in steady state (after 15 generations of growth at an OD600 below 0.1) were labeled with 90% ^{15}N for periods of **(A)** 0 min. **(B)** 2 min. **(C)** 4 min **(D)** 8 min. **(E)** 16 min. **(F)** 32 min. **(G)** 64 min. **(H)** and **(I)** 128 min. In **(I)** the cells were fixed with formaldehyde and some outlined for analysis. The ratios of $^{12}C^{15}N/(^{12}C^{14}N+^{12}C^{15}N)$ were obtained with a NanoSIMS 50. The arrowheads show cells with mass doubling times estimated using isotope incorporation as 61 min and 82 min in **(G)**, and as 70 min and 80 min in **(H)**. Scale bars 2 μm.

is focused on the surface and rastered across it; this fragments molecules contained in a nanovolume and sputters them out; a proportion of these fragments is collected as secondary ions and counted with a mass spectrometer (the useful yield), hence the name *Secondary Ion Mass Spectrometry*. These ions counted in each nanovolume can then be displayed as an image. In our conditions, the chip was bombarded with a primary beam of Cs^+ ions (the impact energy for the primary ions was set to 16 kV and the primary current to 1.3 pA or to 0.8 pA for the *B. subtilis* and *E. coli* experiments, respectively), the mass spectrometer set at a mass resolution of 5000 = M/ΔM (where ΔM is the difference between the masses of two secondary ions with the same mass number, M); five out of the six following secondary ions were counted simultaneously from the same place on the surface of the sample: ^{12}C, ^{13}C, $^{12}C^{14}N$, $^{12}C^{15}N$ or $^{13}C^{14}N$, and $^{13}C^{15}N$.

In a "sputtered section," all material containing carbon and nitrogen is sputtered out and a proportion then detected (the useful yield); the labeled nitrogen is sufficient to allow detection of membrane and cytoplasm which both contain this element. Three successive sections of the cells were sputtered out in our conditions and all the counts in the middle section were used for imaging in all the figures shown except for Supplementary Figures 4, 5. Assuming that the density of the sample is 5.10^{22} atoms/cm^3 and that the sputtering yield (the number of sputtered particles per incident primary ion) was in the range 2 to 10, about 5 nm of material was sputtered out per section of *B. subtilis* (1.3 pA, raster 8 μm, pixels 128, dwell time 40 ms/px) and about 5 nm per section of *E. coli* (0.8 pA, raster 10 μm, pixels 256, dwell time 10 ms/px). ImageJ was then used for the extraction, treatment and assembly of the data (Mutterer and Zinck, 2013). Excel and OpenOffice were also used for data collection and statistical analysis. The naturally occurring ratios of ^{15}N:^{14}N and ^{13}C:^{12}C are 0.0036 and 0.011, respectively. Isotope fractions such $^{12}C^{15}N/(^{12}C^{14}N+^{12}C^{15}N)$ were used to both estimate mass doubling times (as equaling $^{15}N/(^{14}N+^{15}N)$, see below) and avoid artifacts due to matrix effects (Lhuissier et al., 2000; Peteranderl and Lechene, 2004); the latter arise because of different useful yields in different matrices and can be allowed for by using the fraction $^{12}C^{15}N/(^{12}C^{14}N+^{12}C^{15}N)$ because both ions are affected in the same way.

The mean values of $^{13}C^{15}N/(^{13}C^{15}N+^{12}C^{15}N)$ obtained for *E. coli*, 0.0112 ± 0.0003 after 128 min, were the same as the natural fraction of ^{13}C, as expected. To ensure the validity of our results, we excluded those images in the *E. coli* experiments that had a bacterium with a mean value of $^{13}C^{15}N/(^{13}C^{15}N+^{12}C^{15}N)$ >0.016 or <0.006, that is, those bacteria with fractions out of the range 0.011 ± 0.005. This choice was because 0.005 is the standard deviation typically obtained from the pixels of a single bacterium.

Instrumental isotope fractionation in SIMS might be considered a potential problem. This fractionation means that, globally, two different numbers of secondary ions are counted for the same number of atoms of two different isotopes of the same element present in the sample (so that, for example, the isotope ratio of $^{12}C^{15}N/(^{12}C^{14}N+^{12}C^{15}N)$ counted by the machine differs from the actual ratio). The reason this might be a problem is because the fractionating effects during ionization and analysis are likely to contribute to the isotope ratios on which our conclusions are based. However, a biological variability in a reference sample (a single cell with the normal isotope ratio) has been reported as being <2% (Kopf et al., 2015). Hence the differences between the real and the counted numbers of isotopes are small compared with (1) the differences due to the Poisson nature of the counting process [the percentage error = 100/(square root of the mean)] which in the case of the 32 min and 128 min labeling, for example, is typically 7 and 3%, respectively, on the same image), (2) the differences between the bacteria (in the text we report that the %CV ranges from 5 to

20) and (3) the level of diversity apparent even within an image, which is acquired with the same settings within a short period of time; admittedly, the counting artifact could become more significant when comparing acquisitions obtained at different times and on different samples. However, it should be noted that the diversity we describe below is apparent even within a single image. And even if there were a significant error in our fractionation, this would apply to all the bacteria and simply shift the mean of the distribution of isotope ratios without affecting its variance (i.e., the growth rate diversity we observe would still be true); this is because there is a linear relationship between the isotope ratio of $^{12}C^{15}N/(^{12}C^{14}N+^{12}C^{15}N)$ measured by SIMS and bulk isotope ratios measured by other techniques (see Table 1 and Figure C8 in Kopf et al., 2015). Finally, our estimation of the mass doubling time of the population based on the isotope ratios matches the estimation of the mass doubling time based on optical density, which it would not do if there were a significant error in our measurements.

Mass Spectrometry

Electrospray ionization-mass spectrometry (ESI-MS) experiments were performed using a Bruker HCT Ultra ETD II quadrupole ion-trap (QIT) equiped with an ESI source, Esquire control 6.2 and Data Analysis 4.0 software package (Bruker, Bremen, Germany). The ESI parameters were capillary and end plate voltages set respectively to +3.5 and +3.0 kV in negative ion mode. The skimmer and the capillary exit voltages were set respectively to −30 and −80V and the injection low mass cut-off (LMCO, corresponding to the "trap drive" parameter) value was *m/z* 40. Sample solutions were either infused into the ESI source at a flow-rate of 3 μL.min^{-1} by means of a syringe pump (Cole-Palmer, Vernon Hills, Illinois, USA) for full scan data or injected into the ESI source at a flow-rate of 100 μL.min^{-1} by means of a liquid chromatographic (LC) system (Agilent 1200 chromatographic system equipped with a G1379B degasser, a G1312A high pressure binary pump and a G1329A autosampler, Agilent technologies, Waghaeusel-Wiesental, Germany) for full scan data as well for the more specific precursor-to-product ion transition termed selected reaction monitoring (SRM). For infusion, the nebulizer gas (N_2) pressure, drying gas (N_2) flow rate and drying gas temperature were 10 psi, 7.0 L/min and 300°C, respectively. For LC-injection, the nebulizer gas (N_2) pressure, drying gas (N_2) flow rate and drying gas temperature were 30 psi, 10.0 L/min and 300°C, respectively. Helium pressure in the ion trap was 1.1×10^{-5} mbar. Full scan spectra were acquired in the *m/z* 50–1,000 range, using a scan rate of 8100 *m/z* per second ("Standard-Enhanced" mode). The number of ions entering the ion trap was automatically adjusted by controlling the accumulation time with the ion charge control (ICC) mode (target 50,000) with a maximum accumulation time of 50 ms. The values of spectra averages and rolling average were 5 and 2 respectively. The selected reaction monitoring (SRM) experiments using glutamate specific precursor-to-product ion transition "*m/z* 146 → *m/z* 128" were carried out by collision induced dissociation (CID) using a resonant excitation frequency with ramping amplitude from 0.06 to 0.42 V_{p-p}, helium as the collision gas, isolation width of 1 *m/z* unit for the precursor ion (*m/z* 146) and 1 *m/z* unit for the product ion (*m/z* 128).

Estimation of Population Growth Rate

We took growth to be the increase in cell mass (irrespective of its molecular nature) as determined by nitrogen uptake thereby disregarding the question of whether cells have significantly different densities (Poole, 1977; Martinez-Salas et al., 1981; Makinoshima et al., 2003). After addition of ^{15}N to the *E. coli* culture, we measured the isotope fraction of nitrogen, x(t), using $^{12}C^{15}N/(^{12}C^{14}N+^{12}C^{15}N)$ after different periods, t. Two independent series of experiments, A and B, were performed and from 2 to 11 images were acquired and analyzed after each period of labeling. The values at 4 min for one of the B series were discarded (see SIMS analysis above). A total of 2174 bacteria in 83 images were analyzed. Given that an unsynchronized population of bacteria grows exponentially:

$$x(t) = \{x_{ext} \times (2^{t/g} - 1) + x_0\}/2^{t/g} \quad (1)$$

Where t is the period of labeling, g is the mass doubling time, x_0 is the natural level of ^{15}N (0.00366), and x_{ext} is the fraction of ^{15}N to total N in the final medium after addition of the ^{15}N. x_{ext} is obtained from adding 9 volumes of 98% ^{15}N (as estimated by the supplier) to 1 volume of natural nitrogen hence $x_{ext} = (0.9 \times 0.98) + (0.1 \times 0.00366) = 0.882$

To be coherent with the model of exponential growth of a population of bacteria where it is the population mass which is considered, all the values of the x(t) measured at each pixel of all the bacteria visible in a given image j were pooled and the mean of the isotope fractions of the pixels in an image, $\overline{x_j(t)}$, and standard deviations were calculated. In exponential growth where $\gamma = (\ln 2)/g$, the growth of the population can be expressed as:

$$Y(t) = (x_{ext} - x_0)/(x_{ext} - x(t)) = \exp(\gamma t) = 2^{t/g} \quad (2)$$

Hence, this can be expressed in terms of the image means:

$$\overline{Y_j(t)} = (x_{ext} - x_0)/(x_{ext} - \overline{x_j(t)}) = \exp(\gamma t) \quad (3)$$

Supplementary Figure 6 shows that all the image means $\overline{Y_j(t)}$, are well fitted, as expected, by an exponential function $a \times \exp(bt)$ with a determination coefficient of 0.9903 and agreement with equation (3) since $a = 0.9938$ (close to 1) and $\gamma = b = 0.0106$ min^{-1} corresponds to a population doubling time of $\ln(2)/0.0106 = 65$ min whilst the value obtained using OD_{600} was 64 min. Supplementary Figures 7, 8 show other representations of these results highlighting perturbations of growth at short labeling periods even though these perturbations do not affect cell division (Supplementary Figure 9).

Estimation of Growth Rates of Individual Cells

The nature of the growth of individual bacteria has a long history. For many years, there was a controversy over whether the growth of individual bacteria in steady state conditions

should be described by an exponential or by some other function (Kubitschek, 1986; Cooper, 2006). It is now generally believed that individual bacteria grow exponentially. This belief is supported by the observations using optical microscopy of bacteria growing on surfaces or in channels (Wang et al., 2010; Osella et al., 2014) and, with less certainty, by observations based on the buoyant density of bacteria (Godin et al., 2010).

Our estimation of the mass doubling times of individual cells using ^{15}N incorporation assumes the exponential growth of the individual bacterium, the conservation of nitrogen, the relatively slight effect of differential segregation of ^{14}N and ^{15}N (see below) and no significant changes in the media during the experiment. To grasp rapidly the rationale for our estimation, imagine that all of the unlabeled material in a new-born cell at the start of the labeling period remains within that cell during the labeling whilst all the material labeled during the period goes into the other cells. The ratio of unlabeled to labeled material is therefore 1:1 after 1 mass doubling time in the label, 1:3 after 2 mass doubling times etc. Hence:

$$x(t) = \{x_{ext} \times (2^{t/g} - 1) + x_0\}/2^{t/g} \quad \text{(S1)}$$

Where x_{ext} = the fraction of ^{15}N to total N in the final medium after addition of the ^{15}N, x_0 = the natural fraction of ^{15}N, t is the period of labeling, and g = the mass doubling time.

$$x(t) = [x_0 + \{x_{ext} \times (2^{t/g} - 1)\}]/2^{t/g} \quad \text{(S2)}$$

$$2^{t/g} = \{x_0/x(t) - x_{ext}/x(t)\}/[1 - (x_{ext}/x(t))] \quad \text{(S3)}$$

$$\ln 2^{t/g} = \ln\{(x_0/x(t) - x_{ext}/x(t))/[1 - (x_{ext}/x(t))]\} \quad \text{(S4)}$$

$$(t/g) \times \ln 2 = \ln\{(x_0/x(t) - x_{ext}/x(t))/[1 - (x_{ext}/x(t))]\} \quad \text{(S5)}$$

$$g = (t \times \ln 2)/\ln\{(x_0 - x_{ext})/x(t) \times [x(t)/(x(t) - x_{ext})]\} \quad \text{(S6)}$$

Hence:

$$g = (t \times \ln 2)/\ln\{(x_0 - x_{ext})/(x(t) - x_{ext})\} \quad \text{(S7)}$$

where $x_0 = 0.00366$ and, in the case of *E. coli*, x_{ext} is the isotope fraction in the medium obtained from adding 9/10 volumes of 98% ^{15}N (as estimated by the supplier) to 1/10 volumes of natural nitrogen:

$0.9 \times 0.98 = 0.882$
plus $0.1 \times 0.00366 = 0.000366$
so x_{ext} effectively equals 0.882

Hence in this *E. coli* experiment:

$$g = (t \times \ln 2)/\ln\{(0.00366 - 0.882)/(x(t) - 0.882)\} \quad \text{(S8)}$$

As an example, the population after 4 min labeling contains a cell with an isotope rate $x(4) = 0.0436$ which therefore has a mass doubling time of $(4 \times \ln 2)/\ln\{(0.00366–0.882)/(0.0436–0.882)\} = 59.6$ min

To validate investigations of growth rate using isotope-labeling and SIMS, we confirmed that the isotope fractions (Supplementary Figure 10) and mass doubling times (Supplementary Table 1) estimated for an individual bacterium did not vary significantly in serial sputtered sections. We then plotted the size of each bacterium against ^{15}N incorporation (Supplementary Figure 11), but found no evidence that cells deviated significantly from exponential growth.

It is important to note that two individual bacteria can have different growth rates but that these growth rates are still exponential–in other words, the exponents are different (e.g., the mass of bacterium A is proportional to $2^{(t/gA)}$ whilst the mass of bacterium B is proportional to $2^{(t/gB)}$ where gA and gB are the generation times of the bacteria A and B, respectively). This exponential growth means that as bacterium A gets bigger it grows faster and that as bacterium B gets bigger it also grows faster but that, at a particular moment, bacterium A could be growing faster than bacterium B even if B were bigger than A at that same moment.

Significance of Intercellular Diversity

Differences in the distribution of isotope fractions between cells are commonly used to determine whether these cells have significantly different mass doubling times. However, such differences would not be significant if they could be generated by a random distribution of isotope fractions. We therefore used simulations to determine whether the differences of isotope fractions between bacteria after a particular labeling period were significant. We did this in two ways. Firstly, we obtained the median value of all the isotope fractions of all the pixels of all the images of bacteria after a particular labeling period. We then used Maple 9.5 to simulate the isotope fractions in a population of bacteria that would be obtained by SIMS (Supplementary Figure 12). We defined a square of 240 × 240 pixels to correspond to a real SIMS image of 256 × 256 pixels. We filled this square completely with 192 bacteria each measuring 10 × 30 pixels corresponding to the region of interest (ROI) of a bacterium of 400 × 1,200 nm (in which each pixel is 40 × 40 nm). We supposed that the isotope fraction $^{12}C^{15}N/(^{12}C^{14}N+^{12}C^{15}N)$ is the same for all the bacteria and corresponds to the fraction really measured for a particular labeling period. For each pixel, we then chose as a reference the numbers of counts of $^{12}C^{14}N$ and of $^{12}C^{15}N$ that would give both this isotope fraction and correspond to the average of the counts per pixel of $^{12}C^{14}N$ and $^{12}C^{15}N$ actually measured. To represent the statistics of secondary ion counting in SIMS (Fleming and Bekken, 1995; Nikolov et al., 1996), these reference pixel values of $^{12}C^{14}N$ and $^{12}C^{15}N$ were then considered as means that were used in Maple to generate random values following a Poisson distribution. These random values then replaced the reference values in all pixels and the isotope fractions calculated. We simulated 5 images containing a total of 288,000 pixels corresponding to 960 bacteria. We calculated the median of the 288,000 pixels. For each bacterium, we then calculated the percentage of its pixels with a value below this median; we made a histogram from the numbers of bacteria (converted into a percentage) that have a particular percentage of their pixels below this median of the population and compared this histogram with one obtained from the experimentally measured values. We found in this simulation

that, in a population of 192 cells with 300 pixels per cell, all cells had between 42 and 59% of their pixels below the population median.

We also repeated this simulation in a simpler way using Visual Basic 6 to obtain a random distribution of pixels either above or below the median of all the pixels in all the bacteria. This was done by taking all the pixels (equals the number of bacteria multiplied by 600 pixels per bacterium) and setting them to be blue or yellow at random whilst making the total number of blue and yellow pixels the same. These pixels were then allocated to bacteria, 600 pixels at a time, and the distribution per bacterium was analyzed. The result was similar: in a population of 200,000 bacteria, each containing 600 pixels there were no bacteria that had more than 353 pixels below the median (that is, 100% of the bacteria had between 247 and 353 blue pixels, i.e., between 42 and 59%) as shown in Supplementary Figure 13 (compare this with the experimental results shown in Supplementary Figure 14 where only 37% of the bacteria have between 42 and 59% blue pixels). Moreover, the standard deviation obtained in this simulation, 12%, was the same as that obtained for the experimental control of unlabeled bacteria.

Index of Intracellular Asymmetry

To calculate the index, the pixels constituting the ROI of each bacterium were divided into two equal or nearly equal parts, P1 and P2, by a line perpendicular to the long axis such that P1 contains a total of N(P1) pixels and P2 a total of N(P2) pixels [ideally N(P1) = N(P2)]. To do this automatically, we wrote a program that first determined the rectangle that inscribed the bacterium and that then divided that rectangle into two halves (Supplementary Figure 15). If the longer side of the rectangle was an odd number of pixels, the pixels on the line bisecting this side were suppressed to prevent them from being counted twice. The median of the isotope fractions of the pixels in the cell was taken for each cell and the pixels above or below the median colored yellow or cyan, respectively. The asymmetry index, I_a, was then calculated as the absolute value of the difference between the fraction of the cyan pixels in P1, $N_C(P1)/N(P1)$, and P2, $N_C(P2)/N(P2)$:

$$I_a = \mathrm{abs}(N_C(P1)/N(P1) - N_C(P2)/N(P2)) \quad (4)$$

I_a is therefore positive and lies between 0, corresponding to no asymmetry, and 1, corresponding to a complete asymmetry. I_a is only weakly dependent on small differences between N(P1) and N(P2); in the ensemble of our experiments the mean of the differences between N(P1) and N(P2) was 9% which would give a deviation from the I_a obtained from the case of N(P1) = N(P2) of the same order of magnitude.

Statistical Analysis of Intracellular Asymmetry

To determine the significance of apparent intracellular asymmetries we modeled the probability of obtaining by chance a particular asymmetrical distribution of the cyan (or yellow) pixels between the two parts P1 and P2 (see above, Index of intracellular asymmetry). To simplify, we consider here that the image of the bacterium contains 2N pixels and that the parts P1 and P2 each contain N pixels. To further simplify the calculation, we assume that N is even and that N/2 is therefore an integer. Consider then a set of 2N objects ("pixels"), N being yellow and the other N, cyan. N "pixels" are drawn from the set of 2N "pixels" without replacement and are placed at arbitrary positions in the P1 part of the bacterium image. If, among the N "pixels", a total of ((N/2)+n) cyan "pixels" are drawn from the 2N set and placed in P1, the remaining ((N/2)–n) cyan "pixels" are automatically placed in P2. The asymmetry index is therefore $I_a(n) = 2n/N$ with $n = 0,\ldots, N/2$. Hence the probability $p[I_a(n)]$ of observing this index by chance is equal to the probability to draw (N/2+n) plus the probability to draw (N/2−n) cyan "pixels" (both have the same value of I_a). These probabilities are given by a hypergeometric distribution in which the C(Q, r) is the classical binomial coefficient defined by Q!/[(Q-r)! r!] for positive integers Q and r and with Q ≥ r:

$$C(2N, N) \times p[I_a(n)] = 2 \times C(N, (N/2) + n) \times C(N, (N/2) - n)$$

for $n = 1,\ldots, N/2$ and $C(2N, N) \times p[I_a(0)] = 2 \times C(N, N/2) \times C(N, N/2)$ for $n = 0$ (there is only a single draw corresponding to a null asymmetry index). We verified that: $\sum_{n=0}^{N/2} p[Ia(n)] = 1$ as it should.

Thus, the proportion of bacteria (with 2N pixels) that have an asymmetry index lower than or equal to 2n/N is approximately cP[Ia(n)] (Supplementary Figure 16) with:

$$cP[Ia(n)] = \sum_{j=0}^{j=n} p[Ia(j)]$$

For each bacterium, we tested the null hypothesis in which the proportion of cyan pixels in P1 is the same as the proportion of cyan pixels in P2 (i.e., no asymmetry) and the alternative hypothesis in which the proportion of cyan pixels in P1 is not the same as in P2 (i.e., asymmetry). We used the R software to carry out an exact Fisher test based on the hypergeometric law so as to compare two proportions. We obtained a *p*-value per bacterium and made a histogram for each labeling time (Supplementary Figure 17).

Finally, we compared our index of intracellular asymmetry with the normalized difference between the average isotope ratios in each half of the cell. The two measures are very similar but the median-based index has the advantage that it is clear to the reader why we argue that the asymmetries are significant (Supplementary Figure 18).

Choosing Cells for Intracellular Asymmetry Analysis

Two cells with different mass doubling times that come together by chance might be mistaken for a single, asymmetric cell. This possibility can be eliminated because such cells are usually at an angle to one another; where there was a doubt, we excluded the cell. Secondly, and importantly, any such "doublet" cells would

be bigger than most cells but we found no evidence for an increase in intracellular asymmetry with cell size (Supplementary Figure 19).

Estimation of Diversity

A general, quantitative measure of population diversity would facilitate comparisons within and between different species of bacteria and, indeed, of eukaryotic cells; it would facilitate investigation of the effects on heterogeneity of a wide variety of growth conditions and treatments. Ideally, such a yardstick would be easy to obtain and to interpret and would be free of evident artifacts. To determine the feasibility of obtaining a measure of diversity based on isotope incorporation, we excluded labeling bacteria for short periods because estimations of the growth rates revealed significant variations from the actual growth rate (that may reflect a combination of bacterial sensitivity to slight perturbations, residual growth during chilling, variations in the samples, in detection by the NanoSIMS 50 and in the nature of growth) that would be difficult to avoid (Supplementary Figures 7, 8).

We therefore explored the possibility of using bacteria labeled for a long period. We obtained the median value of the isotope fraction $[^{12}C^{15}N/(^{12}C^{14}N+^{12}C^{15}N)]$ for all of the pixels in a population of *E. coli* labeled for 128 minutes (Supplementary Figure 14A); each bacterium therefore has a percentage, p, of its own pixels above this median and (100-p) below it. A histogram was then used to give an idea of the diversity of incorporation (Supplementary Figure 14B). Since the form of the histogram depends on the arbitrary choice of the bin, we used kernel density estimation (Supplementary Figure 14C); this entails replacing each sample point of the data with a Gaussian-shaped kernel, and then summing these kernels (via Matlab). This gave distributions that could readily be compared with one another.

Growth Rate Diversity and Loss of Material

The growth rate diversity we observe is unlikely to result from different losses of small molecules by different bacteria during sample preparation for several reasons. Firstly, glutamate, the principal intracellular source of nitrogen in *E. coli*, is at a concentration of 96 mM (Bennett et al., 2009). Differential losses of the small pool during sample preparation should therefore have released detectable quantities of glutamate into the supernatants. However, we found no evidence for the release of glutamate in any of the preparative steps (Supplementary Figure 20).

Secondly, the pool of small molecules is too low a proportion of the bacterial mass for losses in this pool to account for the CVs and mean values we observe. Metabolites, cofactors and ions constitute <4% of the dry weight of *E. coli* (and this includes molecules and ions that do not contain nitrogen; Neidhardt, 1996). Moreover, the half-lives of the small molecules containing nitrogen is very short before they are incorporated into macromolecules. Since macromolecules are made—and only made—out of small precursor molecules, it could be argued that the pool of these precursors should be incorporated into macromolecules in <4% of the generation time: consider that $M.(104/100).2^{T/g} = M.2^{(T+t)/g}$ where M is the mass of the bacterium at time zero, T is the time after zero for which the bacterium has been growing, and t is the time needed to increase the bacterial mass by 4%; this equation gives t = 3.6 min. Hence, if it were true that the short labeling times had large CVs due to the loss of these molecules, the highest CV should be for 2 min labeling and all the subsequent CVs (e.g., for 4 and 8 min) should be much smaller. To quantify this, we wrote a program in Visual Basic 6 to simulate the effect of the random loss of the pool to different degrees in different cells. We set the program's variables for the isotope concentrations to the values corresponding to our growth rate calculations. We then used a random distribution of losses of the pool that gave the maximum CV we observed experimentally (20% after labeling for 2 min); exactly the same distribution of losses of the pools was subsequently used for the other labeling times. For a couple of 100 cells that initially had a pool of small molecules of 3%, the program gave CVs of 20, 14, 7.8, 3.9, 1.9, 0.94, and 0.47% for 2, 4, 8, 16, 32, 64, and 128 min labeling, respectively (Supplementary Table 2); these values are significantly different from the corresponding experimental values of 18, 20, 17, 12, 8, 6, and 5%. Moreover, the program shows that the random losses of the pool necessarily increase the apparent mass doubling times (losses of the pool cannot decrease them); in the case of the values obtained above by the program, the mass doubling time was estimated to be as much as 78 min, which is significantly more than the 64 min given by both our optical density and experimental SIMS measurements.

Thirdly, there is no evidence of loss of molecules from specific regions of the cell. Serial sputtered sections of the same bacterium gave essentially the same isotope fractions (and hence the same estimates of the corresponding mass doubling times), consistent with any intracellular diversity resulting from losses having little effect on intercellular diversity (Supplementary Figure 10 and Supplementary Table 1). In this context, suppose that the distribution of small molecules within growing cells is homogeneous and that the loss of these molecules from regions within some of the cells during preparation is responsible for the high intercellular diversity at the short labeling periods; this loss of homogeneity within the cells should cause a high intracellular asymmetry, particularly after short labeling periods when the ratio of labeled small molecules to labeled macromolecules is highest. The opposite, however, is observed (**Figure 2A**).

Fourthly, differences in the binding of the ^{15}N-ammonium ion to the membrane—and the loss of such ions—are unlikely to contribute significantly to the diversity since varying the regions of interest (ROIs) analyzed to include or exclude the membrane made little difference to the estimated mass doubling times (data not shown). Comparison of three successive sputtered sections of the *E. coli* cells after a short period of labeling showed that the high variation of ^{15}N incorporation observed in these periods is not due to small regions of high or low incorporation that may be fortuitously present in the section analyzed. In addition, population growth rates estimated from the averages of isotope counts corresponded to those measured by optical density (Supplementary Figures 6, 8) consistent with a relatively small effect of isotope losses, particularly for the longer labeling periods.

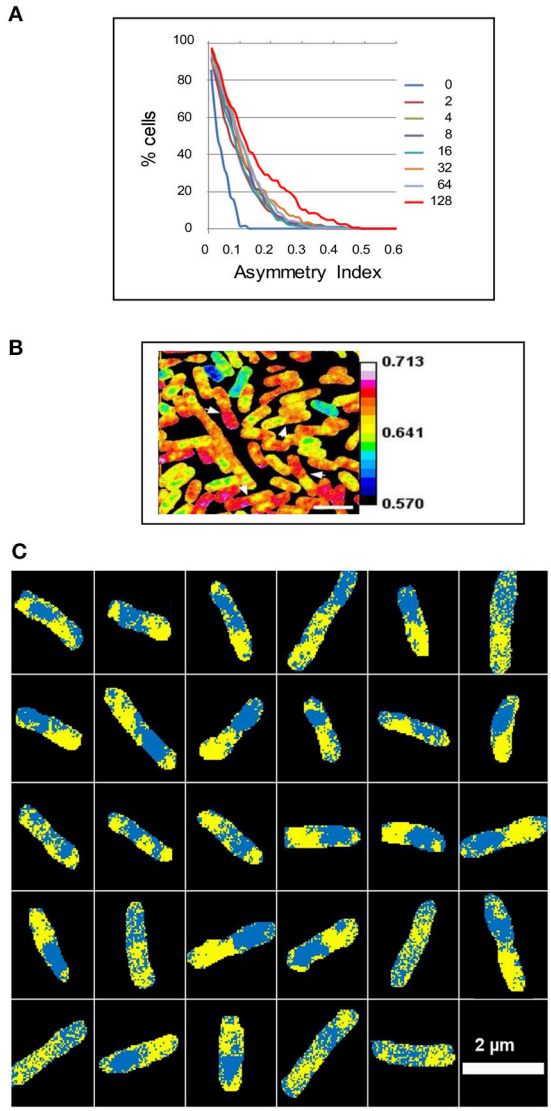

FIGURE 2 | Intracellular asymmetry of isotope distribution in *E. coli*. A steady state culture was labeled with ^{15}N for 2 to 128 min and analyzed using a NanoSIMS 50 to show the ratio of $^{12}C^{15}N/(^{12}C^{14}N+^{12}C^{15}N)$. **(A)** The cumulative percentage of cells 100*cP[I_a] above a given asymmetry index I_a in the A series. The median was taken for each cell and the asymmetry index then calculated as the proportion of pixels above the median in one half of the cell minus the proportion above the median in the other half of the cell (see Materials and Methods). **(B)** The white arrowheads show some daughter cells that have an asymmetric distribution of the isotope after labeling for 128 min. **(C)** The median was taken for each cell after labeling for 128 min and pixels above or below the median were colored yellow or cyan, respectively, to show 29 asymmetric cells within a sample of 111 cells. Scale bar 2 µm.

Finally, it might be contended that adding ^{15}N perturbs bacteria and thereby generates or simply exacerbates diversity. This is formally possible given that adding ^{15}N can result in changes to the proteome and metabolome of *E. coli* but these changes are only minor (Filiou et al., 2012) and growing *E. coli* in a 1:1 ratio of ^{15}N:^{14}N is reported to result in <1% difference in growth rates (Xie and Zubarev, 2015).

Contribution of Asymmetric Segregation to the Estimation of Growth Rates

Estimation of the growth rates of the individual bacteria in the population based on isotope ratios is subject to a possible artifact, namely that an asymmetric segregation of labeled and unlabeled material into daughter cells would result in them having different isotope ratios even if their actual growth rates were the same. Hence, it might be argued that the intercellular diversity we observe is due not only to different metabolic rates but also to an asymmetric segregation of labeled and unlabeled material (Chai et al., 2014; Gupta et al., 2014). Suppose, for example, all the cells in our experiments grew with the same growth rate, then, after one generation in the ^{15}N medium, up to half the cellular material would be unlabeled and, in the limit, if all this ^{14}N material were concentrated in one of the two daughter cells (or, after two generations, in one of the four granddaughter cells), it would appear that this cell had not grown at all. In support of this reasoning, much of the cellular material exists in the form of large *hyperstructures* with different turnover characteristics (Norris et al., 2007; Pelletier et al., 2012; Saier, 2013), which, if they had different isotope fractions and segregated separately into the future daughter cells, might generate significant asymmetry, particularly if they affected diffusion (Parry et al., 2014).

To estimate the contribution of asymmetrical segregation to growth rate diversity, we performed three analyses: (1) we calculated the proportion of cells in the population that would have been born during the labeling period, (2) we plotted the relationship between the diversity of incorporation (which is the basis for estimating growth rates) and cell size, and (3) we calculated the growth rates that would correspond to a subpopulation of half-size cells (where each half of a cell is considered a future daughter cell); each cell therefore has a "faster-growing" half and a "slower-growing half"; these half-size cells were then classed into two subpopulations of "faster growing" or "slower growing" half-size cells; we then compared the "growth rates" of these half-size cells with the estimated growth rates of the cells themselves.

(1) The total number of cells in the population after the labeling time, t, is:

$$N_0 2^{t/g}$$

where N_0 is the number of cells at the start of the labeling time and g is the mass doubling time. Noting that the number of labeled "newborn" cells is twice the increase in the number of cells over the labeling time, the number of cells born during the labeling time is:

$$2(N_0 2^{t/g} - N_0)$$

Hence the proportion of labeled cells resulting from a division during labeling is:

$$\frac{2(N_0 2^{t/g} - N_0)}{N_0 2^{t/g}}$$

or

$$\frac{2(2^{t/g}-1)}{2^{t/g}}$$

This shows that the proportion of cells that result from a division during short labeling times is small being, for example, only 4% after 2 min (Supplementary Table 3).

(2) Newborn cells are small so if the apparent intercellular diversity in growth rates were mainly due to asymmetric segregation of material, this diversity should only be characteristic of small cells at the short labeling times. This is clearly not the case (Supplementary Figure 11).

(3) By imagining two populations of half-size cells that would be formed by the parts P1 and P2 (see above) if each cell were to divide, the isotope ratios in P1 and P2 were used to estimate their "mass doubling times" (see below) and then, for each real cell, to plot these doubling times against the estimated doubling time of the cell itself (Supplementary Figure 21); the fact that the differences within cells are much smaller than the differences between cells means that intracellular segregation can only make a small contribution to our estimates of growth rate heterogeneity even in the worst scenario where the entire population comprises cells that have divided during the labeling period, which cannot be the case for short periods (Supplementary Table 3).

RESULTS

Controls Based on the Differentiating Bacterium, *B. Subtilis*

As a positive control for our investigation of phenotypic diversity in the form of metabolic diversity, an overnight culture of *B. subtilis*, a bacterium known to differentiate readily (Kerravala et al., 1964; Schaeffer et al., 1965; Veening et al., 2008), was diluted into fresh medium and grown again, as typically done in studies of its cell cycle. Once in exponential phase, ^{15}N-ammonium sulfate and ^{13}C-glucose were added to the culture. Cells were then collected after around two (90 min) and three (120 min) generations, and analyzed by SIMS (Supplementary Figures 4, 5). This revealed an intercellular diversity in the distribution of ^{15}N and ^{13}C (Supplementary Figure 4), with the distribution of ^{13}C mirroring that of ^{15}N (compare Supplementary Figures 2C,D). Moreover, depth-profiling the labeled cells showed that a particular pattern of incorporation extended throughout an individual bacterium (Supplementary Figure 5) and excluded the possibility that intercellular diversity upon long exposure to the label might be due entirely to a combination of intracellular heterogeneity and position of the section of the analysis.

Using Isotope Fractions to Estimate the Mass Doubling Time of an *E. Coli* Population

We first estimated the mass doubling time from the *global* isotope fraction, namely, the values of all the pixels in all the bacteria analyzed after a particular period of labeling with ^{15}N (Supplementary Figures 6–8). It should be noted that each point in these three figures corresponds to the isotope fraction of all the bacteria in a single image; note that the average of the isotope fractions of the individual images is not the same as the real global isotope fraction since the number of individual bacteria—and their corresponding isotope fractions—in an image varies. That said, these results do suggest a considerable variation in the mass doubling times estimated for the shorter labeling periods (Supplementary Figures 7, 8). One explanation is that the high sensitivity of the combination of isotope-labeling and SIMS reveals a bacterial response to a mechanical or other perturbation that occurred despite our best efforts (and that may missed by other techniques). The results of short labeling periods must therefore be interpreted with caution. However, for labeling periods over 32 min, the mass doubling time converged on 65 min which is close to the 64 min measured by the independent method of optical density. This gives us confidence that the isotope fraction is a valid measure of growth rate diversity within a population.

Growth Rate Diversity and Individual *E. coli* Cells

Many aspects of metabolism are captured by the growth rate. This rate can be expressed as the mass doubling time, which is sometimes estimated using the isotope fractions of elements such as nitrogen as detected by SIMS following the labeling of cells (Musat et al., 2012). SIMS is a very precise technique for measuring isotope fractions particularly when the isotopes are abundant in the sample and have a high useful yield (ratio of isotopes detected to those present in the volume analyzed), as is the case for carbon and nitrogen in many biological samples (Lechene et al., 2006) (section Materials and Methods). This means that the isotope fraction $^{15}N/(^{15}N+^{14}N)$ can be used to estimate with precision the mass doubling time of individual cells (section Materials and Methods); we therefore labeled cultures of *E. coli* with ^{15}N for periods varying from 2 to 128 min. This revealed that the isotope fraction characteristic of each cell varied significantly in every image analyzed (**Figures 1**, **2**). The intercellular diversity in labeling was then estimated in terms of the mass doubling times of individual cells; these times varied from 34 min to 123 min in the 4-min-labeled sample and from 65 min to 102 min in the 128-min-labeled sample (Supplementary Figure 2). The statistical significance of the intercellular diversity was confirmed using a simulation program (Supplementary Figure 12).

Size Distributions

The growth of populations of *E. coli* with different mass doubling times is associated with major changes in cell volume (Sloan and Urban, 1976; Kepes and Kepes, 1985; Ehrenberg et al., 2013). To investigate whether the differences in the mass doubling times of the individual cells in our study are related to differences in cell sizes, we estimated the sizes of these cells and obtained size distributions for the 10% of the fastest growing cells and the 10% of the slowest growing cells and compared them with the size distribution of the whole population. These distributions are similar (Supplementary Figure 22). This means that the growth of *E. coli* cells with different mass doubling times, that we report

here, were *not* accompanied by major changes in cell volume. At first sight, then, our results may seem at variance with those that form the cornerstone of microbial physiology. However, the above, classical studies are based on correlating the sizes of cells with the average mass doubling times of populations growing in different media whilst our results can be likened to snapshots of the mass doubling times of individual cells within a population growing in a single medium. To put it differently, at the level of populations growing in different media, the size of the cell is correlated with the mass doubling time conferred on the population by the growth medium whereas at the level of cells *within the same population*, the size of the cell is not correlated with its mass doubling time. One possible explanation is that the mechanism responsible for the global variation in mass doubling times *between* populations growing in different media differs fundamentally from the mechanism responsible for the variation of these times *within* a single population growing in the same medium. If so, what is the nature of the mechanism responsible for generating a diversity of mass doubling times for the cells *within* a single population?

Segregation and Correct Estimation of Growth Rates

It might be thought that if asymmetric segregation of material were indeed an important mechanism for generating different growth rates (as we propose) such asymmetric segregation would be important enough to give rise to false estimates of these growth rates. In fact, only a small proportion of cells actually divide during the short labeling times (where the growth rate diversity is greatest); moreover, the unequal distribution of label on division does not affect the *calculation* of mass doubling times significantly because the differences in label between the daughters is small. The argument that we develop below is that though this difference in distribution is sufficient to underpin the hypothesis that asymmetric segregation is responsible for generating different growth rates, it is too slight in itself to affect the estimates of growth rate.

In principle, both differences in growth rates and differences in the segregation of labeled or unlabeled material into daughter cells could contribute to the intercellular diversity in ^{15}N distributions. Labeling for periods shorter than the mass doubling time of the population might be expected to give a snapshot of differences in growth rates. Labeling for periods longer than the mass doubling time (which should decrease the growth-rate-dependent diversity of ^{15}N distributions) might nevertheless show persistence of an artifactual, growth-rate-*independent*, intercellular diversity if the asymmetric segregation of labeled and unlabeled material followed by cell division were an important factor in the *estimation* of growth rates.

To try to evaluate the relative contributions of growth rate and segregation-division to intercellular ^{15}N distributions, we therefore compared the distributions of mass doubling times estimated after different periods of labeling (Supplementary Figure 2); the coefficients of variation (CV% = 100 × standard deviation/mean) at 2, 4, 8, 16, 32, 64, and 128 min were 18, 20, 17, 12, 8, 6, and 5%, respectively. The higher coefficients at the shorter periods are consistent with an important role for growth rate in the intercellular diversity of ^{15}N incorporation whilst the fact that the coefficients remain relatively high at the longer periods is consistent with a possible role for the asymmetric segregation of labeled and unlabeled material. To investigate further the contribution of this type of asymmetric segregation to our estimates of growth rates, we reasoned that it could only affect our calculation of the growth rate of those cells that originated from a division occurring during the labeling period (which would have inherited different amounts of the label). The proportion of cells that might be affected in this way is small for brief labeling periods, being only 4% of the population labeled for 2 min (Supplementary Table 3), whereas the proportion of cells that actually differ from one another is much greater; moreover, if asymmetric segregation were responsible, only newborn cells—which are short—should be affected for brief labeling periods but there is no evidence that the subpopulation of short cells has a greater intercellular diversity than that of long cells (Supplementary Figure 11). To estimate the *maximum* contribution that intracellular asymmetry of labeled and unlabeled material might make to the estimation of intercellular growth rates, the pixels constituting the image of each bacterium were divided into two equal or nearly equal parts (Supplementary Figure 15) and the 'growth rates' corresponding to each part were estimated separately. Plotting the estimated growth rate of each of these imaginary, half-size cells against the estimated growth rate of the cell itself shows that the variation in incorporation within cells is too small to generate the observed variation in incorporation between cells from which growth rates are estimated (Supplementary Figure 21). Taken together, these results mean that the asymmetric segregation of labeled and unlabeled material can only have a small effect on the actual estimation of growth rates, particularly after periods of labeling much briefer than the mass doubling time.

Growth Rate Diversity and the Cell Cycle

What are the origins of the extensive growth rate diversity we and others observe (Godin et al., 2010; Campos et al., 2014; Taheri-Araghi et al., 2015; Wallden et al., 2016)? One possibility is that it originates in the cell cycle, which is intimately linked to growth rate diversity in differentiating bacteria such as *Caulobacter crescentus*. We have previously proposed that the cell cycle in both differentiating and non-differentiating bacteria generates a coherent metabolic diversity because the parental DNA strands and physically associated macromolecules are segregated during the replication of the chromosome such that subsequent division results in one daughter cell receiving macromolecules responsible for slow growth and the other daughter cell receiving macromolecules responsible for fast growth (Rocha et al., 2003). These sets of macromolecules are part of the class of molecular assemblies termed *hyperstructures* that perform specific functions at intracellular locations defined in part by their association with the chromosome (Norris et al., 2007; Llopis et al., 2010). It might therefore be expected that these hyperstructures would have different rates of turnover according to their function, composition and location. We reasoned that these different rates of turnover might, in principle, translate

into differences in our labeling experiments in the intracellular distribution of ^{15}N so, to explore the possible involvement of the cell cycle in the generation of growth rate diversity, we obtained the median value of the pixels of each individual cell and displayed pixels above or below that value in yellow or cyan, respectively; we then divided each cell roughly into two halves (corresponding to the future daughter cells) and estimated asymmetry as an index, I_a, calculated as the absolute value of the fraction of cyan pixels in one half minus the fraction of cyan pixels in the other half. To determine the significance of these estimates, we obtained the probability distributions of the asymmetry index (Supplementary Figure 17). Except for the control, most of the *p*-values are small and the null hypothesis of no significant asymmetry can be rejected. We then plotted the cumulative percentage of bacteria as a function of the asymmetry index after each labeling period. An increase in asymmetry was striking after 128 min labeling (**Figure 2**). To quantify the significance of this asymmetry, we used the hypergeometric distribution of yellow and cyan pixels within a cell. This showed that the probability of observing by chance a bacterium with an asymmetry index >0.16 is <0.001 (Supplementary Figure 16). This probability distribution corresponds to that obtained for the unlabeled control bacteria (**Figure 2A** and Supplementary Figure 16). For the labeled bacteria, however, all curves show many bacteria with asymmetry indices >0.16 which is highly unlikely to occur by chance (Supplementary Figure 16); for example, 15% of the bacteria after 16 min labeling have an asymmetry index >0.16 although the probability of observing by chance a single bacterium with an asymmetry index >0.16 is <0.001, whilst at 128 min, over 30% of the bacteria had an index over 0.16 (**Figure 2A**). Why does asymmetry increase up to 128 min? 128 min corresponds to the time that would be needed for cells growing with the same rate of 64 min to undergo two mass doublings. In the classic experiment of Meselson and Stahl (Meselson and Stahl, 1958), an increase in asymmetry of labeled material from one to two mass doublings revealed the semi-conservative replication of DNA. Our results may therefore be explained if the labeled and unlabeled DNA strands plus associated hyperstructures (themselves containing different proportions of labeled and unlabeled material) were to follow the pattern of DNA distribution characteristic of semi-conservative replication and hence if the cell cycle itself via the distribution of these different hyperstructures were indeed to be a general and major determinant of growth rate diversity (**Figure 3**).

Toward a Standard Measure of Growth Rate Diversity

The distribution of growth rates of the individuals in a population is an important characteristic of a species because it reflects the overall capacity of the species to respond to its environment. This environment can include, of course, the presence of antibiotics. There are several ways that the isotope fraction, $[^{12}C^{15}N/(^{12}C^{14}N+^{12}C^{15}N)]$, might be used to measure growth rate diversity. Ideally, such measurements should be standardized and, for example, samples might be taken at times based on the mass doubling time of the population as here where samples

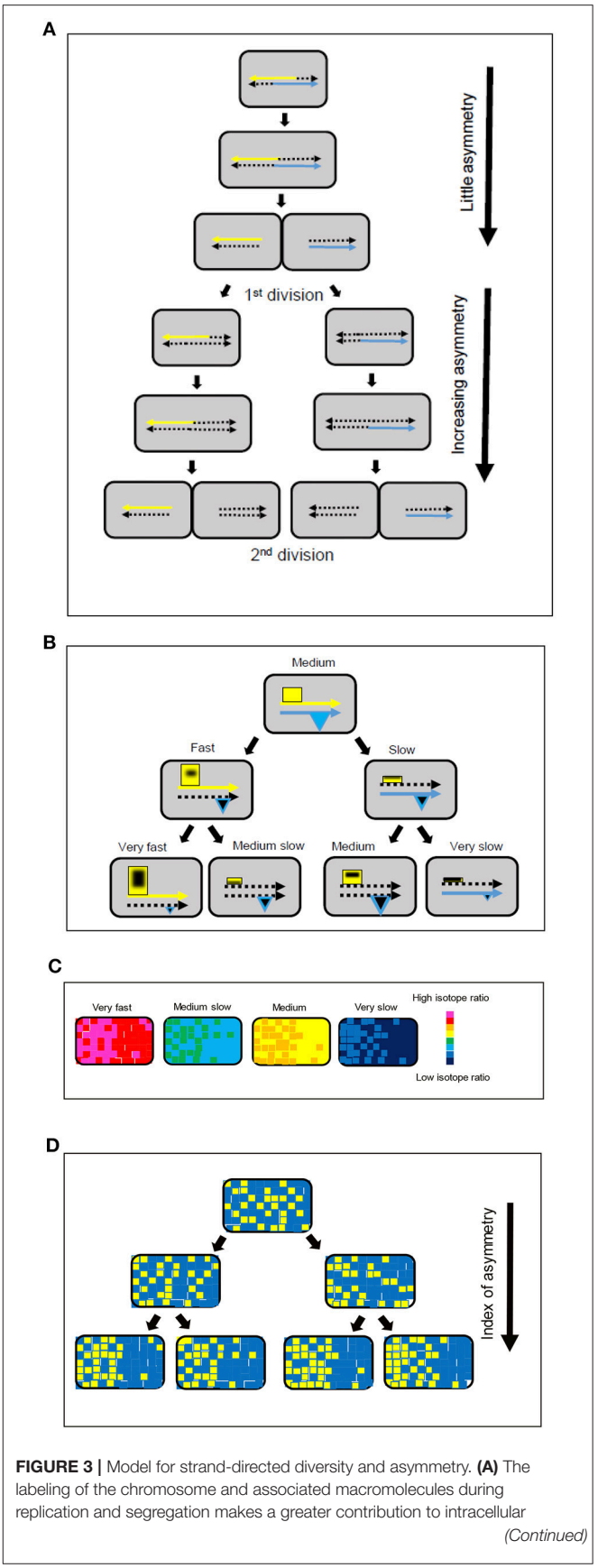

FIGURE 3 | Model for strand-directed diversity and asymmetry. **(A)** The labeling of the chromosome and associated macromolecules during replication and segregation makes a greater contribution to intracellular

(Continued)

FIGURE 3 | asymmetry after the first division. **(B)** Positive feedback and association with the parental DNA strands leads to an increase in the size of hyperstructures (yellow rectangles) responsible for fast growth in one daughter cell and a decrease in the size of these hyperstructures in the other daughter cell, as shown in the left-hand branch; this tendency continues into the next generation. There is a corresponding decrease in expression of the hyperstructures responsible for fast growth, as shown in the right-hand branch; in parallel, expression of the hyperstructures responsible for survival (blue triangles) can either be maintained or decrease. The continuous yellow and blue arrows represent the parental DNA strands, the dotted arrows represent newly synthesized strands, and the black shapes within the hyperstructures represent ^{15}N-labeled material. **(C)** Growth rate diversity in the four, second generation cells in the bottom line of **(B)** shown using a chromatic scale. **(D)** Increase in index of intracellular asymmetry (arrow) shown by classing pixels above (yellow) or below (blue) the median of the isotope ratio for the pixels within a single bacterium for the four, second generation, cells in **(B)**. Comparison of the same cells in **(C,D)** shows that there is no contradiction between the evidence for the lack of importance of the intracellular asymmetry of labeled/unlabeled material in the actual estimation of mass doubling times **(C)** and the evidence for the importance of strand-based asymmetry as a mechanism for generating intercellular diversity **(D)**.

were taken at 2, 4, 8, 16, 32, 64, and 128 min, that is, 2^x (where $-5 \leq x \leq 1$) of the doubling time of 64 min as measured by optical density. The shorter periods of labeling show the sensitivity of isotope incorporation to physical and/or chemical stimuli, which, though interesting in its own right, means that such periods are unsuitable for estimating doubling times in steady state (section Materials and Methods). For the A series, the estimated doubling times after 2, 4, 8, and 16 min labeling periods are clearly too different from the steady state doubling time (as measured by optical density) to be useful whereas, for the B series, only the 2 and 4 min periods are different. The distribution of growth rates is one measure of diversity (see above) whilst the distribution of the asymmetry indices, I_a, is another. The distribution of growth rates can be usefully expressed as the distribution of mass doubling times (Supplementary Figure 2); to facilitate comparisons between different species growing in different conditions with very different average growth rates, we propose to represent the diversity of estimated growth rates using the growth rate index of the single cell, I_g, defined as:

(the difference between the estimated mass doubling time of the bacterium and the mass doubling time of the sample population)/the mass doubling time of the sample population

where the mass doubling time of the sample population is estimated using the mean isotope fraction of all the bacteria in the sample after a particular labeling period. Hence, $I_g = 0$, $I_g > 0$ and $I_g < 0$ for a bacterium growing with a mass doubling time that is the same as, greater than, or less than of the population, respectively. One advantage of using I_g is that the standard deviation of its distribution is identical to the familiar coefficient of variation of the mass doubling times. The relative growth rate measured by I_g is underpinned by the structuring of intracellular activity that is measured by I_a. We therefore propose that each cell sampled after each labeling period be characterized by these two indices (Supplementary Figure 23) whilst the population at each time be characterized by the standard deviation of I_g (since the mean of I_g is zero by definition) and by the mean and standard deviation of I_a (Supplementary Table 4), thereby providing quantitative measures for studies of growth rate diversity.

DISCUSSION

Growth Rate Diversity

It has been argued that the laws underlying cell growth—and, in particular, those directly relevant to the cell cycle such as growth rate—are to be found not by studying single cells but rather by studying cells as an aggregate (Cooper, 2006). This argument is weakened by evidence for growth rate diversity in exponentially growing cultures of *E. coli* cells, which video-microscopy has shown grow with different rates (Kiviet et al., 2014) that may vary two- to four-fold (Wang et al., 2010; Campos et al., 2014; Osella et al., 2014). A very different, high precision technique, which depends on trapping individual *E. coli* in a resonator and determining their buoyant densities, has also shown a wide variety of growth rates (Godin et al., 2010). To complement these approaches, we have investigated growth rate diversity using the combination of labeling with stable isotopes and analysis by SIMS, as commonly used for studies of metabolism in microbial ecology. This combination has the advantages of being quantitative and precise and of allowing isotopes to be localized on the scale of 50–100 nm; using this combination, we have obtained evidence for a considerable intercellular diversity of incorporation of isotopes for all labeling periods in a population of the non-differentiating bacterium, *E. coli*, growing in liquid medium in steady state conditions. This diversity largely reflects growth rates that can vary four-fold even in a sample of a couple of 100 cells. We then extended this study to the very different model system of *B. subtilis* where we also obtained evidence for a considerable intercellular diversity (Supplementary Figure 4).

What then is the explanation for this growth rate diversity? Clearly, this explanation may involve fluctuations in gene expression and metabolic cycles (Korobkova et al., 2004; Tu et al., 2007; Peterson et al., 2015). An alternative or additional possibility is that the cell cycle—which comprises the replication of the chromosome, the segregation of the chromosomes, and cell division—is itself responsible for generating growth rate diversity. In support of this possibility, cell division is important in establishing growth rates (Reshes et al., 2008) and in generating diversity in bacteria (Musat et al., 2008; Rego et al., 2017; Yu et al., 2017). The segregation of intracellular material in *E. coli* is characterized by asymmetry (Lindner et al., 2008; Wang et al., 2010; Chai et al., 2014; Bergmiller et al., 2017). Such segregation, followed by cell division, might also generate a coherent metabolic diversity: in the strand-specific model, which has a eukaryotic echo (Klar, 1987), the strand-specific hyperstructures that separately accompany each of the parental DNA strands are segregated to separate positions during the replication of the chromosome; this results in one of the daughter cells receiving hyperstructures that steer it toward a slow growth phenotype whilst the other daughter cell receives hyperstructures that steer it toward a fast growth phenotype (Rocha et al., 2003). It has indeed been found that genes and

their products are located together (Llopis et al., 2010) and that the leading and lagging strands are in different locations (White et al., 2008). To explore further this idea, we analyzed the asymmetric distributions of ^{15}N within cells after different periods of labeling. This distribution was striking after 128 min, that is, after an average of two mass doubling times (**Figure 2**). One seductive interpretation is that this reflects the combination of the semi-conservative nature of DNA replication (Meselson and Stahl, 1958) and the strand-specific phenotype (Rocha et al., 2003).

How exactly might the strand-based separation of hyperstructures generate coherent diversity? Our results are consistent with the operation of two related processes (**Figure 3**). In this hypothesis, the first process is the positive feedback nature of the distribution of transcriptional and translational resources according to the parental DNA inherited by the daughter cell (the areas of the rectangles and the triangles in **Figure 3B** correspond to the sizes of the different hyperstructures); this positive feedback occurs because there is competition within the cell for these resources during chromosome replication such that the hyperstructures that are physically associated with a parental strand (e.g., by coupled transcription-translation) and, in particular, the hyperstructures responsible for fast growth, outcompete their equivalents on the new strand (left branch, **Figure 3B**); hence there is a corresponding decrease in those "fast growth" hyperstructures that are associated with the new strand (e.g., cell labeled "medium slow," **Figure 3B**). The second process is the positive feedback nature of the distribution of resources between growth strategies (which includes RNA polymerases, ribosomes and transcription-translation in general) and survival strategies (which includes DNA-binding proteins and storage materials). There are several reasons why this positive feedback might occur; for example, transcriptional activators might preferentially associate with one another and with their binding sites on one DNA strand, or the accumulation of survival-related material might reduce transcription-translation from the chromosome of one of the future daughter cells; this latter possibility is illustrated by the greater combined area of the hyperstructures in the "medium growth" cell compared with the combined area of these hyperstructures in the "very slow growth" cell at the right of the bottom line of **Figure 3B**. Material that is synthesized during the labeling (black shapes within the hyperstructures in **Figure 3B**) is distributed differently across the bacterial population to give the isotope ratios per pixel shown schematically in **Figure 3C**.

Semi-conservative Distribution of Hyperstructures

The combination of isotope ratios and medians is extremely sensitive and, by taking the median value of the isotope ratios of all the pixels in a bacterium and displaying these pixels as yellow or blue according to whether they are above or below this median, respectively, we find that labeled and unlabeled material is distributed heterogeneously (**Figure 2C**). This is to be expected since much of this material is in the form of hyperstructures. This material is, however, also distributed asymmetrically; again, this might be expected since the location of certain hyperstructures will be determined by the location of corresponding regions of DNA, which are themselves located in particular places in the cell (as, for example, in *C. crescentus* Viollier et al., 2004). In analyzing this asymmetry, it is significant that the first generation of daughter cells has a relatively low asymmetry index but that the second generation of cells has a high asymmetry index (**Figure 3**), which echoes the evidence for semi-conservative replication (Meselson and Stahl, 1958) and which is consistent with the major role of strand separation and hyperstructures in producing diversity or, more precisely, is consistent with hyperstructures with different metabolic activities segregating with one or other of the DNA strands into the future daughter cells (Rocha et al., 2003).

The results presented here on intracellular and intercellular diversity, taken together with the results from other approaches, have implications for the control of the phenotype by the cell cycle. These results are consistent with a major role for the cell cycle in the generation of a heterogeneous but phenotypically coherent population of cells that travel between the two attractors of growth and survival and that are ready to deal with a wide diversity of challenges and opportunities. This role would entail the growth rate being reset during the cell cycle; the operation of a mechanism to do this might explain the puzzling observation that the cells in our experiments had similar diameters despite their different growth rates. *E. coli* growing with generation times shorter than the time required for replication of the chromosome should be undergoing multi-fork replication and be wider (to accommodate the extra DNA) than cells growing much more slowly (Schaechter et al., 1958; Zaritsky and Pritchard, 1973; Zaritsky, 2015). A cell growing rapidly would not need to change its diameter if its growth rate were not maintained beyond division and, consistent with this, no significant differences in diameter were reported in a microfluidics study showing widely different growth rates (Wang et al., 2010).

The results presented here also have implications for the control of the cell cycle itself. Control over cell division has recently been attributed to the combination of a "sizer" and a "timer" (Osella et al., 2014) or to a constant increase in volume between divisions (Campos et al., 2014; Taheri-Araghi et al., 2015). In the latter case, the hypothesis has been extended to the control over the initiation of DNA replication (Taheri-Araghi, 2015). Control over the cell cycle can, however, be attributed to factors that are directly related to phenotypic diversity such as (1) the composition in terms of macromolecular assemblies or hyperstructures, responsible for survival and growth, and (2) the intensity of activity of these hyperstructures (Norris and Amar, 2012). In this hypothesis, the cell cycle not only generates cells with different combinations of hyperstructures appropriate for growth or survival but also *is itself driven* by these combinations. Evidence for this role of hyperstructure dynamics in cell cycle control may come from more information about the activity of hyperstructures via isotope labeling and SIMS.

Measures of Growth Rate Diversity

In 1949, Jacques Monod remarked: "The study of the growth of bacterial cultures does not constitute a specialized subject

or branch of research: it is the basic method of Microbiology" (Monod, 1949). The growth rate diversity of a culture might therefore be considered basic to Microbiology. Certain aspects of this diversity are captured by the distribution of isotope incorporation in a steady state population and it could also be argued that this distribution is a unique characteristic of a species. As such, the growth rate distribution could serve as a yardstick to estimate the effects of treatments that include alterations to the genome and addition of antibiotics. One question therefore is how best to represent the growth rate distribution. In addition to the usual distribution of mass doubling times and their means and standard deviations, in the case of SIMS analysis of isotope-labeled cells, we suggest that at least two other parameters should be measured: the growth rate index, I_g, and the intracellular asymmetry index, I_a. I_g can be obtained from the estimated growth rates; these estimates do not require correcting since the calculations themselves are not greatly affected by the segregation of labeled and unlabeled material. That said, our data indicate that the strand-specific segregation of hyperstructures is an important determinant of growth rate; the extent of this segregation is revealed by I_a. Given the importance of the cell cycle in generating diversity, we also suggest that cells should be labeled for periods that are directly related to the mass doubling time.

AUTHOR CONTRIBUTIONS

GYG: Performed experiments and analyzed data; CR, AC-F, AD, GG, GC, and VN: Analyzed data; DG, CL-B, EL, PG, LJ, and J-NA: Performed experiments. All authors helped write the paper.

ACKNOWLEDGMENTS

For technical and statistical assistance, we thank Laurent Quillet, Josselin Bodilis, Sylvaine Buquet, Sylvie Bertin, and Angela Flores Ribeiro. For advice, we thank Arieh Zaritsky, Conrad Woldringh, Itzhak Fishov, Alfonso Jimenez-Sanchez, Silvia Zaoli, Marco Lagomarsino-Cosentino, and Dick D'Ari. For support, we thank the Epigenomics Project, Genopole, DYCOEC (GDR 2984) and the European Network in Systems Biology (GDRE 513), Conseil Général de l'Eure, the Labex SynOrg (ANR-11-LABX-0029), the Région Haute-Normandie (CRUNCH network) and the European Regional Development Fund (ERDF 31708).

SUPPLEMENTARY MATERIAL

The Supplementary Material for this article can be found online at: https://www.frontiersin.org/articles/10.3389/fmicb.2018.00849/full#supplementary-material

REFERENCES

Balaban, N. Q., Merrin, J., Chait, R., Kowalik, L., and Leibler, S. (2004). Bacterial persistence as a phenotypic switch. *Science* 305, 1622–1625. doi: 10.1126/science.1099390

Bennett, B. D., Kimball, E. H., Gao, M., Osterhout, R., Van Dien, S. J., and Rabinowitz, J. D. (2009). Absolute metabolite concentrations and implied enzyme active site occupancy in *Escherichia coli*. *Nat. Chem. Biol.* 5, 593–599. doi: 10.1038/nchembio.186

Bergmiller, T., Andersson, A. M. C., Tomasek, K., Balleza, E., Kiviet, D. J., Hauschild, R., et al. (2017). Biased partitioning of the multidrug efflux pump AcrAB-TolC underlies long-lived phenotypic heterogeneity. *Science* 356, 311–315. doi: 10.1126/science.aaf4762

Bowman, G. R., Perez, A. M., Ptacin, J. L., Ighodaro, E., Folta-Stogniew, E., Comolli, L. R., et al. (2013). Oligomerization and higher-order assembly contribute to sub-cellular localization of a bacterial scaffold. *Mol. Microbiol.* 90, 776–795. doi: 10.1111/mmi.12398

Boxer, S. G., Kraft, M. L., and Weber, P. K. (2009). Advances in imaging secondary ion mass spectrometry for biological samples. *Annu. Rev. Biophys.* 38, 53–74. doi: 10.1146/annurev.biophys.050708.133634

Burkholder, P. R., and Giles, N. H. Jr. (1947). Induced biochemical mutations in *Bacillus subtilis*. *Am. J. Bot.* 34, 345–348. doi: 10.1002/j.1537-2197.1947.tb12999.x

Campos, M., Surovtsev, I. V., Kato, S., Paintdakhi, A., Beltran, B., Ebmeier, S. E., et al. (2014). A constant size extension drives bacterial cell size homeostasis. *Cell* 159, 1433–1446. doi: 10.1016/j.cell.2014.11.022

Chai, Q., Singh, B., Peisker, K., Metzendorf, N., Ge, X., Dasgupta, S., et al. (2014). Organization of ribosomes and nucleoids in *Escherichia coli* cells during growth and in quiescence. *J. Biol. Chem.* 289, 11342–11352. doi: 10.1074/jbc.M114.557348

Cooper, S. (2006). Distinguishing between linear and exponential cell growth during the division cycle: single-cell studies, cell-culture studies, and the object of cell-cycle research. *Theor. Biol. Med. Model.* 3:10. doi: 10.1186/1742-4682-3-10

Ecker, R. E., and Kokaisl, G. (1969). Synthesis of protein, ribonucleic acid, and ribosomes by individual bacterial cells in balanced growth. *J. Bacteriol.* 98, 1219–1226.

Ehrenberg, M., Bremer, H., and Dennis, P. P. (2013). Medium-dependent control of the bacterial growth rate. *Biochimie* 95, 643–658. doi: 10.1016/j.biochi.2012.11.012

Filiou, M. D., Varadarajulu, J., Teplytska, L., Reckow, S., Maccarrone, G., and Turck, C. W. (2012). The 15N isotope effect in *Escherichia coli*: a neutron can make the difference. *Proteomics* 12, 3121–3128. doi: 10.1002/pmic.201200209

Fleming, R. H., and Bekken, B. M. (1995). Isotope ratio and trace element imaging of pyrite grains in gold ores. *Int. J. Mass Spectrom. Ion Process.* 143, 213–224. doi: 10.1016/0168-1176(94)04138-W

Godin, M., Delgado, F. F., Son, S., Grover, W. H., Bryan, A. K., Tzur, A., et al. (2010). Using buoyant mass to measure the growth of single cells. *Nat. Methods* 7, 387–390. doi: 10.1038/nmeth.1452

Gupta, A., Lloyd-Price, J., Neeli-Venkata, R., Oliveira, S. M., and Ribeiro, A. S. (2014). *In vivo* kinetics of segregation and polar retention of MS2-GFP-RNA complexes in *Escherichia coli*. *Biophys. J.* 106, 1928–1937. doi: 10.1016/j.bpj.2014.03.035.

Kepes, F., and Kepes, A. (1985). Postponement of cell division by nutritional shift-up in *Escherichia coli*. *J. Gen. Microbiol.* 131, 677–685. doi: 10.1099/00221287-131-3-677.

Kerravala, Z. J., Srinivasan, V. R., and Halvorson, H. O. (1964). Endogenous factor in sporogenesis in bacteria. Ii. growth and sporulation in *Bacillus Subtilis*. *J. Bacteriol.* 88, 374–380.

Kim, J. S., and Wood, T. K. (2016). Persistent persister misperceptions. *Front. Microbiol.* 7:2134. doi: 10.3389/fmicb.2016.02134

Kiviet, D. J., Nghe, P., Walker, N., Boulineau, S., Sunderlikova, V., and Tans, S. J. (2014). Stochasticity of metabolism and growth at the single-cell level. *Nature* 514, 376–379. doi: 10.1038/nature13582

Klar, A. J. (1987). Differentiated parental DNA strands confer developmental asymmetry on daughter cells in fission yeast. *Nature* 326, 466–470. doi: 10.1038/326466a0

Kopf, S. H., McGlynn, S. E., Green-Saxena, A., Guan, Y., Newman, D. K., and Orphan, V. J. (2015). Heavy water and (15) N labelling with NanoSIMS analysis reveals growth rate-dependent metabolic heterogeneity in chemostats. *Environ. Microbiol.* 17, 2542–2556. doi: 10.1111/1462-2920.12752

Korobkova, E., Emonet, T., Vilar, J. M. G., Shimizu, T. S., and Cluzel, P. (2004). From molecular noise to behavioural variability in a single bacterium. *Nature* 428, 574–578. doi: 10.1038/nature02404

Kubitschek, H. E. (1986). Increase in cell mass during the division cycle of *Escherichia coli* B/rA. *J. Bacteriol.* 168, 613–618. doi: 10.1128/jb.168.2.613-618.1986

Lechene, C., Hillion, F., McMahon, G., Benson, D., Kleinfeld, A. M., Kampf, J. P., et al. (2006). High-resolution quantitative imaging of mammalian and bacterial cells using stable isotope mass spectrometry. *J. Biol.* 5:20. doi: 10.1186/jbiol42

Lhuissier, F., Lefebvre, F., Gibouin, D., Demarty, M., Thellier, M., and Ripoll, C. (2000). Secondary ion mass spectrometry imaging of the fixation of 15N-labelled NO in pollen grains. *J Microsc.* 198(Pt 2), 108–115. doi: 10.1046/j.1365-2818.2000.00690.x

Lindner, A. B., Madden, R., Demarez, A., Stewart, E. J., and Taddei, F. (2008). Asymmetric segregation of protein aggregates is associated with cellular aging and rejuvenation. *Proc. Natl. Acad. Sci. U.S.A.* 105, 3076–3081. doi: 10.1073/pnas.070893110

Llopis, P. M., Jackson, A. F., Sliusarenko, O., Surovtsev, I., Heinritz, J., Emonet, T., et al. (2010). Spatial organization of the flow of genetic information in bacteria. *Nature* 466, 77–81. doi: 10.1038/nature09152

Maisonneuve, E., and Gerdes, K. (2014). Molecular mechanisms underlying bacterial persisters. *Cell* 157, 539–548. doi: 10.1016/j.cell.2014.02.050

Makinoshima, H., Aizawa, S., Hayashi, H., Miki, T., Nishimura, A., and Ishihama, A. (2003). Growth phase-coupled alterations in cell structure and function of *Escherichia coli*. *J. Bacteriol.* 185, 1338–1345. doi: 10.1128/JB.185.4.1338-1345.2003

Martinez-Salas, E., Martin, J. A., and Vicente, M. (1981). Relationship of *Escherichia coli* density to growth rate and cell age. *J. Bacteriol.* 147, 97–100.

Meselson, M., and Stahl, F. W. (1958). The Replication of DNA in *Escherichia Coli*. *Proc. Natl. Acad. Sci. U.S.A.* 44, 671–682. doi: 10.1073/pnas.44.7.671

Monod, J. (1949). The growth of bacterial cultures. *Annu. Rev. Microbiol.* 3, 371–394. doi: 10.1146/annurev.mi.03.100149.002103

Musat, N., Foster, R., Vagner, T., Adam, B., and Kuypers, M. M. (2012). Detecting metabolic activities in single cells, with emphasis on nanoSIMS. *FEMS Microbiol. Rev.* 36, 486–511. doi: 10.1111/j.1574-6976.2011.00303.x

Musat, N., Halm, H., Winterholler, B., Hoppe, P., Peduzzi, S., Hillion, F., et al. (2008). A single-cell view on the ecophysiology of anaerobic phototrophic bacteria. *Proc. Natl. Acad. Sci. U.S.A.* 105, 17861–17866. doi: 10.1073/pnas.0809329105

Mutterer, J., and Zinck, E. (2013). Quick-and-clean article figures with FigureJ. *J. Microsc.* 252, 89–91. doi: 10.1111/jmi.12069

Neidhardt, F. C. (1996). In *Escherichia coli and Salmonella: Cellular and Molecular Biology, 2nd Edn.* eds F. C. Neidhardt, R. Curtiss, J. L. Ingraham, E. C. C. Lin, K. B. Low, B. Magasanik, W. S. Reznikoff, M. Riley, M. Schaechter and H. E. Umbarger. Washington, DC: American Society for Microbiology), 14.

Nikolov, S. G., Hutter, H., and Grasserbauer, M. (1996). De-noising of SIMS images via wavelet shrinkage. *Chemomet. Intell. Lab. Syst.* 34, 263–273. doi: 10.1016/0169-7439(96)00003-2

Norris, V., and Amar, P. (2012). Chromosome replication in *Escherichia coli*: life on the Scales. *Life* 2, 286–312. doi: 10.3390/life2040286

Norris, V., Blaauwen, T. D., Doi, R. H., Harshey, R. M., Janniere, L., Jimenez-Sanchez, A., et al. (2007). Toward a hyperstructure taxonomy. *Annu. Rev. Microbiol.* 61, 309–329. doi: 10.1146/annurev.micro.61.081606.103348

Osella, M., Nugent, E., and Cosentino Lagomarsino, M. (2014). Concerted control of *Escherichia coli* cell division. *Proc. Natl. Acad. Sci. U.S.A.* 111, 3431–3435. doi: 10.1073/pnas.1313715111.

Parry, B. R., Surovtsev, I. V., Cabeen, M. T., O'Hern, C. S., Dufresne, E. R., and Jacobs-Wagner, C. (2014). The bacterial cytoplasm has glass-like properties and is fluidized by metabolic activity. *Cell* 156, 183–194. doi: 10.1016/j.cell.2013.11.028.

Pelletier, J., Halvorsen, K., Ha, B. Y., Paparcone, R., Sandler, S. J., Woldringh, C. L., et al. (2012). Physical manipulation of the *Escherichia coli* chromosome reveals its soft nature. *Proc. Natl. Acad. Sci. U.S.A.* 109, E2649–E2656. doi: 10.1073/pnas.1208689109

Peteranderl, R., and Lechene, C. (2004). Measure of carbon and nitrogen stable isotope ratios in cultured cells. *J. Am. Soc. Mass Spectrom.* 15, 478–485. doi: 10.1016/j.jasms.2003.11.019

Peterson, J. R., Cole, J. A., Fei, J., Ha, T., and Luthey-Schulten, Z. A. (2015). Effects of DNA replication on mRNA noise. *Proc. Natl. Acad. Sci. U.S.A.* 112, 15886–15891. doi: 10.1073/pnas.1516246112.

Petroff, A. P., Wu, T. D., Liang, B., Mui, J., Guerquin-Kern, J. L., Vali, H., et al. (2011). Reaction-diffusion model of nutrient uptake in a biofilm: theory and experiment. *J. Theor. Biol.* 289, 90–95. doi: 10.1016/j.jtbi.2011.08.004

Poole, R. K. (1977). Fluctuations in buoyant density during the cell cycle of *Escherichia coli* K12: significance for the preparation of synchronous cultures by age selection. *J. Gen. Microbiol.* 98, 177–186. doi: 10.1099/00221287-98-1-177

Rego, E. H., Audette, R. E., and Rubin, E. J. (2017). Deletion of a mycobacterial divisome factor collapses single-cell phenotypic heterogeneity. *Nature* 546, 153–157. doi: 10.1038/nature22361.

Reshes, G., Vanounou, S., Fishov, I., and Feingold, M. (2008). Timing the start of division in *E. coli:* a single-cell study. *Phys. Biol.* 5:46001. doi: 10.1088/1478-3975/5/4/046001

Rocha, E. P., Fralick, J., Vediyappan, G., Danchin, A., and Norris, V. (2003). A strand-specific model for chromosome segregation in bacteria. *Mol. Microbiol.* 49, 895–903. doi: 10.1046/j.1365-2958.2003.03606.x

Saier, M. H. Jr. (2013). Microcompartments and protein machines in prokaryotes. *J. Mol. Microbiol. Biotechnol.* 23, 243–269. doi: 10.1159/000351625

Schaechter, M., Maaloe, O., and Kjeldgaard, N. O. (1958). Dependency on medium and temperature of cell size and chemical composition during balanced grown of *Salmonella typhimurium*. *J. Gen. Microbiol.* 19, 592–606. doi: 10.1099/00221287-19-3-592

Schaechter, M., Williamson, J. P., Hood, J. R. Jr., and Koch, A. L. (1962). Growth, cell and nuclear divisions in some bacteria. *J. Gen. Microbiol.* 29, 421–434. doi: 10.1099/00221287-29-3-421.

Schaeffer, P., Millet, J., and Aubert, J. P. (1965). Catabolic repression of bacterial sporulation. *Proc. Natl. Acad. Sci. U.S.A.* 54, 704–711. doi: 10.1073/pnas.54.3.704

Sloan, J. B., and Urban, J. E. (1976). Growth response of *Escherichia coli* to nutritional shift-up: immediate division stimulation in slow-growing cells. *J. Bacteriol.* 128, 302–308.

Smits, W. K., Kuipers, O. P., and Veening, J. W. (2006). Phenotypic variation in bacteria: the role of feedback regulation. *Nat. Rev. Microbiol.* 4, 259–271. doi: 10.1038/nrmicro1381

Taheri-Araghi, S. (2015). Self-consistent examination of Donachie's constant initiation size at the single-cell level. *Front. Microbiol.* 6:1349. doi: 10.3389/fmicb.2015.01349

Taheri-Araghi, S., Bradde, S., Sauls, J. T., Hill, N. S., Levin, P. A., Paulsson, J., et al. (2015). Cell-size control and homeostasis in bacteria. *Curr. Biol.* 25, 385–391. doi: 10.1016/j.cub.2014.12.009

Tu, B. P., Mohler, R. E., Liu, J. C., Dombek, K. M., Young, E. T., Synovec, R. E., et al. (2007). Cyclic changes in metabolic state during the life of a yeast cell. *Proc. Natl. Acad. Sci. U.S.A.* 104, 16886–16891. doi: 10.1073/pnas.0708365104

Veening, J. W., Stewart, E. J., Berngruber, T. W., Taddei, F., Kuipers, O. P., and Hamoen, L. W. (2008). Bet-hedging and epigenetic inheritance in bacterial cell development. *Proc. Natl. Acad. Sci. U.S.A.* 105, 4393–4398. doi: 10.1073/pnas.0700463105

Viollier, P. H., Thanbichler, M., McGrath, P. T., West, L., Meewan, M., McAdams, H. H., et al. (2004). Rapid and sequential movement of individual chromosomal loci to specific subcellular locations during bacterial DNA replication. *Proc. Natl. Acad. Sci. U.S.A.* 101, 9257–9262. doi: 10.1073/pnas.0402606101

Wallden, M., Fange, D., Lundius, E. G., Baltekin, O., and Elf, J. (2016). The synchronization of replication and division cycles in individual *E. coli* Cells. *Cell* 166, 729–739. doi: 10.1016/j.cell.2016.06.052.

Wang, P., Robert, L., Pelletier, J., Dang, W. L., Taddei, F., Wright, A., et al. (2010). Robust growth of *Escherichia coli*. *Curr. Biol.* 20, 1099–1103. doi: 10.1016/j.cub.2010.04.045

Weart, R. B., Lee, A. H., Chien, A. C., Haeusser, D. P., Hill, N. S., and Levin, P. A. (2007). A metabolic sensor governing cell size in bacteria. *Cell* 130, 335–347. doi: 10.1016/j.cell.2007.05.043

White, M. A., Eykelenboom, J. K., Lopez-Vernaza, M. A., Wilson, E., and Leach, D. R. (2008). Non-random segregation of sister chromosomes in *Escherichia coli*. *Nature* 455, 1248–1250. doi: 10.1038/nature07282

Xie, X., and Zubarev, R. A. (2015). Isotopic resonance hypothesis: experimental verification by *Escherichia coli* growth measurements. *Sci. Rep.* 5:9215. doi: 10.1038/srep09215

Yu, F. B., Willis, L., Chau, R. M., Zambon, A., Horowitz, M., Bhaya, D., et al. (2017). Long-term microfluidic tracking of coccoid cyanobacterial cells reveals robust control of division timing. *BMC Biol.* 15:11. doi: 10.1186/s12915-016-0344-4

Zaritsky, A. (2015). Cell-shape homeostasis in *Escherichia coli* is driven by growth, division, and nucleoid complexity. *Biophys. J.* 109, 178–181. doi: 10.1016/j.bpj.2015.06.026

Zaritsky, A., and Pritchard, R. H. (1973). Changes in cell size and shape associated with changes in the replication time of the chromosome of *Escherichia coli*. *J. Bacteriol.* 114, 824–837.

Conflict of Interest Statement: The authors declare that the research was conducted in the absence of any commercial or financial relationships that could be construed as a potential conflict of interest.

The reviewer TDB and handling Editor declared their shared affiliation.

frontiers in Microbiology

REVIEW
published: 10 July 2017
doi: 10.3389/fmicb.2017.01264

Determinants of Bacterial Morphology: From Fundamentals to Possibilities for Antimicrobial Targeting

Muriel C. F. van Teeseling[1†], Miguel A. de Pedro[2] and Felipe Cava[1]*

[1] *Laboratory for Molecular Infection Medicine Sweden, Department of Molecular Biology, Umeå Centre for Microbial Research, Umeå University, Umeå, Sweden,* [2] *Centro de Biología Molecular "Severo Ochoa" – Consejo Superior de Investigaciones Científicas, Universidad Autónoma de Madrid, Madrid, Spain*

Bacterial morphology is extremely diverse. Specific shapes are the consequence of adaptive pressures optimizing bacterial fitness. Shape affects critical biological functions, including nutrient acquisition, motility, dispersion, stress resistance and interactions with other organisms. Although the characteristic shape of a bacterial species remains unchanged for vast numbers of generations, periodical variations occur throughout the cell (division) and life cycles, and these variations can be influenced by environmental conditions. Bacterial morphology is ultimately dictated by the net-like peptidoglycan (PG) sacculus. The species-specific shape of the PG sacculus at any time in the cell cycle is the product of multiple determinants. Some morphological determinants act as a cytoskeleton to guide biosynthetic complexes spatiotemporally, whereas others modify the PG sacculus after biosynthesis. Accumulating evidence supports critical roles of morphogenetic processes in bacteria-host interactions, including pathogenesis. Here, we review the molecular determinants underlying morphology, discuss the evidence linking bacterial morphology to niche adaptation and pathogenesis, and examine the potential of morphological determinants as antimicrobial targets.

Keywords: bacterial morphology, peptidoglycan, cytoskeleton, antimicrobials, cell shape inhibitors

OPEN ACCESS

Edited by:
Arieh Zaritsky, Ben-Gurion University of the Negev, Israel

Reviewed by:
Waldemar Vollmer, Newcastle University, United Kingdom
Kevin D. Young, University of Arkansas for Medical Sciences, United States

****Correspondence:***
Felipe Cava
felipe.cava@umu.es

†Present address:
Muriel C. F. van Teeseling, Faculty of Biology, Philipps-Universität, Marburg, Germany

Specialty section:
This article was submitted to Microbial Physiology and Metabolism, a section of the journal Frontiers in Microbiology

Received: *05 May 2017*
Accepted: *23 June 2017*
Published: *10 July 2017*

Citation:
van Teeseling MCF, de Pedro MA and Cava F (2017) Determinants of Bacterial Morphology: From Fundamentals to Possibilities for Antimicrobial Targeting. Front. Microbiol. 8:1264. doi: 10.3389/fmicb.2017.01264

INTRODUCTION

The variation of bacterial cell shapes is often underappreciated. In addition to the well-known rods and cocci, more exotic shapes such as stars, mustaches, serpentines, and branches represent a large, although undefined, proportion (Young, 2006; Kysela et al., 2016). The characteristic morphology of a bacterial species is maintained through countless generations but is periodically modified within set limits during bacterial division and life cycles (**Figure 1**). Bacterial shape is genetically determined, but physical forces (internal and external) exerted on cells are increasingly recognized as major players in morphogenesis. To ensure constant bacterial morphology over generations despite these forces, shape maintenance must be an active process guided by robust regulatory circuits. This is evidenced by the development of aberrant morphology upon mutations. Shape dictates the interactions between a bacterial cell and its environment, most notably small-molecule traffic (via the surface/volume ratio), motility, formation of multicellular aggregates, habitat

colonization (including eukaryotic hosts and consequently pathogenesis and symbiosis), predation, and resistance (see Young, 2006, for a comprehensive review). Therefore, morphogenesis should be viewed as a major evolutionary and adaptive process that contributes greatly to prokaryotic ubiquity and versatility.

Bacterial shape is primarily dictated by the peptidoglycan (PG) sacculus (Salton and Horne, 1951; Weidel et al., 1960), a polymeric macromolecular structure that surrounds the cytoplasmic membrane and is the only "solid" element in the bacterial envelope. PG is present in essentially all bacteria [the number of exceptions is quickly dwindling as better detection methods are developed (Pilhofer et al., 2013; Liechti et al., 2014; Jeske et al., 2015; van Teeseling et al., 2015; Rast et al., 2017)] and wraps the cytoplasmic membrane like an elastic net (de Pedro and Cava, 2015). PG is a polymer of glycan chains crosslinked by peptides. The structure of the monomeric subunit, *N*-acetyl-glucosaminyl-*N*-acetyl-muramyl-L-alanyl-D-glutaminyl-L-(meso)diaminopimelyl-D-alanyl-D-alanine (GlcNAc-MurNAc-L-Ala-D-Glu-L-mesoDAP-D-Ala-D-Ala), is remarkably conserved throughout the bacterial phylogenetic tree. The few variations are either a change in the amino acid sequence of the stem peptide (almost always the di-amino acid at position 3) or the consequence of accessory reactions that modify the basic subunit (e.g., O-acetylation of sugars or amidation of dicarboxylic amino acids) (Vollmer, 2008; Cava and de Pedro, 2014).

The precursors for PG biosynthesis, uridine diphosphate -*N*-acetylglucosamine (UDP-GlcNAc) and UDP-MurNAc-pentapeptide, are synthesized in the cytoplasm by the enzymes MurA-F (Barreteau et al., 2008). The enzyme MraY couples the UDP-MurNAc-pentapeptide to undecaprenyl phosphate to produce the membrane-anchored lipid I (Manat et al., 2014). Subsequent addition of GlcNAc to lipid I by MurG results in inward-oriented lipid II molecules. Translocation to the outer face of the cytoplasmic membrane is performed by the flippase MurJ (Sham et al., 2014), with the likely participation in some species of AmiJ (Meeske et al., 2015) and the SEDS (shape, elongation, division and sporulation) proteins RodA and FtsW (Mohammadi et al., 2011; Scheffers and Tol, 2015; Leclercq et al., 2017). Once transferred to the external side of the cytoplasmic membrane, the GlcNAc-MurNAc-pentapeptide moiety of lipid II becomes accessible to enzymes with glycosyltransferase

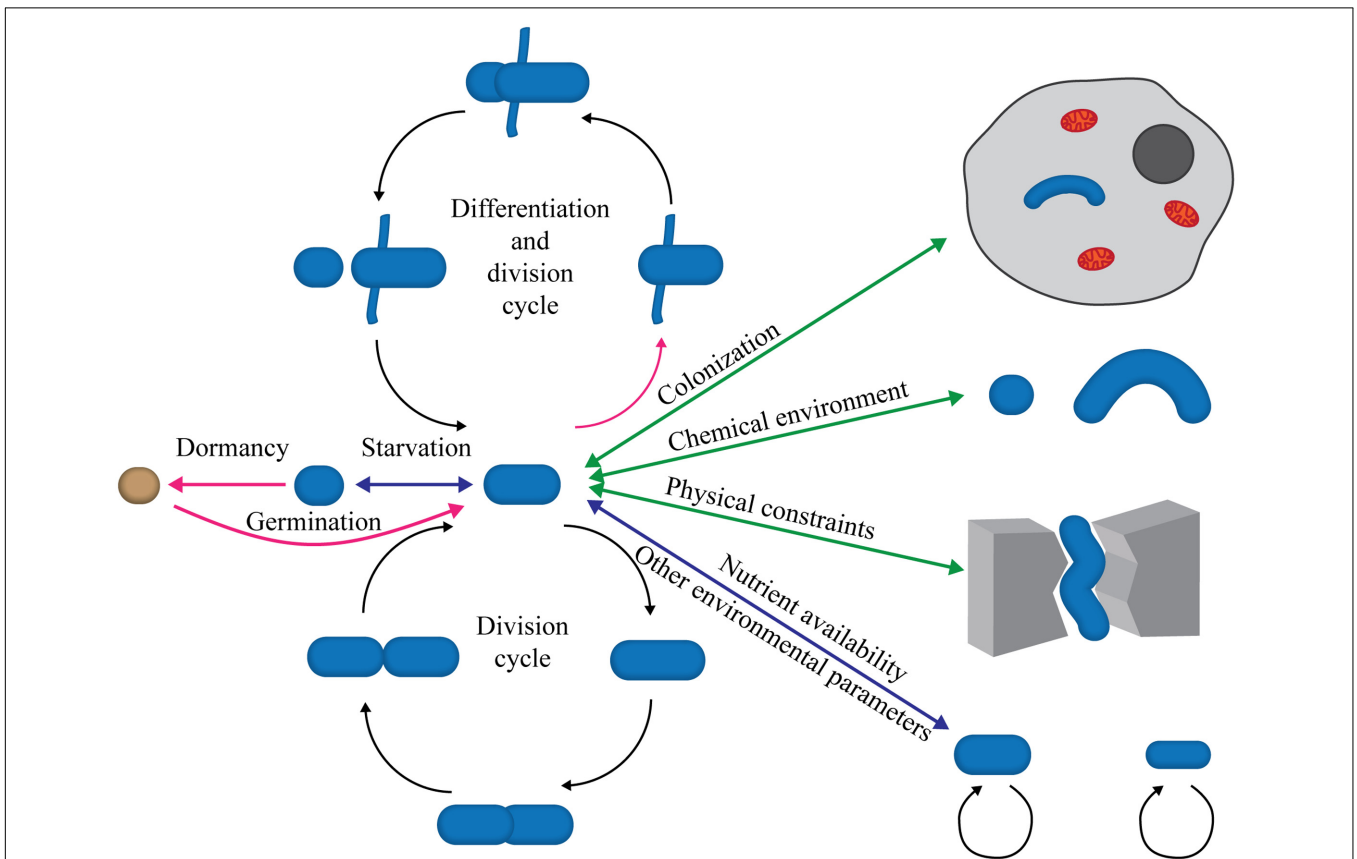

FIGURE 1 | Morphological plasticity and the bacterial life cycle. The scheme illustrates the continuous modulations affecting bacterial shape throughout the life cycle. These changes can be either cyclic (division cycles) or sporadic in response to changing conditions, the presence of chemicals, colonization of other organisms or environments, nutrient depletion or abundance, etc. Most shape alterations are reversible (double-headed arrows) and could be considered adaptive phenomena, whereas others are irreversible (single-headed magenta arrows) and represent bona fide morphological differentiation processes, such as sporulation (orange sphere) or polymorphic cell cycles.

(GT) and transpeptidase (TP) activities, which catalyze linear polymerization and peptide crosslinking, respectively. The undecaprenyl diphosphate released in the polymerization reaction is flipped back, dephosphorylated and reused for the cyclical transport of new precursors (Manat et al., 2014). Bifunctional proteins with GT and TP activities are universal and concurrent with monofunctional representatives of both activities. The SEDS protein RodA was recently identified as a novel GT enzyme *in Bacillus subtilis*, and seems to play the same role *in Escherichia coli* (Cho et al., 2016; Meeske et al., 2016). A ubiquitous class of enzymes involved in crosslinking is DD-transpeptidases, which are inhibited by covalent binding of beta-lactams and accordingly were first identified as penicillin-binding proteins (PBPs) (Sauvage et al., 2008). In mature PG, D,D-crosslinks between the D-Ala at position 4 in the stem peptide of one subunit and the di-amino acid at position 3 (either directly or through intermediate peptides) of a nearby stem peptide are universal. Additional crosslinking mechanisms involving specific sets of enzymes and distinctive stereochemistry are relatively common (Vollmer et al., 2008a).

As the PG layer is a covalently closed structure, the addition of new material requires concomitant cleavage of pre-existing bonds by PG hydrolases to permit enlargement of the sacculus. PG remodeling and maturation are mostly mediated by PG hydrolases (Vollmer et al., 2008b). As a group, these enzymes target every bond (glycosidic and peptidic) sustaining the PG fabric. Organisms can encode many hydrolases, which are often redundant (35 and counting in *E. coli*) (van Heijenoort, 2011). In addition to the enlargement process, the sacculus is subject to a complex and dynamic metabolism involving a large number of proteins that are not directly involved in the integration of precursors. Modifications related to subunit aging, growth state, nutritional conditions, population density, and stress response have been reported (Cava and de Pedro, 2014). Of particular interest to the present work are modifications causing changes in shape and the differentiation of new structures during the cell and life cycles of bacteria.

In this review, we will discuss how sacculi are molded and altered to produce typical bacterial morphologies, primarily in Gram-negative bacteria. The proteins involved and the underlying mechanisms will be elaborated.

GENERATION OF CELL SHAPE

Because of its covalently closed, net-like structure, the PG sacculus retains a specific shape and imposes this shape on the bacterial cell body. Despite a certain degree of deformability due to the elastic nature of the PG fabric (Männik et al., 2009), isolated sacculi faithfully retain the shape of the corresponding cell. However, the sacculi themselves lack the inbuilt information and/or features to determine their precise shape. Coding of epigenetic structural information in the 3D organization of the molecule has been proposed (Turner et al., 2010). However, no hard evidence supports this hypothesis. Furthermore, the current view of the sacculus as a relatively disordered array (de Pedro and Cava, 2015) and the ability of "cell wall-less" forms to regenerate bacillary shapes (Billings et al., 2014; Kawai et al., 2014) argue against such coding. Even if a particular disposition of incoming new precursors might be favored by the pre-existing order (or lack thereof) of the older material, this does not necessarily indicate a global shape-defining role. Therefore, it seems reasonable to assume that while the sacculus is the element that confers and preserves a defined shape and size, the generation of that shape depends on the dynamics and topology of biosynthetic complexes rather than the sacculus itself.

The simple growth of a closed net subjected to cytoplasmic turgor pressure poses some critical constraints on the incorporation of new material to cause an effective enlargement. These constraints must be overcome by morphogenetic mechanisms. Simple attachment of incoming precursors to the sacculus would result only in thickening. Indeed, PG endopeptidases that permit expansion by cleaving existing crosslinked peptides have been identified in *E. coli, Vibrio cholerae,* and *B. subtilis* (Hashimoto et al., 2012; Singh et al., 2012; Dörr et al., 2013). However, if insertion of new material, and concomitant cleavage of old crosslinks, would happen constantly and evenly over the whole surface of the sacculus, this would lead to a homogeneous expansion of the growing structure. This mechanism by itself would not allow for the differentiation of new features. To generate shapes other than a sphere, incorporation must occur at distinct rates in different locations and for defined periods of time. Budding, for instance, would require a faster rate of precursor incorporation at the budding site than in the surrounding area. The morphogenetic process in bacteria not only requires physical enlargement, but also must allow periodic division events to increase the number of individuals.

As the mode of division of common model organisms, symmetrical binary fission is the best-known division mechanism and represents an elegant, intuitive mechanism to ensure shape conservation (Angert, 2005). However, alternative ways of division also occur (Angert, 2005). The only critical condition for division is the equitable distribution of both the genetic material and the biochemical components required to express the genetic potential. Division must be regulated in such a way that further divisions are not allowed before these conditions are fulfilled by the daughter cells. Many bacterial species divide by alternative mechanisms, often producing offspring cells that are quite dissimilar in size, shape and physiology from the mother cells (**Figure 1**). In these instances, the "juvenile" cells must undergo complex developmental programs to generate the characteristic morphology before committing to a subsequent round of division (e.g., Hirsch, 1974; Curtis and Brun, 2010; Williams et al., 2016; Cserti et al., 2017).

Cytokinesis implies the scission of the bacterial cell wall at genetically determined locations and cell cycle times while preserving cell integrity. The sacculus is a common substrate in cytokinesis and growth (enlargement and differentiation), which are mediated by closely related enzymatic complexes. As described below, the elements responsible for the dynamics and topology of PG biosynthetic complexes are slowly

being unraveled, thanks to current advances in genetics and visualization techniques.

Positioning and Guiding Peptidoglycan Synthesis: Cytoskeletal Elements

Since PG dictates bacterial cell shape, regulation of the location and timing of the synthesis and degradation of PG throughout the cell cycle is of key importance. Bacteria use cytoskeletal elements to position proteins involved in PG synthesis and hydrolysis in large, intricately regulated protein complexes. The cytoskeletal elements FtsZ and MreB are relatively conserved, but the exact composition of the protein complexes associated with FtsZ and MreB varies from species to species. Unless stated otherwise, we base our description on the model organism *E. coli*.

Actin-Like Cytoskeletal Elements

The actin-like cytoskeletal protein MreB influences bacterial morphogenesis by coordinating cell wall biosynthesis spatiotemporally (Carballido-López, 2007; Errington, 2015). The MreB protein is important for maintaining the rod shape in bacteria (Wachi et al., 1987; Doi et al., 1988; Levin et al., 1992), is conserved in many non-spherical bacteria (Jones et al., 2001), and forms actin-like filaments (Jones et al., 2001; van den Ent et al., 2001), thus motivating extensive studies of this protein. Multiple roles of MreB have been identified (Carballido-López, 2007; Busiek and Margolin, 2015), although directing PG insertion during elongation appears to be the main role of MreB in most organisms.

Although the exact localization pattern of MreB in bacterial cells has been highly debated (Errington, 2015), it is widely accepted that MreB forms membrane-bound patches or filaments in an ATP-dependent manner (Salje et al., 2011). Multiple studies show that these filaments move along the periphery of the cell (Errington, 2015). MreB interacts with numerous proteins involved in PG biosynthesis and hydrolysis, which are clustered in a large protein complex called the elongasome (Szwedziak and Löwe, 2013; Laddomada et al., 2016). These proteins include the PBPs PBP1A and PBP2; the hydrolase LytE (in *B. subtilis*) (Carballido-López et al., 2006); the enzymes DapI, MurC, MurD, MurE, MurF, MurG, and MraY, which are involved in the synthesis of lipid II; and the protein FtsW, for which functions as a flippase of lipid II (Mohammadi et al., 2011) and as a PG polymerase (Meeske et al., 2016) have been described.

The movement of MreB filaments along the membrane is correlated with active PG biosynthesis (Domínguez-Escobar et al., 2011; Garner et al., 2011; van Teeffelen et al., 2011; Cho et al., 2016). Originally, this movement was proposed to be caused by treadmilling of the MreB filaments (Soufo and Graumann, 2004; Kim et al., 2006). A revised hypothesis posited that the movement of the elongasome depends on PG synthesis, either by insertion of new glycan strands of PG by a bifunctional PBP in a pushing movement or by pulling of hydrolases degrading old PG strands (Errington, 2015). Recent studies in *E. coli* have shown that MreB filaments only move if RodA can polymerize the glycan backbone of PG, thereby demonstrating that polymerization by the SEDS protein RodA, and not bifunctional PBPs, drives MreB movement (Cho et al., 2016).

The combination of time-lapse microscopy with biophysical simulations has provided a deeper understanding of how MreB localization and subsequent cell wall synthesis lead to elongation of bacterial cells (Ursell et al., 2014). MreB localizes preferentially to negatively curved membrane regions, where it directs local cell growth by PG incorporation, leading to a more positive curvature. MreB then moves to another membrane region with negative curvature, where it stimulates PG insertion. Simulations show that this pattern of dynamic growth bursts in regions of negative cell curvature leads to a straight morphology. Recent results suggest that MreB also affects cell diameter, as the helical pitch angle of MreB filaments correlates with the diameter of the model organism *E. coli* (Ouzounov et al., 2016). These findings imply a sophisticated relationship between bacterial morphology and the structure and orientation of the MreB filaments with respect to the membrane.

Actin-like cytoskeletal elements other than MreB have been identified in bacteria (Carballido-López, 2007; Busiek and Margolin, 2015). The functions of only a few of the 35 known families of actin-like proteins have been studied (Derman et al., 2009). Of these, the membrane-associated, filament-forming FtsA is involved in the formation and function of the divisome (see below) in multiple bacteria (Pinho et al., 2013). There, the role of FtsA is hypothesized to be comparable to that of MreB (Szwedziak and Löwe, 2013). In this scenario, FtsA has a crucial role in guiding cell wall synthesis and remodeling during cell division. Several actin-like proteins, notably ParM (Jensen and Gerdes, 1997) and AlfA (Becker et al., 2006), are involved in DNA segregation.

Tubulin-Like Cytoskeletal Elements

The bacterial tubulin-homolog FtsZ is a key protein in cell division that is present in nearly all bacteria (Vaughan et al., 2004; Bernander and Ettema, 2010). FtsZ polymerizes into (proto)filaments that curve and thereby constrict the cytoplasmic membrane in a GTP hydrolysis-dependent fashion (Erickson et al., 1996; Li et al., 2013). During constriction, septal PG must be synthesized and/or the existing PG must be remodeled to create new poles for both daughter cells. The divisome, a protein complex associated with the ring formed by FtsZ (the Z ring), coordinates constriction and septal PG biosynthesis and remodeling (Haeusser and Margolin, 2016). Because FtsZ cannot bind the membrane, other proteins, such as the widely conserved actin homolog FtsA and ZipA, are required to tether FtsZ to the membrane. FtsA and ZipA are thought to affect the polymerization dynamics of FtsZ as well as the orientation of the protofilaments in the Z ring to contribute to proper Z ring function (Loose and Mitchison, 2014; Haeusser and Margolin, 2016). Different membrane anchors have been described in different species; the newly described anchor FzlC in *Caulobacter crescentus* has been shown to affect PG hydrolysis during cell division (Meier et al., 2016).

Multiple proteins involved in PG synthesis and remodeling are recruited to the divisome. In addition to PBP1B and PBP3, the divisome includes the flippase/PG synthase FtsW, PG hydrolases and hydrolase activators (van Heijenoort, 2011; Haeusser and Margolin, 2016). Multiple proteins in the divisome

have been shown to directly or indirectly stimulate PG synthesis or hydrolysis. ATP hydrolysis by the ABC-like complex FtsEX, which interacts with FtsA, is required for PG synthesis, and FtsEX also plays a role in PG hydrolysis (Du et al., 2016). The protein FtsN, which binds directly to FtsA and PBP1B, stimulates septal PG synthesis (Müller et al., 2007). The function of PBP1B requires interaction with the lipoprotein LpoB (Paradis-Bleau et al., 2010; Typas et al., 2010). CpoB stimulates PBP1B in response to the state of the Tol-Pal system, which is responsible for constricting the outer membrane to ensure coordinated constriction of the cell envelope during cytokinesis (Gray et al., 2015). In *C. crescentus*, a flexible linker sequence inside FtsZ itself may be important for PG remodeling by affecting the degree of crosslinking and the length of the glycan chains (Sundararajan et al., 2015). Very recent studies have shown that the PG biosynthesis enzymes in the divisome synthesize PG at discrete sites that move around the cell division plane by treadmilling of FtsZ (Bisson-Filho et al., 2016; Yang X. et al., 2016).

Several studies indicate that FtsZ is not only important for PG biosynthesis during cell division but also contributes to sidewall synthesis, in a process known as preseptal PG synthesis. Preseptal PG synthesis has been described in *E. coli* (de Pedro et al., 1997) and *C. crescentus* (Aaron et al., 2007) and appears to be important during a larger part of the cell cycle in the latter. Many open questions remain, although two different mechanisms have been described for this preseptal PG incorporation in *E. coli*. The first mechanism requires the interaction of FtsZ with PBP2 (Varma et al., 2007; Varma and Young, 2009), a PBP that normally interacts with the elongasome instead of the divisome. In the second mechanism, FtsZ and ZipA, but not MreB and PBP2, are required for insertion of PG that appears to lack pentapeptides (Potluri et al., 2012). This mechanism is known as PIPS (PBP3-independent peptidoglycan synthesis). PIPS is thought to occur after elongation ends and before constriction of the cell begins (Potluri et al., 2012). Other studies suggest the occurrence of a different mechanism between elongation and division in *E. coli*. A direct interaction of MreB and FtsZ is crucial for proper cell division (Fenton and Gerdes, 2013), and the corresponding PBPs PBP2 and PBP3 colocalize and interact before division begins (van der Ploeg et al., 2013). These observations led to the hypothesis that at least part of the PG biosynthetic machinery might be transferred from MreB to FtsZ in preparation for cell division (Fenton and Gerdes, 2013). Further studies are needed to better understand which processes occur between elongation and division and how, if at all, the mechanisms described above are coordinated.

Bacterial tubulin-like proteins other than FtsZ exist (Busiek and Margolin, 2015). A function in DNA partitioning has been identified for several members of the TubZ family (Larsen et al., 2007), thus paralleling the function of some actin-like proteins (see above). Two other tubulin homologs, BtubA, and BtubB, have been identified in the phylum Verrucomicrobia (Jenkins et al., 2002). BtubAB forms filaments in the presence of GTP (Schlieper et al., 2005), but the function of these filaments remains unknown.

Intermediate-Like Cytoskeletal Elements

Bacterial intermediate filament (IF)-like structures are also involved in positioning the PG biosynthesis machinery. IF-like structures can polymerize into filaments or sheets, but in contrast to actin- and tubulin-like cytoskeletal structures, this polymerization occurs without binding and hydrolysis of nucleotides (Lin and Thanbichler, 2013). The three main classes of bacterial IF-like elements are bactofilins, coiled-coil-rich proteins (CCRPs) and cytoskeletal-like scaffolding proteins. In the domain Bacteria, IF-like proteins are widespread, and studies of several representative proteins support multiple roles, including morphogenesis, locomotion, cell division and intracellular localization of proteins.

The bactofilins BacA and BacB have a direct role in positioning the proteins involved in PG synthesis by localizing the bifunctional PBP PbpC to the base of the stalk in *C. crescentus* during the transition from swarmer to stalked cell (Kühn et al., 2010). PbpC contributes to elongation of the stalk (Kühn et al., 2010), although it might also contribute to PG biosynthesis at other cellular locations and interact with divisome proteins as well as with other bifunctional PBPs (Strobel et al., 2014). Although conclusive evidence is lacking, it has been hypothesized that the bactofilins CcmA in *Proteus mirabilis* and BacM in *Myxococcus xanthus* are also involved in recruiting and positioning cell wall biosynthesic proteins (Hay et al., 1999; Koch et al., 2011). In the helical bacterium *Helicobacter pylori*, a CcmA protein has been implicated in cell shape (Sycuro et al., 2010). However, whether CcmA forms a cytoskeleton in this bacterium and, if so, how this putative cytoskeleton is involved in helical cell shape remains unclear. Several other proteins necessary for helical morphology have been described, the majority of which are PG hydrolases (see below and Bonis et al., 2010; Sycuro et al., 2010, 2012, 2013). An inviting hypothesis is that the CcmA protein forms a cytoskeleton that is involved in positioning these hydrolases so that they modify the degree of PG crosslinking only at specific sites. A similar mechanism may occur in the helical *Campylobacter jejuni*, although the role of its CcmA homolog in morphology has not been established (Frirdich et al., 2012, 2014). We expect that follow-up studies of the function of bactofilins, which are present in many bacteria (Kühn et al., 2010), will reveal more examples of bactofilins as tethers for PG enzymes (potentially organized in protein complexes) to permit more complex morphologies.

The role of the CCRP crescentin, the protein responsible for the curvature of *C. crescentus* cells (Ausmees et al., 2003), in PG biosynthesis is less direct (Cabeen et al., 2009). According to the current model, the lining of the crescentin filament along the inner curvature of the cell provides a compressive force that results in a higher PG synthesis rate at the outer curvature than at the inner curvature of the cell (Cabeen et al., 2009). The involvement of CCRP filaments in morphology has also been reported for *H. pylori* (Waidner et al., 2009; Specht et al., 2011; Schätzle et al., 2015). However, whether these CCRPs influence PG biosynthesis and, if so, via which underlying mechanism remains unclear. A mechanism similar to that of CreS has been proposed for the recently discovered CCRP CrvA, which is

responsible for the curved morphology of *V. cholerae* (Bartlett et al., 2017). CrvA self-assembles at the inner face of the cell curvature and asymmetrically patterns PG insertion, resulting in more insertions in the outer face than the inner face. Strikingly, however, CrvA localizes in the periplasm and therefore forms a periskeleton rather than a typical cytoskeleton.

DivIVA is the most-studied protein in the third class of IF-like elements, the cytoskeletal-like scaffolding elements. This protein is restricted to Gram-positive bacteria. In some of these bacteria, notably the actinomycetes, DivIVA activates and recruits PG biosynthetic enzymes to the cell pole to establish polar growth (Lin and Thanbichler, 2013). No hard evidence supports the ability of the Gram-negative (evolutionarily unrelated) variant PopZ to recruit PG biosynthetic enzymes. However, PopZ (Grangeon et al., 2015), one PBP with a transglycosylase activity and an L,D-transpeptidase (Cameron et al., 2014) all localize to the growing pole in *Agrobacterium tumefaciens*. As the involvement of other likely candidates in recruitment of the PG biosynthesis machinery to the growing pole has recently been excluded, PopZ could very well be involved in localizing PG biosynthesis in at least some Gram-negative bacteria (Howell and Brown, 2016).

The first Gram-negative IF-like structure was identified only in 2003 in the form of crescentin (Ausmees et al., 2003), but the involvement of multiple IF-like structures in positioning or guiding PG biosynthesis has been demonstrated in several cases. We expect that further research will establish positioning of PG biosynthesis and modification as one of the functions of IF-like structures. We envision that IF-like proteins might even tether protein complexes reminiscent of the elongasome and divisome for this purpose. In that case, all three classes of cytoskeletal elements would have a complementary cell wall synthesizing protein complex. The first few examples of proteins interacting with IF-like cytoskeletal elements suggest that these protein complexes might be involved in shape modification (especially when compared with the canonical coccoid and rod shapes). If this role were to be verified, we expect the compositions of these protein complexes to be more diverse and considerably less conserved than those of elongasome and divisome complexes, given the morphological diversity with which the IF-like cytoskeletal elements might be associated.

Post-Insertional Modifications of the Sacculus

In addition to positioning of PG synthesis by cytoskeletal elements, enzymes that affect the chemical composition of the PG can impact cell shape. One of the first indications that PG hydrolytic enzymes could influence morphology was the altered phenotype, with respect to diameters and contours, of the PBP5 mutant in *E. coli* (Nelson and Young, 2000, 2001). The role of PG hydrolases in shaping bacterial morphology has major relevance in *H. pylori*, in which Csd1 and Csd2 (endopeptidases), Csd3 (a bifunctional endo- and carboxypeptidase) and Csd4 and Csd6 (carboxypeptidases) dictate helical shape (Bonis et al., 2010; Sycuro et al., 2010, 2012, 2013; Kim et al., 2014, 2015; An et al., 2015). Csd4 and Csd6, probably together with the hypothetical scaffolding protein Csd5, trim PG monomers to dipeptides, resulting in cell curvature, possibly because the trimming is localized and decreases the local availability of crosslinkable PG precursors (Sycuro et al., 2012, 2013). Csd1 and Csd2, together with the bactofilin CcmA discussed above, determine the helical twist of *H. pylori*, probably by locally cutting tetra-pentapeptide crosslinks (Sycuro et al., 2012). Csd3 appears to participate in both of these networks (Sycuro et al., 2012). Similarly, the carboxypeptidases Pgp1 and Pgp2 in *C. jejuni* are major determinants of the morphology of this bacterium (Frirdich et al., 2012, 2014; Frirdich and Gaynor, 2013).

Chemical modifications of the murein sacculus, such as amidation of the D-center of DAP in *Lactobacillus plantarum*, have also been reported to be important in cell morphology and growth (Bernard et al., 2011). The amount of PG O-acetylation affects morphology, at least in *C. jejuni* (Ha et al., 2016); an increase in PG O-acetylation caused by inactivation of the gene *ape1* leads to a significant difference in the amount and variance of curvature of these cells and a decreased colonization phenotype. However, for both examples, it is unknown whether the effects on bacterial shape and fitness are caused by the PG composition directly or by misregulation of PG-associated enzymes that are less efficient in recognizing the altered PG.

Peptidoglycan-Independent Morphological Determinants

In addition to morphological determinants affecting the PG sacculus, PG-independent determinants are known. In some spirochetes, periplasmic flagella are responsible for the characteristic spiral or flat-wave shape (Motaleb et al., 2000) or additional twisting of the bacteria (Charon et al., 1991; Ruby et al., 1997; Picardeau et al., 2001). The periplasmic flagella deform the sacculus, which in turn deforms the flagella, resulting in the particular cell shape. This is a dynamic process that causes the bacteria to move, even in highly viscous media (Wolgemuth et al., 2006; Dombrowski et al., 2009; Harman et al., 2013). This motility is a necessary prerequisite for the virulence of the spirochete *Borrelia burgdorferi* (Sultan et al., 2013, 2015).

Another PG-independent morphological determinant is membrane composition, as demonstrated for the rod-shaped *Rhodobacter sphaeroides* (Lin et al., 2015). *R. sphaeroides* with a reduced amount of the membrane lipid cardiolipin is nearly spherical. It is not yet understood by which mechanism a reduced amount of cardiolipins leads to altered cell shape in *R. sphaeroides*. The geometry of cardiolipin molecules dictates preferential localization at sites with increased membrane curvature, notably the cell poles and the cell division site (Huang et al., 2006). Because a higher percentage of the membrane is in a curved state in spherical cells than in rod-shaped cells, one would intuitively presume that spherical cells contain more instead of less (as was the case in the *R. sphaeroides* mutant) cardiolipin. Indeed, *E. coli* minicells, in which a very high percentage of the membrane is in a highly curved state, are enriched in cardiolipin (Koppelman et al., 2001). Thus, the effect of membrane composition on cell shape might be indirect, such as by affecting the localization of lipid II or MreB, which are both

linked to specific membrane organization (Ganchev et al., 2006; Strahl et al., 2014).

CHANGING CELL SHAPE DURING THE LIFE OF A BACTERIAL CELL

Many bacterial species undergo dramatic shape changes throughout the cell cycle (dimorphic or polymorphic bacteria). Modification of the shape of sacculi might be achieved by remodulation of the spatiotemporal activation patterns of PG biosynthetic complexes and/or the frequency of cell division relative to the rate of growth. However, in many instances, shape change includes "*de novo*" differentiation of cell regions or appendages, such as "points" in *Stella vacuolata* (Vasilyeva, 1985) or prostheca in *Asticcacaulis biprosthecum* (Pate et al., 1973) and *Hyphomonas neptunium* (Leifson, 1964). These situations require additional elements that dictate when and where new complexes are assembled and activated. The recently discovered proteins from *C. crescentus* and related species (Biondi et al., 2006; Jiang et al., 2014; Persat and Gitai, 2014) are the first morphogenetic elements with such abilities. If these types of shape modifications are dependent on "sufficient and necessary" modular elements, such elements could provide excellent tools to manipulate shape in species of biotechnological interest.

Morphological Changes throughout the Cell Cycle

The alphaproteobacterium *C. crescentus* is the best-studied bacterial model organism with a cell cycle-dependent morphology. Juvenile flagellated swarmer cells have a curved rod shape, and during development, a stalk grows from the previously flagellated cell pole. The cell eventually divides in an asymmetric fashion: the stalked mother cell can immediately undergo a new round of division, whereas the daughter cell must develop into a stalked cell before undergoing a new round of division. These cell cycle-dependent phenomena are dictated by a robust regulatory circuit that combines transcriptional and translational regulation, proteolysis, and phosphorylation (Tsokos and Laub, 2012; Woldemeskel and Goley, 2017). Cell division only occurs in the stalked cell and depends on how Z ring assembly is temporally and spatially coordinated with chromosome segregation through the actions of MipZ, CtrA, and DnaA, among other proteins (Laub et al., 2000; Thanbichler and Shapiro, 2006; Curtis and Brun, 2010). The transcriptional regulators TacA and StaR are involved in the development of the stalk (Biondi et al., 2006), but *tacA* and *staR* mutants still form stalks when starved of phosphate (Biondi et al., 2006), indicating additional regulators of stalk formation. The precise mechanisms via which the stalk is elongated remain obscure, although involvement of the elongasome components RodA and MreB (Wagner et al., 2005) and the above-mentioned bactofilins and PbpC, which localize at the base of the stalk (Kühn et al., 2010), has been demonstrated.

Asticcacaulis species are related to *C. crescentus* and also form stalks during their cell cycle. The location of the stalk differs between different *Asticcacaulis* species: *A. excentricus* displays one subpolar stalk, whereas *A. biprosthecum* has two bilateral stalks at midcell. These species have repurposed an ancestral regulatory protein, SpmX (Radhakrishnan et al., 2008), by adding a new domain to the C-terminus to function as a localization marker for stalk synthesis (Jiang et al., 2014). The factors recruited by SpmX for local PG synthesis for stalk production are unknown.

Hyphomonas neptunium, another alphaproteobacterium, is an example of a budding bacterium with a cell cycle-dependent morphology. New offspring arise from a stalk that emerges from the mother cell. As in *C. crescentus*, this cell division is asymmetric: the ovococcoid daughter cell can only divide after developing into a stalked cell itself. The cell cycle-dependent morphology of these bacteria originates from PG incorporation at specific cellular locations dependent on the stage of the cell cycle (Cserti et al., 2017). In addition, buds originate from the stalk by remodeling of the tip of the stalk. Further research is needed to understand the mechanisms that regulate and establish this morphogenetic program.

As the discussed examples show, studies of di- or polymorphic bacteria have provided a deeper understanding of the regulation and coordination of morphogenesis. As only very few bacteria with cell cycle-dependent morphologies have been investigated, many more regulatory networks will likely be discovered upon further research in this field.

Morphological Changes Dependent on Environmental Conditions

Bacteria are strongly affected by changes in environmental conditions. Multiple species undergo morphological changes under certain conditions. These changes may be related to a transition to a metabolically inactive state or to a need to increase nutrient uptake or escape threats. Some bacteria induce a dormant state known as viable but not culturable (VBNC) upon low-temperature exposure and/or nutrient deprivation. The development of VBNC forms is associated with morphological changes in some species (Baker et al., 1983; Rollins and Colwell, 1986; Effendi and Austin, 1995; Citterio et al., 2004; Liu et al., 2017). Many Gram-negative pathogens change from rod to coccoid forms. (Barer et al., 1993). These morphological changes are in some cases correlated with regulation of the expression of cell envelope/wall genes (Asakura et al., 2007; Hung et al., 2013; Meng et al., 2015). Resuscitation of *V. parahaemolyticus* VBNC forms generates shape heterogeneity apparently caused by the increased expression of the DD-carboxypeptidase DacB (Hung et al., 2013). The morphological transition of *H. pylori* during VBNC to coccoid forms is the result of the activity of the PG hydrolase AmiA (Chaput et al., 2006, 2016), which alters PG composition to increase levels of disaccharide dipeptides (Costa et al., 1999). Remodeling of the cell wall appears to be a shared feature of VBNC induction in diverse organisms, although further research is needed to understand the relevance of this remodeling to morphogenesis.

Diverse bacteria respond to starvation conditions by forming metabolically inert spores that are smaller and often more coccoid than the cells themselves. Upon this major metabolic

reprogramming (beyond simple morphological adaptation), the PG in the spores of *Bacillus* species is remodeled (Tan and Ramamurthi, 2014) to a specialized PG called the cortex. The cortex has a much lower degree of crosslinking and fewer peptide stems, with regular distribution of the atypical modification muramic δ-lactam at every second muramic acid along the PG strand (Gilmore et al., 2004). The main enzymes involved in these changes are D,D-carboxypeptidases (Popham et al., 1999) and, in the case of muramic δ-lactam, the concerted action of the amidase CwlD and the deacetylase PdaA (Gilmore et al., 2004).

Bacterial morphology and PG topology can also be influenced by bacterial growth stage. In stationary phase, the stringent response of *E. coli* governs downregulation of PG synthesis (Ishiguro and Ramey, 1976), and the sacculus undergoes a number of structural changes, including increased crosslinking (including LD-crosslinks) and reduced chain length (Pisabarro et al., 1985). *V. cholerae* follows the same dynamics but also displays RpoS-dependent cell wall chemical editing mediated by non-canonical D-amino acids (Lam et al., 2009; Cava et al., 2011). *C. crescentus* undergoes a morphological adaptation during stationary phase that causes the cells to elongate, decrease in width, and become helical (Wortinger et al., 1998). Another morphological adaptation by *C. crescentus* (and relatives such as *Asticcacaulis* species) is substantial elongation of the stalk in response to phosphate limitation (Schmidt and Stanier, 1966). This stalk elongation appears to be a strategy to either increase phosphate absorption capacity and/or elevate the cell body away from the surface (Wagner et al., 2006). The mechanisms responsible for these adaptations in *C. crescentus* remain obscure (Woldemeskel and Goley, 2017).

Upon environmental stresses, multiple bacteria (Chauhan et al., 2006; Justice et al., 2006; Stackhouse et al., 2012) increase drastically in length via a process called filamentation, which is achieved by inhibiting cell division while maintaining cell growth (Justice et al., 2008). In *E. coli*, the SOS response can trigger cell filamentation by inducing the division inhibitor SulA (Huisman and D'Ari, 1981; Bi and Lutkenhaus, 1993). In uropathogenic *E. coli* (UPEC), filamentation during urinary tract infections depends on the cell division gene *damX* (Khandige et al., 2016). UPEC undergoes additional morphological transitions in addition to filamentation, as it forms non-motile, rod-shaped intracellular bacterial communities (IBCs) (Schwartz et al., 2011). These arise upon initial invasion within the cytoplasm of bladder umbrella cells and then eventually transitions into slower-growing coccoids that form more organized biofilm-like communities (mid-IBCs). At this point, a small subset of cells further differentiates into filaments within these mid-IBCs. Eventually, the coccoid UPEC cells become motile and bacillary (late IBCs), lysing the host cell and releasing both filaments and motile rods for further rounds of invasion into neighboring bladder cells (egress and second-generation IBCs). Since each IBC represents a single invasion event, the morphological changes observed within these communities are likely part of a developmental program in which each morphotype presumably functions to facilitate intracellular growth and subsequent rounds of infection (Schwartz et al., 2011).

Many bacteria change morphology during the transition to swarming motility. This transition is induced by surface contact. Swarmer cells are characterized by increased cell length and number of flagella (Jansen et al., 2003; Kearns and Losick, 2003; Armbruster and Mobley, 2012; Partridge and Harshey, 2013). In *P. mirabilis*, PG O-acetylation decreases from 51 to 29% upon differentiation to swarmer cells (Strating et al., 2012). This differentiation is accompanied by additional changes in the PG composition as well as the autolysin profile (Strating et al., 2012).

THE IMPORTANCE OF BACTERIAL CELL SHAPE

Morphology affects bacterial life in multiple ways (Young, 2006). Direct evidence of roles of morphology in multiple processes has only been collected in some species. Below, we will discuss several recent studies elucidating the impact of altered morphology on multiple processes, including bacterial survival and pathogenicity.

Colonization of surfaces can be facilitated by cell shape, as shown for the curved model organism *C. crescentus* (Persat et al., 2014). *C. crescentus* mother cells use their stalk to attach to surfaces, and the daughter cells expresses pili and a flagellum at the opposite pole (Curtis and Brun, 2010). Persat et al. (2014) followed the colonization of surfaces by both curved and uncurved *C. crescentus* cells under flow in a microfluidic set-up to mimic the natural environment, i.e., freshwater lakes and streams. Curved cells formed larger and taller microcolonies than straight cells under moderate flow. The study demonstrated that in dividing cells, the daughter cell pole with the pilus is positioned closer to the surface of the microfluidic device because of the cell curvature. This positioning facilitates attachment to this same surface via retraction of the pilus and thus enhances colonization by curved cells in moderate flow.

The importance of cell shape in biofilm formation was demonstrated in a study of the alphaproteobacterium *R. sphaeroides*, which inhabits soil and anoxic water bodies (Lin et al., 2015). The wild-type rod-shaped bacteria readily form biofilms. Ellipsoidal (shortened rods) mutants and coccoid cells treated with *S*-(3,4-dichlorobenzyl)isothiourea (A22), an inhibitor of MreB, were impaired for surface attachment and biofilm formation. These results suggest that the morphological changes decrease the surface area of the bacteria in contact with the surface and neighboring cells, leading to a defect in attachment to the surface and other cells. In *Burkholderia cepacia*, an opportunistic pathogen that causes pneumonia, a spherical mutant was detected in a screening for altered biofilm formation (Huber et al., 2002). The structure of the biofilms formed by these coccoid *rodA* mutants was clearly different from those formed by rod-shaped wild-type cells and featured exceptionally thick aggregates alternating with uncolonized surface areas. These studies in *R. sphaeroides* and *B. cepacia* thus provide evidence for the relationship between morphology and biofilm formation postulated by Young (Young, 2006).

Alignment of bacterial cells is also important in some forms of social motility. *P. mirabilis* is a rod-shaped bacterium that

can infect the urinary tract and can move in groups of cells aligned in parallel in a process called swarming (Schaffer and Pearson, 2015). Altering morphology by increasing the amount of bactofilin protein CcmA, expressing a truncated CcmA, or knocking out *ccmA* leads to curved *P. mirabilis* cells with inferior swarming compared with wild-type (Hay et al., 1999). This swarming defect was attributed to the inability of (irregularly) curved cells to form the neatly parallel alignment of cells required for swarming. The importance of swarming in the pathogenicity of *P. mirabilis* remains controversial: some mutants that have lost the ability to swarm are less virulent, whereas several non-motile mutants are fully virulent (Schaffer and Pearson, 2015).

The motility of single cells can also be affected by cell shape, as shown for the helical pathogens *H. pylori* and *C. jejuni* and the curved *V. cholerae*. The cell shape of these pathogens is important in colonization of the GI tract by *H. pylori* (Bonis et al., 2010; Sycuro et al., 2010, 2012), a pathogen that can cause inflammation, gastric ulcers and cancers in the human stomach (Kusters et al., 2006); *V. cholerae*, which can cause the diarrheal disease cholera; and *C. jejuni* (Frirdich et al., 2012, 2014; Stahl et al., 2016), which invades epithelial cells (Young et al., 2007). During infection, all three pathogens move through the mucus layer lining the GI tract. This environment has been simulated using gel-like substances [whose suitability for mimicking the mucus layer remains under debate (Celli et al., 2009; Yang D.C. et al., 2016)] or viscous liquids. Two straight rod-shaped mutants and two curved rod-shaped mutants of *C. jejuni* both display decreased motility in soft agar compared to wild-type (Frirdich et al., 2012, 2014; Ha et al., 2016; Stahl et al., 2016). Experiments in gel-like substances showed that the motility of some *H. pylori* mutants with altered helicity is reduced compared with wild-type (Sycuro et al., 2010, 2012), whereas other mutants do not show reduced motility (Bonis et al., 2010; Sycuro et al., 2010). Although initial studies in viscous liquids did not reveal a decrease in motility of straight *H. pylori* mutants (Sycuro et al., 2010), a recent in-depth study in a mucus-mimicking solution showed that the amount of motile cells and the median speed were both lower for non-helical mutants (Martínez et al., 2016). This finding explains the advantage of the helical cell shape for *H. pylori* during colonization by showing that helical cells are better adapted to move through the mucus layer covering the stomach epithelium. A similar process appears to occur in *V. cholerae*, in which the CrvA-driven curvature promotes motility in hydrogels and confers an advantage in host colonization and pathogenesis (Bartlett et al., 2017). In *C. jejuni*, rod-shaped mutants colonize the lumen in a mouse infection model, whereas straight-rod mutants do not cross the mucus layer to infect the intestinal crypts and therefore are not pathogenic (Stahl et al., 2016). In addition, straight *C. jejuni* mutants are also less capable of forming biofilms; biofilm formation has been linked to cell survival under stressful conditions (Murphy et al., 2006; Reuter et al., 2010). Further research might demonstrate whether this decreased biofilm-forming capacity has any relevance for the survival of *C. jejuni* inside or outside its host.

Cell shape might facilitate reduced detection of bacteria by the immune system (Veyrier et al., 2015). The opportunistic pathogens *Neisseria meningitidis* and *Moraxella catarrhalis* are both adapted to live in the human nasopharynx. Both species are coccoid, but their ancestors were rod-shaped and ovococcoid, respectively. A recent study showed that loss of the gene *yacF*, which encodes a protein involved in the transition from elongation to division, could explain the morphological evolution of both species (Veyrier et al., 2015). In addition to this morphological change, the amount of pentapeptides is increased in the PG of *N. meningitidis* cocci. These PG sacculi are recognized less efficiently by the Nod1 and Nod2 receptors of the innate immune system. Veyrier et al. (2015) hypothesized that the smaller cell surface of the coccoid bacteria might also reduce attacks from the immune system. The entire cell surface of the coccoid cells is covered in pili, whereas rod-shaped cells display pili on the poles only. Thus, coccoid cells might attach to the nasopharyngeal mucosa more efficiently.

Morphology might also play a role in the infection process itself. *Shigella flexneri* is a rod-shaped pathogen that infects epithelial cells in the large intestine in a multi-step process in which its type III secretion system (T3SS) plays an important role (Schroeder and Hilbi, 2008). Although A22-treated coccoid cells still attach to eukaryotic cells *in vitro*, invasion of these cells is clearly impaired (Noguchi et al., 2008). Furthermore, the coccoid cells secrete less T3SS effector proteins, suggesting that the altered morphology leads to a decrease in effector secretion through T3SS, possibly due to mislocalization of the T3SS proteins. Further research is needed to establish if the reduced pathogenicity is directly caused by the altered morphology or (in)directly by inactivation of the MreB cytoskeleton. Indeed, in the enteric pathogen *Salmonella typhimurium*, inactivation of the MreB cytoskeleton by depletion of the accessory proteins MreC and MreD leads to spherical cells that are impaired in the disruption of epithelial tight junctions *in vitro* and colonization in a mouse model (Bulmer et al., 2012). In this case, however, the altered morphology plays only a minor role, if any, in the attenuated virulence. Instead, the disruption of the MreB cytoskeleton leads to downregulation of genes involved in pathogenicity (Bulmer et al., 2012; Doble et al., 2012).

Moreover, certain bacteria change shape as a strategy to boost survival when confronting environmental stresses, as discussed in the previous section. Filamentation protects UPEC cells from phagocytosis by neutrophils during infection of the bladder (Justice et al., 2004, 2006; Horvath et al., 2011). *Legionella pneumophila* filamentous cells are less easily engulfed by phagocytes (Prashar et al., 2012, 2013). In *Haemophilus influenza* causing otitis, the influence of filamentous cells on biofilm architecture increases the persistence of the pathogen in an animal model (Szelestey et al., 2013). Filamentous cells of *S. enterica* (Humphrey et al., 2011) and *Edwardsiella tarda* (Wang et al., 2014) are less able to invade epithelial cells. Filamentation is also used by multiple bacteria as a strategy to escape predation by protists (Güde, 1979; Hahn et al., 1999; Corno and Jürgens, 2006), although in some cases filamentation can't prevent bacteria from being eaten (Wu et al., 2004).

MORPHOLOGICAL DETERMINANTS AS TARGETS FOR ANTIMICROBIALS

The rise of antibiotic resistance in pathogenic bacteria and the very limited success in developing new antibiotics drives the search for novel targets in antimicrobial research (Spellberg et al., 2008; Fishbach and Walsh, 2009). The majority of antibiotics currently in use as well as those under development (Boucher et al., 2013) act on membrane stability, PG biosynthesis, folate biosynthesis, DNA replication, transcription and translation (Hurley et al., 2016). Strategies under investigation include hijacking toxin-antitoxin systems (Chan et al., 2015), inhibiting bacterial cell division (Lock and Harry, 2008; Hurley et al., 2016) and blocking the T3SS to render bacteria non-pathogenic (McShan and De Guzman, 2015).

As exemplified by this last strategy, it might be possible to develop antimicrobials that are not bactericidal *per se* but that target the ability of bacteria to cause unwanted effects, such as disease. A meta-analysis showed that the curing efficiencies of bacteriostatic and bactericidal antibiotics are equivalent (Nemeth et al., 2015), supporting the validity of this strategy to address infectious diseases. However, the use of bacteriostatic antibiotics might increase the incidence of antibiotic resistance as living bacteria can mutate and develop resistance, whereas dead bacteria cannot (Stratton, 2003). However, if the targeted pathways are of key importance for bacterial survival or proliferation, it is expected that the bacteria will eventually die, even if the drugs are mechanistically bacteriostatic. This indeed appears to be the case for antibiotics targeting cell division (Lock and Harry, 2008).

As bacterial cell shape can impact the ability of bacteria to survive in their specific niche as well as colonize hosts, escape the immune system and cause disease, shape might be a good target for antimicrobials. The exploration of morphological determinants of bacteria as drug targets has been limited and has focused primarily on bacterial cytoskeletal elements (Vollmer, 2006). In the following paragraphs, we will discuss the potential indications for morphology inhibitors and the possible advantages and disadvantages of morphology as a target for inhibitors. Furthermore, we will introduce examples of inhibitors currently under development and outline possibilities for future research directions.

Possible Applications of Inhibitors of Bacterial Cell Shape

Multiple applications might benefit from inhibitors of bacterial morphology. The most obvious use would be to make pathogenic bacteria unfit to colonize their host, escape the immune system and cause disease. This strategy will only be effective if the morphology of the bacterium is important for survival or virulence in the host. The most obvious host is humans, but this strategy is also applicable to plant or animal species, such as food crops or endangered species. Indeed, antibiotics are commonly used in agriculture, where antibiotic resistance is also a problem (Thanner et al., 2016).

Another possible application is inhibition of biofilm formation. Bacterial biofilms are a substantial problem in the food and beverage industries (Brooks and Flint, 2008), medicine (Francolini and Donelli, 2010) and water treatment (Nguyen et al., 2012). As discussed above, bacterial morphology has been shown to influence biofilm formation (Huber et al., 2002; Lin et al., 2015), and therefore targeting cell shape might be a very useful strategy to combat biofilm formation.

Furthermore, it might be promising to use shape inhibitors to change the characteristics of bacteria to increase their suitability for biotechnological applications. Cell shape dictates the ratio between the membrane area and volume of a bacterial cell, a parameter that affects both substrate uptake (Schulz and Jørgensen, 2001) and product excretion. If bacteria are used to degrade certain substances, the uptake efficiency of the bacteria is of high interest. The ability of bacteria to efficiently export proteins or other substances is crucial in many biotechnological applications.

Targeting Morphological Determinants: Advantages and Disadvantages

An important advantage of morphological determinants as drug targets is the potential for broad-spectrum as well as narrow-spectrum antibiotics. Successfully targeting widespread determinants, such as MreB, will lead to broad-spectrum antibiotics. Other determinants, such as the PG hydrolases that shape *H. pylori* (Sycuro et al., 2012) and *C. jejuni* (Frirdich et al., 2012; Stahl et al., 2016), are only conserved in certain bacteria, in this case, several helical or curved delta- and epsilonproteobacteria (Sycuro et al., 2012). Targeting these determinants thus allows for drugs against a specific class of pathogens. In addition to the morphological determinants themselves, the interactions of these proteins with other macromolecules can possibly be used as targets (Zoraghi and Reiner, 2013). This strategy can be used to tune the specificity of these drugs. For example, bacterial IF-like filaments such as bactofilins are widespread, but their interaction partners appear to vary. Therefore, targeting the site of interaction between bactofilins and the interacting proteins in complexes responsible for a certain morphology might be an excellent strategy to obtain very specific antimicrobials. As research into the morphological determinants of various bacteria proceeds, it is probable that multiple new potential drug targets will be identified, of which the majority are likely to be rather specific.

Why would it be relevant to develop both broad-range and narrow-range antibiotics? With respect to the curative success rate, broad-spectrum and pathogen-directed antibiotic treatments show very similar efficiency, at least in pneumonia (van der Eerden et al., 2005; Williams et al., 2013). In the case of serious bacterial infections requiring immediate treatment, broad-spectrum antibiotics are the drugs of choice because they enable treatment to start before the pathogen is identified (Kollef, 2008). However, the use of broad-spectrum antibiotics also poses problems. Broad-spectrum antibiotics kill bacteria other than pathogens (Rea et al., 2011), including beneficial microbiome species (Brown and Wright, 2005), creating a

more favorable environment for antibiotic-resistant bacteria (Harbarth et al., 2002). When the pathogen is known (although routine identification would require considerable effort from the healthcare system), the use of narrow-range antibiotics is favorable because of the reduced collateral damage to other microbiome species (Rea et al., 2011) and the reduced risk of secondary infections (Palmer et al., 1995).

Another advantage of morphological determinants over some other possible targetable pathways is that most are specific to prokaryotes, thus reducing the likelihood of toxicity to the host due to binding to eukaryotic proteins with structures similar to the bacterial targets.

As discussed above, a potential disadvantage of morphological determinants as drug targets is that most of these drugs might not be bactericidal, facilitating development of resistance. Further research on different inhibitors at relevant concentrations and in different species is required; in some cases, the negative effect of the alteration of morphology might ultimately result in bacterial death. More research is also needed to establish whether changing bacterial morphology leads to unwanted side effects, such as reduced detectability or less efficient clearing by the immune system. The use of these inhibitors will probably impact microbial community composition in unexpected ways since inhibiting the target species might free up niches for other bacteria, including pathogens or biofilm-forming bacteria.

Existing Inhibitors Targeting Morphological Determinants

Multiple inhibitors targeting FtsZ have been described (Hurley et al., 2016), but these inhibitors impact cell division more than cell shape *per se* and will therefore be discussed only briefly. The six known classes of FtsZ inhibitors function via either decreasing or increasing the GTPase activity of FtsZ (Hurley et al., 2016) or altering the interactions between monomers or protofilaments (Vollmer, 2006). Other cell-division inhibitors target the interaction between FtsZ and its membrane anchor ZipA (Sutherland et al., 2003; Jennings et al., 2004a,b; Tsao et al., 2006) or stimulate uncontrolled proteolysis of FtsZ by the protease ClpP (Sass et al., 2011).

Several inhibitors targeting MreB derived from both chemical synthesis (Iwai et al., 2002; Robertson et al., 2007; Takacs et al., 2010) and natural sources (Rodríguez et al., 2008; Molshanski-Mor et al., 2014) have been described. The two most common inhibitors, *S*-(3,4-dichlorobenzyl)isothiourea (A22) and its derivative *S*-(4-chlorobenzyl)isothiourea (MP265), bind close to but not in the nucleotide-binding site of MreB (van den Ent et al., 2014). As illustrated in recent molecular dynamics studies, binding of these inhibitors leads to slower release of γ-phosphate upon ATP hydrolysis (Awuni et al., 2016). Inhibitor-bound MreB can still polymerize in an ATP-dependent fashion (Robertson et al., 2007), but its dimerization into stable double protofilaments is hindered (van den Ent et al., 2014). The indole-class inhibitor CBR-4830 binds in the nucleotide-binding site and prevents ATP-dependent polymerization (Robertson et al., 2007). No detailed mechanistic understanding of the inhibition process is available for the other MreB inhibitors, although the binding site of the T7 phage gene product 0.6 on MreB is known (Molshanski-Mor et al., 2014). Strikingly few studies have investigated the toxicity of MreB inhibitors against eukaryotic cells, even though this is an obvious prerequisite for the development of MreB inhibitors into antibiotics. The only study that has been performed suggests that the inhibitor A22 is cytotoxic and genotoxic to human blood cells at concentrations exceeding 4.3 μM (Bonez et al., 2016), which is lower than the minimal inhibitory concentration (MIC) for multiple bacterial species (Foss et al., 2011). In addition, the structurally similar *S*-benzylisothiourea was shown to be toxic to rats (Shirota et al., 1997).

A phosphonic acid-based pseudopeptide inhibitor of the PG hydrolases Csd4 and Pgp1, which are required for the helical cell shapes of *H. pylori* and *C. jejuni*, respectively, was recently developed via targeted drug design (Liu et al., 2016). The pseudopeptide binds in the active site of the enzyme and mimics an intermediate stage in the cleavage of mesoDAP from the uncrosslinked PG stem peptide (Liu et al., 2016). The inhibitor can cross the outer membrane to induce cell straightening of both *H. pylori* and, albeit with lower efficiency due to the polysaccharide capsule, *C. jejuni* (Liu et al., 2016).

Future Perspectives for Drugs Targeting Morphological Determinants

The availability of several inhibitors targeting morphological determinants is a good first step toward the development of drugs for use in the clinic. However, extensive work remains, and it is unclear if pharmaceutical companies find drugs targeting morphology sufficiently promising for investment. Many of the potential shape-targeting drugs are expected to be narrow-range antibiotics. Developing new antibiotics is very expensive, and pharmaceutical companies are unlikely to invest considerable resources in developing drugs with a very limited market (Walsh, 2003). Initial screening for lead structures with shape-inhibiting action has always been very tedious, requiring screening by manual microscopy, further adding to the unattractiveness of these inhibitors to companies developing antimicrobials. This problem has recently been solved by the application of automated microscopy and image analysis (Choi et al., 2014) and flow cytometry cell sorting (Laubacher et al., 2013; Sycuro et al., 2013) to screen for bacterial morphology, enabling high-throughput, low-cost screening of large compound libraries for effects on bacterial morphology.

Further research by the academic community might aid further investigation of the drug potential of inhibitors targeting morphological determinants. This research should focus on multiple goals. First, the importance of shape in bacterial survival (in the environment as well as in the host) and virulence should be studied in many more bacteria. Much more research is also needed to identify additional morphological determinants and molecular mechanisms underlying cell shape, particularly in (pathogenic) bacteria with non-standard cell shapes [as eloquently proposed elsewhere (Kysela et al., 2016)]. These two research lines will form the basis for the development of novel inhibitors via targeted design or high-throughput screening of compound libraries.

In parallel, more research is needed on existing inhibitors. These endeavors should focus on investigating the effects of these inhibitors on additional species and establishing their toxicity in eukaryotic hosts. Further elucidation of the working mechanism of these inhibitors might enable targeted optimization to develop next-generation inhibitors that are effective at lower (more practical) doses. Studies of the occurrence of resistant strains could provide information on whether these inhibitors represent good drugs alone or in combination with drugs that suppress resistance through elevated efflux.

Morphological determination continues to be an important field of fundamental research in which many open questions remain. The development of several inhibitors demonstrates the need for further study and might ultimately lead to drugs targeting bacterial morphology to control bacterial survival and virulence.

AUTHOR CONTRIBUTIONS

All authors listed have made a substantial, direct and intellectual contribution to the work, and approved it for publication.

ACKNOWLEDGMENTS

Research in the Cava lab is supported by the Laboratory for Molecular Infection Medicine Sweden (MIMS), the Knut and Alice Wallenberg Foundation (KAW), the Swedish Research Council, the Kempe Foundation and Umeå University. MvT is supported by an EMBO Long-Term Fellowship (ALTF 1396-2015), co-funded by the European Commission via the Marie Curie Actions (LTFCOFUND2013, GA-2013-609409).

REFERENCES

Aaron, M., Charbon, G., Lam, H., Schwarz, H., Vollmer, W., and Jacobs-Wagner, C. (2007). The tubulin homologue FtsZ contributes to cell elongation by guiding cell wall precursor synthesis in *Caulobacter crescentus*. *Mol. Microbiol.* 64, 938–952. doi: 10.1111/j.1365-2958.2007.05720.x

An, D. R., Kim, H. S., Kim, J., Im, H. N., Yoon, H. J., Jang, J. Y., et al. (2015). Structure of Csd3 from *Helicobacter pylori*, a cell shape-determining metallopeptidase. *Acta Crystallogr. D Biol. Crystallogr.* 71, 675–686. doi: 10.1107/S1399004715000152

Angert, E. R. (2005). Alternatives to binary fission in bacteria. *Nat. Rev. Microbiol.* 3, 214–224. doi: 10.1038/nrmicro1096

Armbruster, C. E., and Mobley, H. L. T. (2012). Merging mythology and morphology: the multifaceted lifestyle of *Proteus mirabilis*. *Nat. Rev. Microbiol.* 10, 743–754. doi: 10.1038/nrmicro2890

Asakura, H., Ishiwa, A., Arakawa, E., Makino, S., Okada, Y., Yamamoto, S., et al. (2007). Gene expression profile of *Vibrio cholerae* in the cold stress-induced viable but non-culturable state. *Environ. Microbiol.* 9, 869–879. doi: 10.1111/j.1462-2920.2006.01206.x

Ausmees, N., Kuhn, J. R., and Jacobs-Wagner, C. (2003). The bacterial cytoskeleton: an intermediate filament-like function in cell shape. *Cell* 115, 705–713. doi: 10.1016/S0092-8674(03)00935-8

Awuni, Y., Jiang, S., Robinson, R. C., and Mu, Y. (2016). Exploring the A22-bacterial actin MreB interaction through molecular dynamics simulations. *J. Phys. Chem. B* 120, 9867–9874. doi: 10.1021/acs.jpcb.6b05199

Baker, R. M., Singleton, F. L., and Hood, M. A. (1983). Effects of nutrient deprivation on *Vibrio cholerae*. *Appl. Environ. Microbiol.* 46, 930–940.

Barer, M. R., Gribbon, L. T., Harwood, C. R., and Nwoguh, C. E. (1993). The viable but non-culturable hypothesis and medical bacteriology. *Rev. Med. Microbiol.* 4, 183–191. doi: 10.1097/00013542-199310000-00001

Barreteau, H., Kovač, A., Boniface, A., Sova, M., Gobec, S., and Blanot, D. (2008). Cytoplasmic steps of peptidoglycan biosynthesis. *FEMS Microbiol. Rev.* 32, 168–207. doi: 10.1111/j.1574-6976.2008.00104.x

Bartlett, T. M., Bratton, B. P., Duvshani, A., Miguel, A., Sheng, Y., Martin, N. R., et al. (2017). A periplasmic polymer curves *Vibrio cholerae* and promotes pathogenesis. *Cell* 168, 172–185. doi: 10.1016/j.cell.2016.12.019

Becker, E., Herrera, N. C., Gunderson, F. Q., Derman, A. I., Dance, A. L., Sims, J., et al. (2006). DNA segregation by the bacterial actin lfA during *Bacillus subtilis* growth and development. *EMBO J.* 25, 5919–5931. doi: 10.1038/sj.emboj.7601443

Bernander, R., and Ettema, T. J. G. (2010). FtsZ-less cell division in archaea and bacteria. *Curr. Opin. Microbiol.* 13, 747–752. doi: 10.1016/j.mib.2010.10.005

Bernard, E., Rolain, T., Courtin, P., Hols, P., and Chapot-Chartier, M.-P. (2011). Identification of the amidotransferase AsnB1 as being responsible for *meso*-diaminopimelic acid amidation in *Lactobacillus plantarum* peptidoglycan. *J. Bacteriol.* 193, 6323–6330. doi: 10.1128/JB.05060-11

Bi, E., and Lutkenhaus, J. (1993). Cell division inhibitors SulA and MinCD prevent formation of the FtsZ ring. *J. Bacteriol.* 175, 1118–1125. doi: 10.1128/jb.175.4.1118-1125.1993

Billings, G., Ouzounov, N., Ursell, T., Desmarais, S. M., Shaevitz, J., Gitai, Z., et al. (2014). *De novo* morphogenesis in L-forms via geometric control of cell growth. *Mol. Microbiol.* 93, 883–896. doi: 10.1111/mmi.12703

Biondi, E. G., Skerker, J. M., Arif, M., Prasol, M. S., Perchuk, B. S., and Laub, M. (2006). A phosphorelay system controls stalk biogenesis during cell cycle progression in *Caulobacter crescentus*. *Mol. Microbiol.* 59, 386–401. doi: 10.1111/j.1365-2958.2005.04970.x

Bisson-Filho, A. W., Hsu, Y.-P., Squyres, G., Kuru, E., Wu, F., Jukes, C., et al. (2016). Treadmilling by FtsZ filaments drives peptidoglycan synthesis and bacterial cell division. *Science* 355, 739–743. doi: 10.1126/science.aak9973

Bonez, P. C., Ramos, A. P., Nascimento, K., Copetti, P. M., Souza, M. E., Rossi, G. G., et al. (2016). Antibacterial, cyto and genotoxic activities of A22 compound ((S-3,4-dichlorobenzyl) isothiourea hydrochloride). *Microb. Pathog.* 99, 14–18. doi: 10.1016/j.micpath.2016.07.007

Bonis, M., Ecobichon, C., Guadagnini, S., Prévost, M.-C., and Boneca, I. G. (2010). A M23B family metallopeptidase of *Helicobacter pylori* required for cell shape, pole formation and virulence. *Mol. Microbiol.* 78, 809–819. doi: 10.1111/j.1365-2958.2010.07383.x

Boucher, H. W., Talbot, G. H., Benjamin, D. K. Jr., Bradley, J., Guidos, R. J., Jones, R. N., et al. (2013). 10 × ′20 progress-development of new drugs active against Gram-negative bacilli: an update from the infectious diseases society of America. *Clin. Infect. Dis.* 56, 1685–1694. doi: 10.1093/cid/cit152

Brooks, J. D., and Flint, S. H. (2008). Biofilms in the food industry: problems and potential solutions. *Int. J. Food Sci. Technol.* 43, 2163–2176. doi: 10.1111/j.1365-2621.2008.01839.x

Brown, E. D., and Wright, G. D. (2005). New targets and screening approaches in antimicrobial drug discovery. *Chem. Rev.* 105, 759–774. doi: 10.1021/cr030116o

Bulmer, D. M., Kharraz, L., Grant, A. J., Dean, P., Morgan, F. J. E., Karavolos, M. H., et al. (2012). The bacterial cytoskeleton modulates motility, type 3 secretion, and colonization in *Salmonella*. *PLoS Pathog.* 8:e1002500. doi: 10.1371/journal.ppat.1002500

Busiek, K. K., and Margolin, W. (2015). Bacterial actin and tubulin homologs in cell growth and division. *Curr. Biol.* 25, R243–R254. doi: 10.1016/j.cub.2015.01.030

Cabeen, M. T., Charbon, G., Vollmer, W., Born, P., Ausmees, N., Weibel, D. B., et al. (2009). Bacterial cell curvature through mechanical control of cell growth. *EMBO J.* 28, 1208–1219. doi: 10.1038/emboj.2009.61

Cameron, T. A., Anderson-Furgeson, J., Zupan, J. R., Zik, J. J., and Zambryski, P. C. (2014). Peptidoglycan synthesis machinery in *Agrobacterium tumefaciens* during unipolar growth and cell division. *mBio* 5:e01219-14. doi: 10.1128/mBio.01219-14

Carballido-López, R. (2007). The bacterial actin-like cytoskeleton. *Microbiol. Mol. Biol. Rev.* 70, 888–909. doi: 10.1128/MMBR.00014-06

Carballido-López, R., Formstone, A., Li, Y., Ehrlich, S. D., Noirot, P., and Errington, J. (2006). Actin homolog MreBH governs cell morphogenesis by

localization of the cell wall hydrolase LytE. *Dev. Cell* 11, 399–409. doi: 10.1016/j.devcel.2006.07.017

Cava, F., and de Pedro, M. A. (2014). Peptidoglycan plasticity in bacteria: emerging variability of the murein sacculus and their associated biological functions. *Curr. Opin. Microbiol.* 18, 46–53. doi: 10.1016/j.mib.2014.01.004

Cava, F., de Pedro, M. A., Lam, H., Davis, B. M., and Waldor, M. K. (2011). Distinct pathways for modification of the bacterial cell wall by non-canonical D-amino acids. *EMBO J.* 30, 3442–3453. doi: 10.1038/emboj.2011.246

Celli, J. P., Turner, B. S., Afdhal, N. H., Keates, S., Ghiran, I., Kelly, C. P., et al. (2009). *Helicobacter pylori* moves through mucus by reducing mucin viscoelasticity. *Proc. Natl. Acad. Sci. U.S.A.* 106, 14321–14326. doi: 10.1073/pnas.0903438106

Chan, W. T., Balsa, D., and Espinosa, M. (2015). One cannot rule them all: are bacterial toxins-antitoxins druggable? *FEMS Microbiol. Rev.* 39, 522–540. doi: 10.1093/femsre/fuv002

Chaput, C., Ecobichon, C., Cayet, N., Girardin, S. E., Werts, S., Guadagnini, S., et al. (2006). Role of AmiA in the morphological transition of *Helicobacter pylori* and immune escape. *PLoS Pathog.* 2:e97. doi: 10.1371/journal.ppat.0020097

Chaput, C., Ecobichon, C., Pouradier, N., Rouselle, J.-C., Namane, A., and Boneca, I. G. (2016). Role of the N-acetylmuramoyl-L-alanyl amidase, AmiA, of *Helicobacter pylori* in peptidoglycan metabolism, daughter cell separation and virulence. *Microb. Drug Resist.* 22, 477–486. doi: 10.1089/mdr.2016.0070

Charon, N. W., Goldstein, S. F., Curci, K., and Limberger, R. J. (1991). The bent-end morphology of *Treponema phagedenis* is associated with short, left-handed, periplasmic flagella. *J. Bacteriol.* 173, 4820–4826. doi: 10.1128/jb.173.15.4820-4826.1991

Chauhan, A., Madiraju, M. V. V. S., Fol, M., Lofton, H., Maloney, E., Reynolds, R., et al. (2006). Mycobacterium tuberculosis cells growing in macrophages are filamentous and deficient in FtsZ rings. *J. Bacteriol.* 188, 1856–1865. doi: 10.1128/JB.188.5.1856-1865.2006

Cho, H., Wivagg, C. N., Kapoor, M., Barry, Z., Rohs, P. D. A., Suh, H., et al. (2016). Bacterial cell wall biogenesis is mediated by SEDS and PBP polymerase families functioning semi-autonomously. *Nat. Microbiol.* 1:16172. doi: 10.1038/nmicrobiol.2016.172

Choi, J., Yoo, J., Lee, M., Kim, E.-G., Lee, J. S., Lee, S., et al. (2014). A rapid antimicrobial susceptibility test based on single-cell morphological analysis. *Sci. Transl. Med* 6, 267ra174. doi: 10.1126/scitranslmed.3009650

Citterio, B., Cassaroli, A., Pierfelici, L., Battistelli, M., Falcieri, E., and Baffone, W. (2004). Morphological changes and outer membrane protein patterns in *Helicobacter pylori* during conversion from bacillary to coccoid form. *New Microbiol.* 27, 353–360.

Corno, G., and Jürgens, K. (2006). Direct and indirect effects of protist predation on population size structure of a bacterial strain with high phenotypic plasticity. *Appl. Environ. Microbiol.* 72, 78–86. doi: 10.1128/AEM.72.1.78-86.2006

Costa, K., Bacher, G., Allmaier, G., Dominguez-Bello, M. G., Engstrand, L., Falk, P., et al. (1999). The morphological transition of *Helicobacter pylori* cells from spiral to coccoid is preceded by a substantial modification of the cell wall. *J. Bacteriol.* 181, 3710–3715.

Cserti, E., Rosskopf, S., Chang, Y.-W., Eisheuer, S., Selter, L., Shi, J., et al. (2017). Dynamics of the peptidoglycan biosynthetic machinery in the stalked budding bacterium *Hyphomonas neptunium*. *Mol. Microbiol.* 103, 875–895. doi: 10.1111/mmi.13593

Curtis, P. D., and Brun, Y. V. (2010). Getting in the loop: regulation of development in *Caulobacter crescentus*. *Microbiol. Mol. Biol. Rev.* 74, 13–41. doi: 10.1128/MMBR.00040-09

de Pedro, M. A., and Cava, F. (2015). Structural constraints and dynamics of bacterial cell wall architecture. *Front. Microbiol.* 6:449. doi: 10.3389/fmicb.2015.00449

de Pedro, M. A., Quintela, J. C., Höltje, J. V., and Schwarz, H. (1997). Murein segregation in *Escherichia coli*. *J. Bacteriol.* 179, 2823–2834. doi: 10.1128/jb.179.9.2823-2834.1997

Derman, A. I., Becker, E. C., Truong, B. D., Fujioka, A., Tucey, T. M., Erb, M. L., et al. (2009). Phylogenetic analysis identifies many uncharacterized actin-like proteins (Alps) in bacteria: regulated polymerization, dynamic instability, and treadmilling in Alp7A. *Mol. Microbiol.* 73, 534–552. doi: 10.1111/j.1365-2958.2009.06771.x

Doble, A. C., Bulmer, D. M., Kharraz, L., Karavolos, M. H., and Khan, C. M. A. (2012). The function of the bacterial cytoskeleton in *Salmonella* pathogenesis. *Virulence* 3, 446–458. doi: 10.4161/viru.20993

Doi, M., Wachi, M., Ishino, F., Tomioka, S., Ito, M., Sakagami, Y., et al. (1988). Determinants of the DNA sequence of the *mreB* gene and of the gene products of the *mre* region that function in formation of the rod shape of *Escherichia coli*. *J. Bacteriol.* 170, 4619–4624. doi: 10.1128/jb.170.10.4619-4624.1988

Dombrowski, C., Kan, W., Motaleb, M. A., Charon, N. W., Goldstein, R. E., and Wolgemuth, C. W. (2009). The elastic basis for the shape of *Borrelia burgdorferi*. *Biophys. J.* 96, 4409–4417. doi: 10.1016/j.bpj.2009.02.066

Domínguez-Escobar, J., Chastanet, A., Crevenna, A. H., Fromion, V., Wedlich-Söldner, R., and Carballido-López, R. (2011). Processive movement of MreB-associated cell wall biosynthetic complexes in bacteria. *Science* 333, 225–228. doi: 10.1126/science.1203466

Dörr, T., Cava, F., Lam, H., Davis, B. M., and Waldor, M. K. (2013). Substrate specificity of an elongation-specific peptidoglycan endopeptidase and its implications for cell wall architecture and growth of *Vibrio cholerae*. *Mol. Microbiol.* 89, 949–962. doi: 10.1111/mmi.12323

Du, S., Pichoff, S., and Lutkenhaus, J. (2016). FtsEX acts on FtsA to regulate divisome assembly and activity. *Proc. Natl. Acad. Sci. U.S.A.* 113, E5052–E5061. doi: 10.1073/pnas.1606656113

Effendi, I., and Austin, B. (1995). Dormant/unculturable cells of the fish pathogen *Aeromonas salmonicida*. *Microb. Ecol.* 30, 183–192. doi: 10.1007/BF00172573

Erickson, H. P., Taylor, D. W., Taylor, K. A., and Bramhill, D. (1996). Bacterial cell division protein FtsZ assembles into protofilament sheets and minirings, structural homologs of tubulin polymers. *Proc. Natl. Acad. Sci. U.S.A.* 93, 519–523. doi: 10.1073/pnas.93.1.519

Errington, J. (2015). Bacterial morphogenesis and the enigmatic MreB helix. *Nat. Rev. Microbiol.* 13, 241–248. doi: 10.1038/nrmicro3398

Fenton, A. K., and Gerdes, K. (2013). Direct interaction of FtsZ and MreB is required for septum synthesis and cell division in *Escherichia coli*. *EMBO J.* 32, 1953–1965. doi: 10.1038/emboj.2013.129

Fishbach, M. A., and Walsh, C. T. (2009). Antibiotics for emerging pathogens. *Science* 325, 1089–1093. doi: 10.1126/science.1176667

Foss, M. H., Eun, Y. J., and Weibel, D. B. (2011). Chemical-biological studies of subcellular organization in bacteria. *Biochemistry* 50, 7719–7734. doi: 10.1021/bi200940d

Francolini, I., and Donelli, G. (2010). Prevention and control of biofilm-based medical-device-related infections. *FEMS Immunol. Med. Microbiol.* 59, 227–238. doi: 10.1111/j.1574-695X.2010.00665.x

Frirdich, E., Biboy, J., Adams, C., Lee, J., Ellermeier, J., Davis Gielda, L., et al. (2012). Peptidoglycan-modifying enzyme pgp1 is required for helical cell shape and pathogenicity traits in *Campylobacter jejuni*. *PLoS Pathog.* 8:e1002602. doi: 10.1371/journal.ppat.1002602

Frirdich, E., and Gaynor, E. C. (2013). Peptidoglycan hydrolases, bacterial shape, and pathogenesis. *Curr. Opin. Microbiol.* 16, 767–778. doi: 10.1016/j.mib.2013.09.005

Frirdich, E., Vermeulen, J., Biboy, J., Soares, F., Taveirne, M. E., Johnson, J. G., et al. (2014). Peptidoglycan LD-carboxypeptidase pgp2 influences *Campylobacter jejuni* helical cell shape and pathogenic properties and provides the substrate for the DL-carboxypeptidase pgp1. *J. Biol. Chem.* 289, 8007–8018. doi: 10.1074/jbc.M113.491829

Ganchev, D. N., Hasper, H. E., Breukink, E., and de Kruijff, B. (2006). Size and orientation of the lipid II headgroup as revealed by AFM imaging. *Biochemistry* 45, 6195–6202. doi: 10.1021/bi051913e

Garner, E. C., Bernard, R., Wang, W., Zhuang, X., Rudner, D. Z., and Mitchison, T. (2011). Coupled, circumferential motions of the cell wall synthesis machinery and MreB filaments in *B. subtilis*. *Science* 333, 222–225. doi: 10.1126/science.1203285

Gilmore, M. E., Bandyopadhyay, D., Dean, A. M., Linnstaedt, S. D., and Popham, D. L. (2004). Production of muramic δ-lactam in *Bacillus subtilis* spore peptidoglycan. *J. Bacteriol.* 186, 80–89. doi: 10.1128/JB.186.1.80-89.2004

Grangeon, R., Zupan, J. R., Anderson-Furgeson, J., and Zambryski, P. C. (2015). PopZ identifies the new pole, and PodJ identifies the old pole during polar growth in *Agrobacterium tumefaciens*. *Proc. Natl. Acad. Sci. U.S.A.* 112, 11666–11671. doi: 10.1073/pnas.1515544112

Gray, A. N., Egan, A. J. F., van 't Veer, I. L., Verheul, J., Colavin, A., Koumoutsi, A., et al. (2015). Coordination of peptidoglycan synthesis and outer membrane

constriction druing *Escherichia coli* cell division. *eLife* 4:e07118. doi: 10.7554/eLife.07118

Güde, H. (1979). Grazing by protozoa as selection factor for activated sludge bacteria. *Microb. Ecol.* 5, 225–237. doi: 10.1007/BF02013529

Ha, R., Frirdich, E., Sychantha, D., Biboy, J., Taveirne, M. E., Johnson, J. G., et al. (2016). Accumulation of peptidoglycan O-acetylation leads to altered cell wall biochemistry and negatively impacts pathogenesis factors of *Campylobacter jejuni*. *J. Biol. Chem.* 291, 22686–22702. doi: 10.1074/jbc.M116.746404

Haeusser, D. P., and Margolin, W. (2016). Splitsville: structural and functional insights into the dynamic bacterial Z ring. *Nat. Rev. Microbiol.* 14, 305–319. doi: 10.1038/nrmicro.2016.26

Hahn, M. W., Moore, E. R. B., and Höfle, M. G. (1999). Mechanism against flagellate grazing, is growth rate controlled in bacteria of different phyla. *Appl. Environ. Microbiol.* 65, 25–35.

Harbarth, S., Cosgrove, S., and Carmeli, Y. (2002). Effects of antibiotics on nosocomial epidemiology of vancomycin-resistant enterococci. *Antimicrob. Agents Chemother.* 46, 1619–1628. doi: 10.1128/AAC.46.6.1619-1628.2002

Harman, M., Vig, D. K., Radolf, J. D., and Wolgemuth, C. W. (2013). Viscous dynamics of lyme disease and syphilis spirochetes reveal flagellar torque and drag. *Biophys. J.* 105, 2273–2280. doi: 10.1016/j.bpj.2013.10.004

Hashimoto, M., Ooiwa, S., and Sekiguchi, J. (2012). Synthetic lethality of the *lytE cwlO* genotype in *Bacillus subtilis* is caused by lack of D,L-endopeptidase activity at the lateral cell wall. *J. Bacteriol.* 194, 796–803. doi: 10.1128/JB.05569-11

Hay, N. A., Tipper, D. J., Gygi, D., and Hughes, C. (1999). A novel membrane protein influencing cell shape and multicellular swarming of *Proteus mirabilis*. *J. Bacteriol.* 181, 2008–2016.

Hirsch, P. (1974). Budding bacteria. *Ann. Rev. Microbiol.* 28, 391–440. doi: 10.1146/annurev.mi.28.100174.002135

Horvath, D. J. Jr., Li, B., Casper, T., Partida-Sanchez, S., Hunstad, D. A., Hultgren, S. J., et al. (2011). Morphological plasticity promotes resistance to phagocyte killing of uropathogenic *Escherichia coli*. *Microb. Infect.* 13, 426–437. doi: 10.1016/j.micinf.2010.12.004

Howell, M., and Brown, P. J. B. (2016). Building the bacterial cell wall at the pole. *Curr. Opin. Microbiol.* 34, 53–59. doi: 10.1016/j.mib.2016.07.021

Huang, K. C., Mukhopadhyay, R., and Wingreen, N. S. (2006). A curvature-mediated mechanism for localization of lipids to bacterial poles. *PLoS Comput. Biol.* 2:e151. doi: 10.1371/journal.pcbi.0020151

Huber, B., Riedel, K., Köthe, M., Givskov, M., Molin, S., and Eberl, L. (2002). Genetic analysis of functions involved in the late stages of biofilm development in *Burkholderia cepacia* H111. *Mol. Microbiol.* 46, 411–426. doi: 10.1046/j.1365-2958.2002.03182.x

Huisman, O., and D'Ari, R. (1981). An inducible DNA replication-cell division coupling mechanism in *E. coli*. *Nature* 290, 797–799. doi: 10.1038/290797a0

Humphrey, S., MacVicar, T., Stevenson, A., Roberts, M., Humphrey, T. J., and Jepson, M. A. (2011). SulA-induced filamentation in *Salmonella enterica* serovar Typhimurium: effects on SPI-1 expression and epithelial infection. *J. Appl. Microbiol.* 111, 185–196. doi: 10.1111/j.1365-2672.2011.05022.x

Hung, W., Jane, W.-N., and Wong, H. (2013). Association of D-alanyl-D-alanine carboxypeptidase gene with the formation of aberrantly shaped cells during the induction of viable but nonculturable *Vibrio parahaemolyticus*. *Appl. Environ. Microbiol.* 79, 7305–7312. doi: 10.1128/AEM.01723-13

Hurley, K. A., Santos, T. M. A., Nepomuceno, G. M., Huynh, V., Shaw, J. T., and Weibel, D. B. (2016). Targeting the bacterial division protein FtsZ. *J. Med. Chem.* 59, 6975–6998. doi: 10.1021/acs.jmedchem.5b01098

Ishiguro, E. E., and Ramey, W. D. (1976). Stringent control of peptidoglycan biosynthesis in *Escherichia coli* K-12. *J. Bacteriol.* 127, 1119–1126.

Iwai, N., Nagai, K., and Wachi, M. (2002). Novel S-benzylisothiourea compound that induces spherical cells in *Escerichia coli* probably by acting on a rod-shape-determining protein(s) other than penicillin-binding protein 2. *Biosci. Biotechnol. Biochem.* 66, 2658–2662. doi: 10.1271/bbb.66.2658

Jansen, A., Lockatell, C., Johnson, D., and Mobley, H. L. T. (2003). Visualization of *Proteus mirabilis* morphotypes in the urinary tract: the elongated swarmer cell is rarely observed in ascending urinary tract infection. *Infect. Immun.* 71, 3607–3613. doi: 10.1128/IAI.71.6.3607-3613.2003

Jenkins, C., Samudrala, R., Anderson, I., Hedlund, B. P., Petroni, G., Michailova, N., et al. (2002). Genes for the cytoskeletal protein tubulin in the bacterial genus *Prosthecobacter*. *Proc. Natl. Acad. Sci. U.S.A.* 99, 17049–17054. doi: 10.1073/pnas.012516899

Jennings, L. D., Foreman, K. W., Rush, T. S. III., Tsao, D. H. H., Mosyak, L., Kincaid, S. L., et al. (2004a). Combinatorial synthesis of substituted 3-(2-indolyl)piperidines and 2-phenyl indoles as inhibitors of ZipA-FtsZ interaction. *Bioorg. Med. Chem.* 1, 5115–5131.

Jennings, L. D., Foreman, K. W., Rush, T. S. III., Tsao, D. H. H., Mosyak, L., Li, Y., et al. (2004b). Design and synthesis of indolo[2,3-a]quinolizin-7-one inhibitors of the ZipA-FtsZ interaction. *Bioorg. Med. Chem. Lett.* 14, 1427–1431.

Jensen, R. B., and Gerdes, K. (1997). Partitioning of plasmid R1. The ParM protein exhibits ATPase activity and interacts with the centromere-like ParR-*parC* complex. *J. Mol. Biol.* 269, 505–513. doi: 10.1006/jmbi.1997.1061

Jeske, O., Schüler, M., Schumann, P., Schneider, A., Boedeker, C., Jogler, M., et al. (2015). Planctomycetes do posess a peptidoglycan cell wall. *Nat. Commun.* 6:7116. doi: 10.1038/ncomms8116

Jiang, C., Brown, P. J. B., Ducret, A., and Brun, Y. V. (2014). Sequential evolution of bacterial morphology by co-option of a developmental regulator. *Nature* 506, 489–493. doi: 10.1038/nature12900

Jones, L. J. F., Carballido-López, R., and Errington, J. (2001). Control of cell shape in bacteria: helical, actin-like filaments in *Bacillus subtilis*. *Cell* 104, 913–922. doi: 10.1016/S0092-8674(01)00287-2

Justice, S. S., Hung, C., Theriot, J. A., Fletcher, D. A., Anderson, G. G., Footer, M. J., et al. (2004). Differentiation and developmental pathways of uropathogenic *Escherichia coli* in urinary tract infections. *Proc. Natl. Acad. Sci. U.S.A.* 101, 1333–1338. doi: 10.1073/pnas.0308125100

Justice, S. S., Hunstad, D. A., Cegelski, L., and Hultgren, S. J. (2008). Morphological plasticity as a bacterial survival strategy. *Nat. Rev. Microbiol.* 6, 162–168. doi: 10.1038/nrmicro1820

Justice, S. S., Hunstad, D. A., Seed, P. C., and Hultgren, S. J. (2006). Filamentation by *Escherichia coli* subverts innate defenses during urinary tract infection. *Proc. Natl. Acad. Sci. U.S.A.* 103, 19884–19889. doi: 10.1073/pnas.0606329104

Kawai, Y., Mercier, R., and Errington, J. (2014). Bacterial cell morphogenesis does not require a preexisting template structure. *Curr. Biol.* 24, 863–867. doi: 10.1016/j.cub.2014.02.053

Kearns, D. B., and Losick, R. (2003). Swarming motility in undomesticated Bacillus subtilis. *Mol. Microbiol.* 49, 581–590. doi: 10.1046/j.1365-2958.2003.03584.x

Khandige, S., Asferg, C. A., Rasmussen, K. J., Larsen, M. J., Overgaard, M., Andersen, T. E., et al. (2016). DamX controls reversible cell morphology switching in uropathogenic *Escherichia coli*. *mBio* 7:e00642-16. doi: 10.1128/mBio.00642-16

Kim, H. S., Im, H. N., An, D. R., Yoon, J. Y., Jang, J. Y., Mobashery, S., et al. (2015). The cell shape-determining Csd6 protein from *Helicobacter pylori* constitutes a new family of L,D-carboxypeptidases. *J. Biol. Chem.* 290, 25103–25117. doi: 10.1074/jbc.M115.658781

Kim, H. S., Kim, J., Im, H. N., An, D. R., Lee, M., Hesek, D., et al. (2014). Structural basis for the recognition of muramyltripeptide by *Helicobacter pylori* Csd4, a D,L-carboxypeptidase controlling the helical cell shape. *Acta Crystallogr. D Biol. Crystallogr.* 70, 2800–2812. doi: 10.1107/S1399004714018732

Kim, S. Y., Gitai, Z., Kinkhabwala, A., Shapiro, L., and Moerner, W. E. (2006). Single molecules of the bacterial actin MreB undergo directed treadmilling motion in *Caulobacter crescentus*. *Proc. Natl. Acad. Sci. U.S.A.* 103, 10929–10934. doi: 10.1073/pnas.0604503103

Koch, M. K., McHugh, C. A., and Hoiczyk, E. (2011). BacM, an N-terminally processed bactofilin of *Myxococcus xanthus*, is crucial for proper cell shape. *Mol. Microbiol.* 80, 1031–1051. doi: 10.1111/j.1365-2958.2011.07629.x

Kollef, M. H. (2008). Broad-spectrum antimicrobials and the treatment of serious bacterial infections: getting it right up front. *Clin. Infect. Dis.* 47, S3–S13. doi: 10.086/590061

Koppelman, C.-M., Den Blaauwen, T., Duursma, M. C., Heeren, R. M. A., and Nanninga, N. (2001). *Escherichia coli* minicell membranes are enriched in cardiolipin. *J. Bacteriol.* 183, 6144–6147. doi: 10.1128/JB.183.20.6144-6147.2001

Kühn, J., Briegel, A., Mörschel, E., Kahnt, J., Leser, K., Wick, S., et al. (2010). Bactofilins, a ubiquitous class of cytoskeletal proteins mediating polar localization of a cell wall synthase in *Caulobacter crescentus*. *EMBO J.* 20, 327–339. doi: 10.1038/emboj.2009.358

Kusters, J. G., van Vliet, A. H. M., and Kuipers, E. J. (2006). Pathogenesis of *Helicobacter pylori* infection. *Clin. Microbiol. Rev.* 19, 449–490. doi: 10.1128/CMR.00054-05

Kysela, D. T., Randich, A. M., Caccamo, P. D., and Brun, Y. V. (2016). Diversity takes shape: understanding the mechanistic and adaptive basis of bacterial morphology. *PLoS Biol.* 14:e1002565. doi: 10.1371/journal.pbio.1002565

Laddomada, F., Miyachiro, M. M., and Dessen, A. (2016). Structural insights into protein-protein interactions involved in bacterial cell wall biogenesis. *Antibiotics* 5:14. doi: 10.3390/antibiotics5020014

Lam, H., Oh, D. C., Cava, F., Takacs, C. N., Clardy, J., de Pedro, M. A., et al. (2009). D-amino acids govern stationary phase cell wall remodeling in bacteria. *Science* 325, 1552–1555. doi: 10.1126/science.1178123

Larsen, R. A., Cusumano, C., Fujioka, A., Lim-Fong, G., Patterson, P., and Pogliano, J. (2007). Treadmilling of a prokaryotic tubulin-like protein, TubZ, required for plasmid stability in *Bacillus thuringiensis*. *Genes Dev.* 21, 1340–1352. doi: 10.1101/gad.1546107

Laub, M. T., McAdams, H. H., Feldblyum, T., Fraser, C. M., and Shapiro, L. (2000). Global analysis of the genetic network controlling a bacterial cell cycle. *Science* 290, 2144–2148. doi: 10.1126/science.290.5499.2144

Laubacher, M. E., Melquist, A. L., Chandramohan, L., and Young, K. D. (2013). Cell sorting enriches *Escherichia coli* mutants that rely on peptidoglycan endopeptidases to suppress highly aberrant morphologies. *J. Bacteriol.* 195, 855–866. doi: 10.1128/JB.01450-12

Leclercq, S., Derouaux, A., Olatunji, S., Fraipont, C., Egan, A. J., Vollmer, et al. (2017). Interplay between penicillin-binding proteins and SEDS proteins promotes bacterial cell wall synthesis. *Sci. Rep.* 7:43306. doi: 10.1038/srep43306

Leifson, E. (1964). Hyphomicrobium neptunium sp. n. *Antonie van Leeuwenhoek* 30, 249–256. doi: 10.1007/BF02046730

Levin, P. A., Margolis, P. S., Setlow, P., Losick, R., and Sun, D. X. (1992). Identification of *Bacillus subtilis* genes for septum placement and shape determination. *J. Bacteriol.* 174, 6717–6728. doi: 10.1128/jb.174.21.6717-6728.1992

Li, Y., Hsin, J., Zhao, L., Cheng, Y., Shang, W., Huang, K. C., et al. (2013). FtsZ protofilaments use a hinge-opening mechanism for constrictive force generation. *Science* 341, 392–395. doi: 10.1126/science.1239248

Liechti, G. W., Kuru, E., Hall, E., Kalinda, A., Brun, Y. V., VanNieuwenhze, M., et al. (2014). A new metabolic cell-wall labeling method reveals peptidoglycan in *Chlamydia trachomatis*. *Nature* 506, 507–510. doi: 10.1038/nature12892

Lin, L., and Thanbichler, M. (2013). Nucleotide-independent cytoskeletal scaffolds in bacteria. *Cytoskeleton* 70, 409–423. doi: 10.1002/cm.21126

Lin, T.-Y., Santos, T. M. A., Kontur, W. S., Donohue, T. J., and Weibel, D. B. (2015). A cardiolipin-deficient mutant of *Rhodobacter sphaeroides* has an altered cell shape an is impaired in biofilm formation. *J. Bacteriol.* 197, 3446–3455. doi: 10.1128/JB.00420-15

Liu, J., Zhou, R., Peters, B. M., Li, B., Lin, C., Chuang, T.-L., et al. (2017). Viable but non-culturable state and toxin gene expression of enterohemorrhagic *Escherichia coli* O157 under cryopreservation. *Res. Microbiol.* 168, 188–193. doi: 10.1016/j.resmic.2016.11.002

Liu, Y., Frirdich, E., Taylor, J. A., Chan, A. C. K., Blair, K. M., Vermeulen, J., et al. (2016). A bacterial cell shape-determining inhibitor. *ACS Chem. Biol.* 11, 981–991. doi: 10.1021/acschembio.5b01039

Lock, R. L., and Harry, E. J. (2008). Cell-division inhibitors: new insights for future antibiotics. *Nat. Rev. Drug Disc.* 7, 324–338. doi: 10.1038/nrd2510

Loose, M., and Mitchison, T. J. (2014). The bacterial cell division proteins FtsA and FtsZ self-organize into dynamic cytoskeletal patterns. *Nat. Cell Biol.* 16, 38–46. doi: 10.1038/ncb2885

Manat, G., Roure, S., Auger, R., Bouhss, A., Barreteau, H., Mengin-Lecreulx, D., et al. (2014). Deciphering the metabolism of undecaprenyl-phosphate: the bacterial cell-wall unit carrier at the membrane frontier. *Microb. Drug Resist.* 20, 199–214. doi: 10.1089/mdr.2014.0035

Männik, J., Driessen, R., Galajda, P., Keymer, J. A., and Dekker, C. (2009). Bacterial growth and motility in sub-micron constrictions. *Proc. Natl. Acad. Sci. U.S.A.* 106, 14861–14866. doi: 10.1073/pnas.0907542106

Martínez, L. E., Hardcastle, J. M., Wang, J., Pincus, Z., Tsang, J., Hoover, T. R., et al. (2016). *Helicobacter pylori* strainsvary cell shape and flagellum number to maintain robust motility in viscous environments. *Mol. Microbiol.* 99, 88–110. doi: 10.1111/mmi.13218

McShan, A. C., and De Guzman, R. N. (2015). The bacterial type III secretion system as a target for developing new antibiotics. *Chem. Biol. Drug Des.* 85, 30–42. doi: 10.1111/cbdd.12422

Meeske, A. J., Riley, E. P., Robins, W. P., Uehara, T., Mekalanos, J. J., Kahne, D., et al. (2016). SEDS proteins are a widespread family of bacterial cell wall polymerases. *Nature* 537, 634–638. doi: 10.1038/nature19331

Meeske, A. J., Sham, L.-T., Kimsey, H., Koo, B.-M., Gross, C. A., Bernhardt, T. G., et al. (2015). MurJ and a novel lipid II flippase are required for cell wall biogenesis in *Bacillus subtilis*. *Proc. Natl. Acad. Sci. U.S.A.* 112, 6437–6442. doi: 10.1073/pnas.1504967112

Meier, E. L., Razavi, S., Inoue, T., and Goley, E. D. (2016). A novel membrane anchor for FtsZ is linked to cell wall hydrolysis in *Caulobacter crescentus*. *Mol. Microbiol.* 101, 265–280. doi: 10.1111/mmi.13388

Meng, L., Alter, T., Aho, T., and Huehn, S. (2015). Gene expression profiles of *Vibrio* parahaemolyticus in viable but non-culturable state. *FEMS Microbiol. Ecol.* 91:fiv035. doi: 10.1093/femsec/fiv035

Mohammadi, T., van Dam, V., Sijbrandi, R., Vernet, T., Zapun, A., Bouhss, A., et al. (2011). Identification of FtsW as a transporter of lipid-linked cell wall precursors across the membrane. *EMBO J.* 30, 1425–1432. doi: 10.1038/emboj.2011.61

Molshanski-Mor, S., Yosef, I., Kiro, R., Edgar, R., Manor, M., Gershovits, M., et al. (2014). Revealing bacterial targets of growth inhibitors encoded by bacteriophage T7. *Proc. Natl. Acad. Sci. U.S.A.* 111, 18715–18720. doi: 10.1073/pnas.1413271112

Motaleb, M. A., Corum, L., Bono, J. L., Elias, A. F., Rosa, P., Samuels, D. S., et al. (2000). *Borrelia burgdorferi* periplasmic flagella have both skeletal and motility functions. *Proc. Natl. Acad. Sci. U.S.A.* 97, 10899–10904. doi: 10.1073/pnas.200221797

Müller, P., Ewers, C., Bertsche, U., Anstett, M., Kallis, T., Breukink, E., et al. (2007). The essential cell division protein FtsN interacts with the murein (peptidoglycan) synthase PBP1B in *Escherichia coli*. *J. Biol. Chem.* 282, 36394–36402. doi: 10.1074/jbc.M706390200

Murphy, C., Carroll, C., and Jordan, K. N. (2006). Environmental survival mechanisms of the foodborne pathogen *Campylobacter jejuni*. *J. Appl. Microbiol.* 100, 623–632. doi: 10.1111/j.1365-2672.2006.02903.x

Nelson, D. E., and Young, K. D. (2000). Penicillin binding protein 5 affects cell diameter, contour, and morphology of *Escherichia coli*. *J. Bacteriol.* 182, 1714–1721. doi: 10.1128/JB.182.6.1714-1721.2000

Nelson, D. E., and Young, K. D. (2001). Contribution of PBP5 and DD-carboxypeptidase penicillin binding proteins to maintenance of cell shape in *Escherichia coli*. *J. Bacteriol.* 183, 3055–3064. doi: 10.1128/JB.183.10.3055-3064.2001

Nemeth, J., Oesch, G., and Kuster, S. P. (2015). Bacteriostatic versus bactericidal antibiotics for patients with serious bacterial infections: systematic review and meta-analysis. *J. Antimicrob. Chemother.* 70, 382–395. doi: 10.1093/jac/dku379

Nguyen, T., Roddick, F. A., and Fan, L. (2012). Biofouling of water treatment membranes: a review of the underlying causes, monitoring techniques and control measures. *Membranes* 2, 804–840. doi: 10.3390/membranes2040804

Noguchi, N., Yanagimoto, K., Nakaminami, H., Wakabayashi, M., Iwai, N., Wachi, M., et al. (2008). Anti-infectious effect of S-benzylisothiourea compound A22, which inhibits the actin-like protein, MreB, in *Shigella flexneri*. *Biol. Pharm. Bull.* 31, 1327–1332. doi: 10.1248/bpb.31.1327

Ouzounov, N., Nguyen, J. P., Bratton, B. P., Jacobowitz, D., Gitai, Z., and Shaevitz, J. W. (2016). MreB orientation correlates with cell diameter in *Escherichia coli*. *Biophys. J.* 111, 1035–1043. doi: 10.1016/j.bpj.2016.07.017

Palmer, D. L., Pett, S. B., and Akl, B. F. (1995). Bacterial wound colonization after broad-spectrum versus narrow-spectrum antibiotics. *Ann. Thorac. Surg.* 59, 626–631. doi: 10.1016/0003-4975(94)00992-9

Paradis-Bleau, C., Markovski, M., Uehara, T., Lupoli, T. J., Walker, S., Kahne, D. E., et al. (2010). Lipoprotein cofactors located in the outer membrane activate bacterial cell wall polymerases. *Cell* 143, 1110–1120. doi: 10.1016/j.cell.2010.11.037

Partridge, J. D., and Harshey, R. M. (2013). More than motility: *Salmonella* flagella contribute to overriding friction and facilitating colony hydration during swarming. *J. Bacteriol.* 195, 919–929. doi: 10.1128/JB.02064-12

Pate, J. L., Porter, J. S., and Jordan, T. L. (1973). *Asticcacaulis biprosthecum* sp.nov. life cycle, morphology and cultural characteristics. *Antonie van Leeuwenhoek* 39, 569–583. doi: 10.1007/BF02578901

Persat, A., and Gitai, Z. (2014). Bacterial evolution: rewiring modules to get in shape. *Curr. Biol.* 24, R522–R524. doi: 10.1016/j.cub.2014.04.022

Persat, A., Stone, H. A., and Gitai, Z. (2014). The curved shape of *Caulobacter crescentus* enhances surface colonization in flow. *Nat. Commun.* 5:3824. doi: 10.1038/ncomms4824

Picardeau, M., Brenot, A., and Saint Girons, I. (2001). First evidence for gene replacement in *Leptospira* spp. Inactivation of *L. biflexa flaB* results in non-motile mutants deficient in endoflagella. *Mol. Microbiol.* 40, 189–199. doi: 10.1046/j.1365-2958.2001.02374.x

Pilhofer, M., Aistleitner, K., Biboy, J., Gray, J., Kuru, E., Hall, E., et al. (2013). Discovery of chlamydial peptidoglycan reveals bacteria with murein sacculi but without FtsZ. *Nat. Commun.* 4:2856. doi: 10.1038/ncomms3856

Pinho, M. G., Kjos, M., and Veening, J.-W. (2013). How to get (a)round: mechanisms controlling growth and division of coccoid bacteria. *Nat. Rev. Microbiol.* 11, 601–614. doi: 10.1038/nrmicro3088

Pisabarro, A. G., de Pedro, M. A., and Vázquez, D. (1985). Structural modifications in the peptidoglycan of *Escherichia coli* associated with changes in the state of growth of the culture. *J. Bacteriol.* 161, 238–242.

Popham, D. L., Gilmore, M. E., and Setlow, P. (1999). Roles of low-molecular-weight penicillin-binding proteins in *Bacillus subtilis* spore peptidoglycan synthesis and spore properties. *J. Bacteriol.* 181, 126–132.

Potluri, L.-P., Kannan, S., and Young, K. D. (2012). ZipA is required for FtsZ-dependent preseptal peptidoglycan synthesis prior to invagination during cell division. *J. Bacteriol.* 194, 5334–5342. doi: 10.1128/JB.00859-12

Prashar, A., Bhatia, S., Gigliozzi, D., Martin, T., Duncan, C., Guyard, C., et al. (2013). Filamentous morphology of bacteria delays the timing of phagosome morphogenesis in macrophages. *J. Cell Biol.* 203, 1081–1097. doi: 10.1083/jcb.201304095

Prashar, A., Bhatia, S., Tabatabaeiyazdi, Z., Duncan, C., Garduño, R. A., Tang, P., et al. (2012). Mechanism of invasion of lung epithelial cells by filamentous *Legionella pneumophila*. *Cell. Microbiol.* 14, 1632–1655. doi: 10.1111/j.1462-5822.2012.01828.x

Radhakrishnan, S. K., Thanbichler, M., and Viollier, P. H. (2008). The dynamic interplay between a cell fate determinant and a lysozyme homolog drives the asymmetric division cycle of *Caulobacter crescentus*. *Genes Dev.* 22, 212–225. doi: 10.1101/gad.1601808

Rast, P., Glöckner, I., Boedeker, C., Jeske, O., Wiegand, S., Reinhardt, R., et al. (2017). Three novel species with peptidoglycan cell walls from the new genus *Lacunisphaera* gen. nov. in the family Opitutaceae of the verrucomicrobial subdivision 4. *Front. Microbiol.* 8:202. doi: 10.3389/fmicb.2017.00202

Rea, M. C., Dobson, A., O'Sullivan, O., Crispie, F., Fouhy, F., Cotter, P. D., et al. (2011). Effect of broad- and narrow-spectrum antimicrobials on Clostridium difficile and microbial diversity in a model of the distal colon. *Proc. Natl. Acad. Sci. U.S.A.* 108, 4639–4644. doi: 10.1073/pnas.1001224107

Reuter, M., Mallett, A., Pearson, B. M., and van Vliet, A. H. M. (2010). Biofilm formation by *Campylobacter jejuni* is increased under aerobic conditions. *Appl. Environ. Microbiol.* 76, 2122–2128. doi: 10.1128/AEM.01878-09

Robertson, G. T., Doyle, T. B., Du, Q., Duncan, L., Mdluli, K. E., and Lynch, A. S. (2007). A novel indole compound that inhibits *Pseudomonas aeruginosa* growth by targeting MreB is a substrate for MexAB-OprM. *J. Bacteriol.* 189, 6870–6881. doi: 10.1128/JB.00805-07

Rodríguez, A. D., Lear, M. J., and La Clair, J. J. (2008). Identification of the binding of sceptrin to MreB via a bidirectional affinity protocol. *J. Am. Chem. Soc.* 130, 7256–7258. doi: 10.1021/ja7114019

Rollins, D. M., and Colwell, R. R. (1986). Viable but nonculturable stage of *Campylobacter jejuni* and its role in survival in the natural aquatic environment. *Appl. Environ. Microbiol.* 52, 531–538.

Ruby, J. D., Li, H., Kuramitsu, H., Norris, S. J., Goldstein, S. F., Buttle, K. F., et al. (1997). Relationship of *Treponema denticola* periplasmic flagella to irregular cell morphology. *J. Bacteriol.* 179, 1628–1635. doi: 10.1128/jb.179.5.1628-1635.1997

Salje, J., van den Ent, F., de Boer, P., and Löwe, J. (2011). Direct membrane-binding by bacterial actin MreB. *Mol. Cell* 43, 478–487. doi: 10.1016/j.molcel.2011.07.008

Salton, M. R. J., and Horne, R. W. (1951). Studies of the bacterial cell wall I. Electron microscopical observation on heated bacteria. *Biochim. Biophys. Acta* 7, 19–42. doi: 10.1016/0006-3002(51)90003-0

Sass, P., Josten, M., Famulla, K., Schiffer, G., Sahl, H.-G., Hamoen, L., et al. (2011). Antibiotic acyldepsipeptides activate ClpP peptidase to degrade the cell division protein FtsZ. *Proc. Natl. Acad. Sci. U.S.A.* 108, 17474–17479. doi: 10.1073/pnas.1110385108

Sauvage, E., Kerff, F., Terrak, M., Ayala, J. A., and Charlier, P. (2008). The penicillin-binding proteins: structure and role in peptidoglycan biosynthesis. *FEMS Microbiol. Rev.* 32, 234–258. doi: 10.1111/j.1574-6976.2008.00105.x

Schaffer, J. N., and Pearson, M. M. (2015). *Proteus mirabilis* and urinary tract infections. *Microbiol. Spectr.* 3:UTI-0017-2013. doi: 10.1128/microbialspec.UTI-0017-2013

Schätzle, S., Specht, M., and Waidner, B. (2015). Coiled coil rich proteins (Ccrp) influence molecular pathogenicity. *PLoS ONE* 10:e0121463. doi: 10.1371/journal.pone.0121463

Scheffers, D.-J., and Tol, M. B. (2015). LipidII: just another brick in the wall? *PLoS Pathog.* 11:e1005213. doi: 10.1371/journal.ppat.1005213

Schlieper, D., Oliva, M. A., Andreu, J. M., and Löwe, J. (2005). Structure of bacterial tubulin BtubA/B: evidence for horizontal gene transfer. *Proc. Natl. Acad. Sci. U.S.A.* 102, 9170–9175. doi: 10.1073/pnas.0502859102

Schmidt, J. M., and Stanier, R. Y. (1966). The development of cellular stalks in bacteria. *J. Cell Biol.* 28, 423–436. doi: 10.1083/jcb.28.3.423

Schroeder, G. N., and Hilbi, H. (2008). Molecular pathogenesis of Shigella spp.: controlling host cell signaling, invasion, and death by type III secretion. *Clin. Microbiol. Rev.* 21, 134–156. doi: 10.1128/CMR.00032-07

Schulz, H. N., and Jørgensen, B. B. (2001). Big bacteria. *Annu. Rev. Microbiol.* 55, 105–137. doi: 10.1146/annurev.micro.55.1.105

Schwartz, D. J., Chen, S. L., Hultgren, S. J., and Seed, P. C. (2011). Population dynamics and niche distribution of uropathogenic *Escherichia coli* during acute and chronic urinary tract infection. *Infect. Immun.* 79, 4250–4259. doi: 10.1128/IAI.05339-11

Sham, L. T., Butler, E. K., Lebar, M. D., Kahne, D., Bernhardt, T. G., and Ruiz, N. (2014). MurJ is the flippase of lipid-linked precursors for peptidoglycan biogenesis. *Science* 345, 220–222. doi: 10.1126/science.1254522

Shirota, F. N., Stevens-Johnk, J. M., DeMaster, E. G., and Nagasawa, H. T. (1997). Novel prodrugs of cyanamide that inhibit aldehyde dehydrogenase in vivo. *J. Med. Chem.* 40, 1870–1875. doi: 10.1021/jm9606296

Singh, S. K., SaiSree, L., Amrutha, R. N., and Reddy, M. (2012). Three redundant murein endopeptidases catalyse an essential cleavage step in peptidoglycan synthesis of *Escherichia coli* K12. *Mol. Microbiol.* 86, 1036–1051. doi: 10.1111/mmi.12058

Soufo, H. J. D., and Graumann, P. L. (2004). Dynamic movement of actin-like proteins within bacterial cells. *EMBO Rep.* 5, 789–794. doi: 10.1038/sj.embor.7400209

Specht, M., Schätzle, S., Graumann, P. L., and Waidner, B. (2011). *Helicobacter pylori* possesses four coiled-coil-rich proteins that form extended filamentous structures and control cell shape and motility. *J. Bacteriol.* 193, 4523–4530. doi: 10.1128/JB.00231-11

Spellberg, B., Guidos, R., Gilbert, D., Bradley, J., Boucher, H. W., Scheld, W. M., et al. (2008). The epidemic of antibiotic-resistant infections: a call to action for the medical community from the infectious diseases society of America. *Clin. Infect. Dis.* 46, 155–164. doi: 10.1086/524891

Stackhouse, R. R., Faith, N. G., Kaspar, C. W., Czuprynski, C. J., and Lee Wong, A. C. (2012). Survival and virulence of *Salmonella enterica* serovar enteritidis filaments induced by reduced water activity. *Appl. Environ. Microbiol.* 78, 2213–2220. doi: 10.1128/AEM.06774-11

Stahl, M., Frirdich, E., Vermeulen, J., Badayeva, Y., Li, X., Vallance, B. A., et al. (2016). The helical shape of *Campylobacter jejuni* promotes *in vivo* pathogenesis by aiding transit through intestinal mucus and colonization of crypts. *Infect. Immun.* 84, 3399–3407. doi: 10.1128/IAI.00751-16

Strahl, H., Bürmann, F., and Hamoen, L. W. (2014). The actin homologue MreB organizes the bacterial cell membrane. *Nat. Commun.* 5:3442. doi: 10.1038/ncomms4442

Strating, H., Vandenende, C., and Clarke, A. J. (2012). Changes in peptidoglycan structure and metabolism during differentiation of *Proteus mirabilis* into swarmer cells. *Can. J. Microbiol.* 58, 1183–1194. doi: 10.1139/w2012-102

Stratton, C. W. (2003). Dead bugs don't mutate: susceptibility issues in the emergence of bacterial resistance. *Emerg. Infect. Dis.* 9, 10–16. doi: 10.3201/eid0901.020172

Strobel, W., Möll, A., Kiekebusch, D., Klein, K. E., and Thanbichler, M. (2014). Function and localization dynamics of bifunctional penicillin-binding proteins

in *Caulobacter crescentus*. *J. Bacteriol.* 196, 1627–1639. doi: 10.1128/JB.01194-13

Sultan, S. Z., Manne, A., Stewart, P. E., Bestor, A., Rosa, P. A., Charon, N. W., et al. (2013). Motility is crucial for the infectious life cycle of *Borrelia burgdorferi*. *Infect. Immun.* 81, 2012–2021. doi: 10.1128/IAI.01228-12

Sultan, S. Z., Sekar, P., Zhao, X., Manne, A., Liu, J., Wooten, R. M., et al. (2015). Motor rotation is essential for the formation of the periplasmic flagellar ribbon, cellular morphology, and *Borrelia burgdorferi* persistence within *Ixodes scapularis* tick and murine hosts. *Infect. Immun.* 83, 1765–1777. doi: 10.1128/IAI.03097-14

Sundararajan, K., Miguel, A., Desmarais, S. M., Meier, E. L., Huang, K. C., and Goley, E. D. (2015). The bacterial tubulin FtsZ requires its intrinsically disordered linker to direct robust cell wall construction. *Nat. Commun.* 6:7281. doi: 10.1038/ncomms8281

Sutherland, A. G., Alvarez, J., Ding, W., Foreman, K. W., Kenny, C. H., Labthavikul, P., et al. (2003). Structure-based design of carboxybiphenylindole inhibitors of the ZipA-FtsZ interaction. *Org. Biomol. Chem.* 1, 4138–4140. doi: 10.1039/B312016C

Sycuro, L. K., Pincus, Z., Gutierrez, K. D., Biboy, J., Stern, C. A., Vollmer, W., et al. (2010). Peptidoglycan crosslinking relaxation promotes *Helicobacter pylori*'s helical shape and stomach colonization. *Cell* 5, 822–833. doi: 10.1016/j.cell.2010.03.046

Sycuro, L. K., Rule, C. S., Petersen, T. W., Wyckoff, T. J., Sessler, T., Nagarkar, D. B., et al. (2013). Flow cytometry-based enrichment for cell shape mutants identifies multiple genes that influence *Helicobacter pylori* morphology. *Mol. Microbiol.* 90, 869–883. doi: 10.1111/mmi.12405

Sycuro, L. K., Wyckoff, T. J., Biboy, J., Born, P., Pincus, Z., Vollmer, W., et al. (2012). Multiple peptidoglycan modification networks modulate *Helicobacter pylori*'s cell shape, motility, and colonization potential. *PLoS Pathog.* 8:e1002603. doi: 10.1371/journal.ppat.1002603

Szelestey, B. R., Heimlich, D. R., Raffel, F. K., Justice, S. S., and Mason, K. M. (2013). *Haemophilus* responses to nutritional immunity: epigenetic and morphological contribution to biofilm architecture, invasion, persistence and disease severity. *PloS Pathog.* 9:e1003709. doi: 10.1371/journal.ppat.1003709

Szwedziak, P., and Löwe, J. (2013). Do the divisome and elongasome share a common evolutionary past. *Curr. Opin. Microbiol.* 16, 745–751. doi: 10.1016/j.mib.2013.09.003

Takacs, C. N., Poggio, S., Charbon, G., Pucheault, M., Vollmer, W., and Jacobs-Wagner, C. (2010). MreB drives *de novo* rod morphogenesis in *Caulobacter crescentus* via remodeling of the cell wall. *J. Bacteriol.* 192, 1671–1684. doi: 10.1128/JB.01311-09

Tan, I. S., and Ramamurthi, K. S. (2014). Spore formation in *Bacillus subtilis*. *Environ. Microbiol. Rep.* 6, 212–225. doi: 10.1111/1758-2229.12130

Thanbichler, M., and Shapiro, L. (2006). MipZ, a spatial regulator coordinating chromosome segregation with cell division in *Caulobacter*. *Cell* 126, 147–162. doi: 10.1016/j.cell.2006.05.038

Thanner, S., Drissner, D., and Walsh, F. (2016). Antimicrobial resistance in agriculture. *mBio* 7:e02227-15. doi: 10.1128/mBio.02227-15

Tsao, D. H. H., Sutherland, A. G., Jennings, L. D., Li, Y., Rush, T. S. III, Alvarez, J. C., et al. (2006). Discovery of novel inhibitors of the ZipA/FtsZ complex by NMR fragment screening coupled with structure-based design. *Bioorg. Med. Chem.* 14, 7953–7961. doi: 10.1016/j.bmc.2006.07.050

Tsokos, C. G., and Laub, M. T. (2012). Polarity and cell fate asymmetry in *Caulobacter crescentus*. *Curr. Opin. Microbiol.* 15, 744–750. doi: 10.1016/j.mib.2012.10.011

Turner, R. D., Ratcliffe, E. C., Wheeler, R., Golestanian, R., Hobbs, J. K., and Foster, S. J. (2010). Peptidoglycan architecture can specify division planes in *S. aureus*. *Nat. Commun.* 1, 26. doi: 10.1038/ncomms1025

Typas, A., Banzhaf, M., van den Berg van Saparoea, B., Verheul, J., Biboy, J., Nichols, R. J., et al. (2010). Regulation of peptidoglycan synthesis by outer-membrane proteins. *Cell* 143, 1097–1109. doi: 10.1016/j.cell.2010.11.038

Ursell, T. S., Nguyen, J., Monds, R. D., Colavin, A., Billings, G., Ouzounov, N., et al. (2014). Rod-like bacterial shape is maintained by feedback between cell curvature and cytoskeletal localization. *Proc. Natl. Acad. Sci. U.S.A.* 111, E1025–E1034. doi: 10.1073/pnas.1317174111

van den Ent, F., Amos, L. A., and Löwe, J. (2001). Prokaryotic origin of the actin cytoskeleton. *Nature* 413, 39–44. doi: 10.1038/35092500

van den Ent, F., Izoré, T., Bharat, T. A. M., Johnson, C. M., and Löwe, J. (2014). Bacterial actin MreB forms antiparallel double filaments. *eLife* 3:e02634. doi: 10.7554/eLife.02634

van der Eerden, M. M., Vlaspolder, F., de Graaff, C. S., Groot, T., Bronsveld, W., Jansen, H. M., et al. (2005). Comparison between pathogen directed antibiotic treatment and empirical broad spectrum antibiotic treatment in patients with community acquired pneumonia: a prospective randomised study. *Thorax* 60, 672–678. doi: 10.1136/thx.2004.030411

van der Ploeg, R., Verheul, J., Vischer, N. O. E., Alexeeva, S., Hoogendoorn, E., Posma, M., et al. (2013). Colocalization and interaction between elongasome and divisome during a preparative cell division phase in *Escherichia coli*. *Mol. Microbiol.* 87, 1074–1087. doi: 10.1111/mmi.12150

van Heijenoort, J. (2011). Peptidoglycan hydrolases of *Escherichia coli*. *Microbiol. Mol. Biol. Rev.* 75, 636–663. doi: 10.1128/MMBR.00022-11

van Teeffelen, S., Wang, S., Furchtgott, L., Huang, K. C., Wingreen, N., Shaevitz, J. W., et al. (2011). The bacterial actin MreB rotates, and rotation depends on cell-wall assembly. *Proc. Natl. Acad. Sci U.S.A* 108, 15822–15827. doi: 10.1073/pnas.1108999108

van Teeseling, M. C. F., Mesman, R. J., Kuru, E., Espaillat, A., Cava, F., Brun, Y. V., et al. (2015). Anammox planctomycetes have a peptidoglycan cell wall. *Nat. Commun.* 6:6878. doi: 10.1038/ncomms7878

Varma, A., de Pedro, M. A., and Young, K. D. (2007). FtsZ directs a second mode of peptidoglycan synthesis in *Escherichia coli*. *J. Bacteriol.* 189, 5692–5704. doi: 10.1128/JB.00455-07

Varma, A., and Young, K. D. (2009). In *Escherichia coli*, MreB and FtsZ direct the synthesis of lateral cell wall via independent pathways that require PBP 2. *J. Bacteriol.* 191, 3526–3533. doi: 10.1128/JB.01812-08

Vasilyeva, L. V. (1985). *Stella*, a new genus of soil prosthecobacteria, with proposals for *Stella humosa* sp. nov. and *Stella vacuolata* sp. nov. *Int. J. Syst. Bacteriol.* 35, 518–521. doi: 10.1099/00207713-35-4-518

Vaughan, S., Wickstead, B., Gull, K., and Addinall, S. G. (2004). Molecular evolution of FtsZ protein sequences encoded within the genomes of archaea, bacteria and eukaryota. *Mol. Evol.* 58, 19–29. doi: 10.1007/s00239-003-2523-5

Veyrier, F. J., Biais, N., Morales, P., Belkacem, N., Guilhen, C., Ranjeva, S., et al. (2015). Common cell shape evolution of two nasopharyngeal pathogens. *PLoS Genet.* 11:e1005338. doi: 10.1371/journal.pgen.1005338

Vollmer, W. (2006). The prokaryotic cytoskeleton: a putative target for inhibitors ad antibiotics? *Appl. Microbiol. Biotechnol.* 73, 37–47. doi: 10.1007/s00253-006-0586-0

Vollmer, W. (2008). Structural variation in the glycan strands of bacterial peptidoglycan. *FEMS Microbiol. Rev.* 32, 287–306. doi: 10.1111/j.1574-6976.2007.00088.x

Vollmer, W., Blanot, D., and de Pedro, M. A. (2008a). Peptidoglycan structure and architecture. *FEMS Microbiol. Rev.* 32, 149–167. doi: 10.1111/j.1574-6976.2007.00094.x

Vollmer, W., Joris, B., Charlier, P., and Foster, S. (2008b). Bacterial peptidoglycan (murein) hydrolases. *FEMS Microbiol. Rev.* 32, 259–286. doi: 10.1111/j.1574-6976.2007.00099.x

Wachi, M., Doi, M., Tamaki, S., Park, W., Nakajima-Iijima, S., and Matsuhashi, M. (1987). Mutant isolation and molecular cloning of *mre* genes, which determine cell shape, sensitivity to mecillinam, and amount of penicillin-binding proteins in *Escherichia coli*. *J. Bacteriol.* 169, 4935–4940. doi: 10.1128/jb.169.11.4935-4940.1987

Wagner, J. K., Galvani, C. D., and Brun, Y. V. (2005). *Caulobacter crescentus* requires RodA and MreB for stalk synthesis and prevention of ectopic pole formation. *J. Bacteriol.* 187, 544–553. doi: 10.1128/JB.187.2.544-553.2005

Wagner, J. K., Setayeshgar, S., Sharon, L. A., Reilly, J. P., and Brun, Y. V. (2006). A nutrient uptake role for bacterial cell envelope extensions. *Proc. Natl. Acad. Sci. U.S.A.* 103, 11772–11777. doi: 10.1073/pnas.0602047103

Waidner, B., Specht, M., Dempwolff, F., Haeberer, K., Schaetzle, S., Speth, V., et al. (2009). A novel system of cytoskeletal elements in the human pathogen *Helicobacter pylori*. *PLoS. Pathog.* 5:e1000669. doi: 10.1371/journal.ppat.1000669

Walsh, C. (2003). Where will new antibiotics come from? *Nat. Rev. Microbiol.* 1, 65–70.

Wang, L., Xiao, J., Cui, S., Wang, Q., Wu, H., Liu, Q., et al. (2014). HU-induced polymorphous filamentation in fish pathogen *Edwardsiella tarda* leading to reduced invasion and virulence in zebrafish. *Vet. Microbiol.* 171, 165–174. doi: 10.1016/j.vetmic.2014.03.030

Weidel, W., Frank, H., and Martin, H. H. (1960). The rigid layer of the cell wall of *Escherichia coli* strain B. *J. Gen. Microbiol.* 22, 158–166. doi: 10.1099/00221287-22-1-158

Williams, D. J., Hall, M., Shah, S. S., Parikh, K., Tyler, A., Neuman, M. I., et al. (2013). Narrow vs broad-spectrum antimicrobial therapy for children hospitalized with pneumonia. *Pediatrics* 132, e1141-8. doi: 10.1542/peds.2013-1614

Williams, M., Hoffman, M. D., Daniel, J. J., Madren, S. M., Dhroso, A., Korkin, D., et al. (2016). Short-stalked *Prosthecomicrobium hirschii* cells have a *Caulobacter*-like cell cycle. *J. Bacteriol.* 198, 1149–1159. doi: 10.1128/JB.00896-15

Woldemeskel, S. A., and Goley, E. D. (2017). Shapeshifting to survive: shape determination and regulation in *Caulobacter crescentus*. *Trends Microbiol.* doi: 10.1016/j.tim.2017.03.006 [Epub ahead of print].

Wolgemuth, C. W., Charon, N. W., Goldstein, S. F., and Goldstein, R. E. (2006). The flagellar cytoskeleton of the spirochetes. *J. Mol. Microbiol. Biotechnol.* 11, 221–227. doi: 10.1159/000094056

Wortinger, M. A., Quardokus, E. M., and Brun, Y. V. (1998). Morphological adaptation and inhibition of cell division during stationary phase in *Caulobacter crescentus*. *Mol. Microbiol.* 29, 963–973. doi: 10.1046/j.1365-2958.1998.00959.x

Wu, Q. L., Boenigk, J., and Hahn, M. W. (2004). Successful predation of filamentous bacteria by a nanoflagellate challenges current models of flagellate bacterivory. *Appl. Environ. Microbiol.* 70, 332–339. doi: 10.1128/AEM.70.1.332-339.2004

Yang, D. C., Blair, K. M., and Salama, N. R. (2016). Staying in shape: the impact of cell shape on bacterial survival in diverse environments. *Microbiol. Mol. Biol. Rev.* 80, 187–203. doi: 10.1128/MMBR.00031-15

Yang, X., Lyu, Z., Miguel, A., McQuillen, R., Huang, K. C., and Xiao, J. (2016). GTPase activity-coupled treadmilling of the bacterial tubulin FtsZ organizes septal cell-wall synthesis. *Science* 355, 744–747. doi: 10.1126/science.aak9995

Young, K. D. (2006). The selective value of bacterial shape. *Microbiol. Mol. Biol. Rev.* 70, 660–700. doi: 10.1128/MMBR.00001-06

Young, K. T., Davis, L. M., and DiRita, V. J. (2007). *Campylobacter jejuni*: molecular biology and pathogenesis. *Nat. Rev. Microbiol.* 5, 666–679. doi: 10.1038/nrmicro1718

Zoraghi, R., and Reiner, N. E. (2013). Protein interaction networks as starting points to identify novel antimicrobial drug targets. *Curr. Opin. Microbiol.* 16, 566–572. doi: 10.1016/j.mib.2013.07.010

Conflict of Interest Statement: The authors declare that the research was conducted in the absence of any commercial or financial relationships that could be construed as a potential conflict of interest.

frontiers in Microbiology

REVIEW
published: 08 May 2018
doi: 10.3389/fmicb.2018.00822

Is Longitudinal Division in Rod-Shaped Bacteria a Matter of Swapping Axis?

*Tanneke den Blaauwen**

Bacterial Cell Biology and Physiology, Swammerdam Institute for Life Sciences, University of Amsterdam, Amsterdam, Netherlands

The morphology of bacterial species shows a wealth of variation from star-shaped to spherical and rod- to spiral-shaped, to mention a few. Their mode of growth and division is also very diverse and flexible ranging from polar growth and lateral surface increase to midcell expansion and from perpendicular to longitudinal asymmetric division. Gammaproteobacterial rod-shaped species such as *Escherchia coli* divide perpendicularly and grow in length, whereas the genetically very similar rod-shaped symbiotic *Thiosymbion* divide longitudinally, and some species even divide asynchronously while growing in width. The ovococcal *Streptococcus pneumoniae* also lengthens and divides perpendicularly, yet it is genetically very different from *E. coli*. Are these differences as dramatic as is suggested by visual inspection, or can they all be achieved by subtle variation in the regulation of the same protein complexes that synthesize the cell envelope? Most bacteria rely on the cytoskeletal polymer FtsZ to organize cell division, but only a subset of species use the actin homolog MreB for length growth, although some of them are morphologically not that different. Poles are usually negative determinant for cell division. Curved cell poles can be inert or active with respect to peptidoglycan synthesis, can localize chemotaxis and other sensing proteins or other bacterial equipment, such as pili, depending on the species. But what is actually the definition of a pole? This review discusses the possible common denominators for growth and division of distinct and similar bacterial species.

Keywords: division, FtsZ, morphology, MreB, peptidoglycan, symbionts

OPEN ACCESS

Edited by:
Ariel Amir,
Harvard University, United States

Reviewed by:
Richard A. Daniel,
Newcastle University, United Kingdom
Peter Graumann,
Philipps University of Marburg, Germany
Lars Renner,
Leibniz Institute of Polymer Research (LG), Germany

***Correspondence:**
Tanneke den Blaauwen
t.denblaauwen@uva.nl

Specialty section:
This article was submitted to Microbial Physiology and Metabolism, a section of the journal Frontiers in Microbiology

Received: *04 February 2018*
Accepted: *11 April 2018*
Published: *08 May 2018*

Citation:
den Blaauwen T (2018) Is Longitudinal Division in Rod-Shaped Bacteria a Matter of Swapping Axis? Front. Microbiol. 9:822. doi: 10.3389/fmicb.2018.00822

INTRODUCTION

Bacteria can grow with a wealth of variations (Kysela et al., 2016) of which only the morphogenesis of the sphere, the ovococ, the rod-shape, and the crescent-shaped species have been thoroughly investigated in the form of *Staphyloccocus aureus* (Monteiro et al., 2015; Wheeler et al., 2015), *Streptococcus pneumoniae* (Morlot et al., 2003; Land and Winkler, 2011; Fleurie et al., 2014; Tsui et al., 2014; Bajaj et al., 2016), *Escherichia coli* (Egan et al., 2015; Blaauwen et al., 2017), *Bacillus subtilis* (Adams and Errington, 2009), and *Caulobacter crescentus* (Yakhnina and Gitai, 2013; Collier, 2016; Woldemeskel and Goley, 2017), respectively. More recently, other rod-shaped bacteria such as *Myxococcus xanthus* that grow by elongation at lateral sides (Lotte Søgaard-Andersen personal communication) and rods that grow by extension of their

poles [*Mycobacterium tuberculosis* (Singh et al., 2013), *Corynebacterium glutamicum* (Letek et al., 2008), and *Agrobacterium tumefaciens* (Cameron et al., 2015)], from midcell (Rhizobiales; Brown et al., 2012), or as branched filaments (*Streptomyces*; Jakimowicz and van Wezel, 2012; Claessen et al., 2014), are receiving more attention (Eswara and Ramamurthi, 2017). This development is applaudable as it is discovered that our laboratory pets are not the standard for morphological organization and regulation we thought them to be.

A better understanding of the available variation in the organization of bacterial growth (see for a review Yang et al., 2016) will enable the discrimination of key factors that determine survival of bacteria. Likely, if new antibiotics are to be discovered they should preferably interfere with multiple of these key factors to postpone resistance as long as possible. In fact, that is what many of the naturally occurring antibiotics such as beta-lactams and fluoroquinolones do (Hooper, 2001; Cho et al., 2014) and why they have been very successful, until we have started to apply them in quantities that were not meant to be used. Consequently, a dramatic increase in antibiotic resistance developed to a point that some bacterial infections have become untreatable (http://www.who.int/mediacentre/news/releases/2017/bacteria-antibiotics-needed). In addition, detailed molecular knowledge of specific species could be of use for the development of new small spectrum antibiotics, to diminish destruction of the composition of the gut microbiota (Gao et al., 2017).

Even among phylogenetically related species, considerable difference in morphology can be observed despite a very high genomic similarity. For instance, the gammaproteobacteria *Escherichia coli*, *Candidatus* Thiosymbion oneisti, and *Candidatus* Thiosymbion hypermnestrae, share most of the genes known to be involved in morphogenesis, whereas their division modes are very different. The Thiosymbion live in marine sediment attached via one of their cell poles to the cuticle of their nematode host, *Laxus oneistus* and *Robbea hypermnestra*, respectively. *E. coli* is a rod-shaped bacterium that divides perpendicularly to produce two identical daughter cells, whereas the rod-shaped symbionts have approximately the same size as *E. coli* but divide longitudinally (Leisch et al., 2012, 2016; **Figure 1A**). Presumably, they have evolved to divide longitudinally to ensure the daughter cells have an anchor point on the nematode surface. These bacteria can be seen as very fat and short *E. coli* that still divide perpendicularly (**Figure 1B** model 1) or as thin and long bacteria that divide longitudinally (**Figure 1B** model 2). This review will try to discriminate between the two models.

PEPTIDOGLYCAN DETERMINES SHAPE

The peptidoglycan (PG) layer protects bacteria against osmotic and chemical stress and is an absolute requirement to maintain shape for bacteria that live in a hypo-osmotic environments such as the sea and the soil, in contrast to species such as *Chlamydia* that live in Eukaryotic cells, which cytosol is osmotically in balance with their own cytosol (Liechti et al., 2016). The PG layer consists of glycan strands of repeating *N*-acetylglucosamine and *N*-acetylmuramic acid disaccharides of which the latter are interconnected by peptide side bridges (Egan et al., 2015). The fourth and third amino acid of two stem peptides are crosslinked. Alternatively, some bacterial species such as *Mycobacteria* (Gupta et al., 2010) and *Clostridia* (Peltier et al., 2011) make predominantly crosslinks between the third amino acid on both stem peptides (**Figure 2**). The PG network is present as a single layer in Gram-negative bacteria that have an outer membrane and as multiple layers in Gram-positive bacteria that do not have an outer membrane. The well-known Penicillin Binding Proteins (PBP)s that can be inhibited by *beta*-lactams are responsible for the synthesis of peptidoglycan (Vollmer and Bertsche, 2008), together with the penicillin insensitive glycosyl transferases (GTases) RodA and possibly FtsW (Meeske et al., 2015, 2016; Cho et al., 2016). The PG disaccharide pentapeptide building units are synthesized in the cytoplasm and coupled to a lipid linker (undecaprenyl pyrophosphate) by the integral membrane protein MraY to become attached to the cytoplasmic membrane as lipid II, and subsequently flipped to the outer side of the cytoplasmic membrane to be used by the PG synthases (Egan et al., 2015). PG forms a covalently closed network, which intactness is essential for the survival of the cells. Therefore, a well-regulated balance between the insertion of new PG and the cleavage of bonds in the existing layer is needed to allow for the growth and survival of the bacteria. This balance is achieved by the formation of large protein complexes, termed elongasome and divisome for cell elongation and division, respectively (Blaauwen et al., 2008).

FtsZ

Septum synthesis and cell division is initiated by a cytoskeletal protein, the tubulin homolog FtsZ. It polymerizes in a GTP dependent fashion to form protofilaments of about 100 nm in length underneath the cytoplasmic membrane at midcell. In *E. coli*, the polymers are attached to the membrane by the bitopic membrane protein ZipA (Hale and de Boer, 1997) and the membrane associated protein FtsA (Tormo and Vicente, 1984). The FtsZ filaments are connected to each other by ZapA and possibly by other Z-ring organizing proteins such as Zap C, D, and E (Blaauwen et al., 2017). This structure has been termed the proto-ring because initially FtsZ was thought to form a continuous ring based on low resolution fluorescence microscopy. High resolution microscopy such as PALM, STET and SIM has revealed that the proto-ring is discontinuous and that FtsZ polymers likely form a loosely organized network of filaments in three dimensions (Strauss et al., 2012; Buss et al., 2013, 2015; Holden et al., 2014; Jacq et al., 2015), which are dynamically kept together by the aforementioned proteins. The FtsZ polymers were shown to grow on one end and release monomers on the opposite end of the filament, causing them to treadmill (Loose and Mitchison, 2014; Bisson-Filho et al., 2017; Yang et al., 2017). After a measurable delay (Aarsman et al., 2005; Gamba et al., 2009; Wu et al., 2018), the proto-ring recruits all proteins

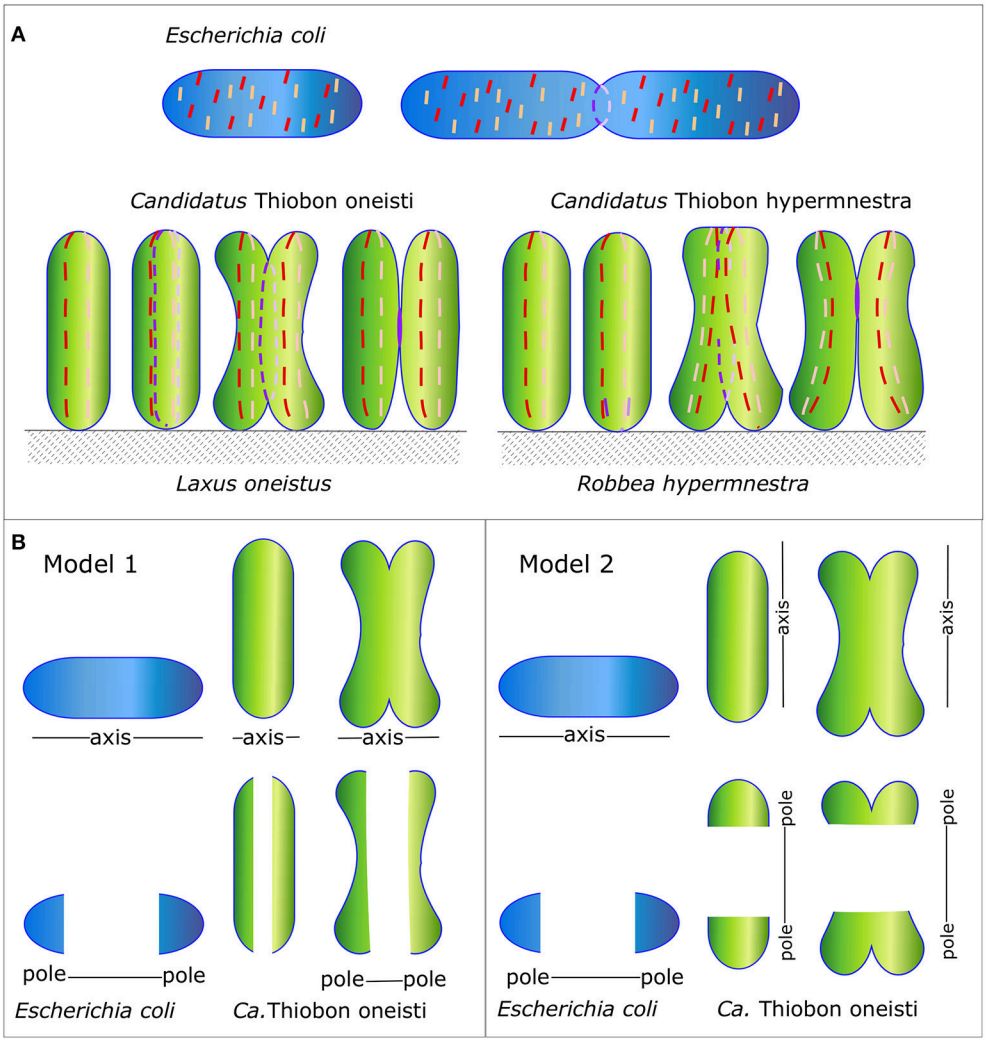

FIGURE 1 | Schematic representation of the Morphology of *E. coli* and *Ca.* T. oneisti and *Ca.* T. hypermnestrae and their MreB and FtsZ localization patterns. **(A)** Orientation of the division plane in the gammaproteobacteria *E. coli* (in blue) and *Ca.*T. oneisti and *Ca.* T. hypermnestae (in green). The very simplified localization of MreB and FtsZ are shown as a dashed red and purple line, respectively. **(B)** Two possible models. *Ca.* T. oneisti can be seen as a short very fat *E. coli* (model 1) or as a cell that has swapped its major axes in comparison to *E. coli* (model 2).

that are needed to coordinate the precisely regulated synthesis and cleavage of the septum that will become the new pole of the two daughter cells. The treadmilling of the FtsZ filaments seems to move the PG synthetic complexes in a circumferential direction guiding the synthesis of the septum. Cephalexin-mediated Inhibition of transpeptidase activity, does not inhibit this movement (Yang et al., 2017). When the class B PBP3 responsible for the crosslinking of the glycan strands during cell division is specifically inhibited by aztreonam (Kocaoglu and Carlson, 2015) the cells are not able to divide, and form filaments while the division machinery remains localized at midcell for at least two mass doublings (Pogliano et al., 1997; Blaauwen et al., 2003; Potluri et al., 2010). Possibly the division machinery does not dissociate while PBP3 is inhibited, because glycosyl transferase (GTase) activity continues in a futile cycle of synthesis and hydrolysis of the glycan strands until the lipid II precursors are depleted (Cho et al., 2014). FtsZ mutants that have a reduced GTPase activity and therefore reduced depolymerization rate, slow down the movement of the PG synthases (Yang et al., 2017), suggesting that FtsZ treadmilling directs PG synthesis.

The Gram-negative gammaproteobacteria *E. coli*, *Ca.* T. oneisti, and *Ca.* T. hypermnestrae all have closely related FtsZ proteins (**Figure 3**) with 74% identical amino acid residues (amino acid residues 1-316, excluding the C-terminal variable region). The longitudinal mode of division of the symbionts is also supported by FtsZ, which forms an interrupted ellipse instead of a ring in *Ca.*T. oneisti (Leisch et al., 2012) and starts as an arc in the basal pole of *Ca.* T. hypermnestrae (Leisch et al., 2016; **Figure 1A**). The localization patterns of the Z-ring

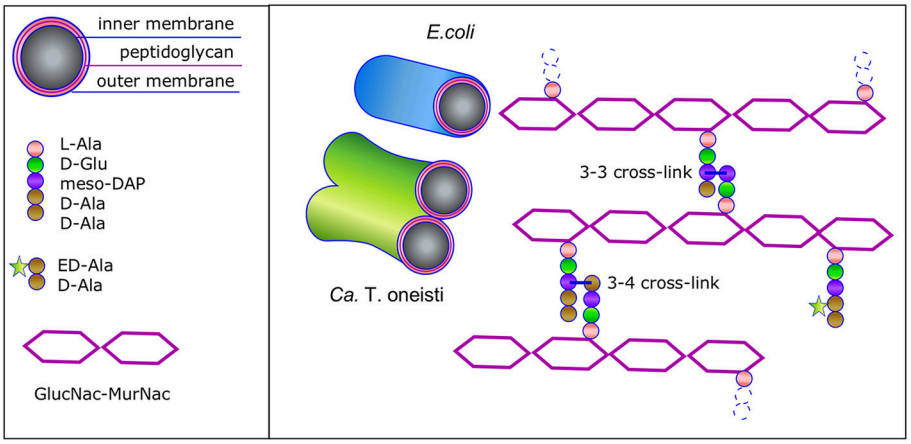

FIGURE 2 | Schematic representation of the Gram-negative envelope and its peptidoglycan structure**.** Gram-negative bacteria have a three-layered envelope. The outer and inner membrane sandwich the single peptidoglycan (PG) layer. The glycan strands are connected by stem peptides that are either 3-4 or 3-3 crosslinked. ED-Ala-D-Ala (Liechti et al., 2014) is a clickable probe that is imported in the cytosol of the Thiosymbon and incorporated in the N-acetyl muramyl(MurNac)pentapeptide. Next the precursor is coupled to the lipid tail undecaprenyl phosphate by MraY and to N-acetyl glucosamine (GlcNac) by MurG to complete the synthesis of Lipid II. The latter is then flipped across the cytoplasmic membrane and the PG precursor is incorporated in the peptidoglycan layer. Consequently, the nascent peptidoglycan synthesis can be monitored by chemical addition of a fluorophore.

in these bacteria exemplify that a closed ring structure is not a requirement for division.

MreB

In rod-shaped bacteria such as *E. coli* and *B. subtilis* two modes of PG synthesis can be discriminated. Elongation occurs by dispersed insertion of new material into the existing PG layer, and division is achieved by the synthesis of a division septum, which is later converted to yield two entirely new cell poles (De Pedro et al., 1997). The second cytoskeletal protein in most rod shaped bacterial species is MreB, an actin homolog that polymerizes as short filaments in an ATP dependent fashion, which attaches to the cytoplasmic membrane with its amphipathic helix (Salje et al., 2011). The distribution of MreB filaments over the entire length of the cell is even (Jones et al., 2001; Carballido-López and Errington, 2003). The filaments themselves are almost perpendicularly oriented to the width axis of the cell (Wang et al., 2012; Olshausen et al., 2013). It is not known what exactly determines this organization. In addition to its own interaction with the membrane, MreB is also attached by its interaction with the bitopic membrane protein RodZ (Shiomi et al., 2008), the integral protein MreD and the bitopic protein MreC that forms a similar organization as MreB in the periplasm (Leaver and Errington, 2005; van den Ent et al., 2006). The MreB filaments of about 300–500 nm move along the membrane with an average speed of half a cell circumference per min in *B. subtilis* and in *E. coli* (Domínguez-Escobar et al., 2011; Garner et al., 2011; van Teeffelen et al., 2011; Olshausen et al., 2013; Ouzounov et al., 2016). In contrast to the treadmilling of FtsZ, inhibition by mecillinam of the transpeptidase activity of the class B PBP2, responsible for the crosslinking of the glycan strands during elongation, stops this movement despite the ongoing futile cycle of GTase and turnover activity (van Teeffelen et al., 2011; Cho et al., 2016). Depletion of Lipid II or induction of the expression of a GTase defective RodA mutant also inhibits the MreB movement (Cho et al., 2016), indicating that MreB movement and PG insertion in the lateral cell wall are coupled. In contrast, depolymerization of MreB by its inhibitor A22 does only affect the number of filaments but not the speed of movement of the filaments that were still intact (van Teeffelen et al., 2011; Olshausen et al., 2013; Lee et al., 2014). The overall consensus is that MreB recruits and organizes the PG synthesis machinery needed for elongation and that insertion of new PG is responsible for the movement of MreB.

Escherchia coli, *Ca.* T. oneisti, and *Ca.* T. hypermnestrae all have closely related MreB proteins (**Figure 3**) with up to 77% identical and 88% similar residues. Surprisingly, the localization of MreB in the symbiotic bacteria is quite different from the well-known patchy distribution observed in *E. coli*, *B. subtilis* and *C. crescentus*. In non-dividing symbiont cells MreB was found in a very thin and restricted area in medially (parallel to the cell long axis) arranged patches (Pende et al., 2018). In dividing cells MreB seemed to associate initially with the Z-ellipse and both proteins co-localize. Upon invagination of the envelope, MreB and FtsZ separate in the proximal and distal poles where MreB reassumes its medial localization and FtsZ follows the constricting septum forming a ring and finally a dot in the almost separated daughter cells (Pende et al., 2018). Because of the large surface of the septum (**Figure 1**) in these longitudinally dividing bacteria, the doubling in volume assuming exponential growth comes to a large extent from the added surface area during cells division (see **Figure 4** and **Supplementary Video 1**).

A Alignment of the amino acid sequences of MreB.

```
Eco MreB M-LKKFRGMFSNDLSIDLGTANTLIYVKGQGIVLNEPSVVAIRQDRAGSPKSVAAVGHDAK 60
CTO MreB MFLRRIRGIFSNDLSIDLGTATTLIYTRGQGIVLNEPSVVAIRQGPGGS-KSVAAVGNEAK 60
CTM MreB MFLRRIRGVFSNDLSIDLGTATTLIYIRGQGIVLNEPSVVAIRQQGGGGPKSVAAVGTEAK 61
         *:*:: *: ***************** :*:***************   *: ******* :**

Eco MreB QMLGRTPGNIAAIRPMKDGVIADFFVTEKMLQHFIKQVHSNSFMRPSPRVLVCVPVGATQV 121
CTO MreB QMLGRTPQNITAIRPLKDGVIADFTVTEKMLQFFIHKVHESRIIRPSPRVLICVPCGSTQV 121
CTH MreB QMLGRTPKNIMAVRPLMDGVIADFTVTEKMLQYFIHKVHESRLIRPSPRVLICVPCGSTQV 122
         *******:**:*:***********:*******:**: **   : *******:***:*:***

Eco MreB ERRAIRESAQGAGAREVFLIEPMAAAIGAGLPVSEATGSMVVDIGGGTEVAVISLNGVVY 183
CTO MreB ERRAIKESAAGAGAREVFLIEPMAAAIGAGLPVDEARGSMVLDVGGGTSEVAITSLNGIVY 183
CTH MreB ERRAIKESAAGAGAREVFLIEPMAAAIGAGLPVEEARGSMVLDIGGGTSEVAILSLNGIVY 184
         *****:*** ********************** ** ******:********: ****:**

Eco MreB SSSVRIGGDRFDEAIINYVRRNYGSLIGEATAERIKHEIGSAYP--GDEVREIEVRGRNLAE 243
CTO MreB SNSVRIGGDRFDDAITAYVRRNYGALIGEVTAEHIKYEIGSAYP--GGEMREIEVMGRNLAE 243
CTH MreB SNSVRIGGDRFNEAIIAYVRRHGALIGEATAEYIKHKIGSAYPDSGNEVREVEFRGRYMAE 246
         * *********::**  ****  *:****:*** **  ******  * *  *:*  **  **

Eco MreB GVPRGFTLNSNEILEALQEPLTGIVSAVMVALEQCPPELASDISERGMVLTGGGALLRNLDR 305
CTO MreB GVPRSFTLNSNEILEALQEPLSGIIEAVKTALEQIPPELGADVAERGIVVTGGGALLADIDR 305
CTH MreB GVPRSFTLNSNDVLEALQEPLAGICGTVKIALEQTPPELAADVAERGIVITGGGALLAHIDR 308
         ***********::********:**   *  **** ****::*::*** *:*******  :**

Eco MreB LLMEETGIPVVVAEDPLTCVARGGGKALEMIDMH-GGDLFSE-E 347
CTO MreB LLEEETGLPVLIADDPLTCVARGGGHALETTNER-SLDLLAMTE 348
CTH MreB LLEEETGLSVVVADDPLTCVARGGGRALEMVDKPSGLDLFTVVE 352
         ** ***** *::*:*********** ***  :   : **    *
```

B alignment of the amino acid sequences of FtsZ

```
Eco FtsZ MFEPMELTN--DAVIKVIGVGGGGGNAVEHMVRERIEGVEFFAVNTDAQALRKTAVGQTIQI 60
CTO FtsZ MFELVD-TNGQDAVIKVIGVGGGGGNAVNQMVESSIEGVDFICANTDSQALKSSNVKTILQL 61
CTH FtsZ MFELMD-TNGQDAVIKVIGVGGGGGNAVNQMVDSAIEGVDFICANTDSQALKHSNAKTILQL 61
         ***  : **  *****************: **   ****:*  :*******: : :   ***

Eco FtsZ GSGITKGLGAGANPEVGRNAADEDRDALRAALEGADMVFIAAGMGGGTGTGAAPVVAEVAKD 122
CTO FtsZ GADITKGLGAGADPKVGKEAALEDKERIHDALEGADMVFITAGMGGGTGTGAAPVVAQVARE 123
CTH FtsZ GADITKGLGAGADPKVGQEAALEDRERIHDALEGADMVFITAGMGGGTGTGAAPIVAQIARE 123
         ** *********:* ** *** **:: :  ************************:**:**::

Eco FtsZ LGILTVAVVTKPFNFEGKKRMAFAEQGITELSKHVDSLITIPNDKLLKVLGRGISLLDAFGA 184
CTO FtsZ LGILTVAVVTKPFAFEGAKRMKVAVEGISELASHVDSLITIPNEKLLAVLGKEMSLLNSFKA 185
CTH FtsZ LGILTVAVVTKPFAFEGAKRMQVALEGISELANHVDSLITIPNEKLLAVLGKEMSLLNAFKA 185
         ************* *** ***  * :**:**  **********:*** ***:  ***: * *

Eco FtsZ ANDVLKGAVQGIAELITRPGLMNVDFADVRTVMSEMGYAMMGSGVASGEDRAEEAAEMAISS 246
CTO FtsZ ANDVLLNATQGIAELITRPGLINVDFADVKTVMAEMGQAMMGTGIASGEQRAREAAEAAINS 247
CTH FtsZ ANDVLLNATQGIAELITCPGLINVDFADIKTVMAEMGQAMMGTGAASGEQRARDAAEAAINS 247
         *****  * ******** *** ******:::*** ********:*:****:***:********

Eco FtsZ PLLEDIDLSGARGVLVNITAGFDLRLDEFETVGNTIRAFASDNATVVIGTSLDPDMNDELRV 308
CTO FtsZ PLLEDIDLAGAKGILVNITAGMSLSIGEFDEVGNTVRDFADDDAIVVVGTVIDPDLSEELRV 309
CTH FtsZ PLLEDIDLAGAKGILVNITAGMSLSIGEFDEVGNTVRDFADDDATVVVGTVIDSNLSEELRV 309
         ******** **:*:******** * * **: ****:* ** *:****:** :* :  *****

Eco FtsZ TVVATGIGMDKRPEIT----------LVTN----------KQVQQPVMDRYQQHGMAPLTQE 350
CTO FtsZ TVVATGLGEGRRAQLSKPAMGESPIHLVPRGGTGSVTPDYRDMERPAVYRKGYQGVAAAA-- 369
CTH FtsZ TVVATGLGKRNKAQPRL-AVGEPALHLVSNGITETATPDYRELDRPAVYRNKGHQGGTAA-- 368
         ********   :              **           :: : *:  *      :

Eco FtsZ QKPVAKVVNDNAPQTAKEPDYLDIPAFLRKQAD 383
CTO FtsZ ---VAQAHPDAVEET--DLDYLDIPAFLKHQAD 397
CTH FtsZ ----AATQAQADTAGEKNLDYLDIPAFLRQAN 398
                    *: ********** **:
```

FIGURE 3 | (Continued)

FIGURE 3 | (A,B) Alignment of *E. coli* (Eco), *Ca.* T. oneisti (CTO) and *Ca. T. hypermnestra* (CTH) MreB and FtsZ. Active site residues in MreB are highlighted in magenta (van den Ent et al., 2001). Amino acids that are in direct contact with A22 are shown in gray (Bean et al., 2009). Amino acids that confer A22 resistance are highlighted in cyan or when overlapping with ATP binding shown in magenta (Gitai et al., 2005; Dye et al., 2011; Ouzounov et al., 2016). Amino acids in MreB that increase the width of *E. coli* are highlighted in green (Shi et al., 2017). Amino acids involved in the interaction of MreB with FtsZ are highlighted in yellow. The amino acid R379 that is essential for degradation of FtsZ by ClpXP in *E. coli* (highlighted magenta) is also conserved in the symbionts. Alignment was made by Clustal Omega (Sievers et al., 2011).

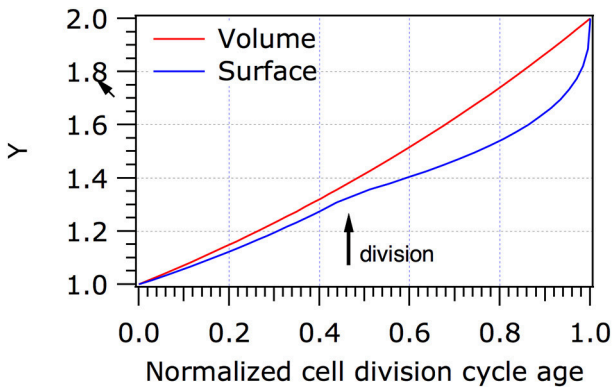

FIGURE 4 | Increase in volume and surface of *Ca.*T. oneisti. When it is assumed that *Ca.* T. onesti is growing exponentially, it increases predominantly (70%) in surface during division. The normalized cell division cycle age is plotted against the volume (red) or the surface (blue) of the cells. Y represents the volume or the surface in arbitrary units. It should be noted that we have no information on the growth mode of the symbiont because they cannot be cultivated, apart from that they clearly grow in width only. The model is purely to show the putative contribution of division to the increase in width.

THE ROLE OF MreB IN CELL DIVISION

MreB filaments also run perpendicular to the long axis of *C. crescentus* cells, like in *E. coli*. In addition, MreB accumulates at midcell in dividing cells in an FtsZ dependent fashion (Figge et al., 2004; Gitai et al., 2004). In bacterial two hybrid experiments FtsZ was found to interact with MreB (White et al., 2010). Upon depletion of MreB, cell division was impaired and diameter control at midcell seemed to be lost implying that MreB is needed for cell division in *C. crescentus*. However, MreB leaves the cell division site at about the same time as the late localizing proteins such as FtsL and FtsW arrive (Goley et al., 2011), suggesting that MreB is only needed at an early stage in which the cells are preparing for cell division. A similar temporal midcell localization of MreB was observed in *E. coli* (Vats and Rothfield, 2007; van der Ploeg et al., 2013), and a specific interaction between FtsZ and MreB was shown *in vivo* and *in vitro* (Fenton and Gerdes, 2013). It was hypothesized that midcell localization of MreB might help to position the lipid II synthesizing complex at midcell because MurG, the last protein involved in lipid II synthesis, could be immunoprecipitated together with MreB in *E. coli* (Mohammadi et al., 2007; van der Ploeg et al., 2013).

In *Caulobacter,* MurG and MreB are both dependent on the presence of a FtsZ ring for midcell localization and treatment of the cells with A22, which inhibits the polymerization of MreB does not affect the localization of MurG (Aaron et al., 2007). MurG midcell localization is not dependent on active PG synthesis in *Caulobacter* (Aaron et al., 2007). These data suggest that if MreB helps to recruit the lipid II synthesis complex to midcell its role is only temporarily.

Cells that do not possess FtsZ, such as *Chlamydia trachomatis,* require MreB to synthesize a temporal thin band of PG at the division plane (Liechti et al., 2016). The deltaproteobacterium *Bdellovibrio bacteriovorus* is a very small Gram-negative bacterial species that preys on Gram-negative species like *E. coli* (Kuru et al., 2017). It has two MreB proteins, one involved in elongation and one involved in division (Fenton et al., 2010). Interestingly, bacteria that grow by dispersed insertion of PG, do not always use MreB for this purpose. For instance, in *Rhodobacter sphaeroides* MreB localizes predominantly at a predivisional stage at the septum in elongating cells, and moves to future division sites when septation starts (Slovak et al., 2005). In the symbiont cells *Ca.* T. oneisti and *Ca.* T. hypermnestrae the MreB inhibitor A22 completely abolished the synthesis of peptidoglycan as monitored by the lack of incorporation of fluorescent PG precursors (**Figure 2**; Pende et al., 2018). In addition, the specific localization and assemblage of FtsZ is lost (Pende et al., 2018). Inhibition by A22 of MreB in *E. coli* results in spherical cells that increase in diameter (Karczmarek et al., 2007; Ouzounov et al., 2016). No change in the width of the symbiont cells was observed after prolonged incubation with A22. Since all PG synthesis stops under these conditions, also no shape changes are observed in the symbionts.

The concentration of FtsZ in non-dividing *Ca.* T. oneisti is only 10–20% of that in dividing cells (Leisch et al., 2012), which could indicate that it is specifically synthesized at the moment the cells are ready to divide. Amino acid residue R379, involved in degradation of FtsZ by the proteolytic system ClpXP in *E. coli* (Viola et al., 2017) is also conserved in the symbionts (**Figure 3**). Possibly a large part of FtsZ is degraded after the symbionts have finished division. As MreB is known to interact with FtsZ in *E. coli* and the involved amino acids in MreB as well as in FtsZ are conserved in *Ca.* T. oneisti, it is conceivable that MreB recruits FtsZ to the potential division site. Because these symbionts double in width predominantly by dividing (Pende et al., 2018), MreB might synthesize a band of preseptal PG and recruit FtsZ. Inhibition of MreB by A22 would not provide the band of preseptal peptidoglycan nor recruit FtsZ and perhaps fails to activate FtsZ synthesis. Consequently, all new peptidoglycan synthesis is completely abrogated by inhibiting MreB. The examples presented above suggest that MreB is directing specific PG synthesis at midcell in at least many Gram-negative bacterial species. The activity of MreB at midcell likely contributes to the maintenance of the correct diameter of the cells and to the precise positioning of their new division plane.

In *C.* T. oneisti FtsZ forms an ellipse that initially colocalizes with MreB. When constriction progresses, FtsZ remains concentrated at the midcell where new PG is synthesized, whereas the MreB signal splits in two, occupying the medial and future division sites of both daughter cells (Pende et al., 2018). PG synthesis during constriction requires a highly active synthesizing machinery to produce the new cell pole, which comprises 22% of the surface of new-born *E. coli* cells. In the symbionts, septal synthesis can surmount to an estimated 45–70% of the surface of the newborn cell (**Figure 4** and **Supplementary Video 1**). Consequently, regions of active PG synthesis were predominantly observed at the leading edge of the constriction where FtsZ was localized (Pende et al., 2018).

WHAT'S IN A POLE?

Conceivably, the symbiotic bacterial species have reoriented their PG synthesizing machinery such that the Z-ring is positioned parallel to the long axis of the cell, which would then correspond to the cylindrical part of an *E. coli* cell (**Figure 1B** model 2). The position where constriction is initiated would then be the equivalent of the cell poles in *E. coli*. This would require the reorientation of the major cytoskeletal elements MreB and FtsZ in the symbiont cells. An alternative interpretation could be that the symbionts are just very fat short *E. coli* cells (**Figure 1B** model 1). This would not require any reorganization of MreB and FtsZ. The medial position of MreB in the symbionts would then correspond to the cylindrical part of *E. coli*. Recently a study has been described in which MreB was randomly mutagenized and cells were selected based on their morphology by FACS (Shi et al., 2017). The mutations in MreB that resulted in very fat *E. coli* cells (almost 2 μm in width) are similar in the symbionts. For instance, the two mutations that cause the largest increase in width in *E. coli* M291V and F86S are an isoleucine (similar to valine) and a threonine (similar to serine) in *Ca.* T. oneisti as well as in *Ca.* T. hypermnestra. This illustrates that subtle changes might be sufficient to change at least one dimension of the morphology of the cells.

Since the symbionts in the latter interpretation would consist of almost only cell pole, the medial part in which MreB is localizing in a thin band would have the same orientation as the cylindrical part in *E. coli*. Since there is very little PG to be synthesized during elongation of the symbionts, MreB has obtained predominantly the function of marking the midcell position by the synthesis of a band of preseptal PG. Not excluding that it might contribute to the synthesis of the new cell poles during septation. FtsZ, is doing exactly what it is doing in *E. coli*, only it occupies a much larger circumference. By now it is clear that this is not really an issue as the Z-ring is discontinuous in all thus far investigated bacterial species (Blaauwen et al., 2017).

The cell poles in *E. coli* are thought to be inert with respect to PG synthesis (De Pedro et al., 1997) and so could be the very large putative poles of the symbionts. The observation in *E. coli* is based on the incorporation of gold labeled D-cysteine, which was diluted in density in the cylindrical wall but not in the cell poles during a chase for two mass doublings (De Pedro et al., 1997). Indicating that these D-cysteines were not accessible to PG turnover enzymes. Although many proteins involved in length growth are not present in the cell poles, many specialized sensor proteins are (for instance, the serine chemoreceptor, the

DcuS/DcuR two-component system, the chemoreceptor Tar, and the Osmosensing transporter ProP; Scheu et al., 2014; Neeli-Venkata et al., 2016; Romantsov et al., 2017; Saaki et al., 2018). Thus, although poles of *E. coli* are inert for PG recycling, they function fully in perception of their environment. *Ca.* T. oneisti and *Ca.* T. hypermnestra cannot be cultivated, which makes experiments with living cells very limited. Consequently, at this moment it is not known whether the very large putative poles of the symbionts are inert with respect to PG turnover. Even if they were, proteins required for nutrient uptake and environmental sensing could be inserted during new cell pole synthesis. In addition, it is not known whether limited reorganization of polar PG occurs in *E. coli*. For instance, for the insertion of envelope spanning proteins. The wealth of available PG hydrolases in *E. coli* (Vollmer et al., 2008) and in the symbionts, could allow the bacteria to make new pores in the PG layer by hydrolysis of the 3–4 crosslinks and insert new protein complexes or remove proteins complexes and subsequently repair the PG layer by creating 3–3 crosslinks (**Figure 2**; Hugonnet et al., 2016; Kuru et al., 2017). This provides sufficient flexibility to insert whatever is needed in the envelope of the symbionts. This leaves the very short length axis of the symbionts of which the top and bottom look like a pole as the only available place for nascent PG synthesis, which is exactly what is observed in the symbiont cells (Pende et al., 2018).

MreB is reported to avoid the poles of *E. coli* because of the presence of anionic phospholipids such as cardiolipin and phosphatidylglycerol, which are there because of the increased curvature of the poles (Renner et al., 2013; Billings et al., 2014; Ursell et al., 2014; Kawazura et al., 2017). However, in a case where MreB was forced to bind to the poles it would stimulate PG synthesis and create Y-shaped cells, which is how division starts in *Ca* T. hypermnestra (Kawazura et al., 2017). Presently it is unknown what the lipid composition is of symbiont envelopes, but marine gammaproteobacteria, especially sulfuroxidizing bacteria, can have a very different lipid composition (Sebastián et al., 2016; Favre et al., 2018). For MreB to localize in the top or bottom of the symbiont cell, where the curvature is high, possibly one of the requirements is to adapt the lipid composition. The amount of RodZ is reported to affect the sensitivity of MreB for curvature (Shi et al., 2018). The organization and amount of RodZ and MreCD (only ± 15% amino acid identity with *E. coli* versions) in the symbionts might be able to overrule the negative influence of the membrane curvature for MreB localization. For the symbionts to survive on the cuticle of the host longitudinal division was an essential adaptation. In general, evolution works best if increased fitness can be achieved by relatively small changes. MreB and FtsZ of the symbionts are very conserved and their minor changes might explain some of the changes in morphology, but likely the adaptation are to be found in the other proteins that are part of the elongasome and divisome. The alternative model (**Figure 1B** model 2) in which the symbionts have swapped their axes and the orientation of their cytoskeletal proteins would require different adaptations. For instance, what would prevent MreB to orient perpendicular to their short axis and what would restrict MreB to the medial position only? During septation, the synthetic machinery should discriminate between the top and bottom of the cells, which would have to become inactive with respect to PG synthesis and the envelope in between these parts should remain active areas of PG synthesis. Due to our present lack of knowledge on the morphogenesis of the symbionts, it is not possible to choose between the two models. However, from an evolutionary point of view, Model 1 in **Figure 1B** might be realized with the least complicated adaptations.

AUTHOR CONTRIBUTIONS

The author confirms being the sole contributor of this work and approved it for publication.

ACKNOWLEDGMENTS

I would like to thank Norbert O. E. Vischer for modeling the growth of *Ca.* T. oneisti. I would like to thank Silvia Bulgheresi and Leendert Hamoen for critically reading the manuscript. Special thanks to Silvia Bulgheresi for sharing the symbionts and their wonderful world with me.

SUPPLEMENTARY MATERIAL

The Supplementary Material for this article can be found online at: https://www.frontiersin.org/articles/10.3389/fmicb.2018.00822/full#supplementary-material

Supplementary Video 1 | Simulation of the growth and division of a *Ca.* Thiosymbion oneisti cell.

REFERENCES

Aaron, M., Charbon, G., Lam, H., Schwarz, H., Vollmer, W., and Jacobs-Wagner, C. (2007). The tubulin homologue FtsZ contributes to cell elongation by guiding cell wall precursor synthesis in *Caulobacter crescentus*. *Mol. Microbiol.* 64, 938–952. doi: 10.1111/j.1365-2958.2007.05720.x

Aarsman, M. E., Piette, A., Fraipont, C., Vinkenvleugel, T. M., Nguyen-Distèche, M., and Blaauwen, d. T. (2005). Maturation of the *Escherichia coli* divisome occurs in two steps. *Mol. Microbiol.* 55, 1631–1645. doi: 10.1111/j.1365-2958.2005.04502.x

Adams, D. W., and Errington, J. (2009). Bacterial cell division: assembly, maintenance and disassembly of the Z ring. *Nat. Rev. Microbiol.* 7, 642–653. doi: 10.1038/nrmicro2198

Bajaj, R., Bruce, K. E., Davidson, A. L., Rued, B. E., Stauffacher, C. V., and Winkler, M. E. (2016). Biochemical characterization of essential cell division proteins FtsX and FtsE that mediate peptidoglycan hydrolysis by PcsB in *Streptococcus pneumoniae*. *Microbiologyopen* 5, 738–752. doi: 10.1002/mbo3.366

Bean, G. J., Flickinger, S. T., Westler, W. M., McCully, M. E., Sept, D., Weibel, D. B., et al. (2009). A22 disrupts the bacterial actin cytoskeleton by directly binding and inducing a low-affinity state in MreB. *Biochemistry* 48, 4852–4857. doi: 10.1021/bi900014d

Billings, G., Ouzounov, N., Ursell, T., Desmarais, S. M., Shaevitz, J., Gitai, Z., et al. (2014). *De novo* morphogenesis in L-forms via geometric control of cell growth. *Mol. Microbiol.* 93, 883–896. doi: 10.1111/mmi.12703

Bisson-Filho, A. W., Hsu, Y. P., Squyres, G. R., Kuru, E., Wu, F., Jukes, C., et al. (2017). Treadmilling by FtsZ filaments drives peptidoglycan synthesis and bacterial cell division. *Science* 355, 739–743. doi: 10.1126/science.aak9973

Brown, P. J. B., De Pedro, M. A., Kysela, D. T., Van der Henst, C., Kim, J., De Bolle, X., et al. (2012). Polar growth in the Alphaproteobacterial order *Rhizobiales*. *Proc. Natl. Acad. Sci. U.S.A.* 109, 1697–1701. doi: 10.1073/pnas.1114476109

Buss, J., Coltharp, C., Huang, T., Pohlmeyer, C., Wang, S. C., Hatem, C., et al. (2013). *In vivo* organization of the FtsZ-ring by ZapA and ZapB revealed by quantitative super-resolution microscopy. *Mol. Microbiol.* 89, 1099–1120. doi: 10.1111/mmi.12331

Buss, J., Coltharp, C., Shtengel, G., Yang, X., Hess, H., and Xiao, J. (2015). A multi-layered protein network stabilizes the *Escherichia coli* FtsZ-ring and modulates constriction dynamics. *PLoS Genet.* 11:e1005128. doi: 10.1371/journal.pgen.1005128

Cameron, T. A., Zupan, J. R., and Zambryski, P. C. (2015). The essential features and modes of bacterial polar growth. *Trends Microbiol.* 23, 347–353. doi: 10.1016/j.tim.2015.01.003

Carballido-López, R., and Errington, J. (2003). The bacterial cytoskeleton: *in vivo* dynamics of the actin-like protein Mbl of *Bacillus subtilis*. *Dev. Cell* 4, 19–28. doi: 10.1016/S1534-5807(02)00403-3

Cho, H., Uehara, T., and Bernhardt, T. G. (2014). Beta-lactam antibiotics induce a lethal malfunctioning of the bacterial cell wall synthesis machinery. *Cell* 159, 1300–1311. doi: 10.1016/j.cell.2014.11.017

Cho, H., Wivagg, C. N., Kapoor, M., Barry, Z., Rohs, P. D. A., Suh, H., et al. (2016). Bacterial cell wall biogenesis is mediated by SEDS and PBP polymerase families functioning semi-autonomously. *Nat. Microbiol.* 1:16172. doi: 10.1038/nmicrobiol.2016.172

Claessen, D., Rozen, D. E., Kuipers, O. P., Søgaard-Andersen, L., and van Wezel, G. P. (2014). Bacterial solutions to multicellularity: a tale of biofilms, filaments and fruiting bodies. *Nat. Rev. Microbiol.* 12, 115–124. doi: 10.1038/nrmicro3178

Collier, J. (2016). Cell cycle control in Alphaproteobacteria. *Curr. Opin. Microbiol.* 30, 107–113. doi: 10.1016/j.mib.2016.01.010

de Pedro, M. A., Quintela, J. C., Höltje, J. V., and Schwarz, H. (1997). Murein segregation in *Escherichia coli*. *J. Bacteriol.* 179, 2823–2834. doi: 10.1128/jb.179.9.2823-2834.1997

Domínguez-Escobar, J., Chastanet, A., Crevenna, A. H., Fromion, V., Wedlich-Söldner, R., and Carballido-López, R. (2011). Processive movement of MreB-associated cell wall biosynthetic complexes in bacteria. *Science* 333, 225–228. doi: 10.1126/science.1203466

Dye, N. A., Pincus, Z., Fisher, I. C., Shapiro, L., and Theriot, J. A. (2011). Mutations in the nucleotide binding pocket of MreB can alter cell curvature and polar morphology in *Caulobacter*. *Mol. Microbiol.* 81, 368–394. doi: 10.1111/j.1365-2958.2011.07698.x

Egan, A. J., Biboy, J., van't Veer, I., Breukink, E., and Vollmer, W. (2015). Activities and regulation of peptidoglycan synthases. *Philos. Trans. R. Soc. Lond. B. Biol. Sci.* 370:20150031. doi: 10.1098/rstb.2015.0031

Eswara, P. J., and Ramamurthi, K. S. (2017). Bacterial cell division: nonmodels poised to take the spotlight. *Annu. Rev. Microbiol.* 71, 393–411. doi: 10.1146/annurev-micro-102215-095657

Favre, L., Ortalo-Magné, A., Pichereaux, C., Gargaros, A., Burlet-Schiltz, O., Cotelle, V., et al. (2018). Metabolome and proteome changes between biofilm and planktonic phenotypes of the marine bacterium *Pseudoalteromonas lipolytica* TC8. *Biofouling* 50, 1–17. doi: 10.1080/08927014.2017.1413551

Fenton, A. K., and Gerdes, K. (2013). Direct interaction of FtsZ and MreB is required for septum synthesis and cell division in *Escherichia coli*. *EMBO J.* 32, 1953–1965. doi: 10.1038/emboj.2013.129

Fenton, A. K., Lambert, C., Wagstaff, P. C., and Sockett, R. E. (2010). Manipulating Each MreB of Bdellovibrio bacteriovorus gives diverse morphological and predatory phenotypes. *J. Bacteriol.* 192, 1299–1311. doi: 10.1128/JB.01157-09

Figge, R. M., Divakaruni, A. V., and Gober, J. W. (2004). MreB, the cell shape-determining bacterial actin homologue, co-ordinates cell wall morphogenesis in *Caulobacter crescentus*. *Mol. Microbiol.* 51, 1321–1332. doi: 10.1111/j.1365-2958.2003.03936.x

Fleurie, A., Lesterlin, C., Manuse, S., Zhao, C., Cluzel, C., Lavergne, J. P., et al. (2014). MapZ marks the division sites and positions FtsZ rings in *Streptococcus pneumoniae*. *Nature* 516, 259–262. doi: 10.1038/nature13966

Gamba, P., Veening, J.-W., Saunders, N. J., Hamoen, L. W., and Daniel, R. A. (2009). Two-step assembly dynamics of the *Bacillus subtilis* divisome. *J. Bacteriol.* 191, 4186–4194. doi: 10.1128/JB.01758-08

Gao, P., Ma, C., Sun, Z., Wang, L., Huang, S., Su, X., et al. (2017). Feed-additive probiotics accelerate yet antibiotics delay intestinal microbiota maturation in broiler chicken. *Microbiome* 5:91. doi: 10.1186/s40168-017-0315-1

Garner, E. C., Bernard, R., Wang, W., Zhuang, X., Rudner, D. Z., and Mitchison, T. (2011). Coupled, circumferential motions of the cell wall synthesis machinery and MreB filaments in *B. subtilis*. *Science* 333, 222–225. doi: 10.1126/science.1203285

Gitai, Z., Dye, N. A., Reisenauer, A., Wachi, M., and Shapiro, L. (2005). MreB actin-mediated segregation of a specific region of a bacterial chromosome. *Cell* 120, 329–341. doi: 10.1016/j.cell.2005.01.007

Gitai, Z., Dye, N., and Shapiro, L. (2004). An actin-like gene can determine cell polarity in bacteria. *Proc. Natl. Acad. Sci. U.S.A.* 101, 8643–8648. doi: 10.1073/pnas.0402638101

Goley, E. D., Yeh, Y. C., Hong, S. H., Fero, M. J., Abeliuk, E., McAdams, H. H., et al. (2011). Assembly of the *Caulobacter* cell division machine. *Mol. Microbiol.* 80, 1680–1698. doi: 10.1111/j.1365-2958.2011.07677.x

Gupta, R., Lavollay, M., Mainardi, J.-L., Arthur, M., Bishai, W. R., and Lamichhane, G. (2010). The *Mycobacterium tuberculosis* protein Ldt Mt2 is a nonclassical transpeptidase required for virulence and resistance to amoxicillin. *Nat. Med.* 16, 466–469. doi: 10.1038/nm.2120

Hale, C. A., and de Boer, P. A. (1997). Direct binding of FtsZ to ZipA, an essential component of the septal ring structure that mediates cell division in *E. coli*. *Cell* 88, 175–185. doi: 10.1016/S0092-8674(00)81838-3

Holden, S. J., Pengo, T., Meibom, K. L., Fernandez Fernandez, C., Collier, J., and Manley, S. (2014). High throughput 3D super-resolution microscopy reveals *Caulobacter crescentus in vivo* Z-ring organization. *Proc. Natl. Acad. Sci. U.S.A.* 111, 4566–4571. doi: 10.1073/pnas.1313368111

Hooper, D. C. (2001). Mechanisms of action of antimicrobials: focus on fluoroquinolones. *Clin. Infect. Dis.* 32, S9–S15. doi: 10.1086/319370

Hugonnet, J. E., Mengin-Lecreulx, D., Monton, A., Blaauwen, d. T., Carbonnelle, E., Veckerlé, C., et al. (2016). Factors essential for L,D-transpeptidase-mediated peptidoglycan cross-linking and β-lactam resistance in *Escherichia coli*. *Elife* 5:e19469. doi: 10.7554/eLife.19469

Jacq, M., Adam, V., Bourgeois, D., Moriscot, C., Di Guilmi, A. M., Vernet, T., et al. (2015). Remodeling of the Z-Ring Nanostructure during the *Streptococcus pneumoniae* cell cycle revealed by photoactivated localization microscopy. *MBio* 6:e01108-15. doi: 10.1128/mBio.01108-15

Jakimowicz, D., and van Wezel, G. P. (2012). Cell division and DNA segregation in Streptomyces: how to build a septum in the middle of nowhere? *Mol. Microbiol.* 85, 393–404. doi: 10.1111/j.1365-2958.2012.08107.x

Jones, L. J., Carballido-López, R., and Errington, J. (2001). Control of cell shape in bacteria: helical, actin-like filaments in *Bacillus subtilis*. *Cell* 104, 913–922. doi: 10.1016/S0092-8674(01)00287-2

Karczmarek, A., Martínez-Arteaga, R., Baselga, R. M.-A., Alexeeva, S., Hansen, F. G., Vicente, M., et al. (2007). DNA and origin region segregation are not affected by the transition from rod to sphere after inhibition of *Escherichia coli* MreB by A22. *Mol. Microbiol.* 65, 51–63. doi: 10.1111/j.1365-2958.2007.05777.x

Kawazura, T., Matsumoto, K., Kojima, K., Kato, F., Kanai, T., Niki, H., et al. (2017). Exclusion of assembled MreB by anionic phospholipids at cell poles confers cell polarity for bidirectional growth. *Mol. Microbiol.* 104, 472–486. doi: 10.1111/mmi.13639

Kocaoglu, O., and Carlson, E. E. (2015). Profiling of β-lactam selectivity for penicillin-binding proteins in *Escherichia coli* strain DC2. *Antimicrob. Agents Chemother.* 59, 2785–2790. doi: 10.1128/AAC.04552-14

Kuru, E., Lambert, C., Rittichier, J., Till, R., Ducret, A., Derouaux, A., et al. (2017). Fluorescent D -amino-acids reveal bi-cellular cell wall modifications important for *Bdellovibrio bacteriovorus* predation. *Nat. Microbiol.* 2, 1648–1657. doi: 10.1038/s41564-017-0029-y

Kysela, D. T., Randich, A. M., Caccamo, P. D., and Brun, Y. V. (2016). Diversity takes shape: understanding the mechanistic and adaptive basis of bacterial morphology. *PLoS Biol.* 14:e1002565. doi: 10.1371/journal.pbio.1002565

Land, A. D., and Winkler, M. E. (2011). The requirement for pneumococcal MreC and MreD is relieved by inactivation of the gene encoding PBP1a. *J. Bacteriol.* 193, 4166–4179. doi: 10.1128/JB.05245-11

Leaver, M., and Errington, J. (2005). Roles for MreC and MreD proteins in helical growth of the cylindrical cell wall in *Bacillus subtilis*. *Mol. Microbiol.* 57, 1196–1209. doi: 10.1111/j.1365-2958.2005.04736.x

Lee, T. K., Tropini, C., Hsin, J., Desmarais, S. M., Ursell, T. S., Gong, E., et al. (2014). A dynamically assembled cell wall synthesis machinery buffers cell growth. *Proc. Natl. Acad. Sci. U.S.A.* 111, 4554–4559. doi: 10.1073/pnas.1313826111

Leisch, N., Pende, N., Weber, P. M., Gruber-Vodicka, H. R., Verheul, J., Vischer, N. O., et al. (2016). Asynchronous division by non-ring FtsZ in the gammaproteobacterial symbiont of *Robbea hypermnestra*. *Nat. Microbiol.* 2:16182. doi: 10.1038/nmicrobiol.2016.182

Leisch, N., Verheul, J., Heindl, N. R., Gruber-Vodicka, H. R., Pende, N., den Blaauwen, T., et al. (2012). Growth in width and FtsZ ring longitudinal positioning in a gammaproteobacterial symbiont. *Curr. Biol.* 22, R831–R832. doi: 10.1016/j.cub.2012.08.033

Letek, M., Fiuza, M., Ordóñez, E., Villadangos, A. F., Ramos, A., Mateos, L. M., et al. (2008). Cell growth and cell division in the rod-shaped actinomycete *Corynebacterium glutamicum*. *Antonie Van Leeuwenhoek* 94, 99–109. doi: 10.1007/s10482-008-9224-4

Liechti, G., Kuru, E., Packiam, M., Hsu, Y. P., Tekkam, S., Hall, E., et al. (2016). Pathogenic *Chlamydia* lack a classical sacculus but synthesize a narrow, mid-cell peptidoglycan ring, regulated by MreB, for cell division. *PLoS Pathog.* 12:e1005590. doi: 10.1371/journal.ppat.1005590

Liechti, G. W., Kuru, E., Hall, E., Kalinda, A., Brun, Y. V., VanNieuwenhze, M., et al. (2014). A new metabolic cell-wall labelling method reveals peptidoglycan in *Chlamydia trachomatis*. *Nature* 506, 507–510. doi: 10.1038/nature12892

Loose, M., and Mitchison, T. J. (2014). The bacterial cell division proteins FtsA and FtsZ self-organize into dynamic cytoskeletal patterns. *Nat. Cell Biol.* 16, 38–46. doi: 10.1038/ncb2885

Meeske, A. J., Riley, E. P., Robins, W. P., Uehara, T., Mekalanos, J. J., Kahne, D., et al. (2016). SEDS proteins are a widespread family of bacterial cell wall polymerases. *Nature* 537, 634–638. doi: 10.1038/nature19331

Meeske, A. J., Sham, L. T., Kimsey, H., Koo, B.-M., Gross, C. A., Bernhardt, T. G., et al. (2015). MurJ and a novel lipid II flippase are required for cell wall biogenesis in *Bacillus subtilis*. *Proc. Natl. Acad. Sci. U.S.A.* 112, 6437–6442. doi: 10.1073/pnas.1504967112

Mohammadi, T., Karczmarek, A., Crouvoisier, M., Bouhss, A., Mengin-Lecreulx, D., den Blaauwen, T. (2007). The essential peptidoglycan glycosyltransferase MurG forms a complex with proteins involved in lateral envelope growth as well as with proteins involved in cell division in *Escherichia coli*. *Mol. Microbiol.* 65, 1106–1121. doi: 10.1111/j.1365-2958.2007.05851.x

Monteiro, J. M., Fernandes, P. B., Vaz, F., Pereira, A. R., Tavares, A. C., Ferreira, M. T., et al. (2015). Cell shape dynamics during the staphylococcal cell cycle. *Nat. Commun.* 6:8055. doi: 10.1038/ncomms9055

Morlot, C., Zapun, A., Dideberg, O., and Vernet, T. (2003). Growth and division of *Streptococcus pneumoniae*: localization of the high molecular weight penicillin-binding proteins during the cell cycle. *Mol. Microbiol.* 50, 845–855. doi: 10.1046/j.1365-2958.2003.03767.x

Neeli-Venkata, R., Startceva, S., Annila, T., and Ribeiro, A. S. (2016). Polar localization of the serine chemoreceptor of *Escherichia coli* is nucleoid exclusion-dependent. *Biophys. J.* 111, 2512–2522. doi: 10.1016/j.bpj.2016.10.024

Olshausen, P. V., Defeu Soufo, H. J., Wicker, K., Heintzmann, R., Graumann, P. L., and Rohrbach, A. (2013). Superresolution imaging of dynamic MreB filaments in *B. subtilis*-a multiple-motor-driven transport? *Biophys. J.* 105, 1171–1181. doi: 10.1016/j.bpj.2013.07.038

Ouzounov, N., Nguyen, J. P., Bratton, B. P., Jacobowitz, D., Gitai, Z., and Shaevitz, J. W. (2016). MreB orientation correlates with cell diameter in *Escherichia coli*. *Biophys. J.* 111, 1035–1043. doi: 10.1016/j.bpj.2016.07.017

Peltier, J., Courtin, P., Meouche El, I., Lemée, L., Chapot-Chartier, M. P., and Pons, J. L. (2011). Clostridium difficile has an original peptidoglycan structure with a high level of N-acetylglucosamine deacetylation and mainly 3-3 cross-links. *J. Biol. Chem.* 286, 29053–29062. doi: 10.1074/jbc.M111.259150

Pende, N., Wang, J., Weber, P. M., Verheul, J., Kuru, E., Rittmann, S. K. M. R., et al. (2018). Host-Polarized cell growth in animal symbionts. *Curr. Biol.* 28, 1039.e5–1051.e5. doi: 10.1016/j.cub.2018.02.028

Pogliano, J., Pogliano, K., Weiss, D. S., Losick, R., and Beckwith, J. (1997). Inactivation of FtsI inhibits constriction of the FtsZ cytokinetic ring and delays the assembly of FtsZ rings at potential division sites. *Proc. Natl. Acad. Sci. U.S.A.* 94, 559–564. doi: 10.1073/pnas.94.2.559

Potluri, L., Karczmarek, A., Verheul, J., Piette, A., Wilkin, J. M., Werth, N., et al. (2010). Septal and lateral wall localization of PBP5, the major D,D-carboxypeptidase of *Escherichia coli*, requires substrate recognition and membrane attachment. *Mol. Microbiol.* 77, 300–323. doi: 10.1111/j.1365-2958.2010.07205.x

Renner, L. D., Eswaramoorthy, P., Ramamurthi, K. S., and Weibel, D. B. (2013). Studying biomolecule localization by engineering bacterial cell wall curvature. *PLoS ONE* 8:e84143. doi: 10.1371/journal.pone.0084143

Romantsov, T., Culham, D. E., Caplan, T., Garner, J., Hodges, R. S., and Wood, J. M. (2017). ProP-ProP and ProP-phospholipid interactions determine the subcellular distribution of osmosensing transporter ProP in *Escherichia coli*. *Mol. Microbiol.* 103, 469–482. doi: 10.1111/mmi.13569

Saaki, T. N. V., Strahl, H., and Hamoen, L. W. (2018). Membrane curvature and the Tol-Pal complex determine polar localization of the chemoreceptor Tar in *E. coli*. *J. Bacteriol.* doi: 10.1128/JB.00658-17. [Epub ahead of print].

Salje, J., van den Ent, F., De Boer, P., and Löwe, J. (2011). Direct membrane binding by bacterial actin MreB. *Mol. Cell* 43, 478–487. doi: 10.1016/j.molcel.2011.07.008

Scheu, P. D., Steinmetz, P. A., Dempwolff, F., Graumann, P. L., and Unden, G. (2014). Polar localization of a tripartite complex of the two-component system DcuS/DcuR and the transporter DctA in *Escherichia coli* depends on the sensor kinase DcuS. *PLoS ONE* 9:e115534. doi: 10.1371/journal.pone.0115534

Sebastián, M., Smith, A. F., González, J. M., Fredricks, H. F., Van Mooy, B., Koblížek, M., et al. (2016). Lipid remodelling is a widespread strategy in marine heterotrophic bacteria upon phosphorus deficiency. *ISME J.* 10, 968–978. doi: 10.1038/ismej.2015.172

Shi, H., Bratton, B. P., Gitai, Z., and Huang, K. C. (2018). How to Build a Bacterial Cell: MreB as the Foreman of *E. coli* Construction. *Cell* 172, 1294–1305. doi: 10.1016/j.cell.2018.02.050

Shi, H., Colavin, A., Bigos, M., Tropini, C., Monds, R. D., and Huang, K. C. (2017). Deep phenotypic mapping of bacterial cytoskeletal mutants reveals physiological robustness to cell size. *Curr. Biol.* 27, 3419.e4–3429.e4. doi: 10.1016/j.cub.2017.09.065

Shiomi, D., Sakai, M., and Niki, H. (2008). Determination of bacterial rod shape by a novel cytoskeletal membrane protein. *EMBO J.* 27, 3081–3091. doi: 10.1038/emboj.2008.234

Sievers, F., Wilm, A., Dineen, D., Gibson, T. J., Karplus, K., Li, W., et al. (2011). Fast, scalable generation of high-quality protein multiple sequence alignments using Clustal Omega. *Mol. Syst. Biol.* 7, 539–539. doi: 10.1038/msb.2011.75

Singh, B., Nitharwal, R. G., Ramesh, M., Pettersson, B. M., Kirsebom, L. A., and Dasgupta, S. (2013). Asymmetric growth and division in *Mycobacterium spp.*: compensatory mechanisms for non-medial septa. *Mol. Microbiol.* 88, 64–76. doi: 10.1111/mmi.12169

Slovak, P. M., Wadhams, G. H., and Armitage, J. P. (2005). Localization of MreB in *Rhodobacter sphaeroides* under conditions causing changes in cell shape and membrane structure. *J. Bacteriol.* 187, 54–64. doi: 10.1128/JB.187.1.54-64.2005

Strauss, M. P., Liew, A. T., Turnbull, L., Whitchurch, C. B., Monahan, L. G., and Harry, E. J. (2012). 3D-SIM super resolution microscopy reveals a bead-like arrangement for FtsZ and the division machinery: implications for triggering cytokinesis. *PLoS Biol.* 10:e1001389. doi: 10.1371/journal.pbio.1001389

Blaauwen, d. T., Aarsman, M. E. G., Vischer, N. O. E., and Nanninga, N. (2003). Penicillin-binding protein PBP2 of *Escherichia coli* localizes preferentially in the lateral wall and at mid-cell in comparison with the old cell pole. *Mol. Microbiol.* 47, 539–547. doi: 10.1046/j.1365-2958.2003.03316.x

den Blaauwen, T., de Pedro, M. A., Nguyen-Distèche, M., and Ayala, J. A. (2008). Morphogenesis of rod-shaped sacculi. *FEMS Microbiol. Rev.* 32, 321–344. doi: 10.1111/j.1574-6976.2007.00090.x

den Blaauwen, T., Hamoen, L. W., and Levin, P. A. (2017). The divisome at 25: the road ahead. *Curr. Opin. Microbiol.* 36, 85–94. doi: 10.1016/j.mib.2017.01.007

Tormo, A., and Vicente, M. (1984). The ftsA gene product participates in formation of the *Escherichia coli* septum structure. *J. Bacteriol.* 157, 779–784.

Tsui, H. C. T., Boersma, M. J., Vella, S. A., Kocaoglu, O., Kuru, E., Peceny, J. K., et al. (2014). Pbp2x localizes separately from Pbp2b and other peptidoglycan synthesis proteins during later stages of cell division of *Streptococcus pneumoniae* D39. *Mol. Microbiol.* 94, 21–40. doi: 10.1111/mmi.12745

Ursell, T. S., Nguyen, J., Monds, R. D., Colavin, A., Billings, G., Ouzounov, N., et al. (2014). Rod-like bacterial shape is maintained by feedback between cell curvature and cytoskeletal localization. *Proc. Natl. Acad. Sci. U.S.A.* 111, E1025–E1034. doi: 10.1073/pnas.1317174111

van den Ent, F., Amos, L. A., and Löwe, J. (2001). Prokaryotic origin of the actin cytoskeleton. *Nature* 413, 39–44. doi: 10.1038/35092500

van den Ent, F., Leaver, M., Bendezu, F., Errington, J., de Boer, P., and Löwe, J. (2006). Dimeric structure of the cell shape protein MreC and its functional implications. *Mol. Microbiol.* 62, 1631–1642. doi: 10.1111/j.1365-2958.2006.05485.x

van der Ploeg, R., Verheul, J., Vischer, N. O. E., Alexeeva, S., Hoogendoorn, E., Postma, M., et al. (2013). Colocalization and interaction between elongasome and divisome during a preparative cell division phase in *Escherichia coli*. *Mol. Microbiol.* 87, 1074–1087. doi: 10.1111/mmi.12150

van Teeffelen, S., Wang, S., Furchtgott, L., Huang, K. C., Wingreen, N. S., Shaevitz, J. W., et al. (2011). The bacterial actin MreB rotates, and rotation depends on cell-wall assembly. *Proc. Natl. Acad. Sci. U.S.A.* 108, 15822–15827. doi: 10.1073/pnas.1108999108

Vats, P., and Rothfield, L. (2007). Duplication and segregation of the actin (MreB) cytoskeleton during the prokaryotic cell cycle. *Proc. Natl. Acad. Sci. U.S.A.* 104, 17795–17800. doi: 10.1073/pnas.0708739104

Viola, M. G., LaBreck, C. J., Conti, J., and Camberg, J. L. (2017). Proteolysis-dependent remodeling of the tubulin homolog FtsZ at the division septum in *Escherichia coli*. *PLoS ONE* 12:e0170505. doi: 10.1371/journal.pone.0170505

Vollmer, W., and Bertsche, U. (2008). Murein (peptidoglycan) structure, architecture and biosynthesis in *Escherichia coli*. *Biochim. Biophys. Acta* 1778, 1714–1734. doi: 10.1016/j.bbamem.2007.06.007

Vollmer, W., Joris, B., Charlier, P., and Foster, S. (2008). Bacterial peptidoglycan (murein) hydrolases. *FEMS Microbiol. Rev.* 32, 259–286. doi: 10.1111/j.1574-6976.2007.00099.x

Wang, S., Furchtgott, L., Huang, K. C., and Shaevitz, J. W. (2012). Helical insertion of peptidoglycan produces chiral ordering of the bacterial cell wall. *Proc. Natl. Acad. Sci. U.S.A.* 109, E595–E604. doi: 10.1073/pnas.1117132109

Wheeler, R., Turner, R. D., Bailey, R. G., Salamaga, B., Mesnage, S., Mohamad, S. A., et al. (2015). Bacterial cell enlargement requires control of cell wall stiffness mediated by peptidoglycan hydrolases. *MBio* 6:e00660. doi: 10.1128/mBio.00660-15

White, C. L., Kitich, A., and Gober, J. W. (2010). Positioning cell wall synthetic complexes by the bacterial morphogenetic proteins MreB and MreD. *Mol. Microbiol.* 76, 616–633. doi: 10.1111/j.1365-2958.2010.07s108.x

Woldemeskel, S. A., and Goley, E. D. (2017). Shapeshifting to survive: shape determination and regulation in *Caulobacter crescentus*. *Trends Microbiol.* 25, 673–687. doi: 10.1016/j.tim.2017.03.006

Wu, K. J., Zhang, J., Baranowski, C., Leung, V., Rego, E. H., Morita, Y. S., et al. (2018). Characterization of conserved and novel septal factors in *Mycobacterium smegmatis*. *J. Bacteriol.* 200:e00649-17. doi: 10.1128/JB.00649-17

Yakhnina, A. A., and Gitai, Z. (2013). Diverse functions for six glycosyltransferases in *Caulobacter crescentus* cell wall assembly. *J. Bacteriol.* 195, 4527–4535. doi: 10.1128/JB.00600-13

Yang, D. C., Blair, K. M., and Salama, N. R. (2016). Staying in shape: the impact of cell shape on bacterial survival in diverse environments. *Microbiol. Mol. Biol. Rev.* 80, 187–203. doi: 10.1128/MMBR.00031-15

Yang, X., Lyu, Z., Miguel, A., McQuillen, R., Huang, K. C., and Xiao, J. (2017). GTPase activity-coupled treadmilling of the bacterial tubulin FtsZ organizes septal cell wall synthesis. *Science* 355, 744–747. doi: 10.1126/science.aak9995

Conflict of Interest Statement: The author declares that the research was conducted in the absence of any commercial or financial relationships that could be construed as a potential conflict of interest.

frontiers in Microbiology

REVIEW
published: 02 March 2018
doi: 10.3389/fmicb.2018.00174

Dividing the Archaeal Way: The Ancient Cdv Cell-Division Machinery

Yaron Caspi†* and *Cees Dekker**

Department of Bionanoscience, Kavli Institute of Nanoscience, Delft University of Technology, Delft, Netherlands

Cell division in most prokaryotes is mediated by the well-studied fts genes, with FtsZ as the principal player. In many archaeal species, however, division is orchestrated differently. The Crenarchaeota phylum of archaea features the action of the three proteins, CdvABC. This Cdv system is a unique and less-well-studied division mechanism that merits closer inspection. *In vivo*, the three Cdv proteins form a composite band that contracts concomitantly with the septum formation. Of the three Cdv proteins, CdvA is the first to be recruited to the division site, while CdvB and CdvC are thought to participate in the active part of the Cdv division machinery. Interestingly, CdvB shares homology with a family of proteins from the eukaryotic ESCRT-III complex, and CdvC is a homolog of the eukaryotic Vps4 complex. These two eukaryotic complexes are key factors in the endosomal sorting complex required for transport (ESCRT) pathway, which is responsible for various budding processes in eukaryotic cells and which participates in the final stages of division in Metazoa. There, ESCRT-III forms a contractile machinery that actively cuts the membrane, whereas Vps4, which is an ATPase, is necessary for the turnover of the ESCRT membrane-abscission polymers. In contrast to CdvB and CdvC, CdvA is unique to the archaeal Crenarchaeota and Thaumarchaeota phyla. The Crenarchaeota division mechanism has often been suggested to represent a simplified version of the ESCRT division machinery thus providing a model system to study the evolution and mechanism of cell division in higher organisms. However, there are still many open questions regarding this parallelism and the division mechanism of Crenarchaeota. Here, we review the existing data on the role of the Cdv proteins in the division process of Crenarchaeota as well as concisely review the ESCRT system in eukaryotes. We survey the similarities and differences between the division and abscission mechanisms in the two cases. We suggest that the Cdv system functions differently in archaea than ESCRT does in eukaryotes, and that, unlike the eukaryotic case, the Cdv system's main function may be related to surplus membrane invagination and cell-wall synthesis.

Keywords: the Cdv system, Crenarchaeota, archaeal division, the ESCRT system, membrane remodeling

OPEN ACCESS

Edited by:
Arieh Zaritsky,
Ben-Gurion University of the Negev, Israel

Reviewed by:
William Margolin,
University of Texas Health Science Center at Houston, United States
Joe Lutkenhaus,
University of Kansas Medical Center Research Institute, United States

***Correspondence:**
Yaron Caspi
y.caspi@umcutrecht.nl
Cees Dekker
C.Dekker@tudelft.nl

†Present Address:
Yaron Caspi,
Brain Center Rudolf Magnus, University Medical Center Utrecht, Utrecht, Netherlands

Specialty section:
This article was submitted to Microbial Physiology and Metabolism, a section of the journal Frontiers in Microbiology

Received: *20 November 2017*
Accepted: *25 January 2018*
Published: *02 March 2018*

Citation:
Caspi Y and Dekker C (2018) Dividing the Archaeal Way: The Ancient Cdv Cell-Division Machinery. Front. Microbiol. 9:174. doi: 10.3389/fmicb.2018.00174

INTRODUCTION

Cell division (cytokinesis) is an essential process that, in most biological model systems, is mediated by a proteinaceous cytosolic machinery that binds the plasma membrane. Cytokinesis can be separated into four distinct conceptual stages: (i) localization of the early division components to the division site; (ii) recruitment of later components by the early ones; (iii) application of an ingression force on the membrane, leading to constriction; and (iv) final membrane abscission

leading to the daughter cells separation. For example, in a large span of bacterial species, selection of the division site is regulated by the Min protein system and the nucleoid occlusion mechanism that together localize the eukaryote tubulin homolog FtsZ to the cell center (Rowlett and Margolin, 2015). Subsequently, FtsZ recruits late division proteins. The source of ingression force has so far remained unclear but likely includes active cell wall synthesis (while it may also be aided by direct force application by FtsZ itself) (Haeusser and Margolin, 2016; Du and Lutkenhaus, 2017). As of today, it has also remained unclear what drives the final abscission stage (Söderström et al., 2014). Another example of this four steps gradation is found in Metazoa. Here, localization of the division apparatus is mediated by signals that are emitted from the spindle asters and central zone (Barr and Gruneberg, 2007). Subsequently, RhoA is localized to the division site and activates the actomyosin network by indirectly regulating the myosin-II ATPase activity, while the furrow-ingression force is provided by myosin and active actin polymerization (Cheffings et al., 2016). Interestingly, in most animal cells, the end-result of this process is the formation of a thin intracellular bridge between daughter cells (Nähse et al., 2017). At that point, a "NoCut" checkpoint prevents cytokinesis completion until all chromosomal bridges are cleared (Mierzwa and Gerlich, 2014). Subsequently, the Endosomal Sorting Complex Required for Transport (ESCRT) proteins are recruited to the intracellular bridge and mediate abscission, thus completing the cell separation (see **Figure 1A**).

From a topological point of view, cytokinesis is equivalent to various other membrane remodeling processes such as exovesicle secretion. In all of these cases, a proteinaceous machinery acts from the inner side of the membrane to induce its abscission (accordingly, these processes are called reverse-topology remodeling). In the last few years it became clear that in eukaryotes, the ESCRT system functions as a generalized machinery that cuts the membrane from within and mediates abscission in reverse topology processes. In that sense, ESCRT applies the opposite abscission strategy compared to protein machineries that remodel the membrane from the outer surface (Faini et al., 2013; Daumke et al., 2014). Thus, HIV-1 virus release and the formation of Endosomal Multivesicular Bodies (MVB) became model pathways to study the ESCRT machinery (see **Figure 1B**).

Relative to the well-studied bacteria and eukaryotes, the process of cell division in archaea is poorly understood. Yet, it follows the same four conceptual division stages, as archaeal cells face the same topological challenges during cell division. In particular, in some archaeal orders that belong to the TACK (Thaumarchaeota, Aigarchaeota, Crenarchaeota, and Korarchaeota) super-phylum, a group of Cdv (Cell division) proteins participates in cell division and equivalent topology membrane-remodeling processes (see **Figure 1C**). Importantly, some Cdv proteins are homologous to ESCRT proteins (Obita et al., 2007; Hobel et al., 2008). Unlike in Metazoa, however, the Cdv proteins act from early to late stages of the division process. As of today, the exact way in which the Cdv system achieves its function is not yet deciphered.

Often it is suggested that the Cdv system is an evolutionary precursor of ESCRT. Current views regarding the Cdv system largely rely on our understanding of the homologous ESCRT mechanism in eukaryotes. To test this hypothesis, we set out to both extensively review the Cdv function and to critically assess similarities and differences between the ESCRT and the Cdv systems. We will start with a concise review of the division mechanisms of archaea. Next, we review, side-by-side, the repertoire of ESCRT and Cdv proteins and their mutual interactions. We continue by reviewing the *in vitro* reconstitution of ESCRT and Cdv proteins. Following that, we emphasize the role of ESCRT proteins in eukaryotic cytokinesis and the role of the Cdv proteins in the archaeal one. Subsequently, we discuss the different models that were proposed for the ESCRT functioning and critically compare the match between these models and the current knowledge regarding the Cdv system. Finally, we discuss important open questions, and we point out future directions for the Cdv field. From this discussion, we suggest that the Cdv system functions differently in archaea than the ESCRT one functions in eukaryotes. That is, we hypothesize that the archaeal Cdv system is mainly coupled to cell-wall synthesis, like the FtsZ-based bacterial divisome, and/or is responsible for vesicle trafficking into or away from the division site.

Please note that, due to the homology of Cdv and ESCRT proteins, the first group has sometimes been referred to by the corresponding name of the second (which can be quite confusing). To maintain a clear distinction between the two cases, and to stress relevant differences, we will maintain the unique archaeal Cdv terminology. For convenience of the reader, we provide a glossary of Cdv proteins and their relation to the eukaryotic ESCRT proteins in **Table 1**.

DIVISION MECHANISMS OF ARCHAEA

For many years, the mainstream thinking regarding archaea put them in proximity to the bacterial domain. Hence, attempts have been made to identify and characterize homologs of the pivotal bacterial division protein FtsZ in archaeal organisms. In the early days, two main archaeal kingdoms, namely the Euryarchaeota and the Crenarchaeota were identified (Woese et al., 1990). Indeed, an archaeal homolog of FtsZ, which in some cases also localized to the division site was identified in several Euryarchaeota species (Baumann and Jackson, 1996; Margolin et al., 1996; Wang and Lutkenhaus, 1996; Nogales et al., 1998; Nagahisa et al., 2000; Poplawski et al., 2000). Subsequent studies showed that FtsZ homologs are found across all classes of the Euryarchaeota kingdom (Makarova et al., 2010). Thus, it was suggested that Euryarchaeota divide via an FtsZ-based mechanism that is similar to the bacterial one.

The current view, however, places the eukaryotes branching point inside the archaea domain so that the TACK super-phylum shares the same phylogenetic ancestor with eukaryotes (Williams et al., 2013). In fact, recently, a deep-sequencing metagenomic

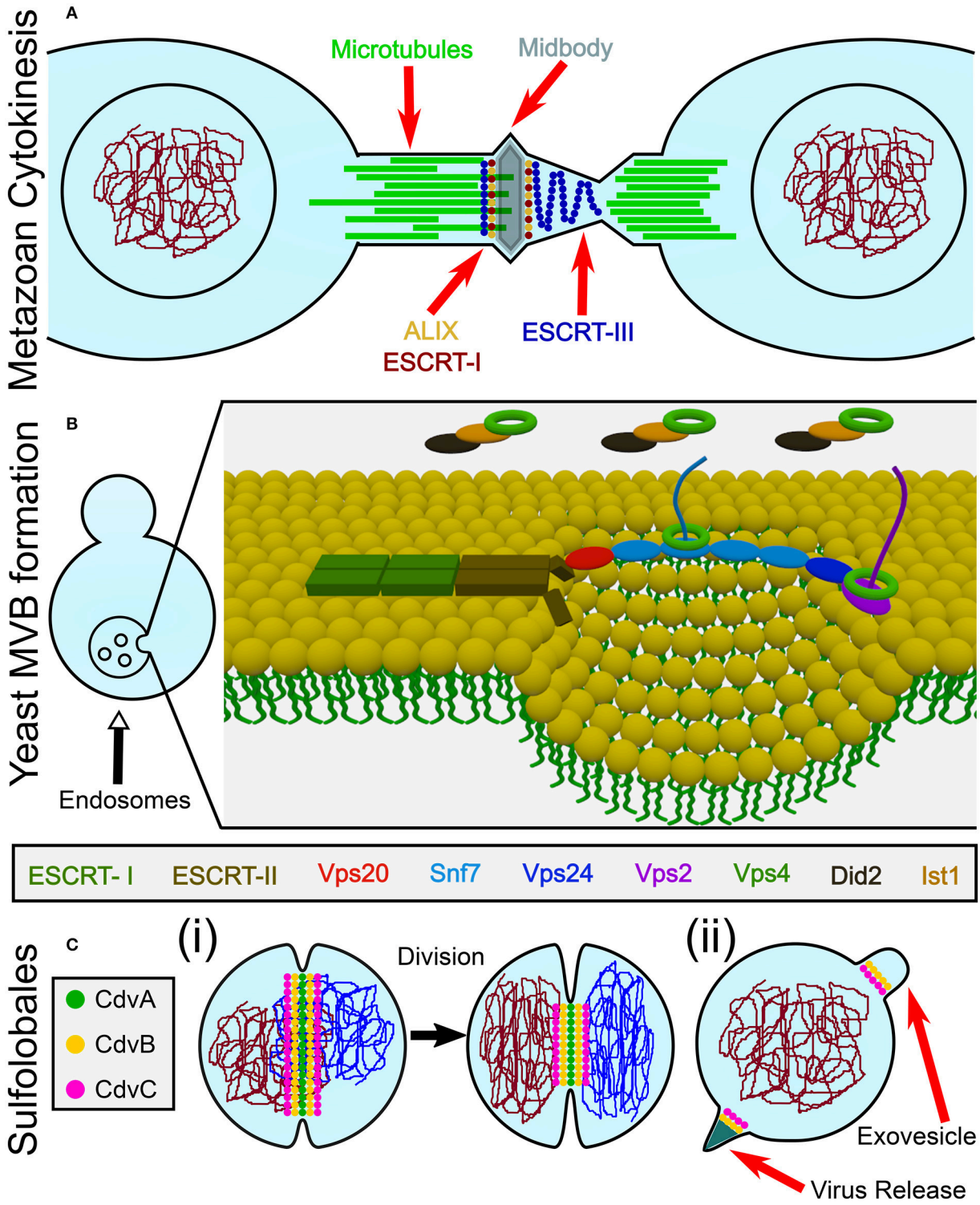

FIGURE 1 | Overview of the biological functions of ESCRT and CdvB proteins. **(A)** In animal cells, ESCRT proteins participate in the last stage of cytokinesis (abscission). **(B)** In Fungi and Animalia, ESCRT proteins are responsible for cargo sorting into the endosomes and for the biogenesis of multivesicular bodies (MVB). For participation of ESCRT proteins in other biological pathways, see the main text. **(C)** In Crenarchaeota, the Cdv system participates in (i) cell division, as well as in (ii) viral release and exovesicle secretion.

TABLE 1 | Glossary of ESCRT and Cdv proteins.

Complex	Yeast name	Human name	Crenarchaea homolog	Asgard homolog	
CdvA	–	–	CdvA	–	Membrane recruitment
Alix	Bro1	ALIX	–	–	
ESCRT-I	Vps23	TSG101	–	Lokiarch_16740	Adapter and recruitment
	Vps28	VPS28	–	Lokiarch_10170	
	Vps37	VPS37A,B,C,D	–	–	
	Mvb12	MVB12A,B UBAP1	–	–	
ESCRT-II	Vps22	EAP30	–	Lokiarch_37450	
	Vps25	EAP20	–	Lokiarch_37460	
	Vps36	EAP45	–	–	
ESCRT-III	Did2 (Vps46)	CHMP1A,B	CdvB	Lokiarch_37480	Membrane remodeling
	Vps2 (Did4)	CHMP2A,B	CdvB1, CdvB2		
	Vps24	CHMP3	CdvB3		
	Ist1	IST1	–	–	
	snf7 (Vps32)	CHMP4A,B,C	–	Lokiarch_16760	
	Vps60	CHMP5			
	Vps20	CHMP6			
	Chm7	CHMP7			
Vps4	Vps4	VPS4A,B	CdvC	Lokiarch_37470	Dynamical behavior
	Vta1	LIP5	–	–	

Synonyms of the ESCRT system proteins names in Yeast, Human, and Archaea are outlined. The two classes of ESCRT-III proteins are denoted in yellow and brown, and the Vps2/24 class related Ist1 protein is denoted in dark yellow.

analysis inferred the existence of a new archaeal super-phylum that is related to the TACK super-phylum and was named Asgard. It was suggested that Asgard are the archaeal organisms that are closest to eukaryotes (Zaremba-Niedzwiedzka et al., 2017). Interestingly, Asgard cells possess protein signatures that once were thought to be unique to eukaryotes. In particular, they have orthologs for (de)ubiquitination proteins as well as orthologs for proteins that belong to the ESCRT pathway (see **Figure 2A** and Tables S1, S2 of the Supporting Information; Spang et al., 2015). Since the ESCRT proteins participate in eukaryotes cell division, it can be assumed that their homologs in the Asgard super-phylum are also responsible for cell division. Note, however, that, as of today, none of the Asgard organisms has been cultivated or even isolated, and knowledge regarding their cell biology has been limited to sequencing studies. Thus, no direct evidence connects Asgard ESCRT homologs to cell division.

In contrast, Crenarchaeota organisms, from the TACK super-phylum, especially those from the Sulfolobales order, have become the leading archaeal model organisms. They can be cultivated, and their cell biology is starting to be deciphered (Leigh et al., 2011). While they do not possess homologs of the ftsZ gene, Crenarchaeota organisms do possess homologs to ESCRT proteins—the Cdv proteins. Since ample evidence connects the Cdv proteins to all classical ESCRT pathways, including cytokinesis, the rest of this review will concentrate on Crenarchaeota organisms (and Thaumarchaeota organisms that also possess Cdv paralogs). In particular, references to Cdv proteins will, unless stated otherwise, be to *Sulfolobus acidocaldarius*. For completeness, we mention that homologs of CdvB and CdvC are also found in the Euryarchaeota kingdom (Makarova et al., 2010). However, nothing is known about their cellular function, or whether they participate in cell division. For examples of homology between the *S. acidocaldarius* CdvB and CdvC proteins and their Euryarchaeota counterparts, see Table S3 of the Supporting Information. The fact that CdvB/C appear only sparsely in this kingdom, on top of the fact that Euryarchaea possess functional ftsZ genes, suggests that Euryarchaea Cdv proteins do not play a dominant role in Euryarchaeota cytokinesis.

Interestingly, the Crenarchaeota are further classified into three orders: Thermoproteales, Desulfurococcales, and Sulfolobales. While genes encoding Cdv homologous were identified in the latter two orders, no such genes were identified in the Thermoproteales (Makarova et al., 2010). Instead, it was suggested that Thermoproteales make use of a division system that is based on crenactin, a close homolog of the eukaryotic F-actin (Izorè et al., 2016). However, an identification of the division mechanism of Thermoproteales is still missing, and some experimental evidence suggests that the actin-based division picture is too simplified. For example, in the Thermoproteale *Pyrobaculum calidifontis*, the crenactin is distributed in an extended helical structure that does not localize to the division site (Ettema et al., 2011). By contrast, arcadin 2, which depolymerizes crenactin polymers (Izorè et al., 2016), is

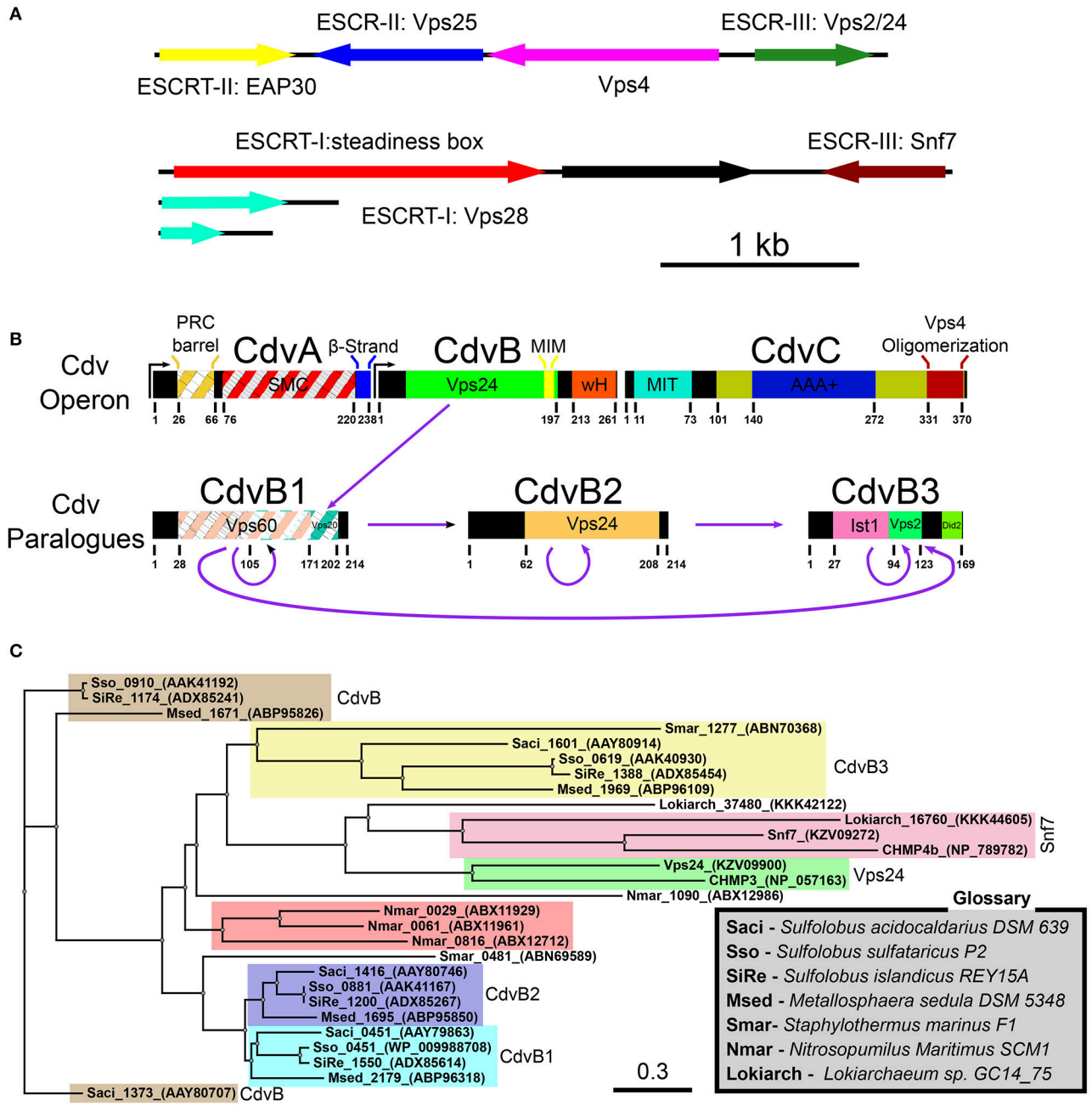

FIGURE 2 | Cdv proteins of archaea. **(A)** Chromosomal distribution of Lokiarchaeota sp. GC14_75 genes that share common features with the ESCRT pathway. ESCRT homologoues (including ESCRT-I and ESCRT-II) are in color. Black, genes that are unrelated to the ESCRT pathway. Based on Spang et al. (2015); Zaremba-Niedzwiedzka et al. (2017). **(B)** Genome organization, domain analysis and interaction network of *S. acidocaldarius* Cdv proteins. The highest homologies of each Cdv protein to the *S. cerevisiae* ESCRT-III proteins are also indicated. Striped boxes indicate homology below statistical significance. Purple arrows, interaction network of *S. acidocaldarius* CdvB proteins. **(C)** Phylogenetic tree of Cdv proteins. Groups of CdvB paralogs are emphasized in colors. Representative members of the two *S. cerevisiae* ESCRT-III protein families as well as the Lokiarchea Cdv proteins are also included. Scale bar, nucleotide substitutions per site.

localized between segregated chromosomes. This may suggest that, in Thermoproteales, division occurs by destabilization of the cell cortex at the division site while maintaining its rigidity at the poles. In this scenario, the concurrent increase of the rigidity of the cell cortex far away from the division site due to crenactin polymerization, together with destabilization of the crenactin network at the division site, results in a global deformation of cell shape due to energy minimization. In fact, such a mechanism was demonstrated theoretically for lipid-vesicle deformation (Božič et al., 2014) and was suggested as an auxiliary

mechanism supporting division in eukaryotes (Wang, 2005). Interestingly, in the Thermoproteale *Pyrobaculum aerophilum* no constriction of the plasma membrane was observed during division (Lundgren et al., 2008), and in *Thermoproteus tenax* a constriction-independent "snapping" mechanism was suggested (Horn et al., 1999). These data suggest that in Thermoproteales division may occur independently of septa formation.

OVERVIEW OF THE ESCRT AND Cdv PROTEINS

To facilitate the discussion about the Cdv system, we will next review the repertoire of Cdv proteins in relation to their ESCRT counterparts. We particularly emphasize here their shared and different structural biology properties.

The ESCRT Pathway

The eukaryotic ESCRT system is composed of five complexes ESCRT-0, -I, -II, -III and VPS4, as well as several associated proteins (see **Table 1**). It is highly conserved in opisthokont cells (animals and fungi; Field and Dacks, 2009). However, in many non-Metazoa eukaryotes, ESCRT-0 is absent, and while not all components of ESCRT-I were identified, upstream ESCRT elements widely exist (Leung et al., 2008). The abundant existence of upstream ESCRT components in the entire eukaryotic kingdom suggests that the last common universal eukaryotic ancestor already possessed a developed ESCRT machinery. For a recent extensive review about the ESCRT system (see Schöneberg et al., 2017).

Initially identified in the context of MVB formation (Coonrod and Stevens, 2010), the number of biological functions that are assigned to the ESCRT system has increased considerably over the years (see Hurley, 2015; Campsteijn et al., 2016 and references therein). As of today, it includes MVB formation, exovesicles secretion, retrovirus release, cytokinesis, neuronal pruning, plasma membrane healing, nuclear envelope sealing and removal of malfunctioning nuclear pore complexes. In the classical MVB pathway, ESCRT-0 first binds ubiquitinated endosomal membrane proteins that are designated for transport to the lysozyme. Next, ESCRT-0 recruits the ESCRT-I complex, which then recruits the ESCRT-II complex, a complex whose structure best fits a membrane with one concave and one convex curvatures (such as the one that is formed in bud necks; Im et al., 2009; Boura et al., 2012). It was suggested that the ESCRT-II shape is particularly important for the stabilization of narrow membrane necks. Subsequently, ESCRT-II recruits the ESRTC-III complex, which is believed to be the main player in membrane deformation and induces membrane fission through the formation of higher-order polymeric structures. Finally, ESCRT-III recruits the de-ubiquitinated proteins AMSH and Doa4 as well as the Vps4 complex. Vps4, an ATPase and the sole energy-coupled enzyme in the ESCRT pathway, finally disassembles the ESCRT-III proteins from the complex, thus ensuring its turnover. In some cases, ESCRT-III is directly recruited to the membrane by another adapter protein, ALIX.

In yeast, the main component of the ESCRT pathway, the ESCRT-III complex, is composed of 8 protein [6 Vacuolar protein sorting (Vps) proteins, Chm7, and Ist1]. In humans, there are corresponding 12 proteins [11 Charged MVB Proteins (CHMP) and IST1]. Although there are 12 CHMP proteins in humans, several are paralogs (e.g., CHMP4A/B/C), and hence, the human ESCRT-III proteins can also be grouped into eight protein families, parallel to those in yeast. The eight protein families can be further classified into two main classes that share very low sequence homology, Vps2/Vps24/Did2/Ist1 (CHMP2/CHMP3/CHMP1 and IST1), and Snf7/Vps20/Vps60/Chm7 (CHMP4/CHMP6/CHMP5/CHMP7).

The Cdv System

In Sulfolobales, the Cdv proteins are composed of two groups. The first group includes the cdvA, cdvB, and cdvC genes that are organized in one chromosomal locus. The second group contains three cdvB paralogs, namely, cdvB1, cdvB2, and cdvB3, that are spread at different locations along the chromosome (see **Figure 2B**). These four cdvB genes are homologs of the eukaryotic Vps2/24/Did2 ESCRT-III class. In addition, the cdvC gene is a homolog of vps4. However, no homologs of the Snf7/Vps20/60 class were identified in Sulfolobales. In addition, cdvA is unique to Sulfolobales, and is not found elsewhere except in Thaumarchaeota and Desulfurococcales. It was suggested that the main function of CdvA is to recruit CdvB to the membrane (Samson et al., 2011). In particular, while the presence of CdvC and CdvB homologs is the definite signature for the existence of a Cdv-like system, CdvA is not generally found in Asgard phylum. Assuming that the main function of CdvA is to recruit CdvB to the membrane, this is understandable, since Asgard organisms possess ESCRT-I/II homologs that can substitute for CdvA. Experimental evidence connects the Cdv proteins to three cellular functions: Exovesicle secretion, viral release, and cell division. In this review, we will mainly concentrate on cell division. For a discussion of the putative role of the Cdv system in exovesicle and viruses release (similar to the ESCRT system), we refer the reader to the Supporting Information. For a detailed recap of the experimental evidence that connects the Cdv system to its different functions in several Crenarchaeota and Asgard organisms, we refer to Tables S1, S2 of the Supporting Information.

Note that the quartet organization of CdvB paralogs in Sulfolobales with four distinct families (CdvB, CdvB1, CdvB2, and CdvB3) is not a universal feature in the TACK superphylum or even in Crenarchaeota. For example, most of the Desulfurococcales organisms possess only three CdvB paralogs and some organisms possess only two CdvB paralogs (one at the main Cdv locus and the second one at a different location on the chromosome; Makarova et al., 2010). In addition, none of the Desulfurococcales cdvB paralogs belong to the same family as the Sulfolobales cdvB gene. Similarly, the Thermoproteale *Nitrosopumilus Maritimus* possesses four CdvB paralogs, but three out of them form a unique separate family that is not directly related to either the CdvB1/2 or the CdvB3 families. Moreover, the main locus cdvB gene is short (like the Sulfolobales

CdvB3), but is not closely related to any Sulfolobales cdvB gene (see Table S2 of the Supporting Information, **Figure 2C** and Makarova et al., 2010). Thus, a wide variety of CdvB paralogs organization exist in the TACK super-phylum, and it is of interest to study how these different organizations relate to the biological functions of the Cdv system.

Importantly, in contrast to Crenarchaeota and Thaumarchaeota, Asgard organisms such as Lokiarchaeota possess two ESCRT-III-like genes. One belongs to the Vps2/24/Did2 class and is a homolog of CdvB, and one is related to the other ESCRT-III class, that of Snf7/Vps20/60. The existence of proteins from the two ESCRT-III classes in Asgard organisms suggests that the core ESCRT machinery evolved before eukaryogenesis, and that it was followed by ESCRT-III gene duplication for specialization and division of labor. It will be of interest to study how do the different organizations of Cdv proteins contribute to the biological functions of the system.

The ESCRT-III Complex

Although the two classes of ESCRT-III proteins (Vps2/Vps24/Did2/Ist1 and Snf7/Vps20/Vps60/Chm7) share very low sequence homology, they do share the same secondary structure that is the definite signature of an ESCRT-III protein (see **Figure 3A**). At the N-terminus of all ESCRT-III proteins, four α-helices are located. Together these four helices form the ESCRT-III core domain (Tang et al., 2015). Two additional, regulatory, α-helices (α5 and α6) are located at the C-terminus. ESCRT-III proteins also share the same overall tertiary structure. In solution, ESCRT-III subunits are found in a "closed" conformation where α5 and α6 fold over the ESCRT-III core domain and inhibit polymerization (Shim et al., 2007; Bajorek et al., 2009b; Tang et al., 2015). Once the auto-inhibition is released (e.g., after binding the membrane), a conformational change transfers the proteins into their "open" form, which enables them to establish higher-order structures (see **Figures 3B–E** for examples of ESCRT-III proteins in their open and closed conformations). Interestingly, in all ESCRT-III proteins (except Ist1), α1–α3 are highly basic (e.g., pI = 10.71 for Snf7 residues 1-118), while α4–α5 are highly acidic (pI = 3.52 for Snf7 residues 119-240; Babst et al., 2002; Shim et al., 2007). This separation of charge is responsible for the ability of ESCRT-III proteins to bind acidic lipids by creating a highly basic surface. For example, for CHMP3 a basic patch which is conserved from yeast to human was implicated in the membrane binding (Muzioł et al., 2006).

In vivo, only 4 proteins are essential for ESCRT-III function (Vps20/Snf7/Vps24/Vps2). The rest of the ESCRT-III proteins act as helper proteins (Ist1, Vps60, and Did2) or are needed for special functions (e.g., Cmp7, in the clearance of nuclear pores). Vps20/CHMP6 is the initiator of ESCRT-III polymerization and recruits Snf7/CHMP4. Snf7/CHMP4 is the major structural protein in the ESCRT-III complex and occupies at least 50% of the complex content (Teis et al., 2008). Vps2/CHMP2 and Vps24/CHMP3, which are recruited to the ESCRT-III complex by Snf7/CHMP4, cap the polymers and recruit the downstream Vps4 complex (Saksena et al., 2009).

The recruitment of CHMP6 (Vps20) to the membrane is achieved through its interaction with the winged helix (wH) motif of the ESCRT-II protein EAP20 (Vps25) (see **Figure 4A**; Im et al., 2009). wH motifs are a subgroup of the helix-turn-helix motifs that are composed of 3 α-helices and 3 β-strands and that, many times, act as transcription factors (Gajiwala and Burley, 2000). For the ESCRT machinery, the interaction between CHMP6 and EAP20 has a K_d of 7 μM. Since ESCRT-II binds the membrane with a nM affinity, this constitutes an efficient pathway to initiate ESCRT-III polymerization.

The CdvB Paralogs

As mentioned above, CdvB and its paralogs belong to the Vps2/24/Did2 protein class (see **Figure 2B**, and also Figure S1 of the Supporting Information for a full homology repository between the *S. acidocaldarius* CdvB paralogs and *S. cerevisiae* ESCRT-III proteins). Like all other ESCRT-III proteins, they are predicted to share the same overall ESCRT-III secondary structure organization, however, with some differences (**Figure 3A**). In CdvB, the four ESCRT-III core α-helices are present, as well as the auto-inhibitory helix α5, but CdvB lacks the last terminal helix α6. A tertiary structure prediction program that is based on sequence homology and alignment (Phyre, see Kelley and Sternberg, 2009) predicted a CdvB 3D structure that is highly similar to that of Ist1 in the "closed" state (see **Figure 3G**). However, the N-terminus of CdvB is less basic than that of ESCRT-III proteins, and the C-terminus is only mildly acidic (residues 1–116 pI 10.23; residues 117–212 pI 5.17). This lower ionic charge of the CdvB N-terminal end is probably responsible for CdvB inability to bind the membrane directly. In particular, the basic patch in CHMP3 that was implicated in the membrane binding has, in fact, an acidic pI in CdvB, rendering it unfitted for membrane interaction (Samson et al., 2011). At the far end of CdvB C-terminal end, a wH domain is located, which was implicated in its interaction with CdvA as is discussed below. This wH domain is slightly more acidic than the rest of the C-terminus part (residues 213–261, pI 4.12).

CdvB1 and CdvB2 form two closely related protein subfamilies. They are shorter than CdvB and lack the wH domain. While the N-terminal half of CdvB1 and CdvB2 has a pI similar to CdvB, the C-terminus part of CdvB1 and CdvB2 is somewhat more acidic (CdvB1 residues 117–214 pI 4.06, CdvB2 residues 117–219 pI 4.3). Interestingly, unlike for CdvB, the peptide of CdvB1 and CdvB2 that is a homolog to the membrane binding patch on CHMP3, is somewhat basic (pI 9.8 compare to pI 11.7 in CHMP3). This might suggest that CdvB1 and CdvB2 can bind membrane directly, though less efficient than CHMP3. However, currently, there is no experimental evidence for such an interaction.

In contrast to Sulfolobales CdvB, the Asgard ESCRT-III homologs proteins do share the fundamental ESCRT-III property of a highly basic N-terminus moiety and a highly acidic C-terminus moiety (Lokiarch_37480: residues 1–120 pI 11.12, residues 121–209 pI 3.23; Lokiarch_16760 residues 1–122 pI 11.06, residues 123–218 pI 3.34). In particular, the Lokiarch_37480 peptide that is homolog to the CHMP3 membrane binding patch is even more basic in Lokiarch_37480 than in CHNP3 (pI 12.2). Hence, it will be interesting to study

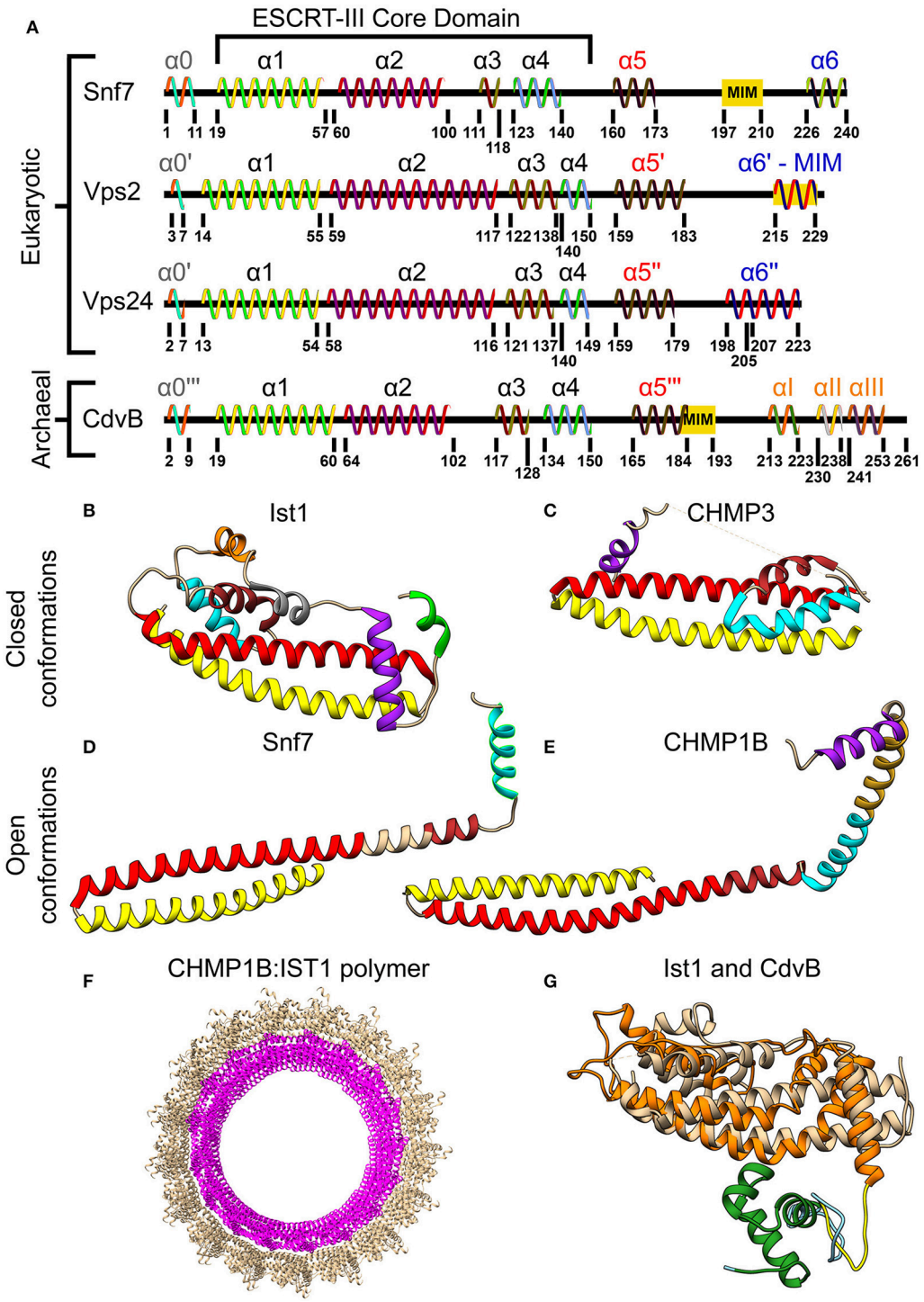

FIGURE 3 | Molecular structure of ESCRT-III and CdvB proteins. **(A)** Secondary structure of several *S. cerevisiae* ESCRT-III (Tang et al., 2015) and *S. acidocaldarius* CdvB proteins. ESCRT-III proteins—helices that are not part of the ESCRT-III core domain are shown with tags. For CdvB, the wH helices are numbered using Greek letters. Since no high-resolution structure of either Vps2 or CdvB exists, the numbering of the helices in these cases is only putative. **(B,C)** Closed conformation of the ESCRT-III proteins. **(B)** IST1 from Cryo-EM (PDB #3JC1) (McCullough et al., 2015). α1, Yellow; α2, Red; α3, Brown; α4, Cyan; α5, Purple; α6, Green. IST1 non-canonical helices are in orange and gray. **(C)** Crystal structure of CHMP3 (Residues 8–222, PDB # 3FRT) (Bajorek et al., 2009b). **(D,E)** Open conformation of ESCRT-III proteins. **(D)** *S. cerevisiae* Snf7 core domain (PDB #5FD9) (Tang et al., 2015). **(E)** CHMP1B from Cryo-EM (PDB #3JC1) (McCullough et al., 2015). Color code for **(C–E)** same as **(B)**. Note that for CHMP1B the interfaces between α2 to α3 and α4 to α5 are only putative. **(F)** Cryo-EM structure of a reconstituted ESCRT-III positive curvature membrane binding ring (PDB ##3JC1). IST1 molecule in tan and CHMP1B in magenta. **(G)** Alignment of *S. acidocaldarius* CdvB Phyre2 based predicted structure and IST1 (PDB #3FRS, residues 1–189; Bajorek et al., 2009b). IST1 is shown in light tan. CdvB core domain is shown in orange, the wH domain in green and the MIT motif in yellow (the rest of the chain in cyan). RMSD distance between 131 atoms 4.916 Å.

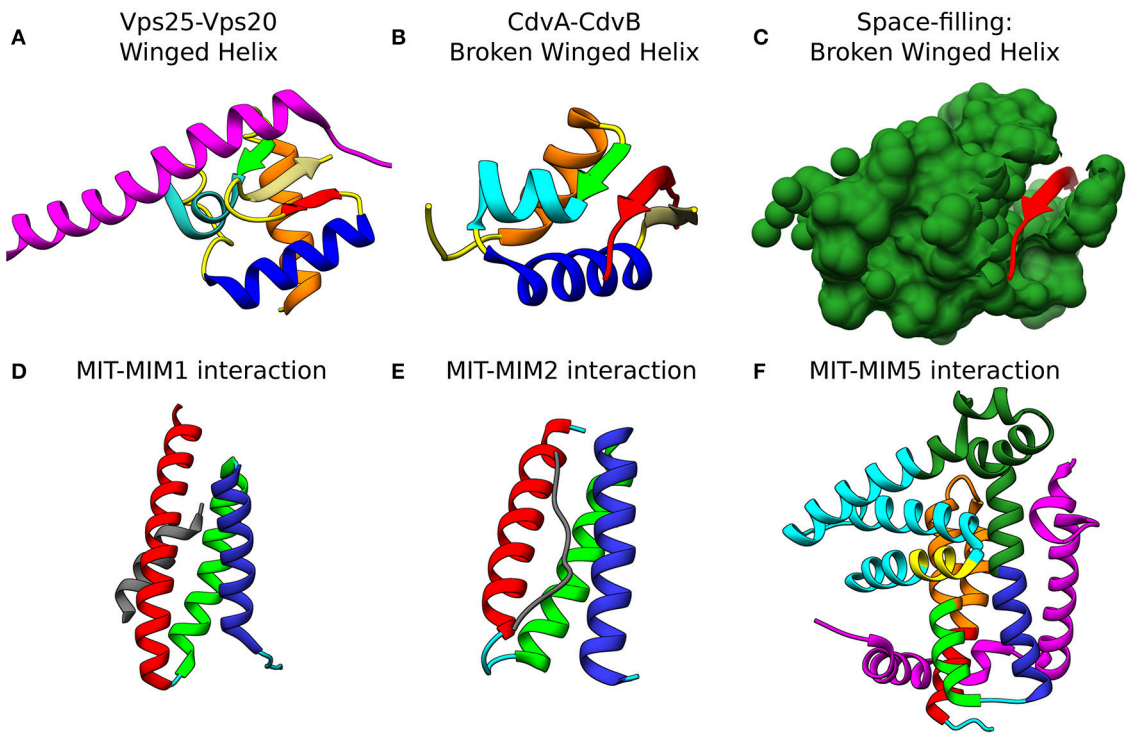

FIGURE 4 | Molecular basis for the interaction of ESCRT-III and CdvB proteins. Top row: wH interactions of ESCRT-III and CdvB proteins with upstream components. **(A)** Crystal structure of the Vps25-Vps20 interaction zone. Vps25 wH domain: αI, orange; $\beta 1$, green; αII, cyan; αIII, Blue; $\beta 2$, Khaki; $\beta 3$, Red; unstructured regions, yellow. Vps20 interaction peptide in purple (PDB #3HTU) (Im et al., 2009). **(B)** *S. solfataricus* CdvA-CdvB "broken" wH interaction zone. Color representation—same as in (a) with the appropriate modification of the β-strands numbering (PDB #2XVC) (Samson et al., 2011). E3B peptide of CdvA in red. **(C)** Same as **(B)** with the CdvB wH (light sea green) in space filled representation. Bottom row: ESCRT-III and CdvB interact with downstream components through a MIM-MIT interactions. **(D)** Interaction between the Vps2 MIM1 (gray) and Vps4 MIT domain. (MIT helices; $\alpha 1$, red; $\alpha 2$, green; $\alpha 3$, medium blue; the rest of the chain in cyan). Based on PDB #2V6X (Obita et al., 2007). **(E)** Interaction of *S. acidocaldarius* CdvB MIM2 (gray) with CdvC MIT (PDB #2W2U). Helices colors, same as in **(D)** (Samson et al., 2008). **(F)** Interaction of Vps60 MIM5 (magenta) with Vta1 MIT (PDB #2LUH) (Yang et al., 2012). Helices colors, same as in **(D)**. Homology regions between Vta1 and *S. islandicus* CdvC in orange and green. Homology between Vta1 and *S. islandicus* CdvB1 in yellow. The rest of the Vta1 chain is in cyan.

if Asgard ESCRT-III homologs can bind the membrane directly, and if they do, what is the implication on their function.

A yeast two-hybrid system has predicted an intricate network of interactions between the CdvB paralogs, where CdvB1/2/3 each interact with itself as well as with the other two CdvB paralogs (see **Figure 2B**) (Samson et al., 2008). In addition, CdvB interacts with CdvB1. It is interesting to note that CdvB3, the shortest CdvB paralog that can probably accommodate only the ESCRT-III core domain (helices $\alpha 1$–$\alpha 5$), shares homology with the ELYC domain of Ist1. The ELYC domain is involved in the interaction between the human IST1 homolog and CHMP1 (Dimaano et al., 2008). Thus, this homologous domain might enable the interaction between CdvB3 and CdvB1/CdvB2. To the best of our knowledge, this is the first time that such a homology is noted.

CdvA and Its Interaction With CdvB

As mentioned above, CdvA is unique to the TACK superphylum. It does not share significant homology with any known protein families. The only significant homology that we were able to identify outside the TACK superphylum is to two distant proteins in *Thorarchaeota*, an organism from the Asgard superphylum. CdvA probably has a tripartite structural organization. Secondary structure prediction suggests the existence of a β-strand-rich domain at its N-terminus, which is followed by a long α-helix-rich domain. The latter domain occupies the major part of the protein sequence and is followed by an unstructured region. Several non-significant homologies were previously noted between CdvA and other proteins. For example, the β-strand-rich moiety was suggested to form a PRC barrel domain (Samson et al., 2011) and the α-helix-rich moiety was suggested to belong to the lamins, golgins and cingulin protein of eukaryotes (Lindås et al., 2008). In the NIH database, the α-helix-rich domain is suggested to belong to the Structural-Maintenance of the Chromosome (SMC) fork B family for *S. acidocaldarius* and to the BAR domain family for *Metallosphaera sedula*. Indeed, we have noted some homology between the CdvA α-helices-rich domain and the SMC protein of *B. subtilis*. In addition, we noted some non-significant homology between the *S. acidocaldarius* α-helices-rich domain and one of the helices of ALIX. Overall, this set of non-significant homologies probably only represents the double function of CdvA as a membrane and a DNA binder as discussed below.

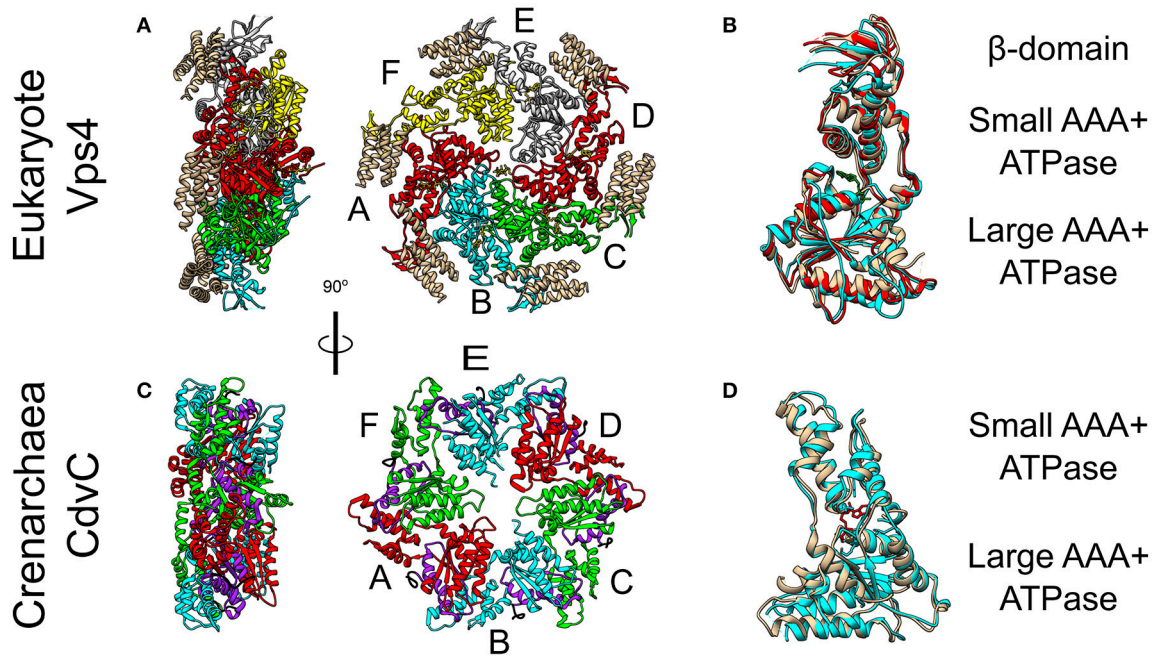

FIGURE 5 | Crystal Structure of the Vps4 and CdvC proteins. **(A)** Crystal structure in side (left) and front (right) views of the yeast Vps4 hexamer together with the VSL domain of Vta1 (tan). Protomers are marked as A–F. Equivalent monomers share color. Gray protomers bind either ADP or ADP+Pi. The yellow protomer is empty (PDB #5UIE) (Monroe et al., 2017). **(B)** Alignment of monomers F (tan), E (red) and C (cyan). F to C protomers alignment—RMSD between 300 atom pairs is 3.262 Å. **(C)** Crystal structure side (left) and front (right) views of an empty *M. sedula* CdvCΔMIT hexamer (PDB #4D80) (Caillat et al., 2015). Identical protomers share the same color. The P-Loops NTPase domains (residues 105–156) are highlighted in purple. The N-terminus of every chain is shown in black. **(D)** Alignment of one protomer from **(C)** in tan with *M. sedula* CdvC bound to ADP (PDB #4D82) in cyan. RMSD between 257 atom pairs is 2.717 Å.

At the C-terminus of CdvA another short β-strand is located which was named E3B. The E3B peptide is responsible for the CdvA-CdvB interaction through its binding to the CdvB wH domain with a K_d of 6 μM (similar to the ESCRT-II-Vps20 interaction affinity) (Samson et al., 2011). Interestingly, while Vps20 binds an exterior surface of the ESCRT-II wH domain (see **Figure 4A**), in the CdvB-CdvC interaction interface, the wH domain is broken, and one of the β-strands is missing. In that case, the broken wH domain is supplemented by the CdvA E3B peptide that together form a full wH domain, albeit with three parallel β-strands (see **Figures 4B,C**). This forms a unique wH domain interaction that was probably developed in Crenarchaeota. Since CdvA can bind the membrane, as is discussed below, it is customary to model CdvA as the recruiter of CdvB to the membrane. Indeed, from all CdvB paralogs, only CdvB possess a wH domain.

The Vps4 Complex

The Vps4 complex couples the recurring action of the ESCRT-III complex to energy expenditure through its ATPase activity. Thus, Vps4 sets the directionality of the membrane remodeling pathway. In yeast, in the ATP-bound form, the Vps4 complex is a hetero-hexamer of Vps4 and the Vps4 cofactor Vta1 (see **Figure 5A**) (Monroe et al., 2014). In fact, ATP is necessary for the Vps4 oligomerization. Each Vps4 monomer is composed of a Microtubule Interacting and Trafficking (MIT) domain, a large ATPase subunit, a small ATPase subunit, and a β-domain (see **Figure 5B**). Vta1 binds the β-domain and stimulates Vps4 ATPase activity (Azmi et al., 2008). Multiple experiments have recently shown that although Vps4 appears as a hexamer, it does not form a closed hexameric ring (Monroe et al., 2017; Su et al., 2017; Sun et al., 2017). Instead, it possesses a helical form where ATP hydrolysis and ADP release result in structural modifications of the interfaces between the monomers (see **Figure 5A**). To pull out and recycle ESCRT-III subunits, Vps4 first binds MIT Interaction Motives (MIMs) of the ESCRT-III subunits. This reveals part of the α5 helix of the ESCRT-III subunit for a high-affinity interaction (K_d ~2 μM) with loops in the Vsp4 central pore (Han et al., 2015). In addition, the Vps4-ESCRT-III binding also stimulates the ATPase activity of Vps4. Consequently, the helical form of Vps4 allows it to "walk" along the ESCRT-III polypeptide chain and pull it out of the ESCRT-III complex as a thread through the Vps4 complex central pore (Yang et al., 2015). Interestingly, in addition to the Vps4 monomers, Vta1 also possesses 2 MIT domains. Thus, overall, the Vps4 complex exposes 18 MIT domains, which interact selectively with different ESCRT-III subunits.

CdvC

CdvC shares both a high sequence (37% identical, 52% positive over 345 amino acids) and high structure (*S. solfataricus* RMSD 1.62 Å over 237 pairs of C^{α} atoms) similarities to Vps4 from

S. cerevisiae (Monroe et al., 2014). However, archaea lack the Vta1 cofactor. In addition, two small structural differences exist between CdvC and the Vps4 protein. First, CdvC lacks the Vps4 major β-domain that connects the two parts of the small AAA+ ATPase subunit, and which is responsible for the binding of Vta1 (see **Figures 5B,D** and Monroe et al., 2014; Caillat et al., 2015). Instead, for CdvC, the two parts of the small subunit are connected by a well-ordered short loop. Second, in its empty form, the large AAA+ ATPase subunit of CdvC contains only 4 β-strands in comparison to 5 in its eukaryote counterpart. The small fifth β-strand (annotated as β') that is located at the beginning of the large subunit, next to the MIT domain, is unstructured in the empty state of CdvB. Only in the ADP-bound form of the protein, this moiety becomes structured into a short β'-strand and an α-helix.

Crystal structure studies as well as size exclusion chromatography of the Crenarchaeota *M. sedula* CdvC, showed that it oligomerizes into hexamers, similar to Vps4 (see **Figures 5A,C**; Monroe et al., 2014). However, unlike Vps4, CdvC can form a hexameric ring even without ATP. In the empty form, the hexameric ring shows a 3-fold symmetry with 3 pairs of identical protomers that together form a planar asymmetric structure (see **Figure 5C**). When ADP binds CdvC, a 23° rotation between the two ATPase domains is induced. This rotation is a manifestation of the structural flexibility of the protein that is necessary for its proper function. Also in its tertiary structure, like in its secondary structure, there are several differences between CdvC and Vps4. First, ADP bound to CdvC occupies a position that is similar to that of ATPγS when it binds the yeast Vps4. Second, ADP bound to Vps4 penetrates less into the binding pocket than ADP that binds CdvC. In addition, isothermal titration calorimetry showed that CdvC binds with a similar affinity six ATP molecules with $K_d = 3.3$ μM, while for ADP, five molecules had a similar affinity of 5 μM, and one ADP had a high affinity of 0.4 μM (Caillat et al., 2015). For Vps4 in yeast, however, only a negligible amount of bound ADP was detected in a purified non-hydrolyzable version of the hexamer, so the K_d of ADP is probably much lower than that of ATP (Sun et al., 2017). Moreover, although biochemical assays showed that it hydrolyzes ATP in the hexameric active form (Moriscot et al., 2011; Caillat et al., 2015), in contrast to Vps4, CdvC's ATPase activity is only marginal at 37°C and becomes substantial only at high temperatures [16 $\frac{ATP}{min}$ at 60°C (Caillat et al., 2015), compared to 45 $\frac{ATP}{min}$ for Vps4-Vta1 at 30°C (Azmi et al., 2008)]. These differences may suggest a somehow different ATP cycle for CdvC action than for the yeast Vps4.

The Interaction Between ESCRT-III and Vps4

Similar to their MIM-MIT based interactions with Vps4, ESCRT-III proteins utilize their MIM peptide for the interactions with other downstream components such as the de-ubiquitinated protein AMSH (Hurley and Yang, 2008; Shestakova et al., 2010). Different MIM sequences in various ESCRT-III proteins and different MIT domains in various down-stream components permits differential binding and division-of-labor specialization. In general, the MIM peptides are located at the C-terminal domain of the ESCRT-III subunits (see **Figure 3A**). As of today, at least five types of MIM-MIT interactions were identified (Yang et al., 2012). Two out of these are being utilized for the ESCRT-III interactions with Vps4 (see **Figures 4D,E**). MIM1 peptide, found in proteins from the Vps2/Did2 class, forms a α-helix and complements the interface between α2 and α3 of the MIT domain. The characteristic feature of MIM1 is the formation of leucine-based hydrophobic interactions and charged amino acids based salt bridges with the MIT domain. In contrast, the MIM2 peptide binds the opposite side of the MIT domain, between α1 and α3, and is found at the C-terminal domain of proteins from the Snf7/Vps20/Vps60 class. A consensus sequence of the MIM2 motif based on archaeal and eukaryotic organisms was suggested to be: $\phi_1 P_1 x \phi_2 P_2 x x P_3 \phi_3 P_4$, where P is proline, x a polar residue and ϕ a hydrophobic residue (Kojima et al., 2016). Thus, the characteristics feature of the MIM2 motif is a high enrichment of proline residues. Exceptionally, Ist1 possesses both MIM1 and MIM2 motifs, showing that proteins from the Vps2/24/Did2 class can also possess an MIT2 motif.

The MIM-MIT interactions exhibit a wide span of binding affinities, from a high binding efficiency (1–2 μM, to tens of μM), to a very low binding efficiency (more than 100 μM) (Obita et al., 2007; Stuchell-Brereton et al., 2007; Kieffer et al., 2008; Bajorek et al., 2009a). In particular, CHMP4, the main constituent of the ESCRT-III complex binds Vps4 with a very low binding affinity, while Vps2, the essential factor for the recruitment of Vps4 to the ESCRT-III structure binds Vps4 with an affinity of about 30 μM. In addition, IST1 binds VPS4 with a very high binding efficiency (about 1 μM), which enables it to bind VPS4 in the cytoplasm and recruit it to the ESCRT-III complex thus assuring the efficient function of the ESCRT pathway (see **Figure 1B**). In contrast, proteins with lower binding affinities have to be incorporated into the ESCRT-III complex before they can bind Vps4 efficiently. Thus, this broad span of interaction strengths implies functional consequences.

The Interaction Between CdvB and CdvC

Similar to the ESCRT-III-Vps4 interaction, also the CdvB-CdvC interaction is mediated through an MIM-MIT binding. Interestingly, although CdvB is a homolog of the Vps2/24/Did2 class, it does not possess an MIM1 motif. Instead, it possesses an MIM2 peptide at the end of the C-terminal region, immediately after the α5 (**Figure 4E**). CdvB thus exhibits mixed characteristics. On the one hand, it possesses a Vps2/24/Did2 core domain. On the other hand, it possesses an Snf7/Vps20/60-family MIM2 peptide for its interaction with CdvC.

For CdvB, the MIM2 peptide sequence is: RELLPELPHPP (underbar, hydrophobic; double underbar, acidic or basic). Thus, the main characteristic of the MIM2 motif, namely an enrichment of plorine residues is maintained. Residues 177-261 of CdvC, which contain this motif, bind the CdvC MIT domain with a $K_d \approx 30$ μM, thus situating the CdvB-CdvC interaction

on the middle range of ESCRT-III-Vps4 binding efficiencies, similar to the Vps2-Vps4 interaction strength (Samson et al., 2008).

By contrast to CdvB, C-terminus peptides from *S. acidocaldarius* CdvB1 and CdvB2 show only a marginal binding affinity to the MIT domain ($K_d > 100\,\mu M$). This is consistent with the fact that CdvB1 and CdvB2 lack the end part of the proline-rich MIM2 motif (KEKFPSLPAAG and KEKFPSLPSFA respectively; wavy underbar - polar). Thus, in *S. acidocaldarius,* CdvB is probably the sole recruiter of CdvC *in vivo*. However, this picture was different in *S. islandicus*, as here a yeast two-hybrid system detected interactions also between CdvB1 or CdvB2 with CdvC (Liu et al., 2017). This difference in the CdvC interaction repertoire probably has a causal effect on the mechanisms of action during division, as is discussed below.

We would like to suggest a structural hypothesis that may explain this different binding profiles of CdvB1-CdvC in these two species. The Vta1 ESCRT-III interacting domain is composed of two tandem MIT domains that are packed one against each other at a 90° organization. Vta1 interacts with Vps60 through a unique MIM5-MIT interaction mode (Yang et al., 2012). In that case, two interfaces are implicated in the interaction, one between helix 1 and helix 3 of the MIT domain and a separate one with helix 1 of Vta1 MIT (see **Figure 4F**). We noticed some homology between the Vta1 MIT domain and CdvC. However, while for *S. acidocaldarius* the sequence homology is low and the homologous region is continuous and is part of the ATPase domain, for *S. islandicus* the homologous sequence is divided into two regions. One of these regions is part of the CdvC MIT domain. Interestingly, in addition, CdvB1 possess a short α-helix that is also a homolog to the Vta1 MIT domain, and this α-helix is involved in the packing of the two Vta1 MIT domains one against the other. This suggests that for *S. islandicus*, the less-proline-rich MIM2 motif may be supported by an additional interaction between the CdvB1 protein body and the CdvC MIT domain, in the same fashion as in Vta1 MIT-MIT packing. If that is the case, this will constitute an additional class of MIM-MIT interaction. It will be interesting to test this hypothesis experimentally.

IN VITRO RECONSTITUTION OF Cdv AND ESCRT–III PROTEINS

Higher-Order Structures Formed by ESCRT-III Proteins

The hallmark of ESCRT-III proteins is their ability to form higher-order structures such as domes, filaments or spirals. Although the exact membrane-remodeling mechanism of ESCRT-III is still under intensive debate (Chiaruttini and Roux, 2017; Schöneberg et al., 2017), it is generally believed that the key for the membrane deformation and abscission depends on the formation of these ESCRT-III structures.

One of the most impressive *in vivo* examples of ESCRT-III polymers appeared when CHMP4A or CHMP4B were over-expressed (Hanson et al., 2008). Under this condition, both proteins formed highly ordered arrays of curved filaments at the plasma membrane. When, in addition, the dominant-negative Vps4B^{E23Q} was expressed, the CHMP4A filaments created an extensive array of protrusions that bulged out of the plasma membrane (see **Figure 6A**). The diameter of the protrusions was about 100 nm, and they contained highly dense CHMP4A spiral filaments. Similarly, depletion of VPS4A/B and over-expressing of CHMP2B resulted in the formation of plasma membrane protrusions that could be as long as tens of microns (Bodon et al., 2011). These protrusions were filled with helical CHMP2B filaments throughout their entire length. In fact, ESCRT-III spiral polymers were also observed on the plasma membrane upon Vps4 deletion, without the need for protein over-expression (Cashikar et al., 2014). Thus, members from either of the two ESCRT-III classes assemble on the plasma membrane and can lead to the formation of long protrusions *in cellulo*.

Many ESCRT-III proteins also form complex structures *in vitro*. For example, Snf7 proteins, with a mutation that removed the auto-inhibition, formed flat spirals and ring-like structures when incubated together with a lipid monolayer (see **Figure 6B**; Henne et al., 2012). When the Snf7 mutant was incubated together with Vps24, Vps2 (molar ratio 2:1:1) and a lipid monolayer, 3D coiled-helical structures were formed (see **Figure 6B**). The average diameter of these 3D helices was about 85 nm, approximately the size of an endosome-bud neck. Not only did Vps24 and Vps2 determine the geometrical pattern of Snf7 polymers, but they also reshaped preformed flat Snf7 spirals into the 3D helices, suggesting a regulation mechanism for ESCRT-III membrane-remodeling.

By themselves, members of the Vps2/24/Did2 class tend to form long rigid tubes or long linear/branched protofilaments, but not spirals or rings (Bajorek et al., 2009b). For example, Vps24 form a network of branched long (hundreds of nm) helical protofilaments with a typical diameter of 15 nm (Ghazi-Tabatabai et al., 2008), while CHMP2AΔC:CHMP3ΔC, both lacking the auto-inhibition region, formed hundreds of microns long tubes with a width of about 40 nm. In some cases, these tubes ended up with a dome-like structure (see **Figure 6C**; Lata et al., 2008). Similar structures were also observed for CHMP2A:CHMP3ΔC (Effantin et al., 2013). Yet, under certain conditions, proteins from the Vps2/24/Did2 class can also form coil-like polymers or rings (for example, CHMP2AΔC polymers; Lata et al., 2008; Effantin et al., 2013).

It is interesting to note that the CHMP2AΔC:CHMP3ΔC tubes expose their outer side for interaction with a membrane while Vps4 interacts with the inner surface of the tubes. This arrangement is consistent with the expected topology of the ESCRT-III machinery. By contrast, CHMP1B formed cones and funnels alone or with the N-terminus domain of IST1, but these structures wrapped around the outside surface of vesicles (see **Figure 6D**). Thus, the CHMP1B structures exhibit an opposite topology to the regular one of the ESCRT machinery (McCullough et al., 2015). High-resolution cryo-EM showed that these CHMP1B:IST1$_{NTD}$ tubes consisted of two layers. The inner layer was composed of CHMP1B monomers in the "open" conformation. The outer layer consisted of IST1 in a "closed" conformation (see **Figure 3F**).

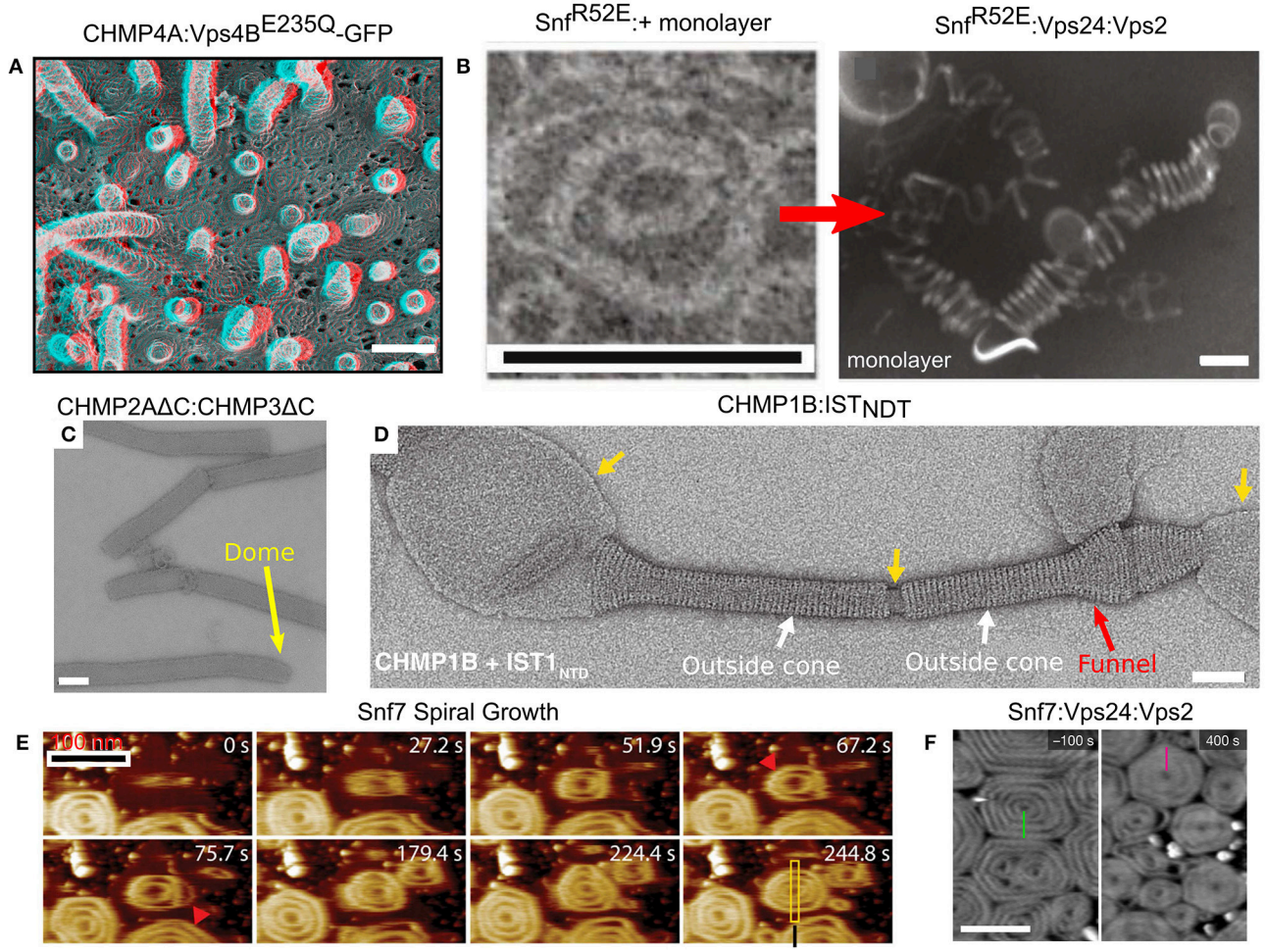

FIGURE 6 | Membrane remodeling by ESCRT-III proteins. **(A)** Protrusions and spirals on the plasma membrane as result of an overexpression of CHMP4A:Vps4B^{E235Q}-GFP in COM-7 cells. Scale bar 100 nm. **(B–F)** *In vitro* reconstituted ESCRT-III polymers. **(B)** Rings and helices: typical 2D Snf^{R52E} rings and Snf^{R52E}:Vps24:Vps2 3D helices (formed when a lipid monolayer is present). Scales bar 100 nm. **(C)** Tubes of CHMP2AΔC:CHMP3ΔC. Scale bar 100 nm. The dome structure at the tip of the tubes (yellow arrow). **(D)** Cones and funnels: CHMP1B:IST$_{NTD}$ coating a lipid vesicle to form an outside sheath. Cf. also **Figure 3F**. Scale bar 50 nm. **(E)** Growth of Snf7 spirals (red arrowheads) on a supported lipid membrane over time, measured in high-speed liquid AFM. Scale bar 100 nm. **(F)** Pre-formed Snf7 spirals on a supported lipid bilayer (left) are flattened and shrink upon Vps24 and Vps2 addition. Scale bar 200 nm. **(A)** Is reproduced from Hanson et al. (2008). **(B)** is reproduced from Henne et al. (2012). **(C)** Is reproduced from Lata et al. (2008). **(D)** Is reproduced from McCullough et al. (2015). **(E)** Is reproduced from Chiaruttini et al. (2015). **(F)** is reproduced from Mierzwa et al. (2017). All panels are reproduced with permission.

In spite of the fact that various proteins from both ESCRT-III classes assemble into higher order structures, it is believed that Snf7/CHMP4 spirals are the main player in the membrane deformation. By its nature, a spiral does not have a constant curvature. As the spiral ring grows bigger, its curvature grows smaller. Measurements on Snf7 polymers suggested a preferred diameter of about 35 nm (Shen et al., 2014). When Snf7 formed spiral polymers on a supported lipid bilayer, it nucleated from a ring with a typical diameter of about 25 nm (Chiaruttini et al., 2015). As additional turns are added to the spiral, the innermost rings were compressed to about 17 nm and outer rings continued to grow. In addition, the spiral structure evolved into a polygon-like shape, probably to accumulate the stress induced from the non-ideal curvature of the spiral rings (see **Figure 6E**). These data suggest the Snf7 spirals acts as a tensed spring that deform the membrane by releasing its tension.

Interestingly, when Vps2 or Vps24 were added to Snf7 spirals on a supported lipid bilayer, they inhibited the growth of the Snf7 spirals by bundling with them to form co-filaments with a typical width of 15 nm (Mierzwa et al., 2017). In addition, the Snf7-Vps2-Vps24 polygons compacted to a disc-like structure (see **Figure 6F**). Addition of Vps4 to the Snf7-Vps24-Vps2 spiral-disks resulted in a massive rearrangement of the network. Pre-existing spirals depolymerized and reduced their size, and new spirals were formed at the expense of the pre-existing ones. Thus, Vps4 confers dynamical-behavior capabilities to the ESCRT-III polymers.

Two of the most impressing examples for the ability of ESCRT-III proteins to remodel membranes *in vitro* occurred when

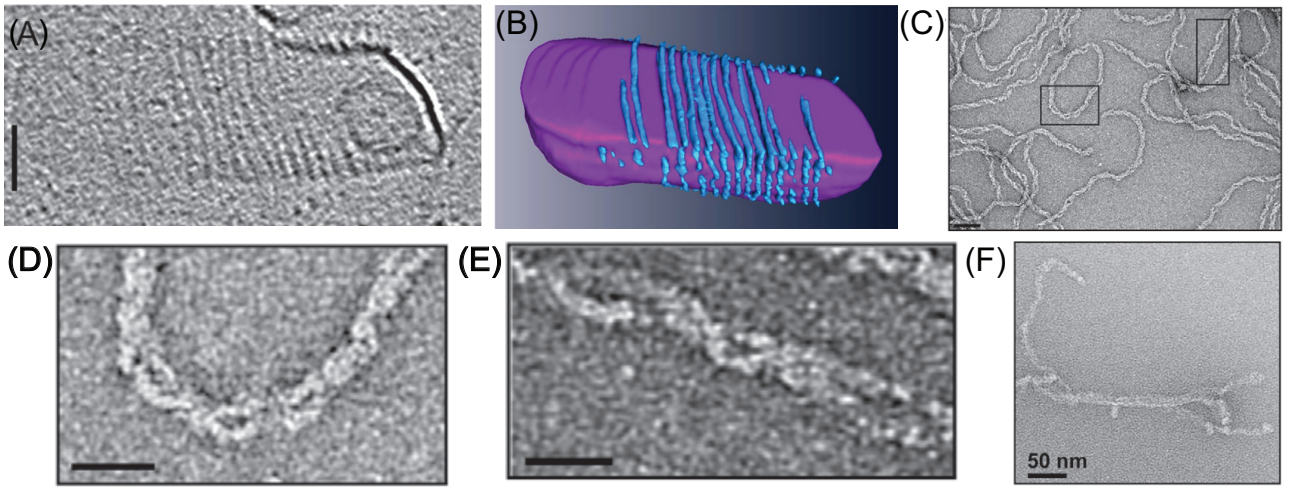

FIGURE 7 | *In vitro* reconstitution of Cdv protein. **(A)** Cryo-EM microscopy of CdvA from *S. acidocaldarius* that polymerize on the other surface of a liposome made from tetraether polar lipid fraction **(E)**. Scale bar - 50 nm. **(B)** 3D reconstruction of the CdvA filaments from **(A)**. **(C)** Negatively stained EM of *M. sedula* CdvA double-helical polymers reconstituted *in vitro* that contained DNA. **(D,E)** Zooms of the emphasized areas indicated in panel **(C)**. scale bars 20 nm. **(F)** Negatively stained EM image of CdvBΔC polymers (Residues 1–167 -ΔMIM domain) from *M. sedula*. **(A,B)** are reproduced from Dobro et al. (2013) with permission. **(C–F)** Are reproduced from Moriscot et al. (2011) with permission.

several ESCRT-III proteins were incubated together with lipid vesicles. In the first case, when the four ESCRT-III core proteins were incubated with small unilamellar vesicles, inward-facing buds were produced in a Vps4-independent manner (Saksena et al., 2009). In the second case, incubating the ESCRT-III core proteins with giant unilamellar vesicles resulted in the formation of completely encapsulated vesicles, similar to the MVB, again in a Vps4 independent manner (Wollert et al., 2009). Adding the ESCRT-0/I/II proteins to the giant liposomes *in vitro* assay, enabled Wollert et al. to obtain completely encapsulated vesicles even at a physiologically relevant concentration of the ESCRT-III proteins (Wollert and Hurley, 2010).

Reconstitution of Cdv Proteins Into Higher-Order Structures

As mentioned above, unlike the ESCRT-III proteins, CdvB does not bind membranes *in vitro,* likely because it lacks the CHMP3 basic patch that was implicated in its membrane binding (Samson et al., 2011). In contrast, CdvA does bind the archaeal tetraether polar lipid fraction E (PLFE) membranes. Cryo-electron microscopy has shown that CdvA polymerizes on the outside surface of PLFE liposomes and forms long polymers with a typical spacing of about 8 nm (see **Figures 7A,B**; Dobro et al., 2013). Furthermore, using the *S. acidocaldarius* CdvA-CbvB system, it was shown that CdvA could recruit CdvB to the membrane, and transform, in an CdvC-independent manner, small unilamellar PLFE vesicles into an extensive network of connected membrane tubes with a typical diameter of 10–20 nm (Samson et al., 2011). This might suggest that CdvB, like ESCRT-III complex, can directly cut narrow membrane necks. However, a note of caution should be added. Such a tubulation effect does not resemble the ordered bud-like structures that are formed when Vps20:Snf7:Vps24:Vps2 were incubated with small unilamellar vesicles (see Figure 6 in Saksena et al., 2009), and neither is it reminiscent of the intralumenal vesicles that were obtained by ESCRT-III from giant unilamellar vesicles (Wollert et al., 2009; Wollert and Hurley, 2010). In fact, it is not surprising that a membrane-associated dynamic polymer can tubulate membranes. Thus, the physiological relevance of this observation is not clear.

Another interesting feature of the CdvA filaments is their interaction with DNA. When *M. sedula* CdvA was purified from *E. coli*, it formed extended double helical filaments that copolymerized with the host DNA (see **Figures 7C–E**). It was impossible to remove the DNA from the filaments (Moriscot et al., 2011). Treatment of the CdvA filaments with DNAase resulted in disassembly of a large fraction of the filaments. This is probably a manifestation of the affinity of CdvA to the chromosome and may hint to CdvA participation in the chromosome segregation processes or suggest an inverse nucleoid-occlusion type localization mechanism for the archaeal divisome. Supplementing the CdvA filaments with CdvB did not cause any noticeable structural changes in the *M. sedula* CdvA filaments, which suggests a rather rigid structure for the CdvA filaments.

In contrast to CdvA, full-length *M. sedula* CdvB did not form *in vitro* polymers. Only a truncated version of *M. sedula* CdvB (CdvBΔC, residues 1–167), which includes only the ESCRT-III core domain, polymerized into extended filamentous structures *in vitro* (see **Figure 7F**). However, these unordered CdvB polymeric structures do not resemble the structurally defined reconstituted spirals or tubes that were found in ESCRT-III assays. At best, *M. sedula* CdvBΔ*C* polymers vaguely resemble the Vps24 reconstitution linear polymers (Ghazi-Tabatabai et al., 2008) or polymers of Snf7 mutants that are impaired in their function (Henne et al., 2012; Shen et al., 2014). Importantly,

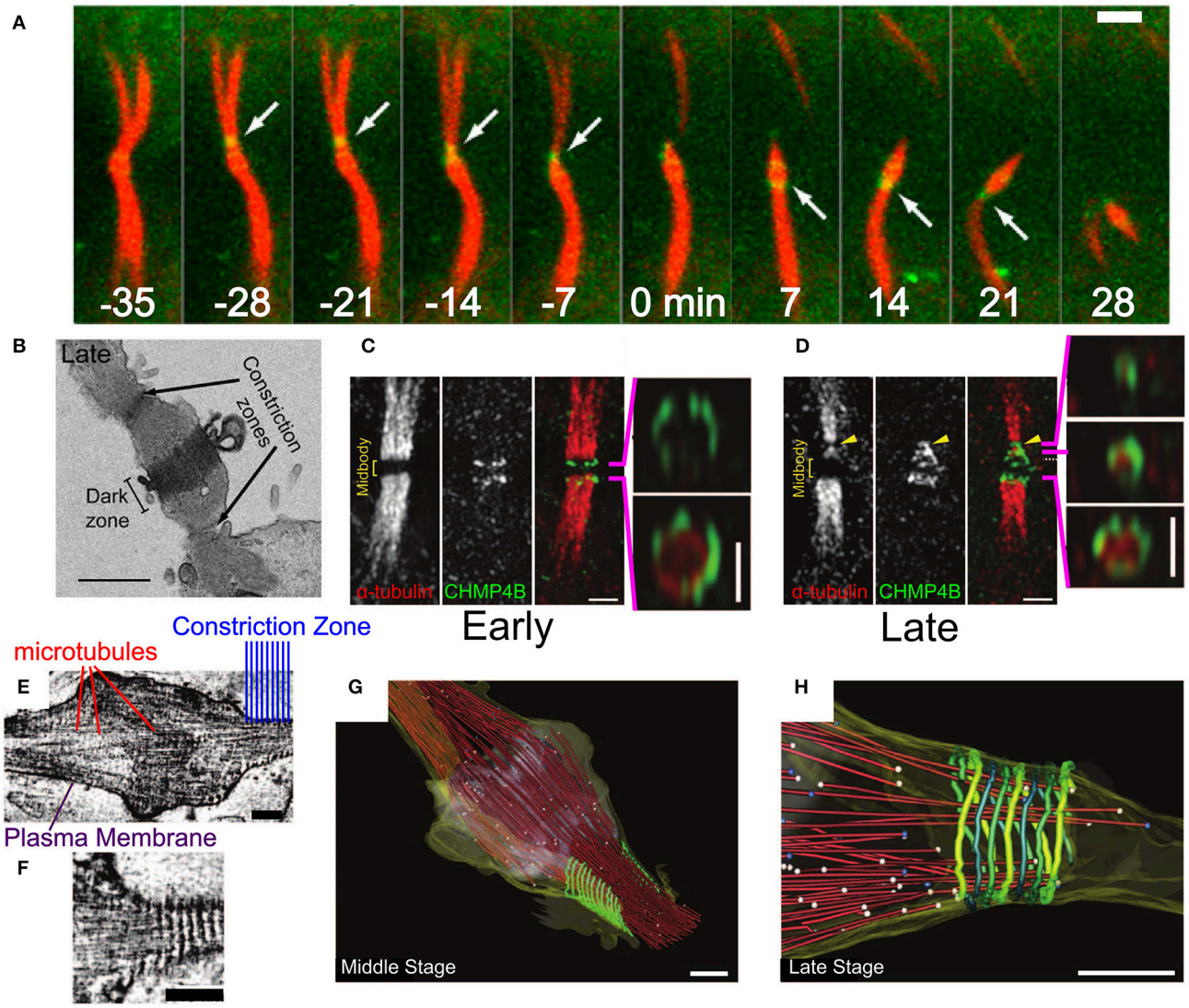

FIGURE 8 | Abscission in eukaryotic cells during cytokinesis. **(A)** Abscission process of the intracellular bridge in Madin-Darby Canine Kidney (MDCK) Epithelial cells. CHMP4B in green and tubulin in red. White arrow—abscission site. Scale bar 2 μm. **(B)** Structure of the intracellular bridge in MDCK cells. Arrows indicate the future abscission sites. Scale bar 2 μm. **(C)** Early localization of GFP-CHMP4B (green) and mRFP α-tubulin to the division site of a HeLa cell. Panels on the right are 3D structured illumination (SIM) reconstructions of CHMP4B rings. Scale bar 1 μm. **(D)** Same as **(C)** at the late stage of abscission. Panels on the right are 3D SIM reconstruction of ESCRT-III cone. **(E,F)** Cryo-EM images of the Hela cell intracellular bridge at the middle stage of abscission. Scale bars—200 nm. **(E)** Shows the overall structure while **(F)** shows the cortical helical filaments. **(G–H)** Cryo-EM 3D reconstruction of a constriction zone. Red—microtubules, yellow—plasma membrane, green - 17 nm cortical filaments. **(G,H)** Shows the Middle and Late abscission stages, respectively. Scale bars—200 nm. **(A,B)** Is reproduced from Elia et al. (2011) with permission. **(C–H)** are reproduced from Guizetti et al. (2011) with permission.

however, sucrose gradient centrifugation showed that, in spite of the proximity of the wH domain and the MIM2 motif, *the M. sedula* CdvB interacts in a non-mutually exclusive manner with both CdvA and CdvC (Moriscot et al., 2011), which supports the notion that the three proteins act synergistically.

Long and linear polymers of Cdv proteins were also detected when one of the Thaumarchaeota *Nitrosopumilus Maritimus* CdvB paralogs was expressed in yeast or mammalian cells (Ng et al., 2013). In that case, the polymers were dynamic, as judged by fluorescence recovery after photobleaching experiments. Similar to the *in vitro* CdvB polymers reconstitution, *N. Maritimus* CdvB paralog polymers needed only the core domain (residues 1–192) to polymerize. No other *N. Maritimus* CdvB paralogs formed polymers in yeast, leaving open questions regarding the operational state of the *N. Maritimus* CdvB paralogs *in vivo*.

THE ESCRT AND Cdv MACHINERIES IN CYTOKINESIS

The ESCRT-III in Cell Division

The last stage of Metazoan cytokinesis involves the formation of a microtubules-rich intracellular bridge with a width of about 1 μm (see **Figures 1**, **8A,B**). At the intracellular bridge middle, a protein-rich structure that is called the mid body (or Flemming

body), is located. During late mitosis, Cep55 recruits ALIX and the ESCRT-I protein TSG101 to the mid body (Carlton and Martin-Serrano, 2007). These two factors recruit CHMP4 and initiate its polymerization (Morita et al., 2007; Carlton et al., 2008; Lee et al., 2008). Multiple experiments have shown that ESCRT-III is essential for cell separation in Metazoa (Elia et al., 2011; Guizetti et al., 2011; Lafaurie-Janvore et al., 2013). Here, we briefly describe its role in abscission. For a more detailed recent review on ESCRT in cytokinesis, see Stoten and Carlton (2017).

Initially, CHMP4 assembles in two parallel bands at the periphery arms of the Flemming body (see **Figure 8C**; Guizetti et al., 2011). Approximately 20–40 min later, ESCRT-III shuttles about 1 μm away from the mid body toward the abscission site that is located between the mid body and the cell (see **Figures 8A,B**) (Elia et al., 2011). There, it forms a cone-like structure that ends at the abscission site (see **Figure 8D**). Electron (Guizetti et al., 2011) and soft X-ray (Sherman et al., 2016) microscopy studies have detected a set of cortical filaments, each with a width of 17 nm, that are organized as a cone-like structure, similarly to the ESCRT-III complex (see **Figures 8E–G**). Just before abscission occurs, the ends of these cortical filaments structure correlate with the location of microtubules ends and with the abscission site (see **Figure 8H**). Although the cortical filaments are quite spaced and have a diameter of about 200 nm at their pointed end (about 2 times larger than the membrane neck at virus escape sites or the MVB buds), it is common to identify them with the ESCRT-III filaments. Thus, it was suggested that ESCRT-III is responsible for cell separation by remodeling the membrane at the abscission site. It is interesting to note that a cell-fate program determines whether abscission will also occur on the opposite side of the Flemming body, to leave an orphan mid body, or whether, alternatively, the mid body will be absorbed into the daughter cell cytoplasm (Chen et al., 2013).

Similar to other functions of the ESCRT machinery, also in cytokinesis, the ESCRT-III complex works concomitantly with VPS4. However, unlike in HIV-1 release or MVB formation, recruitment of VPS4A and VPS4B to the division site depends on IST1 ($K_d \approx 1\,\mu M$ between IST1 and the Vps4 MIT domain; Agromayor et al., 2009; Bajorek et al., 2009a). Since the yeast homolog of CHMP1 (DId2) is responsible for the recruitment of Ist1 to the ESCRT-III complex at the MVB sites (Dimaano et al., 2008; Tan et al., 2015), it seems that IST1 is recruited to the ESCRT-III filaments at the abscission site by CHMP1. In addition, CHMP1A can bind VPS4 directly through its MIM1 motif with a $K_d \approx 4.5\,\mu M$, and recruit it to the ESCRT-III filament (Stuchell-Brereton et al., 2007). These data suggest that, at least for cytokinesis, the regulation of the VPS4 activity is mediated by high-affinity interactions in solution. After its recruitment to the division site, VPS4 can bind the lower affinity MIM1 of CHMP2B (Obita et al., 2007) or the MIM2 of CHMP6 ($K_d \approx 30\,\mu M$) (Kieffer et al., 2008), or even bind to CHMP4 ($K_d > 100\,\mu M$).

It should be noted that membrane deformation cannot be achieved without the destabilization of the intracellular bridge cytoskeleton components. Therefore, before abscission, spastin, a microtubule-severing protein, is recruited to the intracellular bridge by an interaction between its MIT domain and CHMP1B (Yang et al., 2008; Connell et al., 2009). Similarly, the recruitment of actin depolymerization and oxidation proteins was implicated for the completion of cytokinesis (Schiel et al., 2012; Frémont et al., 2017). These data show the differential mechanical requirements for the deformation of a bare membrane relative to those of the plasma membrane that is protected by a cytoskeleton. Interestingly, Metazoan cells apply an additional level of regulation to prevent premature abscission and persistent chromosomal bridges severing (the "NoCut" checkpoint; Carlton et al., 2012). Differential recruitment and phosphorylation of CHMP4 paralogs play a pivotal part in this checkpoint (Capalbo et al., 2012; Carlton et al., 2012). In particular, CHMP4C dephosphorylation and translocation from the center of the mid body to its periphery, after the "NoCut" checkpoint was resolved, is responsible for the initiation of mature ESCRT-III polymers, thus assuring cytokinesis completion (Capalbo et al., 2016).

Recently, it was found that during the second phase of the CHMP4B recruitment to the mid body, all the core components of the ESCRT-III machinery (CHMP4B, CHMP2B, CHMP3) showed an identical bipartite-population kinetics (Mierzwa et al., 2017). The first, a fast population has a residence time of about 20 s and is constantly exchanged with cytoplasmic proteins. The second, a slow population is exchanged only at the 10 min timescale. VPS4 showed a similar accumulation kinetics at the division site. Thus, the ESCRT-III-VSP4 machinery is highly dynamic during abscission. As discussed below, this might have implications on its membrane deformation mechanism. It is interesting that other components of the ESCRT-I/II complexes (besides TSG101 and ALIX) also play an important role in the recruitment of ESCRT-III components to the intracellular bridge and their dynamical shuttling away from the Flemming body (Christ et al., 2016). In particular, it was suggested that ESCRT-II, together with CHMP6, bridge the gap between the outer arms of the mid body and the abscission site, thus assuring the correct final positioning of the CHMP4B-CHMP2-CHMP3 polymers (Goliand et al., 2014).

Importantly, although the ESCRT system, most likely, directly remodels the membrane during abscission in Metazoan cells, this is not a universal modus operandi. For example, in budding yeast, ESCRT plays only a minor role in cell division. Indeed, it was suggested that ESCRT's primary function in *S. cerevisiae* division is to mediate the turnover of cell-division proteins from the plasma membrane (McMurray et al., 2011), Similarly, in *S. pombe*, the main role of ESCRT was ascribed to the control of membrane trafficking during cytokinesis (Bhutta et al., 2014). Finally, in Arabidopsis, elch, a homolog of the ESCRT-I TSG101 protein, functions in cytokinesis (Spitzer et al., 2006). Yet again, in that case, its main role is related to the regulation of the microtubule cytoskeleton. In the context of cytokinesis, the main relevant difference between plants, fungi, and Metazoa may be the existence of a cell wall in the former cases. Accordingly, for understanding the relationship between the ESCRT and the Cdv systems, it is interesting to check whether the ESCRT system remodels the membrane directly during cytokinesis in other lower cell-walled eukaryotes.

The Cdv System in Division

First experimental evidence that linked Cdv proteins to cell-cycle regulated processes and in particular to cell division came from UV radiation studies. Exposure of *S. solfataricus* cells to UV radiation caused a severe down-regulation of the transcription levels of all cdv genes (Fröls et al., 2007). Similarly, for *S. acidocaldarius*, the main locus cdv genes, as well as cdvB2 and cdvB3, were down-regulated (Götz et al., 2007). In accordance with these observations, in *S. acidocaldarius*, all cdv genes are cell-cycle regulated, with cdvA, cdvB, and cdvB2 showing the largest increase (about 3.5-fold) before entering the division phase (Lindås et al., 2008; Samson et al., 2008).

The most direct evidence that connects the Cdv system to cell division comes from immunofluorescence microscopy experiments. These studies revealed the localization of CdvA and CdvB to the division site between segregated chromosomes, and specifically the formation of a band that shrinks concomitant with the septum formation (see **Figure 9A**). CdvC localizes to the division site as well, but in some cases, a diffusive pattern without a clear-cut localization is observed. Treatment of *S. acidocaldarius* cells with antibiotics that arrest the cell cycle prior to division resulted in the abolishment of the Cdv bands (Lindås et al., 2008). Accordingly, treatment of cells with tunicamycin, an antibiotic that causes cell-cycle arrest at the division phase, resulted in a 3-fold increase in the abundance of Cdv mid-cell bands. Overall, the combined data clearly indicate that the Cdv system is a major player in Sulfolobales cell division.

A detailed analysis of the main Cdv locus showed that it is composed of two transcription units, one for CdvA, and the second one for CdvB and CdvC (see **Figure 2B**). Transcription-level measurements showed that the up-regulation of cdvA preceded that of all four cdvB paralogs by ∼30 min (Samson et al., 2011). This suggests that CdvA mediates the division apparatus localization and recruits the downstream CdvB proteins. In support of this hypothesis, immunofluorescence microscopy showed a large number of CdvA bands that are localized outside the mid-cell, perpendicular to the division site or even across non-segregated chromosomes (Samson et al., 2011). In contrast, the CdvB band was detected only at mid-cell and rarely over non-segregated chromosomes (Lindås et al., 2008). Together, the data suggest that CdvA transduces the information regarding chromosome segregation to the assembly of the division apparatus.

Mutational and over-expression assays further implicated a central role for the Cdv system in Crenarchaeota cell division. Expression of a dominant-negative ATP-hydrolysis-deficient CdvC^{E260Q}, resulted in the formation of large cells that contain less than one (indicating apoptosis) or more than two (indicating a cell-cycle arrest) genome equivalents in the mutant strain (Samson et al., 2008). Similarly, over-expression of the CdvB wH domain resulted in large cells that were devoid of chromosomes (Samson et al., 2011). An additional study showed that deletion of either *S. acidocaldarius* CdvB1 or CdvB2 resulted in the formation of large cells with an increased amount of DNA (Yang and Driessen, 2014). This aberrant phenotype was accompanied by slower growth in liquid and the formation of smaller colonies on agar plates. Yet, these mutants were viable. This might indicate that CdvB1 and CdvB2 can functionally substitute for each other, albeit with some deficiency.

By contrast, deletion of CdvB3 resulted in a more severe phenotype. The growth rate in liquid was very slow, colonies did not grow on agar, and the cells were much larger in comparison to the ΔCdvB1 and the ΔCdvB2 mutants. In addition, the localization pattern of CdvA was aberrant, and many CdvA bands were localized at the edge of the cell, adjacent to the edge of the chromosome. Thus, CdvB3 plays an important but non-essential role in cell division. It will be interesting to check if the Ist1 homology that we identified contributes to this phenotype through interaction with CdvB1.

In contrast to *S. acidocaldarius*, in *S. islandicus* the function of the CdvB paralogs in cytokinesis appears to be reversed (Liu et al., 2017). Here it was found that while CdvB3 is dispensable for cell division and mainly acts in viral release, no viable ΔCdvB1 or ΔCdvB2 mutants could be constructed. Immunofluorescence microscopy detected a band of CdvB1 and CdvB2 at the division site, between segregated chromosomes or even before chromosome segregation (see **Figures 9B,C**). A mutant strain with a negligible expression of CdvB1 showed an aberrant phenotype that occurred in about 35% of the cases (see **Figure 9D**) where cells could not complete their division and stayed connected as a non-separable chain of cells. Over-expression of CdvB1-ΔC (which lacks the truncated MIM2 motif), also resulted in the formation of chains of cells. In contrast, over-expression of CdvB-ΔC arrested the cells in a peanut-like shape in about 33% of the cases. Thus, these data suggest that, while CdvB is mainly important for the execution of the early stage of division, *S. islandicus* CdvB1 acts at a later stage that is related to furrow maturation and final cell separation. Strikingly, over-expression of CdvB2-ΔC resulted in a phenotype where the two daughter *S. islandicus* cells stayed connected by a long (>2 μm) and narrow (∼100 nm) membrane tube with a blob at its center (see **Figure 9E**), a phenotype that clearly is reminiscent of the intracellular bridge and the mid-body of Metazoan cells. Both CdvB1 and CdvB2 localized to these mid-body-like structures, suggesting a role for these proteins (especially for CdvB2) in abscission. It is interesting to ask about the source of these different behaviors of CdvB1/2 mutants in *S. acidocaldarius* and *S. islandicus.* One possible explanation might be related to their interaction with CdvC which was not detected for *S. acidocaldarius* but was detected for *S. islandicus*. In particular, it should be interesting to check if these differences result from the Vta1-like homology in *S. islandicus* that we identified.

The overall picture that emerges from these biochemistry and cell-biology assays is that the Cdv system is a key player in cell division. Yet, a clear understanding of its biophysical mechanics is still missing. In *S. acidocaldarius,* Z-stack reconstruction of the CdvA band showed that it forms both open and closed rings (Samson et al., 2011). These data might suggest a similar biophysical mechanism as that of the bacterial FtsZ, which also forms non-continuous rings (Fu et al., 2010; Strauss et al., 2012; Holden et al., 2014). Cryo-EM tomography of dividing *S. acidocaldarius* cells, however, has detected a full-circle proteinaceous band with a radial thickness of ∼3.5 nm that was

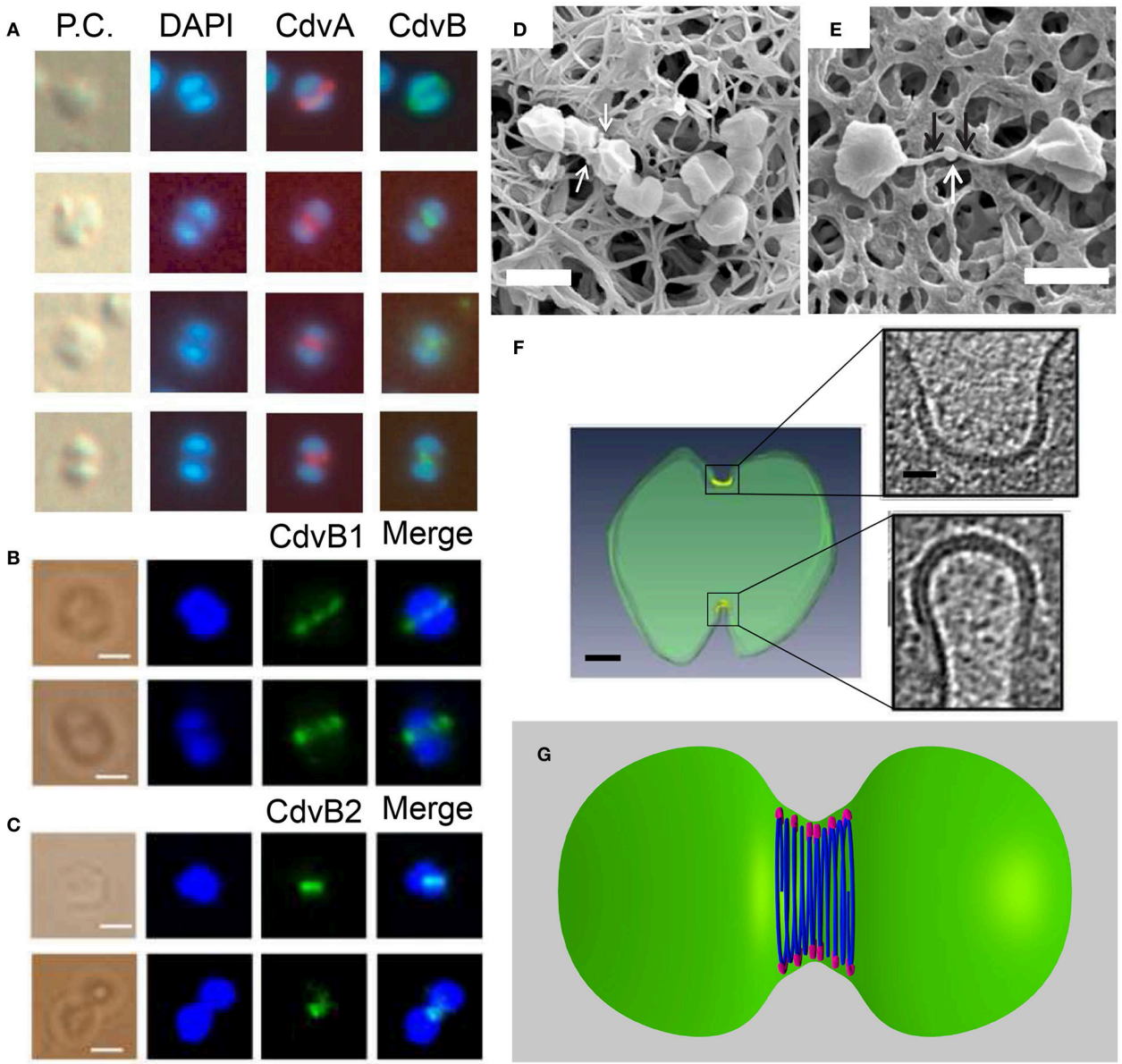

FIGURE 9 | The Cdv system in cytokinesis in Crenarchaeota. Left column: *In situ* immunofluorescence microscopy of Cdv proteins. **(A)** Intermediate steps during *S. acidocaldarius* cytokinesis showing localization of CdvA and CdvB bands that shrink in concomitant with the septum formation. P.C. denotes phase contrast. **(B,C)** Localization of *S. islandicus* CbvB1 **(B)** and CdvB2 **(C)** to the division site. The localization is visualized before chromosomes segregated (upper row in each panel) and during cytokinesis after chromosome segregation (lower raw in each panel). Scale bars 1 μm. **(D)** Mutant *S. islandicus* cells expressing a reduced level of CdvB1 are locked in a "chain-like" phenotype and cannot separate. **(E)** Mutant *S. islandicus* cells over-expressing CdvB2 form a "mid-body" like phenotype. Scale bars for **(D,E)** 2 μm. **(F)** Cryo-EM segmented image of a dividing *S. acidocaldarius* cell. Cell membrane is denoted in green and the thick protein belt at the cleavage furrow is denoted in yellow. Insets - zoom in of the two sides of the cleavage furrow. Scale bars - 150 nm for the whole cell, 40 nm for the insets. **(G)** "Hourglass" model of the Cdv system during cytokinesis in dividing *S. acidocaldarius* cell, showing CdvB polymers (blue) that are connected to the membrane via CdvA (purple). For clarity, CdvA is shown only at the top and bottom of the cell. In reality, it is located along the whole perimeter of the cell. **(A)** Is reproduced from Lindås et al. (2008) with permission, Copyright (2088) National Academy of Sciences. **(B–E)** Are reproduced from Liu et al. (2017) with permission. **(F)** Is reproduced from Dobro et al. (2013) with permission.

separated from the membrane by a distance of ∼6 nm in all cells, irrespective of the furrow ingression stage (see **Figure 9F**; Dobro et al., 2013). As cell division progressed, the width of the belt on the cell surface increased from 150 to 400 nm, while its thickness remained constant. As a result of the progressive septum formation and the increase of the belt surface area, the curvature of the belt also became larger, likely due to an active process of increasing Cdv protein mass at the division site as

cytokinesis progresses. Interestingly, in all cases, the division furrow at one side of the cell was more advanced and differently shaped than that on the other side. In fact, asymmetric division is also observed in many other bacterial and archaeal species, including those that use FtsZ (Yao et al., 2017). In addition, the surface layer (the proteinaceous cell-wall layer of archaea) was often incomplete, and many budding vesicles were detected at the division site. These data suggest a dynamic, asymmetric and cell-wall- and plasma-membrane-coupled division process. It was interpreted as representing a dense "hourglass" belt of CdvB that is coupled to the membrane through a sparse CdvA layer (see **Figure 9G**). According to this model, the increase in belt width represents an addition of CdvB coils, and coils at the middle of the furrow shrink faster than those at the belts side. In this framework, the reduction in diameter of the central CdvB coils is the driving force for cytokinesis. Yet, more data are needed before the full biophysical mechanism of Sulfolobales division can be inferred.

It is interesting to note that the localization picture of Cdv proteins was different for the rod-shaped Thaumarchaeon *N. maritimus* (Pelve et al., 2011). Here, CdvA and CdvC localized to the middle of the cell, in most cases correlated with chromosome segregation, but none of the CdvB paralogs showed the formation of a mid-cell band. The strength of the fluorescence signal of the CdvB1/2 paralogs (Nmar_0816 and Nmar_029) was correlated with the formation of CdvA-CdvC mid-cell localized band, but both CdvB paralogs showed a diffusive fluorescence pattern along the whole cell length and did not localize to a specific location. In fact, such a diffusive fluorescence signal was also observed for the *N. maritimus* FtsZ homolog, which lacks the conserved signature sequence for GTP binding that is crucial for FtsZ polymerization (Busiek and Margolin, 2011).

As is discussed below, these data might suggest that the division mechanism in some TACK organisms is in fact not directly related to the ESCRT-III membrane remodeling mechanism.

THE MECHANISM OF THE Cdv AND ESCRT MACHINERIES

Models of the ESCRT-III Membrane Remodeling

Different classes of theoretical models have attempted to explain membrane deformation by the ESCRT-III complex based on the *in vivo* data and the *in vitro* reconstitution of ESCRT-III higher-order structures. The first of these are dome-like models. The direct dome model was inspired by the dome-like structures that are observed at the tip of the CHMP2A:CHMP3 tubes (see **Figure 6C**; Fabrikant et al., 2009). According to this model, Snf7/CHMP4 polymers encircle a membrane patch and recruit Vps2/CHMP2 and Vps24/CHMP3 to form a dome-like structure within a narrow membrane neck with a typical diameter of 50 nm at its base (see **Figure 10A**). The key ingredient of this model is that a high binding affinity between the charged lipids and dome proteins compensate for the bending energy that is involved in membrane deformation so that the membrane follows the dome shape. At the tip of the dome, spontaneous fission can then occur. Similar to the case of MVB formation, a dome-like structure was predicted to drive membrane abscission during cytokinesis (Elia et al., 2012). However, the ESCRT system cannot remodel the membrane next to the Flemming body due to its size and rigidity. Instead a breakage of the filaments and their sliding away from the Flemming body toward the abscission site is predicted, where mechanic and elastic considerations allow the functioning of the ESCRT dome.

For HIV-I release, the major viral Gag protein binds the cell membrane, produces the early viral bud, and recruits ALIX and TSG101 to initiate CHMP4 polymerization. Thus, according to the dome-like model, the dome would cut the membrane from the virus side. However, deep-etch EM microscopy showed that the ESCRT-III funnel starts at the narrow part of the bud neck and widens toward the cytoplasm (Cashikar et al., 2014). This finding is also consistent with the fact that ESCRT-III proteins are generally not found in viral bodies after their release. Thus, a variation of the dome model, namely the inverse dome model, was suggested (see **Figure 10B**). According to this model, ESCRT-III polymerization is initiated from the virion side and grows from a large radius to a smaller one. At a certain point, the direction of growth is inverted, and the dome ends up as in the original dome model (Schöneberg et al., 2017).

A second class of models is based on the mechanical properties of CHMP4/Snf7 spirals structures. As was discussed above, a 2D spiral polymerization results in stress accumulation (Shen et al., 2014; Chiaruttini et al., 2015), which can be relieved if the spirals buckle into the form of a tube (Lenz et al., 2009). Since the membrane follows the ESCRT-III shape due to binding interactions, a tubular-shaped membrane can thus be formed. This model, however, does not explain how ESCRT-III induces membrane fission. Hence, it was suggested that for membrane fission, buckling occurs in the opposite direction, that is, from a tubular to a flat shape (see **Figure 10C**; Carlson et al., 2015). However, the physical basis for this hypothetical reversed buckling is unclear.

A variation of the buckling model suggests that the unique preferred curvature of various ESCRT-III subunits is the key factor for membrane abscission (Chiaruttini and Roux, 2017). Based on *in vitro* observations, it was suggested that *in vivo*, CHMP2/Vps2 and CHMP3/Vps24 might induce a localized change in the CHMP4/snf7 spirals curvature, and hence buckling (see **Figure 10D**). Still, similar to the simple stress-induced buckling mechanisms, it is not clear what will be the driving force for membrane fission. One possibility is that differential removal of subunits with a certain preferred curvature by Vps4 may drive shape transformation of the ESCRT-III polymers. Such differential removal of CHMP proteins can occur, for example, as result of the fact that different ESCRT-III subunits have a different affinity for Vps4 (as mentioned above there exist two orders of magnitude difference between the affinities of CHMP2A and CHMP4 for Vps4).

Finally, a third class of ESCRT-III abscission model, based on recent *in vitro* measurements of a high turnover rate of ESCRT-III monomers and similar dynamics *in vivo*, suggests that ESCRT-III are "live" polymers that are constantly remodeled by Vps4 (see

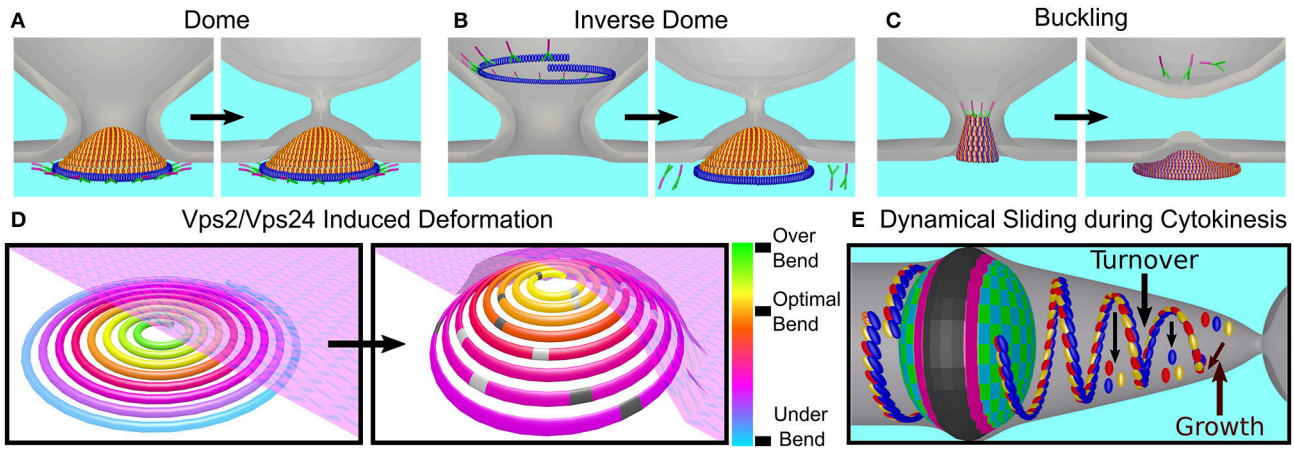

FIGURE 10 | Models of bud neck abscission by ESCRT-III. The function of ESCRT-I-II (green and pink) and ESCRT-III (red, Vps2; yellow, Vps24; and blue, Snf7) are shown for different models for the mechanisms of membrane remodeling by ESCRT proteins. **(A)** Dome model—ESCRT-I/II complex initiates the formation of an Vps2/24 dome from the cytoplasm side. The membrane is remodeled as results of its wrapping up tightly around the dome. **(B)** Reverse dome model - same as the dome model only that the ESCRT-III structure is initiated from the bud lumen. The bud grows but then turn over to end up in a configuration similar to the one in the dome model. The driving force for membrane remodeling is again the tight binding to the ESCRT-III dome. **(C)** Stress-induced buckling model—polymerization of ESCRT-III polymers results in the accumulation of stress due to the deviation from the preferred curvature. As a result, the ESCRT-III structure is transformed from a flat 2D one to a 3D spiral. Reverse buckling than causes the abscission of the membrane. **(D)** Membrane-curvature deformation upon Vps2/Vps24 (light and dark gray) binding to an Snf7 filament. According to this model, the driving force for the deformation of the ESCRT-III structure is the binding of Vps2/Vps24 for the Snf7 polymer. The sporadic binding creates a locally preferred curvature that is different from that of the Snf7 polymer. This promotes the buckling of the ESCRT-III structure. Since the membrane binds the ESCRT-III structure, it is remodeled by its buckling. **(E)** Dynamical polymerization of ESCRT-III filaments leading to membrane ingression - In this model, the ESCRT-III structure is not static, but dynamic. Polymerization and depolymerization from the end of the ESCRT-III structure, as well as from its middle, continually contribute to monomers turnover and global structure deformation that results in the membrane remodeling.

Figure 10E; Mierzwa et al., 2017). In this model, Vps4 may lead to growth of the polymer tip or to a differential removal of ESCRT-III subunits from the polymer core. Very recently, the dynamics of ESCRT proteins during MVB formation was measured using light-sheet microscopy (Adell et al., 2017), yielding also a high turnover rate and number fluctuations of ESCRT-III proteins that were coupled to Vps4 recruitment. The authors suggested that their data were inconsistent with existing ESCRT models. Instead, they suggested that ESCRT-III polymerizes and depolymerizes independently of Vps4. They further suggested that the main function of Vps4 is to bind together two or more ESCRT-III polymers, which can occur as result of the multiple binding sites for ESCRT-III that Vps4 possesses. This may result in condensation of the polymers network that, together with limited cargo space, results in membrane invagination, reduction of the bud neck size, and finally abscission. Yet, a detailed physical understanding of how this process, or alternative processes that depend on a high turnover rate of the ESCRT-III proteins, induce membrane remodeling and fission is still missing.

Comparison of the Cdv and ESCRT-III Systems

A breadth of experimental results has shown that the Cdv system is a key participant in cell division in Sulfolobales (and probably in Thermoproteales). Similar to the scenario in bacteria, there are two options for a mechanism that can underlie the division process. The first is that CdvB paralogs apply a force on the membrane leading to its deformation, similar to the ESCRT-III case. The second is that the Cdv system merely acts as a scaffold to coordinate coupling to cell wall deformation and local vesicle secretion/fusion. Here, we discuss these two possibilities.

The first point to consider in this context is the typical length scale over which the Cdv and ESCRT systems function. During cytokinesis, the ESCRT-III complex is initially assembled at the Flemming body that is about 1 μm in size. However, the ESCRT system cannot remodel the membrane at that site. Instead, it slides to the abscission site, which has a diameter of approximately 100 nm, similar to other ESCRT-III functioning sites (such as MVB or virus release buds). Thus, the ESCRT system acts only in the very last step of membrane abscission, while the diameter of the abscission site probably mainly depends on actin and tubulin remodeling. In contrast, the Cdv system acts throughout the whole phase of septum ingression, from its start where the diameter of the cell is about 1 μm to its end. Thus, it is not clear how the supposedly more primitive system (the Cdv system) can accommodate a more robust function over a broad span of membrane widths if the two systems share the same mechanism.

Another important point relates to the CdvB-CdvC affinity. For the ESCRT system, a span of interaction strengths exists between Vps4 and various ESCRT-III subunits. Some of these interactions are high-affinity, and they are necessary for the efficient recruitment of Vps4 from solution to the ESCRT-III complex (e.g., the IST1-VPS4 interactions in cytokinesis). However, for *S. acidocaldarius,* the MIM_{CdvB}-CdvC affinity is only moderate. Indeed, CdvC acts as a hexamer, and thus the apparent affinity to the CdvB band should be higher. Still, as Animalia use the large span of affinities of ESCRT-III proteins

to VPS4 so that abscission will be efficient, it is unclear how an efficient recruitment of CdvC from the cytoplasm is achieved in Crenarchaeota. If the recruitment efficiency of CdvC is much lower than in Metazoa, it may imply that the turnover rate of CdvB is lower. Thus, the recent suggestion that ESCRT-III can cut the membrane because of a high turnover of the subunits might not be relevant in archaea. One way to check this issue is to measure the ATPase-activity simulation of CdvC by CdvB.

An additional point to consider is the current lack of evidence for the formation of higher-order structures such as spirals, tubes or domes by CdvB paralogs *in vitro*. Of course, this can merely be an experimental issue that necessitates more efforts. Still, such evidence is awaiting, and this is especially important if ESCRT-III acts as a spiral spring. Since the sine qua non skeletal component of ESCRT-III spiral is Snf7, while CdvB is a homolog of the Vps2/Vps24/Did2 class, which shares a very low sequence homology with Snf7, it is a priori unclear if CdvB paralogs are geared to form spirals. Moreover, for a spiral-based mechanism to function, there must be an asymmetry between the base of the spiral to its buckled tip where abscission occurs. In the Cdv case, however, the band at the division site has a symmetric "hourglass" shape (Dobro et al., 2013), which probably precludes buckling-like mechanisms for the Cdv system.

A similar problem arises concerning the dome-based models. The dome model is based on the assumption that the membrane has a high affinity to the dome subunits (Fabrikant et al., 2009). These strong interactions compensate for the high energy penalty that is associated with bending the membrane. For the model to work, given reasonable affinity values, it is essential that every subunit will interact with the membrane. However, CdvB does not bind the membrane at all, and it is not clear, theoretically, if the sparse binding of CdvA to the membrane (Dobro et al., 2013) is sufficient to fulfill the model requirements. Of course, one may speculate that other CdvB paralogs may bind the membrane, but this remains to be shown.

Finally, there is a question regarding the actual orientation CdvB relative to the membrane. This problem stems from the fact that CdvA polymerized on the outside surface of liposomes (see **Figure 7B**; Dobro et al., 2013). Indeed, the curvature of these liposomes was not large, but if CdvA, which is supposed to act as the sole recruiter of CdvB, can bind the membrane from both sides, it raises questions regarding the orientation of CdvB relative to the membrane *in vivo*. Recall that for the ESCRT system, inversion of the membrane binding direction transferred the ESCRT-III proteins from an inverse-topology to a direct-topology membrane remodeling machinery (see **Figures 3F**, **6D** for the CHMP1B-IST1 case). Similarly, for bacteria, inversion of the FtsZ membrane binding direction caused it to form bands on the outside surface of vesicles instead of the inside surface (Osawa and Erickson, 2011). Thus, for the development of a comprehensive model of the Cdv system, future experiments will have to clarify the orientation of CdvA relative to the membrane.

Irrespective of the previous arguments, the strongest argument against the Cdv and the ESCRT-III having the same biophysical mechanism is the existence of the proteinaceous Surface-layer (S-layer) in the first case. The Sulfolobales S-layer is a cell-wall-like layer, and the sole protector against the turgor pressure (Engelhardt, 2007; Albers and Meyer, 2011). For a thin porous S-layer to function as a mechanical protection against turgor, the crystalline distance between adjacent S-layer monomers should be small, on the order of a few nm (Engelhardt, 2016). Otherwise, the membrane will bulge out. For Sulfolobales division, it was reported that, surprisingly, the S-layer was often incomplete (Dobro et al., 2013). Large voids in the S-layer would undoubtedly result in bulging out of the membrane, suggesting the presence of another supportive layer that can replace the S-layer locally and temporarily. We speculate that one of the functions of the dark band that was detected at the *S. acidocaldarius* division site (Dobro et al., 2013) is to protect the cell during membrane ingression (see **Figure 9F**). This might explain why this band was highly dense, in comparison to the sparsely distributed 17 nm cortical eukaryotic filaments (see **Figures 8G,H**). As mentioned above, at the *S. acidocaldarius* division site, many budding vesicles were observed. Note that also in Fungi and plants, the participation of the ESCRT system in cell division is related to vesicles delivery. In addition, it was suggested that the function of the ESCRT system during the abscission phase of the *C. elegans* embryo first division is to facilitate membrane removal (König et al., 2017). Thus, if the Sulfolobales division apparatus is composed of several proteins in addition to the Cdv system, the function of the Cdv system may be to deal with surplus membrane invagination, while other proteins may provide the mechanical support. Concomitantly, during cytokinesis, the S-layer should first be removed and then rebuilt at the septum site to reshaping the cell.

In light of this discussion we prefer the explanation that, in Crenarchaeota, the primary function of the Cdv system is related to vesiculation of the plasma membrane while other cofactors establish an inner protection layer against turgor. A comparison to the bacterial FtsZ may be fitting here: For many years, it was assumed that the primary function of FtsZ is to apply force on the membrane. However, it was recently shown that a major role of FtsZ is to coordinate the synthesis of cell wall material (Bisson-Filho et al., 2017; Yang et al., 2017). We also would like to suggest that CdvA's role in cytokinesis is more important than merely to recruit CdvB to the membrane. It will be interesting to check these hypotheses experimentally.

While above we discussed the mechanistic aspects of the Cdv and ESCRT-III systems, it also is of interest to discuss their evolutionary relationship. There are two possible evolutionary scenarios. According to the first, the Cdv system was a reversed-topology membrane-remodeling machinery that continued to develop in eukaryotes but sometimes lost its cytokinetic functionality (e.g., for yeast and plants). According to the second, the Cdv system developed its cytokinesis function independently in Crenarchaeota and Animalia and that this pattern represents a form of functional convergent evolution, where homologous protein systems participate in a similar biological pathway, but their role in this pathway is different due to a lack of evolutionary continuity. We argue that if indeed our mechanistic hypothesis is correct, and the Cdv system does not remodel the membrane directly, the second evolutionary scenario is more likely. One way to further study the evolutionary relationship of the ESCRT/Cdv systems

is to study their functional mechanics in protists and the archaeal Asgard phylum, to see if they function similarly as in animals.

CONCLUSIONS AND OUTLOOK

During the last two decades, the eukaryotic ESCRT field was established and matured. We hope that, similarly, the next decade will considerably expand our understanding of the archaeal Cdv system. We envision that structural biology studies will continue to shed light on the function of Cdv proteins. In particular, high-resolution structures of CdvA and the different CdvB paralogs would be beneficial to assess their role in cytokinesis. Similarly, high-resolution structure of CdvC in its ATP-bound form should show whether it forms a helical hexamer, like Vps4, or whether it forms a hexameric ring also in its active ATP-bound state.

In vivo studies, and especially the application of advanced light microscopy tools to study the Cdv system in real time, bear great potential to expand our understanding of the Cdv system. In particular, such studies should be able to disentangle the exact relations between chromosome segregation and CdvA localization. They should also allow to identify the possible existence of regulatory mechanisms similar to the "NoCut" check-point, which assures DNA clearance from the division site before cytokinesis. In this context, it will also be interesting to study the possible interaction of CdvA and the DNA and, if found *in vivo*, to understand its possible physiological consequences. A particular emphasis should be directed to study the exact function of CdvB paralogs in different Crenarchaeota species, and to decipher the coupling to CdvC and the S-layer synthesis machinery. The study of mutations of Cdv proteins will undoubtedly contribute significantly in future work on the system, and will likely serve as a valuable source for deciphering its mechanism of action. More advanced i*n vitro* studies that will reconstitute the Cdv system in vesicles and synthetic cells (Caspi and Dekker, 2014; Härtel and Schwille, 2014) or on supported lipid membranes will add invaluable information regarding the different higher-order structures that the CdvA/CdvB paraloges system can form. In particular, such studies will be able to show if CdvB paralogs can form spirals or domes like the ESCRT-III subunits.

Altogether, we are optimistic that future experiments will clarify the biophysical mechanism as well as the evolutionary role of the Cdv system. We hope that this review has been of help to clarify some important points and expand the discussion regarding the archaeal Cdv system in cytokinesis. We also hope that it will attract new scientists to study archaeal division, which, in every sense, constitutes a fascinating topic to study in the context of the great variety of cell-division modes that exist in nature.

AUTHOR CONTRIBUTIONS

All authors listed have made a substantial, direct and intellectual contribution to the work, and approved it for publication.

ACKNOWLEDGMENTS

We thank Federico Fanalista and Alberto Blanch Jover and the two referees for a critical reading of the manuscript. CD is supported by the European Research Council Advanced Grant SynDiv (No. 669598).

SUPPLEMENTARY MATERIAL

The Supplementary Material for this article can be found online at: https://www.frontiersin.org/articles/10.3389/fmicb.2018.00174/full#supplementary-material

REFERENCES

Adell, M. A. Y., Migliano, S. M., Upadhyayula, S., Bykov, Y. S., Sprenger, S., Pakdel, M., et al. (2017). Recruitment dynamics of ESCRT-III and Vps4 to endosomes and implications for reverse membrane budding. *eLife* 6:e31652. doi: 10.7554/eLife.31652

Agromayor, M., Carlton, J. G., Phelan, J. P., Matthews, D. R., Carlin, L. M., Ameer-Beg, S., et al (2009). Essential role of hIST1 in cytokinesis. *Mol. Biol. Cell,* 20, 1374–1387. doi: 10.1091/mbc.E08-05-0474

Albers, S.-V., and Meyer, B. H. (2011). The archaeal cell envelope. *Nat. Rev. Microbiol.* 9, 414–426. doi: 10.1038/nrmicro2576

Azmi, I. F., Davies, B. A., Xiao, J., Babst, M., Xu, Z., and Katzmann, D. J. (2008). ESCRT-III family members stimulate Vps4 ATPase activity directly or via Vta1. *Dev. Cell* 14, 50–61. doi: 10.1016/j.devcel.2007.10.021

Babst, M., Katzmann, D. J., Estepa-Sabal, E. J., Meerloo, T., and Emr, S. D. (2002). Escrt-III: an endosome-associated heterooligomeric protein complex required for mvb sorting. *Dev. Cell* 3, 271–282. doi: 10.1016/S1534-5807(02)00220-4

Bajorek, M., Morita, E., Skalicky, J. J., Morham, S. G., Babst, M., and Sundquist, W. I. (2009a). Biochemical analyses of human IST1 and its function in cytokinesis. *Mol. Biol. Cell* 20, 1360–1373. doi: 10.1091/mbc.E08-05-0475

Bajorek, M., Schubert, H. L., McCullough, J., Langelier, C., Eckert, D. M., Stubblefield, W.-M. B., et al. (2009b). Structural basis for ESCRT-III protein autoinhibition. *Nat. Struct. Mol. Biol.* 16, 754–762. doi: 10.1038/nsmb.1621

Barr, F. A., and Gruneberg, U. (2007). Cytokinesis: placing and making the final cut. *Cell* 131, 847–860. doi: 10.1016/j.cell.2007.11.011

Baumann, P., and Jackson, S. P. (1996). An archaebacterial homologue of the essential eubacterial cell division protein FtsZ. *Proc. Natl. Acad. Sci. U.S.A.* 93, 6726–6730. doi: 10.1073/pnas.93.13.6726

Bhutta, M. S., Roy, B., Gould, G. W., and McInerny, C. J. (2014). A complex network of interactions between mitotic kinases, phosphatases and ESCRT proteins regulates septation and membrane trafficking in *S. pombe*. *PLoS ONE* 9:e111789. doi: 10.1371/journal.pone.0111789

Bisson-Filho, A. W., Hsu, Y.-P., Squyres, G. R., Kuru, E., Wu, F., Jukes, C., et al. (2017). Treadmilling by FtsZ filaments drives peptidoglycan synthesis and bacterial cell division. *Science* 355, 739–743. doi: 10.1126/science.aak9973

Bodon, G., Chassefeyre, R., Pernet-Gallay, K., Martinelli, N., Effantin, G., Hulsik, D. L., et al. (2011). Charged multivesicular body protein 2B (CHMP2B) of the endosomal sorting complex required for transport-III (ESCRT-III) polymerizes into helical structures deforming the plasma membrane. *J. Biol. Chem.* 286, 40276–40286. doi: 10.1074/jbc.M111.283671

Boura, E., Różycki, B., Chung, H. S., Herrick, D. Z., Canagarajah, B., Cafiso, et al. (2012). Solution structure of the ESCRT-I and -II supercomplex: implications for membrane budding and scission. *Structure* 20, 874–886. doi: 10.1016/j.str.2012.03.008

Božič, B., Guven, J., Vázquez-Montejo, P., and Svetina, S. (2014). Direct and remote constriction of membrane necks. *Phys. Rev. E* 89:052701. doi: 10.1103/PhysRevE.89.052701

Busiek, K. K., and Margolin, W. (2011). Split decision: a thaumarchaeon encoding both FtsZ and Cdv cell division proteins chooses Cdv for cytokinesis. *Mol. Microbiol.* 82, 535–538. doi: 10.1111/j.1365-2958.2011.07833.x

Caillat, C., Macheboeuf, P., Wu, Y., McCarthy, A. A., Boeri-Erba, E., Effantin, G., et al. (2015). Asymmetric ring structure of Vps4 required for ESCRT-III disassembly. *Nat. Commun.* 6:8781. doi: 10.1038/ncomms9781

Campsteijn, C., Vietri, M., and Stenmark, H. (2016). Novel ESCRT functions in cell biology: spiraling out of control? *Curr. Opin. Cell Biol.* 41, 1–8. doi: 10.1016/j.ceb.2016.03.008

Capalbo, L., Mela, I., Abad, M. A., Jeyaprakash, A. A., Edwardson, J. M., and D'Avino, P. P. (2016). Coordinated regulation of the ESCRT-III component CHMP4C by the chromosomal passenger complex and centralspindlin during cytokinesis. *Open Biol.* 6:160248. doi: 10.1098/rsob.160248

Capalbo, L., Montembault, E., Takeda, T., Bassi, Z. I., Glover, D. M., and D'Avino, P. P. (2012). The chromosomal passenger complex controls the function of endosomal sorting complex required for transport-III Snf7 proteins during cytokinesis. *Open Biol.* 2:120070. doi: 10.1098/rsob.120070

Carlson, L.-A., Shen, Q.-T., Pavlin, M. R., and Hurley, J. H. (2015). ESCRT filaments as spiral springs. *Dev. Cell* 35, 397–398. doi: 10.1016/j.devcel.2015.11.007

Carlton, J. G., Agromayor, M., and Martin-Serrano, J. (2008). Differential requirements for Alix and ESCRT-III in cytokinesis and HIV-1 release. *Proc. Natl. Acad. Sci. U.S.A.* 105, 10541–10546. doi: 10.1073/pnas.0802008105

Carlton, J. G., Caballe, A., Agromayor, M., Kloc, M., and Martin-Serrano, J. (2012). ESCRT-III governs the Aurora B-mediated abscission checkpoint through CHMP4C. *Science* 336, 220–225. doi: 10.1126/science.1217180

Carlton, J. G., and Martin-Serrano, J. (2007). Parallels between cytokinesis and retroviral budding: a role for the ESCRT machinery. *Science* 316, 1908–1912. doi: 10.1126/science.1143422

Cashikar, A. G., Shim, S., Roth, R., Maldazys, M. R., Heuser, J. E., and Hanson, P. I. (2014). Structure of cellular ESCRT-III spirals and their relationship to HIV budding. *eLife* 3:e02184. doi: 10.7554/eLife.02184

Caspi, Y., and Dekker, C. (2014). Divided we stand: splitting synthetic cells for their proliferation. *Sys. Synth. Biol.* 8, 249–269. doi: 10.1007/s11693-014-9145-7

Cheffings, T. H., Burroughs, N. J., and Balasubramanian, M. K. (2016). Actomyosin ring formation and tension generation in eukaryotic cytokinesis. *Curr. Biol.* 26, R719–R737. doi: 10.1016/j.cub.2016.06.071

Chen, C.-T., Ettinger, A. W., Huttner, W. B., and Doxsey, S. J. (2013). Resurrecting remnants: the lives of post-mitotic midbodies. *Trends Cell Biol.* 23, 118–128. doi: 10.1016/j.tcb.2012.10.012

Chiaruttini, N., Redondo-Morata, L., Colom, A., Humbert, F., Lenz, M., Scheuring, S., et al. (2015). Relaxation of loaded ESCRT-III spiral springs drives membrane deformation. *Cell* 163, 866–879. doi: 10.1016/j.cell.2015.10.017

Chiaruttini, N., and Roux, A. (2017). Dynamic and elastic shape transitions in curved ESCRT-III filaments. *Curr. Opin. Cell. Biol.* 47, 126–135. doi.org/10.1016/j.ceb.2017.07.002

Christ, L., Wenzel, E. M., Liestøl, K., Raiborg, C., Campsteijn, C., and Stenmark, H. (2016). ALIX and ESCRT-I/II function as parallel ESCRT-III recruiters in cytokinetic abscission. *J. Cell Biol.* 212, 499–513. doi: 10.1083/jcb.201507009

Connell, J. W., Lindon, C., Luzio, J. P., and Reid, E. (2009). Spastin couples microtubule severing to membrane traffic in completion of cytokinesis and secretion. *Traffic* 10, 42–56. doi: 10.1111/j.1600-0854.2008.00847.x

Coonrod, E. M., and Stevens, T. H. (2010). The yeast vps class E mutants: the beginning of the molecular genetic analysis of multivesicular body biogenesis. *Mol. Biol. Cell* 21, 4057–4060. doi: 10.1091/mbc.E09-07-0603

Daumke, O., Roux, A., Haucke, V. (2014). BAR domain scaffolds in dynamin-mediated membrane fission. *Cell* 156, 882–892. doi: 10.1016/j.cell.2014.02.017

Dimaano, C., Jones, C. B., Hanono, A., Curtiss, M., and Babst, M. (2008). Ist1 regulates Vps4 localization and assembly. *Mol. Biol. Cell* 19, 465–474. doi: 10.1091/mbc.E07-08-0747

Dobro, M. J., Samson, R. Y., Yu, Z., McCullough, J., Ding, H. J., Chong, P. L.-G., et al. (2013). Electron cryotomography of ESCRT assemblies and dividing Sulfolobus cells suggests that spiraling filaments are involved in membrane scission. *Mol. Biol. Cell* 24, 2319–2327. doi: 10.1091/mbc.E12-11-0785

Du, S., and Lutkenhaus, J. (2017). Assembly and activation of the Escherichia coli divisome. *Mol. Microbiol.* 105, 177–187. doi: 10.1111/mmi.13696

Effantin, G., Dordor, A., Sandrin, V., Martinelli, N., Sundquist, W. I., Schoehn, G., et al. (2013). ESCRT-III CHMP2A and CHMP3 form variable helical polymers in vitro and act synergistically during HIV-1 budding. *Cell. Microbiol.* 15, 213–226. doi: 10.1111/cmi.12041

Elia, N., Fabrikant, G., Kozlov, M. M., and Lippincott-Schwartz, J. (2012). Computational model of cytokinetic abscission driven by ESCRT-III polymerization and remodeling. *Biophys. J.* 102, 2309–2320. doi: 10.1016/j.bpj.2012.04.007

Elia, N., Sougrat, R., Spurlin, T. A., Hurley, J. H., and Lippincott-Schwartz, J. (2011). Dynamics of endosomal sorting complex required for transport (ESCRT) machinery during cytokinesis and its role in abscission. *Proc. Natl. Acad. Sci. U.S.A.* 108, 4846–4851. doi: 10.1073/pnas.1102714108

Engelhardt, H. (2007). Are S-layers exoskeletons? The basic function of protein surface layers revisited. *J. Struct. Biol.* 160, 115–124. doi: 10.1016/j.jsb.2007.08.003

Engelhardt, H. (2016). *S-Layers, eLS.* Hoboken, NJ: John Wiley and Sons, Ltd.

Ettema, T. J. G., Lindås, A.-C., and Bernander, R. (2011). An actin-based cytoskeleton in archaea. *Mol. Microbiol.* 80, 1052–1061. doi: 10.1111/j.1365-2958.2011.07635.x

Fabrikant, G., Lata, S., Riches, J. D., Briggs, J. A. G., Weissenhorn, W., and Kozlov, M. M. (2009). Computational model of membrane fission catalyzed by ESCRT-III. *PLoS Comput. Biol.* 5:e1000575. doi: 10.1371/journal.pcbi.1000575

Faini, M., Beck, R., Wieland, F. T., and Briggs, J. A. G. (2013). Vesicle coats: structure, function, and general principles of assembly. *Trends Cell Biol.* 23, 279–288. doi: 10.1016/j.tcb.2013.01.005

Field, M. C., and Dacks, J. B. (2009). First and last ancestors: reconstructing evolution of the endomembrane system with ESCRTs, vesicle coat proteins, and nuclear pore complexes. *Curr. Opin. Cell Biol.* 21, 4–13. doi: 10.1016/j.ceb.2008.12.004

Frémont, S., Hammich, H., Bai, J., Wioland, H., Klinkert, K., Rocancourt, M., et al. (2017). Oxidation of F-actin controls the terminal steps of cytokinesis. *Nat. Commun.* 8:14528. doi: 10.1038/ncomms14528

Fröls, S., Gordon, P. M. K., Panlilio, M. A., Duggin, I. G., Bell, S. D., Sensen, C. W., et al. (2007). Response of the hyperthermophilic archaeon Sulfolobus solfataricus to UV damage. *J. Bacteriol.* 189, 8708–8718. doi: 10.1128/JB.01016-07

Fu, G., Huang, T., Buss, J., Coltharp, C., Hensel, Z., and Xiao, J. (2010). *In vivo* structure of the E. coli FtsZ-ring revealed by photoactivated localization microscopy (PALM). *PLoS ONE* 5:e12680. doi: 10.1371/journal.pone.0012680

Gajiwala, K. S., and Burley, S. K. (2000). Winged helix proteins. *Curr. Opin. Struct. Biol.* 10, 110–116. doi: 10.1016/S0959-440X(99)00057-3

Ghazi-Tabatabai, S., Saksena, S., Short, J. M., Pobbati, A. V., Veprintsev, D. B., Crowther, R. A., et al. (2008). Structure and disassembly of filaments formed by the ESCRT-III subunit Vps24. *Structure* 16, 1345–1356. doi: 10.1016/j.str.2008.06.010

Goliand, I., Nachmias, D., Gershony, O., and Elia, N. (2014). Inhibition of ESCRT-II-CHMP6 interactions impedes cytokinetic abscission and leads to cell death. *Mol. Biol. Cell* 25, 3740–3748. doi: 10.1091/mbc.E14-08-1317

Götz, D., Paytubi, S., Munro, S., Lundgren, M., Bernander, R., and White, M. F. (2007). Responses of hyperthermophilic crenarchaea to UV irradiation. *Genome Biol.* 8:R220. doi: 10.1186/gb-2007-8-10-r220

Guizetti, J., Schermelleh, L., Mäntler, J., Maar, S., Poser, I., Leonhardt, H., et al. (2011). Cortical constriction during abscission involves helices of ESCRT-III-dependent filaments. *Science* 331, 1616–1620. doi: 10.1126/science.1201847

Haeusser, D. P., and Margolin, W. (2016). Splitsville: structural and functional insights into the dynamic bacterial Z ring. *Nat. Rev. Microbiol.* 4:305. doi: 10.1038/nrmicro.2016.26

Han, H., Monroe, N., Votteler, J., Shakya, B., Sundquist, W. I., and Hill, C. P. (2015). Binding of substrates to the central pore of the Vps4 ATPase is autoinhibited by the Microtubule Interacting and Trafficking (MIT) domain and activated by MIT interacting motifs (MIMs). *J. Biol. Chem.* 290, 13490–13499. doi: 10.1074/jbc.M115.642355

Hanson, P. I., Roth, R., Lin, Y., and Heuser, J. E. (2008). Plasma membrane deformation by circular arrays of ESCRT-III protein filaments. *J. Cell Biol.* 180, 389–402. doi: 10.1083/jcb.200707031

Härtel, T., and Schwille, P. (2014). ESCRT-III mediated cell division in Sulfolobus acidocaldarius - a reconstitution perspective. *Front. Microbiol.* 5:257. doi: 10.3389/fmicb.2014.00257

Henne, W. M., Buchkovich, N. J., Zhao, Y., and Emr, S. D. (2012). The endosomal sorting complex ESCRT-II mediates the assembly and architecture of ESCRT-III helices. *Cell* 151, 356–371. doi: 10.1016/j.cell.2012.08.039

Hobel, C. F., Albers, S. V., Driessen, A. J., and Lupas, A. N. (2008). The Sulfolobus solfataricus AAA protein Sso0909, a homologue of the eukaryotic ESCRT Vps4 ATPase. *Biochem. Soc. Trans.* 36, 94–98. doi: 10.1042/BST 0360094

Holden, S. J., Pengo, T., Meibom, K. L., Fernandez, C. F., Collier, J., and Manley, S. (2014). High throughput 3D super-resolution microscopy reveals Caulobacter crescentus *in vivo* Z-ring organization. *Proc. Natl. Acad. Sci. U.S.A.* 111, 4566–4571. doi: 10.1073/pnas.1313368111

Horn, C., Paulmann, B., Kerlen, G., Junker, N., and Huber, H. (1999). *In vivo* observation of cell division of anaerobic hyperthermophiles by using a high-intensity dark-field microscope. *J. Bacteriol.* 181, 5114–5118.

Hurley, J. H. (2015). ESCRTs are everywhere. *EMBO J.* 34, 2398–2407. doi: 10.15252/embj.201592484

Hurley, J. H., and Yang, D. (2008). MIT domainia. *Dev. Cell* 14, 6–8. doi: 10.1016/j.devcel.2007.12.013

Im, Y. J., Wollert, T., Boura, E., and Hurley, J. H. (2009). Structure and function of the ESCRT-II-III interface in multivesicular body biogenesis. *Dev. Cell* 17, 234–243. doi: 10.1016/j.devcel.2009.07.008

Izoré, T., Kureisaite-Ciziene, D., McLaughlin, S. H., and Löwe, J. (2016). Crenactin forms actin-like double helical filaments regulated by arcadin-2. *eLife* 5:e21600. doi: 10.7554/eLife.21600

Kelley, L. A., and Sternberg, M. J. (2009). Protein structure prediction on the Web: a case study using the Phyre server. *Nat. Protoc.* 4, 363–371. doi: 10.1038/nprot.2009.2

Kieffer, C., Skalicky, J. J., Morita, E., De Domenico, I., Ward, D. M., Kaplan, J., et al. (2008). Two distinct modes of ESCRT-III recognition are required for VPS4 functions in lysosomal protein targeting and HIV-1 budding. *Dev. Cell* 15, 62–73. doi: 10.1016/j.devcel.2008.05.014

Kojima, R., Obita, T., Onoue, K., and Mizuguchi, M. (2016). Structural fine-tuning of MIT-Interacting Motif 2 (MIM2) and allosteric regulation of ESCRT-III by Vps4 in yeast. *J. Mol. Biol.* 428, 2392–2404. doi: 10.1016/j.jmb.2016.04.007

König, J., Frankel, E., Audhya, A., and Müller-Reichert, T. (2017). Membrane remodeling during embryonic abscission in caenorhabditis elegans. *J. Cell Biol.* 216, 1277–1286. doi: 10.1083/jcb.201607030

Lafaurie-Janvore, J., Maiuri, P., Wang, I., Pinot, M., Manneville, J.-B., Betz, T., et al. (2013). ESCRT-III assembly and cytokinetic abscission are induced by tension release in the intercellular bridge. *Science* 339, 1625–1629. doi: 10.1126/science.1233866

Lata, S., Roessle, M., Solomons, J., Jamin, M., Gottlinger, H. G., Svergun, D. I., et al. (2008). Structural basis for autoinhibition of ESCRT-III CHMP3. *J. Mol. Biol.* 378, 818–827. doi: 10.1016/j.jmb.2008.03.030

Lee, H. H., Elia, N., Ghirlando, R., Lippincott-Schwartz, J., and Hurley, J. H. (2008). Midbody targeting of the ESCRT machinery by a noncanonical coiled coil in CEP55. *Science* 322, 576–580. doi: 10.1126/science.1162042

Leigh, J. A., Albers, S.-V., Atomi, H., and Allers, T. (2011). Model organisms for genetics in the domain Archaea: methanogens, halophiles, Thermococcales and Sulfolobales. *FEMS Microbiol. Rev.* 35, 577–608. doi: 10.1111/j.1574-6976.2011.00265.x

Lenz, M., Crow, D. J. G., and Joanny, J.-F. (2009). Membrane buckling induced by curved filaments. *Phys. Rev. Lett.* 103:038101. doi: 10.1103/PhysRevLett.103.038101

Leung, K. F., Dacks, J. B., and Field, M. C. (2008). Evolution of the multivesicular body ESCRT machinery; retention across the eukaryotic lineage. *Traffic* 9, 1698–1716. doi: 10.1111/j.1600-0854.2008.00797.x

Lindås, A.-C., Karlsson, E. A., Lindgren, M. T., Ettema, T. J., and Bernander, R. (2008). A unique cell division machinery in the Archaea. *Proc. Natl. Acad. Sci. U.S.A.* 105, 18942–18946. doi: 10.1073/pnas.0809467105

Liu, J., Gao, R., Li, C., Ni, J., Yang, Z., Zhang, Q., et al. (2017). Functional assignment of multiple ESCRT-III homologs in cell division and budding in Sulfolobus islandicus. *Mol. Microbiol.* 105, 540–553. doi: 10.1111/mmi.13716

Lundgren, M., Malandrin, L., Eriksson, S., Huber, H., and Bernander, R. (2008). Cell cycle characteristics of crenarchaeota: unity among diversity. *J. Bacteriol.* 190, 5362–5367. doi: 10.1128/JB.00330-08

Makarova, K. S., Yutin, N., Bell, S. D., and Koonin, E. V. (2010). Evolution of diverse cell division and vesicle formation systems in Archaea. *Nat. Rev. Microbiol.* 8:731. doi: 10.1038/nrmicro2406

Margolin, W., Wang, R., and Kumar, M. (1996). Isolation of an ftsZ homolog from the archaebacterium halobacterium salinarium: implications for the evolution of FtsZ and tubulin. *J. Bacteriol.* 178, 1320–1327. doi: 10.1128/jb.178.5.1320-1327.1996

McCullough, J., Clippinger, A. K., Talledge, N., Skowyra, M. L., Saunders, M. G., Naismith, T. V., et al. (2015). Structure and membrane remodeling activity of ESCRT-III helical polymers. *Science* 350, 1548–1551. doi: 10.1126/science.aad8305

McMurray, M. A., Stefan, C. J., Wemmer, M., Odorizzi, G., Emr, S. D., and Thorner, J. (2011). Genetic interactions with mutations affecting septin assembly reveal ESCRT functions in budding yeast cytokinesis. *Biol. Chem.* 392, 699–712. doi: 10.1515/BC.2011.091

Mierzwa, B., and Gerlich, D. W. (2014). Cytokinetic abscission: molecular mechanisms and temporal control. *Dev. Cell* 31, 525–538. doi: 10.1016/j.devcel.2014.11.006

Mierzwa, B. E., Chiaruttini, N., Redondo-Morata, L., von Filseck, J. M., König, J., Larios, J., et al (2017). Dynamic subunit turnover in ESCRT-III assemblies is regulated by Vps4 to mediate membrane remodelling during cytokinesis. *Nat. Cell Biol.* 19, 787–798. doi: 10.1038/ncb3559

Monroe, N., Han, H., Gonciarz, M. D., Eckert, D. M., Karren, M. A., Whitby, F. G., et al. (2014). The oligomeric state of the active Vps4 AAA ATPase. *J. Mol. Biol.* 426, 510–525. doi: 10.1016/j.jmb.2013.09.043

Monroe, N., Han, H., Shen, P. S., Sundquist, W. I., and Hill, C. P. (2017). Structural basis of protein translocation by the Vps4-Vta1 AAA ATPase. *eLife* 6:e24487. doi: 10.7554/eLife.24487

Moriscot, C., Gribaldo, S., Jault, J.-M., Krupovic, M., Arnaud, J., Jamin, M., et al. (2011). Crenarchaeal CdvA forms double-helical filaments containing DNA and interacts with ESCRT-III-like CdvB. *PLoS ONE* 6:e21921. doi: 10.1371/journal.pone.0021921

Morita, E., Sandrin, V., Chung, H.-Y., Morham, S. G., Gygi, S. P., Rodesch, C. K., et al. (2007). Human ESCRT and ALIX proteins interact with proteins of the midbody and function in cytokinesis. *EMBO J.* 26, 4215–4227. doi: 10.1038/sj.emboj.7601850

Muzioł, T., Pineda-Molina, E., Ravelli, R. B., Zamborlini, A., Usami, Y., Göttlinger, H., et al. (2006). Structural basis for budding by the ESCRT-III factor CHMP3. *Dev. Cell* 10, 821–830. doi: 10.1016/j.devcel.2006.03.013

Nagahisa, K., Nakamura, T., Fujiwara, S., Imanaka, T., and Takagi, M. (2000). Characterization of FtsZ homolog from hyperthermophilic archaeon Pyrococcus kodakaraensis kod1. *J. Biosci. Bioeng.* 89, 181–187. doi: 10.1016/S1389-1723(00)88734-4

Nähse, V., Christ, L., Stenmark, H., and Campsteijn, C. (2017). The abscission checkpoint: making it to the final cut. *Trends Cell Biol.* 27, 1–11. doi: 10.1016/j.tcb.2016.10.001

Ng, K.-H., Srinivas, V., Srinivasan, R., and Balasubramanian, M. (2013). The Nitrosopumilus maritimus CdvB, but not FtsZ, assembles into polymers. *Archaea* 2013, 1–10. doi: 10.1155/2013/104147

Nogales, E., Downing, K. H., Amos, L. A., and Löwe, J. (1998). Tubulin and FtsZ form a distinct family of GTPases. *Nat. Struct. Biol.* 5, 451–458. doi: 10.1038/nsb0698-451

Obita, T., Saksena, S., Ghazi-Tabatabai, S., Gill, D. J., Perisic, O., Emr, S. D., et al. (2007). Structural basis for selective recognition of ESCRT-III by the AAA ATPase Vps4. *Nature* 449:735. doi: 10.1038/nature06171

Osawa, M., and Erickson, H. P. (2011). Inside-out Z rings–constriction with and without GTP hydrolysis. *Mol. Microbiol.* 81, 571–579. doi: 10.1111/j.1365-2958.2011.07716.x

Pelve, E. A., Lindås, A.-C., Martens-Habbena, W., de la Torre, J. R., Stahl, D. A., and Bernander, R. (2011). Cdv-based cell division and cell cycle organization in the thaumarchaeon Nitrosopumilus maritimus. *Mol. Microbiol.* 82, 555–566. doi: 10.1111/j.1365-2958.2011.07834.x

Poplawski, A., Gullbrand, B., and Bernander, R. (2000). The ftsZ gene of Haloferax mediterranei: sequence, conserved gene order, and visualization of the FtsZ ring. *Gene* 242, 357–367. doi: 10.1016/S0378-1119(99)00517-X

Rowlett, V. W. and Margolin, W. (2015). The Min system and other nucleoid-independent regulators of Z ring positioning. *Front. Microbiol.* 6:478. doi: 10.3389/fmicb.2015.00478

Saksena, S., Wahlman, J., Teis, D., Johnson, A. E., and Emr, S. D. (2009). Functional reconstitution of ESCRT-III assembly and disassembly. *Cell* 136, 97–109. doi: 10.1016/j.cell.2008.11.013

Samson, R. Y., Obita, T., Freund, S. M., Williams, R. L., and Bell, S. D. (2008). A role for the ESCRT system in cell division in archaea. *Science* 322, 1710–1713. doi: 10.1126/science.1165322

Samson, R. Y., Obita, T., Hodgson, B., Shaw, M. K., Chong, P. L.-G., Williams, R. L., et al. (2011). Molecular and structural basis of ESCRT-III recruitment to membranes during archaeal cell division. *Mol. Cell* 41, 186–196. doi: 10.1016/j.molcel.2010.12.018

Schiel, J. A., Simon, G. C., Zaharris, C., Weisz, J., Castle, D., Wu, C. C., et al. (2012). FIP3-endosome-dependent formation of the secondary ingression mediates ESCRT-III recruitment during cytokinesis. *Nat. Cell Biol.* 14, 1068–1078. doi: 10.1038/ncb2577

Schöneberg, J., Lee, I.-H., Iwasa, J. H., and Hurley, J. H. (2017). Reverse-topology membrane scission by the ESCRT proteins. *Nat. Rev. Mol. Cell Biol.* 18, 5–17. doi: 10.1038/nrm.2016.121

Shen, Q.-T., Schuh, A. L., Zheng, Y., Quinney, K., Wang, L., Hanna, M., et al. (2014). Structural analysis and modeling reveals new mechanisms governing ESCRT-III spiral filament assembly. *J. Cell Biol.* 206, 763–777. doi: 10.1083/jcb.201403108

Sherman, S., Kirchenbuechler, D., Nachmias, D., Tamir, A., Werner, S., Elbaum, M., et al. (2016). Resolving new ultrastructural features of cytokinetic abscission with soft-X-ray cryo-tomography. *Sci. Rep.* 6:27629. doi: 10.1038/srep27629

Shestakova, A., Hanono, A., Drosner, S., Curtiss, M., Davies, B. A., Katzmann, D. J., et al. (2010). Assembly of the AAA ATPase Vps4 on ESCRT-III. *Mol. Biol. Cell* 21, 1059–1071. doi: 10.1091/mbc.E09-07-0572

Shim, S., Kimpler, L. A., and Hanson, P. I. (2007). Structure/function analysis of four core ESCRT-III proteins reveals common regulatory role for extreme C-terminal domain. *Traffic* 8, 1068–1079. doi: 10.1111/j.1600-0854.2007.00584.x

Söderström, B., Skoog, K., Blom, H., Weiss, D. S., Heijne, G., and Daley, D. O. (2014). Disassembly of the divisome in Escherichia coli: evidence that FtsZ dissociates before compartmentalization. *Mol. Microbiol.* 92, 1–9. doi: 10.1111/mmi.12534

Spang, A., Saw, J. H., Jørgensen, S. L., Zaremba-Niedzwiedzka, K., Martijn, J., Lind, A. E., et al. (2015). Complex archaea that bridge the gap between prokaryotes and eukaryotes. *Nature* 521, 173–179. doi: 10.1038/nature14447

Spitzer, C., Schellmann, S., Sabovljevic, A., Shahriari, M., Keshavaiah, C., Bechtold, N., et al. (2006). The Arabidopsis elch mutant reveals functions of an ESCRT component in cytokinesis. *Development* 133, 4679–4689. doi: 10.1242/dev.02654

Stoten, C. L., and Carlton, J. G. (2017). ESCRT-dependent control of membrane remodeling during cell division. *Semin. Cell Dev. Biol.* 74, 50–65. doi: 10.1016/j.semcdb.2017.08.035

Strauss, M. P., Liew, A. T., Turnbull, L., Whitchurch, C. B., Monahan, L. G., and Harry, E. J. (2012). 3D-SIM super resolution microscopy reveals a bead-like arrangement for FtsZ and the division machinery: implications for triggering cytokinesis. *PLoS Biol.* 10:e1001389. doi: 10.1371/journal.pbio.1001389

Stuchell-Brereton, M. D., Skalicky, J. J., Kieffer, C., Karren, M. A., Ghaffarian, S., and Sundquist, W. I. (2007). ESCRT-III recognition by VPS4 ATPases. *Nature* 449, 740–744. doi: 10.1038/nature06172

Su, M., Guo, E. Z., Ding, X., Li, Y., Tarrasch, J. T., Brooks, C. L., et al. (2017). Mechanism of Vps4 hexamer function revealed by cryo-EM. *Sci. Adv.* 3:e1700325. doi: 10.1126/sciadv.1700325

Sun, S., Li, L., Yang, F., Wang, X., Fan, F., Yang, M., et al. (2017). Cryo-EM structures of the ATP-bound Vps4(E233Q) hexamer and its complex with Vta1 at near-atomic resolution. *Nat. Commun.* 8:16064. doi: 10.1038/ncomms16064

Tan, J., Davies, B. A., Payne, J. A., Benson, L. M., and Katzmann, D. J. (2015). Conformational changes in the Endosomal Sorting Complex Required for the Transport III subunit Ist1 lead to distinct modes of ATPase Vps4 regulation. *J. Biol. Chem.* 290, 30053–30065. doi: 10.1074/jbc.M115.665604

Tang, S., Henne, W. M., Borbat, P. P., Buchkovich, N. J., Freed, J. H., Mao, Y., et al. (2015). Structural basis for activation, assembly and membrane binding of ESCRT-III Snf7 filaments. *eLife* 4:e12548. doi: 10.7554/eLife.12548

Teis, D., Saksena, S., and Emr, S. D. (2008). Ordered assembly of the ESCRT-III complex on endosomes is required to sequester cargo during MVB formation. *Dev. Cell* 15, 578–589. doi: 10.1016/j.devcel.2008.08.013

Wang, X., and Lutkenhaus, J. (1996). FtsZ ring: the eubacterial division apparatus conserved in archaebacteria. *Mol. Microbiol.* 21, 313–319. doi: 10.1046/j.1365-2958.1996.6421360.x

Wang, Y.-l. (2005). The mechanism of cortical ingression during early cytokinesis: thinking beyond the contractile ring hypothesis. *Trends Cell Biol.* 15, 581–588. doi: 10.1016/j.tcb.2005.09.006

Williams, T. A., Foster, P. G., Cox, C. J., and Embley, T. M. (2013). An archaeal origin of eukaryotes supports only two primary domains of life. *Nature* 504, 231–236. doi: 10.1038/nature12779

Woese, C. R., Kandler, O., and Wheelis, M. L. (1990). Towards a natural system of organisms: proposal for the domains Archaea, Bacteria, and Eucarya. *Proc. Natl. Acad. Sci. U.S.A.* 87, 4576–4579. doi: 10.1073/pnas.87.12.4576

Wollert, T., and Hurley, J. H. (2010). Molecular mechanism of multivesicular body biogenesis by ESCRT complexes. *Nature* 464, 864–869. doi: 10.1038/nature08849

Wollert, T., Wunder, C., Lippincott-Schwartz, J., and Hurley, J. H. (2009). Membrane scission by the ESCRT-III complex. *Nature* 458:172. doi: 10.1038/nature07836

Yang, B., Stjepanovic, G., Shen, Q., Martin, A., and Hurley, J. H. (2015). Vps4 disassembles an ESCRT-III filament by global unfolding and processive translocation. *Nat. Struct. Mol. Biol.* 2, 492–498. doi: 10.1038/nsmb.3015

Yang, D., Rismanchi, N., Renvoisé, B., Lippincott-Schwartz, J., Blackstone, C., and Hurley, J. H. (2008). Structural basis for midbody targeting of spastin by the ESCRT-III protein CHMP1B. *Nat. Struc. Mol. Biol.* 15, 1278–1286. doi: 10.1038/nsmb.1512

Yang, N., and Driessen, A. J. M. (2014). Deletion of cdvB paralogous genes of sulfolobus acidocaldarius impairs cell division. *Extremophiles* 18, 331–339. doi: 10.1007/s00792-013-0618-5

Yang, X., Lyu, Z., Miguel, A., McQuillen, R., Huang, K. C., and Xiao, J. (2017). GTPase activity-coupled treadmilling of the bacterial tubulin FtsZ organizes septal cell wall synthesis. *Science* 355, 744–747. doi: 10.1126/science.aak9995

Yang, Z., Vild, C., Ju, J., Zhang, X., Liu, J., Shen, J., et al. (2012). Structural basis of molecular recognition between ESCRT-III-like protein Vps60 and AAA-ATPase regulator Vta1 in the multivesicular body pathway. *J. Biol. Chem.* 287, 43899–43908. doi: 10.1074/jbc.M112.390724

Yao, Q., Jewett, A. I., Chang, Y.-W., Oikonomou, C. M., Beeby, M., Iancu, C. V., et al. (2017). Short FtsZ filaments can drive asymmetric cell envelope constriction at the onset of bacterial cytokinesis. *EMBO J.* 36, 1577-1589. doi: 10.15252/embj.201696235

Zaremba-Niedzwiedzka, K., Caceres, E. F., Saw, J. H., Bäckström, D., Juzokaite, L., Vancaester, E., et al. (2017). Asgard archaea illuminate the origin of eukaryotic cellular complexity. *Nature* 541, 353–358. doi: 10.1038/nature21031

Conflict of Interest Statement: The authors declare that the research was conducted in the absence of any commercial or financial relationships that could be construed as a potential conflict of interest.

frontiers in Microbiology

ORIGINAL RESEARCH
published: 09 April 2018
doi: 10.3389/fmicb.2018.00681

Absence of the Min System Does Not Cause Major Cell Division Defects in *Agrobacterium tumefaciens*

*Sue A. Flores†, Matthew Howell†, Jeremy J. Daniel, Rebecca Piccolo and Pamela J. B. Brown**

Division of Biological Sciences, University of Missouri, Columbia, MO, United States

In *A. tumefaciens*, the essential FtsZ protein is located at the growth pole before shifting to the mid-cell right before division. Loss of FtsZ causes a halt in cell separation and lysis of cells. To understand how FtsZ polymerization is regulated to properly localize the FtsZ ring at the mid-cell, we have conducted a systematic characterization of the Min system in *A. tumefaciens*. Our findings indicate that the Min system is not required for cell survival. Yet, we find that the deletion of either *minE* or *minCDE* results in a broad cell size distribution, including an increase in the proportion of short and long cells. We observe that the site of constriction is misplaced in the *minE* or *minCDE* deletion strains allowing for short cells to arise from sites of constriction near the cell poles. Remarkably, the short cells are viable and contain DNA. In order to observe chromosome replication and segregation in these strains, YFP-ParB is used as a proxy to track the origin of replication as cells elongate and divide. In the absence of the Min proteins, duplication and segregation of the origin of replication is frequently delayed. Taken together, our data suggest that the Min system contributes to the proper regulation of FtsZ placement and subsequent cell division. Furthermore, the failure to precisely place FtsZ rings at mid-cell in the *min* mutants impacts other cell cycle features including chromosome segregation.

Keywords: *Agrobacterium*, cell division, Min system, FtsZ, chromosome segregation

OPEN ACCESS

Edited by:
Jaan Männik,
University of Tennessee, Knoxville, United States

Reviewed by:
Martin Thanbichler,
Philipps University of Marburg, Germany
Tanneke Den Blaauwen,
University of Amsterdam, Netherlands

***Correspondence:**
Pamela J. B. Brown
brownpb@missouri.edu

†These authors have contributed equally to this work.

Specialty section:
This article was submitted to Microbial Physiology and Metabolism, a section of the journal Frontiers in Microbiology

Received: *11 January 2018*
Accepted: *22 March 2018*
Published: *09 April 2018*

Citation:
Flores SA, Howell M, Daniel JJ, Piccolo R and Brown PJB (2018) Absence of the Min System Does Not Cause Major Cell Division Defects in Agrobacterium tumefaciens. Front. Microbiol. 9:681. doi: 10.3389/fmicb.2018.00681

INTRODUCTION

Most bacteria precisely place the site of cell division at or near mid-cell through proper positioning of FtsZ to initiate divisome assembly. FtsZ forms a ring-like structure at or near the mid-cell along the cytoplasmic surface of the inner membrane (Bi and Lutkenhaus, 1991). FtsZ is stabilized along the membrane by interactions with FtsA leading to the formation of FtsZ filaments (Szwedziak et al., 2014). The FtsZ filaments form a ring-like structure at the future site of cell division and guide other divisome proteins, including peptidoglycan synthases, to the mid-cell (Ma et al., 1996; Sun and Margolin, 1998; Den Blaauwen et al., 1999; Li et al., 2007; Goley et al., 2011). The order of recruitment and essentiality of individual cell division proteins varies across species, but the general mechanism of cell division appears to be broadly conserved (Lutkenhaus and Du, 2017). After assembly of the cell division machinery is complete, peptidoglycan biosynthesis is activated at mid-cell (Addinall et al., 1997; Müller et al., 2007; Möll and Thanbichler, 2009). As the ring constricts, septal peptidoglycan is synthesized inwards to build the new poles of the daughter cells. Septal peptidoglycan synthesis requires the monofunctional PBP3, the SEDS protein FtsW, and the bifunctional PBP1b (Botta and Park, 1981; Bertsche et al., 2006; Cho et al., 2016).

The GTPase-dependent treadmilling motion of the FtsZ filaments drives the movement of the peptidoglycan biosynthesis machinery around the circumference of the cell division site, enabling the synthesis of concentric rings of peptidoglycan to form the septum (Bisson-Filho et al., 2017; Yang et al., 2017).

How is FtsZ properly positioned at mid-cell? There are several well characterized mechanisms to ensure proper positioning of the FtsZ rings (for review see Wu and Errington, 2011; Rowlett and Margolin, 2015). In rod-shaped bacteria such as *Escherichia coli* and *Bacillus subtilis*, the Min system and nucleoid occlusion (NO) prevent FtsZ rings from forming near cell poles or over nucleoids, respectively. In *E. coli*, the MinCDE proteins rapidly oscillate from pole to pole guiding FtsZ to the mid-cell (Hu and Lutkenhaus, 1999; Raskin and de Boer, 1999a,b; Fu et al., 2001; Hale et al., 2001). Since MinC is an inhibitor of FtsZ-ring assembly (Hu and Lutkenhaus, 2000; Justice et al., 2000; Dajkovic et al., 2008), FtsZ rings only form in mid-cell regions where the concentration of MinC is low. MinC forms a complex with MinD, an ATPase which dimerizes and binds to the cell membrane when bound to adenosine triphosphate (ATP) (de Boer et al., 1991, 1992; Hu and Lutkenhaus, 2003). MinE binds to MinD-ATP causing ATP hydrolysis and release of the MinCD complex from the membrane (Hu and Lutkenhaus, 2001). Remarkably, MinE can remain bound to the membrane at the pole to dislodge additional MinCD complexes (Loose et al., 2011; Park et al., 2011, 2017). Meanwhile, MinD-ATP is regenerated and cooperatively binds the membrane at the opposite pole. After removing the MinCD complexes from one cell pole, MinE will travel to the opposite pole. Thus, MinE chases MinCD from pole to pole giving rise to regular oscillations. The oscillation of the Min proteins results in a minimum of FtsZ inhibitory activity at mid-cell (Hale et al., 2001; Bonny et al., 2013).

When the genes encoding the Min proteins in *E. coli* are removed simultaneously or individually, cell division and survival is adversely impacted. In the absence of MinE, the cells usually cannot divide and the cells form long, smooth filaments. The block in cell division occurs because inhibition of FtsZ polymerization by MinC occurs throughout the cell (de Boer et al., 1989; Hu and Lutkenhaus, 2000). In the absence of MinC, or its activator MinD, a broad distribution of cell lengths is observed (de Boer et al., 1989). Both mini cells and long filaments are observed since FtsZ polymerization can occur at the cell poles or near mid-cell leading to asymmetric cell division events. FtsZ polymerization is restricted to poles and mid-cell in the absence of the Min system due to the presence of the nucleoid occlusion protein, SlmA (Bernhardt and de Boer, 2005). The FtsZ inhibitory activity of SlmA is activated by binding specific sites on the DNA near the origin of replication (Cho et al., 2011; Tonthat et al., 2011). Thus, as DNA replication is completed and the origins segregate to the cell poles, a minimal inhibitory zone is formed at mid-cell. SlmA binding to DNA activates its ability to bind the C-terminal tail of FtsZ causing depolymerization of FtsZ filaments (Du and Lutkenhaus, 2014). Under nutrient rich conditions, loss of the Min system and nucleoid occlusion is synthetically lethal; however under nutrient limited conditions the cells continue to grow and divide relatively well (Bernhardt and de Boer, 2005). When both the Min proteins and SlmA are absent, FtsZ ring placement is more accurate than in cells with only SlmA suggesting that other mechanisms contribute to the proper placement of FtsZ-ring in the absence of both Min proteins and SlmA (Bailey et al., 2014; Cambridge et al., 2014).

Indeed, the Min system is not universally distributed among bacteria suggesting the existence of alternative mechanisms of FtsZ positioning. MinCD is present in diverse bacteria, MinE is found in a more restricted range of bacteria, and other bacteria do not contain a Min system (Rothfield et al., 2005). For example, the Caulobacterales clade of alphaproteobacteria do not contain obvious homologs of the Min proteins. Furthermore, in *Caulobacter crescentus*, a bacterial model system within the Caulobacterales, only the final step of cell division takes place after completion of chromosome segregation suggesting that nucleoid occlusion does not occur (Jensen, 2006). Instead, *Caulobacter cresentus* uses at least two distinct mechanisms for regulation of cell division (Thanbichler and Shapiro, 2006; Radhakrishnan et al., 2010; Kiekebusch et al., 2012). MipZ is a distinct member of the MinD/ParA family of ATPases that contribute to spatial organization with bacterial cells (Lutkenhaus, 2012). MipZ forms a bipolar gradient on the nucleoid by binding to DNA sites near the origin of replication and directly interacts with FtsZ, inhibiting filament formation near the cell poles (Thanbichler and Shapiro, 2006; Kiekebusch et al., 2012). KidO is an NAD(H)-binding oxidoreductase that provides temporal regulation of FtsZ-ring assembly (Radhakrishnan et al., 2010). KidO binds FtsZ and prevents premature filament assembly at mid-cell. KidO is proteolytically cleared from the cell during elongation and the initiation of cell division, enabling efficient FtsZ-ring formation at mid-cell. KidO reappears late during cell division and is recruited to the mature divisome where it likely contributes to FtsZ-ring disassembly during constriction. Thus, together MipZ and KidO restrict FtsZ-ring formation to the mid-cell of predivisional cells.

Remarkably, not all alphaproteobacterial species lack a Min system. Among the alphaproteobacteria, the MinCDE proteins are found among the Rhodospirallales, Rhodobacterales, and Rhizobiales clades. The *minCDE* cluster is likely regulated by CtrA, the master cell cycle regulator, in several Rhizobiales species including *Brucella abortus* (Bellefontaine et al., 2002), *Prosthecomicrobium hirschii* (Williams et al., 2016), and *Sinorhizobium meliloti* (Pini et al., 2015). In *S. meliloti*, CtrA negatively regulates *minCD* expression (Pini et al., 2015) and overexpression of MinCD inhibits cell division (Cheng et al., 2007). Together, these observations suggest that the Min system may contribute to the regulation of cell division in the Rhizobiales. Here, we expand our knowledge about the function of the Min system in Rhizobiales by characterizing its contribution to regulation of cell division in *Agrobacterium tumefaciens*. The *A. tumefaciens* genome reveals the presence of an operon predicted to encode the MinCDE proteins, but there is not an obvious nucleoid occlusion system or MipZ homolog (Curtis and Brun, 2014). The MinCDE proteins from *Agrobacterium* share significant sequence similarity with the *E. coli* proteins (percent identities: MinC 31.70%, MinD 61.05%, and MinE 39.29%) suggesting that they may have conserved

functions. In this work, we have systematically characterized the role of the Min proteins on cellular morphology, constriction site placement, and chromosome segregation. Our results suggest that the Min system contributes to the regulation of cell division; however, other FtsZ-positioning proteins likely exist in *A. tumefaciens*.

MATERIALS AND METHODS

Bacterial Strains and Culture Conditions

A list of all bacterial strains and plasmids used in this study is provided in **Table 1**. *A. tumefaciens* C58 and derived strains were grown in AT minimal media with 0.5% glucose (ATGN) (Morton and Fuqua, 2012b) without exogenous iron at 28°C with shaking. For *sacB* counterselection during construction of deletion mutants 5% sucrose replaced glucose as the sole carbon source (ATSN). *E. coli* DH5α and S17-1 λ *pir* were routinely cultivated in Luria-Bertani (LB) medium at 37°C with shaking. When appropriate, kanamycin was used at 300 μg/ml for *A. tumefaciens* and 50 μg/ml for *E. coli.* When indicated, IPTG was used as an inducer at a concentration of 1 mM.

TABLE 1 | Bacterial strains and plasmids used in this study.

Strain or plasmid	Relevant characteristics	References/Source
PLASMIDS		
pNTPS138/139	Km^r; Suicide vector containing *oriT* and *sacB*	D. Alley
pNTPS139Δ*minC*	Km^r Suc^S; deletion plasmid for *minC*	This study
pNTPS139Δ*minD*	Km^r Suc^S; deletion plasmid for *minD*	This study
pNTPS139Δ*minE*	Km^r Suc^S; deletion plasmid for *minE*	This study
pNTPS139Δ*minCDE*	Km^r Suc^S; deletion plasmid for *minCDE*	This study
pRV-Pvan-FtsZ-GFP	Km^r; replicating plasmid for constitutive expression of FtsZ-GFP	Howell et al., 2017a
pSRKKm-Plac-YFP-ParB	Km^r; replicating plasmid for inducible expression of YFP-ParB	Ehrle et al., 2017
E. COLI STRAINS		
DH5α	Cloning strain	Life Technologies
S17-1	Sm^r; RP4-2, Tc::Mu,Km-Tn7, for plasmid mobilization	Simon et al., 1983
A. TUMEFACIENS STRAINS		
C58	Nopaline type strain; pTiC58; pAtC58	Watson et al., 1975
C58 Δ*minC*	C58 with deletion of *minC*	This study
C58 Δ*minD*	C58 with deletion of *minD*	This study
C58 Δ*minE*	C58 with deletion of *minE*	This study
C58 Δ*minCDE*	C58 with deletion of *minCDE*	This study

Plasmid Construction

PCR was used to amplify ∼ 500 bp of flanking sequence upstream (primers 1 and 2) and downstream (primers 3 and 4) of the gene targeted for deletion. Primers used for amplification of regions upstream and downstream of *minC* (Atu 3249), *minD* (Atu3248), *minE* (Atu3247) are shown in **Table 2**. For regions upstream and downstream of the *minCDE* locus, primers Atu 3249 P1-SpeI, Atu 3249 P2, Atu 3247 P3, and Atu 3247 P4-BamHI were used. All PCR reactions contained 10 μM of each primer, 100 ng of genomic DNA purified from wildtype *A. tumefaciens* C58, 10 mM deoxynucleotides (dNTPs; New England Biolabs), 0.5 U Phusion DNA Polymerase (Thermo scientific), 1.5% DMSO, and 5X Phusion GC Buffer (Thermo Scientific). Upstream and downstream DNA fragments were amplified by routine PCR reactions with the following cycling conditions: denaturation 98°C for 30 s, annealing 2° higher than the calculated annealing temperature of the primers for 30s, extension 72°C for 30 s, and final extension was done at 72°C for 5 min. The PCR ran for 30 cycles. PCR products were run on a 0.8% agarose gel by electrophoresis, stained with DNA SafeStain (Midwest Scientific) and gel purified using GeneJet PCR purification kit (Thermo Scientific). A second PCR reaction was done using PCR SOEing (synthesis by overlap extension) to anneal linker sequence from the 500 bp upstream and downstream together as described previously (Merritt et al., 2007). Briefly, purified PCR products were used as both templates and primers for a five-cycle PCR. A final PCR step with primers 1 and 4, using 2 μl of the second-step reaction mix as the template, generates the full-length spliced product. PCR products were then gel purified. PCR products and the pNTPS139 vector were then digested overnight at 37°C using enzymes SpeI and BamHI (New England Biolabs). Digested products were gel purified and ligated together using T4 DNA ligase (New England Biolabs). Ligations were transformed into *E.coli* DH5α competent cells using the suggested manufacturer protocol (Invitrogen). Transformants were plated on LB-agar plates containing kanamycin. Individual colonies from the transformation where then grown up overnight in LB with Kan50 and plasmid extraction was done using GenJet plasmid miniprep kit (Thermo Scientific). Plasmid inserts were verified by sequencing and the plasmids were transformed into *E. coli* S-17 by electroporation.

Deletion of Target Genes in *A. tumefaciens*

Nonpolar, markerless deletions of the *A. tumefaciens* individual *minC* (Atu 3249), minD (Atu 3248), and minE (Atu 3247) genes and the entire locus were generated using the plasmids pNPTS139Δ*minC*, pNPTS139Δ*minD*, pNPTS139Δ*minE, and* pNTPS139Δ*minCDE* following an established protocol (Morton and Fuqua, 2012a). Deletion of target genes was confirmed by colony PCR using the indicated primer pairs: Δ*minC* (Atu 3249 P1-SpeI and MinCDE P6), Δ*minD* (Atu 3248 P1-SpeI and Atu 3249 P4-BamHI), Δ*minE* (Atu 3247 P1-SpeI and Atu 3248 P4-BamHI), and Δ*minCDE* (MinCDE P5 and Atu 3249 P4-BamHI). PCR products were gel purified and sequence verified to confirm deletion of the target gene.

TABLE 2 | Synthesized DNA primers used in this study.

Primers	Sequence
Atu 3249 P1-SpeI	5′-ACA CGT ACT AGT CAG GCC GAT GCG G–3′
Atu 3249 P2	5′-AAG CTT GGT ACC GAAA TTC GCG AAG CTC G–3′
Atu 3249 P3	5′-GAA TTC GGT ACC AAGCTT CGA ACGCTG G–3′
Atu 3249 P4-BamHI	5′-CGC GCG GGA TCC GCA ATC GAA TTG ACC A–3′
Atu 3248 P1-SpeI	5′-ACA CGT ACT AGT TAT GGC CTG ATG CTG C–3′
Atu 3248 P2	5′-AAG CTT GGT ACC GAA TTC AGG AGG GCT G–3′
Atu 3248 P3	5′-GAA TTC GGT ACC AAG CTT TAC AAC GAC TA–3′
Atu 3248 P4-BamHI	5′-CGC GCG GGA TCC GTT CGC CCG TCG ATG A–3′
Atu 3247 P1-SpeI	5′-ACA CGT ACT AGT GCC GAT CTT GCC GGG C–3′
Atu 3247 P2	5′-AAG CTT GGT ACC GAA TTC CTG CGC GCT–3′
Atu 3247 P3	5′-GAA TTC GGT ACC AAG CTT GAT GCT CAT GC–3′
Atu 3247 P4-BamHI	5′-CGC GCG GGA TCC GAA TGG GTC ATC GCC G–3′
MinCDE P5	5′-CAT GGA ATG CGT GGC GAG CAC GAA TAC G–3′
MinCDE P6	5′-GAA GCC CGC ATG CCA TAGG ATA CGT TGC AG–3′

Growth Curve Analysis

Strains were grown in ATGN until exponential phase was reached, then back diluted to reach an OD_{600} = 0.1 in 1 ml of ATGN. 200 μl of culture was placed into 3 wells of a 96-well plate. A BioTek Synergy H1 Hybrid Reader was programed to read the optical density at 600 nm every 5 min after shaking for 1 min. The plate reader was maintained at a temperature of 28°C for a period of 36 h. Growth curve experiments were completed in triplicate and a total of four biological replicates were completed.

Cell Viability Assays

Serial dilutions of *A. tumefaciens* cells were spotted on ATGN plates to assess the viability of the *min* mutants. Exponential cultures (OD_{600} = 0.4–0.6) were diluted to OD_{600} 0.05 in ATGN. Cells were then serially diluted and 4 μl of each dilution was spotted onto ATGN plates. Plates were grown for 3 days at 28°C and imaged.

Phase Contrast Microscopy, Cell Length Analysis, and Quantitation of Constriction Position

Cells were grown in ATGN media until exponential phase was reached. A small volume (0.6–0.8 μl) of live cells were then placed onto a 1% agarose ATGN pad as described previously (Brown et al., 2012; Howell et al., 2017b). Phase contrast microscopy was performed with an inverted Nikon Eclipse TiE with a QImaging Rolera em-c^2 1 K EMCCD camera and Nikon Elements Imaging Software. Cell length distributions of 948 cells per strain were determined using the longest medial axis measured using MicrobeJ software (Ducret et al., 2016). Sites of cell constrictions were determined for ∼1,000 individual cells for each strain using stacked phase contrast images. Sites of constriction were autodetected using a preset MicrobeJ constriction detection function. To determine the polar orientation of each cell, old poles were identified using the lipophilic dye FM4-64 as previously described (Howell et al., 2017b).

Fluorescence Microscopy

For DNA staining, 1 ml of cells at an OD_{600} = 0.4–0.6 were treated with 1 μl of Sytox Orange (Invitrogen) for 5 min in the dark. Cells were pelleted and washed with PBS two times to remove excess dye. Cell pellets were resuspended in PBS and cells were imaged immediately on an agarose pad. Replicating plasmids pRV-Pvan-FtsZ-GFP and pSRKKm-Plac-YFP-ParB were introduced in wildtype cells and *min* mutants via an established electroporation protocol (Morton and Fuqua, 2012a). For imaging of YFP-ParB, exponential phase cells were diluted to OD_{600} = 0.2 and were induced with IPTG for 4 h until reaching an OD_{600} = 0.4–0.6 and were then imaged on agarose pads. Dual channel images were stacked and cell outlines and YFP-ParB foci were automatically detected using MicrobeJ (Ducret et al., 2016). Demographs depicting YFP-ParB localization were created by capturing the fluorescent intensity along the midline of the longitudinal axis of each cell and ordering these images by cell length. Both cell outlines and identified YFP-ParB foci were manually reviewed to ensure that the plots reflect accurate sites of YFP-ParB foci. For imaging of cells expressing constitutive FtsZ-GFP, cells were grown to OD_{600} = 0.4–0.6 and placed on agarose pads. Cells were imaged using phase contrast and epifluorescence microscopy with the appropriate filters. For timelapse microscopy cells were grown on ATGN 1.5% agarose pads with images collected either every 5 or 10 min.

RESULTS

Deletion of *min* Genes Does Not Have a Large Impact on Cell Growth or Viability, but Causes a Broader Cell Length Distribution

Transposons accumulate in the *min* region of *A. tumefaciens* during saturating transposon mutagenesis experiments in *A. tumefaciens* suggesting that the Min system is not required for cell survival (Curtis and Brun, 2014). To verify these results, we constructed markerless deletions in each *min* gene and the entire *min* locus. Growth curves of *min* mutants were indistinguishable from the growth curve of the parent strain (**Figure 1A**). The *min* mutants are viable (**Figure 1B**) with only a slight decrease in viability in Δ*minE*, suggesting that unregulated MinCD is more problematic than loss of the entire *min* locus. Although the *min* mutants are viable, phase contrast images of the cell populations revealed a small but consistent proportion of cells with atypical morphologies, including short cells (**Figure 2A**). Quantitative image analysis was used to determine the cell length distributions of the *min* mutants (**Figure 2B**). While the medians of the cell length distributions of the *min* mutants are actually slightly longer than that of the parent strain, the length of the whiskers is significantly increased suggesting that both short and long cells are accumulating in the *min* mutants. Next, we determined

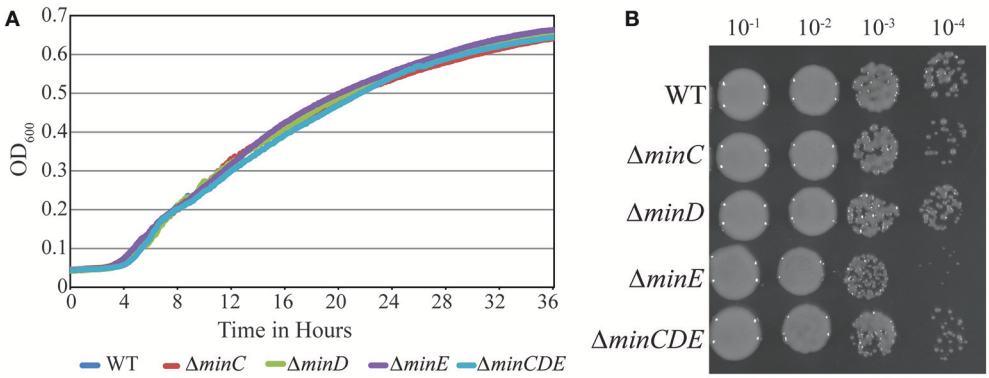

FIGURE 1 | Growth and viability of *min* mutants is not compromised. **(A)** Growth of Wildtype *A. tumefaciens* strain C58 and *min* mutants is monitored over 36 h by observing the increase in optical density. **(B)** Exponentially growing cells were diluted to OD $_{600}$ = 0.05 and serial dilutions were spotted on nutrient rich medium to observe viability.

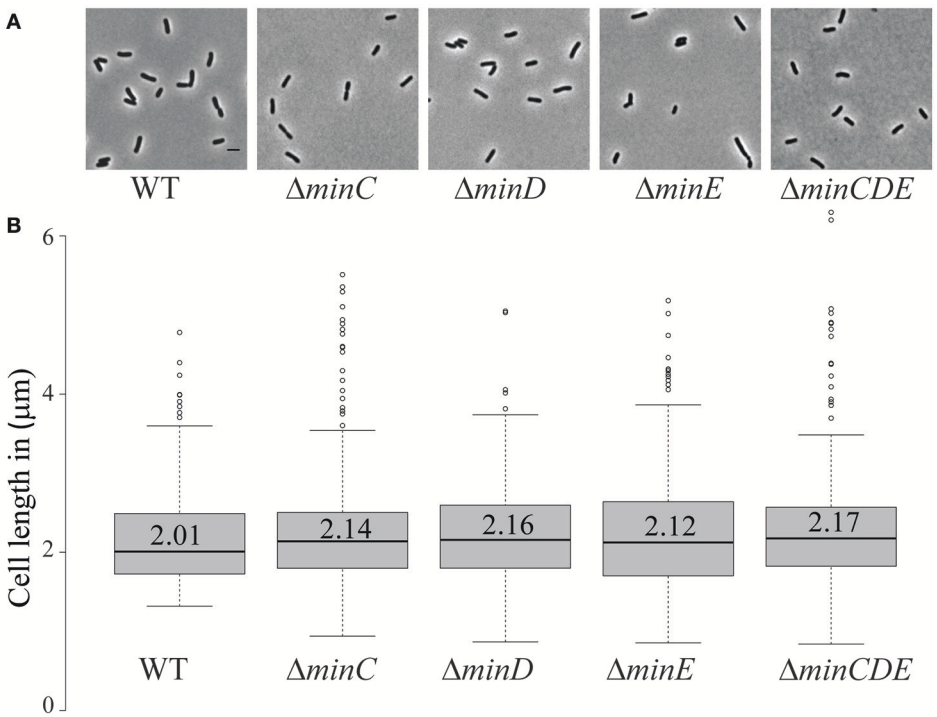

FIGURE 2 | Short cells accumulate in *min* mutants. **(A)** Phase contrast images of representative wildtype and *min* mutant cells. Scale bar = 2 μm. **(B)** Box plots illustrate cell length distributions of wildtype cells and *min* mutants. Medians are shown by the labeled center lines. Box limits indicate the 25th and 75th percentiles as determined by R software; whiskers extend 1.5 times the interquartile range and outliers are represented by dots. Cell lengths measured from 948 cells for each strain.

the percentage of cells with typical cell lengths (defined as 1.5–3.5 μm), cells with branches or bulges, short cells (< 1.5 μm), and cells with visible constrictions (**Figure 3**). Indeed, these observations confirm the presence of a small but reproducible proportion of short cells in the *min* mutant cells (**Figure 3**, panel iii). Furthermore, although the overall proportion of cells with constrictions is not impacted by the loss of individual *min* genes or the entire locus, we observe an increase in cells with obvious asymmetric constrictions or multiple constrictions (**Figure 3**, panel iv).

The Min System Contributes to Precise Placement of Constriction Sites

The previous observations suggest that the Min system may contribute to the proper placement of the site of cell division in *A. tumefaciens*. To better understand the function of the Min

system in the establishment of constriction sites, we quantitated the position of constriction sites in wildtype cells ($n = 186$). In this analysis, the true-mid cell is defined as 0 and negative values indicate positions of constrictions closer to the old pole whereas positive values indicate positions of constrictions closer to the new pole. Using the wildtype data set, we define a typical constriction placement to occur near mid-cell with a bias toward the new pole: 95% of constrictions formed between −0.1 and 0.35 μm from the true mid-cell position (**Figure 4A**, left). In addition, constrictions are consistently observed in cells with lengths between 2.5 and 3.5 μm (**Figure 4A**, right). These observations indicate that the site of constriction is established well before the cell has completed elongation. Cells longer than 4 μm in length with constrictions are rarely observed, presumably because the cells have successfully completed cell division.

In the *min* mutants, constrictions form in ∼20% of the cell population which is similar to what is observed in wildtype (**Figure 3**); however, the placement of the constrictions is perturbed. The *min* mutants have a broader distribution of constriction placement (**Figure 4A**). The Δ*minE* mutant in particular has lost the ability to maintain the proper bias of constriction site placement near the new pole. In contrast, when the entire *min* locus is absent 82% of constrictions are observed in the typical position and the bias for constriction placement toward the new pole is retained. These observations suggest that the unregulated activity of MinCD results in a more random positioning of constrictions, but proper positioning of constrictions is frequently retained when the *min* locus is entirely deleted. Although constriction sites form more randomly in *min* mutants, we rarely observe constriction sites immediately adjacent to the cell poles (**Figure 4B**) and short cells, rather than mini cells are formed. Since constriction sites are not biased only toward the new pole in *min* mutants, this phenotype cannot be readily explained by the continuation of growth at the new pole and may indicate the existence of another mechanism to protect the poles. Furthermore, an increase in long cells (>4 μm) with visible constrictions (**Figure 4B**) is observed in *min* mutants. This observation suggests that cell division efficiency is adversely impacted in the *min* mutants. It is possible that the perturbations of the Min system result in a delay in cell division or an increase in the frequency of constrictions that do not lead to a productive cell division event.

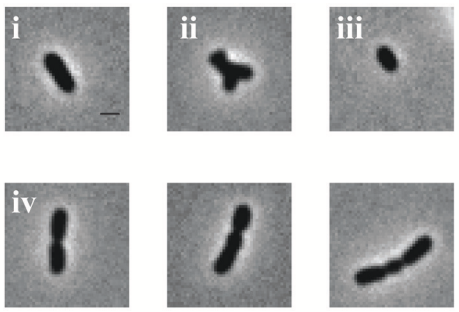

	(i) Rod-shaped	(ii) Branched	(iii) Small <1.5μm	(iv) Constricting
WT	75%	<1%	5%	20%
Δ*minC*	71%	1%	8%	20%
Δ*minD*	70%	1%	8%	21%
Δ*minE*	61%	1%	12%	25%
Δ*minCDE*	71%	1%	8%	20%

FIGURE 3 | Atypical morphologies are observed in *min* mutants. Phase contrast images of representative morphologies. All images taken from the Δ*minE* cell population. Scale bar = 1 μm. (**top**) Quantitation of bacterial morphologies. (**bottom**) The percentage of cells with a rod-shaped morphology (i: 1.5–3.5 μm in length), branched morphology (ii), short cell morphology (iii: <1.5 μm in length), and cells with visible constrictions (iv) are shown in the table. Cell morphologies were categorized from at least 948 cells for each strain.

FtsZ-Rings Form in *min* Mutants

In order to provide additional insights into the position of constriction placement, we introduced a plasmid which constitutively expresses *ftsZ-gfp* at a low level (Howell et al., 2017a) into wildtype and *min* mutant cells. In wildtype cells, FtsZ-rings initially form at an asymmetric position near the new pole and mark the future site of cell division (**Figures 5A,B**, Movie S1). As the cell continues to elongate at the new pole, the FtsZ ring is ultimately positioned near mid-cell and constriction leads to the appearance of a discrete focus of FtsZ in late predivisional cells. In the *min* mutants, FtsZ rings are observed at asymmetric positions, near mid-cell and in some cells multiple FtsZ rings form (**Figure 5A**). Unlike the pattern of FtsZ ring formation in wildtype cells which is very consistent, the pattern of FtsZ ring formation is variable in the *min* mutants. For example, asymmetric FtsZ rings form in positions biased toward either the new or old pole in Δ*minE* mutants (**Figure 5C**, top two panels, Movies S2, S3). In either case, the establishment of an FtsZ ring can lead to a cell division event which creates daughter cells of different cell sizes. These observations are consistent with the broader cell length distribution of the *min* mutants which includes both short and long cells (**Figure 2**) and with the asymmetric positioning of constrictions (**Figure 4**). In addition, Δ*minC*, Δ*minE,* and Δ*minCDE* cells with multiple FtsZ rings are readily observed (**Figure 5A**). In Δ*minE* cells with two FtsZ rings, both sites marked with FtsZ undergo constriction leading to the production of a bow-tie morphology and cell division ultimately occurs at either both or a single site marked by an FtsZ ring (**Figure 5C**, bottom two panels, Movies S4, S5).

Cell Division Is Initiated Prior to Nucleoid Separation

After observing that FtsZ rings are present in wildtype cells without visible constrictions (**Figure 5B**), we next aimed to determine if FtsZ rings form over DNA (**Figure 6**). In elongating wildtype cells, FtsZ is typically observed either as a polar focus or in an asymmetric FtsZ ring, whereas Sytox Orange labeling

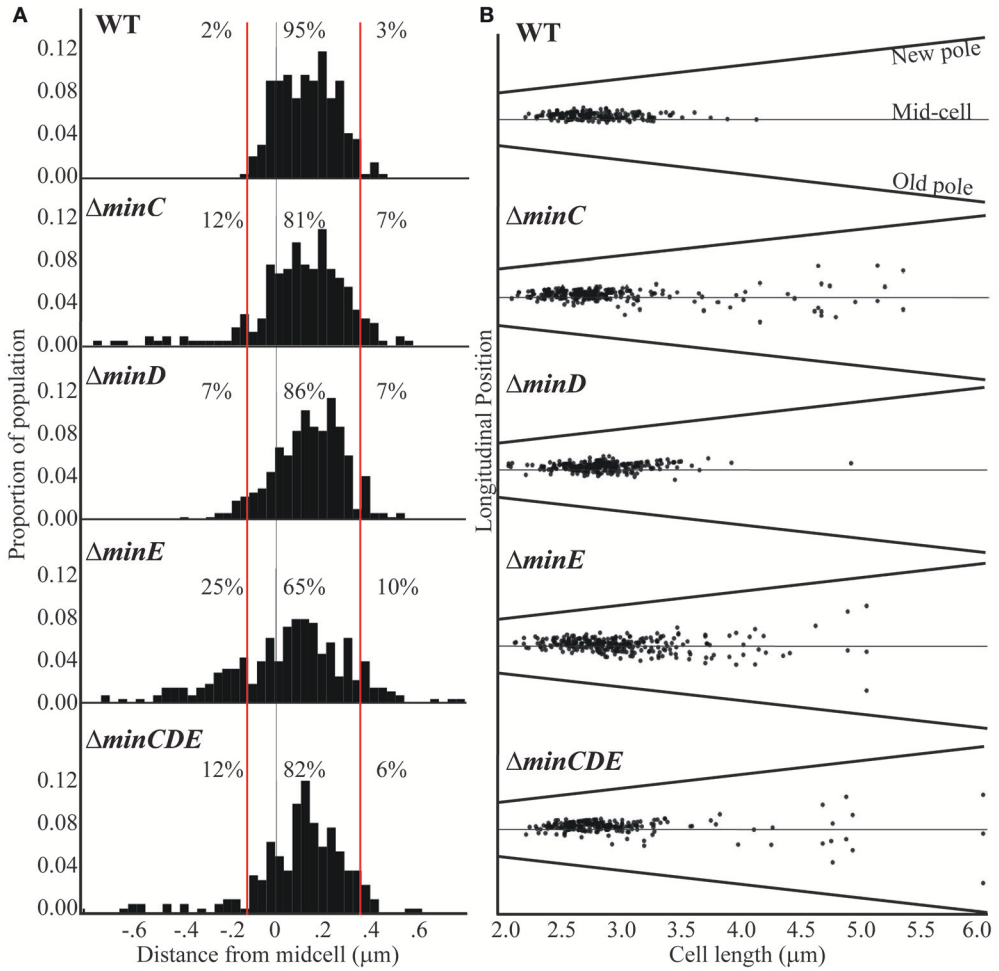

FIGURE 4 | Cell constriction placement in wildtype and *min* mutant cells. **(A)** Histograms of constriction position relative to distance from the midcell (gray line; relative position = 0). The red lines at −0.1 and 0.35 μm mark the region where constrictions typically form in wildtype cells. Negative numbers are closer to the old pole whereas the positive numbers are closer to the new pole. Percentages indicate the proportion of constrictions placed farther than −0.1 μm from mid-cell, placed between −0.1 and 0.35 μm, and placed more than 0.35 μm from mid-cell. **(B)** The longitudinal position of constrictions is plotted against cell length. For this analysis, cells are ordered by cell length and black dots indicate the position of the constriction. Mid-cell is indicated by the center gray line and the slanted lines indicate the position of the new and old pole for each cell. For these analysis, the predivisional cells within a population of ∼1,000 cells were analyzed ($n = 186$ for wildtype; $n = 242$ for Δ*minC*, $n = 262$ for Δ*minD*, $n = 285$ for Δ*minE*, and $n = 225$ for Δ*minCDE*).

indicates that the DNA is diffuse (**Figure 6A**, columns 1-2). The DNA remains diffuse in cells with early constrictions (**Figure 6A**, column 3) and only forms separated nucleoids in deeply constricted cells (**Figure 6A**, column 4). These observations are consistent with the possibility that *A. tumefaciens* does not use a nucleoid occlusion mechanism to position FtsZ at mid-cell. Similar results are observed in the *min* mutants, as exemplified by Δ*minE* (**Figure 6B**). Notably, in the Δ*minE* mutant FtsZ rings form over the top of DNA at asymmetric positions and when multiple FtsZ rings are present. Finally, we observed that short cells in the Δ*minE* population typically contain diffuse DNA (**Figure 6B**, right column).

In the wildtype cells and each of the *min* mutants, 90–95% of the cell population (based on observations of ∼230 cells/strain) has diffuse DNA. In the *min* mutants, DNA is diffuse in cells without constrictions irrespective of cell shape (shown for Δ*minE* in **Figure 6C**, panel i), including short and branched cells. Two distinct nucleoids are observed in 5–10% of the wildtype and *min* cell populations (shown for Δ*minE* in **Figure 6C**, panel ii). As expected due to the formation of asymmetric sites of cell constriction, the *min* mutants contain a higher proportion of cells with asymmetrically separated nucleoids. In <1% of the Δ*minC and* Δ*minE* cells, the presence of more than 2 nucleoids is observed (**Figure 6C**, panel iii).

Chromosome Segregation Is Delayed in Single *min* Mutants

Since the inefficiency of cell division in the *min* mutants may cause a delay in chromosome segregation, we next tracked the early stages of chromosome segregation by introducing an IPTG

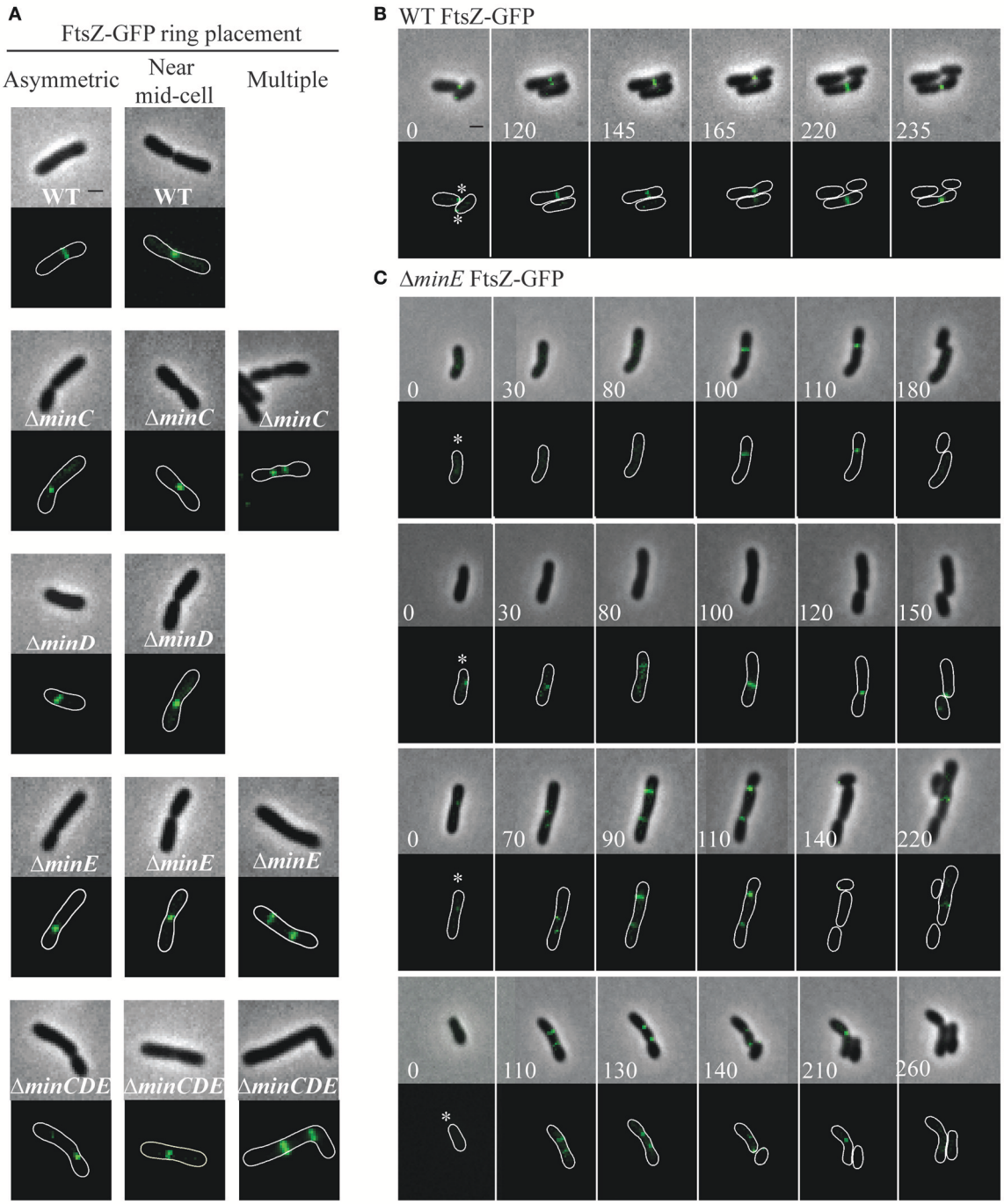

FIGURE 5 | FtsZ-GFP ring position in wildtype and *min* mutant cells. **(A)** Representative images of FtsZ-GFP localization patterns in wildtype and *min* mutants including asymmetric localization, near mid cell localization, and multiple ring formation. The absence of an image indicates that the localization pattern is not observed in the strain. **(B)** Timelapse microscopy showing typical FtsZ-GFP localization patterns in wildtype cells. Asterisks mark the growing poles. **(C)** Timelapse microscopy of FtsZ-GFP localization in Δ*minE* cells. Asterisks mark the growing poles. Images shown in panels **B** and **C** are at the same scale. Scale bars = 1 μm.

inducible plasmid expressing *yfp-parB* (Ehrle et al., 2017) into the *min* mutants. ParB attaches to the *parS* site near the origin of replication, making it suitable to track the movement of newly replicated origin (Ehrle et al., 2017). In *A. tumefaciens* ParB localizes at the old pole and as the cell nears division a second focus appears and rapidly tracks across the cell to the new pole ensuring both cells receive a copy of the chromosome (**Figure 7**; Ehrle et al., 2017). The longitudinal profile of over 500 cells expressing YFP-ParB were aligned in order of cell length to create a demograph depicting the localization of YFP-ParB

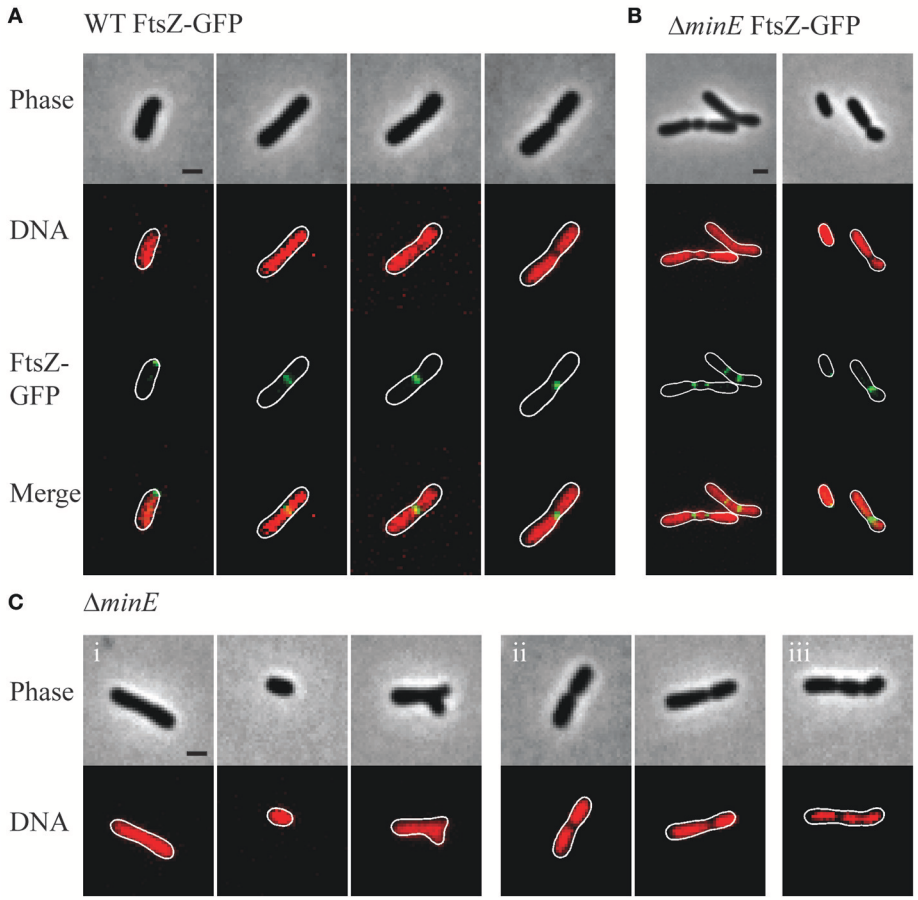

FIGURE 6 | Nucleoid position in wildtype and *min* mutant cells. **(A)** Representative images demonstrating FtsZ-GFP localization in wildtype cells with Sytox Orange stained DNA. **(B)** Representative images of FtsZ-GFP localization in Δ*minE* cells with Sytox Orange stained DNA. **(C)** Representative images from the Δ*minE* mutant population. Sytox Orange was used to label DNA and observe localization patterns including (i) diffuse, (ii) separated nucleoids, and (iii) other patterns. Scale bars = 1 μm.

throughout the cell cycle (**Figure 7A**). In wildtype cells, YFP-ParB is observed in three patterns: first, a single focus is observed in short cells, next we observe a brief transition period where a second focus of YFP-ParB appears and transits along the longitudinal axis of the cell, finally in predivisional cells, both foci are anchored at opposite poles. To examine the YFP-ParB localization pattern at the population level, the positions of the YFP-ParB foci were normalized by cell length and plotted along the cell axis (**Figure 7B**). In wildtype cells, a larger number of foci are observed at the old pole than at the new pole due to the presence of a single focus in short cells and two foci near the old pole at the onset of DNA replication. Notably, very few YFP-ParB foci are observed transiting from old pole to new pole presumably due to the rapid rate of DNA replication and chromosome segregation.

The deletion of single *min* genes results in less consistent patterns of YFP-ParB localization throughout the cell cycle. In the absence of MinC, MinD, or MinE, YFP-ParB is located at a single focus in short cells; however, not all of the foci are found at the old pole (**Figure 7A**). Furthermore, we observe an increase in the number of foci observed between the poles (**Figures 7A,B**). This phenotype is due to a combination of cells which accumulate more than 2 YFP-ParB foci and cells in which the duplicated origin is not efficiently transited from pole to pole. Although MinD has been described as a candidate protein to tether DNA to the membrane during chromosome segregation in *E. coli* (Di Ventura et al., 2013), we do not observe a more severe phenotype in the Δ*minD* mutant compared to the Δ*minC* or Δ*minE* mutants. Furthermore, deletion of the entire *min* locus results in a localization pattern of YFP-ParB which is more similar to wildtype. Since the *min* mutants are viable (**Figure 1**) and even short cells are capable of resuming growth (**Figure 5C**, bottom panel), we infer that chromosome segregation is delayed presumably due to inefficient cell division in the *min* mutants.

DISCUSSION

In this work, we have characterized the impact of the Min system on the cell division of *A. tumefaciens*. Similar to findings in *S. meliloti* (Cheng et al., 2007) and consistent with a saturating

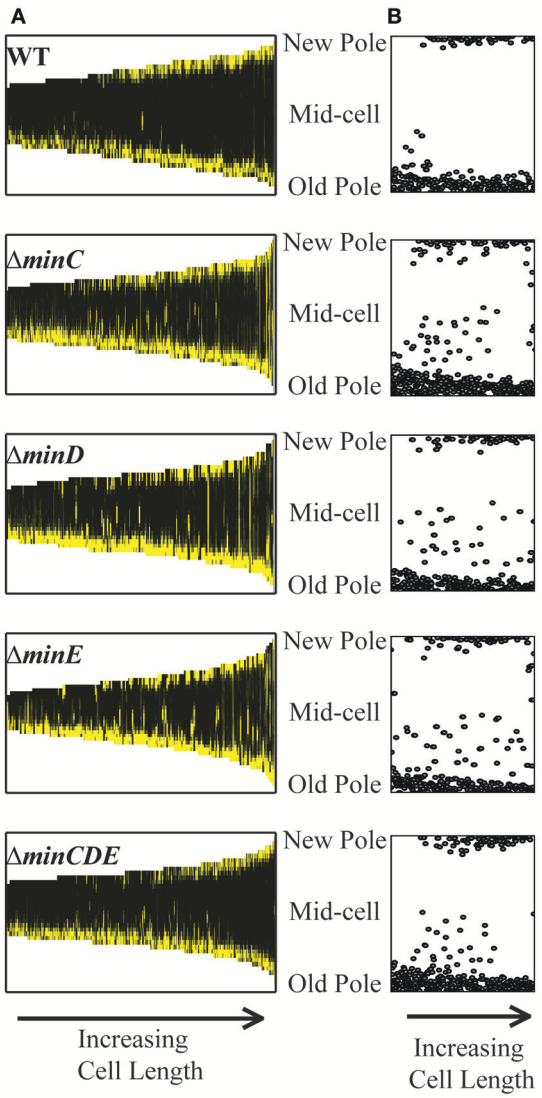

FIGURE 7 | YFP-ParB localization in wildtype and *min* mutant cells. **(A)** Demographs of YFP-ParB localization. Cells are ordered according to cell length and positions of the new pole, mid-cell, and old pole are indicated. **(B)** Position of YFP-ParB foci are plotted relative to longitudinal position in the cells. At least 500 cells were analyzed for each strain.

transposon screen in *A. tumefaciens* suggesting that the *min* genes are not essential (Curtis and Brun, 2014), we have confirmed that the *min* genes are not required for cell viability (**Figure 1**). Quantitative image analysis of cell morphology reveals that cell length distributions and placement of sites of cell constrictions are perturbed when single *min* genes are deleted compared to wildtype cells (**Figures 2–4**). In particular, the absence of MinE leads to the accumulation of both long and short cells suggesting that the placement of the septum is perturbed. Indeed, the sites of cell constriction (**Figure 4**) and localization of FtsZ-GFP is more variable in the Δ*minE* strain (**Figure 5**) suggesting that the misregulation of MinCD is detrimental to efficient cell division. These observations are consistent with the *E. coli* model of the Min system where MinE regulates the activity of the MinCD complex by driving the oscillation of MinC and MinD from pole-to-pole and preventing the establishment of polar FtsZ rings (Lutkenhaus, 2007; Rowlett and Margolin, 2015). In *A. tumefaciens*, the absence of MinE leads to a more random distribution of active of MinCD complexes, allowing the observed misplacement of FtsZ-rings and constriction sites. Remarkably, asymmetric FtsZ-GFP rings are not observed immediately adjacent to the cell poles in *min* mutants (**Figures 5A,C**) and can form over DNA in both wildtype cells and *min* mutants (**Figure 6**). Finally, the absence of the entire Min system has a relatively mild phenotype enabling most cells to divide near mid-cell (**Figures 2**, **4**). Together, these results suggest that other mechanisms for proper placement of FtsZ-rings must exist in *A. tumefaciens*.

While the *A. tumefaciens min* mutant phenotypes are generally consistent with *E. coli* Min model, a key component of this model remains to be tested in *A. tumefaciens*. In *E. coli*, the Min proteins oscillate from pole-to-pole producing a local minimum inhibition zone at mid-cell in which FtsZ-rings can form (Raskin and de Boer, 1999a,b; Meinhardt and de Boer, 2001). In contrast, in *B. subtilis* the MinCDJ system does not use protein oscillation. DivIVA binds to regions of the membrane with negative curvature (Lenarcic et al., 2009; Ramamurthi and Losick, 2009). Next, MinJ acts as an adaptor protein and enables the recruitment of MinD and subsequently MinC to sites of DivIVA localization (Bramkamp et al., 2008; Patrick and Kearns, 2008). Initially, it was thought that the MinCD complexes formed a static bipolar gradient which protects the poles from FtsZ ring assembly (Adams and Errington, 2009; Bramkamp and van Baarle, 2009); however, DivIVA is recruited to the nascent division site when constriction is initiated leading to the formation of DivIVA rings on either side of the division site (Eswaramoorthy et al., 2011). MinCDJ complexes are assembled at these DivIVA rings and presumably prevent the formation of additional FtsZ rings near mid-cell. Based on the presence of *minE* and the absence of *divIVA* and *minJ* in the genome of *A. tumefaciens*, we hypothesize that the MinCD proteins should localize at cell poles and oscillate from pole-to-pole and MinE should exhibit a dynamic localization pattern with enrichment at sub-polar region. Our initial efforts to construct C-terminal fluorescent protein fusions to the *A. tumefaciens* Min proteins have been unsuccessful. A rigorous effort will be needed to observe the localization patterns of the Min proteins in *A. tumefaciens* to determine if pole-to-pole oscillation of the Min proteins contributes to the efficient establishment of constriction sites at the proper position.

In addition to cell division defects, single deletion of *min* genes results in delayed chromosome segregation (**Figure 7**). At first glance, this finding appears to be consistent with observations of chromosome partitioning defects in *E. coli min* mutants (Akerlund et al., 1992, 2002; Di Ventura et al., 2013); however, there are notable phenotypic differences. First, in *E. coli*, the production of mini-cells devoid of DNA due to polar cell division events is a hallmark of *min* mutants (de Boer et al., 1989). In contrast, short cells arising from misplacement of constriction

sites in *A. tumefaciens min* mutants typically contain DNA. This difference may suggest that *A. tumefaciens* does not employ a nucleoid occlusion system to prevent the establishment of FtsZ rings over unsegregated nucleoids (Wu and Errington, 2004; Bernhardt and de Boer, 2005) and is consistent with the absence of an obvious nucleoid occusion protein in the *A. tumefaciens genome* (Goodner et al., 2001; Wood et al., 2001) and the formation of FtsZ-GFP rings over DNA in unconstricted cells (**Figure 6A**). Second, in *E. coli*, a Δ*minCDE* mutant has a more severe defect in chromosome segregation than a Δ*minC* mutant leading to the hypothesis that MinD may directly contribute to chromosome segregation (Di Ventura et al., 2013). The MinD/ParA family of proteins share an evolutionary history and MinD and ParA function in providing positional information for spatial organization of the FtsZ ring and segregating chromosome, respectively (Lutkenhaus, 2012). *E. coli* MinD can nonspecifically bind chromosomal DNA and may provide polar gradients of DNA tethering sites during chromosome segregation (Di Ventura et al., 2013). If *A. tumefaciens* MinD is capable of binding DNA and tethering chromosomes to the membrane, the predicted random distribution of MinCD complexes in the absence of MinE may explain why the YFP-ParB foci do not rapidly transit from pole-to-pole. Nevertheless, if *A. tumefaciens* MinD is involved in chromosome segregation we would expect to observe segregation defects in the Δ*minD* and Δ*minCDE* strains. Remarkably, the Δ*minC,* Δ*minD,* and Δ*minE* strains exhibit a strikingly similar phenotype with a delay in transition of the YFP-ParB focus from the old pole to the new pole (**Figure 7**). Furthermore, the Δ*minCDE* strain has a less severe phenotype and YFP-ParB is bipolar in the longest cells. Together, these data suggest that the chromosome segregation defect in the *min* mutants likely arises indirectly as a consequence of less efficient cell division.

Remarkably, in some *C. crescentus* cells lacking MipZ, productive cell division events occur resulting in the production of mini cells which contain DNA (Thanbichler and Shapiro, 2006). Although constrictions form over chromosomes that have not completed segregation, most isolated mini cells contain both an origin of replication and a terminus. These observations suggest that cell division is delayed until DNA replication is finished and the complete chromosome is delivered to the mini cell compartment (Thanbichler and Shapiro, 2006). In most bacteria, DNA replication and chromosome segregation occur simultaneously. These processes consist of three major stages: separation and translocation of the duplicated origin, segregation of the bulk chromosome, and separation of the terminus region (Badrinarayanan et al., 2015; Surovtsev and Jacobs-Wagner, 2018). *C. crescentus* uses the widely distributed ParABS system (Livny et al., 2007) to segregate the *ori* region of the chromosome. Briefly, ParB binds to DNA at the *parS* site which is proximal to the origin of replication. Following duplication of *ori*, one of the ParB-bound *ori* regions remains at the old pole and the other is translocated across the cell to the opposite pole following a receding cloud of ParA (Shebelut et al., 2009; Ptacin et al., 2010; Schofield et al., 2010). ParB is anchored to the poles through a direct interaction with the polar organizing protein PopZ (Bowman et al., 2008; Ebersbach et al., 2008). When PopZ is absent, the chromsomes become untethered from the pole and mini cells without DNA are formed (Ebersbach et al., 2008). MipZ not only inhibits FtsZ-ring assembly, it also binds to ParB, protecting the *ori* proximal regions from FtsZ-ring formation (Thanbichler and Shapiro, 2006). Thus, the processes of cell division and *ori* partitioning are tightly coupled through MipZ. Later stages of cell division and chromosome segregation are also coupled through FtsK. In *C. crescentus,* the N-terminus of FtsK contributes to the stability of FtsZ-rings and the C-terminus of FtsK is responsible for clearing the termini from the division plane (Wang et al., 2006).

The observation that the *A. tumefaciens min* mutants produce short cells that contain DNA may suggest that *A. tumefaciens* also couples the processes of cell division and chromosome segregation. Indeed, the deletion of *popZ* in *A. tumefaciens* results in untethered chromosomes and the production of cells devoid of DNA (Ehrle et al., 2017). In some Δ*popZ* cells, DNA appears to be segregated in the wrong direction across the division plane. FtsK functions as a DNA translocase that assists in the completion of cell division by moving DNA across the division plane in the direction of the termini (Besprozvannaya and Burton, 2014; Badrinarayanan et al., 2015). If a terminus is trapped on the wrong side of the division plane in the absence of PopZ, FtsK may pump DNA in the wrong direction leading to the production of cells without DNA. Notably, whereas the deletion of *popZ* leads to the production of mini cells in *C. crescentus* (Ebersbach et al., 2008), the loss of *popZ* results in the production of a broad distribution of cell lengths in *A. tumefaciens* (Howell et al., 2017a) suggesting that the poles are still largely protected from FtsZ-ring formation. Similarly, when the Min system is removed the short cells sometimes arise (**Figure 2**) and although *ori* partitioning appears to be delayed (**Figure 7**), most cells are viable (**Figure 1**) suggesting that even short cells inherit an intact chromosome. Timelapse microscopy of the Δ*minE* mutant illustrates that short cells are capable of resuming growth following cell division (**Figure 5C**, bottom panel). Together, these observations suggest that *A. tumefaciens* must use another FtsZ-positioning mechanism to protect the poles and that the processes of DNA replication, chromosome segregation, and cell division must be coordinated.

How might DNA replication, chromosome segregation, and cell division be properly coordinated in *A. tumefaciens*? In *S. meliloti,* expression of *minC* and *minD* was upregulated during depletion of CtrA, implicating this master cell cycle regulator as a transcriptional repressor of this operon (Pini et al., 2015). Remarkably, *minCD* are the only known cell division genes directly regulated by CtrA; however, introduction of a deletion of *minCDE* into the CtrA depletion strain did not rescue the cell division defect suggesting the Min overexpression is not exclusively responsible for the cell division phenotype. Depletion of CtrA in *A. tumefaciens* leads to a block in cell division (Figueroa-Cuilan et al., 2016) and a putative consensus CtrA binding site (TTAA-N_7-TTAA) is present upstream of *minC* in the *A. tumefaciens* genome. Thus, it is tempting to speculate that the transcription of the *min* genes is under the control of CtrA. Cell-cycle regulation of the Min system may ensure that these proteins are functioning as needed when the cells approach

cell division. In *C. crescentus* the expression of *ftsZ* is directly regulated by CtrA (Kelly et al., 1998; Laub et al., 2002) and FtsZ is subject to proteolysis by ClpAP and ClpXP (Williams et al., 2014) leading to cell-cycle variability of FtsZ levels. Even when *ftsZ* is expressed constitutively, it is subject to post-translational control leading to cell cycle variability of FtsZ levels (Williams et al., 2014). The cell cycle variability in FtsZ levels may be a common feature among bacteria with an alphaproteobacterial cell cycle. Thus, in *A. tumefaciens* the cell cycle regulation of the Min system may temporally coordinate the expression levels of the Min and FtsZ proteins. Future studies will be necessary to determine if FtsZ, other divisome components, and the Min proteins are coordinated through cell-cycle regulation in *A. tumefaciens*. Such studies are necessary to better understand how the processes of DNA replication, chromosome segregation, and cell division are coordinated in *A. tumefaciens*.

Overall these results suggest that while the *A. tumefaciens* Min system contributes to the precise positioning of an FtsZ-ring and constriction site near mid-cell, other mechanisms must exist to ensure proper spatial organization during cell division. In *A. tumefaciens,* the phenotype of the Δ*minCDE* strain is milder than that of the individual Δ*minC,* Δ*minD,* or Δ*minE* strains suggesting that this FtsZ positioning system is dispensable for the completion of cell division. There are a number of alternative FtsZ positioning proteins including nucleoid occlusion proteins, MipZ in *C. crescentus* which forms a bipolar gradient and directly inhibits FtsZ-ring assembly near the poles (Thanbichler and Shapiro, 2006; Kiekebusch et al., 2012), and positive regulators which localize to mid-cell and promote FtsZ-ring assembly (Rowlett and Margolin, 2015). Other than the *min* locus, genes encoding candidate FtsZ-positioning proteins cannot be readily identified in the *A. tumefaciens* genome (Goodner et al., 2001; Wood et al., 2001). Thus, further studies of *A. tumefaciens* cell division are likely to reveal novel strategies to ensure proper mid-cell assembly of the divisome.

AUTHOR CONTRIBUTIONS

SF, MH, JD, and PB designed the experiments. SF, MH, JD, and RP conducted the experiments. SF, MH, RP, and PB analyzed the data. All authors contributed to writing and editing of the manuscript.

FUNDING

Research in the Brown lab on *A. tumefaciens* cell growth and division is supported by the National Science Foundation (IOS1557806).

ACKNOWLEDGMENTS

We thank Grant Bowman (University of Wyoming) for the plasmid containing YFP-ParB and members of the Brown lab for feedback during the preparation of this manuscript.

SUPPLEMENTARY MATERIAL

The Supplementary Material for this article can be found online at: https://www.frontiersin.org/articles/10.3389/fmicb.2018.00681/full#supplementary-material

REFERENCES

Adams, D. W., and Errington, J. (2009). Bacterial cell division: assembly, maintenance and disassembly of the Z ring. *Nat. Rev. Microbiol.* 7, 642–653. doi: 10.1038/nrmicro2198

Addinall, S. G., Cao, C., and Lutkenhaus, J. (1997). FtsN, a late recruit to the septum in *Escherichia coli*. *Mol. Microbiol.* 25, 303–309. doi: 10.1046/j.1365-2958.1997.4641833.x

Akerlund, T., Bernander, R., and Nordstrom, K. (1992). Cell division in *Escherichia coli minB* mutants. *Mol. Microbiol.* 6, 2073–2083. doi: 10.1111/j.1365-2958.1992.tb01380.x

Akerlund, T., Gullbrand, B., and Nordstrom, K. (2002). Effects of the Min system on nucleoid segregation in *Escherichia coli*. *Microbiology* 148(Pt 10), 3213–3222. doi: 10.1099/00221287-148-10-3213

Badrinarayanan, A., Le, T. B., and Laub, M. T. (2015). Bacterial chromosome organization and segregation. *Annu. Rev. Cell Dev. Biol.* 31, 171–199. doi: 10.1146/annurev-cellbio-100814-125211

Bailey, M. W., Bisicchia, P., Warren, B. T., Sherratt, D. J., and Mannik, J. (2014). Evidence for divisome localization mechanisms independent of the Min system and SlmA in Escherichia coli. *PLoS Genet.* 10:e1004504. doi: 10.1371/journal.pgen.1004504

Bellefontaine, A. F., Pierreux, C. E., Mertens, P., Vandenhaute, J., Letesson, J. J., and De Bolle, X. (2002). Plasticity of a transcriptional regulation network among alpha-proteobacteria is supported by the identification of CtrA targets in *Brucella abortus*. *Mol. Microbiol.* 43, 945–960. doi: 10.1046/j.1365-2958.2002.02777.x

Bernhardt, T. G., and de Boer, P. A. (2005). SlmA, a nucleoid-associated, FtsZ binding protein required for blocking septal ring assembly over chromosomes in *E. coli*. *Mol. Cell* 18, 555–564. doi: 10.1016/j.molcel.2005.04.012

Bertsche, U., Kast, T., Wolf, B., Fraipont, C., Aarsman, M. E., Kannenberg, K., et al. (2006). Interaction between two murein (peptidoglycan) synthases, PBP3 and PBP1B, in *Escherichia coli*. *Mol. Microbiol.* 61, 675–690. doi: 10.1111/j.1365-2958.2006.05280.x

Besprozvannaya, M., and Burton, B. M. (2014). Do the same traffic rules apply? Directional chromosome segregation by SpoIIIE and FtsK. *Mol. Microbiol.* 93, 599–608. doi: 10.1111/mmi.12708

Bi, E. F., and Lutkenhaus, J. (1991). FtsZ ring structure associated with division in *Escherichia coli*. *Nature* 354, 161–164.

Bisson-Filho, A. W., Hsu, Y. P., Squyres, G. R., Kuru, E., Wu, F., Jukes, C., et al. (2017). Treadmilling by FtsZ filaments drives peptidoglycan synthesis and bacterial cell division. *Science* 355, 739–743. doi: 10.1126/science.aak9973

Bonny, M., Fischer-Friedrich, E., Loose, M., Schwille, P., and Kruse, K. (2013). Membrane binding of MinE allows for a comprehensive description of Min-protein pattern formation. *PLoS Comput. Biol.* 9:e1003347. doi: 10.1371/journal.pcbi.1003347

Botta, G. A., and Park, J. T. (1981). Evidence for involvement of penicillin-binding protein 3 in murein synthesis during septation but not during cell elongation. *J. Bacteriol.* 145, 333–340.

Bowman, G. R., Comolli, L. R., Zhu, J., Eckart, M., Koenig, M., Downing, K. H., et al. (2008). A polymeric protein anchors the chromosomal origin/ParB complex at a bacterial cell pole. *Cell* 134, 945–955. doi: 10.1016/j.cell.2008.07.015

Bramkamp, M., Emmins, R., Weston, L., Donovan, C., Daniel, R. A., and Errington, J. (2008). A novel component of the division-site selection system

of *Bacillus subtilis* and a new mode of action for the division inhibitor MinCD. *Mol. Microbiol.* 70, 1556–1569. doi: 10.1111/j.1365-2958.2008.06501.x

Bramkamp, M., and van Baarle, S. (2009). Division site selection in rod-shaped bacteria. *Curr. Opin. Microbiol.* 12, 683–688. doi: 10.1016/j.mib.2009.10.002

Brown, P. J., de Pedro, M. A., Kysela, D. T., Van der Henst, C., Kim, J., De Bolle, X., et al. (2012). Polar growth in the Alphaproteobacterial order Rhizobiales. *Proc. Natl. Acad. Sci. U.S.A.* 109, 1697–1701. doi: 10.1073/pnas.1114476109

Cambridge, J., Blinkova, A., Magnan, D., Bates, D., and Walker, J. R. (2014). A replication-inhibited unsegregated nucleoid at mid-cell blocks Z-ring formation and cell division independently of SOS and the SlmA nucleoid occlusion protein in *Escherichia coli*. *J. Bacteriol.* 196, 36–49. doi: 10.1128/JB.01230-12

Cheng, J., Sibley, C. D., Zaheer, R., and Finan, T. M. (2007). A *Sinorhizobium meliloti minE* mutant has an altered morphology and exhibits defects in legume symbiosis. *Microbiology* 153(Pt 2), 375–387. doi: 10.1099/mic.0.2006/001362-0

Cho, H., McManus, H. R., Dove, S. L., and Bernhardt, T. G. (2011). Nucleoid occlusion factor SlmA is a DNA-activated FtsZ polymerization antagonist. *Proc. Natl. Acad. Sci. U.S.A.* 108, 3773–3778. doi: 10.1073/pnas.1018674108

Cho, H., Wivagg, C. N., Kapoor, M., Barry, Z., Rohs, P. D., Suh, H., et al. (2016). Bacterial cell wall biogenesis is mediated by SEDS and PBP polymerase families functioning semi-autonomously. *Nat. Microbiol.* 1:16172. doi: 10.1038/nmicrobiol.2016.172

Curtis, P. D., and Brun, Y. V. (2014). Identification of essential alphaproteobacterial genes reveals operational variability in conserved developmental and cell cycle systems. *Mol. Microbiol.* 93, 713–735. doi: 10.1111/mmi.12686

Dajkovic, A., Lan, G., Sun, S. X., Wirtz, D., and Lutkenhaus, J. (2008). MinC spatially controls bacterial cytokinesis by antagonizing the scaffolding function of FtsZ. *Curr. Biol.* 18, 235–244. doi: 10.1016/j.cub.2008.01.042

de Boer, P. A., Crossley, R. E., Hand, A. R., and Rothfield, L. I. (1991). The MinD protein is a membrane ATPase required for the correct placement of the *Escherichia coli* division site. *EMBO J.* 10, 4371–4380.

de Boer, P. A., Crossley, R. E., and Rothfield, L. I. (1989). A division inhibitor and a topological specificity factor coded for by the minicell locus determine proper placement of the division septum in *E. coli*. *Cell* 56, 641–649. doi: 10.1016/0092-8674(89)90586-2

de Boer, P. A., Crossley, R. E., and Rothfield, L. I. (1992). Roles of MinC and MinD in the site-specific septation block mediated by the MinCDE system of *Escherichia coli*. *J. Bacteriol.* 174, 63–70. doi: 10.1128/jb.174.1.63-70.1992

Den Blaauwen, T., Buddelmeijer, N., Aarsman, M. E., Hameete, C. M., and Nanninga, N. (1999). Timing of FtsZ assembly in *Escherichia coli*. *J. Bacteriol.* 181, 5167–5175.

Di Ventura, B., Knecht, B., Andreas, H., Godinez, W. J., Fritsche, M., Rohr, K., et al. (2013). Chromosome segregation by the *Escherichia coli* Min system. *Mol. Syst. Biol.* 9:686. doi: 10.1038/msb.2013.44

Du, S., and Lutkenhaus, J. (2014). SlmA antagonism of FtsZ assembly employs a two-pronged mechanism like MinCD. *PLoS Genet.* 10:e1004460. doi: 10.1371/journal.pgen.1004460

Ducret, A., Quardokus, E. M., and Brun, Y. V. (2016). MicrobeJ, a tool for high throughput bacterial cell detection and quantitative analysis. *Nat. Microbiol.* 1:16077. doi: 10.1038/nmicrobiol.2016.77

Ebersbach, G., Briegel, A., Jensen, G. J., and Jacobs-Wagner, C. (2008). A self-associating protein critical for chromosome attachment, division, and polar organization in *Caulobacter*. *Cell* 134, 956–968. doi: 10.1016/j.cell.2008.07.016

Ehrle, H. M., Guidry, J. T., Iacovetto, R., Salisbury, A. K., Sandidge, D. J., and Bowman, G. R. (2017). Polar organizing protein PopZ Is required for chromosome segregation in *Agrobacterium tumefaciens*. *J. Bacteriol.* 199:e00111-17. doi: 10.1128/JB.00111-17

Eswaramoorthy, P., Erb, M. L., Gregory, J. A., Silverman, J., Pogliano, K., Pogliano, J., et al. (2011). Cellular architecture mediates DivIVA ultrastructure and regulates min activity in *Bacillus subtilis*. *MBio* 2:e00257-11. doi: 10.1128/mBio.00257-11

Figueroa-Cuilan, W., Daniel, J. J., Howell, M., Sulaiman, A., and Brown, P. J. (2016). Mini-Tn7 insertion in an artificial *att*Tn7 site enables depletion of the essential master regulator CtrA in the Phytopathogen *Agrobacterium tumefaciens*. *Appl. Environ. Microbiol.* 82, 5015–5025. doi: 10.1128/AEM.01392-16

Fu, X., Shih, Y. L., Zhang, Y., and Rothfield, L. I. (2001). The MinE ring required for proper placement of the division site is a mobile structure that changes its cellular location during the *Escherichia coli* division cycle. *Proc. Natl. Acad. Sci. U.S.A.* 98, 980–985. doi: 10.1073/pnas.98.3.980

Goley, E. D., Yeh, Y. C., Hong, S. H., Fero, M. J., Abeliuk, E., McAdams, H. H., et al. (2011). Assembly of the *Caulobacter* cell division machine. *Mol. Microbiol.* 80, 1680–1698. doi: 10.1111/j.1365-2958.2011.07677.x

Goodner, B., Hinkle, G., Gattung, S., Miller, N., Blanchard, M., Qurollo, B., et al. (2001). Genome sequence of the plant pathogen and biotechnology agent *Agrobacterium tumefaciens* C58. *Science* 294, 2323–2328. doi: 10.1126/science.1066803

Hale, C. A., Meinhardt, H., and de Boer, P. A. (2001). Dynamic localization cycle of the cell division regulator MinE in *Escherichia coli*. *EMBO J.* 20, 1563–1572. doi: 10.1093/emboj/20.7.1563

Howell, M., Aliashkevich, A., Salisbury, A. K., Cava, F., Bowman, G. R., and Brown, P. J. B. (2017a). Absence of the polar organizing protein PopZ results in reduced and asymmetric cell division in *Agrobacterium tumefaciens*. *J. Bacteriol.* 199:e00101-17. doi: 10.1128/JB.00101-17

Howell, M., Daniel, J. J., and Brown, P. J. B. (2017b). Live cell fluorescence microscopy to observe essential processes during microbial cell growth. *J. Vis. Exp.* e56497. doi: 10.3791/56497

Hu, Z., and Lutkenhaus, J. (1999). Topological regulation of cell division in *Escherichia coli* involves rapid pole to pole oscillation of the division inhibitor MinC under the control of MinD and MinE. *Mol. Microbiol.* 34, 82–90. doi: 10.1046/j.1365-2958.1999.01575.x

Hu, Z., and Lutkenhaus, J. (2000). Analysis of MinC reveals two independent domains involved in interaction with MinD and FtsZ. *J. Bacteriol.* 182, 3965–3971. doi: 10.1128/JB.182.14.3965-3971.2000

Hu, Z., and Lutkenhaus, J. (2001). Topological regulation of cell division in *E. coli*. Spatiotemporal oscillation of MinD requires stimulation of its ATPase by MinE and phospholipid. *Mol. Cell* 7, 1337–1343. doi: 10.1016/S1097-2765(01)00273-8

Hu, Z., and Lutkenhaus, J. (2003). A conserved sequence at the C-terminus of MinD is required for binding to the membrane and targeting MinC to the septum. *Mol. Microbiol.* 47, 345–355. doi: 10.1046/j.1365-2958.2003.03321.x

Jensen, R. B. (2006). Coordination between chromosome replication, segregation, and cell division in *Caulobacter crescentus*. *J. Bacteriol.* 188, 2244–2253. doi: 10.1128/JB.188.6.2244-2253.2006

Justice, S. S., Garcia-Lara, J., and Rothfield, L. I. (2000). Cell division inhibitors SulA and MinC/MinD block septum formation at different steps in the assembly of the *Escherichia coli* division machinery. *Mol. Microbiol.* 37, 410–423. doi: 10.1046/j.1365-2958.2000.02007.x

Kelly, A. J., Sackett, M. J., Din, N., Quardokus, E., and Brun, Y. V. (1998). Cell cycle-dependent transcriptional and proteolytic regulation of FtsZ in *Caulobacter*. *Genes Dev.* 12, 880–893. doi: 10.1101/gad.12.6.880

Kiekebusch, D., Michie, K. A., Essen, L. O., Lowe, J., and Thanbichler, M. (2012). Localized dimerization and nucleoid binding drive gradient formation by the bacterial cell division inhibitor MipZ. *Mol. Cell* 46, 245–259. doi: 10.1016/j.molcel.2012.03.004

Laub, M. T., Chen, S. L., Shapiro, L., and McAdams, H. H. (2002). Genes directly controlled by CtrA, a master regulator of the *Caulobacter* cell cycle. *Proc. Natl. Acad. Sci. U.S.A.* 99, 4632–4637. doi: 10.1073/pnas.062065699

Lenarcic, R., Halbedel, S., Visser, L., Shaw, M., Wu, L. J., Errington, J., et al. (2009). Localisation of DivIVA by targeting to negatively curved membranes. *EMBO J.* 28, 2272–2282. doi: 10.1038/emboj.2009.129

Li, Z., Trimble, M. J., Brun, Y. V., and Jensen, G. J. (2007). The structure of FtsZ filaments *in vivo* suggests a force-generating role in cell division. *EMBO J.* 26, 4694–4708. doi: 10.1038/sj.emboj.7601895

Livny, J., Yamaichi, Y., and Waldor, M. K. (2007). Distribution of centromere-like parS sites in bacteria: insights from comparative genomics. *J. Bacteriol.* 189, 8693–8703. doi: 10.1128/JB.01239-07

Loose, M., Fischer-Friedrich, E., Herold, C., Kruse, K., and Schwille, P. (2011). Min protein patterns emerge from rapid rebinding and membrane interaction of MinE. *Nat. Struct. Mol. Biol.* 18, 577–583. doi: 10.1038/nsmb.2037

Lutkenhaus, J. (2007). Assembly dynamics of the bacterial MinCDE system and spatial regulation of the Z ring. *Annu. Rev. Biochem.* 76, 539–562. doi: 10.1146/annurev.biochem.75.103004.142652

Lutkenhaus, J. (2012). The ParA/MinD family puts things in their place. *Trends Microbiol.* 20, 411–418. doi: 10.1016/j.tim.2012.05.002

Lutkenhaus, J., and Du, S. (2017). *E. coli* cell cycle machinery. *Subcell Biochem.* 84, 27–65. doi: 10.1007/978-3-319-53047-5_2

Ma, X., Ehrhardt, D. W., and Margolin, W. (1996). Colocalization of cell division proteins FtsZ and FtsA to cytoskeletal structures in living *Escherichia coli* cells by using green fluorescent protein. *Proc. Natl. Acad. Sci. U.S.A.* 93, 12998–13003. doi: 10.1073/pnas.93.23.12998

Meinhardt, H., and de Boer, P. A. (2001). Pattern formation in *Escherichia coli*: a model for the pole-to-pole oscillations of Min proteins and the localization of the division site. *Proc. Natl. Acad. Sci. U.S.A.* 98, 14202–14207. doi: 10.1073/pnas.251216598

Merritt, P. M., Danhorn, T., and Fuqua, C. (2007). Motility and chemotaxis in *Agrobacterium tumefaciens* surface attachment and biofilm formation. *J. Bacteriol.* 189, 8005–8014. doi: 10.1128/JB.00566-07

Möll, A., and Thanbichler, M. (2009). FtsN-like proteins are conserved components of the cell division machinery in proteobacteria. *Mol. Microbiol.* 72, 1037–1053. doi: 10.1111/j.1365-2958.2009.06706.x

Morton, E. R., and Fuqua, C. (2012a). Genetic manipulation of *Agrobacterium*. *Curr. Protoc. Microbiol.* Chapter 3:Unit 3D.2. doi: 10.1002/9780471729259.mc03d02s25

Morton, E. R., and Fuqua, C. (2012b). Laboratory maintenance of *Agrobacterium*. *Curr. Protoc. Microbiol.* Chapter 1:Unit3D.1. doi: 10.1002/9780471729259.mc03d01s24

Müller, P., Ewers, C., Bertsche, U., Anstett, M., Kallis, T., Breukink, E., et al. (2007). The essential cell division protein FtsN interacts with the murein (peptidoglycan) synthase PBP1B in *Escherichia coli*. *J. Biol. Chem.* 282, 36394–36402. doi: 10.1074/jbc.M706390200

Park, K. T., Villar, M. T., Artigues, A., and Lutkenhaus, J. (2017). MinE conformational dynamics regulate membrane binding, MinD interaction, and Min oscillation. *Proc. Natl. Acad. Sci. U.S.A.* 114, 7497–7504. doi: 10.1073/pnas.1707385114

Park, K. T., Wu, W., Battaile, K. P., Lovell, S., Holyoak, T., and Lutkenhaus, J. (2011). The Min oscillator uses MinD-dependent conformational changes in MinE to spatially regulate cytokinesis. *Cell* 146, 396–407. doi: 10.1016/j.cell.2011.06.042

Patrick, J. E., and Kearns, D. B. (2008). MinJ (YvjD) is a topological determinant of cell division in *Bacillus subtilis*. *Mol. Microbiol.* 70, 1166–1179. doi: 10.1111/j.1365-2958.2008.06469.x

Pini, F., De Nisco, N. J., Ferri, L., Penterman, J., Fioravanti, A., Brilli, M., et al. (2015). Cell cycle control by the master regulator CtrA in *Sinorhizobium meliloti*. *PLoS Genet.* 11:e1005232. doi: 10.1371/journal.pgen.1005232

Ptacin, J. L., Lee, S. F., Garner, E. C., Toro, E., Eckart, M., Comolli, L. R., et al. (2010). A spindle-like apparatus guides bacterial chromosome segregation. *Nat. Cell Biol.* 12, 791–798. doi: 10.1038/ncb2083

Radhakrishnan, S. K., Pritchard, S., and Viollier, P. H. (2010). Coupling prokaryotic cell fate and division control with a bifunctional and oscillating oxidoreductase homolog. *Dev. Cell* 18, 90–101. doi: 10.1016/j.devcel.2009.10.024

Ramamurthi, K. S., and Losick, R. (2009). Negative membrane curvature as a cue for subcellular localization of a bacterial protein. *Proc. Natl. Acad. Sci. U.S.A.* 106, 13541–13545. doi: 10.1073/pnas.0906851106

Raskin, D. M., and de Boer, P. A. (1999a). MinDE-dependent pole-to-pole oscillation of division inhibitor MinC in *Escherichia coli*. *J. Bacteriol.* 181, 6419–6424.

Raskin, D. M., and de Boer, P. A. (1999b). Rapid pole-to-pole oscillation of a protein required for directing division to the middle of *Escherichia coli*. *Proc. Natl. Acad. Sci. U.S.A.* 96, 4971–4976.

Rothfield, L., Taghbalout, A., and Shih, Y. L. (2005). Spatial control of bacterial division-site placement. *Nat. Rev. Microbiol.* 3, 959–968. doi: 10.1038/nrmicro1290

Rowlett, V. W., and Margolin, W. (2015). The Min system and other nucleoid-independent regulators of Z ring positioning. *Front. Microbiol.* 6:478. doi: 10.3389/fmicb.2015.00478

Schofield, W. B., Lim, H. C., and Jacobs-Wagner, C. (2010). Cell cycle coordination and regulation of bacterial chromosome segregation dynamics by polarly localized proteins. *EMBO J.* 29, 3068–3081. doi: 10.1038/emboj.2010.207

Shebelut, C. W., Jensen, R. B., and Gitai, Z. (2009). Growth conditions regulate the requirements for *Caulobacter* chromosome segregation. *J. Bacteriol.* 191, 1097–1100. doi: 10.1128/JB.00862-08

Simon, R., Priefer, U., and Puhler, A. (1983). A broad host range mobilization system for *in vivo* genetic engineering: transposon mutagenesis in gram negative bacteria. *Nat. Biotechnol.* 1, 784–791. doi: 10.1038/nbt1183-784

Sun, Q., and Margolin, W. (1998). FtsZ dynamics during the division cycle of live *Escherichia coli* cells. *J. Bacteriol.* 180, 2050–2056.

Surovtsev, I. V., and Jacobs-Wagner, C. (2018). Subcellular organization: a critical feature of bacterial cell replication. *Cell* 172, 1271–1293. doi: 10.1016/j.cell.2018.01.014

Szwedziak, P., Wang, Q., Bharat, T. A., Tsim, M., and Lowe, J. (2014). Architecture of the ring formed by the tubulin homologue FtsZ in bacterial cell division. *Elife* 3:e04601. doi: 10.7554/eLife.04601

Thanbichler, M., and Shapiro, L. (2006). MipZ, a spatial regulator coordinating chromosome segregation with cell division in *Caulobacter*. *Cell* 126, 147–162. doi: 10.1016/j.cell.2006.05.038

Tonthat, N. K., Arold, S. T., Pickering, B. F., Van Dyke, M. W., Liang, S., Lu, Y., et al. (2011). Molecular mechanism by which the nucleoid occlusion factor, SlmA, keeps cytokinesis in check. *EMBO J.* 30, 154–164. doi: 10.1038/emboj.2010.288

Wang, S. C., West, L., and Shapiro, L. (2006). The bifunctional FtsK protein mediates chromosome partitioning and cell division in *Caulobacter*. *J. Bacteriol.* 188, 1497–1508. doi: 10.1128/JB.188.4.1497-1508.2006

Watson, B., Currier, T. C., Gordon, M. P., Chilton, M. D., and Nester, E. W. (1975). Plasmid required for virulence of *Agrobacterium tumefaciens*. *J. Bacteriol.* 123, 255–264.

Williams, B., Bhat, N., Chien, P., and Shapiro, L. (2014). ClpXP and ClpAP proteolytic activity on divisome substrates is differentially regulated following the *Caulobacter* asymmetric cell division. *Mol. Microbiol.* 93, 853–866. doi: 10.1111/mmi.12698

Williams, M., Hoffman, M. D., Daniel, J. J., Madren, S. M., Dhroso, A., Korkin, D., et al. (2016). Short-stalked *Prosthecomicrobium hirschii* cells have a *Caulobacter*-like cell cycle. *J. Bacteriol.* 198, 1149–1159. doi: 10.1128/JB.00896-15

Wood, D. W., Setubal, J. C., Kaul, R., Monks, D. E., Kitajima, J. P., Okura, V. K., et al. (2001). The genome of the natural genetic engineer *Agrobacterium tumefaciens* C58. *Science* 294, 2317–2323. doi: 10.1126/science.1066804

Wu, L. J., and Errington, J. (2004). Coordination of cell division and chromosome segregation by a nucleoid occlusion protein in *Bacillus subtilis*. *Cell* 117, 915–925. doi: 10.1016/j.cell.2004.06.002

Wu, L. J., and Errington, J. (2011). Nucleoid occlusion and bacterial cell division. *Nat. Rev. Microbiol.* 10, 8–12. doi: 10.1038/nrmicro2671

Yang, X., Lyu, Z., Miguel, A., McQuillen, R., Huang, K. C., and Xiao, J. (2017). GTPase activity-coupled treadmilling of the bacterial tubulin FtsZ organizes septal cell wall synthesis. *Science* 355, 744–747. doi: 10.1126/science.aak9995

Conflict of Interest Statement: The authors declare that the research was conducted in the absence of any commercial or financial relationships that could be construed as a potential conflict of interest.

frontiers in Microbiology

MINI REVIEW
published: 31 January 2018
doi: 10.3389/fmicb.2018.00111

Turgor Pressure and Possible Constriction Mechanisms in Bacterial Division

Masaki Osawa and Harold P. Erickson*

Department of Cell Biology, Duke University Medical Center, Durham, NC, United States

Bacterial cytokinesis begins with the assembly of FtsZ into a Z ring at the center of the cell. The Z-ring constriction in Gram-negative bacteria may occur in an environment where the periplasm and the cytoplasm are isoosmotic, but in Gram-positive bacteria the constriction may have to overcome a substantial turgor pressure. We address three potential sources of invagination force. (1) FtsZ itself may generate force by curved protofilaments bending the attached membrane. This is sufficient to constrict liposomes *in vitro*. However, this force is on the order of a few pN, and would not be enough to overcome turgor. (2) Cell wall (CW) synthesis may generate force by pushing the plasma membrane from the outside. However, this would probably require some kind of Brownian ratchet to separate the CW and membrane sufficiently to allow a glycan strand to slip in. The elastic element is not obvious. (3) Excess membrane production has the potential to contribute significantly to the invagination force. If the excess membrane is produced under the CW, it would force the membrane to bleb inward. We propose here that a combination of FtsZ pulling from the inside, and excess membrane pushing membrane inward may generate a substantial constriction force at the division site. This combined force generation mechanism may be sufficient to overcome turgor pressure. This would abolish the need for a Brownian ratchet for CW growth, and would permit CW to operate by reinforcing the constrictions generated by FtsZ and excess membrane.

Keywords: ftsZ, bacterial division, tubulin, cytokinesis, turgor pressure

OPEN ACCESS

Edited by:
Arieh Zaritsky,
Ben-Gurion University of the Negev,
Beersheba, Israel

Reviewed by:
Daniel Haeusser,
Canisius College, United States
Mario Feingold,
Ben-Gurion University of the Negev,
Beersheba, Israel

****Correspondence:***
Masaki Osawa
masaki.osawa@duke.edu

Specialty section:
This article was submitted to Microbial Physiology and Metabolism, a section of the journal Frontiers in Microbiology

Received: *19 November 2017*
Accepted: *17 January 2018*
Published: *31 January 2018*

Citation:
Osawa M and Erickson HP (2018) Turgor Pressure and Possible Constriction Mechanisms in Bacterial Division. Front. Microbiol. 9:111. doi: 10.3389/fmicb.2018.00111

INTRODUCTION

The cytokinesis system of almost all bacteria and many archaea is based on a ring of the tubulin homolog FtsZ (Bi and Lutkenhaus, 1991), termed the Z ring, which recruits up to a dozen downstream proteins to achieve constriction of the membranes and cell wall (CW). FtsZ polymerizes into short protofilaments (~150–300 nm) which further associate into the Z ring. In many bacteria the protofilaments are tethered to the plasma membrane (PM) by FtsA, which binds the C-terminal peptide of FtsZ and inserts its own C-terminal amphipathic helix into the PM (Pichoff and Lutkenhaus, 2005). FtsA also plays a role in recruitment of downstream molecules that remodel the peptidoglycan CW (Weiss et al., 1999).

An important question for cytokinesis is whether the invagination of the PM needs to overcome the turgor force. The turgor force is considerable, with estimates ranging from 0.3 atm (Deng et al., 2011) to 3 atm (Cayley et al., 2000) for *Escherichia coli*, and up to 20 atm for *Bacillus subtilis* (Whatmore and Reed, 1990). For comparison a racing bicycle tire has a pressure of about 10 atm. If cytokinesis has to overcome this turgor force it will need very high forces. Whether it does has been a question of controversy in the field, and even between the two present authors.

Erickson has suggested that bacterial cytokinesis might "cheat turgor pressure" by taking place completely within the high pressure environment (Erickson, 2017). This seems well-established for Gram-negative bacteria, where the turgor pressure is generated and sustained by the outer membrane plus the CW, and the periplasm is isoosmotic with the cytoplasm. Then both PM ingression and adding peptidoglycan to the inner surface of the CW to grow the septum take place without fighting turgor. Erickson argued that this is likely also true for Gram-positive bacteria. The strongest argument for this is that cryo EM shows a periplasmic space of ∼20 nm between the PM and CW for Gram-positive bacteria. If the periplasm were not isoosmotic, the PM should be pressed against the CW. Isoosmolarity would be achieved if the thicker CW itself functions as a semipermeable membrane, with a porosity excluding proteins and molecules larger than ∼1,000 Da.

On the contrary, Osawa notes several lines of evidence that the CW of Gram-positive bacteria is leakier than the CW plus outer membrane of Gram-negative bacteria. First, at least one study of the CW of *B. subtilis* proposed a sieving size of 2 nm, which corresponds to the diameter of a 20 kDa globular protein (Demchick and Koch, 1996).

Second, the Sec and Tat secretion systems of *B. subtilis* have been well-delineated for transport across the PM, but no dedicated system has been described for transport across the CW. The simplest mechanism would be that once transported across the PM, small proteins such as beta-lactamase (29 kDa), cutinase (24 kDa), and GFP (28 kDa) diffusely pass through the CW into the extracellular medium (Palva et al., 1982; Tjalsma et al., 2004; Brockmeier et al., 2006; Vrancken et al., 2007). In contrast Gram-negative bacteria have a "main terminal branch" for transport of secretory proteins across the CW and outer membrane. In fact, an *E. coli* strain K 12 that does not express this transporter virtually does not secrete the periplasmic proteins to the media (Pugsley et al., 1997).

Third, many bacteriocins, which are peptides and proteins up to ∼20 kDa, are known to attack the PM of various Gram-positive bacteria, which means they are able to cross the CW. For example cyclic antibacterial peptide Enterocin AS-48 (7 kDa), which has a compact globular structure, kills a wide variety of Gram-positive bacteria by damaging the PM (Grande Burgos et al., 2014). Phospholipase A2 (14 kDa) also kills actively growing Gram-positive bacteria by extensive degradation of phospholipid (Foreman-Wykert et al., 1999). Dysgalacticin (21.5 kDa), a heat-labile bacteriocin, can kill both growing and non-growing *Streptococcus pyogenes* (Gram-positive bacteria) (Swe et al., 2009).

These results suggest the possibility that ∼20 kDa molecules can diffusively pass through the CW of Gram-positive bacteria. If this is the case, how could Gram-positive bacteria maintain a periplasm isoosmolar with cytoplasm? One possibility is that negatively charged lipoteichoic acids tethered to the PM create a Donnan-like equilibrium that mitigates the difference of osmotic pressure between cytoplasm and periplasm. This has been suggested by two studies (Oku et al., 2009; Percy and Grundling, 2014). Quantitative analysis is needed here. It remains possible that cell division might cheat the turgor force in Gram-negative bacteria, but would have to constrict against the full and much larger turgor force in Gram-positive bacteria.

Here we would like to discuss three potential sources for constriction force, and how they might function even in the presence of turgor force: (A) FtsZ bending the PM from the inside; (B) peptidoglycan assembly pushing the PM from the outside; and (C) excess membrane synthesis pushing the membrane to expand inward. The idea of membrane pushing suggests a new force mechanism in which the combined force of FtsZ pulling and membrane pushing could divide bacteria even against turgor pressure.

(A) FtsZ bending the PM from the inside: A number of mechanisms have been proposed for how FtsZ might generate a constriction force, which we have discussed previously (Erickson, 2009; Erickson et al., 2010; Erickson and Osawa, 2017). We favor a model where curved protofilaments generate a bending force on the membrane (Osawa et al., 2009). The strongest evidence came from experiments where FtsZ was tethered to liposomes by an artificial membrane tether. With the tether [(mts) membrane targeting sequence] on the normal C-terminal side, FtsZ-mts assembled Z rings inside tubular liposomes that constricted from the inside (Osawa et al., 2008). When the tether was switched to the opposite side, mts-FtsZ assembled Z rings on the outside, and these constricted the liposomes by squeezing (Osawa and Erickson, 2011). See Supplementary Figure S1 in Supplemental Material for images and diagram. These results are consistent with the FtsZ protofilaments having a defined curvature, and the direction of force determined by whether the tether was on the outside or inside of the curve.

A curved protofilament conformation was first observed for *E. coli* FtsZ adsorbed to cationic lipid monolayers (**Figure 1a**) (Erickson et al., 1996). These 24 nm diameter minirings were favored by GDP, suggesting a hydrolysis-linked conformational change. However, they have only been found for FtsZ from a few bacterial species (discussed in Erickson and Osawa, 2017). Also, GTPase deficient FtsZ can function in suppressor strains, suggesting that GTP hydrolysis is not essential for force generation and cell division (Bi and Lutkenhaus, 1992; Osawa and Erickson, 2006).

There is an alternative curved conformation that we have called "intermediate curved" (Erickson et al., 2010; Erickson and Osawa, 2017) with a diameter 100–200 nm. In many cases, these curved filaments appear mixed with straight protofilaments by negative stain EM, but they were more prominently developed after adsorption to a mica surface (Mingorance et al., 2005; Hamon et al., 2009; Mateos-Gil et al., 2012) or in crowding conditions (Popp et al., 2009) (**Figure 1b**). Intermediate curved

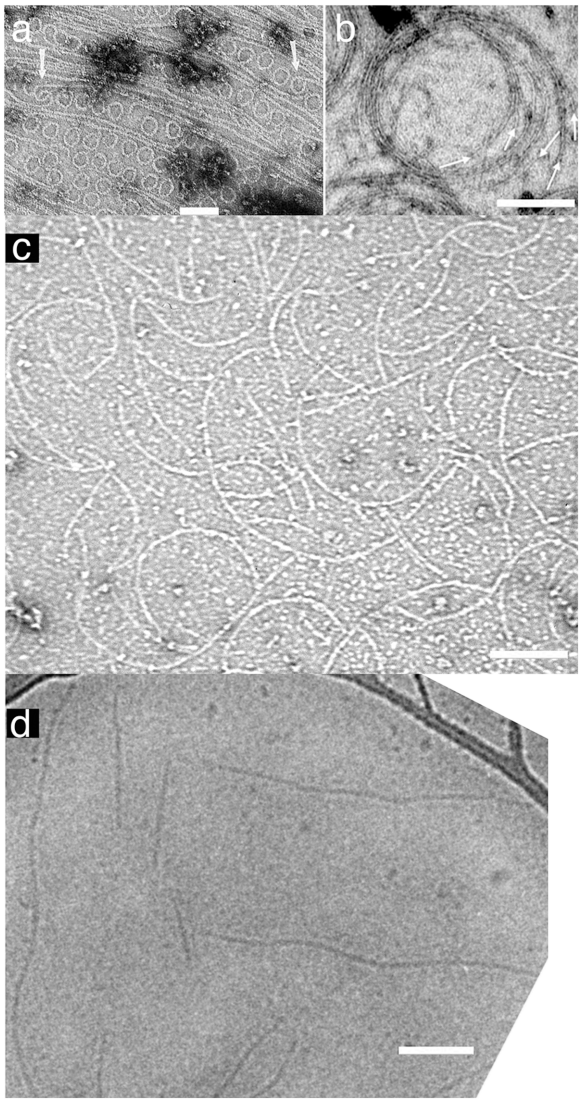

FIGURE 1 | Straight and curved protofilaments. **(a)** FtsZ protofilaments were absorbed on a cationic lipid membrane and then negatively stained for observation by EM. Many minirings approximately 24 nm diameter were observed. These minirings were probably stabilized with GDP-FtsZ (reprinted from Erickson et al., 1996). **(b)** FtsZ was polymerized into protofilaments in crowding buffer solution and then negatively stained. The protofilaments attached loosely to each other and formed curved bundles (inner diameter of the toroid is approximately 200 nm) (reprinted from Popp et al., 2009). **(c)** Protofilament assembly was observed without Mg^{2+}. In this condition all subunits in protofilaments were FtsZ-GTP. *Pseudomonas aeruginosa* FtsZ was used in this image (micrograph courtesy of Dr. Yaodong Chen, Northwest University, Xi'an, China). **(d)** FtsZ was polymerized into protofilaments in solution and then observed by cryo EM. These protofilaments, which apparently made no lateral contact with each other or a substrate, appear straight with some wavy structure (reprinted from Turner et al., 2012). Bars are 100 nm.

protofilaments could also be assembled in GTP plus EDTA, where the absence of Mg completely blocks GTP hydrolysis (Chen et al., 2005) (**Figure 1c**). Intermediate curved filaments were observed in a reconstitution system *in vitro* with FtsZ-mts (Osawa et al., 2009) or FtsZ/FtsA on a supported lipid bilayer (Szwedziak et al., 2014). Furthermore, the diameter of this curvature fits ∼200–300 nm minimum diameter of the Z ring *in vivo* (Soderstrom et al., 2014; Coltharp et al., 2016). We consider this intermediate curvature the likely conformation that generates bending force on the membrane (Erickson and Osawa, 2017).

Two recent studies have shown FtsI moving in circular paths around the Z ring, driven by patches of treadmilling FtsZ (Bisson-Filho et al., 2017; Yang et al., 2017). This may be important for distribution of the CW remodeling molecules, but may not be essential for constriction, because the treadmilling is governed by GTP hydrolysis which is not essential for division.

If GTP hydrolysis is not involved, then what drives the conformational change from straight to curved? One possibility is that the protofilaments are intrinsically curved and may bend the membrane like Bar domains in eukaryotic systems (Saarikangas et al., 2009). Another possibility is a transition from twist to curvature. Although FtsZ protofilaments with no attachment to any surfaces appear mostly straight in cryo EM (**Figure 1d**) (Turner et al., 2012), those filaments might be naturally twisted. Previous studies have suggested that the protofilament conformation might be a balance of twist and curvature (Arumugam et al., 2012; Gonzalez de Prado Salas et al., 2014). When a twisted filament binds the membrane the twist must straighten (so that all subunits face the membrane) and the energy is transferred to a curvature. Lateral interactions of several types seem to induce the curved conformation, perhaps by forcing untwisting (Mingorance et al., 2005; Hamon et al., 2009; Popp et al., 2009; Mateos-Gil et al., 2012). This hypothesis seems to be contradicted by the existence of straight, untwisted protofilaments in crystals of *Staphylococcus aureus* FtsZ (Matsui et al., 2012), but it remains an interesting idea.

(A1) Estimation of energy and force generated by Z rings: Knowing that reconstituted Z rings can divide unilamellar liposomes (**Figure 2A**), a minimum requirement of energy and force for liposome division can be estimated. Certain geometries, such as that shown in **Figure 2B** (Supplementary Material), generate daughters with surface area and volume equal to the mother. We assume that successful divisions of liposomes *in vitro* (**Figure 2A**) (Osawa and Erickson, 2013) approximate this geometry.

To estimate the minimum energy needed to achieve liposome division, we used Helfrich's equation (Helfrich, 1973), and calculated the bending energy of the membrane before and after division (**Figure 2B**). The derivation is given in Supplementary Material. A second calculation gave the minimum initial constriction force that could be generated by a Z ring based on the bending energy/force of isotropic rods (Lan et al., 2009). The minimum energy for full constriction of the liposome shown in **Figure 2B** is 8.0×10^{-19} J, which also estimates 0.35 pN as the minimum initial constriction force for a liposome of 1 μm diameter. The second calculation gives 5.6×10^{-18} J and 2.45 pN as the potential energy and force that could be generated by FtsZ filaments for initial constriction of a 1 μm diameter bacterium. These are similar to values described previously with different parameters (Lan et al., 2009). Both the energy and force for FtsZ bending are about 10 times larger than the minimum

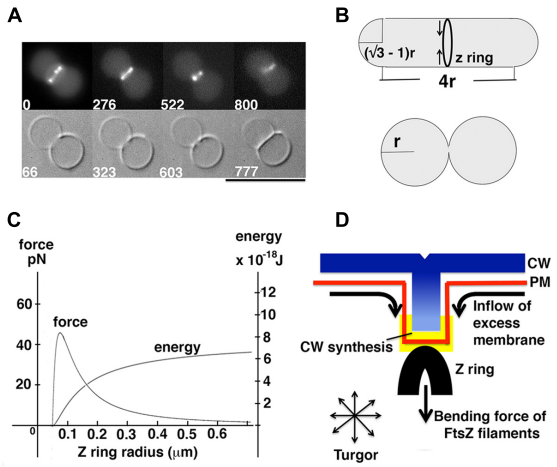

FIGURE 2 | Model for force generation by the Z ring *in vitro* and *in vivo*. **(A)** FtsZ formed Z rings in unilamellar liposomes with FtsA* (R286W), and the reconstituted Z rings divided liposomes with a clear septum (reprinted from Osawa and Erickson, 2013). A constraint on liposome division is posed by the fact that the membrane cannot be stretched more than 4% of the original area (Needham and Nunn, 1990). Because the membrane is impermeable to ions, reducing the volume by removing water would lead to higher salt inside and consequent osmotic pressure. With these constraints one cannot divide a spherical liposome, because the two daughter liposomes would have to shed 20% of the water of the mother. **(B)** Schematic view of liposome division by Z rings. In this particular geometry surface area and volume of the liposome does not change after division, in which case the Z ring only needs to bend the membrane. The successful division of the liposome in **(A)** probably approximates this geometry. **(C)** The relationship between force and energy with different Z ring radius. The graph was made from the equations for bending an isotropic rod (Supplementary Material) (Lan et al., 2009). **(D)** A model showing how excess phospholipid production can play a key role in Z ring constriction.

requirements for liposome division, consistent with the observed constriction *in vitro* (Osawa and Erickson, 2013). As shown in **Figure 2C**, the constriction force actually increases up to 45 pN at 200 nm diameter, which is approximately where FtsZ leaves the Z ring (Soderstrom et al., 2014; Coltharp et al., 2016).

In the absence of turgor, this force would be sufficient to divide a liposome of appropriate geometry. FtsZ bending membranes is almost certainly the major source of constriction force in mycoplasma and some archaea, which lack a CW and have minimal turgor force. If excess membrane were provided it could divide almost any geometry. However, it would probably not be sufficient to constrict the PM in the face of strong turgor.

(B) Peptidoglycan assembly pushing the PM from the outside: Another source of constriction force could be inward growth of the CW. Because the CW is a rigid structure, it should be capable of supporting the PM even if it is pressing against it with full turgor pressure. Coltharp and colleagues have suggested recently that the inward growth of the CW should be the major source of constriction force, while FtsZ serves primarily as a scaffold to define the location and orientation of the CW remodeling proteins (Coltharp et al., 2016; Coltharp and Xiao, 2017). In this case the curvature of FtsZ filaments may just work for fitting to the diameter of constriction site.

A detailed mechanism of pushing by CW ingrowth has not yet been developed. If the CW is to push the PM, it would seem necessary for it to contact the PM directly or indirectly through a membrane protein. This would need to eliminate the periplasmic space at the site of the site of contact. The invaginating CW must then insert glycan strands against the force on the PM. This would likely require a Brownian ratchet mechanism, in which either the CW or the PM were moving with sufficient distance and frequency to permit the glycan strands to slip in. In models of actin pushing membranes it was found that a simple Brownian ratchet would not work. The key was an elastic Brownian ratchet, in which flexing of the actin filaments provided the gaps for insertion (Mogilner and Oster, 1996). It is not clear where the Brownian motion would occur for CW pushing the PM against turgor. This may not work.

Plant and yeast cells are in a similar situation where the PM is surrounded by a rigid CW and is exposed to turgor pressure (Tepfer and Taylor, 1981; De Nobel et al., 1989). A recent paper proposed that the actin-myosin contractile ring for yeast division cannot constrict against this high turgor pressure (Proctor et al., 2012). This study found that constriction often continued after disruption of the actin-myosin ring, and concluded that the major constriction force is generated by the CW invagination.

Another consideration is that both plant and yeast cells can achieve endocytosis with an intracellular apparatus made of protein molecules (Samaj et al., 2005; Goode et al., 2015). This indicates that intracellular proteins can deform the membrane against high turgor pressure, without any contribution from CW invagination. It is not known how this works, but the mechanism may apply also to how bacteria divide even under turgor pressure. We suggest that the mechanism may utilize force from excess membrane synthesis, discussed next.

(C) Excess membrane synthesis pushing the membrane to expand inward: During cell elongation, membrane synthesis must match the expansion of the CW. If, however, membrane is synthesized in excess, it could only be accommodated by blebbing of the membrane. For a bacterial, plant or yeast cell, where the membrane is trapped by the rigid CW, the membrane can only bleb inward. Importantly, if a bleb is initiated by even a small force from a Z ring (or an endocytic apparatus), the excess membrane synthesis may contribute to further extension, perhaps even matching the turgor pressure (**Figure 2D**).

The extension of the rod during bacterial elongation is constant in both *E. coli* and *B. subtilis*, but this extension is reduced during Z ring constriction in both species (Burdett et al., 1986; Coltharp et al., 2016). If membrane synthesis continues at the same rate, it would be produced in excess during the constriction phase. One study actually showed that phospholipid production increased in both species during cross wall formation (Carty and Ingram, 1981), although another study of *E. coli* suggested that the productions of CW and phospholipid are synchronized (Gally et al., 1993). These studies were done 20–30 years ago and there has been no update. Because phospholipids are produced in the PM in bacteria (Zhang and Rock, 2008), phospholipid synthesis directly increases the area of PM and may largely cancel the effect of turgor pressure pressing the PM against the CW, especially once the PM initiates bending.

Because of the constraining CW, excess phospholipid production must push the membrane inward. A possible example is in Gram-positive *Streptomyces* species that grow as vegetative hyphae, where the PM can invaginate and form membrane cross walls without Z ring or CW support (Celler et al., 2016). This suggests that membrane production may be sufficient for membrane invagination against turgor pressure [However, the existence of cross walls in *Streptomyces* lacking FtsZ has been questioned by a recent study (Santos-Beneit et al., 2017)]. Membrane septa without CW were also observed in *B. subtilis* when one peptidoglycan synthase, PBP2B, was deleted (Daniel et al., 2000). Similar membrane septa were observed in *E. coli* with deletion of several lytic hydrolases (Heidrich et al., 2002), or with mutations in FtsK (Berezuk et al., 2014). Internalized PM was also observed in *B. subtilis* when membrane was overproduced by overexpression of AccDA, the enzyme for fatty acid synthesis (Mercier et al., 2013). That study also made a strong case that excess membrane synthesis was necessary and sufficient for division of *B. subtilis* L forms, lacking the CW and FtsZ. We suggest that septum formation without CW invagination is probably driven by excess membrane pushing the membrane inward, in some cases directed and assisted by the constriction force of the Z ring.

Combined Forces of FtsZ Pulling and Membrane Pushing May Divide Bacteria Even under Turgor Pressure

Assuming a substantial contribution from excess membrane production, the requirement of force generation by Z rings can probably be much smaller than expected previously (Lan et al., 2007). If excess membrane is exerting a lateral compressive force on the PM, a bleb may be initiated with only a small invagination force from FtsZ. A force of 2.45 pN or even 0.35 pN may suffice, depending on factors such as the pushing force of membrane and the initial bending curvature of membrane. Continued membrane synthesis would add substantially to any invagination force.

Excess membrane production may also facilitate CW ingrowth by canceling the effect of turgor pressure that pushes the PM against the ingressing CW. This could facilitate or eliminate the need for a Brownian ratchet to insert new glycan strands. In this case CW production might contribute to constriction by working as a ratchet to stabilize the newly constricted membrane. This could also explain how CW synthesis could be rate limiting for constriction (Coltharp et al., 2016). Bisson-Filho et al. (2017) suggested that dynamic FtsZ filaments may deform the membrane, and PG synthesis could reinforce the deformation on the other side. The PG reinforcement could be rate limiting.

The force generated by membrane synthesis could be sufficient to power invagination against a turgor force. Even in Gram-negative bacteria, whose PM is thought to be in an isoosmotic balance between cytoplasm and periplasm, membrane synthesis is needed to keep up with the invagination, and to avoid developing turgor pressure as cytoplasmic volume is reduced by septal ingrowth. This proposal might be also extend to yeast division and to endocytosis in yeast and plant cells, with excess PM providing an essential part of the force for membrane invagination.

Future Directions

A major problem is lack of information about the osmolarity of the periplasmic space in Gram-positive bacteria. Without this we don't even know whether cell division needs to overcome turgor pressure. Important new tools would be bacterial strains where FtsZ bending, CW synthesis and membrane synthesis can be regulated up and down. Biosensors that can measure the force generated by FtsZ and CW would be especially useful.

AUTHOR CONTRIBUTIONS

MO wrote and performed the theoretical analysis; HE assisted writing and deeply discussed a wide range of problems.

FUNDING

This work was supported by NIH grant R01-GM066014.

SUPPLEMENTARY MATERIAL

The Supplementary Material for this article can be found online at: https://www.frontiersin.org/articles/10.3389/fmicb.2018.00111/full#supplementary-material

REFERENCES

Arumugam, S., Chwastek, G., Fischer-Friedrich, E., Ehrig, C., Monch, I., and Schwille, P. (2012). Surface topology engineering of membranes for the mechanical investigation of the tubulin homologue FtsZ. *Angew. Chem. Int. Ed. Engl.* 51, 11858–11862. doi: 10.1002/anie.201204332

Berezuk, A. M., Goodyear, M., and Khursigara, C. M. (2014). Site-directed fluorescence labeling reveals a revised N-terminal membrane topology and functional periplasmic residues in the *Escherichia coli* cell division protein FtsK. *J. Biol. Chem.* 289, 23287–23301. doi: 10.1074/jbc.M114.569624

Bi, E., and Lutkenhaus, J. (1991). FtsZ ring structure associated with division in *Escherichia coli*. *Nature* 354, 161–164. doi: 10.1038/354161a0

Bi, E., and Lutkenhaus, J. (1992). Isolation and characterization of *ftsZ* alleles that affect septal morphology. *J. Bacteriol.* 174, 5414–5423. doi: 10.1128/jb.174.16.5414-5423.1992

Bisson-Filho, A. W., Hsu, Y. P., Squyres, G. R., Kuru, E., Wu, F., Jukes, C., et al. (2017). Treadmilling by FtsZ filaments drives peptidoglycan synthesis and bacterial cell division. *Science* 355, 739–743. doi: 10.1126/science.aak9973

Brockmeier, U., Wendorff, M., and Eggert, T. (2006). Versatile expression and secretion vectors for *Bacillus subtilis*. *Curr. Microbiol.* 52, 143–148. doi: 10.1007/s00284-005-0231-7

Burdett, I. D., Kirkwood, T. B., and Whalley, J. B. (1986). Growth kinetics of individual *Bacillus subtilis* cells and correlation with nucleoid extension. *J. Bacteriol.* 167, 219–230. doi: 10.1128/jb.167.1.219-230.1986

Carty, C. E., and Ingram, L. O. (1981). Lipid synthesis during the *Escherichia coli* cell cycle. *J. Bacteriol.* 145, 472–478.

Cayley, D. S., Guttman, H. J., and Record, M. T. Jr. (2000). Biophysical characterization of changes in amounts and activity of *Escherichia coli* cell and compartment water and turgor pressure in response to osmotic stress. *Biophys. J.* 78, 1748–1764. doi: 10.1016/S0006-3495(00)76726-9

Celler, K., Koning, R. I., Willemse, J., Koster, A. J., and Van Wezel, G. P. (2016). Cross-membranes orchestrate compartmentalization and morphogenesis in *Streptomyces*. *Nat. Commun.* 7:11836. doi: 10.1038/ncomms11836

Chen, Y., Bjornson, K., Redick, S. D., and Erickson, H. P. (2005). A rapid fluorescence assay for FtsZ assembly indicates cooperative assembly with a dimer nucleus. *Biophys. J.* 88, 505–514. doi: 10.1529/biophysj.104.044149

Coltharp, C., Buss, J., Plumer, T. M., and Xiao, J. (2016). Defining the rate-limiting processes of bacterial cytokinesis. *Proc. Natl. Acad. Sci. U.S.A.* 113, E1044–E1053. doi: 10.1073/pnas.1514296113

Coltharp, C., and Xiao, J. (2017). Beyond force generation: why is a dynamic ring of FtsZ polymers essential for bacterial cytokinesis. *Bioessays* 39, 1–11. doi: 10.1002/bies.201600179

Daniel, R. A., Harry, E. J., and Errington, J. (2000). Role of penicillin-binding protein PBP 2B in assembly and functioning of the division machinery of *Bacillus subtilis*. *Mol. Microbiol.* 35, 299–311. doi: 10.1046/j.1365-2958.2000.01724.x

Demchick, P., and Koch, A. L. (1996). The permeability of the wall fabric of *Escherichia coli* and *Bacillus subtilis*. *J. Bacteriol.* 178, 768–773. doi: 10.1128/jb.178.3.768-773.1996

Deng, Y., Sun, M., and Shaevitz, J. W. (2011). Direct measurement of cell wall stress stiffening and turgor pressure in live bacterial cells. *Phys. Rev. Lett.* 107:158101. doi: 10.1103/PhysRevLett.107.158101

De Nobel, J. G., Dijkers, C., Hooijberg, E., and Klis, F. M. (1989). Increased cell-wall porosity in *Saccharomyces cerevisiae* after treatment with Dithiothreitol or EDTA. *J. Gen. Microbiol.* 135, 2077–2084. doi: 10.1099/00221287-135-7-2077

Erickson, H. P. (2009). Modeling the physics of FtsZ assembly and force generation. *Proc. Natl. Acad. Sci. U.S.A.* 106, 9238–9243. doi: 10.1073/pnas.0902258106

Erickson, H. P. (2017). How bacterial cell division might cheat turgor pressure - a unified mechanism of septal division in Gram-positive and Gram-negative bacteria. *Bioessays* 39:1700045. doi: 10.1002/bies.201700045

Erickson, H. P., Anderson, D. E., and Osawa, M. (2010). FtsZ in Bacterial cytokinesis: cytoskeleton and force generator all in one. *Microbiol. Mol. Biol. Rev.* 74, 504–528. doi: 10.1128/MMBR.00021-10

Erickson, H. P., and Osawa, M. (2017). FtsZ constriction force - curved protofilaments bending membranes. *Subcell. Biochem.* 84, 139–160. doi: 10.1007/978-3-319-53047-5_5

Erickson, H. P., Taylor, D. W., Taylor, K. A., and Bramhill, D. (1996). Bacterial cell division protein FtsZ assembles into protofilament sheets and minirings, structural homologs of tubulin polymers. *Proc. Natl. Acad. Sci. U.S.A.* 93, 519–523. doi: 10.1073/pnas.93.1.519

Foreman-Wykert, A. K., Weinrauch, Y., Elsbach, P., and Weiss, J. (1999). Cell-wall determinants of the bactericidal action of group IIA phospholipase A2 against Gram-positive bacteria. *J. Clin. Invest.* 103, 715–721. doi: 10.1172/JCI5468

Gally, D., Bray, K., and Cooper, S. (1993). Synthesis of peptidoglycan and membrane during the division cycle of rod-shaped, gram-negative bacteria. *J. Bacteriol.* 175, 3121–3130. doi: 10.1128/jb.175.10.3121-3130.1993

Gonzalez de Prado Salas, P., Horger, I., Martin-Garcia, F., Mendieta, J., Alonso, A., Encinar, M., et al. (2014). Torsion and curvature of FtsZ filaments. *Soft Matter* 10, 1977–1986. doi: 10.1039/c3sm52516c

Goode, B. L., Eskin, J. A., and Wendland, B. (2015). Actin and endocytosis in budding yeast. *Genetics* 199, 315–358. doi: 10.1534/genetics.112.145540

Grande Burgos, M. J., Pulido, R. P., Del Carmen Lopez Aguayo, M., Galvez, A., and Lucas, R. (2014). The cyclic antibacterial peptide enterocin AS-48: isolation, mode of action, and possible food applications. *Int. J. Mol. Sci.* 15, 22706–22727. doi: 10.3390/ijms151222706

Hamon, L., Panda, D., Savarin, P., Joshi, V., Bernhard, J., Mucher, E., et al. (2009). Mica surface promotes the assembly of cytoskeletal proteins. *Langmuir* 25, 3331–3335. doi: 10.1021/la8035743

Heidrich, C., Ursinus, A., Berger, J., Schwarz, H., and Holtje, J. V. (2002). Effects of multiple deletions of murein hydrolases on viability, septum cleavage, and sensitivity to large toxic molecules in *Escherichia coli*. *J. Bacteriol.* 184, 6093–6099. doi: 10.1128/JB.184.22.6093-6099.2002

Helfrich, W. (1973). Elastic properties of lipid bilayers: theory and possible experiments. *Z. Naturforsch. C* 28, 693–703. doi: 10.1515/znc-1973-11-1209

Lan, G., Daniels, B. R., Dobrowsky, T. M., Wirtz, D., and Sun, S. X. (2009). Condensation of FtsZ filaments can drive bacterial cell division. *Proc. Natl. Acad. Sci. U.S.A.* 106, 121–126. doi: 10.1073/pnas.0807963106

Lan, G., Wolgemuth, C. W., and Sun, S. X. (2007). Z-ring force and cell shape during division in rod-like bacteria. *Proc. Natl. Acad. Sci. U.S.A.* 104, 16110–16115. doi: 10.1073/pnas.0702925104

Mateos-Gil, P., Paez, A., Horger, I., Rivas, G., Vicente, M., Tarazona, P., et al. (2012). Depolymerization dynamics of individual filaments of bacterial cytoskeletal protein FtsZ. *Proc. Natl. Acad. Sci. U.S.A.* 109, 8133–8138. doi: 10.1073/pnas.1204844109

Matsui, T., Yamane, J., Mogi, N., Yamaguchi, H., Takemoto, H., Yao, M., et al. (2012). Structural reorganization of the bacterial cell-division protein FtsZ from *Staphylococcus aureus*. *Acta Crystallogr. D Biol. Crystallogr.* 68, 1175–1188. doi: 10.1107/S0907444912022640

Mercier, R., Kawai, Y., and Errington, J. (2013). Excess membrane synthesis drives a primitive mode of cell proliferation. *Cell* 152, 997–1007. doi: 10.1016/j.cell.2013.01.043

Mingorance, J., Tadros, M., Vicente, M., Gonzalez, J. M., Rivas, G., and Velez, M. (2005). Visualization of single *Escherichia coli* FtsZ filament dynamics with atomic force microscopy. *J. Biol. Chem.* 280, 20909–20914. doi: 10.1074/jbc.M503059200

Mogilner, A., and Oster, G. (1996). Cell motility driven by actin polymerization. *Biophys. J.* 71, 3030–3045. doi: 10.1016/S0006-3495(96)79496-1

Needham, D., and Nunn, R. S. (1990). Elastic deformation and failure of lipid bilayer membranes containing cholesterol. *Biophys. J.* 58, 997–1009. doi: 10.1016/S0006-3495(90)82444-9

Oku, Y., Kurokawa, K., Matsuo, M., Yamada, S., Lee, B. L., and Sekimizu, K. (2009). Pleiotropic roles of polyglycerolphosphate synthase of lipoteichoic acid in growth of *Staphylococcus aureus* cells. *J. Bacteriol.* 191, 141–151. doi: 10.1128/JB.01221-08

Osawa, M., Anderson, D. E., and Erickson, H. P. (2008). Reconstitution of contractile FtsZ rings in liposomes. *Science* 320, 792–794. doi: 10.1126/science.1154520

Osawa, M., Anderson, D. E., and Erickson, H. P. (2009). Curved FtsZ protofilaments generate bending forces on liposome membranes. *EMBO J.* 28, 3476–3484. doi: 10.1038/emboj.2009.277

Osawa, M., and Erickson, H. P. (2006). FtsZ from divergent foreign bacteria can function for cell division in *Escherichia coli*. *J. Bacteriol.* 188, 7132–7140. doi: 10.1128/JB.00647-06

Osawa, M., and Erickson, H. P. (2011). Inside-out Z rings - constriction with and without GTP hydrolysis. *Mol. Microbiol.* 81, 571–579. doi: 10.1111/j.1365-2958.2011.07716.x

Osawa, M., and Erickson, H. P. (2013). Liposome division by a simple bacterial division machinery. *Proc. Natl. Acad. Sci. U.S.A.* 110, 11000–11004. doi: 10.1073/pnas.1222254110

Palva, I., Sarvas, M., Lehtovaara, P., Sibakov, M., and Kaariainen, L. (1982). Secretion of *Escherichia coli* beta-lactamase from *Bacillus subtilis* by the aid of alpha-amylase signal sequence. *Proc. Natl. Acad. Sci. U.S.A.* 79, 5582–5586. doi: 10.1073/pnas.79.18.5582

Percy, M. G., and Grundling, A. (2014). Lipoteichoic acid synthesis and function in gram-positive bacteria. *Annu. Rev. Microbiol.* 68, 81–100. doi: 10.1146/annurev-micro-091213-112949

Pichoff, S., and Lutkenhaus, J. (2005). Tethering the Z ring to the membrane through a conserved membrane targeting sequence in FtsA. *Mol. Microbiol.* 55, 1722–1734. doi: 10.1111/j.1365-2958.2005.04522.x

Popp, D., Iwasa, M., Narita, A., Erickson, H. P., and Maeda, Y. (2009). FtsZ condensates: an in vitro electron microscopy study. *Biopolymers* 91, 340–350. doi: 10.1002/bip.21136

Proctor, S. A., Minc, N., Boudaoud, A., and Chang, F. (2012). Contributions of turgor pressure, the contractile ring, and septum assembly to forces in

cytokinesis in fission yeast. *Curr. Biol.* 22, 1601–1608. doi: 10.1016/j.cub.2012.06.042

Pugsley, A. P., Francetic, O., Possot, O. M., Sauvonnet, N., and Hardie, K. R. (1997). Recent progress and future directions in studies of the main terminal branch of the general secretory pathway in Gram-negative bacteria–a review. *Gene* 192, 13–19. doi: 10.1016/S0378-1119(96)00803-7

Saarikangas, J., Zhao, H., Pykalainen, A., Laurinmaki, P., Mattila, P. K., Kinnunen, P. K., et al. (2009). Molecular mechanisms of membrane deformation by I-BAR domain proteins. *Curr. Biol.* 19, 95–107. doi: 10.1016/j.cub.2008.12.029

Samaj, J., Read, N. D., Volkmann, D., Menzel, D., and Baluska, F. (2005). The endocytic network in plants. *Trends Cell Biol.* 15, 425–433. doi: 10.1016/j.tcb.2005.06.006

Santos-Beneit, F., Roberts, D. M., Cantlay, S., Mccormick, J. R., and Errington, J. (2017). A mechanism for FtsZ-independent proliferation in *Streptomyces*. *Nat. Commun.* 8:1378. doi: 10.1038/s41467-017-01596-z

Soderstrom, B., Skoog, K., Blom, H., Weiss, D. S., Von Heijne, G., and Daley, D. O. (2014). Disassembly of the divisome in *Escherichia coli*: evidence that FtsZ dissociates before compartmentalization. *Mol. Microbiol.* 92, 1–9. doi: 10.1111/mmi.12534

Swe, P. M., Cook, G. M., Tagg, J. R., and Jack, R. W. (2009). Mode of action of dysgalacticin: a large heat-labile bacteriocin. *J. Antimicrob. Chemother.* 63, 679–686. doi: 10.1093/jac/dkn552

Szwedziak, P., Wang, Q., Bharat, T. A., Tsim, M., and Lowe, J. (2014). Architecture of the ring formed by the tubulin homologue FtsZ in bacterial cell division. *Elife* 3:e04601. doi: 10.7554/eLife.04601

Tepfer, M., and Taylor, I. E. (1981). The permeability of plant cell walls as measured by gel filtration chromatography. *Science* 213, 761–763. doi: 10.1126/science.213.4509.761

Tjalsma, H., Antelmann, H., Jongbloed, J. D., Braun, P. G., Darmon, E., Dorenbos, R., et al. (2004). Proteomics of protein secretion by *Bacillus subtilis*: separating the "secrets" of the secretome. *Microbiol. Mol. Biol. Rev.* 68, 207–233. doi: 10.1128/MMBR.68.2.207-233.2004

Turner, D. J., Portman, I., Dafforn, T. R., Rodger, A., Roper, D. I., Smith, C. J., et al. (2012). The mechanics of FtsZ fibers. *Biophys. J.* 102, 731–738. doi: 10.1016/j.bpj.2012.01.015

Vrancken, K., De Keersmaeker, S., Geukens, N., Lammertyn, E., Anne, J., and Van Mellaert, L. (2007). pspA overexpression in *Streptomyces lividans* improves both Sec- and Tat-dependent protein secretion. *Appl. Microbiol. Biotechnol.* 73, 1150–1157. doi: 10.1007/s00253-006-0571-7

Weiss, D. S., Chen, J. C., Ghigo, J. M., Boyd, D., and Beckwith, J. (1999). Localization of FtsI (PBP3) to the septal ring requires its membrane anchor, the Z ring, FtsA, FtsQ, and FtsL. *J. Bacteriol.* 181, 508–520.

Whatmore, A. M., and Reed, R. H. (1990). Determination of turgor pressure in *Bacillus subtilis*: a possible role for K+ in turgor regulation. *J. Gen. Microbiol.* 136, 2521–2526. doi: 10.1099/00221287-136-12-2521

Yang, X., Lyu, Z., Miguel, A., Mcquillen, R., Huang, K. C., and Xiao, J. (2017). GTPase activity-coupled treadmilling of the bacterial tubulin FtsZ organizes septal cell wall synthesis. *Science* 355, 744–747. doi: 10.1126/science.aak9995

Zhang, Y. M., and Rock, C. O. (2008). Membrane lipid homeostasis in bacteria. *Nat. Rev. Microbiol.* 6, 222–233. doi: 10.1038/nrmicro1839

Conflict of Interest Statement: The authors declare that the research was conducted in the absence of any commercial or financial relationships that could be construed as a potential conflict of interest.

The reviewer MF and handling Editor declared their shared affiliation.

frontiers in Microbiology

ORIGINAL RESEARCH
published: 11 September 2017
doi: 10.3389/fmicb.2017.01670

Z-ring Structure and Constriction Dynamics in *E. coli*

Pramod Kumar[1,2], *Amarjeet Yadav*[1,2], *Itzhak Fishov*[3] *and Mario Feingold*[1,2]*

[1] Department of Physics, Ben-Gurion University of the Negev, Beer Sheva, Israel, [2] The Ilse Katz Center for Nanotechnology, Ben-Gurion University of the Negev, Beer Sheva, Israel, [3] Department of Life Sciences, Ben-Gurion University of the Negev, Beer Sheva, Israel

The Z-ring plays a central role in bacterial division. It consists of FtsZ filaments, but the way these reorganize in the ring-like structure during septation remains largely unknown. Here, we measure the effective constriction dynamics of the ring. Using an oscillating optical trap, we can switch individual rod-shaped *E. coli* cells between horizontal and vertical orientations. In the vertical orientation, the fluorescent Z-ring image appears as a symmetric circular structure that renders itself to quantitative analysis. In the horizontal orientation, we use phase-contrast imaging to determine the extent of the cell constriction and obtain the effective time of division. We find evidence that the Z-ring constricts at a faster rate than the cell envelope such that its radial width (inwards from the cytoplasmic membrane) grows during septation. In this respect, our results differ from those recently obtained using photoactivated localization microscopy (PALM) where the radial width of the Z-ring was found to be approximately constant as the ring constricts. A possible reason for the different behavior of the constricting Z-rings could be the significant difference in the corresponding cell growth rates.

Keywords: bacterial division, Z-ring, optical tweezers, fluorescence microscopy, sub-pixel measurements

OPEN ACCESS

Edited by:
Conrad L. Woldringh, Retired, Naarden, Netherlands

Reviewed by:
Anirban Sain, Indian Institute of Technology Bombay, India
Yuval Garini, Bar-Ilan University, Israel

***Correspondence:**
Mario Feingold
mario@exchange.bgu.ac.il

Specialty section:
This article was submitted to Microbial Physiology and Metabolism, a section of the journal Frontiers in Microbiology

Received: *08 June 2017*
Accepted: *17 August 2017*
Published: *11 September 2017*

Citation:
Kumar P, Yadav A, Fishov I and Feingold M (2017) Z-ring Structure and Constriction Dynamics in E. coli. Front. Microbiol. 8:1670. doi: 10.3389/fmicb.2017.01670

INTRODUCTION

The investigation of bacterial cell division is imperative both for understanding the fundamentals of the life cycle of microorganisms and for numerous applications to biomedical problems. The core of the division machinery is the so-called Z-ring, formed from polymers of the tubulin-like protein FtsZ, and acting as an internal scaffold that correctly localizes synthetic enzymes (Margolin, 2005; Dajkovic and Lutkenhaus, 2006; Erickson et al., 2010). Moreover, it was suggested that FtsZ leads the septal peptidoglycan building machinery driving septum constriction (Bisson-Filho et al., 2017; Yang et al., 2017). Crystallographic, phylogenetic, and biochemical evidence indicate that FtsZ is the prokaryotic ancestor of tubulin (Erickson, 1997; Lowe and Amos, 1998). FtsZ contains a highly conserved N-terminus and a highly conserved C-terminal tail that are connected by a region of variable sequence and length. FtsZ polymerization *in vivo* and *in vitro* requires the N-terminus but not the C-terminus (Ma et al., 1996; Yu and Margolin, 1997). The C-terminus is important for interactions with other FtsZ molecules and other proteins such as FtsA and ZipA (Ma et al., 1996). In addition to Mg^{2+}, the GTPase activity of FtsZ is dependent on FtsZ protein concentration, suggesting that GTPase activity is coupled to assembly (de Boer et al., 1992; RayChaudhuri and Park, 1992; Mukherjee et al., 1993; Lu et al., 1998; Sossong et al., 1999; Salvarelli et al., 2011). These data are also supported by the FtsZ crystal structure, which revealed an active site shared by two FtsZ monomers.

Z-rings on the cytoplasmic membrane have been observed by both immunogold electron microscopy (Bi and Lutkenhaus, 1991) and fluorescence microscopy (Addinall and Lutkenhaus, 1996; Levin and Losick, 1996; Ma et al., 1996). GFP-tagged FtsZ expressed at low levels co-polymerizes with native FtsZ in the cell without inhibition of cell division, allowing to study its localization and dynamic behavior in living cells. As the septum grows inward, the Z-ring contracts at its leading edge until cytokinesis is nearly complete, at which time FtsZ disperses, perhaps by looping out subunits from the central core (Sun and Margolin, 1998). Under certain conditions, FtsZ can form spirals and arcs that successfully invaginate to form asymmetric septa (Addinall and Lutkenhaus, 1996). FtsZ does not seem to interact directly with membrane phospholipids *in vivo*. Instead, it binds to the membrane only via a complex with ZipA and/or FtsA. Positioning of the Z-ring in the cell, and consequently of the division site, is determined by two regulatory systems—MinCDE (see Rothfield et al., 2005; Lutkenhaus, 2007 for reviews) and nucleoid occlusion (Wu and Errington, 2004; Bernhardt and de Boer, 2005).

Z-ring dynamics *in vivo* was monitored by wide-field fluorescence microscopy (Sun and Margolin, 1998; Thanedar and Margolin, 2004; Monahan et al., 2009) and other related methods (Stricker et al., 2002). One of the important results of these works is that FtsZ displays a highly dynamic behavior, oscillating along the cell presumably driven by the regulatory MinCDE system. Spatially, these oscillations follow an extended helically shaped pattern. In *B. subtilis*, it was suggested that the helix-to-ring transition of FtsZ is promoted by ZapA, stimulating lateral FtsZ association (Monahan et al., 2009). Fluorescence recovery after photobleaching (FRAP) was also used to study the Z-ring dynamics showing a fast exchange of FtsZ between the ring and the cytoplasm (Stricker et al., 2002). Moreover, Optical Tweezers assisted imaging allowed to view the Z-ring as a circular structure (axial view) and measure its width inwards from the cytoplasmic membrane, Δ (**Figure 1**) (Carmon et al., 2012, 2014). Prior to the onset of constriction, it was shown that Δ is about 100 nm. This result lead to the suggestion that the Z-ring consists of a random network of FtsZ filaments (Piro et al., 2013) which, in turn, is consistent with results from polarization microscopy indicating that the FtsZ filaments in the ring are randomly oriented (Si et al., 2013).

More recently, the Z-ring was also studied using a wide range of super-resolution microscopy techniques. Fu et al. used photoactivated localization microscopy (PALM) showing that in *E. coli* the ring has a helical structure along the cytoplasmic membrane on a sub-optical resolution length scale (Fu et al., 2010). A similarly structured Z-ring was also observed in *B. subtilis* using stimulated emission depletion (STED) (Jennings et al., 2010). Biteen et al. were the first to obtain 3D super-resolution images of the Z-ring using astigmatism to determine the height of individual fluorophores in a PALM system (Biteen et al., 2012). Imaging the axial view of the Z-ring in pre-divisional *C. crescentus* cells they show that it has a significant radial width, consistent with the results of Carmon et al. (2012, 2014). Another 3D super-resolution microscopy approach, 3D structured illumination microscopy (3D-SIM), also allows obtaining an axial view of the Z-ring (Strauss et al., 2012; Rowlett and Margolin, 2014). 3D-SIM imaging revealed that the Z-ring in both *B. subtilis* and *E. coli* is inhomogeneous along its circumference displaying 120–200 nm gaps and a bead-like structure. Astigmatism 3D-PALM (Holden et al., 2014) and 2D-PALM of vertically immobilized cells (Jacq et al., 2015) were used to show that the Z-rings of *C. crescentus* and *S. pneumoniae*, respectively, exhibit a similar structure.

3D-SIM and 3D-PALM were also used to monitor the dynamics of the ring structure on the different time scales (Strauss et al., 2012; Holden et al., 2014; Coltharp et al., 2016). Strauss et al. (2012) have shown that the distribution of FtsZ along the Z-ring circumference in both *B. subtilis* and *S. aureus* significantly changes within 10 s. This behavior was observed for cells before the onset of constriction, during constriction and at a non-permissive temperature where cell division is inhibited. While providing much better resolution than 3D-SIM, 3D-PALM requires relatively long acquisition times (e.g., 80 s; Holden et al., 2014) and may lead to some photodamage, limiting its use for single cell time-lapse microscopy. Instead, 3D-PALM was used to obtain the effective dynamics of Z-ring constriction (Holden et al., 2014; Coltharp et al., 2016). The ring geometry was measured for a set of cells that were at different stages in

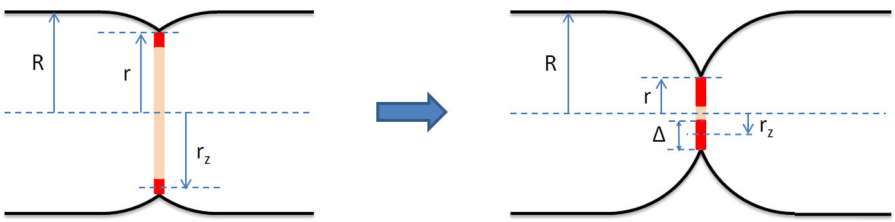

FIGURE 1 | Geometrical model of the bacterial septum and the Z-ring (red) at early **(Left)** and late **(Right)** stages of constriction. It assumes that before the onset of division the cell shape is that of a cylinder with two hemispherical caps. The cell radius, R, is defined as the radius of the cylindrical section of the cell enclosed by the cytoplasmic membrane. We assume that R is constant throughout the septation process. During division, the septum consists of two incomplete hemispheres joined at midcell. We define the constriction radius, r, as the radius of the circle joining the two septal incomplete hemispheres. The Z-ring is modeled as a wide ring centered in the septal plane and attached to the cytoplasmic membrane. Its radius, r_Z, is measured from the middle of its radial width to the long cell axis and its radial width, Δ, is twice the difference between r and r_Z, $\Delta = 2(r - r_Z)$. Our results indicate that for fast growing *E. coli* cells the radial width of the Z-ring, Δ, grows during septation.

the division process. For both *C. crescentus* and *E. coli* cells, it was shown that the radial and the longitudinal widths of the ring remain approximately constant until a certain stage of the constriction when the Z-ring rapidly collapses. To determine the time along the cell cycle for each individual cell, Holden et al. used a synchronous population, measuring time from the onset of synchrony till the imaging of the live cell (Holden et al., 2014). In contrast, Coltharp et al. used interferometric PALM (iPALM) to image the Z-ring in fixed *E. coli* (Coltharp et al., 2016). In their approach, the various ring characteristics are measured as a function of the corresponding ring diameter, that, in turn, is calibrated to indicate the effective time along the cell division period. In both Holden et al. (2014) and Coltharp et al. (2016) the effective time is obtained as a population average and the timing variability between the cells in the population is only partially accounted for. This may explain the large fluctuations in their single cell data for the radial and longitudinal widths of the Z-ring, contrasting with the high precision of 3D-PALM imaging.

Another important observation of the recent 3D-PALM studies of Z-ring constriction is that most of the rings that were imaged were incomplete and a significant fraction appeared as arcs shorter than semicircles (Holden et al., 2014; Coltharp et al., 2016). A possible reason for this behavior might be the fact that in both studies cells were grown in minimal media corresponding to long generation times, e.g., 181 min and 193 min in *E. coli* (Coltharp et al., 2016). In this slow growth regime, the amount of FtsZ available for Z-ring formation may be limited leading to strongly inhomogeneous rings. This seems consistent with the fact that there is much less FtsZ in slow growing than in fast growing cells (Link et al., 1997; Lu et al., 1998; Rueda et al., 2003; Ishihama et al., 2008; Vendeville et al., 2011). Specifically, there are ∼300 FtsZ proteins in low growth rate *E. coli* cells (generation time $>$ 100 min) (Link et al., 1997) and 3,000–15,000 in high growth rate *E. coli* (generation time $\simeq$ 20 min) (Lu et al., 1998; Rueda et al., 2003). Another result of Coltharp et al. (2016) that, following the onset of constriction, the cylindrical cell segment stops growing and the only contribution to cell elongation is from the new cap region may also provide support for such scenario. It has been suggested that the ending of cylindrical growth is due to the competition with the growth of the new caps over the limited resources of peptidoglycan precursor materials (Begg et al., 1990; Lleo et al., 1990), analogously to the limit on the amount of FtsZ. In contrast, for fast growing cells it was shown that cylindrical growth continues throughout constriction with only a moderate slowdown, ∼30%, from its predivisional rate (Reshes et al., 2008a,b).

To test whether the behavior of the Z-ring is different for *E. coli* cells in the high growth rate regime, we study the dynamics of Z-ring constriction for cells growing in Luria broth at 37°C. Although in our imaging approach we use conventional optical microscopy, optical trapping allows us to view the Z-ring as a circular structure without the need of image reconstruction. This feature of our system together with a combination of both spatial and temporal averaging leads to measurements of the Z-ring radius that are of comparable accuracy to those obtained using iPALM (Coltharp et al., 2016).

Specifically, we use optical trapping to image the Z-ring while the *E. coli* cell is oriented with its long axis either in the imaging plane or perpendicular to it. For each orientation, first the cell is imaged using fluorescence to view the GFP labeled Z-ring and next with phase contrast microscopy to obtain the cell shape. Recently, we have used this approach to measure the width of the Z-ring in unconstricted *E. coli* (Carmon et al., 2012, 2014). Here, we analyze constricting cells at different stages of the division process. Since exposure to the trapping laser of more than ∼20 s interferes with normal cell growth (Neuman et al., 1999; Ayano et al., 2006), we cannot measure the ring constriction dynamics of individual cells (see Supplementary Material). Instead, we use the measured septal width to obtain an effective time of division, t', for each of the individual cells (Reshes et al., 2008a,b). Together with the measured radius of the Z-ring, r_z , this leads to the effective Z-ring constriction dynamics, $r_z(t')$. We find that the Z-rings of fast growing *E. coli* appear to be much more uniform along their circumference than those in Holden et al. (2014) and Coltharp et al. (2016). Moreover, we present evidence that Z-rings constrict at a faster rate than the cell envelope and their radial width grows during septation.

MATERIALS AND METHODS

Bacterial Strains and Growth Conditions

To study the effective constriction dynamics of the Z-ring, we used the EC448 strain of *E. coli* [courtesy of Weiss (Weiss et al., 1999)]. Its chromosome contains *ftsZ-gfp* under the control of a weakened *trc* promoter at the lambda attachment site (*attB*). In turn, the *trc* promoter is regulated by isopropyl-β-D-thiogalactoside (IPTG). While FtsZ-GFP displays a similar localization pattern as the wild type FtsZ, it does not fulfill its function in the septation process (Ma et al., 1996). At low levels of IPTG induction (40μM), it was shown that in EC448 the fraction of FtsZ-GFP of the total amount of FtsZ in the cell is between 30 and 40% and cells manifest normal growth (Thanedar and Margolin, 2004). In our experiments, FtsZ-GFP expression was induced at two IPTG concentrations: (1) weak induction at 40μM and (2) strong induction at 500μM. We found that the growth rate of strong induction cells was not affected by the addition of the IPTG and the 3D structure of the Z-ring appears to be similar in both weak and strong induction cells. Note that the induction time used in this work (1 h) is significantly shorter than in Thanedar and Margolin (2004) and Tsukanov et al. (2011) (2–3 and 1.5–2h, respectively). Our approach, namely, using high IPTG concentration and short induction time, leads to relatively uniform expression levels in the cell population (Siegele and Hu, 1997), reducing the effect of expression level variability on Z-ring images from different cells. To estimate the relative FtsZ-GFP expression level, we have compared the average fluorescence intensity within cells and found that it is only twice larger in strong induction experiments than in weak induction experiments (despite a 12.5 ratio in IPTG concentration). Therefore, in our strong induction experiments the amount of FtsZ-GFP/cell is

in the same range as in the work of Thanedar and Margolin (2004).

Cells were grown at 37°C in Luria broth (LB) until $OD_{600} = 0.1$ in the exponential regime. At this optical density we added the IPTG to the cell medium and allowed cells to grow for another 1 h. For microscopy, the cell solution was further diluted 100 times in LB with IPTG.

Microscopy and Optical Trapping

The experimental system was described in detail elsewhere (Carmon et al., 2012, 2014). Briefly, we use an inverted microscope (IX70, Olympus) with a 100X objective (UPLFLN 100XO2PH, 1.3 NA, oil immersion) and a cooled CCD (CoolSNAP ES^2, Photometrics) to image individual *E. coli* cells. The optical trap consists of a laser beam (SDL, $\lambda = 830$ nm) that is focused onto the (x, y) imaging plane via the microscope objective. The trap is stiffer in the (x, y) plane than along the optical axis (z axis), such that trapped cells are aligned with their long axis in the z direction (vertical orientation). This allows imaging the Z-ring as a circular structure. To view cells with their long axis in the (x, y) plane (horizontal orientation), we use a galvanometric mirror that oscillates the trap along the x axis with a frequency of ∼100 Hz and an amplitude equal to the cell length. This leads to an effective linear trap and to horizontal aligning of the trapped cell. Cells can be imaged in either phase contrast or fluorescence for both horizontal and vertical orientations. Our system allows switching within a few seconds between each of these four different imaging modes.

RESULTS

Constricting cells, in which the FtsZ-GFP expression was induced at 500 μ M IPTG, were imaged in each of the four modes starting with the vertical GFP fluorescence. The latter and the horizontal phase contrast mode were used to obtain quantitative data on the Z-ring dynamics. We use the vertical GFP fluorescence images to measure the ring radius, r_z (see **Figure 1**), whenever the contrast was beyond a certain level previously shown to ensure accurate values of r_z (Carmon et al., 2012, 2014). The threshold contrast level was determined in calibration experiments where r_z is computed for an individual cell while the fluorescence intensity is gradually bleached due to repeated exposures. We find the best fitting circle to the ring image and compute radial intensity profiles along 360 rays that radiate from the center of this circle at 1° intervals (Carmon et al., 2012, 2014). Next, we average the radial profiles and define r_z as the distance from the center to the point where the average radial profile is maximal. Unlike in 3D-PALM imaging of the Z-ring where it was shown that most rings are incomplete (Holden et al., 2014; Coltharp et al., 2016), we obtain ring images that are remarkably homogeneous along their circumference (**Figures 2A–D** and Figures S2A–D). This difference in the appearance of the Z-ring can only partially be due to the limited resolution of our system. Diffraction will not obscure gaps in the circumference of the Z-ring with an angular extent of more than about 30°, while most of the Z-ring gaps in Holden et al. (2014) and Coltharp et al. (2016) are much larger. Instead, the large gaps found in the 3D-PALM studies are due to the low level of FtsZ in the slow growing cells. The

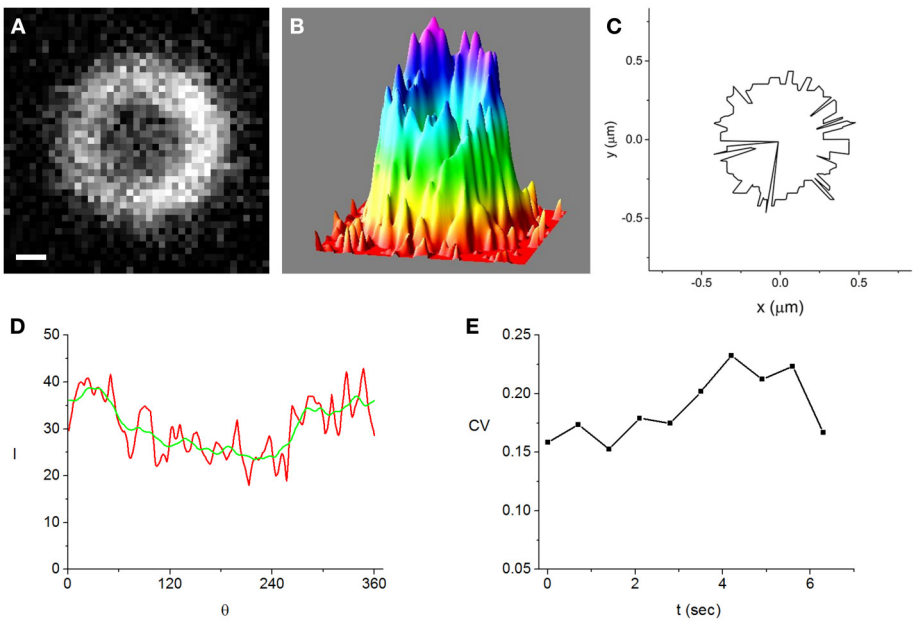

FIGURE 2 | A Z-ring that is among the most inhomogeneous of the cells that we analyzed in strong induction experiments (500 μM IPTG). Bar = 0.2 μm. **(A)** fluorescence image of the ring obtained while the cell is trapped in the vertical orientation, **(B)** intensity distribution corresponding to the image shown in **(A)**, **(C)** maximal intensity angular contour tracing the position where the radial profiles are maximal, $r_Z(\theta)$, **(D)** intensity along the maximal intensity angular contour, $I(\theta)$ (red). It is radially averaged over a 21 nm wide strip centered at $r_Z(\theta)$. For comparison, the angularly smoothed $I(\theta)$ over a range of the order of the optical resolution, ∼250 nm, is also shown (green), **(E)** time-dependence of the coefficient of variation (CV) (see text). It measures the degree of inhomogeneity of the angularly smoothed $I(\theta)$.

ring homogeneity that we find in our experiments is consistent with the results from 3D-SIM (Rowlett and Margolin, 2014), where Z-rings of fast growing *E. coli* were found to be continuous aside from holes typically smaller than the diffraction limit. Accordingly, in our images such holes represent an extremely rare occurrence found only in the most inhomogeneous ring images that were recorded (**Figures 2A–D**). We note that Rowlett et al. (Rowlett and Margolin, 2014) used either FtsZ-GFP at weak induction (30 μ M IPTG) or immunofluorescence to image Z-rings, obtaining similar, relatively homogeneous distributions of FtsZ along the ring circumference with no gaps larger than ∼250 nm. This suggests that, in their experiments, the absence of large gaps in the Z-ring is not due to the additional FtsZ-GFP in the cell, which seems to have no visible effect on the FtsZ distribution in the ring.

To characterize the inhomogeneity in the ring images we use the angular intensity profiles averaged over a strip of 21 nm centered at r_z, $I(\theta)$ (**Figure 2D** and Figures S1D, S2D, S3). We find that the angular profiles are noisy but do not vary much on scales larger than the optical resolution, ∼250 nm. Using the coefficient of variation (CV ≡ standard deviation/average) of the $I(\theta)$ smoothed over an angular range corresponding to the optical resolution to quantify the ring inhomogeneity, we note that it is similar in the most homogeneous and most inhomogeneous rings. Moreover, the CV's are roughly constant on a 10 s time scale (**Figure 2E** and Figure S2E) and in the same range for weak induction cells (Figure S1E). Although the fluctuations in the time dependence of the CV for weak induction cells (Figure S1E) appear to be larger than those of strong induction cells (**Figure 2E**), the difference between them is not statistically significant (see Supplementary Material).

Although the degree of inhomogeneity in the angular profiles is approximately constant on short time scales and at different levels of induction, several factors lead to significant errors in the measured values of r_z. Due to the angular inhomogeneity of the ring in an individual cell, the maximal intensity in the radial profiles corresponding to different angles is located at slightly different radial distances, $r_z(\theta)$ (**Figure 2C** and Figure S2C). Since $r_z \approx < r_z(\theta) >$, the error of r_z, Δr_z, contains a contribution due to the deviations of $r_z(\theta)$ from its average. Another contribution to Δr_z is due to the Brownian motion of the trapped cell. In the vertical orientation, the peak to peak amplitude of these fluctuations is about 100 nm. Although this length scale is below optical resolution, ∼250 nm, these fluctuations will lead to an additional smearing of the ring image. Moreover, the Brownian cell motion affects the ring image by varying its distance from the focal plane. To reduce Δr_z, we average the measured values of r_z over multiple frames (exposure time = 0.5 s, time between frames = 0.2 s). Out of the 50 frame movies recorded for each cell, we select only the N frames for which the ring image satisfies our minimal contrast requirement. For the time averaged r_z, the error is defined as the standard deviation divided by $\sqrt{N}$. For most cells, this error is of the order of only a few nm and its average over all cells is 4.6 nm.

We have used the procedure described above to measure r_z for 25 cells that displayed varying depths of constriction. To compare the geometry of the Z-ring with that of the septum at different stages of cell division, we also measured the constriction radius, r, and the cell radius, R, for each of these cells (**Figure 1**). To this end, we use the horizontal phase contrast imaging mode and obtain cell contours with sub-pixel accuracy. Our approach to computing such contours from phase contrast images was described in Reshes et al. (2008a). We stain the cytoplasmic membrane with FM4-64 to obtain the average value of the normalized phase contrast intensity that corresponds to the edge of the cell. For this calibration, we analyzed seven trapped cells and obtained a phase contrast threshold value. On a rescaled intensity axis where the background is set to unity and the interior of the cell to zero, we find that the cell edge corresponds to an intensity value of 0.56. Using 2D linear interpolation to obtain intensity values at positions in between pixel centers allows determining the cell contour with an accuracy of ∼30 nm. The value of the constriction radius, r, is best estimated as half the shortest distance between two contour points on opposite sides of the cell not too far from midcell (see **Figure 1**). Moreover, we approximate the cell radius, R, as half the average distance between the opposite cell sides away from the constriction region and from the cell caps (**Figure 1**). Similar to the case of r_z, here as well, the measurement errors of r and R, Δr, and ΔR, although much smaller than the optical resolution, are nevertheless too large to obtain the behavior of $r_z(r)$ with sufficient accuracy. Specifically, 25 nm $< \Delta r <$ 53 nm and 7 nm $< \Delta R <$ 19 nm. As before, we use time averaging to reduce Δr and ΔR. We record a 50 frames movie in the horizontal phase contrast mode (exposure time = 0.02 s, time between frames = 0.2 s) instead of a single image and average the values of r and R over all frames. The errors of these averages are all less than 3 nm.

Since individual cells have slightly different radii, it is expected that normalizing the Z-ring radius, r_z, and the constriction radius, r, by the cell radius, R, will reduce the effect of the population variability. Accordingly, we find that the normalized Z-ring radius, $W_z \equiv r_z/R$, appears to vary linearly as a function of the normalized constriction width, $W \equiv r/R$, up to fluctuations that are probably due to population variability (**Figure 3**). The best linear fit to the data, $W_z = aW + b$, corresponds to $a = 1.47 \pm 0.02$ and $b = -0.52 \pm 0.01$, indicating that the Z-ring constricts faster than the cell septum (see Supplementary Material). Since the outer edge of the Z-ring is attached to the cytoplasmic membrane and its radius, r_z, the position of the maximal intensity of the radial profile, corresponds to the middle of the ring's radial width, the behavior of $W_z(W)$ suggests that, for fast growing cells, the radial width of the ring grows as the constriction is progressing. While this behavior is different from the approximately constant radial width found in slow growing cells (Coltharp et al., 2016) (see Figure S6), it represents an analogous trend to the significantly more homogeneous Z-rings than those of Coltharp et al. (2016). We expect that both these differences between our results and those of Coltharp et al. (2016) are due to the larger amount of FtsZ available in fast growing cells.

To obtain the constriction dynamics of the Z-ring, we establish the effective division time for each individual cell using the corresponding values of r and R. We have previously shown that the normalized constriction width of individual cells, W,

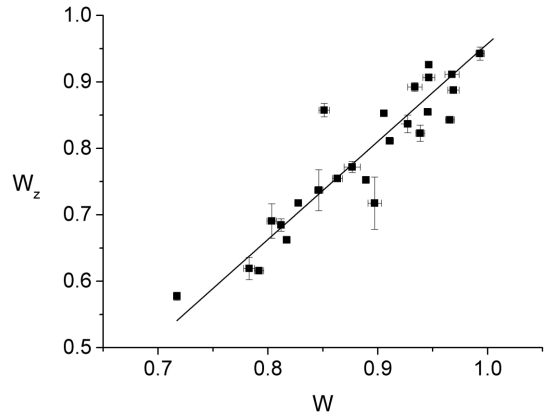

FIGURE 3 | Dependence of the normalized Z-ring radius, $W_z \equiv r_z/R$, on the normalized radius of the constriction, $W \equiv r/R$. Each of the data points (squares with error bars) represents the measurement from an individual cell. The error bars are due to the fluctuations in the values of either W_z or W between the frames used for the time averaging. While for W we averaged over 50 consecutive frames, in the case of W_z the number of frames entering the average varied between 4 and 40 as only images with sufficient contrast were included. The 25 cells of the data set were measured in 9 different strong induction experiments (500 μM IPTG). The corresponding best linear fit to the data is also shown (line).

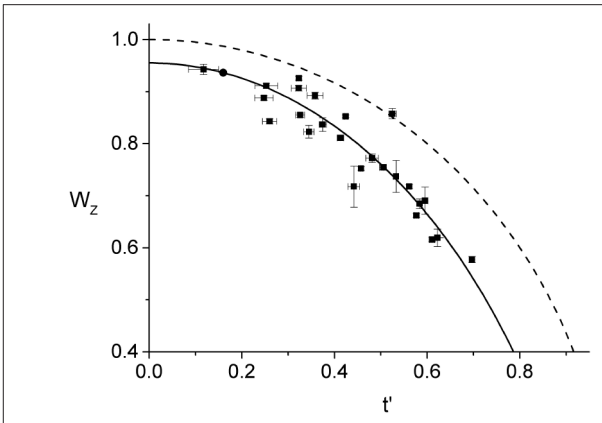

FIGURE 4 | Effective dynamics of the Z-ring constriction, $W_Z(t')$ (squares with error bars). We use the same data set as in **Figure 3**, only here the normalized radius of the Z-ring is plotted as a function of the effective division time. The prediction of Equation (1) (dashed line) together with the curve corresponding to the linear fit in **Figure 3** (full line) are also shown.

follows a simple dynamics

$$W(t) = \sqrt{1 - \left(\frac{t - \tau_c}{\tau_g - \tau_c}\right)^2} \equiv \sqrt{1 - (t')^2} \qquad (1)$$

where τ_c is the time at the onset of constriction, τ_g is the generation time and $t' \equiv \frac{t-\tau_c}{\tau_g-\tau_c}$ is the effective division time. The time interval between τ_c and τ_g, $\tau_g - \tau_c$, corresponds to the T-period of the cell cycle (Den Blaauwen et al., 1999). Equation (1) was derived in Reshes et al. (2008a) using the following four assumptions (see **Figure 1**): (1) the cell is shaped as a cylinder with two hemispherical caps, (2) its septum consists of two incomplete hemispheres; as division proceeds these grow to form the new caps, (3) the septal area grows at a constant rate, and (4) the cell radius, R, is constant in time. Its prediction was compared to measurements from individual fast growing *E. coli* cells and found to be in excellent agreement with experiment (Reshes et al., 2008a,b). Inverting Equation (1) we obtain $t'(r/R)$ and the error of t', $\Delta t'$, as a function of r, R, Δr, and ΔR.

In **Figure 4**, we show the behavior of $W_z(t')$ for all the 25 cells that we have analyzed. As one would expect, using the parameters from the best linear fit of **Figure 3** to obtain the effective time, t', for each individual ring, leads to a $W_z(t')$ curve that is in good agreement with the corresponding data. In contrast, assuming that the ring radius constricts at the same rate as the cell septum provides a relatively poor description of the observed behavior (see Figure S6). Comparing between $W_z(t')$ and $W(t)$, indicates that the ring radius constricts at a faster rate than the cell septum and, correspondingly, the radial width of the ring grows as a function of the effective division time.

Note that the data for $W_z(t')$ only represents cells with rings that are not too small, $r_z > 0.6R$, and not too late during septation, $t' < 0.7$. The restricted range of the data is due to two inherent limitations of our experimental approach. First, the cell edge calibration is performed on unconstricted cells and its validity for the case of the septal geometry holds only as long as the contributions from the two incomplete caps are sufficiently well-separated. In previous work we have determined that our edge calibration fails whenever the septation is deeper than 55%, $W < 0.55$ (Reshes et al., 2008a). Second, we found that the vertical trapping stability of cells that exceed a certain length is gradually deteriorating. For such cells fluctuations become too large and the corresponding ring images cannot be used for quantitative analysis due to the additional blur.

A necessary ingredient in our experimental approach is using time averaging to reduce the measurement error. Prior to averaging, errors in the effective time, t', were as large as 45%, and in the normalized ring radius, W_z, up to 7%, making the data practically useless. In fact, the larger errors bars on several of the W_z data of **Figures 3**, **4** are due to the small number of frames used for the averaging, e.g., at $W = 0.9$ (corresponding to $t' = 0.44$) only four frames were used since for later ones bleaching reduced contrast below the required value. The averaging procedure is reducing both the random errors, like those due to Brownian motion and imaging, and those due to the angular inhomogeneity of the Z-ring intensity distribution. The error due to inhomogeneity is reduced since the angular distribution of FtsZ in the ring varies on a time scale shorter than that of the averaging (see Supplementary Material and Figure S3).

DISCUSSION

We have used Optical Tweezers and subpixel image analysis to monitor the changes in the geometry of the Z-ring during division in *E. coli*. The optical trap allows orienting a cell either

horizontally or vertically and fast switching between the two alignments. Previously, we employed this system to measure the radial width of the Z-ring in cells that had not yet started to septate (Carmon et al., 2012, 2014). Here, our Optical Tweezers assisted imaging approach is used to monitor the constriction dynamics of the Z-ring. Specifically, we use the horizontal view to determine the size of the constriction. It allows establishing the effective time along the division process in a particular cell. In addition, the vertical view of the Z-ring appears as a circular structure that can be quantitatively analyzed to obtain the radius of the ring, r_z. Combining the information from the vertical fluorescence and horizontal phase contrast imaging modes, our data indicates that the Z-ring constricts faster than the cell envelope suggesting that the radial width of the ring grows during cell division. Moreover, we find that the Z-rings are significantly more homogeneous than those of slow growing cells. Our results together with those of Coltharp et al. (2016) suggest that both the geometry and the constriction dynamics of the Z-ring are different between fast and slow growing cells.

A possible mechanism that leads to the different behaviors of the Z-ring in fast and slow growing cells assumes that there is a limited amount of FtsZ protein available in slow growing cells. In contrast, in fast growing cells the amount of FtsZ is sufficient to build a Z-ring that appears roughly homogeneous on the scale of the diffraction limited optical resolution, ∼250 nm. This assumption is consistent with earlier results showing that the number of FtsZ proteins/cell is much larger in fast growing than in slow growing cells (Link et al., 1997; Lu et al., 1998; Rueda et al., 2003; Ishihama et al., 2008; Vendeville et al., 2011). Moreover, a recent study found that the Z-rings become gradually more homogeneous as the expression level of FtsZ is enhanced providing further support for this scenario (Lyu et al., 2016).

Although 3D-PALM is certainly a more advanced microscopy technique than our Optical Tweezers assisted imaging approach, for the particular purpose of measuring the radius of the bacterial Z-ring the two methods provide results of comparable accuracy and are complementary with respect to the conditions that optimize their performance. First, we bypass the optical resolution limit using pixel interpolation together with space and time averaging to obtain the radius of the Z-ring for individual cells, r_z, with an average error of only 4.6 nm. This accuracy is comparable to that obtained using iPALM (Coltharp et al., 2016). However, the high accuracy of our approach is partly due to the relatively homogeneous Z-rings that were measured in this study and will deteriorate as the ring under investigation becomes more inhomogeneous as in Coltharp et al. (2016). Second, the error of the measured Z-ring radius of individual cells is not specified in Holden et al. (2014) and Coltharp et al. (2016). Since most of the quantitative analysis is performed on the population averages, the errors of the different Z-ring characteristics are obtained from the variations between cells. This approach does not distinguish between measurement errors and population variability. In contrast, in our analysis of the Z-ring constriction dynamics we use the Z-ring radii from individual cells together with their corresponding measurement errors (**Figures 3**, **4**), allowing to isolate the effect of population variability. Third, Coltharp et al. (2016) use fixed cells to image the Z-ring with 3D-PALM. In their experiments, cells were fixed with 4% formaldehyde, potentially causing various artifacts. Such a high concentration of formaldehyde could shift the equilibrium in dynamic protein complexes, as is the case for most other cross-linkers. Moreover, the small size of formaldehyde limits its spatial and temporal cross-linking ability (Kiernan, 2000), leading to a wide variability in the extent it is immobilizing different proteins (Tanaka et al., 2010). In contrast, we study live cells therefore avoiding artifacts due to fixation. This also allows us to monitor the short time dynamics of the FtsZ distribution along the circumference of the ring (**Figure 2E**, Figures S1E, S2E, S3).

Our main assumption leading to the conclusion that the ring constricts faster than the cell septum is that the maximal intensity of the average radial profile corresponds to the radius of the Z-ring. It ignores the potential contribution of the FtsZ-GFP that is distributed in the cell cytoplasm, about 70% of the total amount of FtsZ-GFP in the cell (Anderson et al., 2004; Geissler et al., 2007). However, it was shown in previous work that most of this FtsZ-GFP is outside the depth of field and accordingly has a negligible contribution to the value of r_z (Carmon et al., 2014). To this end, we have simulated the image of the Z-ring with and without the FtsZ-GFP in the cytoplasm using the appropriate 3D point spread function for our microscope. Nevertheless, the spread of the $W_z(W)$ and $W_z(t')$ data (**Figures 3**, **4**, respectively) could be partially due to this effect and the variability in the partition of FtsZ-GFP between the ring and the cytoplasm between the different cells.

To obtain the effective division time, t', we also had to make the four geometrical assumptions leading to Equation (1). While the prediction of Equation (1) was extensively verified for fast growing *E. coli* cells (Reshes et al., 2008a,b), it apparently contradicts the behavior observed by Coltharp et al. for slow growing cells (Coltharp et al., 2016). They found that the septum constricts at an almost constant rate, such that using a generalized version of Equation (1)

$$W(t') = \left[1 - (t')^{\alpha}\right]^{1/\alpha} \tag{2}$$

they obtain $\alpha = 1.3 \pm 0.1$. However, it is possible that, in a regime where cells are growing at a slow rate, their septum will tend to display a more linear constriction dynamics. That is, we suggest that the different septation rates correspond to the different growth rate regimes, such that, for fast growing cells, $\alpha \simeq 2$ (Reshes et al., 2008a,b), while for slow growing cells, $\alpha \simeq 1.3$ (Coltharp et al., 2016). The fact that one of the wild type strains analyzed in Coltharp et al. (2016), MC4100, with an intermediate generation time, $\tau_g = 114 \pm 3$ min, was found to constrict with $\alpha = 1.9 \pm 0.2$, consistent with the prediction of Equation (1), lends some support to this view (although the BW25113 strain when grown in rich medium, $\tau_g = 94 \pm 2$ min, constricted according to Equation 2 with $\alpha = 1.3 \pm 0.1$). Moreover, the two constriction rate regimes scenario is compatible with the other differences between fast and slow growing *E. coli* cells, namely: (1) the growth of the cylindrical cell region stops at the onset of septation in slow growing cells while it is only slightly reduced in fast growing cells, (2) the Z-ring is much more homogeneous

along its circumference in fast growing than in slow growing cells and (3) the radial width of the Z-ring grows during septation in fast growing cells while it remains approximately constant in slow growing cells.

Despite recent progress understanding the role of the Z-ring in cytokinesis (Bisson-Filho et al., 2017; Yang et al., 2017), the mechanism that enables the constriction of the ring is still being debated (Ghosh and Sain, 2008; Allard and Cytrynbaum, 2009; Erickson, 2009). Recently, Coltharp et al. (2016) have shown that several properties of the Z-ring, namely, its density, the GTPase activity of FtsZ and the timing of its assembly and disassembly, had practically no effect on the rate of constriction. Moreover, the significant difference in the homogeneity of Z-rings in normally dividing cells between the fast and slow growth regimes, including incomplete rings with an angular range of less than 180°, also indicates that Z-ring constriction is not due to force exerted by the ring itself. Specifically, a less than 180° arch-like Z-ring cannot constrict toward the cell axis without guidance from the circularly symmetric cell wall, a necessary pathway to obtaining a circularly symmetric septum at midcell. These findings suggest that Z-ring constriction is led by the assembly of the septating peptidoglycan cell wall.

AUTHOR CONTRIBUTIONS

PK performed the experiments and analyzed the data. AY assisted with the experiments and the optical alignment of the Optical Tweezers. MF designed the research. IF and MF supervised the experiments and data analysis and wrote the paper.

FUNDING

This research was supported in part by the Israel Academy of Science and Humanities (Grant No. 1701/13) and the German-Israeli Foundation for Scientific Research and Development (Grant No. 1160-137.14/2011).

ACKNOWLEDGMENTS

We thank Y. Meir and O. Piro for useful discussions.

SUPPLEMENTARY MATERIAL

The Supplementary Material for this article can be found online at: http://journal.frontiersin.org/article/10.3389/fmicb.2017.01670/full#supplementary-material

REFERENCES

Addinall, S. G., and Lutkenhaus, J. (1996). FtsZ-spirals and -arcs determine the shape of the invaginating septa in some mutants of *Escherichia coli*. *Mol. Microbiol.* 22, 231–237. doi: 10.1046/j.1365-2958.1996.00100.x

Allard, J. F., and Cytrynbaum, E. N. (2009). Force generation by a dynamic Z-ring in *Escherichia coli* cell division. *Proc. Natl. Acad. Sci. U.S.A.* 106, 145–150. doi: 10.1073/pnas.0808657106

Anderson, D. E., Gueiros-Filho, F. J., and Erickson, H. P. (2004). Assembly dynamics of FtsZ rings in *Bacillus subtilis* and *Escherichia coli* and effects of FtsZ-regulating proteins. *J. Bacteriol.* 186, 5775–5781. doi: 10.1128/JB.186.17.5775-5781.2004

Ayano, S., Wakamoto, Y., Yamashita, S., and Yasuda, K. (2006). Quantitative measurement of damage caused by 1064-nm wavelength optical trapping of *Escherichia coli* cells using on-chip single cell cultivation system. *Biochem. Biophys. Res. Commun.* 350, 678–684. doi: 10.1016/j.bbrc.2006.09.115

Begg, K. J., Takasuga, A., Edwards, D. H., Dewar, S. J., Spratt, B. G., Adachi, H., et al. (1990). The balance between different peptidoglycan precursors determines whether *Escherichia coli* cells will elongate or divide. *J. Bacteriol.* 172, 6697–6703. doi: 10.1128/jb.172.12.6697-6703.1990

Bernhardt, T. G., and de Boer, P. A. (2005). SlmA, a nucleoid-associated, FtsZ binding protein required for blocking septal ring assembly over chromosomes in *E. coli*. *Mol. Cell* 18, 555–564. doi: 10.1016/j.molcel.2005.04.012

Bi, E. F., and Lutkenhaus, J. (1991). FtsZ ring structure associated with division in *Escherichia coli*. *Nature* 354, 161–164. doi: 10.1038/354161a0

Bisson-Filho, A. W., Hsu, Y. P., Squyres, G. R., Kuru, E., Wu, F., Jukes, C., et al. (2017). Treadmilling by FtsZ filaments drives peptidoglycan synthesis and bacterial cell division. *Science* 355, 739–743. doi: 10.1126/science.aak9973

Biteen, J. S., Goley, E. D., Shapiro, L., and Moerner, W. E. (2012). Three-dimensional super-resolution imaging of the midplane protein FtsZ in live *Caulobacter crescentus* cells using astigmatism. *Chemphyschem* 13, 1007–1012. doi: 10.1002/cphc.201100686

Carmon, G., Fishov, I., and Feingold, M. (2012). Oriented imaging of 3D subcellular structures in bacterial cells using optical tweezers. *Opt. Lett.* 37, 440–442. doi: 10.1364/OL.37.000440

Carmon, G., Kumar, P., and Feingold, M. (2014). Optical tweezers assisted imaging of the Z-ring in *Escherichia coli*: measuring its radial width. *New J Phys.* 16:013043. doi: 10.1088/1367-2630/16/1/013043

Coltharp, C., Buss, J., Plumer, T. M., and Xiao, J. (2016). Defining the rate-limiting processes of bacterial cytokinesis. *Proc. Natl. Acad. Sci. U.S.A.* 113, E1044–E1053. doi: 10.1073/pnas.1514296113

Dajkovic, A., and Lutkenhaus, J. (2006). Z ring as executor of bacterial cell division. *J Mol. Microbiol. Biotechnol.* 11, 140–151. doi: 10.1159/000094050

de Boer, P., Crossley, R., and Rothfield, L. (1992). The essential bacterial cell-division protein FtsZ is a GTPase. *Nature* 359, 254–256. doi: 10.1038/359254a0

Den Blaauwen, T., Buddelmeijer, N., Aarsman, M. E., Hameete, C. M., and Nanninga, N. (1999). Timing of FtsZ assembly in *Escherichia coli*. *J. Bacteriol.* 181, 5167–5175.

Erickson, H. P. (1997). FtsZ, a tubulin homologue in prokaryote cell division. *Trends Cell Biol.* 7, 362–367. doi: 10.1016/S0962-8924(97)01108-2

Erickson, H. P. (2009). Modeling the physics of FtsZ assembly and force generation. *Proc. Natl. Acad. Sci. U.S.A.* 106, 9238–9243. doi: 10.1073/pnas.0902258106

Erickson, H. P., Anderson, D. E., and Osawa, M. (2010). FtsZ in bacterial cytokinesis: cytoskeleton and force generator all in one. *Microbiol. Mol. Biol. Rev.* 74, 504–528. doi: 10.1128/MMBR.00021-10

Fu, G., Huang, T., Buss, J., Coltharp, C., Hensel, Z., and Xiao, J. (2010). *In vivo* structure of the *E. coli* FtsZ-ring revealed by photoactivated localization microscopy (PALM). *PLoS ONE* 5:e12680. doi: 10.1371/journal.pone.0012680

Geissler, B., Shiomi, D., and Margolin, W. (2007). The ftsA* gain-of-function allele of *Escherichia coli* and its effects on the stability and dynamics of the Z ring. *Microbiology* 153, 814–825. doi: 10.1099/mic.0.2006/001834-0

Ghosh, B., and Sain, A. (2008). Origin of contractile force during cell division of bacteria. *Phys. Rev. Lett.* 101:178101. doi: 10.1103/PhysRevLett.101.178101

Holden, S. J., Pengo, T., Meibom, K. L., Fernandez Fernandez, C., Collier, J., and Manley, S. (2014). High throughput 3D super-resolution microscopy reveals *Caulobacter crescentus in vivo* Z-ring organization. *Proc. Natl. Acad. Sci. U.S.A.* 111, 4566–4571. doi: 10.1073/pnas.1313368111

Ishihama, Y., Schmidt, T., Rappsilber, J., Mann, M., Hartl, F. U., Kerner, M. J., et al. (2008). Protein abundance profiling of the *Escherichia coli* cytosol. *BMC Genomics* 9:102. doi: 10.1186/1471-2164-9-102

Jacq, M., Adam, V., Bourgeois, D., Moriscot, C., Di Guilmi, A. M., Vernet, T., et al. (2015). Remodeling of the Z-ring nanostructure during the *Streptococcus pneumoniae* Cell Cycle revealed by photoactivated localization microscopy. *MBio* 6, e01108–e01115. doi: 10.1128/mBio.01108-15

Jennings, P. C., Cox, G. C., Monahan, L. G., and Harry, E. J. (2010). Super-resolution imaging of the bacterial cytokinetic protein FtsZ. *Micron* 42, 336–341. doi: 10.1016/j.micron.2010.09.003

Kiernan, J. A. (2000). Formaldehyde, formalin, paraformaldehyde and glutaraldehyde: What they are and what they do. *Microsc. Today* 8, 8–12.

Levin, P. A., and Losick, R. (1996). Transcription factor Spo0A switches the localization of the cell division protein FtsZ from a medial to a bipolar pattern in *Bacillus subtilis*. *Genes Dev.* 10, 478–488. doi: 10.1101/gad.10.4.478

Link, A. J., Robison, K., and Church, G. M. (1997). Comparing the predicted and observed properties of proteins encoded in the genome of *Escherichia coli* K-12. *Electrophoresis* 18, 1259–1313. doi: 10.1002/elps.1150180807

Lleo, M. M., Canepari, P., and Satta, G. (1990). Bacterial cell shape regulation: testing of additional predictions unique to the two-competing-sites model for peptidoglycan assembly and isolation of conditional rod-shaped mutants from some wild-type cocci. *J. Bacteriol.* 172, 3758–3771. doi: 10.1128/jb.172.7.3758-3771.1990

Lowe, J., and Amos, L. A. (1998). Crystal structure of the bacterial cell-division protein FtsZ. *Nature* 391, 203–206. doi: 10.1038/34472

Lu, C., Stricker, J., and Erickson, H. P. (1998). FtsZ from *Escherichia coli*, *Azotobacter vinelandii*, and *Thermotoga maritima*–quantitation, GTP hydrolysis, and assembly. *Cell. Motil. Cytoskeleton* 40, 71–86. doi: 10.1002/(SICI)1097-0169(1998)40:1<71::AID-CM7>3.0.CO;2-I

Lutkenhaus, J. (2007). Assembly dynamics of the bacterial minCDE system and spatial regulation of the Z ring. *Ann. Rev. Biochem.* 76, 539–562. doi: 10.1146/annurev.biochem.75.103004.142652

Lyu, Z., Coltharp, C., Yang, X., and Xiao, J. (2016). Influence of FtsZ GTPase activity and concentration on nanoscale Z-ring structure *in vivo* revealed by three-dimensional Superresolution imaging. *Biopolymers* 105, 725–734. doi: 10.1002/bip.22895

Ma, X., Ehrhardt, D. W., and Margolin, W. (1996). Colocalization of cell division proteins FtsZ and FtsA to cytoskeletal structures in living *Escherichia coli* cells by using green fluorescent protein. *Proc. Natl. Acad. Sci. U.S.A.* 93, 12998–13003. doi: 10.1073/pnas.93.23.12998

Margolin, W. (2005). FtsZ and the division of prokaryotic cells and organelles. *Nat. Rev. Mol. Cell. Biol.* 6, 862–871. doi: 10.1038/nrm1745

Monahan, L. G., Robinson, A., and Harry, E. J. (2009). Lateral FtsZ association and the assembly of the cytokinetic Z ring in bacteria. *Mol. Microbiol.* 74, 1004–1017. doi: 10.1111/j.1365-2958.2009.06914.x

Mukherjee, A., Dai, K., and Lutkenhaus, J. (1993). *Escherichia coli* cell division protein FtsZ is a guanine nucleotide binding protein. *Proc. Natl. Acad. Sci. U S A* 90, 1053–1057. doi: 10.1073/pnas.90.3.1053

Neuman, K. C., Chadd, E. H., Liou, G. F., Bergman, K., and Block, S. M. (1999). Characterization of photodamage to *Escherichia coli* in optical traps. *Biophys. J.* 77, 2856–2863. doi: 10.1016/S0006-3495(99)77117-1

Piro, O., Carmon, G., Feingold, M., and Fishov, I. (2013). Three-dimensional structure of the Z-ring as a random network of FtsZ filaments. *Environ. Microbiol.* 15, 3252–3258. doi: 10.1111/1462-2920.12197

RayChaudhuri, D., and Park, J. T. (1992). *Escherichia coli* cell-division gene ftsZ encodes a novel GTP-binding protein. *Nature* 359, 251–254. doi: 10.1038/359251a0

Reshes, G., Vanounou, S., Fishov, I., and Feingold, M. (2008a). Cell shape dynamics in *Escherichia coli*. *Biophys. J.* 94, 251–264. doi: 10.1529/biophysj.107.104398

Reshes, G., Vanounou, S., Fishov, I., and Feingold, M. (2008b). Timing the start of division in *E. coli*: a single-cell study. *Phys. Biol.* 5:046001. doi: 10.1088/1478-3975/5/4/046001

Rothfield, L., Taghbalout, A., and Shih, Y.-L. (2005). Spatial control of bacterial division-site placement. *Nat. Rev. Microbiol.* 3, 959–968. doi: 10.1038/nrmicro1290

Rowlett, V. W., and Margolin, W. (2014). 3D-SIM super-resolution of FtsZ and its membrane tethers in *Escherichia coli* cells. *Biophys. J.* 107, L17–L20. doi: 10.1016/j.bpj.2014.08.024

Rueda, S., Vicente, M., and Mingorance, J. (2003). Concentration and assembly of the division ring proteins FtsZ, FtsA, and ZipA during the *Escherichia coli* cell cycle. *J. Bacteriol.* 185, 3344–3351. doi: 10.1128/JB.185.11.3344-3351.2003

Salvarelli, E., Krupka, M., Rivas, G., Vicente, M., and Mingorance, J. (2011). Independence between GTPase active sites in the *Escherichia coli* cell division protein FtsZ. *FEBS Lett.* 585, 3880–3883. doi: 10.1016/j.febslet.2011.10.046

Si, F., Busiek, K., Margolin, W., and Sun, S. X. (2013). Organization of FtsZ filaments in the bacterial division ring measured from polarized fluorescence microscopy. *Biophys. J.* 105, 1976–1986. doi: 10.1016/j.bpj.2013.09.030

Siegele, D. A., and Hu, J. C. (1997). Gene expression from plasmids containing the araBAD promoter at subsaturating inducer concentrations represents mixed populations. *Proc. Natl. Acad. Sci. U.S.A.* 94, 8168–8172. doi: 10.1073/pnas.94.15.8168

Sossong, T. M. Jr., Brigham-Burke, M. R., Hensley, P., and Pearce, K. H. Jr. (1999). Self-activation of guanosine triphosphatase activity by oligomerization of the bacterial cell division protein FtsZ. *Biochemistry* 38, 14843–14850. doi: 10.1021/bi990917e

Strauss, M. P., Liew, A. T., Turnbull, L., Whitchurch, C. B., Monahan, L. G., and Harry, E. J. (2012). 3D-SIM super resolution microscopy reveals a bead-like arrangement for FtsZ and the division machinery: implications for triggering cytokinesis. *PLoS Biol.* 10:e1001389. doi: 10.1371/journal.pbio.1001389

Stricker, J., Maddox, P., Salmon, E. D., and Erickson, H. P. (2002). Rapid assembly dynamics of the *Escherichia coli* FtsZ-ring demonstrated by fluorescence recovery after photobleaching. *Proc. Natl. Acad. Sci. U.S.A.* 99, 3171–3175. doi: 10.1073/pnas.052595099

Sun, Q., and Margolin, W. (1998). FtsZ dynamics during the division cycle of live *Escherichia coli* cells. *J. Bacteriol.* 180, 2050–2056.

Tanaka, K. A., Suzuki, K. G., Shirai, Y. M., Shibutani, S. T., Miyahara, M. S., Tsuboi, H., et al. (2010). Membrane molecules mobile even after chemical fixation. *Nat. Methods* 7, 865–866. doi: 10.1038/nmeth.f.314

Thanedar, S., and Margolin, W. (2004). FtsZ exhibits rapid movement and oscillation waves in helix-like patterns in *Escherichia coli*. *Curr. Biol.* 14, 1167–1173. doi: 10.1016/j.cub.2004.06.048

Tsukanov, R., Reshes, G., Carmon, G., Fischer-Friedrich, E., Gov, N. S., Fishov, I., et al. (2011). Timing of Z-ring localization in *Escherichia coli*. *Phys. Biol.* 8:066003. doi: 10.1088/1478-3975/8/6/066003

Vendeville, A., Lariviere, D., and Fourmentin, E. (2011). An inventory of the bacterial macromolecular components and their spatial organization. *FEMS Microbiol. Rev.* 35, 395–414. doi: 10.1111/j.1574-6976.2010.00254.x

Weiss, D. S., Chen, J. C., Ghigo, J. M., Boyd, D., and Beckwith, J. (1999). Localization of FtsI (PBP3) to the septal ring requires its membrane anchor, the Z ring, FtsA, FtsQ, and FtsL. *J. Bacteriol.* 181, 508–520.

Wu, L. J., and Errington, J. (2004). Coordination of cell division and chromosome segregation by a nucleoid occlusion protein in *Bacillus subtilis*. *Cell* 117, 915–925. doi: 10.1016/j.cell.2004.06.002

Yang, X., Lyu, Z., Miguel, A., McQuillen, R., Huang, K. C., and Xiao, J. (2017). GTPase activity-coupled treadmilling of the bacterial tubulin FtsZ organizes septal cell wall synthesis. *Science* 355, 744–747. doi: 10.1126/science.aak9995

Yu, X. C., and Margolin, W. (1997). Ca^{2+}-mediated GTP-dependent dynamic assembly of bacterial cell division protein FtsZ into asters and polymer networks *in vitro*. *Embo J* 16, 5455–5463. doi: 10.1093/emboj/16.17.5455

Conflict of Interest Statement: The authors declare that the research was conducted in the absence of any commercial or financial relationships that could be construed as a potential conflict of interest.

frontiers in Microbiology

ORIGINAL RESEARCH
published: 01 May 2018
doi: 10.3389/fmicb.2018.00871

Analysis of Factors Limiting Bacterial Growth in PDMS Mother Machine Devices

Da Yang[1], *Anna D. Jennings*[1], *Evalynn Borrego*[2], *Scott T. Retterer*[3] *and Jaan Männik*[1]*

[1] *Department of Physics and Astronomy, The University of Tennessee, Knoxville, TN, United States,* [2] *Department of Mechanical, Aerospace and Biomedical Engineering, University of Tennessee, Knoxville, TN, United States,* [3] *Oak Ridge National Laboratory, Center for Nanophase Materials Sciences, Oak Ridge, TN, United States*

The microfluidic mother machine platform has attracted much interest for its potential in studies of bacterial physiology, cellular organization, and cell mechanics. Despite numerous experiments and development of dedicated analysis software, differences in bacterial growth and morphology in narrow mother machine channels compared to typical liquid media conditions have not been systematically characterized. Here we determine changes in *E. coli* growth rates and cell dimensions in different sized dead-end microfluidic channels using high resolution optical microscopy. We find that *E. coli* adapt to the confined channel environment by becoming narrower and longer compared to the same strain grown in liquid culture. Cell dimensions decrease as the channel length increases and width decreases. These changes are accompanied by increases in doubling times in agreement with the universal growth law. In channels 100 μm and longer, cell doublings can completely stop as a result of frictional forces that oppose cell elongation. Before complete cessation of elongation, mechanical stresses lead to substantial deformation of cells and changes in their morphology. Our work shows that mechanical forces rather than nutrient limitation are the main growth limiting factor for bacterial growth in long and narrow channels.

Keywords: mother machine, nutrient shielding, mechanics of cell growth, peptidoglycan synthesis, cell wall, microfluidics

OPEN ACCESS

Edited by:
Manuel Simões, Faculdade de Engenharia da Universidade do Porto, Portugal

Reviewed by:
Roberto Rusconi, Humanitas Università, Italy
Maria Hadjifrangiskou, Vanderbilt University Medical Center, United States

***Correspondence:**
Jaan Männik
jmannik@utk.edu

Specialty section:
This article was submitted to Microbial Physiology and Metabolism, a section of the journal Frontiers in Microbiology

Received: *16 January 2018*
Accepted: *16 April 2018*
Published: *01 May 2018*

Citation:
Yang D, Jennings AD, Borrego E, Retterer ST and Männik J (2018) Analysis of Factors Limiting Bacterial Growth in PDMS Mother Machine Devices. Front. Microbiol. 9:871. doi: 10.3389/fmicb.2018.00871

INTRODUCTION

High resolution optical microscopy is the most widespread method to study bacterial cellular organization and physiology at the single cell level. Most early studies were carried out using fixed cells that were attached to microscope slides. However, both fixation and attachment of cells to slides alter subcellular organization and can lead to imaging artifacts. As a less invasive preparation method, thin agarose pads sandwiched between microscope cover slide and coverslip have been adopted by numerous groups (e.g., in recent reports, Bailey et al., 2014; Adiciptaningrum et al., 2015). Since thin layer of agarose is prone to drying, thicker layers of agarose in Petri dishes with coverslip bottoms can be used (Männik et al., 2017). The dishes and pads allow imaging live cells over several doublings (typically 4–5). Longer imaging is hampered because individual cells start to overlap. Moreover, cells in the interior of the colony experience a different growth environment than the cells at the periphery and consequently grow at different rates. It is unclear for how long exactly, if at all, steady-state growth conditions can be maintained on the pads.

For reproducible quantitative studies, steady-state cell growth is necessary. To be able to grow cells in steady conditions both the physical and chemical environment of cells needs to remain the same over time. Moreover, cells should not overlap as they grow. In practical terms this means that the colony size has to be kept fixed despite exponential growth in cell numbers over time. Different microfluidic platforms have been developed over the past decade to achieve these requirements (Hol and Dekker, 2014). The developed devices either trap cells in narrow channels comparable to bacterial cross-sectional diameter (Wang et al., 2010; Moffitt et al., 2012; Long et al., 2013) or hold them in shallow chambers where bacteria are confined to a single layer (Männik et al., 2012; Ullman et al., 2013). In the latter case bacteria grow packed side-by-side and quantitative analysis of individual cells is more complicated. In addition to providing a steady growth environment, microfluidics can also be used to administer different chemical (Baltekin et al., 2017; Kaiser et al., 2018) and physical stimuli (Yang et al., 2015) to the cells *in situ* while they are imaged under the microscope.

Of these various designs the most wide-spread has been the so-called mother machine platform (Wang et al., 2010) where cells grow in short (10–25 μm long) dead-end channels (**Figure 1A**). The advantage of dead-end channels relative to channels where both ends are open is longer retention time of cells. Pressure fluctuations are more likely to drive cells out from the channels that have both ends open. In mother machine design, all the cells in the channels are clones of the mother cell that resides in the dead-end side of the channel. The size of the colony is maintained fixed in time because flow in the main channel flushes away extra cells that grow out from the dead-end channels. The same flow also maintains a constant media environment in the growth channels by replenishing nutrients and removing metabolic waste products. Both exchanges are thought to occur via diffusion (Wang et al., 2010). Diffusion may set a limit for nutrient availability for cells at the dead-end side of the channel. To increase diffusion rate a design with shallow reservoirs surrounding the dead-end channels has been implemented (Norman et al., 2013; Cabeen et al., 2017). These reservoirs allow diffusion of nutrients from the main channel but are shallow enough to prevent cells from populating them. Faster exchange of media can also be achieved by diverting some flow past the cells via small opening on the "dead-end" side of the channel. While allowing flow of medium, the opening needs to be made small enough to prevent cells from passing through. Such channels have been recently fabricated and tested (Baltekin et al., 2017; Jennings, 2017). However, the fabrication of these devices is rather challenging, especially for smaller size bacteria, such as *E. coli* growing in poor medium, because the opening in the dead-end side needs to be made no more than about 300 nm wide to prevent cells from squeezing through the deformable openings (Männik et al., 2009; Jennings, 2017).

Mother machine platform has been used to study cell aging (Wang et al., 2010), cell cycle control (Taheri-Araghi et al., 2015), and effects of mechanical forces on cell wall growth (Amir et al., 2014). The devices have been also used in studies of gene regulation (Norman et al., 2013; Cabeen et al., 2017; Kaiser et al., 2018) and antibiotic resistance (Baltekin et al., 2017). New open-source computational platforms have been specifically developed to segment and analyze cells in mother machine platform (Sachs et al., 2016; Kaiser et al., 2018). Despite such widespread interest, bacterial growth in narrow dead-end channels has not been systematically compared to their growth in typical liquid media conditions. Nor has it been determined what phenotypic differences appear in cells that grow in such microfluidic devices. Here, we analyze nutritional and mechanical growth limitations to clonal *E. coli* cultures in microfluidic dead-end channels of various widths and lengths (**Figure 1A**). We find that *E. coli* adapt to the confined channel environment by becoming significantly narrower and longer than the same bacteria in liquid cultures. While the aspect ratio is affected, the cell volume remains approximately the same for cells growing in short channels compared to those growing in

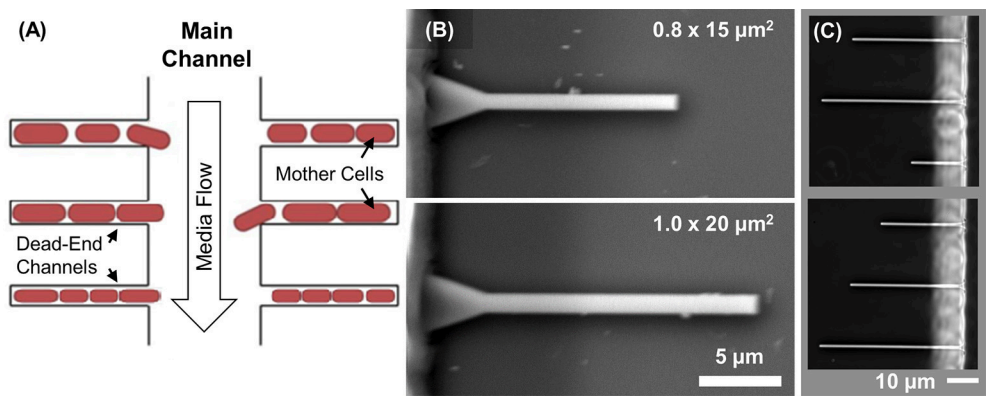

FIGURE 1 | Design of microfluidic chip. **(A)** Schematics showing the mother machine channel layout. Cells grow in dead-end channels. Nutrients diffuse to cells from the main channel where a constant flow is maintained. This flow also removes metabolic waste products and flushes away extra cells. Growth of the mother cell at the end of the channel is studied as a function of channel width and length. **(B)** SEM images of the silicon mold showing patterns of two different size channels. **(C)** Channels form a completed PDMS device imaged using phase contrast microscopy. Channel lengths in the two images vary from 20 to 50 μm. There is a total of 150 channels of each length on a single chip.

the same media conditions in liquid cultures. By increasing the length of the channels, the growth speed and cell volume both decrease until cell growth completely stops in longer channels. We assign the complete cessation of growth to high levels of mechanical stress resulting from colony growth rather than from nutrient limitations. Interestingly, the stress in these 1D colonies can reach levels sufficient to deform cells and to cause them growing into irregular shapes.

MATERIALS AND METHODS

Microfluidic Device Design and Fabrication

The fluidic circuitry in each chip consists of the main channel for media supply and waste product removal and 600 dead-end channels connected to the main channel (**Figure 1A**) following the typical mother machine layout (Wang et al., 2010). The designed length of the dead-end channels varies between 15 and 200 μm, and width from 0.6 to 1.0 μm. The fabrication of microfluidic devices is based on soft-lithography of polydimethylsiloxane (PDMS) elastomers (Weibel et al., 2007).

The channels in PDMS elastomers are created using 4″ silicon (Si) wafer molds. The fabrication of the Si molds follows the process described earlier (Yang et al., 2015). Briefly, the patterns of dead-end channels are defined by e-beam lithography using a JEOL JBX-9300FS electron beam lithography system (JEOL, Japan) with ZEP520A, a positive tone e-beam resist (ZEON Chemical, Japan). After e-beam writing and resist development, a 15 nm chromium layer is deposited. Subsequently, the e-beam resist layer is lifted off using sonication in an acetone bath. A 1.2 μm deep Si etch is carried out in an Oxford Plasmalab 100 inductively coupled plasma reactive ion etching system (Oxford Instruments, MA). The Cr layer acts as a mask for Si etching. The patterns for the larger flow channels are defined using photolithography of SU-8 2015 (MicroChem, MA). The reliefs that result from this step have a typical height of 20 μm. The molds are subsequently silanized in a desiccator using (tridecafluoro-1,1,2,2-tetrahydrooctyl)-1-trichlorosilane (UCT Specialties, CA) for at least 15 min.

PDMS elastomer (Sylgard 184 kit, by Dow Corning, MI) is cast on the mold in a 10:1 base/linker weight ratio. The PDMS is baked at 90°C for 20 min in a convection oven, and then left in the oven for at least two more hours as the oven cools down from 90°C. Individual patterns are cut out, and access holes to the main channels are punched using a biopsy needle. These pieces are subsequently bonded to coverslips. For bonding, #1.5 coverslips are cleaned in isopropyl alcohol (both from Thermo Fisher Scientific, NH) by sonication and then treated in O_2 plasma at 200 mTorr for 70 s. The PDMS elastomer piece and glass coverslips are additionally treated in O_2 plasma for 7s before bonding. After bonding, the chips are left at room temperature at least for 12 h before starting live cell measurements.

The channel heights and widths are measured from the Si mold. For the height measurement, a KLA-Tencor P-6 Stylus (KLA-Tencor Corporation, CA) profilometer is used. The heights of all dead-end channels in different microfluidic chips are within 1.15 ± 0.05 μm. The channels widths are measured using SEM and closely follow their design widths (less than 20 nm differences) (**Figure 1B**). The length of these channels, as measured from the optical images of completed chips (**Figure 1C**), also closely follow their design values.

Bacterial Strain and Culturing

In all measurements, *E. coli* strain AJ5 is used. The strain is created from strain BW25113 (Datsenko and Wanner, 2000) by P1 transduction with lysate from strain FW1401 (Wu et al., 2015). The resulting strain carries a *tagRFP-T* sequence together with kanamycin resistance cassette replacing *leuB*. For an experiment, a colony from LB plate is grown overnight at 28°C with shaking in M9 minimal medium. The medium consists of M9 salts (Teknova, CA), supplemented with 2 mM magnesium sulfate ($MgSO_4$), 0.5% (w/v) glucose (Sigma-Aldrich, MO), 0.2% casamino acids (ACROS Organics, NJ). Liquid media are supplemented with 25 μg/ml kanamycin (Sigma-Aldrich, MO) for selection.

Microfluidic Chip Experiment

Before inoculation of cells to a microfluidic chip, 0.1% (w/v) bovine serum albumin (BSA, Sigma-Aldrich, MO) is added to an overnight liquid culture ($OD_{600} > 0.8$). The cells are then concentrated 100 times in the same medium. About 2 μl of the concentrated culture is injected into the microfluidic device using a pipette and left at 28°C. After a satisfactory amount of dead-end channels are filled with at least one cell (requires a minimum of 20 min), tubing will be connected to the device, and the flow of fresh M9 medium is started. The medium that is used is the same as for the overnight culture, but with 0.1% BSA added to prevent cells from sticking to the main channel surfaces. The medium contains no antibiotics. The flow of this medium is maintained at 4.5 μl/min by an NE-1000 Syringe Pump (New Era Pump Systems, NY). The micro-cultures are grown at 28°C for at least 14 h before imaging is started.

Liquid Culture Measurements

To measure doubling times in liquid culture, the cells are grown in M9 medium overnight ($OD_{600} > 0.8$). The composition of the medium is the same as for the microfluidic chip measurements. The culture is then diluted at least 100× to fresh M9 medium. OD of the culture is measured at $\lambda = 600$ nm using a GENESYS 20 Visible Spectrophotometer (Thermo Fisher Scientific, NH) in 30 min intervals outside the incubator. The linear region of the log(OD) vs. t curve is used to determine the doubling time (Supplementary Figure 1).

To measure cell dimensions in liquid culture, cells are grown to mid-log phase ($OD_{600} \sim 0.15$), concentrated 50×, and then spread onto a 2% agarose pad with the same M9 media composition as in other measurements. The cells are imaged within 30 min after spreading to the pad.

Microscopic Imaging

A Nikon Ti-E inverted epifluorescence microscope (Nikon Instruments, Japan) with a 100X (NA = 1.45) oil immersion phase contrast objective (Nikon Instruments, Japan) is used for imaging the bacteria. Images are captured on an iXon DU-897 EMCCD camera (Andor Technology, UK) and recorded

using NIS-Elements software (Nikon Instruments, Japan). Fluorophores are excited by a 200 W Hg lamp through an ND4 neutral density filter. A Chroma 41004 filtercube (Chroma Technology Corp., VT) is used when capturing fluorescent images. A motorized stage and a perfect focus system are utilized during time-lapse imaging. About 100 dead-end channels for each channel size is imaged in each measurement for 6-h period or longer (at least 5 doublings).

Image Analysis

Image analysis was carried out using Matlab (MathWorks, MA) scripts based on Matlab Image Analysis Toolbox, Signal Processing Toolbox and DipImage Toolbox. ImageJ was used to prepare individual images for the figures and the SI movies.

Cell Length Measurements

Both cell lengths and widths are measured from fluorescent images of the cytoplasmic tagRFP-T label. First, the raw fluorescent images are transformed to the second derivative images using the DipImage function *laplace_plus_dgg*, which computes the Laplacian and the second derivative in the gradient direction of an image (Verbeek and Vanvliet, 1994). Thresholding of the second derivative image based on zero crossing yields a binary image, which is then eroded and dilated to resolve individual cells and to fill them, respectively. Cell lengths are measured from these binary images. The measurement consists of finding the greatest Feret diameter for each cell using the *measure* function from DipImage.

Cell Width Measurements

Based on the binary cell masks from the previous step, the gray value center of mass coordinates and the coordinates of the cell long axes are determined. Next, a line perpendicular to the long axes of the cell that passes through the cell center is calculated. To improve the determination of the cell width, an additional set of lines are calculated, where the orientation relative to the previous line is varied in small angular steps. For each orientation, an intensity profile from the fluorescent image is determined, and the profile is fitted to a Gaussian. The Gaussian with the smallest width is then found among all the fits. Due to diffraction, variance of the Gaussian is about 0.04 μm smaller than the cytoplasmic diameter of the cell in our setup (Männik et al., 2009). An additional 0.04 μm is added to the cytoplasmic diameter to account for the width of the periplasmic space and outer membrane layer of the cell. The final, calculated width thus corresponds to the outer diameter of the cell.

Cell Volume Measurements

For the cell volume determination, we assume that every cell is a cylinder with two hemispherical caps. The volume, V_c, based on cell length, L_c, and width, W_c, is:

$$V_c = \frac{\pi}{6} {W_c}^3 + \frac{\pi}{4} {W_c}^2 (L_c - W_c) \quad (1)$$

Statistical Analysis

Three replicate measurements of cells were performed for each channel size and for liquid cultures. The average cell length, width, volume and doubling time were calculated from the averages of these three measurements. The error bars associated with the above measurements are the standard errors which have been calculated from the averages of the three measurements. For universal growth law plot the error bars were calculated by propagating the random errors for volumes and doubling times. For statistical significance testing Welch's *t*-test was used. This test is more reliable than Student's *t*-test when sample sizes are different. To estimate correlations Pearson R was used.

RESULTS

Dependence of Mother Cell Growth on Channel Width

To investigate how the channel width affects the growth rate and cell dimensions we fabricated channels of 0.6, 0.7, 0.8, 0.9, 1.0, and 1.2 μm in width, 1.15 μm in height and of 15 and 20 μm in length on a single chip. The chosen channel widths were expected to be close to the cell diameter in these growth conditions. The majority of the 0.8, 0.9, and 1.0 μm wide channels had stable bacterial populations that filled the

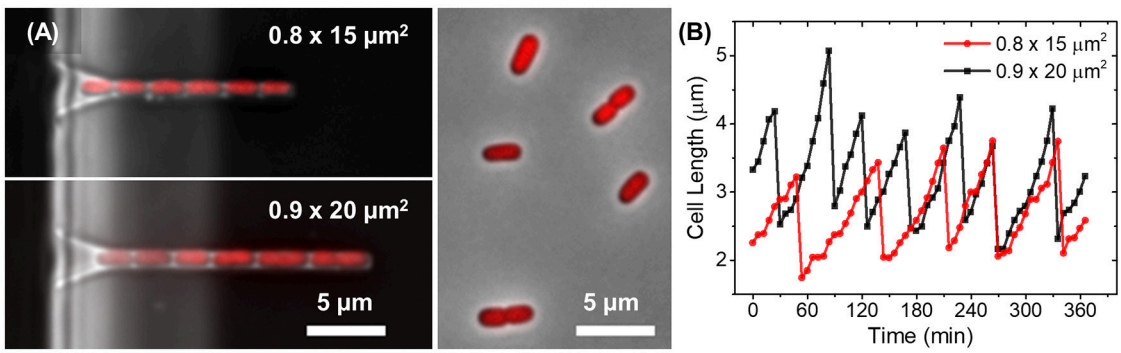

FIGURE 2 | Bacterial growth in channels. **(A)** Composite of phase and fluorescent images of two different size channels filled tagRFP-T labeled *E. coli* (left images). For comparison, composite image of the same strain grown in liquid culture and imaged on agarose pad (right image). The difference in cell width in the two growth environments can be visualized. **(B)** Growth curves of mother cells from channels shown on **(A)**.

whole channel. Cells in these populations grew in single rows (**Figure 2A**, Supplementary Videos 1, 2). In the 1.2 μm wide channels, cells grew in two parallel rows and, as such, these channels were not suitable for analysis. On the other hand, 0.6 μm wide channels were too narrow to support stable colony growth. Although few cells loaded to these channels initially, they all moved out from the channels before imaging started. The same also occurred in the majority of the 0.7 μm wide channels (Supplementary Video 3). However, in some of the 0.7 μm wide channels (8 out of 200), stable populations were present and could be imaged. In both 0.6 and 0.7 μm wide channels the bacteria appeared to be wider than the channel causing deformations to channel walls (Supplementary Figure 2). Note that bacteria from overnight stationary cultures were loaded into channels. These cells are significantly narrower than log phase cells (Männik et al., 2009), and this made their entry to 0.6 and 0.7 μm wide channels possible. As cells started to grow in fresh medium in these channels, their diameter widened beyond the channel width. Higher deformability of open ends of channels may have provided a driving force that pushed the cells out from the channels.

Thus, of all the fabricated channels only those in the range 0.7–1.0 μm were suitable for studying growth of stable 1D bacterial cultures. Cells in these channels were imaged in three independent measurements that each lasted at least 6 h (Supplementary Videos 1, 2, **Figure 2B**). Here, we analyze, in detail, the growth of the mother cell, which is the cell at the dead-end side of the channel. All the cells in the channel are clones of this cell. We use the mother cell for analysis because it is the only cell that strictly grows in steady state conditions. The other cells in the channel move toward the channel entrance during their growth and, because of that movement, we expect both the composition of the growth medium and the mechanical stress that the cells experience to change. Also, to guarantee that mother cells in a channel of a given size grew in comparable conditions we required the channels to be completely full of cells (<1 μm empty space between cells) throughout the entire time-lapse imaging period.

We next compare birth length, width, volume and doubling time measurements of mother cells in differently sized channels to those from cells in liquid cultures. We found cell length (2.12 ± 0.05 μm) to be independent of channel width in the 0.8–1.0 μm range (**Figure 3A**). In 0.7 μm wide channels, where cells appeared to be in contact with channel walls, the cell lengths were significantly (9% difference, $p < 0.02$) smaller than those in other channels. Interestingly, cells were longer in all microfluidic channels than in the test-tube liquid cultures (1.84 μm; $p = 0.19$ for 0.7 μm wide channel, and $p < 10^{-16}$ for all other

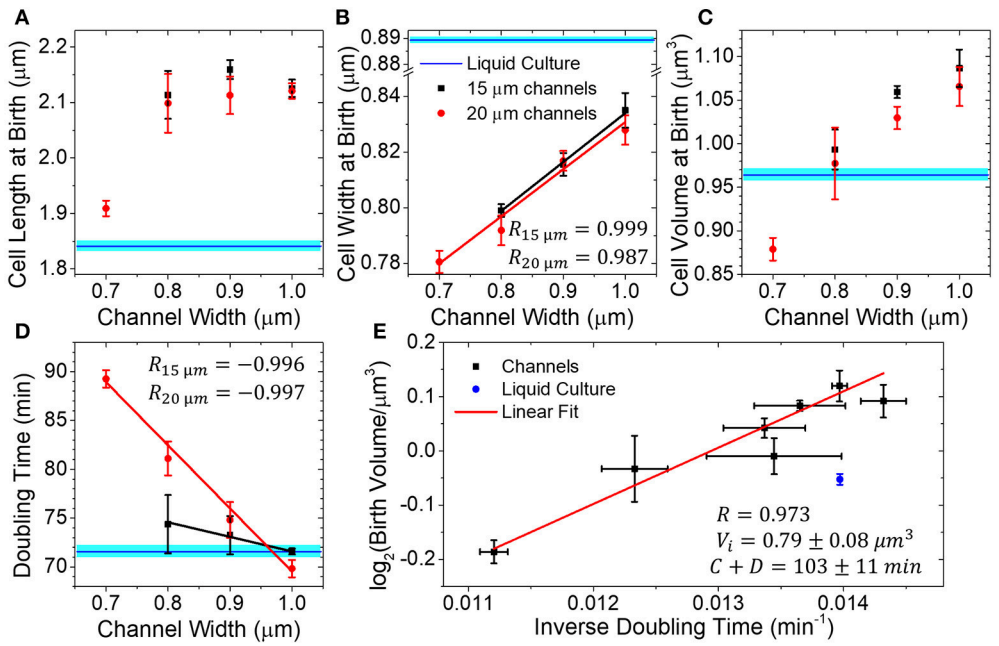

FIGURE 3 | Dimensions of the mother cell and its doubling times in dead-end channels of different widths. **(A–D)** Mother cell length, width, volume and doubling time as a function of channel width in channels of 15 (red circles) and 20 μm (black squares) length. All measurements have been done at 28°C. Data points represent the average of three independent measurements. In each measurement, more than 300 cell births have been analyzed. Error bars are s.e.m. of the three independent measurements. Blue horizontal lines represent measurements of cells from liquid culture tubes. The width of these lines corresponds to s.e.m. All other solid lines are linear fits to the data. **(E)** Logarithm of birth volume, V_b, as a function inverse of doubling time, T_d^{-1}. Solid line shows the fit of the data to the universal growth law, $V_b = \left(\frac{1}{2}\right) V_i \bullet 2^{\frac{C+D}{T_d}}$. In the universal growth law, V_i is cell volume at the initiation of replication, C the time taken to replicate DNA and D the time taken from the end of replication to cell division. Here V_i and $C + D$ are treated as fitting parameters with best fit values $V_i = 0.79 \pm 0.08\ \mu m^3$ and $C + D = 103 \pm 11$ min. The errors are standard error.

channels). At the same time, the coefficients of variation of the cell length at birth distributions were comparable to the values in the liquid culture (all are about 15%) (Supplementary Figure 3). The coefficients of variation determined here are in agreement with previous measurements where values of 12–17% have been reported from agarose pad (Adiciptaningrum et al., 2015) and microfluidic measurements (Campos et al., 2014; Taheri-Araghi et al., 2015).

While cell lengths were longer in microfluidic channels, their widths were significantly smaller (Welch's t-test $p < 10^{-8}$) (**Figure 3B**). Also, coefficients of variation of the cell width distribution were smaller than the ones in liquid culture (4.5%) and decreased as the channel width decreased from 4 to 3% (Supplementary Figure 3). In 0.7 μm wide channels, the cell width was wider than the undeformed channel diameter indicating that channel walls prevented cells from becoming wider. In 0.8 μm wide channels, some cells could still be squeezed by channel walls. In 0.9 and 1.0 μm wide channels, however, the cells were narrower than the channels and not squeezed by the channel walls. Irrespective of squeezing or no squeezing from channel walls, the cell width at birth increased linearly with the channel width (Pearson $R = 0.999$ in 15 μm long and 0.987 in 20 μm long channels). So, in wider channels, the decrease in cell diameter was not linked to a direct mechanical force to cells but must have reflected some form of adaptation of the cells to a confined channel environment.

As expected from the two above measurements, the average mother cell volume also increased with the channel width (**Figure 3C**). Comparison of microfluidic and the liquid culture cells showed that the differences in their lengths and widths, to some degree, compensated each other in cell volumes. In particular, for the 0.8 μm wide channels, the cell volumes matched those in liquid culture.

The doubling times also depended on channel width and increased as the channels become narrower (**Figure 3D**). The effect was pronounced for cells in 20 μm long channels ($R = -0.997$, slope= −65 min/μm), but was less significant in 15 μm channels ($R = -0.996$, slope = −15 min/μm). In the latter case, the doubling times appeared almost indistinguishable from cells grown in liquid cultures despite changes in cell shape. The observed increase in cell doubling times with the decrease of its dimensions is expected. According to the universal growth law, cell volumes at birth depend exponentially on growth rate, which is taken here as an inverse of doubling time (Schaechter et al., 1958; Willis and Huang, 2017). Such correlations are indeed evident in our data (**Figure 3E**). The universal growth law emerged from studies where cells grew unrestricted, and the growth rate was determined by the type of carbon source rather than by its abundance (Schaechter et al., 1958). In later studies, growth rate was also examined in growth limiting conditions and the increase in cell size and growth rate were found to be correlated in most but not all conditions (Shehata and Marr, 1971). Accordingly, we interpreted the exponential decrease in mother cell volume as a function of doubling time to result from nutrient limiting conditions in channels ends which would arise from nutrient shielding in the channel.

Dependence of Mother Cell Growth on Channel Length

To further investigate this hypothesis, we studied how the dimensions and doubling times of mother cell depended on the channel length. We expected that doubling times should increase and cell dimensions should decrease as the length of the channel increases. For these studies, we used microfluidic chips with a fixed channel width of 0.9 μm but varied channel length from about 20–50 μm (19, 29, 39, and 49 μm). We combined results from these measurements with the earlier ones in 15 and 20 μm long channels. Although the 15 and 20 μm long channels had the same designed width as the longer channels, the actual widths of longer channels appeared slightly smaller than 0.9 μm, which likely explains the differences in growth rates of the two data sets.

We found that the mother cell length, width, and volume all decreased in longer channels (**Figures 4A–C**). The decrease was more pronounced in cell length and volume (17 and 33%) than that in cell width (7% change). This contrasts earlier measurements in **Figure 3**, where the cell width showed a larger variation while the length remained approximately constant. The decrease in cell length and volume was in good approximation proportional to channel length ($R = -0.992$ for both cases), while the decrease of cell width showed lower correlations ($R = -0.832$). The doubling time also increased linearly as a function of channel length (**Figure 4D**). In 50 μm long channels, the doubling time was 44% longer than in 15 μm long channels. The increase in doubling time and decrease in cell volumes were, in good approximation ($R = 0.999$), related by the universal growth law (**Figure 4E**). The fit parameters, which determine the cell volume at initiation per replication origin (V_i), and the sum of C and D periods (Cooper and Helmstetter, 1968), matched those found from measurements where the channel width was varied (cf. **Figures 3E**, **4E**). The consistency of these two datasets indicates that growth limitation likely had the same origin in the measurements where channel width and length were varied.

Mechanical Impediments to Cell Growth in 1D Cultures

In the above measurements, the doubling time increased linearly as the function of channel length. We hypothesized that if the channel length increased even further then the doubling time of the mother cell would show a non-linear increase and perhaps cell growth would completely stop as the nutrient levels deplete at the end of the channel. To test if doubling time of mother cells as a function of channel length would deviate from linear at longer channel lengths, we fabricated a new batch of microfluidic chips with channel lengths of 20, 50, 100, 150, and 200 μm.

Unexpectedly, during the initial passivation step of the channel walls with bovine serum albumin (BSA), which preceded cell loading, we observed an accumulation of this protein to the channel ends in 100 μm and longer channels in phase contrast images. The effect was completely missing in channels 50 μm and shorter on the same chip even for long incubation times (>12 h). When the same M9 growth medium was used without BSA, no material accumulated to the ends of any channel. Aggregation of BSA was so strong that it completely excluded

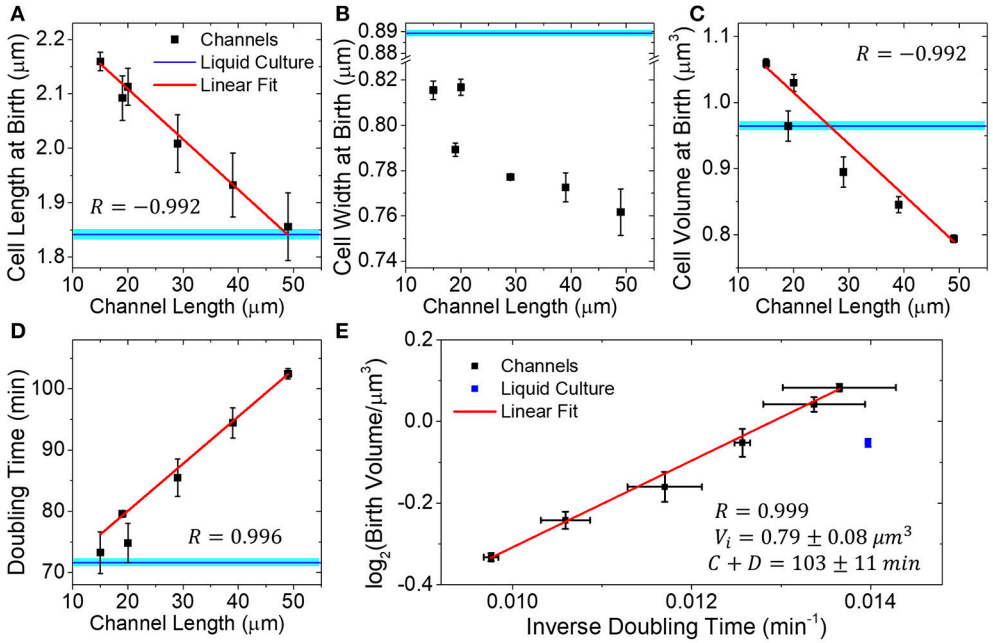

FIGURE 4 | Dimensions and doubling times of mother cells in channels of different lengths. **(A–D)** Mother cell length, width, and volume at birth, and doubling time as a function of channel length. All channels are 0.9 μm wide. Each data point is an average of three independent measurements. In each measurement, more than 300 cell births have been analyzed. Error bars are s.e.m. of the three independent measurements. Blue horizontal lines correspond to measurements of these quantities from liquid culture cells. Solid lines are linear fits to data. **(E)** Logarithm of birth volume, V_b, as a function of inverse doubling time, T_d^{-1}, and it fits to the universal growth law, $V_b = \left(\frac{1}{2}\right)V_i \bullet 2^{\frac{C+D}{T_d}}$.

cells from the channel ends. Further investigation showed that the effect was not specific to BSA because if the channels were left with LB medium that did not contain any BSA, some material still accumulated to the channel ends. Similar effects have been observed before and were explained by water diffusing into PDMS (Randall and Doyle, 2005). The effect depends sensitively on channel length as will be discussed in more details later. Although BSA prevented cells from occupying the ends of 100 μm and longer channels, cells could also be cultivated without BSA. In this case, there was some aggregation of cells near the entrances of the channels. The omission of BSA thus increased sticking of cells to the channel walls, as expected. However, the growth rate of cells in 20–50 μm long channels without BSA passivation were not different from these with BSA (Supplementary Figure 4).

The growth of colonies in 100 μm and longer channels differed significantly from those in shorter channels (≤50 μm). These differences were present irrespective of the presence or absence of BSA in the growth medium. Attachments of cells to channel walls combined with their continued growth lead to considerable pressure buildup, which was evidenced by the widening of the channel in phase contrast images (**Figures 5A–C**). In deformed regions of the channel, the cells grow in multiple rows or were tilted relative to the direction of the channel. Based on our earlier studies (Yang et al., 2015), stress analysis of such channels has shown that pressures in the 0.2 MPa range are needed to widen channels at their midplane by few hundred nanometers. Similar or even larger pressures must have been present in the broadened regions of the channel. From time to time the pressure buildup resulted in a sudden release of cells from the channels as the force resulting from cell growth exceeded some critical value needed to break adhesive contacts between cells and channel walls (**Figure 5A**). However, in some channels, these contacts were likely stronger or differently distributed, and no pressure release occurred during the 12 h observation period.

The pressure buildup had pronounced effects on cell growth and morphology (**Figure 5C**, Supplementary Videos 4, 5). As the pressure increased, cell elongation and division rates slowed down (**Figure 5D**), and the cells started to broaden (**Figure 5E**). For cells that grew tilted relative to the channel axes in the initial stages of pressure buildup, the broadening was not uniform along the cell length due to uneven pushing from other cells (Supplementary Videos 6, 7). The cell regions in contact with the other cells expanded less than the regions where cells were able to expand toward channel walls without these contacts. As a result, the cells acquired irregular pear-shaped morphologies that significantly differed from the regular rod shape (**Figure 5C**). Some mass growth, albeit at a much slower rate than in liquid cultures, still occurred in these conditions (**Figure 5F**). The mass growth in these conditions could be predominantly attributed to cell broadening rather than to elongation. Upon release of pressure, the cell shape immediately returned to the usual elongated rod-shaped morphology. This

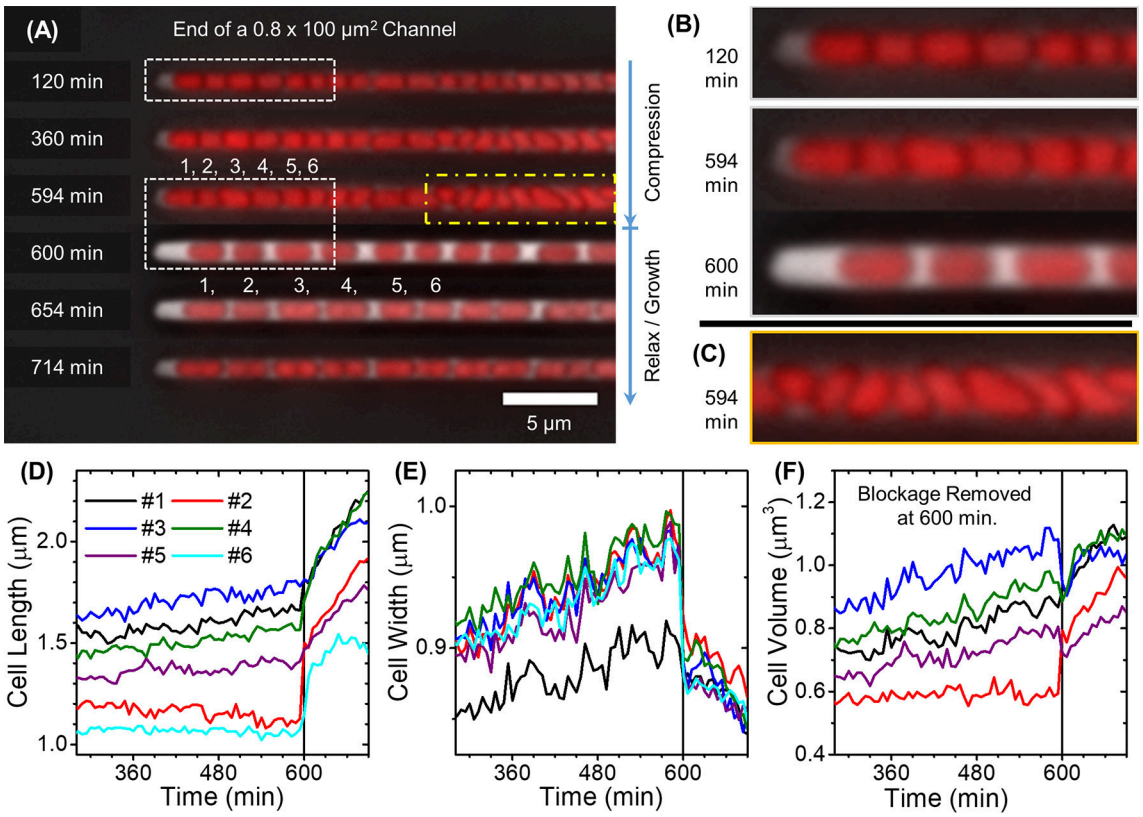

FIGURE 5 | Cell growth in 100 μm long channels. **(A)** Composite time-lapse images of cells growing in a 100 μm long and 0.8 μm wide channel without BSA passivation. Pressure builds up in the channel until the frame at 594 min. Pressure release occurs between 594 and 600 min after which cell growth and division resume. Individual cells are labeled with numbers 1 to 6. **(B,C)** Boxed regions in **(A)** are magnified. **(D–F)** Cell lengths, widths and volumes as a function of time for the first six cells in the channel as labeled on **(A)**. Solid vertical lines show time when the pressure release occurred.

sudden change was accompanied by a decrease in cell width (≈7%) and increase of cell length (≈10%). Interestingly, cell elongation resumed within minutes after pressure was released (**Figure 5D**) even though the elongation rate had been almost zero during the 9 h compression period. Along with resumption of cell elongation, the cell width, after decreasing abruptly upon release of compression, decreased further. Over the course of 1.5 h, it approached its regular value (0.78 μm). The slowdown of cell growth also appeared in measurements in 100 μm and longer channels when BSA was used (Supplementary Figure 5, Supplementary Video 8). The slowdown was followed by a period of faster growth after each pressure release. However, adhesion of cells to the channel wall was clearly weaker in this case; consequently, smaller pressure buildups occurred. In these conditions, cell morphology remained regular, and broadening could not be detected. Altogether, in 100 μm and longer channels, mechanical hindrances were the growth limiting factor instead of nutrient depletion.

DISCUSSION

Cell Shape Shows Adaptations to Channel Geometry

Here we studied how confinement changes the growth of *E. coli* cells in microfluidic channels of different widths and lengths. In 15 and 20 μm long channels with widths of 0.9 and 1.0 μm, the growth rate and cell volume were comparable and even slightly (5–10%) exceeded the values from liquid cultures measurements. Although the confinement related effects to the growth rate in these conditions were negligible, cell morphology was affected. Cells were significantly longer and narrower than in liquid cultures. What factors could have led to the change of cell morphology? In the narrowest channels with widths of 0.7 μm, the cell width was physically limited by the channel walls. The same mechanical constraint could also have limited cell diameter in 0.8 μm wide channels. However, in 0.9 and 1.0 μm wide channels the cells were not squeezed by channel walls, yet they still maintained a higher length to width ratio compared to liquid culture cells (2.7 vs. 2.1, respectively). Even higher ratios (>3.4) can be inferred from previous measurements by another group using mother machine devices at similar growth conditions (Taheri-Araghi et al., 2015). We hypothesize that cell shape in these channels is narrower and longer because of contacts to channel walls. Although the cell adhesion to channel walls was weak, especially to BSA passivated channel walls, these contacts may have had an effect on peptidoglycan synthesizing machinery. Consistent with this idea, the length to diameter ratio of cells was higher when channel walls were not passivated by BSA compared to that when they were (Supplementary Figure 4). By a common view, peptidoglycan synthesis activity

is controlled via MreB and FtsZ polymer scaffolds, which reside in the cytosolic side of the inner membrane (Typas et al., 2012). The data presented here point to the possibility that stresses in the outer envelope may also modulate peptidoglycan synthesis activities directly without being transmitted via MreB and FtsZ scaffolds.

Is Mass Transport Limiting Cell Growth in Channels?

Our measurements showed universal growth law-like dependence between cell volume at birth and growth rate. We interpreted this dependence as arising from nutrient limiting conditions at the channel. We hypothesized that adsorption of nutrients by cells growing between the mother cell and the channel entrance lead to depletion of nutrients at the location of the mother cell. This effect has been also referred to as nutrient shielding (Lavrentovich et al., 2013). Taking the simple geometry of channels and growth of bacteria in single rows without gaps, the nutrient shielding effects in these conditions can be quantitatively analyzed using 1D reaction-diffusion equations. Separate equations can be written for each chemical compound present in the growth medium. Here, we assume that there is just one component in the medium that is growth limiting. Denoting its concentration by c, its diffusion coefficient by D, its absorption coefficient per unit cell surface area by k_{abs}, channel width by W and height by H, and cell radius by R_c a reaction-diffusion equation as a function of distance x from the channel entrance for this component can be written as:

$$\left(W \cdot H - \pi R_c^2\right) \cdot D \frac{d^2 c}{dx^2} = 2\pi R_c k_{abs} \cdot c \tag{2}$$

Here we assumed that the uptake of this nutrient component is a first order process that is far from saturation. If the uptake were saturated (kinetically limited) then the corresponding compound would not be a growth limiting factor. The solution to this equation assuming non-adsorbing boundary condition at channel end is:

$$c\left(x\right) = \frac{c_0 \cosh\left(\frac{x-L}{\lambda}\right)}{\cosh\left(\frac{L}{\lambda}\right)} \quad \lambda = \sqrt{\frac{\left(W \cdot H - \pi R_c^2\right) \cdot D}{2\pi R_c \cdot k_{abs}}} \tag{3}$$

Here L is length of the channel and c_0 is concentration of this compound at the channel entrance. λ defines a characteristic length scale, which is referred to as the nutrient screening length (Lavrentovich et al., 2013). The screening length depends on the cross-sectional area of the channel, being longer for wider channels. We next assume that growth rate (inverse of doubling time), which is controlled by this compound, follows Michelis-Menten type of kinetics (Shehata and Marr, 1971):

$$T_d^{-1}\left(x\right) = \frac{T_{d,min}^{-1}}{1 + \frac{K}{c(x)}} \tag{4}$$

Here T_d is doubling time of cells at position x from the channel entrance, $T_{d,min}$ is the doubling time in conditions where the compound is not growth limiting and K determines the concentration above which nutrient uptake rate starts to saturate. In dilute liquid cultures $T_{d,liquid} = T_{d,min}(1+K/c_0)$. Using the latter expression and the solution for the reaction-diffusion equation for $c(x)$ yields:

$$T_d\left(x\right) = T_{d,min} + \left(T_{d,liquid} - T_{d,min}\right) \cosh\left(\frac{L}{\lambda}\right) / cosh\left(\frac{x-L}{\lambda}\right) \tag{5}$$

Our data concerns mother cells. The doubling time of the mother cell T_d then becomes:

$$T_d = T_{d,min} + \left(T_{d,liquid} - T_{d,min}\right) \cosh\left(\frac{L}{\lambda}\right) \tag{6}$$

Here we assumed the position of the mother cell to be $x \approx L$. The formula predicts that the doubling time in short channels $L \ll \lambda$ is independent of channel length and equals the doubling time in liquid cultures. In channels $L \approx \lambda$ it increases as $T_d \sim L^2$ and in channels $L \gg \lambda$ the increase is exponential $T_d \sim exp(L/\lambda)$. Altogether equation 5 thus predicts a distinctly non-linear relationship between doubling time and channel length. In contrast to this prediction, the data in **Figure 4D** is in good approximation linear (Supplementary Figure 6). The discrepancy between the model and the data also appears when one compares dependence of the doubling time on channel width. The model predicts a smaller variation of doubling time as a function of channel width, in particular for 20 μm long channel (Supplementary Figure 6). It is possible that model treats too simplistically the relationships between concentration of growth-limiting compound and growth rate. For example, some deviations from a single Michelis-Menten type relationship for growth rates were observed in glucose limiting conditions (Shehata and Marr, 1971). However, the underlying relationship between doubling time and channel length should still be distinctly non-linear and as such not consistent with the experimental data. Moreover, there is no obvious compound in our growth medium that can be growth limiting. Concentrations of all media components at channel opening are in the millimolar range and as such exceed several orders of magnitude the growth-limiting concentrations. For example, concentration of glucose in the channel opening is 22 mM. This is about 10^4 higher than its growth-limiting concentration of about 1 μM (Shehata and Marr, 1971). The uptake of glucose by cells is thus completely kinetically limited in the vicinity of channel opening. One can solve the reaction-diffusion equation similar to equation 1 also in kinetically limited regime. The solution shows that the concentration of such nutrients decreases quadratically from the channel entrance as:

$$c = c_0 - c\left(L\right) = L^2 \frac{I_{\max}}{2\left(WH - \pi R_c^2\right) L_c D} \tag{7}$$

Here I_{max} is kinetically limited nutrient uptake rate per cell per second, and L_c is the average cell length. For glucose $I_{max} = 2 \cdot 10^5$ molecules per cell per second (Natarajan and Srienc, 1999) and D=700 μm^2/s (Longsworth, 1953) yields concentration change of 2.7 mM (∼10%) at the end of 50 μm long channel that is

completely filled with bacteria. Resulting 19 mM concentration of glucose in channel end corresponds still to highly saturating level. The same arguments also apply to the casamino acids, which are present in mM concentrations too. Moreover, their depletion with exception of leucine, which is essential for the strain, would not significantly alter the doubling times. If depletion of leucine would have occurred then this would have led to increase in doubling times approximately given by equation 5. Such dependence, however, would not be consistent with the experimentally observed linear dependence in **Figure 4D** as already argued.

The previous analysis assumed mass transport of nutrients to channels is solely via diffusion. However, accumulation of BSA to the ends of 100 μm and longer channels demonstrates that there is significant influx of water into these dead-end channels because of evaporation/diffusion water into PDMS (Randall and Doyle, 2005). This influx was significant even after channels were filled with water for a 12-h period. The steady uptake rate of water to PDMS has been estimated to be $J = 7{\cdot}10^{-6}$ kg/(m^{2}s) (Randall and Doyle, 2005). This update rate explains why BSA accumulates in 100 μm long channels but not in 50 μm long channels. The steady state concentration profile for the BSA in empty channels can be found from equation that balances its diffusive and convection fluxes:

$$W \cdot H \cdot D_{BSA} \frac{dc_{BSA}}{dx} = \frac{J}{\rho} (2H + W) \cdot (L - x) \cdot c_{BSA}(x) \quad (8)$$

Here ρ is density of water. The solution to this equation is:

$$c_{BSA}(x) = c_{0,BSA} \exp\left(\frac{L^2}{2\sigma^2}\right) \exp\left(-\frac{(L-x)^2}{2\sigma^2}\right) \sigma = \sqrt{\frac{\rho \cdot D_{BSA}}{J} \frac{WH}{2H + W}} \quad (9)$$

Here σ is a characteristic length scale for accumulation, which depends on cross-sectional parameters of the channel but not on its length. For BSA, which diffusion coefficient is 70 μm^2/s, $\sigma = 57\ \mu m$ can be estimated for 0.9 μm wide channels. Increase in BSA concentration in channel end is 1.5 times in 50 μm, 5 times in 100 μm and 500 times in 200 μm long channels. 500 times increase corresponds to almost complete precipitation of BSA as observed in our experiments.

While water permeation to PDMS has strong effect on the BSA distribution in the channel, Equation (8) predicts that it does not have significant effect on distribution of nutrients, signaling molecules and metabolic waste products in the channel. The reason is that diffusion coefficients of these small molecules are about an order of magnitude larger (e.g., $D = 700$ μm^2/s for glucose) than for BSA. Even for 200 μm long empty channel one would expect the concentration of these molecules to be less than twice of that in the channel entrance. This increase does not likely have a significant effect on cell growth.

So far we did not consider adsorption of small molecules by channel walls. In current treatment, the adsorption would be completely analogous to adsorption of these molecules by cells. Consequently, adsorption by channel walls can be accounted by increasing k_{abs} in Equation (2) while the functional form of the equations remains the same. Accounting wall adsorption would therefore not lead to better agreement between experiment and model as inclusion of adsorption would not change functional dependence of doubling time on channel length.

Altogether our analysis shows that mass transport related limitations to cell growth in channels $\leq$ 100 μm are not significant in our experimental conditions despite our initial expectations. However, if some of the essential components in the media are present at less than saturating levels then the doubling times of the cells in the channel ends should become strongly affected. Flow of water into channels because of permeability of PDMS should not affect these conclusions because of fast diffusion of nutrients and waste molecules.

Mechanical Constraints to Cell Growth

Our experiments indicate that instead of nutrient limitations, the mechanical impediments set stronger constraints for bacterial growth in channels. In channels 100 μm and longer, friction forces caused cessation of cell elongation. In shorter channels friction could have also been the main growth limiting factor. In accordance with this assumption, friction leads to growth opposing force on a mother cell, F_f, which increases proportionally to channel length $F_f \sim L$. Measurements of *E. coli* growth in agarose hydrogels have shown that forces opposing cell growth decrease elongation rate approximately linearly as the magnitude of the force increases (Tuson et al., 2012). For small forces, this would mean that increase in doubling time from the bulk value is proportional to the opposing force and thus on channel length $\Delta T_d = T_d - T_{d,liquid} \sim F_f \sim L$ in agreement with the experimental data (**Figure 4D**). Increased friction can also explain why in narrower channels doubling time increased (**Figure 3D**).

Although sticking of individual cells to channels walls was weak in channels longer than 50 μm, the cumulative effect of adhesion become strong enough to prevent cell elongation on the dead-end side of the channels. Interestingly, some residual mass growth still occurred in this situation that resulted in broadening of cells. Presumably due to this residual growth cells in some channels were able to overcome static friction forces and release the pressure that opposed their growth. During the release of pressure, the cells behaved similarly to a compressed elastic rod: their length increased (25%) and diameter decreased (7%). The length increase furthermore indicates that cells did synthesize new cell wall during the compression phase. Taken the previously estimated Young modulus in the range of 50–150 MPa for *E. coli* cell for the envelope thickness of 4 nm (Tuson et al., 2012) 25% of compression corresponds to force on the 0.8 μm wide cell of 0.1–0.4 microNewtons (μN). Here we assumed that turgor pressure, during and few minutes after the compression, was the same and that cell wall compression was elastic. The force of 0.1–0.4 μN then corresponds approximately to the stall force for peptidoglycan synthesis in *E. coli*. For comparison, the stalling force has been estimated to be 11 μN in fission yeast (Minc et al., 2009).

Strikingly, the cells were able to restore their growth rates very rapidly (less than 6 min) after more than 9 h of very

limited growth during compression. Here the 6 min estimate corresponds to the frame rate of measurements, but actual lag phase could have been shorter. Very short lag time if any is in contrast with the time needed to restore growth in stationary phase cells upon entering fresh medium. In our measurements, this time has typically been in the range of 0.5–2.0 h depending on the length of time cells spent in stationary state. A period of approximately 30 min appears to be needed to restore transcriptional activity and assemble functional peptidoglycan synthesis complexes. Since the cell growth in channels resumed much faster, the cells must have maintained active peptidoglycan machinery throughout the compression period. The compressed cells in channels were clearly different from stationary phase cells as they had access to nutrients and were metabolically more active. Maintenance of enzymatic machinery, even when no elongation occurred, indicates that mechanical stress opposing cell growth alone is not able to suppress transcriptional peptidoglycan synthesis machinery the way the entry to stationary phase does.

Implications to Bacterial Growth in Microfluidic Devices and in Natural Microenvironments

Our work brings out some differences in the growth of *E. coli* in confined, relative to unconfined, conditions in mother machine platform. We find that for mother machine platform the channels need to be in a rather narrow range of dimensions for not to display growth-limiting effects: for *E. coli* growing in M9 medium with glucose and casamino acids only 15 and 20 μm long and 0.9 and 1.0 μm wide channels did not display these effects. However, even in these channels cell morphology differed from the one in liquid cultures. The different aspect ratio that we observed is not likely significant factor for most experiments, but for those dealing with cell size control and cell wall synthesis, these effects need to be considered. To improve the mother machine design, one can use even shorter ($<$15 μm) channels. However, this comes with the drawback of losing cells from the channel in long-term experiments. On the other hand, our data and analysis indicate that growth limitation due to nutrient and waste diffusion is minimal even in long channels ($>$100 μm). The designs that increase mass transport to channels, such as done recently by diverting some fluid flows through the channels (Baltekin et al., 2017; Jennings, 2017) or using shallow side channels that surround the cells (Norman et al., 2013; Cabeen et al., 2017), is not likely to alleviate growth limitations in these channels.

The mechanical constraints resulting from cell adhesion may be a major limiting factor for bacterial growth not only in microfluidic channels but also in natural environments such as soil where small pores and channels with dimensions comparable to bacterial size are present (Ranjard and Richaume, 2001). These constraints may also limit bacterial growth in unconstrained colonies such as ones on agar plates. Although nutrient limitation has been considered as the main growth limiting factor for growth of bacterial cells in the interior of the colony (Jeanson et al., 2015), our results point out the possibility that mechanical constraints have an equally important role in limiting growth only to the outer layers of the colony.

AUTHOR CONTRIBUTIONS

DY and JM contributed conception and design of the study. DY and SR fabricated the devices used in the study. DY, AJ, EB performed the measurements. DY analyzed the data. DY and JM wrote the manuscript. All authors contributed to manuscript revision, read and approved the submitted version.

FUNDING

This work has been supported in part by NSF research grant MCB-1252890.

ACKNOWLEDGMENTS

The authors thank Cees Dekker and Fabai Wu for the generous gift of the strain and Ariel Amir, Maxim Lavrentovich, Jaana Männik, Bryant Walker, Conrad Woldringh, and Arieh Zaritsky for discussions and critical reading the manuscript. Authors acknowledge technical assistance and material support from the Center for Environmental Biotechnology at the University of Tennessee. A part of this research was conducted at the Center for Nanophase Materials Sciences, which is sponsored at Oak Ridge National Laboratory by the Scientific User Facilities Division, Office of Basic Energy Sciences, U.S. Department of Energy.

SUPPLEMENTARY MATERIAL

The Supplementary Material for this article can be found online at: https://www.frontiersin.org/articles/10.3389/fmicb.2018.00871/full#supplementary-material

REFERENCES

Adiciptaningrum, A., Osella, M., Moolman, M. C., Lagomarsino, M. C., and Tans, S. J. (2015). Stochasticity and homeostasis in the *E. coli* replication and division cycle. *Sci. Rep.* 5:18261. doi: 10.1038/srep18261

Amir, A., Babaeipour, F., McIntosh, D. B., Nelson, D. R., and Jun, S. (2014). Bending forces plastically deform growing bacterial cell walls. *Proc. Natl. Acad. Sci. U.S.A.* 111, 5778–5783. doi: 10.1073/pnas.1317497111

Bailey, M. W., Bissichia, P., Warren, B. T., Sherratt, D. J., and Männik, J. (2014). Evidence for divisome localization mechanisms independent of the Min system and SlmA in *Escherichia coli*. *PLoS Genet.* 10:e1004504. doi: 10.1371/journal.pgen.1004504

Baltekin, Ö., Boucharin, A., Tano, E., Andersson, D. I., and Elf, J. (2017). Antibiotic susceptibility testing in less than 30 min using direct single-cell imaging. *Proc. Natl. Acad. Sci. U.S.A.* 114, 9170–9175. doi: 10.1073/pnas.1708558114

Cabeen, M. T., Russell, J. R., Paulsson, J., and Losick, R. (2017). Use of a microfluidic platform to uncover basic features of energy and environmental

stress responses in individual cells of *Bacillus subtilis*. *PLoS Genet.* 13:e1006901. doi: 10.1371/journal.pgen.1006901

Campos, M., Surovtsev, I. V., Kato, S., Paintdakhi, A., Beltran, B., Ebmeier, S. E., et al. (2014). A constant size extension drives bacterial cell size homeostasis. *Cell* 159, 1433–1446. doi: 10.1016/j.cell.2014.11.022

Cooper, S., and Helmstetter, C. E. (1968). Chromosome replication and division cycle of *Escherichia coli* B/r. *J. Mol. Biol.* 31:519. doi: 10.1016/0022-2836(68)90425-7

Datsenko, K. A., and Wanner, B. L. (2000). One-step inactivation of chromosomal genes in *Escherichia coli* K-12 using PCR products. *Proc. Natl. Acad. Sci. U.S.A.* 97, 6640–6645. doi: 10.1073/pnas.120163297

Hol, F. J., and Dekker, C. (2014). Zooming in to see the bigger picture: Microfluidic and nanofabrication tools to study bacteria. *Science* 346, 438. doi: 10.1126/science.1251821

Jeanson, S., Floury, J., Gagnaire, V., Lortal, S., and Thierry, A. (2015). Bacterial colonies in solid media and foods: a review on their growth and interactions with the micro-environment. *Front. Microbiol.* 6:1284. doi: 10.3389/fmicb.2015.01284

Jennings, A. D. (2017). *Development of Microfluidic Platforms for Studies of Cellular Organization in Escherichia coli*. Master's Thesis, University of Tennessee.

Kaiser, M., Jug, F., Julou, T., Deshpande, S., Pfohl, T., Silander, O. K., et al. (2018). Monitoring single-cell gene regulation under dynamically controllable conditions with integrated microfluidics and software. *Nat. Commun.* 9:212. doi: 10.1038/s41467-017-02505-0

Lavrentovich, M. O., Koschwanez, J. H., and Nelson, D. R. (2013). Nutrient shielding in clusters of cells. *Phys. Rev. E* 87:062703. doi: 10.1103/PhysRevE.87.062703

Long, Z., Nugent, E., Javer, A., Cicuta, P., Sclavi, B., Lagomarsino, M. C., et al. (2013). Microfluidic chemostat for measuring single cell dynamics in bacteria. *Lab Chip* 13, 947–954. doi: 10.1039/c2lc41196b

Longsworth, L. G. (1953). Diffusion measurements, at 25-degrees, of aqueous solutions of amino acids, peptides and sugars. *J. Am. Chem. Soc.* 75, 5705–5709. doi: 10.1021/ja01118a065

Männik, J., Bailey, M. W., O'Neill, J. C., and Männik, J. (2017). Kinetics of large-scale chromosomal movement during asymmetric cell division in *Escherichia coli*. *PLoS Genet.* 13:e1006638. doi: 10.1371/journal.pgen.1006638

Männik, J., Driessen, R., Galajda, P., Keymer, J. E., and Dekker, C. (2009). Bacterial growth and motility in sub-micron constrictions. *Proc. Natl. Acad. Sci. U.S.A.* 106, 14861–14866. doi: 10.1073/pnas.0907542106

Männik, J., Wu, F., Hol, F. J. H., Bissichia, P., Sherratt, D. J., Keymer, J. E., et al. (2012). Robustness and accuracy of cell division in *Escherichia coli* in diverse cell shapes. *Proc. Natl. Acad. Sci. U.S.A.* 109, 6957–6962. doi: 10.1073/pnas.1120854109

Minc, N., Boudaoud, A., and Chang, F. (2009). Mechanical forces of fission yeast growth. *Curr. Biol.* 19, 1096–1101. doi: 10.1016/j.cub.2009.05.031

Moffitt, J. R., Lee, J. B., and Cluzel, P. (2012). The single-cell chemostat: an agarose-based, microfluidic device for high-throughput, single-cell studies of bacteria and bacterial communities. *Lab Chip* 12, 1487–1494. doi: 10.1039/c2lc00009a

Natarajan, A., and Srienc, F. (1999). Dynamics of glucose uptake by single *Escherichia coli* cells. *Metab. Eng.* 1, 320–333. doi: 10.1006/mben.1999.0125

Norman, T. M., Lord, N. D., Paulsson, J., and Losick, R. (2013). Memory and modularity in cell-fate decision making. *Nature* 503:481. doi: 10.1038/nature12804

Randall, G. C., and Doyle, P. S. (2005). Permeation-driven flow in poly(dimethylsiloxane) microfluidic devices. *Proc. Natl. Acad. Sci. U.S.A.* 102, 10813–10818. doi: 10.1073/pnas.0503287102

Ranjard, L., and Richaume, A. (2001). Quantitative and qualitative microscale distribution of bacteria in soil. *Res. Microbiol.* 152, 707–716. doi: 10.1016/S0923-2508(01)01251-7

Sachs, C. C., Grünberger, A., Helfrich, S., Probst, C., Wiechert, W., Kohlheyer, D., et al. (2016). Image-based single cell profiling: high-throughput processing of mother machine experiments. *PLoS ONE* 11:e0163453. doi: 10.1371/journal.pone.0163453

Schaechter, M., Maaloe, O., and Kjeldgaard, N. O. (1958). Dependency on medium and temperature of cell size and chemical composition during balanced growth of *Salmonella Typhimurium*. *J. Gen. Microbiol.* 19, 592–606. doi: 10.1099/00221287-19-3-592

Shehata, T., and Marr, A. G. (1971). Effect of nutrient concentration on growth of *Escherichia coli*. *J. Bacteriol.* 107, 210.

Taheri-Araghi, S., Bradde, S., Sauls, J. T., Hill, N. S., Levin, P. A., Paulsson, J., et al. (2015). Cell-size control and homeostasis in bacteria. *Curr. Biol.* 25, 385–391. doi: 10.1016/j.cub.2014.12.009

Tuson, H. H., Auer, G. K., Renner, L. D., Hasebe, M., Tropini, C., Salick, M., et al. (2012). Measuring the stiffness of bacterial cells from growth rates in hydrogels of tunable elasticity. *Mol. Microbiol.* 84, 874–891. doi: 10.1111/j.1365-2958.2012.08063.x

Typas, A., Banzhaf, M., Gross, C. A., and Vollmer, W. (2012). From the regulation of peptidoglycan synthesis to bacterial growth and morphology. *Nat. Rev. Microbiol.* 10, 123–136. doi: 10.1038/nrmicro2677

Ullman, G., Wallden, M., Marklund, E. G., Mahmutovic, A., Razinkov, I., and Elf, J. (2013). High-throughput gene expression analysis at the level of single proteins using a microfluidic turbidostat and automated cell tracking. *Philos. Trans. R. Soc. B Biol. Sci.* 368:20120025. doi: 10.1098/rstb.2012.0025

Verbeek, P. W., and Vanvliet, L. J. (1994). On the location error of curved edges in low-pass filtered 2-D and 3-D images. *IEEE Trans. Pattern Anal. Mach. Intell.* 16, 726–733. doi: 10.1109/34.297954

Wang, P., Robert, L., Pelletier, J., Dang, W. L., Taddei, F., Wright, A., et al. (2010). Robust growth of *Escherichia coli*. *Curr. Biol.* 20, 1099–1103. doi: 10.1016/j.cub.2010.04.045

Weibel, D. B., DiLuzio, W. R., and Whitesides, G. M. (2007). Microfabrication meets microbiology. *Nat. Rev. Microbiol.* 5, 209–218. doi: 10.1038/nrmicro1616

Willis, L., and Huang, K. C. (2017). Sizing up the bacterial cell cycle. *Nat. Rev. Microbiol.* 15, 606–620. doi: 10.1038/nrmicro.2017.79

Wu, F., van Rijn, E., van Schie, B. G. C., Keymer, J. E., and Dekker, C. (2015). Multicolor imaging of bacterial nucleoid and division proteins with blue, orange and near-infrared fluorescent proteins. *Front. Microbiol.* 6:607. doi: 10.3389/fmicb.2015.00607

Yang, D., Greer, C. M., Jones, B. P., Jennings, A. D., Retterer, S. T., and Männik, J. (2015). Characterization of small microfluidic valves for studies of mechanical properties of bacteria. *J. Vacuum Sci. Technol. B* 33:06F202. doi: 10.1116/1.4929883

Conflict of Interest Statement: The authors declare that the research was conducted in the absence of any commercial or financial relationships that could be construed as a potential conflict of interest.

frontiers in Microbiology

ORIGINAL RESEARCH
published: 05 June 2018
doi: 10.3389/fmicb.2018.01115

Extrachromosomal Nucleolus-Like Compartmentalization by a Plasmid-Borne Ribosomal RNA Operon and Its Role in Nucleoid Compaction

*Carmen Mata Martin, Zhe Sun, Yan Ning Zhou and Ding Jun Jin**

Transcription Control Section, RNA Biology Laboratory, Center for Cancer Research, National Cancer Institute, National Institutes of Health, Frederick, MD, United States

OPEN ACCESS

Edited by:
Conrad L. Woldringh, University of Amsterdam, Netherlands

Reviewed by:
Martin Siemann-Herzberg, University of Stuttgart, Germany
Peter Graumann, Philipps University of Marburg, Germany

***Correspondence:**
Ding Jun Jin
jind@mail.nih.gov

Specialty section:
This article was submitted to Microbial Physiology and Metabolism, a section of the journal Frontiers in Microbiology

Received: *22 January 2018*
Accepted: *11 May 2018*
Published: *05 June 2018*

Citation:
Mata Martin C, Sun Z, Zhou YN and Jin DJ (2018) Extrachromosomal Nucleolus-Like Compartmentalization by a Plasmid-Borne Ribosomal RNA Operon and Its Role in Nucleoid Compaction. Front. Microbiol. 9:1115. doi: 10.3389/fmicb.2018.01115

In the fast-growing *Escherichia coli* cells, RNA polymerase (RNAP) molecules are concentrated and form foci at clusters of ribosomal RNA (rRNA) operons resembling eukaryotic nucleolus. The bacterial nucleolus-like organization, spatially compartmentalized at the surface of the compact bacterial chromosome (nucleoid), serves as transcription factories for rRNA synthesis and ribosome biogenesis, which influences the organization of the nucleoid. Unlike wild type that has seven rRNA operons in the genome in a mutant that has six (Δ6*rrn*) rRNA operons deleted in the genome, there are no apparent transcription foci and the nucleoid becomes uncompacted, indicating that formation of RNAP foci requires multiple copies of rRNA operons clustered in space and is critical for nucleoid compaction. It has not been determined, however, whether a multicopy plasmid-borne rRNA operon (p*rrnB*) could substitute the multiple chromosomal rRNA operons for the organization of the bacterial nucleolus-like structure in the mutants of Δ6*rrn* and Δ7*rrn* that has all seven rRNA operons deleted in the genome. We hypothesized that extrachromosomal nucleolus-like structures are similarly organized and functional *in trans* from p*rrnB* in these mutants. In this report, using multicolor images of three-dimensional superresolution Structured Illumination Microscopy (3D-SIM), we determined the distributions of both RNAP and NusB that are a transcription factor involved in rRNA synthesis and ribosome biogenesis, p*rrnB* clustering, and nucleoid structure in these two mutants in response to environmental cues. Our results found that the extrachromosomal nucleolus-like organization tends to be spatially located at the poles of the mutant cells. In addition, formation of RNAP foci at the extrachromosomal nucleolus-like structure condenses the nucleoid, supporting the idea that active transcription at the nucleolus-like organization is a driving force in nucleoid compaction.

Keywords: RNA polymerase, bacterial nucleolus-like, rRNA synthesis and ribosome biogenesis, nucleoid structure, transcription factories, three-dimensional superresolution Structured Illumination Microscopy, *Escherichia coli*

INTRODUCTION

In *Escherichia coli* (*E. coli*), the growth rate is determined by growth medium (Kjeldgaard et al., 1958; Schaechter et al., 1958; Jin et al., 2012). *E. coli* cells grow rapidly in LB at 37°C with a doubling time about 20 min. In a fast-growing cell, there are multiple copies of the genome (Nielsen et al., 2007) and most RNA polymerase (RNAP) molecules engage in transcription of ribosomal RNA (rRNA) operons (French and Miller, 1989). There are seven almost identical rRNA operons which in total encompass only ∼1% of the genome, four of which are near the origin of chromosome replication *oriC*. Thus, cell size, copy numbers of bacterial chromosome (named nucleoid) and rRNA operon (*rrn*), and the organization of the nucleoid are sensitive to growth conditions (Jin et al., 2013).

Imaging RNAP-GFP using microscopy in bacterial cells has advanced our understanding of the distribution and the organization of the transcription machinery. Images of bacterial RNAP were first reported in *Bacillus subtilis* (Lewis et al., 2000), which showed that most of RNAP lies within the core of the nucleoid but is minimal at the peripheral region of the nucleoid and that, in fast-growing cells, for each nucleoid there are two RNAP foci named transcription foci at rRNA genes clusters in the *oriC* region. However, the effect of RNAP's distribution on the organization of the nucleoid was not determined. Using advanced imaging systems and tools, extensive studies in *E. coli* have revealed that the transcription machineries not only are spatially organized but also influenced the nucleoid structure. Images of RNAP from these two bacteria share similarities but also reveal differences. These differences could be due to microbial diversity, and/or different cell imaging techniques used in different studies. In *E. coli* cells grown in nutrient rich LB, RNAP molecules are concentrated and form foci at clusters of rRNA operons resembling eukaryotic nucleolus-like structure (Cabrera and Jin, 2003). The 3D images of multicolor superresolution Structured Illumination Microscopy (3D-SIM) reveal that under optimal growth conditions (LB at 37°C), RNAP foci, spatially located at the periphery of the compact nucleoid, co-localize with transcriptional factors, NusA and NusB, both of which are involved in rRNA synthesis and ribosome biogenesis (Greenblatt and Li, 1981; Torres et al., 2004; Greive et al., 2005; Stagno et al., 2011; Bubunenko et al., 2013). RNAP foci thus represent transcription factories (Cook, 2010; Papantonis and Cook, 2013) for the expression of growth genes, analogous to the eukaryotic Pol I activity at the nucleolus in the nucleus (Jin et al., 2017). Such an organization of hyperstructure (Norris et al., 2007) would considerably facilitate RNAP recycling and recruitment for synchronized active rRNA synthesis, rRNA processing and ribosome assembly in spatial proximity. However, RNAP is mobile, and RNAP foci and the associated macromolecular organization are dynamic and sensitive to environmental cues (Bakshi et al., 2012; Endesfelder et al., 2013; Jin et al., 2013, 2015; Stracy et al., 2015). For example, the transcription foci and possibly the nucleolus-like structure disappear, leading to an expanded nucleoid when growth is slowing down or arrested during stress responses (Cabrera and Jin, 2003), such as by amino acid starvation, which induces the stringent response (Cashel et al., 1996; Durfee et al., 2008) or with rifampicin treatment, which inhibits transcription initiation. A strong, positive correlation between the presence of transcription foci and the occurrence of relatively compact states of the nucleoid demonstrates an interconnection of the organizations of transcription machinery and the nucleoid (Jin et al., 2013). However, determining whether transcription associated with the bacterial nucleolus-like structure or organization (hereafter they are used interchangeably) plays a direct role in the compaction of the nucleoid has been difficult to dissect.

Having multiple copies of rRNA operons in the bacterial genome is a prerequisite for the formation and organization of RNAP foci in *E. coli*. A series of chromosomal *rrn* deletion(s) has been constructed and characterized (Condon et al., 1993, 1995; Quan et al., 2015). *E. coli* strains in which two out of seven rRNA operons were deleted in the genome behave like wild type in growth rate, formation and organization of RNAP foci, and nucleoid structure. However, mutant strains in which additional multiple chromosomal rRNA were deleted reduce growth rate and cause changes in the distribution of RNAP and nucleoid structure (Jin et al., 2016). For example, in the mutant strain (Δ6*rrn*), in which six out seven rRNA operons were deleted from the genome, there are no apparent transcription foci and the nucleoid becomes uncompacted under optimal growth conditions (LB at 37°C). These phenotypes of Δ6*rrn* can be explained by reduced rRNA synthesis and ribosome biogenesis due to the lack of bacterial nucleolus-like organization in the cell (Cabrera et al., 2009). Thus, this genetic background has provided a unique system to address the potential role of bacterial nucleolus-like organization supplemented *in trans* by a multicopy plasmid-borne rRNA operon in nucleoid compaction. Previously it was briefly reported (Jin et al., 2017) that the RNAP foci reappear in the mutant strain that harbors pKK3535 (in which the *rrnB* operon is cloned into pBR322 vector; hereafter, this plasmid-borne rRNA operon is referred to as p*rrnB*) (Kingston et al., 1981). However, the organization of the transcription machinery and the distribution of p*rrnB* have not been determined. In this study, we characterized the structure and function of RNAP foci in the mutants of Δ6*rrn*/p*rrnB* and Δ7*rrn*/p*rrnB*, in which all seven chromosomal rRNA operons were deleted. Our results showed that analogous to wild type, RNAP forms foci at clusters of p*rrnB* for rRNA synthesis and ribosome biogenesis in the two mutants, and suggested that active transcription at the extrachromosomal nucleolus-like organization is a driving force in nucleoid compaction.

MATERIALS AND METHODS

Bacterial Strains, Growth Conditions, and Technologies

All of the strains used in the study are derivatives of the prototype K-12 MG1655. **Table 1** lists the strains and plasmids used in the study. The MG1655 strain has a doubling time 20 min in LB at 37°C (Jin et al., 2013), as measured by determining the increase of OD at 600 nm (OD_{600}) of bacteria cultures in a shaking flask

TABLE 1 | Bacterial strains and plasmids.

Strains	Relevant Genotype	Source/Reference
CC72	MG1655 *rpoC-Venus*	Cagliero and Jin, 2013
SQZ5	MG1655 Δ6*rrn* [(Δ*rrn*GADEHB)(ptRNA67)]	Cabrera et al., 2009
CC125	SQZ5 *rpoC*-Venus	This work
CC126	CC125(pKK3535)	This work
CC378	CC125(pBR322)	This work
SQ171	MG1655 Δ7*rrn* [(Δ*rrn*GADEHBC)(ptRNA67, pKK3535)]	Quan et al., 2015
CC379	SQ171 *rpoC*-Venus	This work
CC382	CC125 *nusB-mCherry::Kan*	This work
CC383	CC126 *nusB-mCherry::Kan*	This work
CC384	CC378 *nusB-mCherry::Kan*	This work
CC385	CC379 *nusB-mCherry::Kan*	This work
CC386	CC125(pTac-16S)	This work
CC387	CC125[pMKA201(pT7-rpoC)]	This work
CC389	CC125(pK4-16)	This work
Plasmids	**Description**	**Source/Reference**
ptRNA67	tRNA genes cloned in p15 replicon	Cabrera et al., 2009
pKK3535	*rrnB* operon cloned in pBR322	Kingston et al., 1981
pBR322	cloning vector	Bolivar et al., 1977
pDJ2485	pTac-16S (16S rRNA gene inserted into pKK223-3)	Cabrera and Jin, 2006
pMKA201	pT7-rpoC in pTZ19R	Kashlev et al., 1993
pK4-16	rrnB operon cloned in pSC101	Quan et al., 2015

as a function of time. The chromosomal *rpoC-venus* and *nusB-mCherry* fusions were described previously (Cagliero and Jin, 2013; Cagliero et al., 2014) and have no effect on cell growth. They were introduced to different strains either by P1 phage transduction or by phage lambda Red recombineering (Datsenko and Wanner, 2000). The bacterial media and techniques used are described elsewhere (Miller, 1972). All cultures were grown in Luria-Bertani medium (LB which is tryptone 10 g/l, yeast extract 5 g/l, NaCl 5 g/l) with vigorous agitation in a water bath at 37°C. Overnight cultures were diluted 1/200 into fresh medium. Samples used for microscopic observation were removed from cultures at an OD 0.2 at 600 nm (OD_{600}), and when indicated, rifampicin (150 μg/ml), chloramphenicol (200 μg/ml), and freshly made serine hydroxamate (SHX; 100 mM) were added to the log phase cultures at time zero, and sampled at indicated times. These inhibitors stopped cell growth almost immediately. Media downshifts (from LB to minimal medium) were performed by filtering the exponentially growing culture after the absorbance reached OD_{600} 0.2. Cells were then collected on a nitrocellulose Millipore HA WP04700 filter (47 mm diameter with a 0.45 μm pore diameter). The filtration was performed using a vacuum pump (Millipore), allowing a minimal amount of time to obtain the new condition (about 1 min). Filtered cells were washed with 5X filtered-volume of the minimum medium, followed by resuspension (vortexing) for 1 min in the same volume of pre-heated growth minimum medium (as time zero). Later, incubation was performed under the same shaking and temperature conditions. All materials used were preheated at incubation temperature (at 37°C) to avoid abrupt changes in temperature. The downshift minimal medium is a supplement of M63x salt, 0.01 M $CaCl_2$, 0.1 M $MgSO_4$, and 0.4% glucose. The antibiotics and chemicals were from Sigma.

3D Superresolution Microscopy

Because both the distribution of *E. coli* RNAP and the nucleoid structure are extremely sensitive to perturbations in the environment, cells were immediately fixed using formaldehyde (3.7% v/v final) after sampling (Cabrera and Jin, 2003). It is critical and mandatory to use fixed cells on slides to study the dynamic organization of RNAP and DNA in fast growing cells under optimal growth conditions (Jin et al., 2015). The procedure of culture sampling and multicolor 3D SIM imaging was as described (Mata Martin et al., 2018). The 3D superresolution microscopy was performed with a Nikon N-SIM Ti-2E inverted microscope with a CFI SR HP Apochromat TIRF 100XC Oil (NA 1.49) objective and LU-NV series laser units. Images with a high signal-to-noise ratio were captured with a high-resolution ORCA-Flash 4.0 sCMOS camera (Hamamatsu Photonics K.K.). We performed three grid rotations per image and at least 15 *z*-sections of 0.1 μm to acquire the whole cells. The exposure time and setting are determined by the fluorescence proteins. After image acquisition, images were processed to correct for chromatic aberration using the Software NIS-Elements Ar/NIS-Elements C using the inframe calibration beads for optimum alignment, and were reconstituted.

The cells edited and illustrated are representative of the majority of the observed cells. Pictures were processed uniformly using FijiJ to crop and choose the best *z*-slice or maximum intensity projection slide and were false-colored with Adobe Photoshop.

Image Analyses

Relative nucleoid size (RNS) [ratio of size of nucleoid(s) over size of the cell] was measured as described (Cabrera et al., 2009). For each condition, 100 cells were analyzed. Contrast analysis of the distribution of RNAP in nucleoids was described (Cabrera and Jin, 2003). A Java applet named Nucleoid Analyzer was written for the measurements. At each position in the nucleoid, the Venus fluorescence signal is proportional to the concentration of RNAP. The homogeneity in the RNAP distribution can be evaluated by measuring the differences in fluorescence signals between each position of the nucleoid and its neighboring positions. In nucleoids in which RNAP is not distributed homogeneously (nucleoids with transcription foci), there will be more differences on average in the fluorescence signal between neighboring positions than in nucleoids in which the RNAP is distributed homogeneously (nucleoids without transcription foci). For each growth condition, nucleoids of > 100 cells were analyzed and the data were presented as normalized contrast, as described (Cabrera and Jin, 2003). Contrast analysis of the distribution of DNA signals was similarly measured and presented. The measurement of distribution profiles in a

population of cells was performed in FijiJ by Analyzer Plot Profile. Cells were segmented, giving a cell outline and a cell midline. The distances were normalized to 1 and −1 at the cell midline from the outline in one pole to the outline in the opposite pole. The 2D histograms of the distributions were generated by binning cells into different lengths (3.1–4.6 m long); they indicate the probability density distribution of a body in the cell across the *X*-axis for 100 cells.

Live-Cell Imaging Using a Microfluidics System

Overnight cells from 32°C in LB (16 h) were injected into an ONIX Microfluidic Perfusion System (CellASIC) and were allowed to grow at 32°C in LB with a pressure of 2 psi. The cells were growing in the microfluidic device with a continuous flow of fresh LB; the temperature was controlled by Zeiss control temperature module S. The time-lapse images were acquired using an inverted microscope (Zeiss Axio Observer) with a Plan Apochromat 100 × /1.4 oil phase objective and a 1.6 Optovar, with a high signal-to-noise ratio and high-resolution EMCCD camera (Hamamatsu). Each experiment was performed at least three times; in total, 37 cells for each condition were imaged. The cells illustrated are representative observed cells. Pictures were processed uniformly and were false-colored with Adobe Photoshop.

Cell Lysis and Imaging Released Nucleoids and Transcription Factories

Immediately after sampling, the cells were fixed for 20 min at room temperature with formaldehyde (3.7% v/v final). The cells were centrifuged at 5000 *g* for 5 min; resuspended in 50 μl of 10 mM Tris (pH 8.0), 10 mM EDTA, 20% sucrose, 0.2 μl Ready-lyse lysozyme (Epicenter); and incubated for 30 min at 37°C. The cell lysis was completed by the addition of 50 μl of water. After lysis, a 2-μl aliquot of the lysate containing nucleoids was dropped onto a microscopy slide with 2 μl of 1% warm low melting point agarose + 10 μg/ml Hoechst 33342. The slides were imaged immediately with YFP channel for RNAP-Venus, DAPI channel for DNA, mCherry channel for NusB-mCherrry using an inverted microscope (Zeiss Axio Observer) with a Plan Apochromat 100 × /1.4 oil phase objective and a 1.6 Optovar, with a high signal-to-noise ratio and high-resolution EMCCD camera (Hamamatsu).

RNA-Fluorescence *in Situ* Hybridization (FISH)

The RNAI was used as a probe to observe the subcellular localization of the plasmid-borne p*rrnB*. The different probes cover all RNAI regions. Probe design was based on the protocol described by Raj et al. (2008) and Raj and Tyagi (2010). Each probe was ordered with a 3′ amine group, which allows covalent modification with NHS-ester derivatives of fluorescent dye molecules and were labeled with red fluorescence compound Atto 594 NHS ester as described previously (Skinner et al., 2013). Fluorescence *in situ* hybridization was carried out according to the protocol reported previously (Skinner et al., 2013). Briefly, cells were fixed using formaldehyde (37%) and PBS (10%) for 30 min. Fixed cells were centrifuged at 4000 rpm for 5 min and washed three times in PBS and subsequently incubated in 70% Ethanol for 60 min at room temperature. Cells were washed three times in a washing solution (2xSSC and 40% formamide in DEPC water) for 5 min at 37°C. After washing the cells were incubated with the probes in hybridization buffer (2xSSC, 40% formamide, 10% dextran sulfate in DEPC water) overnight at room temperature. After incubation overnight, the cells were washed three times in the washing solution and three times in 2xSSC. A cell suspension was applied to the slides for imaging. All images were imaged and processed as described previously in the Section "3D Superresolution Microscopy."

Plasmid Copy Number Determination by qRT-PCR

The method was used as previously described (Lee et al., 2006; Anindyajati et al., 2016). Briefly, the single-copy gene *tdk* and *bla* on the chromosome and pKK3535, respectively, were chosen to quantify the absolute plasmid copy number. The *tdk* gene was amplified by PCR and cloned into a pBAD24 plasmid to produce pBAD24-*tdk*, which also has one copy of *bla* gene in the backbone. A 10-fold serial dilution series of the plasmid pBAD24-*tdk* extracted from *E. coli*, ranging from 1×10^{-4} to 1×10^{-9} copies/μl, were used to make the standard curve for the *tdk* and *bla* genes. Then the pKK3535 plasmid and genome DNA were extracted from Δ6*rrn* and Δ6*rrn*/p*rrnB* grown in LB at 37°C by Wizard® Genomic DNA Purification Kit (Promega), and diluted to 2 ng/μl. Quantification of the chromosome (*tdk*) and plasmid (*bla*) were performed using SYBR® Green based qRT-PCR. Using the *C*t values, the absolute quantities of the chromosome and plasmid were determined according to the standard curve. The plasmid copy number was then calculated by dividing the above quantity of the plasmid by the amount of the chromosome.

RESULTS

Extrachromosomal Nucleolus-Like Compartmentalization by a Multicopy Plasmid-Borne Ribosomal RNA Operon

RNAP Foci Organization Independent of Chromosomal rRNA Operons

Previously, a comparison was made only between the Δ6*rrn* and Δ6*rrn*/p*rrnB* strains (Jin et al., 2017). Because in pKK3535 (Kingston et al., 1981) the *rrnB* operon was cloned into the pBR322 vector and to eliminate a potential effect by the vector, we introduced the pBR322 into Δ6*rrn* (Δ6*rrn*/pBR322), and examined the phenotypes of the two strains, Δ6*rrn*/pBR322 and Δ6*rrn*/p*rrnB*, under optimal growth conditions (LB at 37°C). We found no differences between Δ6*rrn* and Δ6*rrn*/pBR322, both of which have the same generation time (τ= 37 min). The generation time for Δ6*rrn*/p*rrnB* is longer (τ= 43 min), indicating that p*rrnB* did not suppress the growth defect of the Δ6*rrn* mutant. The slower growth rate of Δ6*rrn*/p*rrnB* compared to Δ6*rrn*/pBR322 is likely due to an unbalanced growth condition

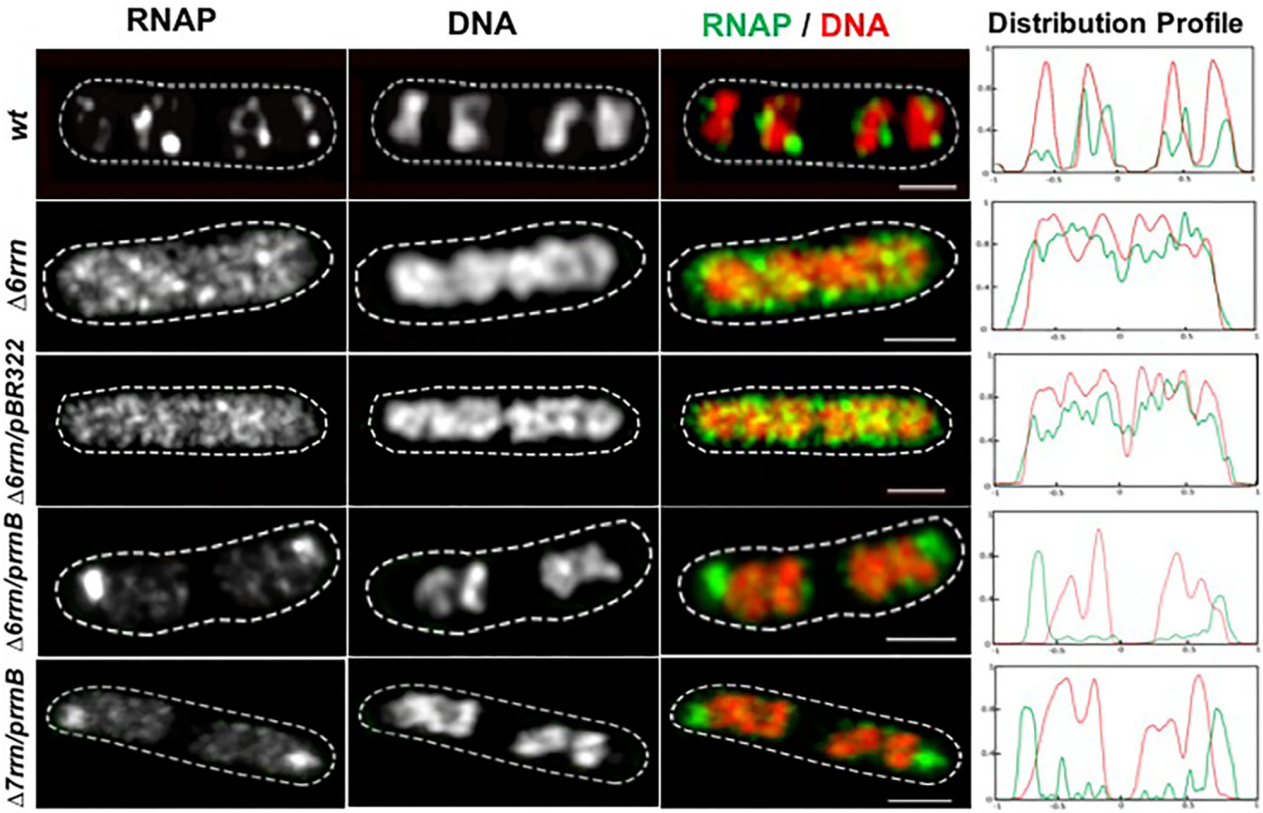

FIGURE 1 | Compartmentalization of RNAP foci and nucleoid condensation caused by the plasmid-borne p*rrnB* in Δ6*rrn* and Δ7*rrn* mutants. Shown are SIM images of RNAP, DNA, and an overlay RNAP (green) and DNA (red) in representative single cells during optimal growth (LB, 37°C). Wild type (*wt*) is included as a control. RNAP is tagged with yellow Venus fluorescent protein (*rpoC*-venus) and DNA is stained with Hoechst 33342, as described in the Section "Materials and Methods." Note that the defects in the Δ6*rrn* or Δ7*rrn* strains in the organization of RNAP foci and nucleoid structure can be complemented by a plasmid-borne rRNA operon (p*rrnB*) in those mutant cells. RNAP foci mainly locate at the cell poles in the two mutants. The cell shape is outlined by a dotted line. The scale bar represents 1 μm. The two-color graphics show the distribution profiles of RNAP and nucleoid in a population of 100 cells; *Y*-axis is the probability density of RNAP (green line) and DNA (red line) across the cell length (*X*-axis) from one pole (–1) to another pole (+1).

caused by the p*rrnB*. SIM images show that there are no RNAP foci in either Δ6*rrn* or Δ6*rrn*/pBR322 strains and the nucleoid is expanded in those cells; however, RNAP foci are evident in Δ6*rrn*/p*rrnB* (**Figure 1**), indicating that the formation of RNAP foci is caused by the plasmid-borne *rrnB*. Unlike wild type, in which multiple RNAP foci are spatially located at the surface of four nascent nucleoids, in Δ6*rrn*/p*rrnB*, there are usually two larger RNAP foci, which are primarily located at the cell poles. To eliminate a potential effect of the remaining chromosomal *rrnC* in the Δ6*rrn* mutant cells on the formation of RNAP foci, we examined the Δ7*rrn*/p*rrnB* mutant cells, in which all seven rRNA operons were deleted in the genome. Like Δ6*rrn*/p*rrnB*, usually two large RNAP foci are apparent and located at cell poles in Δ7*rrn*/p*rrnB* (**Figure 1**), indicating that the formation/organization of RNAP foci is independent of chromosomal rRNA operons but is associated with the plasmid-borne *rrnB*. Each of the Δ6*rrn*/p*rrnB* and Δ7*rrn*/p*rrnB* cells on average has two apparent nascent nucleoids which are compact.

Like their counterparts in wild type, formation/organization of RNAP foci in the Δ6*rrn*/p*rrnB* and Δ7*rrn*/p*rrnB* mutants is also sensitive to environmental cues (**Figures 2A,B**). For example, RNAP foci disappear when the mutant cells were downshifted from LB to minimal medium or starved for amino acids by the addition of SHX. The synthesis of rRNA in cells is significantly reduced by these two treatments. Similarly, there were no RNAP foci when cells were treated with antibiotic rifampicin that inhibits transcription (re)initiation. In addition, similar to wild type, the nucleoids become expanded in those stressed cells compared to those in cells under optimal growth conditions (see details below).

Colocalization of RNAP Foci and Clusters of p*rrnB*

To determine whether RNAP foci are associated with the plasmid-borne p*rrnB*, we attempted to co-image RNAP and the plasmid in the Δ6*rrn*/p*rrnB* and Δ7*rrn*/p*rrnB* cells. Our first approach using DNA-FISH assay failed because of the harsh conditions required in the protocol, including high temperatures, destroyed RNAP foci and the nucleoid structure. We then successfully used the RNA-FISH method, which used mild conditions, to detect the location of p*rrnB* by hybridization of fluorescent DNA probes of the RNAI transcripts (Morita and

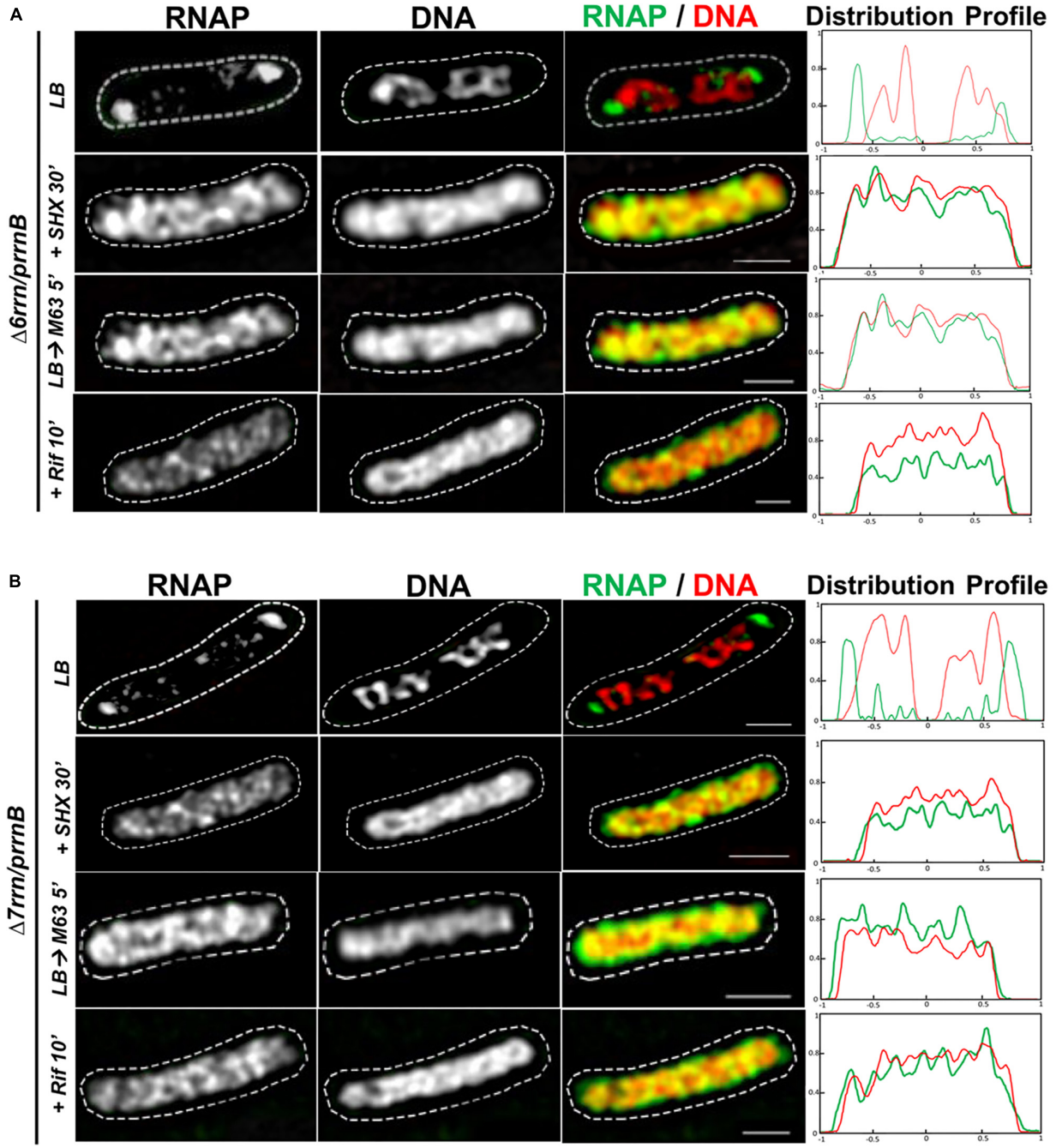

FIGURE 2 | Organizations of RNAP foci and the nucleoids are sensitive to changes in growth medium and/or stress. Shown are SIM images of RNAP, DNA, and two-color overlays of RNAP (green) and DNA (red), from representative single cells of Δ6*rrn*/p*rrnB* **(A)** and Δ7*rrn*/p*rrnB* **(B)** during optimal growth (LB) and after perturbations induced by SHX treatment for 30 min (+SHX 30′), nutrient down shift from LB to minimal medium M63+glucose for 5 min (LB→M63 5′), and after rifampicin treatment for 10 min (+Rif 10′). The cell shape is outlined by a dotted line. The scale bar represents 1 μm. The two-color graphics show the distribution profiles of RNAP and nucleoid in a population of 100 cells, as described in the **Figure 1** caption.

Oka, 1979) made from PBR322 vector portion. We chose RNAI as a tag for the location of p*rrnB* because RNAI targets the replication region of the plasmid (Davison, 1984). Our results showed that, like RNAP's distribution, the distribution of the plasmid-borne p*rrnB* is sensitive to growth conditions. Under optimal growth conditions, there are primarily two clusters of p*rrnB*, which are located at the cell poles and are colocalized with RNAP foci in the mutants (**Figure 3A**). In contrast, signals of pBR322 from the RNA-FISH are scattered in the Δ6*rrn*/pBR322 cells. In addition, both RNAP foci and p*rrnB*

clusters are absent in the cells of stressed mutants, caused by nutrient downshift, amino acid starvation, and rifampicin treatment (**Figures 3B,C**). We concluded from these results that active rRNA synthesis promotes the clustering of plasmid-borne p*rrnB* in the mutants.

We also determined the relative copy number of the plasmid p*rrnB* compared to a single-copy chromosomal gene (*tdk*) in the Δ6*rrn*/p*rrnB* cells grown in LB at 37°C, and found that, on average, there are 12.0 ± 1.2 copies of p*rrnB* per genome (**Figure 3D**), or about 24 copies of p*rrnB* per cell because most of the cells have two nascent nucleoids per cell as revealed by cell images (**Figure 1**). Thus, it is estimated that each of the two RNAP foci is organized at a p*rrnB* cluster of about 12 copies. This could explain why the RNAP foci appear to be larger in the two mutants than those RNAP foci in wild type, in which each of RNAP foci locates at a cluster of about six rRNA operons (Cagliero et al., 2014). We concluded that in both Δ6*rrn*/p*rrnB* and Δ7*rrn*/p*rrnB* mutants, RNAP foci are located at clusters of plasmid-borne *rrnB* resembling extrachromosomal bacteria nucleolus-like organization.

Colocalization of the Foci of RNAP Foci and NusB That Participate in rRNA Synthesis and Ribosome Biogenesis

In wild type, RNAP foci at the bacterial nucleolus-like structure represent transcription factories for rRNA synthesis and ribosome biogenesis because they co-localize with the foci of NusA and NusB (Cagliero et al., 2014; Jin et al., 2017), two transcription factors involved in those processes (Greenblatt and Li, 1981; Torres et al., 2004; Greive et al., 2005; Stagno et al., 2011; Bubunenko et al., 2013). To determine whether RNAP foci also associated with the Nus factors in both Δ6*rrn*/p*rrnB* and Δ7*rrn*/p*rrnB* mutants, we chose to co-image RNAP with NusB that binds to nascent rRNA for rRNA processing. SIM images revealed that NusB foci are apparent and they are colocalized with RNAP foci at the cell poles in the two mutants (**Figure 4A**). Live-cell imaging using a microfluidic system also confirmed colocalization of the foci of RNAP and NusB at the cell poles (**Figures 4B,C**). These results indicate that, despite differences in spatial locations, the compositions of the extrachromosomal bacteria nucleolus-like organization in the two mutants are likely to be the same as that of the bacterial nucleolus-like structure in wild type (Jin et al., 2017). Because p*rrnB* supports cell growth in the Δ7*rrn*/p*rrnB* mutant, we concluded that transcription factories at the extrachromosomal bacteria nucleolus-like organization are fully functional for rRNA synthesis and ribosome biogenesis.

Long-Range Interaction Between RNAP Foci at Extrachromosomal Nucleolus-Like Organization and the Bacterial Chromosome

Condensed Nucleoids in the Mutants Which Have RNAP Foci Associated With p*rrnB* Clusters

We next addressed questions regarding the effect of RNAP foci at the extrachromosomal nucleolus-like organization on nucleoid organization *in trans* in the Δ6*rrn*/p*rrnB* and Δ7*rrn*/p*rrnB* mutants. In wild type, transcription and the distribution of RNAP link to the organization of the nucleoid (Cabrera and Jin, 2003; Jin and Cabrera, 2006; Jin et al., 2013). We used several approaches to determine whether RNAP foci at the extrachromosomal nucleolus-like structure also influence the organization of the nucleoid in these two mutants. First, we measured relative nucleoid size (RNS) [ratio of size of nucleoid(s) over size of the cell], as previously described (Cabrera et al., 2009). In the control Δ6*rrn*/pBR322 cells in which there is no RNAP foci (**Figure 1**), the nucleoids are expanded (**Figure 5A**) with a mean RNS value of 0.79; the distributions of DNA and RNAP are relatively homogeneous, as indicated by contrast analyses (Cabrera and Jin, 2003) (**Figures 5B,C**). In contrast, in the Δ6*rrn*/p*rrnB* and Δ7*rrn*/p*rrnB* cells, RNAP foci are apparent (**Figure 1**) and the nucleoids are compact with a small RNS value of about 0.56–0.58, and the distributions of DNA and particularly RNAP are highly heterogeneous (**Figures 5B,C**) due to the presence of RNAP foci at the cell poles.

Second, we determined the effects of stresses on the formation of RNAP foci, the organization of extrachromosomal nucleolus-like structure and the nucleoid organization. As described above, cells were stressed when the nutrient downshifted, were starved for amino acid, or were treated with rifampicin. Under those stress conditions, RNAP foci are absent (**Figures 2A,B**) and the nucleoids become expanded with increased values of RNS (**Figure 5A**), and the distributions of DNA and RNAP converted to relatively homogeneous states compared to cells prior to the stresses (**Figures 5B,C**). Because the disappearance of RNAP foci is also associated with the dispersing of the clusters of p*rrnB* in the stressed mutants as described above (**Figures 3B,C**), we concluded that active transcription at the extrachromosomal nucleolus-like structure is required for the nucleoid compaction.

Compacted Nucleoids and Transcription Factories Released From Lysed Mutant Cells

We also examined isolated nucleoids by co-imaging RNAP and DNA from lysed cells of different strains (**Figure 6**). The nucleoids released from the Δ6*rrn nusB-mCherry* /pBR322 cells are expanded with large areas (2D images), and are associated with RNAP and NusB. In contrast, the nucleoids released from the Δ6*rrn nusB-mCherry* /p*rrnB* and Δ7*rrn nusB-mCherry* /p*rrnB* cells lysates are compact with much smaller areas, and are associated with RNAP, but not with NusB, suggesting weak interactions between DNA and NusB. In addition, released RNAP foci from those cells lysates are evident as indicated by having strong RNAP-Venus signals but minimal DNA signals, indicating that RNAP foci associated with the extrachromosomal nucleolus-like structure can be physically separated from the nucleoid. The isolated RNAP foci are also colocalized with the foci of NusB, demonstrating that they are isolated transcription factories for rRNA synthesis and ribosome biogenesis.

Hypercondensed Nucleoid in the Mutant Cells Treated With Chloramphenicol

To provide further evidence that transcription activity of the extrachromosomal nucleolus-like organization drives nucleoid

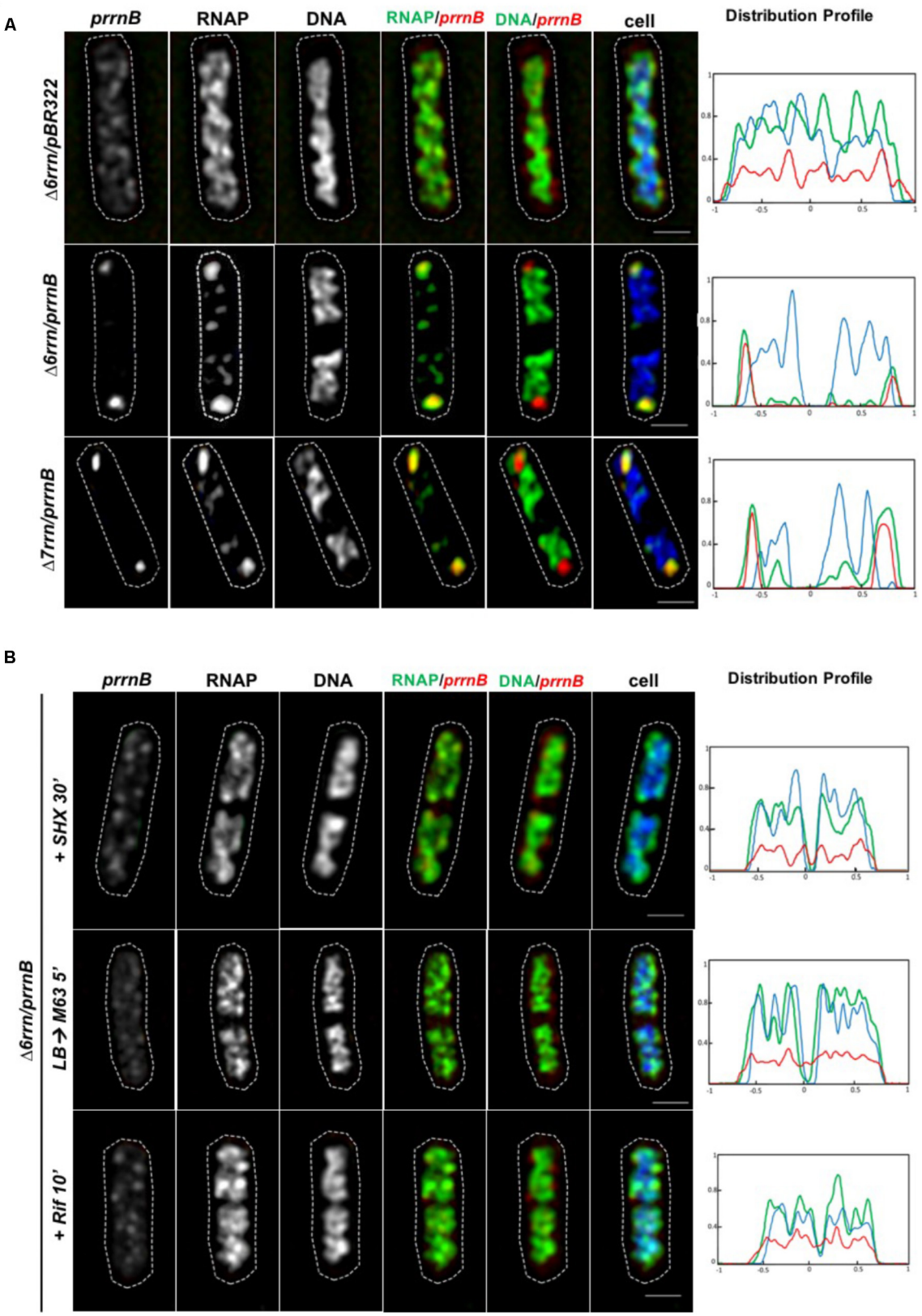

FIGURE 3 | Continued

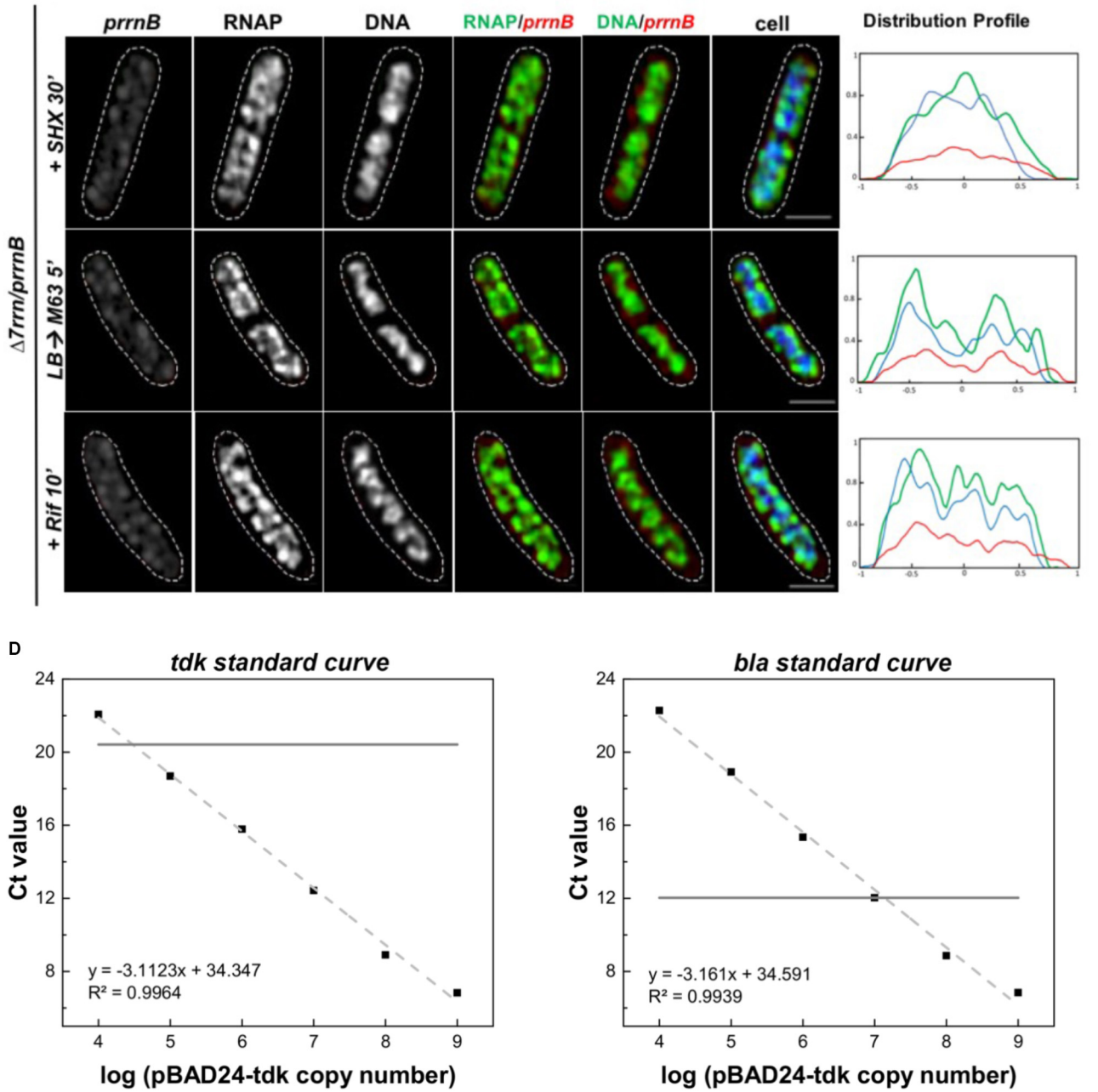

FIGURE 3 | Active transcription of p*rrnB* promotes coordinated organization of RNAP foci and p*rrnB* clusters. **(A–C)** RNA-Fluorescence *in situ* hybridization (FISH). Shown are SIM images of p*rrnB*, RNAP, DNA, two-color overlays of RNAP (green) and p*rrnB* (red), DNA (green) and p*rrnB* (red), and three-color overlays of p*rrnB* (red), RNAP (green) and DNA (blue) from representative single cells during optimal growth (LB) **(A)**, and **(B,C)** after perturbations induced by SHX treatment for 30 min (+SHX 30′), nutrient down shift from LB to minimal medium M63+glucose for 5 min (LB→M63 5′) and after rifampicin treatment for 10 min (+Rif 10′). The distribution of p*rrnB* is determined by RNA-FISH as described in the Section "Materials and Methods." The cell shape is outlined by a dotted line. The scale bar represents 1 μm. The three-color graphics show the distribution profiles of RNAP, nucleoid and p*rrnB* in a population of 100 cells; *Y*-axis is the probability density of the plasmid p*rrnB* (red line), RNAP (green line), nucleoid DNA (blue line) across the cell length (*X*-axis) from one pole (–1) to another pole (+1). Note that p*rrnB* clusters and RNAP foci perfectly colocalize (overall yellow color on the RNAP/p*rrnB* overlay) and are located near the cell poles during optimal growth **(A)**; however, the distributions of both p*rrnB* and RNAP become random without foci and clusters in stressed cells **(B,C)**. **(D)** Plasmid copy number determination by qRT-PCR. A 10-fold serial dilution series of the plasmids pBAD24-*tdk* were used to make the standard curves for the *tdk* and *bla* genes, respectively (dash lines). The pKK3535 plasmid and genome DNA extracted from the strain (Δ6*rrn* and Δ6*rrn*/p*rrnB*) were used by qRT-PCT to determine the *C*t values of *tdk* from genome and *bla* from pKK3535 (solid lines). Based on the differences of the two *C*t values, the copy numbers of pKK3535 relative to genome were calculated, as described in the Section "Materials and Methods."

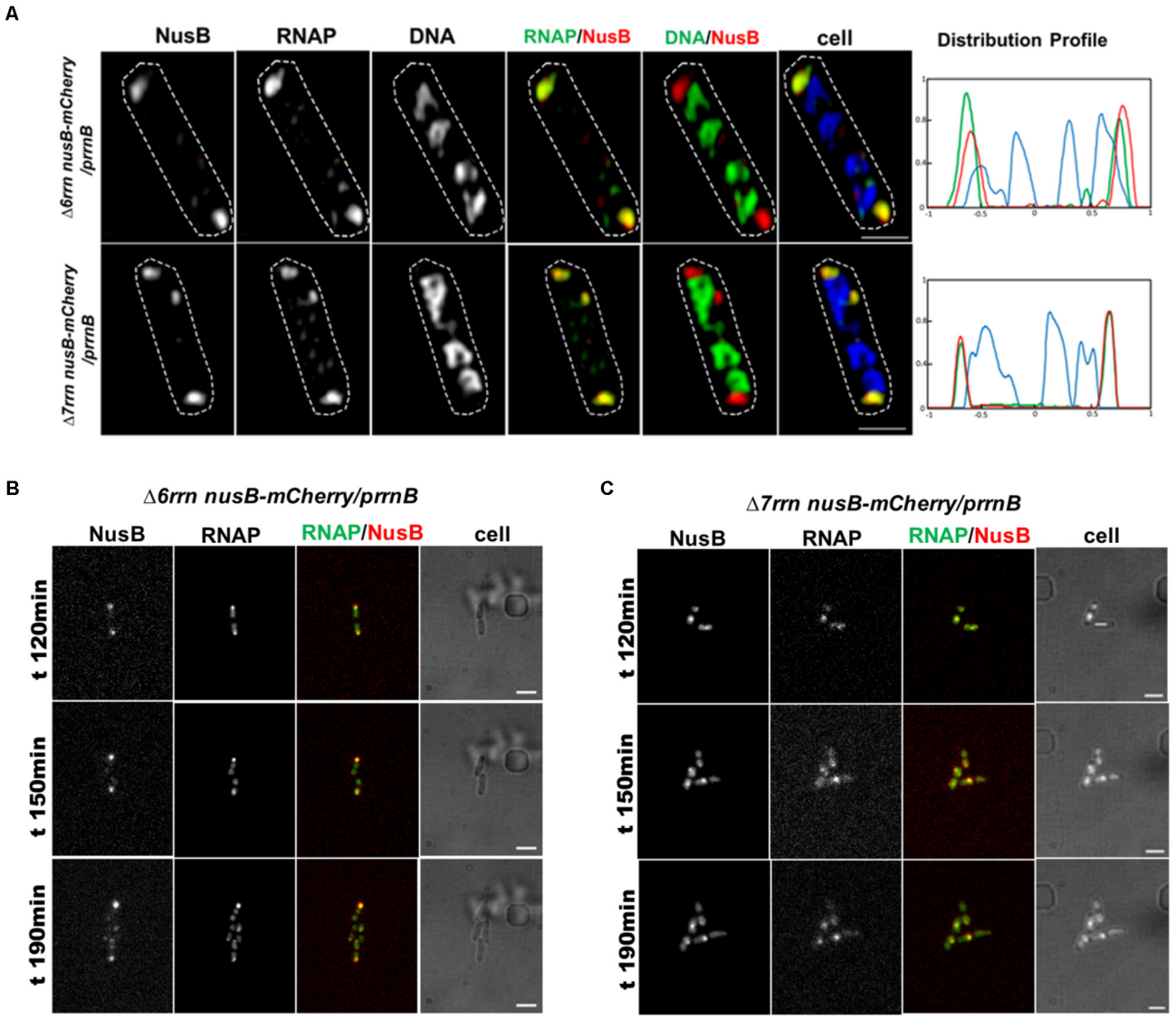

FIGURE 4 | Foci of nascent rRNA-binding protein NusB colocalizes with RNAP foci in the Δ6*rrn*/p*rrnB and* Δ7*rrn*/p*rrnB* mutants containing the chromosomal *nusB-mCherry* fusion **(A)**. Shown are SIM images of NusB, RNAP, DNA, two-color overlays of RNAP (green) and NusB (red), DNA (green) and NusB (red), and three-color overlays of RNAP (green), NusB (red) and DNA (blue) from representative single cells under optimal growth conditions (LB, 37°C). NusB is tagged with m-Cherry fluorescent protein in the two mutant chromosomes. Note that NusB foci are at the cells poles, and the NusB foci signals perfectly colocalize with RNAP foci signals (overall yellow color on the RNAP/NusB overlay). The cell shape is outlined by a dotted line. The scale bar represents 1 μm. The three-color graphics show the distribution profiles of NusB, RNAP and nucleoid in a population of 100 cells; *Y*-axis is the probability density of NusB (red line), RNAPs (green line) and nucleoid (blue line) across the cell length (*X*-axis), as described in the **Figure 1** caption. Live-cells imaging of Δ6*rrn nusB-mCherry*/p*rrnB* **(B)** and Δ7*rrn nusB-mCherry*/p*rrnB* **(C)** using microfluidics confirms that RNAP foci and NusB colocalize at the cell poles in the mutants containing the chromosomal *nusB-mCherry* fusion. Cells were growing in LB using the CellASIC ONIX microfluidic system, as described in the Section "Materials and Methods." Note that RNAP foci and NusB foci are colocalized at the cell poles, and the changes in the cells position and size during the imaging process. The scale bar represents 2 μm.

compaction, we utilized another phenotype of the two mutants after chloramphenicol treatment, which is known to condense nucleoids (van Helvoort et al., 1996; Zimmerman, 2002). It was reported that due to reduced rRNA synthesis, the nucleoid is less condensed after chloramphenicol treatment in the Δ6*rrn* mutant cells compared with wild type (Cabrera et al., 2009). We repeated the experiments with the Δ6*rrn*/pBR322 strain and obtained similar results. We then examined the effect of RNAP foci on the nucleoid compaction in Δ6*rrn*/p*rrnB* and Δ7*rrn*/p*rrnB* after chloramphenicol treatment (**Figure 7**). Our results show that the nucleoids become hyper-condensed after chloramphenicol treatment in the two mutants. This is the same result as wild type but different from Δ6*rrn*/pBR322. For example, image analyses showed that 20 min after the addition of the antibiotic, the RNS value has decreased more than twofold from 0.56 (prior to the treatment) to 0.27 in Δ6*rrn*/p*rrnB* cells. In contrast, in

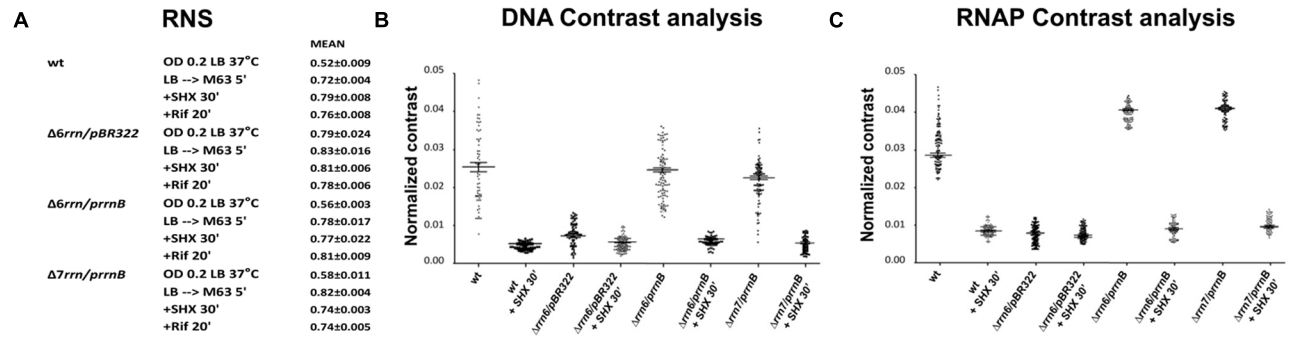

FIGURE 5 | Image analyses of the relative nucleoid size, nucleoid organization, and the distribution of RNAP in different strains under different growth conditions. **(A)** Mean values of relative nucleoid size (RNS) of indicated strains under optimal growth (LB, 37°C) and indicated stressed conditions from a population of 100 cells. RNS was measured as described in the Section "Materials and Methods." Larger values of RNS indicate more expended nucleoids in the cells. **(B)** Normalized contrast parameters of the distributions of DNA signals in indicated strains under different growth conditions. The normalized contrast parameters were measured from 100 nucleoids as described in the Section "Materials and Methods." In this analysis, larger values indicate more heterogeneous distribution of DNA signals with structured features, and are correlated with compact nucleoids. In contrast, smaller values of normalized contrast indicate more homogenous distribution with less structured features, and are correlated with larger values of RNS. **(C)** Normalized contrast parameters of the distributions of RNAP signals in indicated strains under different growth conditions. The normalized contrast parameters were measured from 100 cells as described in the Section "Materials and Methods." In this analysis, larger values of normalized contrast indicate more heterogeneous distributions of the RNAP, which in turn are indicative of the presence of transcription foci. In contrast, smaller values indicate that RNAP is more homogeneously distributed and that there is a lack of RNAP foci.

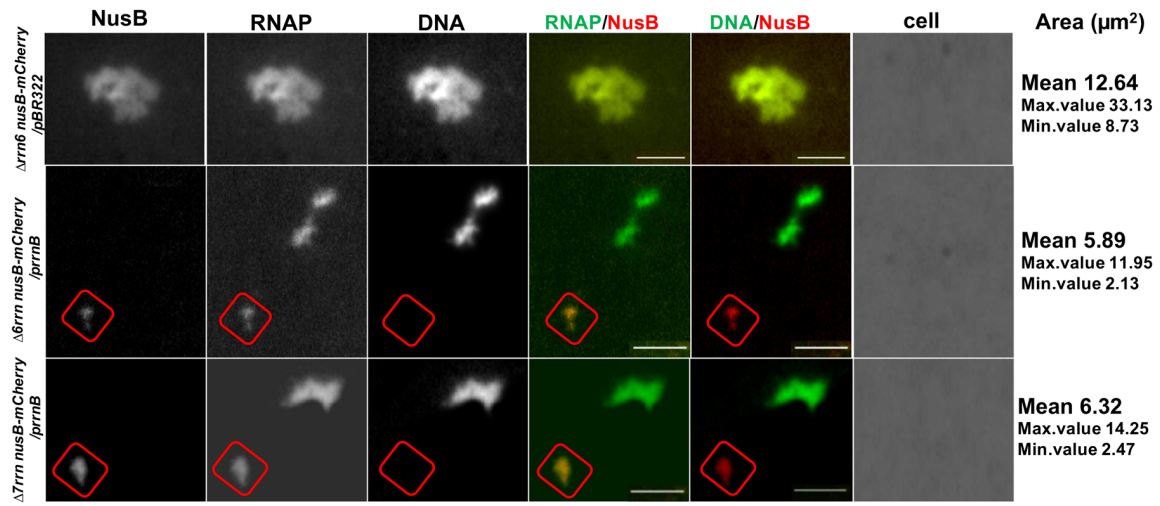

FIGURE 6 | Released nucleoids and transcription factories for rRNA synthesis and ribosome biogenesis from lysed mutant cells. Cells of indicated strains grown in LB at 37°C were lysed followed by coimaging of NusB, RNAP, DNA in released nucleoids, and transcription factories and cells using wide field epifluorescence microscopy, as described in the Section "Materials and Methods." Shown are images of NusB, RNAP, and DNA, and overlays of RNAP (green) and NusB (red) and DNA (green) and NusB (red). No intact cells were visualized because they were completely lysed. Note that there are very low NusB signals in the nucleoid of the Δ6*rrn nusB-mCherry*/p*rrnB* and Δ7*rrn nusB-mCherry*/p*rrnB* cells, in contrast to that in Δ6*rrn nusB-mCherry*/pBR322. The cycles indicated putative transcription factories, which have strong colocalized signals of NusB and RNAP but very low DNA signals, and they are present only in cells harboring the p*rrnB*. The scale bar represents 2 μm. Area mean (μm^2), maximum and minimum values of the areas of 100 isolated nucleoids from different strains are indicated in the last column of the figure. Smaller areas indicate more compact organizations of the nucleoids.

the control Δ6*rrn*/pBR322 cells, the RNS value has reduced only about 1.25-fold from 0.76 (prior to the treatment) to 0.61, 20 min after the treatment, and reduced only about 1.55-fold (0.76 vs. 0.49) 40 min after the addition of chloramphenicol. Similar results were obtained in the Δ7*rrn*/p*rrnB* cells. We concluded that RNAP foci associated with the extrachromosomal nucleolus-like structure *in trans* has a long-range effect in compacting the nucleoid.

There is an intriguing observation indicating that the RNAP–DNA interaction is altered in cells treated with chloramphenicol. We found that, similar to wild type, in both mutants treated with chloramphenicol there are apparent "free" or dissociated RNAP in the cytoplasmic spaces (**Figure 7**). Because RNAP usually binds to DNA strongly, the dissociation of RNAP from the genomic DNA and hyper-condensed nucleoid only reported during osmotic stress (Cagliero and Jin, 2013). It is unlikely

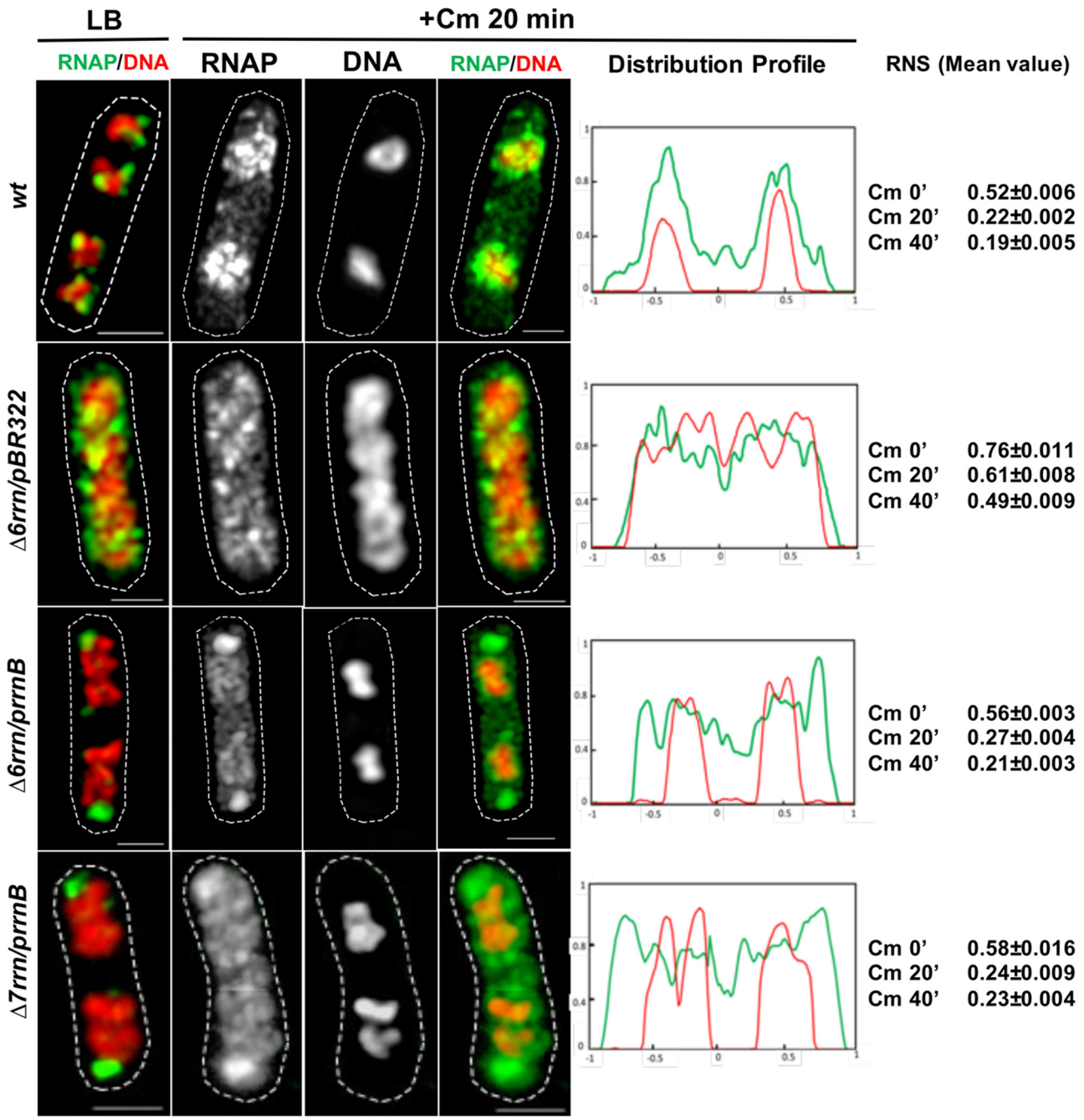

FIGURE 7 | Active transcription of the extrachromosomal nucleolus promotes hyper-condensation of the nucleoids in cells treated with chloramphenicol mimicking wild type (*wt*). Shown are SIM images of indicated cells before and after chloramphenicol treatment. For simplicity, only an overlay RNAP (green) and DNA (red) is shown prior to the antibiotic treatment (LB) because **Figure 1** includes more detailed sets of images. Images of RNAP and DNA and an overlay RNAP (green) and DNA (red) are shown in cells treated with the antibiotic for 20 min. As a control, *wt* is included in the experiments. The cell shape is outlined by a dotted line. The scale bar represents 1 μm. The two-color graphics show the distribution profiles of RNAP (green) and DNA (red) in a population of 100 cells 20 min after the antibiotic treatment, as described in the **Figure 1** caption. Mean values of relative nucleoid size (RNS) in different cells population (100 cells) before, and at 20 and 40 min after chloramphenicol treatment are also shown. Images and image analyses show that, as in *wt*, the nucleoids become hyper-condensed in the Δ6*rrn/prrnB* and Δ7*rrn/prrnB* cells, in contrast, the nucleoids are still relatively expanded in Δ6*rrn/pBR322* after the chloramphenicol treatment.

that the dissociations of RNAP under these two physiological conditions share common mechanisms, and understanding the molecular mechanism whereby RNAP dissociates from the nucleoid after chloramphenicol treatment is beyond the scope of this study. We speculate that the treatment of chloramphenicol causes significant changes in supercoiling states and/or the

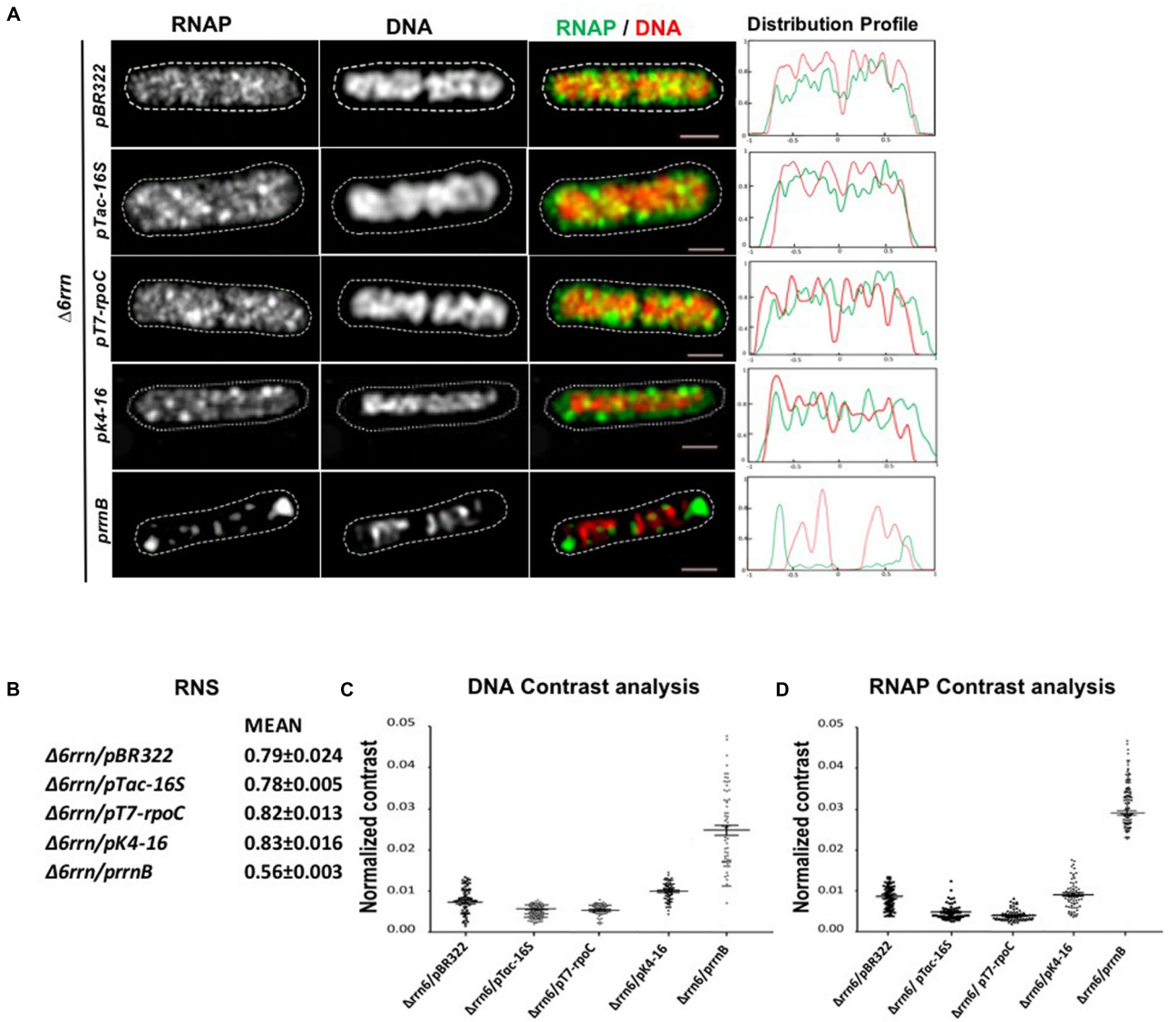

FIGURE 8 | Active transcription at clusters of rRNA operon is essential for the compartmentalization of the extrachromosomal nucleolus-like organization and the nucleoid compaction. **(A)** Shown are SIM images of RNAP, DNA, and an overlay RNAP (green) and DNA (red) in representative single cells harboring different plasmids as indicated during optimal growth (LB, 37°C). Δ6*rrn/pBR322* and Δ6*rrn/prrnB* are included as controls. RNAP is tagged with yellow Venus fluorescent protein (*rpoC*-venus) and DNA is stained with Hoechst 33342, as described in the Section "Materials and Methods." Note that the defects in the Δ6*rrn* strain in the organization of RNAP foci and nucleoid structure cannot be complemented by a low copy plasmid-borne rrnB (*pK4-16*), nor by others two plasmids carrying strong promoters (pTac-16S and *pT7-rpoC*). The cell shape is outlined by a dotted line. The scale bar represents 1 μm. The two-color graphics show the distribution profiles of RNAP and nucleoid in a population of 100 cells, as described in the **Figure 1** caption. **(B–D)** Image analyses of the relative nucleoid size, nucleoid organization, and the distribution of RNAP. **(B)** Mean values of relative nucleoid size (RNS). **(C)** Normalized contrast parameters of the distributions of DNA. **(D)** Normalized contrast parameters of the distributions of RNAP signals in indicated strains. The normalized contrast parameters were measured from 100 cells as described in the Section "Materials and Methods" and in the **Figure 5** caption.

organization of the nucleoid, reducing the binding of RNAP released after completing transcription.

Active Transcription at Clusters of rRNA Operon Is Essential for the Formation of RNAP Foci and Nucleoid Compaction in the Mutants

To determine whether active transcription from other strong promoters in multicopy plasmids also lead to RNAP foci formation, we examined the effects of pTac-16S and pT7-*rpoC* in Δ6*rrn* cells, and found that they behaved similarly to Δ6*rrn*/pBR322 cells in the distribution of RNAP and the nucleoid structure (**Figure 8**). To determine whether active transcription of *rrnB* from a low copy number plasmid has similar effects as multicopy p*rrnB*, we co-imaged RNAP and DNA in Δ6*rrn*/pK4-16. The plasmid pK4-16 contains *rrnB* in the pSC101 vector that has 3–4 copies in a log phase cell (Lutz and Bujard, 1997). The

results showed in contrast to Δ6*rrn*/p*rrnB*, there are only small changes in the distribution of RNAP and the nucleoid structure in Δ6*rrn*/pK4-16 compared to Δ6*rrn*/pBR322 (**Figure 8**). From these results, we concluded that active transcription at clusters of rRNA operon is essential for the compartmentalization of the extrachromosomal nucleolus-like organization and the nucleoid compaction.

DISCUSSION

In this report, we determined the structure and function of the extrachromosomal bacterial nucleolus-like organization from plasmid-borne p*rrnB* in the Δ6*rrn*/p*rrnB* and Δ7*rrn*/p*rrnB* strains. Our study demonstrates that there are many similarities between RNAP foci at clusters of p*rrnB* and their counterparts at clusters of chromosomal rRNA operons. The results from the *rrn* deletion strains harboring p*rrnB* have implications for the formation of bacterial nucleolus-like organization from clustering of the rRNA operon in wild-type *E. coli* cells. This study also suggests that active transcription at transcription factories for rRNA synthesis and ribosome biogenesis is a nucleoid compaction force.

The Transcription Machineries at Chromosomal *rrn* Clusters and at Extrachromosomal p*rrnB* Clusters Share Striking Similarities

There are many parallels in these two systems. First, they have similar compositions. In the Δ6*rrn*/p*rrnB* and Δ7*rrn*/p*rrnB* mutants, RNAP foci co-localize with NusB foci (**Figure 4A**) and function as transcription factories during optimal growth, just like in wild type. In addition to NusA and NusB, there may be other components (both protein and nucleic acids), because transcription factories are likely to be macro-structures containing multiple components. It is proposed that the organization of such macro-structures is entropy-driven (Marenduzzo et al., 2006). Putative transcription factories, which can be separated from the nucleoid, are evident from lysed cells of the two mutants (**Figure 6**). Thus, the mutant can be used as a useful system in the isolation and the identification of the components of transcription factories. Second, they have similar responses to environmental cues. The formation/organization of RNAP foci and p*rrnB* clusters are concurrent and colocalized under optimal growth conditions. However, in nutrient-poor minimal medium and stressed conditions, both RNAP and p*rrnB* are dispersed in the nucleoid (**Figure 3B**). Third, they are fully functional for rRNA synthesis and ribosome biogenesis. Note that in the Δ7*rrn*/p*rrnB* mutant, p*rrnB* is the only source for those functions to support cell growth; it is lethal for Δ7*rrn* in the absence of p*rrnB*.

In addition, transcription factories in both wild type and the Δ6*rrn*/p*rrnB* and Δ7*rrn*/p*rrnB* mutants are spatially compartmentalized at the edge of the nucleoid; however, they are predominantly located toward the cell poles in the mutants. We do not know why the cell poles are the preferred location for transcription factories in these mutants. Considering that the p*rrnB* clusters (on average 12 copies) are larger than the chromosomal *rrn* clusters (on average 6 copies), we speculate that there is more cytoplasmic space in the cell poles of these mutants that can accommodate the macro-structure of multiple components and avoid collision with the nucleoids. Larger chemoreceptor and other complexes are located in the cell poles (Maddock and Shapiro, 1993; Lybarger et al., 2005; Laloux and Jacobs-Wagner, 2014; Draper and Liphardt, 2017).

Active Transcription Is Essential for rRNA Operons Clustering

Our results show that the formation and the organization of both RNAP foci and p*rrnB* clusters are sensitive to growth medium and conditions (**Figure 3B**). RNAP foci and p*rrnB* clusters are evident during optimal growth conditions; however, the distributions of both RNAP and p*rrnB* become random during nutrient downshift and stresses. We conclude from these results that active transcription of rRNA operons is essential for the clustering or assembling of p*rrnB*. In support of this conclusion, it has been reported that active transcription from a constitutive promoter is a driving force in assembling a relatively low copy plasmid (Sanchez-Romero et al., 2012). We further suggest that the same principle also applies to assembling and disassembling of chromosomal *rrn* clusters in response to growth medium and conditions in wild-type cells. Recently it was reported that colocalization of different chromosomal rRNA operons occurred with and without active transcription using epifluorescence microscopy and in living cells (Gaal et al., 2016). However, it has been demonstrated that live-cell imaging protocols, such as those used by Gaal et al. (2016), induce stress response and cause changes in the organization of the nucleoid (Cabrera and Jin, 2003; Jin et al., 2015). In addition, because *E. coli* cells are small it is essential to study the colocalization with superresolution microscopy. Thus, it remains to be determined whether different chromosomal rRNA operons are spatially in proximity under different growth conditions.

Active Transcription at the Bacterial Nucleolus-Like Organization Is a Driving Force in Nucleoid Compaction?

In the absence of multicopy p*rrnB*, or in the presence of low copy plasmid-borne *rrnB*, the nucleoids are uncompacted in the Δ6*rrn* mutant host cells (**Figure 8**). However, when p*rrnB* is supplemented *in trans*, formations of RNAP foci and clusters of p*rrnB* condense the nucleoids in the Δ6*rrn*/p*rrnB* and Δ7*rrn*/p*rrnB* mutants during optimal growth conditions, demonstrating that active transcription at the extrachromosomal nucleolus-like organization is essential for nucleoid compaction. The structure of the nucleoid is proposed to be determined by a balance of expansion and compaction forces (Woldringh et al., 1995). Our study suggests that active transcription at extrachromosomal nucleolus-like organization is a nucleoid compaction force; however, how this force drives nucleoid compaction remains to be determined.

Because of the similarities between the organizations of transcription factories at extrachromosomal p*rrnB* clusters and at chromosomal *rrn* clusters, as detailed above, we argue that the two systems play a similar role in the condensation of the nucleoid in the cell. We speculate that active transcription of transcription factories not only for rRNA synthesis and ribosome biogenesis from clusters of rRNA operons but also for the expression of other growth genes at various locations in the genome through long-range interactions between bacterial nucleolus-like organization and the chromosome (Jin et al., 2017). RNAP is mobile (Bakshi et al., 2012; Endesfelder et al., 2013; Stracy et al., 2015) in transcription factories, and thus able to capture promoters of other growth genes in the genome. Active transcription of transcription factories induces supercoiling. DNA loops and supercoiling (Liu and Wang, 1987; Postow et al., 2004; Booker et al., 2010) could facilitate those long-range interactions, leading to nucleoid compaction. Recently, bacterial condensin has been shown to bind to multiple sites in rDNAs and other regions of the genome (Yano and Niki, 2017), which could provide another means for long-range interaction. In the future, identification and characterization of the components of transcription factories mentioned above will shed light on the mechanism of nucleoid compaction in the cell.

AUTHOR CONTRIBUTIONS

All authors designed the experiments, discussed the results, and contributed to the final manuscript. CM, ZS, and YZ performed the experiments and analyzed the data. CM and DJ wrote the manuscript.

FUNDING

This research was supported by the Intramural Research Program of the NIH, National Cancer Institute, Center for Cancer Research.

ACKNOWLEDGMENTS

The authors acknowledge the support from the NCI, CCR Core Facility (Optical Microscopy and Analysis Laboratory) for the SIM imaging system. They also thank Selwyn Quan and Catherine Squires for the *rrn* deletion strains, and Cedric Cagliero for discussions.

REFERENCES

Anindyajati, Anindyajati, A. A., Riani, C., and Retnoningrum, D. S. (2016). Plasmid copy number determination by quantitative polymerase chain reaction. *Sci. Pharm.* 84, 89–101. doi: 10.3797/scipharm.ISP.2015.02

Bakshi, S., Siryaporn, A., Goulian, M., and Weisshaar, J. C. (2012). Superresolution imaging of ribosomes and RNA polymerase in live *Escherichia coli* cells. *Mol. Microbiol.* 85, 21–38. doi: 10.1111/j.1365-2958.2012.08081.x

Bolivar, F., Rodriguez, R. L., Betlach, M. C., and Boyer, H. W. (1977). Construction and characterization of new cloning vehicles. I. Ampicillin-resistant derivatives of the plasmid pMB9. *Gene* 2, 75–93. doi: 10.1016/0378-1119(77)90074-9

Booker, B. M., Deng, S., and Higgins, N. P. (2010). DNA topology of highly transcribed operons in *Salmonella enterica* serovar Typhimurium. *Mol. Microbiol.* 78, 1348–1364. doi: 10.1111/j.1365-2958.2010.07394.x

Bubunenko, M., Court, D. L., Al Refaii, A., Saxena, S., Korepanov, A., Friedman, D. I., et al. (2013). Nus transcription elongation factors and RNase III modulate small ribosome subunit biogenesis in *Escherichia coli*. *Mol. Microbiol.* 87, 382–393. doi: 10.1111/mmi.12105

Cabrera, J. E., Cagliero, C., Quan, S., Squires, C. L., and Jin, D. J. (2009). Active transcription of rRNA operons condenses the nucleoid in *Escherichia coli*: examining the effect of transcription on nucleoid structure in the absence of transertion. *J. Bacteriol.* 191, 4180–4185. doi: 10.1128/JB.01707-08

Cabrera, J. E., and Jin, D. J. (2006). Active transcription of rRNA operons is a driving force for the distribution of RNA polymerase in bacteria: effect of extrachromosomal copies of *rrnB* on the in vivo localization of RNA polymerase. *J. Bacteriol.* 188, 4007–4014. doi: 10.1128/JB.01893-05

Cabrera, J. E., and Jin, D. J. (2003). The distribution of RNA polymerase in *Escherichia coli* is dynamic and sensitive to environmental cues. *Mol. Microbiol.* 50, 1493–1505. doi: 10.1046/j.1365-2958.2003.03805.x

Cagliero, C., and Jin, D. J. (2013). Dissociation and re-association of RNA polymerase with DNA during osmotic stress response in *Escherichia coli*. *Nucleic Acids Res.* 41, 315–326. doi: 10.1093/nar/gks988

Cagliero, C., Zhou, Y. N., and Jin, D. J. (2014). Spatial organization of transcription machinery and its segregation from the replisome in fast-growing bacterial cells. *Nucleic Acids Res.* 42, 13696–13705. doi: 10.1093/nar/gku1103

Cashel, M., Gentry, D. R., Hernandez, V. J., and Vinella, D. (1996). "The stringent response," in *Escherichia coli and Salmonella: Cellular and Molecular Biology*, ed. F. C. Neidhardt (Washington, DC: American Society for Microbiology), 1458–1496.

Condon, C., French, S., Squires, C., and Squires, C. L. (1993). Depletion of functional ribosomal RNA operons in *Escherichia coli* causes increased expression of the remaining intact copies. *EMBO J.* 12, 4305–4315.

Condon, C., Liveris, D., Squires, C., Schwartz, I., and Squires, C. L. (1995). rRNA operon multiplicity in *Escherichia coli* and the physiological implications of rrn inactivation. *J. Bacteriol.* 177, 4152–4156. doi: 10.1128/jb.177.14.4152-4156.1995

Cook, P. R. (2010). A model for all genomes: the role of transcription factories. *J. Mol. Biol.* 395, 1–10. doi: 10.1016/j.jmb.2009.10.031

Datsenko, K. A., and Wanner, B. L. (2000). One-step inactivation of chromosomal genes in *Escherichia coli* K-12 using PCR products. *Proc. Natl. Acad. Sci. U.S.A.* 97, 6640–6645. doi: 10.1073/pnas.120163297

Davison, J. (1984). Mechanism of control of DNA replication and incompatibility in ColE1-type plasmids–a review. *Gene* 28, 1–15. doi: 10.1016/0378-1119(84)90082-9

Draper, W., and Liphardt, J. (2017). Origins of chemoreceptor curvature sorting in *Escherichia coli*. *Nat. Commun.* 8:14838. doi: 10.1038/ncomms14838

Durfee, T., Hansen, A. M., Zhi, H., Blattner, F. R., and Jin, D. J. (2008). Transcription profiling of the stringent response in *Escherichia coli*. *J. Bacteriol.* 190, 1084–1096. doi: 10.1128/JB.01092-07

Endesfelder, U., Finan, K., Holden, S. J., Cook, P. R., Kapanidis, A. N., and Heilemann, M. (2013). Multiscale spatial organization of RNA polymerase in *Escherichia coli*. *Biophys. J.* 105, 172–181. doi: 10.1016/j.bpj.2013.05.048

French, S. L., and Miller, O. L. Jr. (1989). Transcription mapping of the *Escherichia coli* chromosome by electron microscopy. *J. Bacteriol.* 171, 4207–4216. doi: 10.1128/jb.171.8.4207-4216.1989

Gaal, T., Bratton, B. P., Sanchez-Vazquez, P., Sliwicki, A., Sliwicki, K., Vegel, A., et al. (2016). Colocalization of distant chromosomal loci in space in *E. coli*: a bacterial nucleolus. *Genes Dev.* 30, 2272–2285. doi: 10.1101/gad.290312.116

Greenblatt, J., and Li, J. (1981). Interaction of the sigma factor and the *nusA* gene protein of *E. coli* with RNA polymerase in the initiation-termination cycle of transcription. *Cell* 24, 421–428. doi: 10.1016/0092-8674(81)90332-9

Greive, S. J., Lins, A. F., and von Hippel, P. H. (2005). Assembly of an RNA-protein complex. Binding of NusB and NusE (S10) proteins to boxA RNA nucleates the formation of the antitermination complex involved in controlling

rRNA transcription in *Escherichia coli*. *J. Biol. Chem.* 280, 36397–36408. doi: 10.1074/jbc.M507146200

Jin, D. J., and Cabrera, J. E. (2006). Coupling the distribution of RNA polymerase to global gene regulation and the dynamic structure of the bacterial nucleoid in *Escherichia coli*. *J. Struct. Biol.* 156, 284–291. doi: 10.1016/j.jsb.2006.07.005

Jin, D. J., Cagliero, C., Izard, J., Martin, C. M., and Zhou, Y. N. (2016). "The distribution and spatial organization of RNA polymerase in *Escherichia coli*: growth rate regulation and stress responses," in *Stress and Environmental Regulation of Gene Expression and Adaptation in Bacteria*, Vol. 2, ed. F. J. d. Bruijn (Hoboken, NJ: Wiley).

Jin, D. J., Cagliero, C., Martin, C. M., Izard, J., and Zhou, Y. N. (2015). The dynamic nature and territory of transcriptional machinery in the bacterial chromosome. *Front. Microbiol.* 6:497. doi: 10.3389/fmicb.2015.00497

Jin, D. J., Cagliero, C., and Zhou, Y. N. (2012). Growth rate regulation in *Escherichia coli*. *FEMS Microbiol. Rev.* 36, 269–287. doi: 10.1111/j.1574-6976.2011.00279.x

Jin, D. J., Cagliero, C., and Zhou, Y. N. (2013). Role of RNA polymerase and transcription in the organization of the bacterial nucleoid. *Chem. Rev.* 113, 8662–8682. doi: 10.1021/cr4001429

Jin, D. J., Mata Martin, C., Sun, Z., Cagliero, C., and Zhou, Y. N. (2017). Nucleolus-like compartmentalization of the transcription machinery in fast-growing bacterial cells. *Crit. Rev. Biochem. Mol. Biol.* 52, 96–106. doi: 10.1080/10409238.2016.1269717

Kashlev, M., Martin, E., Polyakov, A., Severinov, K., Nikiforov, V., and Goldfarb, A. (1993). Histidine-tagged RNA polymerase: dissection of the transcription cycle using immobilized enzyme. *Gene* 130, 9–14. doi: 10.1016/0378-1119(93)90340-9

Kingston, R. E., Gutell, R. R., Taylor, A. R., and Chamberlin, M. J. (1981). Transcriptional mapping of plasmid pKK3535. Quantitation of the effect of guanosine tetraphosphate on binding to the rrnB promoters and a lambda promoter with sequence homologies in the CII binding region. *J. Mol. Biol.* 146, 433–449. doi: 10.1016/0022-2836(81)90041-3

Kjeldgaard, N. O., Maaloe, O., and Schaechter, M. (1958). The transition between different physiological states during balanced growth of *Salmonella* typhimurium. *J. Gen. Microbiol.* 19, 607–616. doi: 10.1099/00221287-19-3-607

Laloux, G., and Jacobs-Wagner, C. (2014). How do bacteria localize proteins to the cell pole? *J. Cell Sci.* 127, 11–19. doi: 10.1242/jcs.138628

Lee, C., Kim, J., Shin, S. G., and Hwang, S. (2006). Absolute and relative QPCR quantification of plasmid copy number in *Escherichia coli*. *J. Biotechnol.* 123, 273–280. doi: 10.1016/j.jbiotec.2005.11.014

Lewis, P. J., Thaker, S. D., and Errington, J. (2000). Compartmentalization of transcription and translation in *Bacillus subtilis*. *EMBO J.* 19, 710–718. doi: 10.1093/emboj/19.4.710

Liu, L. F., and Wang, J. C. (1987). Supercoiling of the DNA template during transcription. *Proc. Natl. Acad. Sci. U.S.A.* 84, 7024–7027. doi: 10.1073/pnas.84.20.7024

Lutz, R., and Bujard, H. (1997). Independent and tight regulation of transcriptional units in *Escherichia coli* via the LacR/O, the TetR/O and AraC/I1-I2 regulatory elements. *Nucleic Acids Res.* 25, 1203–1210. doi: 10.1093/nar/25.6.1203

Lybarger, S. R., Nair, U., Lilly, A. A., Hazelbauer, G. L., and Maddock, J. R. (2005). Clustering requires modified methyl-accepting sites in low-abundance but not high-abundance chemoreceptors of *Escherichia coli*. *Mol. Microbiol.* 56, 1078–1086. doi: 10.1111/j.1365-2958.2005.04593.x

Maddock, J. R., and Shapiro, L. (1993). Polar location of the chemoreceptor complex in the *Escherichia coli* cell. *Science* 259, 1717–1723. doi: 10.1126/science.8456299

Marenduzzo, D., Micheletti, C., and Cook, P. R. (2006). Entropy-driven genome organization. *Biophys. J.* 90, 3712-3721. Epub 2006 Feb 3724. doi: 10.1529/biophysj.105.077685

Mata Martin, C., Cagliero, C., Zhe, S., Chen, D., and Jin, D. J. (2018). *Imaging of transcription and replication in the bacterial chromosome with multicolor three-dimensional superresolution structure illumination microscopy. Bacterial Chormatin: Methods and Protocols*. Springer.

Miller, J. H. (1972). *Experiments in Molecular Genetics*. Plainview, NY: Cold Spring Harbor Laboratory Press.

Morita, M., and Oka, A. (1979). The structure of a transcriptional unit on colicin E1 plasmid. *Eur. J. Biochem.* 97, 435–443. doi: 10.1111/j.1432-1033.1979.tb13131.x

Nielsen, H. J., Youngren, B., Hansen, F. G., and Austin, S. (2007). Dynamics of *Escherichia coli* chromosome segregation during multifork replication. *J. Bacteriol.* 189, 8660–8666. doi: 10.1128/JB.01212-07

Norris, V., den Blaauwen, T., Cabin-Flaman, A., Doi, R. H., Harshey, R., Janniere, L., et al. (2007). Functional taxonomy of bacterial hyperstructures. *Microbiol. Mol. Biol. Rev.* 71, 230–253. doi: 10.1128/MMBR.00035-06

Papantonis, A., and Cook, P. R. (2013). Transcription factories: genome organization and gene regulation. *Chem. Rev.* 113, 8683–8705. doi: 10.1021/cr300513p

Postow, L., Hardy, C. D., Arsuaga, J., and Cozzarelli, N. R. (2004). Topological domain structure of the *Escherichia coli* chromosome. *Genes Dev.* 18, 1766–1779. doi: 10.1101/gad.1207504

Quan, S., Skovgaard, O., McLaughlin, R. E., Buurman, E. T., and Squires, C. L. (2015). Markerless *Escherichia coli rrn* deletion strains for genetic determination of ribosomal binding sites. *G3 (Bethesda)* 5, 2555–2557. doi: 10.1534/g3.115.022301

Raj, A., and Tyagi, S. (2010). Detection of individual endogenous RNA transcripts *in situ* using multiple singly labeled probes. *Methods Enzymol.* 472, 365–386. doi: 10.1016/S0076-6879(10)72004-8

Raj, A., van den Bogaard, P., Rifkin, S. A., van Oudenaarden, A., and Tyagi, S. (2008). Imaging individual mrna molecules using multiple singly labeled probes. *Nat. Methods* 5, 877–879. doi: 10.1038/nmeth.1253

Sanchez-Romero, M. A., Lee, D. J., Sanchez-Moran, E., and Busby, S. J. (2012). Location and dynamics of an active promoter in *Escherichia coli* K-12. *Biochem. J.* 441, 481–485. doi: 10.1042/BJ20111258

Schaechter, M., Maaloe, O., and Kjeldgaard, N. O. (1958). Dependency on medium and temperature of cell size and chemical composition during balanced grown of *Salmonella* typhimurium. *J. Gen. Microbiol.* 19, 592–606. doi: 10.1099/00221287-19-3-592

Skinner, S. O., Sepulveda, L. A., Xu, H., and Golding, I. (2013). Measuring mRNA copy number in individual *Escherichia coli* cells using single-molecule fluorescent in situ hybridization. *Nat. Protoc.* 8, 1100–1113. doi: 10.1038/nprot.2013.066

Stagno, J. R., Altieri, A. S., Bubunenko, M., Tarasov, S. G., Li, J., Court, D. L., et al. (2011). Structural basis for RNA recognition by NusB and NusE in the initiation of transcription antitermination. *Nucleic Acids Res.* 39, 7803–7815. doi: 10.1093/nar/gkr418

Stracy, M., Lesterlin, C., Garza de Leon, F., Uphoff, S., Zawadzki, P., and Kapanidis, A. N. (2015). Live-cell superresolution microscopy reveals the organization of RNA polymerase in the bacterial nucleoid. *Proc. Natl. Acad. Sci. U.S.A.* 112, E4390–E4399. doi: 10.1073/pnas.1507592112

Torres, M., Balada, J. M., Zellars, M., Squires, C., and Squires, C. L. (2004). In vivo effect of NusB and NusG on rRNA transcription antitermination. *J. Bacteriol.* 186, 1304–1310. doi: 10.1128/JB.186.5.1304-1310.2004

van Helvoort, J. M., Kool, J., and Woldringh, C. L. (1996). Chloramphenicol causes fusion of separated nucleoids in *Escherichia coli* K-12 cells and filaments. *J. Bacteriol.* 178, 4289–4293. doi: 10.1128/jb.178.14.4289-4293.1996

Woldringh, C. L., Jensen, P. R., and Westerhoff, H. V. (1995). Structure and partitioning of bacterial DNA: determined by a balance of compaction and expansion forces? *FEMS Microbiol. Lett.* 131, 235–242. doi: 10.1111/j.1574-6968.1995.tb07782.x

Yano, K., and Niki, H. (2017). Multiple *cis*-Acting rDNAs contribute to nucleoid separation and recruit the bacterial condensin Smc-ScpAB. *Cell Rep.* 21, 1347–1360. doi: 10.1016/j.celrep.2017.10.014

Zimmerman, S. B. (2002). Toroidal nucleoids in *Escherichia coli* exposed to chloramphenicol. *J. Struct. Biol.* 138, 199–206. doi: 10.1016/S1047-8477(02)00036-9

Conflict of Interest Statement: The authors declare that the research was conducted in the absence of any commercial or financial relationships that could be construed as a potential conflict of interest.

frontiers in Microbiology

REVIEW
published: 21 December 2017
doi: 10.3389/fmicb.2017.02496

The DnaA Cycle in *Escherichia coli*: Activation, Function and Inactivation of the Initiator Protein

Tsutomu Katayama, Kazutoshi Kasho and Hironori Kawakami*

Department of Molecular Biology, Graduate School of Pharmaceutical Sciences, Kyushu University, Fukuoka, Japan

This review summarizes the mechanisms of the initiator protein DnaA in replication initiation and its regulation in *Escherichia coli*. The chromosomal origin (*oriC*) DNA is unwound by the replication initiation complex to allow loading of DnaB helicases and replisome formation. The initiation complex consists of the DnaA protein, DnaA-initiator-associating protein DiaA, integration host factor (IHF), and *oriC*, which contains a duplex-unwinding element (DUE) and a DnaA-oligomerization region (DOR) containing DnaA-binding sites (DnaA boxes) and a single IHF-binding site that induces sharp DNA bending. DiaA binds to DnaA and stimulates DnaA assembly at the DOR. DnaA binds tightly to ATP and ADP. ATP-DnaA constructs functionally different sub-complexes at DOR, and the DUE-proximal DnaA sub-complex contains IHF and promotes DUE unwinding. The first part of this review presents the structures and mechanisms of *oriC*-DnaA complexes involved in the regulation of replication initiation. During the cell cycle, the level of ATP-DnaA level, the active form for initiation, is strictly regulated by multiple systems, resulting in timely replication initiation. After initiation, regulatory inactivation of DnaA (RIDA) intervenes to reduce ATP-DnaA level by hydrolyzing the DnaA-bound ATP to ADP to yield ADP-DnaA, the inactive form. RIDA involves the binding of the DNA polymerase clamp on newly synthesized DNA to the DnaA-inactivator Hda protein. In *datA*-dependent DnaA-ATP hydrolysis (DDAH), binding of IHF at the chromosomal locus *datA*, which contains a cluster of DnaA boxes, results in further hydrolysis of DnaA-bound ATP. SeqA protein inhibits untimely initiation at *oriC* by binding to newly synthesized *oriC* DNA and represses *dnaA* transcription in a cell cycle dependent manner. To reinitiate DNA replication, ADP-DnaA forms oligomers at DnaA-reactivating sequences (*DARS1* and *DARS2*), resulting in the dissociation of ADP and the release of nucleotide-free apo-DnaA, which then binds ATP to regenerate ATP-DnaA. *In vivo*, *DARS2* plays an important role in this process and its activation is regulated by timely binding of IHF to *DARS2* in the cell cycle. Chromosomal locations of *DARS* sites are optimized for the strict regulation for timely replication initiation. The last part of this review describes how DDAH and DARS regulate DnaA activity.

Keywords: DnaA, *oriC*, *DARS*, *datA*, chromosome replication

OPEN ACCESS

Edited by:
Ariel Amir,
Harvard University, United States

Reviewed by:
James Aaron Kraemer,
Massachusetts Institute of Technology, United States
Kirsten Skarstad,
Oslo University Hospital, Norway

****Correspondence:***
Tsutomu Katayama
katayama@phar.kyushu-u.ac.jp

Specialty section:
This article was submitted to Microbial Physiology and Metabolism, a section of the journal Frontiers in Microbiology

Received: *18 October 2017*
Accepted: *30 November 2017*
Published: *21 December 2017*

Citation:
Katayama T, Kasho K and Kawakami H (2017) The DnaA Cycle in Escherichia coli: Activation, Function and Inactivation of the Initiator Protein. Front. Microbiol. 8:2496. doi: 10.3389/fmicb.2017.02496

INTRODUCTION

The genome of *Escherichia coli* consists of a single circular 4.6 Mb chromosome, with a unique replication origin called *oriC*. Replication initiation at *oriC* results in construction of a pair of replisomes, which migrate bi-directionally to replicate the entire chromosome. Replication initiation at *oriC* is regulated to occur only once during each cell cycle, and the timing of initiation is coordinated with the cellular growth rate. Even when cells grow rapidly and the copy number of *oriC* increases to more than two per cell, initiation occurs at sister *oriC* regions simultaneously only once at a specific time during the cell cycle. As such, the time of initiation at *oriC* is regulated and re-initiation during the same cell cycle is strictly repressed (Skarstad and Katayama, 2013; Wolański et al., 2015; Riber et al., 2016).

The 245 bp minimal *oriC* region has multiple binding sites for the chromosomal replication initiator protein DnaA (DnaA boxes), and a single binding site for the integration host factor (IHF), in addition to an AT-rich duplex-unwinding element (DUE) (**Figures 1A**, **2A**; Kaguni, 2011; Leonard and Grimwade, 2015; Wolański et al., 2015; Shimizu et al., 2016). The 9-mer DnaA box consensus sequence is 5′-TTATnCACA-3′. DnaA-initiator-associating protein DiaA is a DnaA-binding protein that stimulates ATP-bound DnaA (ATP-DnaA) assembly on *oriC*, and that is required for timely replication initiation (Ishida et al., 2004; Keyamura et al., 2007). Binding of IHF to DNA causes a sharp (120–180°) bend in the double helix (Swinger and Rice, 2004). A complex consisting of *oriC*, IHF, DiaA, and oligomeric ATP-DnaA is considered to make up the initiation complex in *E. coli* (Keyamura et al., 2007, 2009). This complex unwinds the *oriC* DUE, enabling loading of DnaB helicases onto single-stranded DNA (ssDNA) by specific protein–protein interactions and dissociations, which in turn leads to formation of replisomes (for a review, see Bell and Kaguni, 2013).

Multiple negative and positive regulatory systems target the *oriC*, the *dnaA* gene, and DnaA and work harmoniously to ensure that initiation occurs in a timely manner, in some cases via negative feedback from DNA replication. As for *oriC*, the minimal region contains 11 sites with 5′-GATC-3′ sequences that are specific targets of DNA adenine methylase (Dam) (Waldminghaus and Skarstad, 2009). As GATC is palindromic in duplex DNA, A residues in both strands can be methylated. In newly replicated DNA, only the sites on the parental strand are methylated, whereas those on the daughter strand are unmethylated. The hemimethylated state of *oriC* persists for ∼10 min in cells with a doubling time of 30 min depending on SeqA protein (Lu et al., 1994). SeqA protein has an N-terminal self-oligomerization domain and a C-terminal DNA-binding domain, and binds to the hemimethylated sites, forming self-oligomers. *oriC*–SeqA complexes inhibit binding of DnaA to *oriC*, blocking re-initiation from newly replicated DNA. SeqA sequestration is, therefore, a negative-feedback system coupled to DNA replication (Waldminghaus and Skarstad, 2009; Skarstad and Katayama, 2013). In another negative-feedback system, transcription of *dnaA* is autoregulated by DnaA, and is also repressed by SeqA–Dam-dependent post-replicative regulation (Campbell and Kleckner, 1990; Bogan and Helmstetter, 1997; Speck et al., 1999; Waldminghaus and Skarstad, 2009). These SeqA mechanisms have been well documented elsewhere (Waldminghaus and Skarstad, 2009), and this review will focus instead on regulation of DnaA protein.

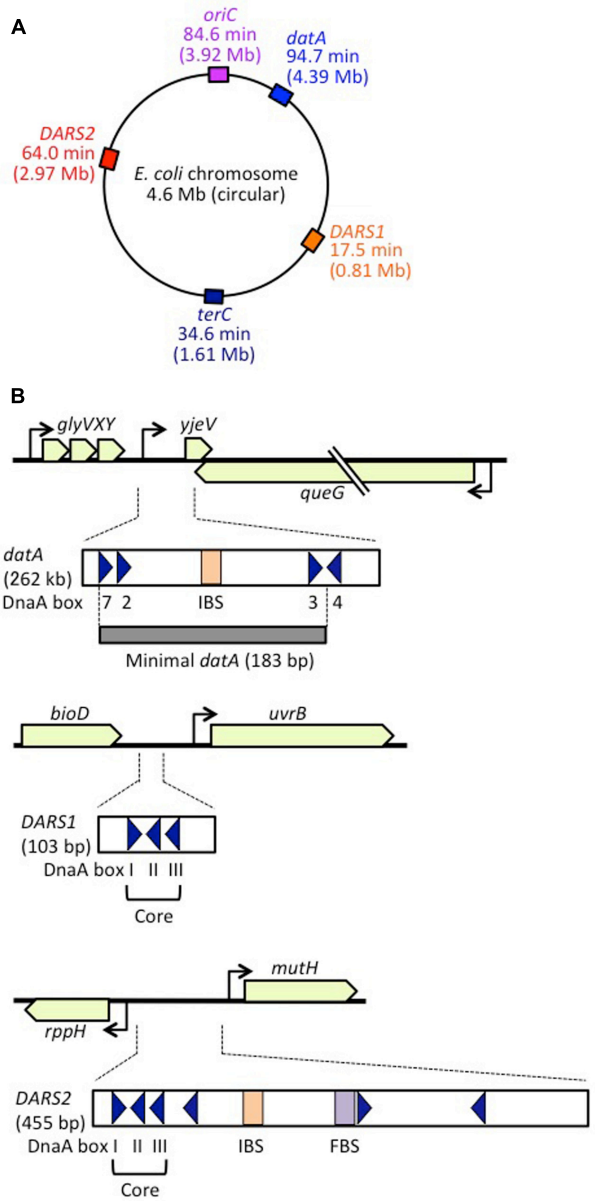

FIGURE 1 | Regulatory DNA elements involved in replication initiation on the *E. coli* genome. **(A)** Schematic representation of the genomic loci of *oriC*, *datA*, *DARS1*, and *DARS2* (and *terC*) in the 4.6 Mb circular *E. coli* genome, with positions also indicated on the scale of 0–100 min. **(B)** Structures of *datA*, *DARS1*, and *DARS2*. Open or gray bars indicate minimal regions. Triangles represent 9 bp DnaA-binding sites (DnaA boxes). Filled squares represent IHF-binding sites (IBS; shown in orange) and a Fis-binding site (FBS; shown in purple). Minimal *datA* consists of DnaA boxes 2, 3, and 7 and a single IBS. DnaA box 4 stimulates DDAH *in vitro*. *DARS1* and *DARS2* both have core regions containing DnaA boxes I–III. *DARS2* also contains additional DnaA boxes and regulatory IBS and FBS.

Escherichia coli cells have at least three regulatory systems for DnaA activity (Skarstad and Katayama, 2013; Riber et al., 2016). In regulatory inactivation of DnaA (RIDA), ATP-DnaA is inactivated in a negative-feedback manner coupled to DNA replication (Katayama et al., 2010). In this system, the clamp subunit of DNA polymerase III holoenzyme has a key role; it remains on the nascent DNA strand after Okazaki-fragment completion, and the clamp–DNA complex binds to the ADP form of DNA regulatory inactivator Hda protein, an 'ATPases associated with various cellular activities' (AAA+) protein with an N-terminal clamp-binding site (Katayama et al., 1998; Kato and Katayama, 2001; Su'etsugu et al., 2008; Baxter and Sutton, 2012; Kim et al., 2017). The resultant ADP-Hda–clamp–DNA complex interacts with ATP-DnaA molecules catalytically, simulating ATP hydrolysis to yield ADP-DnaA. This system is predominant in the inactivation of DnaA after replication initiation, and strongly represses over-initiation of replication. RIDA has been well documented elsewhere (Katayama et al., 2010; Skarstad and Katayama, 2013; Riber et al., 2016), and this review will focus on the two other DnaA regulatory systems.

DDAH (*datA*-dependent DnaA-ATP hydrolysis) regulates the inactivation of DnaA (Kasho and Katayama, 2013; Riber et al., 2016) and requires the non-coding, chromosomal DNA element *datA* (Kitagawa et al., 1996, 1998; **Figure 1**). The 262 bp minimal *datA* region has a specific DnaA-box cluster and a single IHF-binding site (IBS) (Kasho and Katayama, 2013; Kasho et al., 2017; **Figure 1B**). A *datA*–IHF complex forms after replication initiation, and stimulates formation of

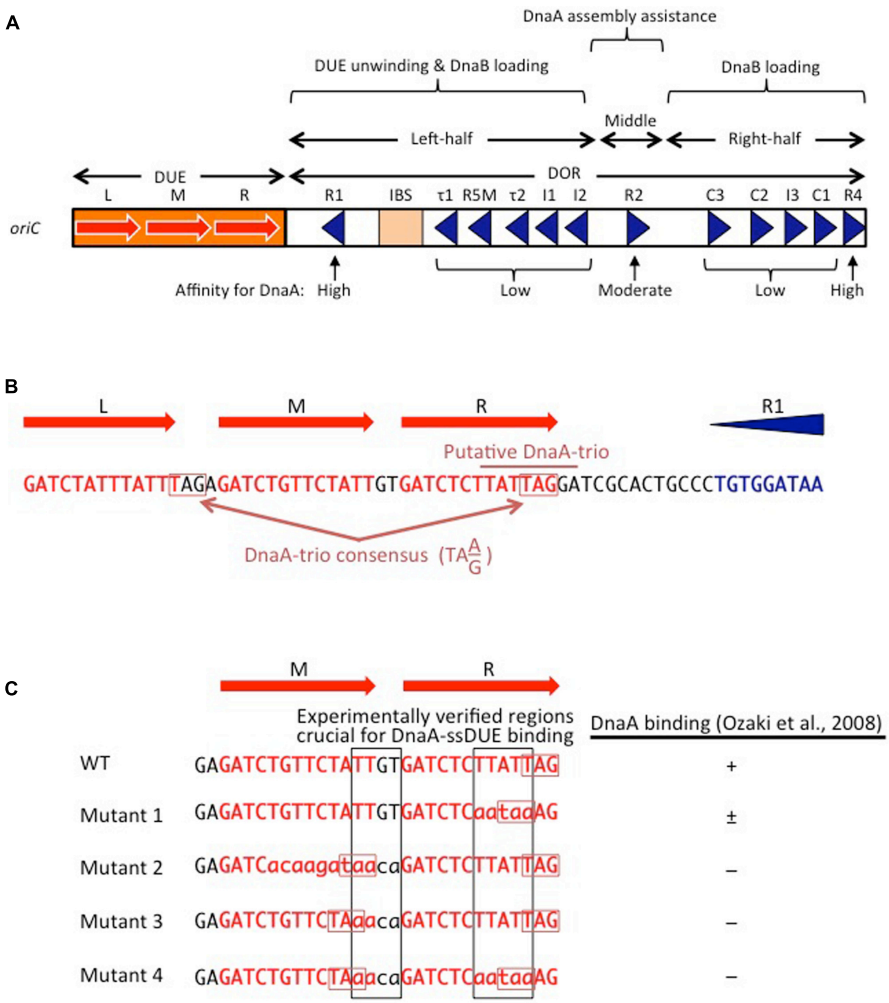

FIGURE 2 | Basic features of *oriC*. **(A)** Structure of *oriC*. Features of the minimal 245 bp *oriC* sequence are shown, including DnaA boxes (triangles), IHF-binding site (IBS; rectangle), and duplex-unwinding element (DUE) AT-rich 13 bp elements (red arrows). Boxes with high, moderate, and low affinity for DnaA are indicated. **(B)** A portion of the *oriC* sequence including the DUE and R1 is shown in detail, with the putative DnaA-trio indicated (Richardson et al., 2016). Perfect DnaA-trio consensus sequences are boxed. **(C)** Effect of mutations on single-stranded DUE (ssDUE) DnaA binding. A portion of the DUE including the M and R 13-mers is indicated in red. Wild-type sequences and mutations are in uppercase and lowercase, respectively. Perfect DnaA-trio consensus sequences are boxed in red. DnaA binding with the indicated ssDUE sequences is summarized (Ozaki et al., 2008). Experimentally verified regions essential for DnaA-ssDUE binding are boxed in black (i.e., TTGT and TTATTT). Note that even if the DnaA-trio consensus is preserved, mutations in the boxed sequences abolish DnaA binding.

specific ATP-DnaA oligomers, and hydrolysis of DnaA-bound ATP, independently of RIDA.

DnaA-reactivating sequence (DARS) sites promote reactivation of DnaA (Fujimitsu et al., 2009). The *E. coli* genome has at least two DARS sites (*DARS1* and *DARS2*) (**Figure 1**), which contain specific DnaA-box clusters (**Figure 1B**), and promote oligomerization of ADP-DnaA, leading to the release of ADP (Fujimitsu et al., 2009; Kasho et al., 2014). The resultant nucleotide-free apo-DnaA preferentially dissociates from the complex, and binds ATP. Both *DARS1* and *DARS2* are required to sustain timely initiation *in vivo*. In particular, *DARS2* is activated by binding of IHF and Fis (a nucleoid-associated factor); IHF binding occurs temporarily before replication initiation (Kasho et al., 2014). The RIDA, DDAH, and DARS DnaA-regulating systems are all required for timely initiation of chromosomal replication.

This review provides an up-to-date detailed synopsis of the various factors and mechanisms involved, particularly from the perspective of the mechanisms involved in the regulation of the timely activation and inactivation of the initiator protein DnaA. Sections "Basic Features of *oriC* and DnaA and DnaA Complex on *oriC*" describe mainly the principal features of *oriC*, DnaA and *oriC*-DnaA complexes, which are based on progress gained over the last 30 years. Sections "DDAH System and DARS System" mainly describe recent developments regarding DDAH and DARS systems and the salient features of DnaA complexes at *datA* and DARS sites. These latter sections provide information on the mechanisms of functionally different DnaA-DNA complexes. Readers who are interested only in DDAH and DARS systems might skip the Section "DnaA Complex on *oriC*," while readers who are interested only in *oriC*-DnaA complexes might skip the Sections "DDAH System and DARS System."

BASIC FEATURES OF *oriC* AND DnaA

oriC

The *E. coli oriC* is a 245 bp DNA element located at 84.6 min of the circular chromosome, and composed of two functionally distinct regions: the DUE and the DnaA-oligomerization region (DOR) (**Figures 1A**, **2A**). The DUE has three AT-rich 13-mer sequences (L, M, and R) with the consensus 5′-GATCTnTTnTTTT-3′, where the Watson and the Crick strands are T-rich and A-rich, respectively (Bramhill and Kornberg, 1988; Messer, 2002). An additional AT-rich region flanking the L sequence assists in DUE unwinding (Messer, 2002). When the DUE is unwound, the single-stranded T-rich DUE strand binds to DnaA oligomers that are bound to the DOR (Ozaki et al., 2008) (also see below). Stable binding of the single-stranded DUE (ssDUE) requires the presence of a region spanning at least the M and R sequences; 5′-TTGT-3′ and 5′-TTATT-3′ sequences are specifically required for the binding (Ozaki et al., 2008; **Figure 2B**). In *Bacillus subtilis oriC*, a repeating trinucleotide motif (DnaA-trio) with the consensus 5′-TA(A/G)-3′ is present in the AT-rich DUE and has been proposed to sustain ssDNA binding by direct interaction with DnaA (**Figure 2**; Richardson et al., 2016). As requirements of specific sequences in DUE are different, *E. coli* and *B. subtilis* may differ in their mechanisms for recognition of ssDUE by DnaA (**Figure 2B**).

The DOR is directly connected to the right edge of the DUE, and contains 12 DnaA boxes, which are present in both orientations (**Figure 2A**). The DOR can be subdivided into three structurally distinct sub-regions: left-half, middle, and right-half (Leonard and Grimwade, 2015; Shimizu et al., 2016). Of these, the left-half sub-region contains six DnaA boxes (R1, τ1, R5M, τ2, I1, I2) in one orientation, and the right-half sub-region contains five boxes (C3, C2, I3, C1, R4) in the opposite orientation, whereas the middle region contains one box (R2) in the right-half orientation (McGarry et al., 2004; Rozgaja et al., 2011; Ozaki and Katayama, 2012; Ozaki et al., 2012a; Shimizu et al., 2016; **Figure 2A**). DnaA complexes assembled on these different sub-regions have specific roles in DUE unwinding and DnaB-helicase loading.

DnaA boxes R1 and R4 (at the left and right ends of the DOR, respectively) match the consensus 5′-TTATnCACA-3′ and have the highest affinity among DOR boxes for DnaA (in both its ATP and ADP bound forms) (Messer, 2002; McGarry et al., 2004; Kawakami et al., 2005; **Figure 2A**). DnaA box R2 has basically moderate affinity, and ATP-DnaA more efficiently binds to this box present in DOR than ADP-DnaA (Messer, 2002; McGarry et al., 2004; Kawakami et al., 2005; Keyamura et al., 2009). All the other DnaA boxes (τ1–I2 and R4–C1 in the left and right halves, respectively) are clustered, and each individual DnaA box only has a low affinity (McGarry et al., 2004; Kawakami et al., 2005; Rozgaja et al., 2011). Although these low-affinity boxes have only moderate similarities to the DnaA-box consensus, ATP-DnaA-specific cooperative binding does occur. This binding depends on DnaA Arg285 for recognition of DnaA-bound ATP (Kawakami et al., 2005; Keyamura et al., 2007, 2009; Kaur et al., 2014; Sakiyama et al., 2017) (for details, see below). ATP-DnaA binding to box τ1 occurs in the absence of IHF binding, but not in the presence of IHF binding, probably because of steric interference (Kawakami et al., 2005; Sakiyama et al., 2017) (see below).

The left-half DOR has a specific binding motif for the nucleoid-associated, DNA-bending protein IHF (**Figure 2A**). The consensus of the IBS is 5′-(A/T)ATCAAnnnnTT(A/G)-3′ (Swinger and Rice, 2004). *In vitro*, IHF binding stimulates DUE unwinding and replication from *oriC*; another nucleoid-associated protein (HU) can substitute for IHF in these reactions (Hwang and Kornberg, 1992). IHF stimulates DnaA binding to moderate-affinity (R2) and low-affinity (R5M and I1-3) sites (Grimwade et al., 2000; McGarry et al., 2004), and promotes binding to ssDUE by DnaA that is complexed with the DOR (Ozaki and Katayama, 2012). Double mutations resulting in deficiency of both IHF and HU severely inhibit cell growth, and cause synthetic lethality at high temperatures (Kano and Imamoto, 1990). Although a Fis binding consensus sequence is present between the R2 and C3 boxes, mutant cells bearing a sequence defective in Fis binding and the results of *in vitro* replication systems suggest that binding of Fis to *oriC* is not an important element in the regulation

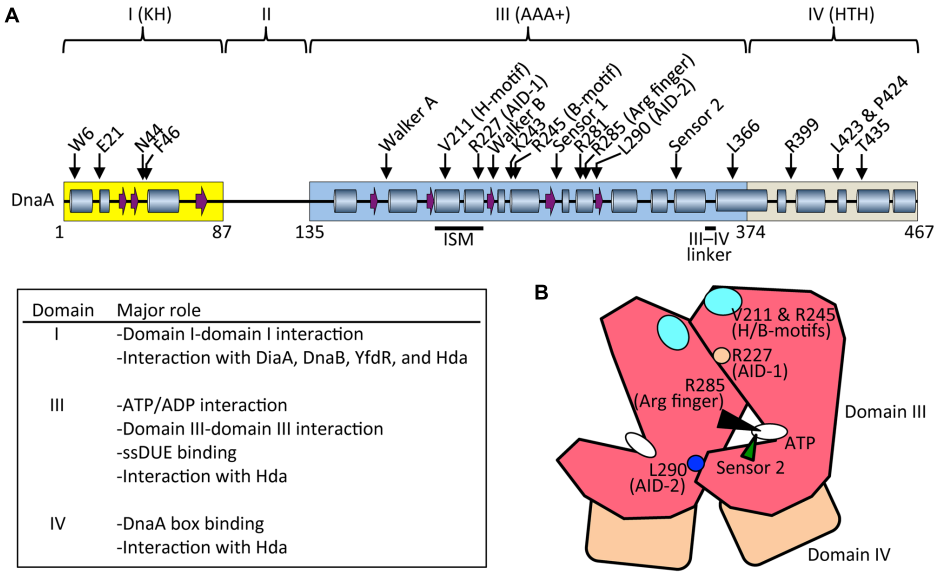

FIGURE 3 | Basic features of DnaA. **(A)** Possible secondary structure of full length DnaA. Domains I, III, and IV are shown in yellow, blue, and gray boxes, respectively. α helices (cylinders) and β strands (arrows) were determined from the NMR structure of DnaA domain I–II (PDB: 2E0G; Abe et al., 2007) and the crystal structure of DnaA domain IV (PDB: 1J1V; Fujikawa et al., 2003), combined with a homology model of DnaA domain III generated using the crystal structure of *Thermotoga maritima* DnaA (PDB: 2Z4S; Ozaki et al., 2008) (SWISS-MODEL Repository: P03004). For clarity, extremely short helices in the homology model are omitted according to the crystal structure of *A. aeolicus* DnaA domain III (Erzberger et al., 2002). Representative motifs in the AAA+ fold and residues crucial for DnaA functions are indicated. Major roles of domains I, II, and IV are summarized. Arg finger, arginine finger (Arg285). **(B)** Schematic presentation of domain III (*red*) and IV (*brown*). Important motifs and residues for DnaA–DnaA interaction and ATP recognition/hydrolysis in DnaA complexes are indicated. ATP, white oval; arginine finger Arg285, black arrowhead; AID-1 Arg227, orange circle; AID-2 Leu270, blue circle; sensor 2, green arrowhead; and H/B-motifs Val211 and Arg245, cyan oval.

of initiation (Margulies and Kaguni, 1998; Weigel et al., 2001).

DnaA

DnaA is a 52.5 kDa basic protein composed of 473 amino acids in four domains (Ozaki and Katayama, 2009; Kaguni, 2011; **Figure 3A**). The largest (domain III) has an AAA+ ATPase fold that contains Walker A and B ATP/ADP-binding/hydrolysis motifs, motifs for domain III–domain III head-to-tail interaction, and motifs for ssDUE binding. Domain III AAA+ sensor 1 motifs and N-linker motif contribute to an extraordinarily high affinity for ATP/ADP (K_d = 10–100 nM) (Kawakami et al., 2006; Ozaki et al., 2012b). ATP binding causes conformational changes in DnaA, and structural differences between ATP-DnaA and ADP-DnaA are thought to occur in domains II and III (Saxena et al., 2015). Lys178, an essential residue within the Walker A motif of DnaA, is acetylated specifically in stationary-phase cells (Zhang et al., 2016).

ATP-DnaA forms oligomers at *oriC* more efficiently than ADP-DnaA. The arginine finger motif (Arg285), ATP-DnaA-specific interactive locus for DUE unwinding (AID) motifs (Arg227, Leu290), box VII motif (Arg281), and Lys243 are required for functional domain III–domain III interactions (Felczak and Kaguni, 2004; Kawakami et al., 2005; Ozaki et al., 2008, 2012a; **Figure 3**) (see section Structure of the DnaA–IHF–*oriC* Complex for DUE Unwinding and DnaB Loading). In particular, Arg285 Arg finger is important for the ATP-dependent activation of DnaA complexes on *oriC* (Kawakami et al., 2005) and is exposed on the side opposite to that of the ATP/ADP-binding site of domain III (**Figure 3B**). Whereas DNA-free DnaA is monomeric in solution, domain III enables DnaA to self-oligomerize in an ATP-dependent, head-to-tail manner via interactions between bound ATP and Arg285 of adjacent protomers, resulting in the binding of multiple DnaA protomers to *oriC* (Kawakami et al., 2005; Ozaki et al., 2008).

During unwinding of DUE by DnaA, hydrophobic (H) and basic (B) motifs (Val211 and Arg245, respectively), which are highly conserved in DnaA orthologs, have a crucial role in binding to the T-rich ssDUE strand (Ozaki et al., 2008; Ozaki and Katayama, 2012; Sakiyama et al., 2017; **Figure 3**) (see Section Structure of the DnaA–IHF–*oriC* Complex for DUE Unwinding and DnaB Loading). The H and B motifs are located in helices between the Walker A and B motifs and the Walker B and sensor 1 motifs, respectively (Ozaki and Katayama, 2009; **Figure 3A**). Whereas typical AAA+ proteins have only a single α helix between Walker A and B motifs, DnaA-related proteins (collectively termed the replication initiator clade) have two α helices in tandem, and the H motif is located on one of the two, giving a structure called an initiator/loader-specific motif (Iyer et al., 2004; Dueber et al., 2007; Mott et al., 2008; Ozaki et al., 2008; Ozaki and Katayama, 2009).

Certain residues in DnaA have distinct roles in its ATPase activity. Sensor 2 Arg334 is important for the intrinsic ATPase activity of DnaA, RIDA, and DDAH, probably via an interaction

between the γ phosphate of ATP and Arg334. However, this residue is dispensable for the formation of functional initiation complexes on *oriC* (Sekimizu et al., 1987; Nishida et al., 2002; Kasho and Katayama, 2013; **Figure 3**). Arginine finger Arg285 is essential for intrinsic ATPase activity and for regulation by DDAH, but not by RIDA (Kawakami et al., 2005; Kasho and Katayama, 2013). Box VII Arg281 represses intrinsic ATPase activity and is dispensable for RIDA, but is required for DDAH (Kawakami et al., 2005; Kasho and Katayama, 2013) (see below).

The DnaA C-terminal domain IV has a typical helix-turn-helix (HTH) motif and binds with sequence specificity to DnaA boxes (Erzberger et al., 2002; Obita et al., 2002; Fujikawa et al., 2003; Yoshida et al., 2003; **Figure 3A**). This binding causes DNA bending by about 20°. An α helix consisting of amino-acid residues 434–451 is part of the HTH motif that is inserted in the major groove of the 9 bp DnaA box, recognizing the 3′ portion (5′-TnCACA-3′) of the consensus sequence (Fujikawa et al., 2003). Arg399, which is located in the turn (or loop) region of the HTH motif, is inserted in the minor groove of the DnaA box, recognizing the 5′ portion (5′-TTA-3′) of the consensus sequence (Fujikawa et al., 2003). In consistent, DnaA T435M and DnaA R399A are defective in DnaA-box binding (Sutton and Kaguni, 1997; Blaesing et al., 2000). The short linker connecting domains III and IV is a structurally flexible loop that enables swiveling of domain IV (Erzberger et al., 2002), and the results of molecular dynamics simulation indicate that it is important in the assembly of DnaA oligomers on *oriC* (Shimizu et al., 2016; **Figure 3A**). Leu366 located in an α helix downstream of the short linker is required for a conformational change in DnaA complexes constructed on *oriC* (Garner and Crooke, 1996; Saxena et al., 2011; **Figure 3A**). In addition, Leu423 and Pro424 contribute to the Hda binding that is crucial for RIDA (Keyamura and Katayama, 2011).

The N-terminal domain I of DnaA has important roles in protein–protein interaction. Weak domain I–domain I binding depends on Trp6, which contributes to DnaA self-oligomerization (Sutton et al., 1998; Simmons et al., 2003; Felczak et al., 2005; **Figure 3A**). Glu21 and Phe46 form a binding site for both DnaB helicase and DiaA protein (Abe et al., 2007; Keyamura et al., 2009). Phe46 contributes more to DiaA binding than Glu21, and is also required for binding to YfdR protein, a potential inhibitor of DnaA–DiaA or DnaA–DnaB interactions that is encoded by a cryptic prophage (Noguchi and Katayama, 2016). Asn44 is thought to interact with Hda to facilitate functional interaction between DnaA domain III and Hda during RIDA (Su'etsugu et al., 2013). Domain I also binds to HU, Dps (DNA protection during starvation protein), and ribosomal L2 protein, but the residues involved in these interactions have not yet been identified (Chodavarapu et al., 2008a,b, 2011). In addition, DnaA domain I contains a K-homology domain, which enables binding to ssDNA and RNA (Abe et al., 2007). However, domain I has only slight activity in ssDUE binding *in vitro* (Abe et al., 2007), and notably, DnaA with deletion of domains I and II retains full DUE-unwinding activity *in vitro* (Sutton et al., 1998), which indicates that domain III plays a predominant role in ssDUE binding sustaining DUE unwinding (Ozaki et al., 2008; Ozaki and Katayama, 2012; Sakiyama et al., 2017). Domain II is an unstructured linker and the least-conserved domain among DnaA orthologs in eubacterial species (Abe et al., 2007; Nozaki and Ogawa, 2008; **Figure 3A**).

DnaA COMPLEX ON *oriC*

The Role of DiaA

The 196 amino acid DiaA protein forms a homotetramer in which each protomer has a DnaA-binding site (Ishida et al., 2004; Keyamura et al., 2007, 2009). DiaA stimulates ATP-DnaA assembly on *oriC* and the unwinding of DUE. A single DiaA tetramer can bind multiple DnaA molecules (theoretically up to four; experimentally at least three), potentially leading to the linkage effect for stimulating cooperative binding. With the linkage effect, it has been demonstrated that, if two proteins each with a weak affinity for DNA are stably connected by a linker molecule, the affinity of the linked molecule for DNA is increases drastically (theoretically by up to 10^3- to 10^5-fold) because it permits binding between the protein and multiple points on the DNA (Zhou, 2001; Stauffer and Chazin, 2004). A mutant that encodes a variant of DiaA with constitutive binding of just two DnaA protomers is defective in stimulation of DnaA assembly on *oriC* and DUE unwinding (Keyamura et al., 2007). The sequence of the *diaA* gene is widely conserved in the genomes of eubacterial species (Keyamura et al., 2007).

The DiaA-binding site is located in domain I of DnaA (and includes residues Glu21 and Phe46), and this site also binds DnaB helicase, as described in Section DnaA (Abe et al., 2007; Keyamura et al., 2009; **Figure 3A**). Both overproduction of DiaA and deletion of the *diaA* gene moderately inhibit initiation *in vivo* (Ishida et al., 2004; Flåtten et al., 2015). DiaA therefore has a positive effect on initiation through stimulation of DnaA assembly, and a negative effect probably via its ability to inhibit DnaA–DnaB binding. DiaA that is bound to the DnaA assembly on *oriC* is thought to dissociate (enabling DnaB binding) at (or after) the time of DUE unwinding, by an unknown mechanism (Keyamura et al., 2009). Regulation of the inhibitory activity of DiaA has not yet been determined.

Structure of the DnaA–IHF–*oriC* Complex for DUE Unwinding and DnaB Loading

The question of the regularity and directionality of DnaA boxes in *oriC* has been resolved by the identification of low-affinity DnaA boxes, and by the correction of previously obtained information. The left-half DOR is now known to contain only DnaA boxes with a leftward directionality (R1, τ1, R5M, τ2, I1, I2), whereas the middle region and right-half DOR contain only DnaA boxes with a rightward directionality (R2, C3, C2, I3, C1, R4) (**Figure 2A**). As explained above, head-to-tail binding of domain III leads to ATP-DnaA-dependent assembly of sub-complexes with opposite orientations in the left-half and right-half DORs (Kawakami et al., 2005; Noguchi et al., 2015; Shimizu et al., 2016; Sakiyama et al., 2017; **Figures 3**, **4**).

In DnaA sub-complexes, nucleotides that are associated with R1 box- and R4 box-bound DnaA protomers are located at the

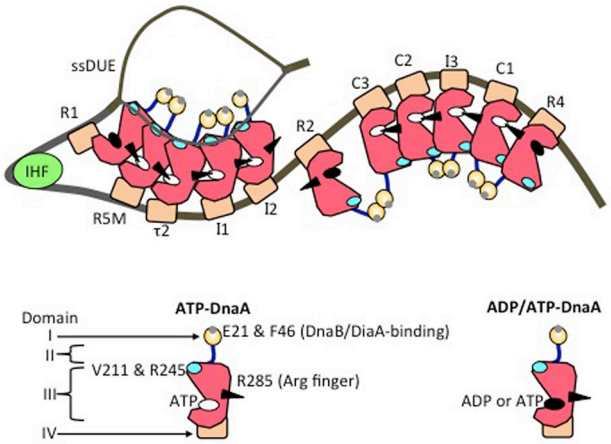

FIGURE 4 | Model of an unwound state of the initiation complex. DnaA domains I (*orange*), II (*blue*), III (*red*), and IV (*brown*) are schematically presented. A small gray circle on domain I shows a patch including Glu21 and Phe46 (for binding of DiaA and DnaB helicase). A black arrowhead, cyan oval, white oval, and black oval on domain III represent the arginine finger Arg285, H/B motifs, ATP, and either ADP or ATP, respectively. IHF is shown as a light green circle. DnaA-box positions are labeled. On the left-half and right-half DnaA-oligomerization regions, head-to-tail DnaA-oligomer sub-complexes assemble, with interactions between ATP and Domain III Arg285. The T-rich ssDUE strand interacts with the DnaA H/B motifs in the left-half sub-complex.

outer edges of the DOR, so that those cannot interact with DnaA protomers bound to other DOR sites (**Figures 2A**, **4**). Thus, even when ADP-DnaA is bound to R1, DUE-unwinding activity is fully sustained (Noguchi et al., 2015). ATP-DnaA assembly at the left-half DOR fundamentally depends on ATP–DnaA binding to the low-affinity R5M box (but not to the R1 box) and is stimulated by R1-bound DnaA (Sakiyama et al., 2017). Cooperative binding of ATP-DnaA molecules would operate effectively in the region from the R5M box to the I2 box (Sakiyama et al., 2017). Also, when ADP-DnaA is bound to the R4 box, assembly of the DnaA sub-complex on the right-half DOR is fully sustained with ATP-DnaA (Noguchi et al., 2015). ATP-DnaA assembly to the low-affinity sites in the right-half DOR depends on DnaA binding to the R4 box (Noguchi et al., 2015).

Evidence suggests that domain III of R2-bound DnaA does not interact with DnaA protomers bound to I2 or C3 (Rozgaja et al., 2011; Shimizu et al., 2016), as expected by the long spacing between R2 and I2 (9 bp) and between R2 and C3 (20 bp) (**Figure 2A**). Each box in the τ1-R5M-τ2-I1-I2 region and the R4-C1-I3-C2-C3 region is separated by 2–4 bp. However, domain I of R2-bound DnaA might interact with that of I2-bound or C3-bound DnaA, simulating cooperative DnaA binding (Miller et al., 2009; Ozaki and Katayama, 2012; Shimizu et al., 2016; **Figure 4**).

The existence of nucleotide-independent activities of DnaA bound to R1, R4, and R2 is consistent with data from *in vivo* dimethyl-sulfate footprint analysis, which suggest that DnaA binding to these boxes is stable throughout the cell cycle (Samitt et al., 1989; McGarry et al., 2004; Kawakami et al., 2005). By contrast, in *in vivo* experiments with DnaA fused to enhanced yellow fluorescent protein, results from photobleaching and high-resolution microscopy suggest that, overall, DnaA complexes bound to *oriC* are rapidly turned over with a time scale of a few seconds (Schenk et al., 2017). These results are consistent with the unstable binding of DnaA to low-affinity sites. Such dynamic features might be important for timely assembly of ATP-DnaA on *oriC* after the DARS system has increased in total level of ATP-DnaA.

The left-half ATP-DnaA sub-complex possesses full activity for DUE unwinding and ssDUE binding (Ozaki and Katayama, 2012; **Figure 4**). In addition to the Arg finger Arg285, AID1 (Arg227) and AID2 (Leu290) motifs, which are highly conserved in DnaA orthologs, are thought to be located at the domain III–domain III interface and to contribute to ATP–DnaA-specific interactions and the establishment of DnaA oligomers within the left-half DOR that are competent for DUE unwinding (Ozaki et al., 2012a; **Figure 3B**). Lys243 also contributes to oligomerization of ATP-DnaA on *oriC* and DUE unwinding (Ozaki et al., 2008). Also, Lys243 can be acetylated *in vivo*. Although the significance of this is unknown, it moderately affects DnaA binding to *oriC in vitro* (Li et al., 2017). Molecular dynamics simulation shows that sharp DNA bending (>120°) caused by IHF binding enables domain III–domain III interaction between DnaA protomers bound to R1 and R5M in the absence of DnaA–τ1 binding (Shimizu et al., 2016; **Figure 4**). Consistently, *in vitro* experiments indicate that DnaA–τ1 interaction is inhibited by IHF binding (Sakiyama et al., 2017).

DUE unwinding depends on temperature and superhelicity of *oriC* DNA, which contribute to destabilization of the duplex state of the DUE (Baker and Kornberg, 1988; Sekimizu et al., 1988). In addition, the unstable ssDUE binds to, and is stabilized by, DnaA domain III, enabling loading of DnaB helicase to the unwound region (Ozaki et al., 2008). In *E. coli* and *B. subtilis*, only a specific strand (the T-rich strand in *E. coli*) binds to DnaA (Ozaki et al., 2008; Richardson et al., 2016). Also, in *E. coli*, the H/B-motif residues of domain III are required for ssDUE binding (Ozaki et al., 2008; Sakiyama et al., 2017). This binding mode is consistent with that seen in the co-crystal structure of the poly-A ssDNA-bound DnaA domain III ortholog from the hyperthermophilic bacterium *Aquifex aeolicus* (Duderstadt et al., 2011).

Notably, when multiple DnaA molecules bind to the DOR, ssDUE binding by DnaA increases dramatically and is much higher than that of DOR-unbound DnaA molecules (Ozaki et al., 2008; Ozaki and Katayama, 2012; Sakiyama et al., 2017). ssDUE directly binds to domain III of DnaA protomers that have associations through domain IV with the left-half DOR (Ozaki et al., 2008; Ozaki and Katayama, 2012; Sakiyama et al., 2017; **Figure 4**). In particular, domain III of the R1- and R5M-bound DnaA protomers play predominant roles in ssDUE binding for replication initiation (Sakiyama et al., 2017). These and the other observations mentioned above support the idea that ssDUE directly binds to R1- and R5M-bound DnaA protomers via sharp DNA bending by IHF, which stimulates ssDUE recruitment to those DnaA molecules. This is referred to as the ssDUE-recruitment mechanism (**Figure 4**; Ozaki et al., 2008; Ozaki

and Katayama, 2012; Noguchi et al., 2015; Shimizu et al., 2016; Sakiyama et al., 2017). This reasonably explains the role of IHF and dispensability of ATP of R1-bound DnaA in DUE unwinding, and the striking stimulation of ssDUE binding by DnaA-oligomer assembly on the DOR, as well as the strict requirements in DUE unwinding for the spacing between the DUE and the DnaA R1 box and between the DnaA R1 box and the IBS, and the requirement for H/B motifs of the DOR-bound DnaA for ssDUE binding (**Figure 4**) (for details, see Sakiyama et al., 2017).

Multiple DnaA molecules bound to the DOR are required for binding of DnaB helicase which is a homohexamer (Abe et al., 2007; Keyamura et al., 2009; Ozaki and Katayama, 2009). Multiple DnaA domain I molecules of the DOR-bound DnaA complexes would be allied so as to stably bind DnaB helicases by using multiple binding points (**Figure 4**). In consistent, Box VII Arg281 stabilizes DnaA oligomers assembled on the DOR, and is required for DnaB-helicase loading, but not for DUE unwinding (Felczak and Kaguni, 2004). This suggests that stability of DnaA complexes is more important for DnaB-helicase loading than for DUE unwinding.

In addition to the basic DnaB-binding/loading activity of the left-half-DOR DnaA sub-complex, the right-half-DOR DnaA sub-complex stimulates DnaB binding/loading (Ozaki and Katayama, 2012; **Figures 2A**, **4**). This activity might result in binding of two DnaB helicases, one to each of the DnaA sub-complexes, enabling bi-directional replication (Ozaki and Katayama, 2012; Noguchi et al., 2015; **Figure 4**). The spacing between the R2 and C3 boxes is important for efficient DnaB loading, suggesting coordination of the left and right DnaA subcomplexes in a DnaB loading process (Shimizu et al., 2016; **Figure 4**).

DDAH SYSTEM

Function

datA-dependent DnaA inactivation has been termed DDAH. Three hundred 9-mer DnaA box consensus sequences are widely distributed throughout the *E. coli* chromosome (Tesfa-Selase and Drabble, 1992; Roth and Messer, 1998; Hansen et al., 2007). Some of these sites regulate the activity of DnaA for replication initiation, whereas some of others function for transcriptional regulation by DnaA (Kitagawa et al., 1996; Messer and Weigel, 1997; Speck et al., 1999; Olliver et al., 2010). The *datA* locus includes a DnaA-box cluster and was originally identified as a potent DnaA-binding locus that can repress untimely replication initiation (Kitagawa et al., 1996; Ogawa et al., 2002; Nozaki et al., 2009; **Figure 1A**). DnaA binding at *datA* is stimulated by IHF (Nozaki et al., 2009); the *datA*–IHF complex stimulates hydrolysis of DnaA-bound ATP independently of RIDA to produce ADP-DnaA (Kasho and Katayama, 2013; Kasho et al., 2017; **Figure 5A**).

Several lines of *in vivo* evidence point to the important role of the *datA*–IHF complex in the repression of untimely replication initiation. Deletion of *datA* or IHF genes (*ihfA* or *ihfB*) increases cellular levels of ATP-DnaA, resulting in higher levels of ATP-DnaA than in wild-type cells and untimely replication initiation without cell growth inhibition (Kitagawa et al., 1996; Nozaki et al., 2009; Kasho and Katayama, 2013). As inhibition of RIDA causes severe over-initiation of replication and arrest of cell growth (Kato and Katayama, 2001; Nishida et al., 2002; Fujimitsu et al., 2008), DDAH is thought to play a supportive role in RIDA. Also, in DDAH-deficient mutants, replication initiation is not completely repressed in the presence of rifampicin, an inhibitor of transcription and replication initiation (von Freiesleben et al., 2000; Morigen, Skarstad and Molina, 2005), probably due to elevated levels of ATP-DnaA.

Structure of *datA*

The minimal *datA* for DDAH function is 183 bp containing high-affinity DnaA boxes 2 and 3, low-affinity DnaA box 7 and a single IBS, which are all essential for efficient ATP–DnaA binding and DDAH activity (Kitagawa et al., 1998; Ogawa et al., 2002; Nozaki et al., 2009; Kasho and Katayama, 2013; Kasho et al., 2017; **Figure 1B**). All the essential DnaA boxes have the same directionality, suggesting the importance of head-to-tail ATP–DnaA interactions. The results of mutation analyses indicate that, as in the *oriC* DORs, the orientations and interval lengths of the *datA* DnaA boxes 2 and 3 and the IBS are optimized for repression of untimely initiations through DDAH (Nozaki et al., 2009; Kasho and Katayama, 2013). The *datA* DnaA box 4 stimulates DnaA assembly and DnaA-ATP hydrolysis *in vitro*, but is not essential for initiation regulation *in vivo* (Ogawa et al., 2002; Kasho and Katayama, 2013; Kasho et al., 2017; **Figure 1B**). Unidentified factor(s) might stimulate DnaA assembly *in vivo* even in the absence of DnaA box 4 (see below).

Mechanism

In the *datA* region, oligomers containing three ATP-DnaA molecules form on and around the core DnaA boxes and higher oligomers form depending on IHF (Kasho and Katayama, 2013; Kasho et al., 2017; **Figure 6A**). IHF binding causes DNA looping, which would promote interaction between the box 2-bound DnaA and the box 3-bound DnaA, thereby stabilizing DnaA complexes in a cooperative manner for the activation of DnaA-ATP hydrolysis. The results of biochemical analyses using mutant DnaA proteins provide evidence that, in *datA*–DnaA complexes, DnaA–DnaA interactions depend on AAA+ domain III arginine finger Arg285, box VII Arg281, and AID2 Leu290, and stimulation of ATP hydrolysis depends on AAA+ sensor 2 motif Arg334 (Kasho and Katayama, 2013; Kasho et al., 2017). DnaA AID-2 Leu290 might facilitate dissociation of the resultant ADP-DnaA, which is unstable in *datA,* thereby enabling catalytic reaction of DDAH (Kasho et al., 2017). Overall, these requirements for specific residues are similar to those of the initiation complex, except for the crucial role of sensor 2 Arg334 in ATP hydrolysis. This seems reasonable because both DDAH complexes and the initiation complex are constructed mainly from head-to-tail DnaA–DnaA interactions (**Figures 3B**, **6A**).

The stimulatory role of IHF in DDAH cannot be replaced by HU, which is a structural homolog of IHF and a widely conserved nucleoid-associated protein in most bacteria, although IHF can be functionally replaced by HU in an *in vitro* reconstituted system

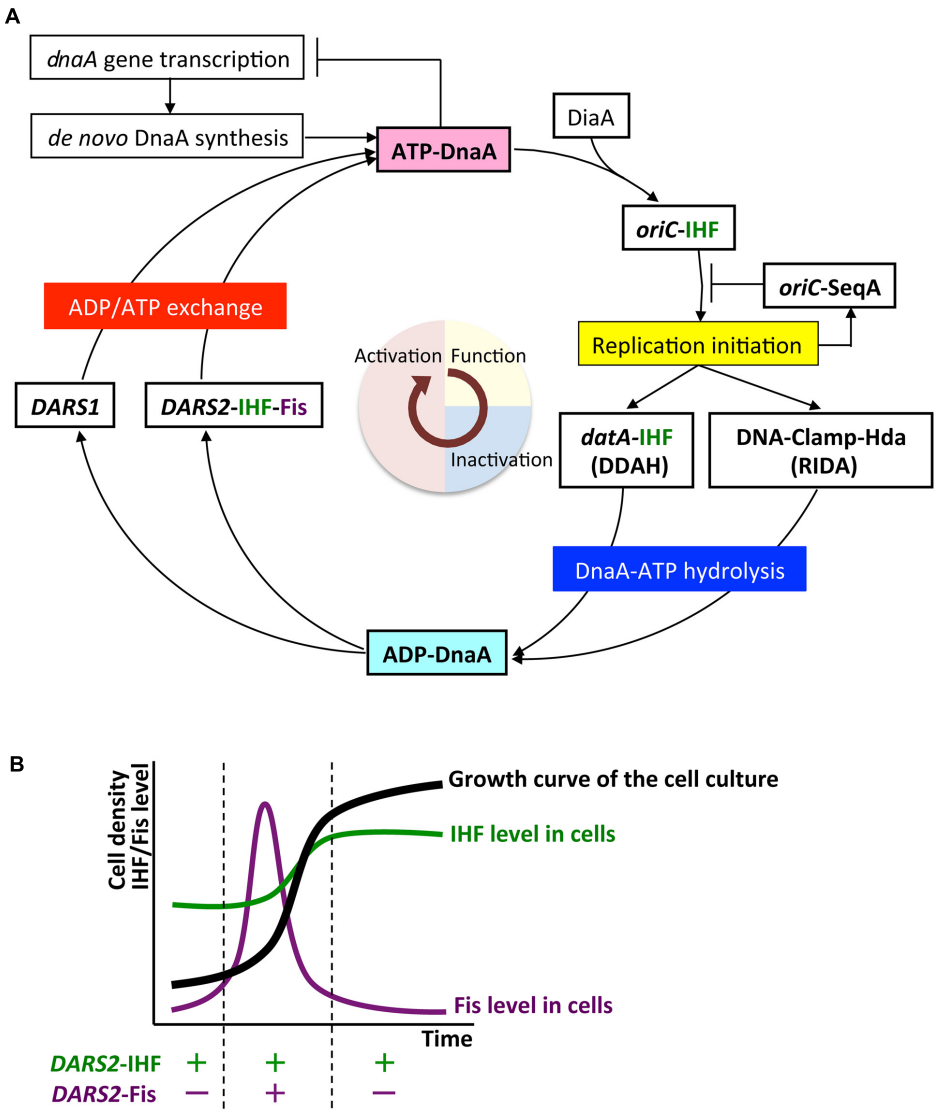

FIGURE 5 | The regulatory cycle of DnaA. **(A)** Schematic presentation of the regulatory cycle of DnaA. ATP-DnaA forms oligomers on *oriC* with the aid of integration host factor (IHF) and DnaA interacting protein DiaA, and initiates replication (period in light yellow). After initiation, ATP-DnaA is converted to replication-inactive ADP-DnaA (RIDA) and *datA*-dependent DnaA-ATP hydrolysis (DDAH) systems (period in light blue). RIDA involves Hda protein and the clamp subunit of DNA polymerase III holoenzyme, and DDAH involves the *datA* locus and IHF. DnaA-reactivating sequence (*DARS1* and *DARS2*) loci stimulate nucleotide exchange of ADP-DnaA and regenerate ATP-DnaA (period in light red). IHF binds to specific sites in *oriC*, *datA*, and *DARS2* in a cell-cycle-coordinated manner. Fis binds to *DARS2* in log-phase cells. **(B)** Growth-phase coordination of regulation of Fis expression. The cellular level of Fis varies through the growth phases, and is much higher in exponential-phase cells (enabling Fis binding to *DARS2*) than in stationary-phase cells. By contrast, the cellular level of IHF is highest in stationary-phase cells.

of replication initiation from *oriC* (Hwang and Kornberg, 1992; Dillon and Dorman, 2010; Kasho and Katayama, 2013). Like IHF, HU induces sharp DNA bending, but unlike IHF, HU binds to DNA without sequence specificity. At *datA* and *oriC,* the IBS is located between DnaA boxes, but the inter-DnaA box region in *datA* (i.e., between box 2 and box 3) is longer than that (i.e., between R1 box and R5M box) at *oriC* (**Figures 1B**, **2A**), suggesting that a functional conformational change in *datA* for activating DDAH is strongly dependent on specific DNA bending at the *datA* IBS induced by IHF binding.

Regulation

Coupling of *datA* Dosage (Copy Number) with Replication

datA is located at 94.7 min (4.39 Mb position) in the *E. coli* genome, near to *oriC* (84.6 min, 3.92 Mb position), which means that *datA* is duplicated soon after replication initiation, resulting in a temporary higher dosage (copy number) of *datA* per cell. This is thought to be important for the repression of untimely initiations under certain growth conditions (Kitagawa et al., 1996; **Figure 1A**). In agreement with these observations, increasing the

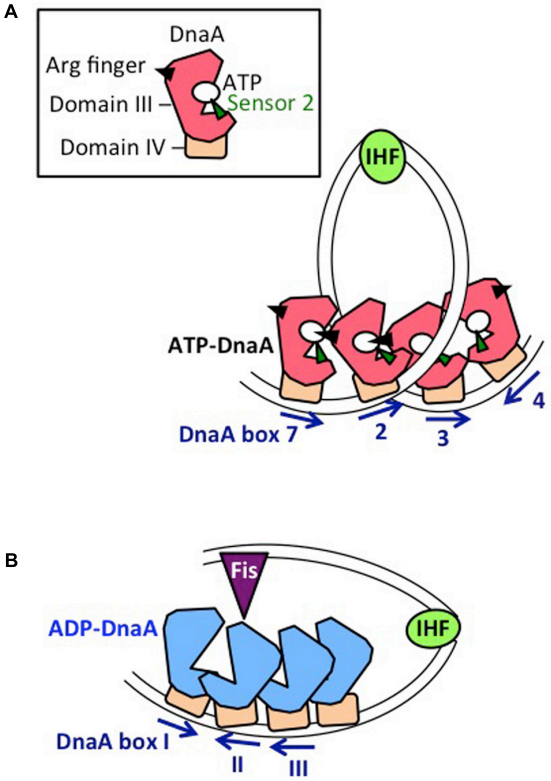

FIGURE 6 | Mechanistic view of DnaA regulation by *datA* and *DARS2*. **(A)** Mechanistic model of *datA*-dependent DnaA-ATP hydrolysis (DDAH). Oligomers of ATP-DnaA (with domain III shown as a red polygon, and domain IV as an brown square) assemble on the *datA* minimal region containing DnaA boxes 7, 2, and 3. Sharp DNA bending by IHF could stimulate contact between DnaA bound at boxes 2 and 3. Cooperative ATP-DnaA binding on *datA* DnaA box 7 might induce conformational change of the DnaA to activate DDAH. **(B)** Mechanistic model of *DARS2*-mediated DnaA activation. Oligomers of ADP-DnaA (with domain III shown as a blue polygon, and domain IV as an brown square) assemble on the *DARS2* core region. IHF and Fis bind to specific sites in the *DARS2* regulatory region, and the resultant complex stimulates conformational changes in the core-bound DnaA oligomer, to induce structural changes in DnaA and ADP dissociation. Nucleotide-free apo-DnaA dissociates from the core region and binds ATP (which is abundant in the cytosol), yielding ATP-DnaA.

datA copy number via a multi-copy plasmid negatively impacts replication initiation and cell growth (Morigen et al., 2003; Kasho et al., 2017). Conversely, translocation of *datA* to the replication-termination locus *terC* at 34.6 min, which is >2 Mb apart from *oriC* (**Figure 1A**), does not result in a temporary increase in its copy number until replication is nearly completed, allowing untimely initiations in nutrition-rich medium, similar to those observed in *datA*-deleted cells (Kitagawa et al., 1998; Frimodt-Møller et al., 2015). The *datA* copy number may also be important for the regulation of cell division (Morigen et al., 2014). Notably, in *B. subtilis* and *Streptomyces coelicolor*, chromosomal DnaA-box clusters analogous to *datA* repress untimely replication initiation (Smulczyk-Krawczyszyn et al., 2006; Okumura et al., 2012), suggesting that the DnaA regulation by *datA* is a conserved feature of most eubacterial species.

Cell-Cycle-Dependent Binding of IHF

The activation of DDAH and RIDA reduces the ATP-DnaA level and represses untimely initiations (Kasho and Katayama, 2013). Regulation of IHF binding to *datA* is essential for the timely activation of DDAH. Cell-cycle analysis of *datA*–IHF binding indicates that IHF dissociates from *datA* before replication initiation and temporarily binds to *datA* after initiation (Kasho and Katayama, 2013). As both IHF binding to and dissociation from *datA* occur during on-going chromosome replication, DDAH is suggested to be regulated by a mechanism that couples certain cell cycle events to *datA*–IHF binding. Conversely, RIDA is activated by DNA replication-coupled feedback (Katayama et al., 2010; Kasho and Katayama, 2013)

The transcription inhibitor rifampicin might inhibit timely dissociation of *datA*–IHF complexes (Kasho and Katayama, 2013). As IHF is abundant in exponentially growing cells (Ali Azam et al., 1999), a specific factor inhibiting *datA*–IHF binding might be required to be transcribed at a particular moment in the cell cycle. DDAH activity is inhibited by translocation of the *datA* sequence to a highly transcribed region (Frimodt-Møller et al., 2016), suggesting that transcription through *datA* might inhibit *datA*–IHF binding. Consistently, the essential core region of *datA* (i.e., box 7-box 2-IBS-box 3) is located at an intergenic region downstream of the *glyVXY* operon and *queG* gene (Kitagawa et al., 1998; Nozaki et al., 2009; Kasho et al., 2017; **Figure 1B**). It remains to be determined whether transcription of these genes oscillates in a coordinated manner during the cell cycle.

Effects of DNA Superhelicity and Nutrition

DDAH is suggested to regulated also by DNA supercoiling. *In vitro* experiments indicate that negative DNA supercoiling, which is modulated by DNA topoisomerases such as DNA gyrase and by nucleoid protein binding (Travers and Muskhelishvili, 2005), stabilizes ATP-DnaA oligomerization and IHF binding on *datA* and increases DDAH activity twofold compared with *datA* activity on relaxed DNA (Kasho et al., 2017). Modulation of negative supercoiling by novobiocin, a DNA-gyrase inhibitor, decreases the function of *datA* on plasmid DNA for repressing replication initiation (Kasho et al., 2017), suggesting supercoiling-dependent regulation of DDAH *in vivo*. Negative supercoiling is predicted to increase under osmotic-stress conditions (Higgins et al., 1988), which might affect *datA* activity for repressing initiation.

Nutrition-dependent regulation of DDAH has been suggested. Untimely initiations in *datA*-null cells are more severely exhibited in nutrient-poor medium containing acetate or glucose than in rich medium containing glucose-casamino acid or LB (Kitagawa et al., 1998; Flåtten et al., 2015). Chromosome-conformation-capture analysis has revealed that *oriC* can physically interact with *datA* under conditions of replication stress induced by serine hydroxamate, which causes amino-acid starvation and inhibits replication initiation (Cagliero et al., 2013). Free DnaA molecules present around *oriC* could efficiently interact with *datA* under poor nutrition conditions. Conversely, in rich medium, the *datA* dosage could be important for the regulation of DDAH. As described above, *datA* translocation to

terC causes excess initiations in rich medium, but not in poor medium (Kitagawa et al., 1998).

DARS SYSTEM

Function

In *E. coli*, ATP-DnaA is produced by binding of apo-DnaA to ATP, which is abundant in the cytosol (Bochner and Ames, 1982). Replication initiation occurs when the cellular level of ATP-DnaA reaches a peak that is high enough to enable assembly on *oriC* (Kurokawa et al., 1999). At least three mechanisms for production of apo-DnaA have been characterized: *de novo* DnaA synthesis; nucleotide dissociation from ADP-DnaA by acidic phospholipids in the cell membrane; and a mechanism involving specific chromosomal DNA elements termed DARS sites (**Figure 1**).

In *de novo* synthesis, newly translated apo-DnaA binds to ATP in the cytosol (**Figure 5A**). In addition to autoregulation by DnaA (Speck et al., 1999), transcription of *dnaA* is down-regulated by the SeqA-Dam system immediately after initiation (Campbell and Kleckner, 1990; Bogan and Helmstetter, 1997). This would contribute to the reduction in *de novo* DnaA synthesis (i.e., production of ATP-DnaA) immediately after initiation and maintain coordination between replication initiation and the cell cycle (Riber and Løbner-Olesen, 2005).

The *E. coli* cell membrane contains acidic phospholipids such as cardiolipin and phosphatidylglycerol that can promote dissociation of ADP or ATP from DnaA by interaction with DnaA domain III. These phospholipids can convert ADP-DnaA to ATP-DnaA *in vitro* (Saxena et al., 2013). In mutant cells with reduction of levels of acidic phospholipids, initiation from *oriC* is repressed (Fingland et al., 2012). The possibility that acidic phospholipids regulate DnaA activity during the cell cycle deserves to be further investigated.

The *DARS1* and *DARS2* chromosomal DNA sequences promote dissociation of ADP from ADP-DnaA, stimulating nucleotide exchange and increasing levels of ATP-DnaA, thereby stimulating replication initiation (Fujimitsu et al., 2009; Kasho et al., 2014; **Figures 1**, **5A**). *In vitro*, *DARS1* can promote ADP dissociation of ADP-DnaA without additional factors, whereas *DARS2* has little activity by itself, but is substantially activated by IHF and Fis, which binds site-specifically and bends DNA by $<60°$ (Fujimitsu et al., 2009; Kasho et al., 2014; **Figure 1B**). In cells, *DARS1* and *DARS2* both have stimulatory roles in ATP-DnaA production and replication initiation, and the deletion of either or both delays initiation (Fujimitsu et al., 2009; Kasho et al., 2014). Deletion of *DARS2* inhibits timely initiation more severely than deletion of *DARS1*, causing asynchronous initiations, and consistently, oversupply of *DARS2* has a greater effect than oversupply of *DARS1* on stimulation of extra initiations, which can cause inhibition of cell growth (Fujimitsu et al., 2009; Kasho et al., 2014). Deletion of *DARS2,* substitution of the IBS or Fis-binding site (FBS), or deletion of Fis gene decreases the cellular ATP-DnaA level more than deletion of *DARS1* under RIDA-deficient conditions (Fujimitsu et al., 2009; Kasho et al., 2014; **Figure 1B**). These observations suggest that the complex formed by *DARS2*, IHF, and Fis is important for increasing the level of ATP-DnaA and determining initiation timing, and that *DARS1* might maintain basal levels of ATP-DnaA.

Structure of *DARS1* and *DARS2*

A common structural feature of *DARS1* (101 bp) and *DARS2* (455 bp) is the presence of a core region containing three DnaA boxes (DnaA boxes I, II, and III): the spacing between these boxes is the same at both *DARS1* and *DARS2*, and box I has the opposite orientation to boxes II and III (**Figure 1B**). In addition to the core regions, *DARS1* and *DARS2* have regulatory regions of different lengths. The ∼50 bp regulatory region of *DARS1* enhances DnaA-ADP-dissociation activity *in vitro*, but its role *in vivo* has not been determined (Fujimitsu et al., 2009). The ∼400 bp *DARS2* regulatory region contains the IBS and FBS, which stimulate ADP-DnaA assembly on *DARS2* and are essential for ADP dissociation from DnaA (Kasho et al., 2014).

Mechanism

Unlike *oriC* or *datA*, DARS sites preferentially bind ADP-DnaA rather than ATP-DnaA. Notably, head-to-head (but not head-to-tail) interactions would occur between the box I-bound DnaA and the box II-bound DnaA, which is a prominent feature at DARS sites (**Figures 1B**, **6B**). Formation of oligomers of four or more ADP-DnaA molecules on the *DARS2* core region depends on DnaA AID-2 Leu290, and results in dissociation of ADP (**Figure 6B**). Formation of similar oligomers on the *DARS1* core region promotes dissociation of ADP and is dependent on DnaA AAA+ sensor 1 Asp269, which would participate in probable heat-dependent conformational change of the DnaA nucleotide-binding pocket (Fujimitsu et al., 2009). DnaA sensor 1 Asp269 is dispensable for ADP dissociation at *DARS2* (Kasho et al., 2014), possibly because of still unknown functions of the activator proteins IHF and Fis (**Figure 6B**). Dissociation of ADP produces apo-DnaA molecules that are unstable in binding to the DARS core region, enabling ATP binding and the production of ATP-DnaA (Fujimitsu et al., 2009; Kasho et al., 2014).

Binding of IHF is essential for *DARS2* activity, and, as with DDAH, IHF cannot be replaced by HU. The complex of *DARS2*–IHF–Fis promotes ∼10 times as much ADP dissociation as *DARS1 in vitro* (Kasho et al., 2014). The results of mutational analyses indicate that the spacing between the core-region DnaA boxes, IBS, and FBS is optimized for efficient activation of *DARS2* (Kasho et al., 2014). The sequences and lengths of the spaces between the *DARS2* core region, IBS, and FBS are highly conserved in *E. coli*-proximal β- or γ-proteobacterial species in which IHF and Fis homologs are conserved, suggesting that the regulatory mechanism for *DARS2* is shared among proteobacterial species, including pathogenic species (Kasho et al., 2014).

Regulation

Cell-Cycle-Dependent IHF Binding

IHF binding to *DARS2* is dynamically regulated in a cell-cycle-coordinated manner (Kasho et al., 2014). In contrast to *datA*–IHF binding, *DARS2*–IHF binding occurs specifically in the pre-initiation period, consistent with its role in timely production

of ATP-DnaA for replication initiation (Kasho et al., 2014). Regulation of *DARS2*–IHF binding and dissociation is resistant to rifampicin (Kasho et al., 2014), suggesting that it is independent of transcription. The timing of *DARS2*–IHF binding is also independent of replication initiation at *oriC* or replication fork progression (Kasho et al., 2014), supporting the suggestion that functional activation of *DARS2* might be controlled by specific cell cycle (but not DNA replication)-coupled events.

Growth-Phase-Dependent Fis Binding

In addition to cell-cycle regulation, growth-phase-dependent regulation contributes to timely activation of *DARS2*. The cellular level of Fis increases specifically in the exponential-growth phase (Ali Azam et al., 1999; Dillon and Dorman, 2010; **Figure 5B**). Fis binding to *DARS2* occurs in the exponential phase, but not in the stationary phase (Kasho et al., 2014). The activation of *DARS2* only in exponential phase is consistent with the requirement for ATP-DnaA for replication initiation.

Chromosomal-Position Effect

Escherichia coli DARS1 (101 bp) and *DARS2* (455 bp) are both located in intergenic regions, at 17.5 min (0.81 Mb position) and 64.0 min (2.97 Mb position), respectively, between *oriC* and *terC* (**Figure 1A**), and these positions are well conserved among related bacteria (Fujimitsu et al., 2009; Kasho et al., 2014; Frimodt-Møller et al., 2015). Translocation of *DARS2* to a *terC*-proximal locus moderately inhibits the timing of initiation, as does its translocation to an *oriC*-proximal locus (Frimodt-Møller et al., 2016; Inoue et al., 2016). Inhibition at the *terC*-proximal locus is sustained in cells lacking MatP, a DNA-binding protein involved in formation of *terC*-specific subchromosomal structure (Mercier et al., 2008; Inoue et al., 2016). The results of 3C (chromosome-conformation-capture) analysis suggest that *oriC* can physically interact with the wild-type *DARS2* locus (Cagliero et al., 2013). These results suggest that the chromosomal location of *DARS2* might be important for efficient interaction with *oriC*. In addition, a specific local chromosomal structure might be important for DARS function.

DnaA activation by *DARS1* and *DARS2* stimulates efficient cell growth under nutrient-poor conditions, and colonization of the large intestine of streptomycin-treated mice (Frimodt-Møller et al., 2015), suggesting a requirement for *DARS1* and *DARS2* for environmental adaptation of *E. coli*. Stimulation of replication initiation by oversupply of *DARS2* has more severe effects on viability under aerobic conditions than under anaerobic conditions (Charbon et al., 2014), suggesting that over-initiation in aerobic conditions leads to lethal levels of encounters between replication forks and sites of oxidative damage (Charbon et al., 2017).

PERSPECTIVES FOR COUPLING BETWEEN DnaA REGULATION AND CELL GROWTH IN *E. coli*

During the *E. coli* cell cycle, levels of ATP-DnaA rise to a peak that induces replication initiation, after which they fall, predominantly as a result of RIDA, a replication-coupled negative-feedback mechanism (Katayama et al., 2010). In the pre-initiation period, *DARS2* is predominant in the conversion of ADP-DnaA to ATP-DnaA. IHF binding to *DARS2* promotes this activity in a timely manner, but IHF is abundant throughout the cell cycle, and the mechanism responsible for its timely binding and dissociation is not yet known. Similarly, the mechanism responsible for the regulation of *datA*–IHF binding, which occurs at a specific time after replication initiation, has not yet been determined. Further studies are required to determine which mechanisms contribute to coupling between these processes and cell-cycle progression. In addition, further studies are required to understand DnaA complex formation/dissociation, ADP dissociation, and ATP hydrolysis during DDAH and in the formation of protein complexes at DARS sites.

Chromosomal positioning of *DARS1*, *DARS2*, and *datA* is important for regulation of the timing of initiation under specific growth conditions. Chromosomal structural determinants such as superhelicity, co-localization of specific loci in the 3D chromosomal structure, or the timing of changes in copy number during replication that is related to the distance from *oriC* might all contribute to the importance of chromosomal location. Further studies can help to determine which of these mechanisms is relevant for the correct timing of replication initiation.

How DnaB helicase binding to *oriC*-DnaA complexes *in vivo* is regulated is an open question. Even in the presence of a high ATP-DnaA level and *oriC* DUE unwinding, DnaB helicase might still not be able to be bind to *oriC*-DnaA complexes because of the stable interaction between DiaA and DnaA. Further studies of the regulatory mechanisms governing the DiaA binding/dissociation to/from DnaA and DnaB helicase loading *in vivo* are required to understand fully how initiation is timed correctly during the cell cycle.

Intensive research over the last 40 years has increased knowledge of the factors and regulatory mechanisms involved in chromosome replication initiation in *E. coli*. Our knowledge has exploded, and it is possible today to provide a considerably detailed outline about the factors involved and how replication initiation is controlled. At the same time, such progress creates further important mysteries, too. Further work in this area will undoubtedly continue to surprise and inform us about how replication is controlled in this erstwhile considered simple organism and advance knowledge about how this process is controlled in other organisms as well.

AUTHOR CONTRIBUTIONS

All authors listed have made a substantial, direct and intellectual contribution to the work, and approved it for publication.

FUNDING

This work was supported by MEXT/JSPS KAKENHI Grant numbers 17H03656, 16H00775, 15K18479 and 17K07338.

REFERENCES

Abe, Y., Jo, T., Matsuda, Y., Matsunaga, C., Katayama, T., and Ueda, T. (2007). Structure and function of DnaA N-terminal domains: specific sites and mechanisms in inter-DnaA interaction and in DnaB helicase loading on *oriC*. *J. Biol. Chem.* 282, 17816–17827. doi: 10.1074/jbc.M701841200

Ali Azam, T., Iwata, A., Nishimura, A., Ueda, S., and Ishihama, A. (1999). Growth phase-dependent variation in protein composition of the *Escherichia coli* nucleoid. *J. Bacteriol.* 181, 6361–6370.

Baker, T. A., and Kornberg, A. (1988). Transcriptional activation of initiation of replication from the *E. coli* chromosomal origin: an RNA-DNA hybrid near *oriC*. *Cell* 55, 113–123. doi: 10.1016/0092-8674(88)90014-1

Baxter, J. C., and Sutton, M. D. (2012). Evidence for roles of the *Escherichia coli* Hda protein beyond regulatory inactivation of DnaA. *Mol. Microbiol.* 85, 648–668. doi: 10.1111/j.1365-2958.2012.08129.x

Bell, S. P., and Kaguni, J. M. (2013). Helicase loading at chromosomal origins of replication. *Cold Spring Harb. Perspect. Biol.* 5:a010124. doi: 10.1101/cshperspect.a010124

Blaesing, F., Weigel, C., Welzeck, M., and Messer, W. (2000). Analysis of the DNA-binding domain of *Escherichia coli* DnaA protein. *Mol. Microbiol.* 36, 557–569. doi: 10.1046/j.1365-2958.2000.01881.x

Bochner, B. R., and Ames, B. N. (1982). Complete analysis of cellular nucleotides by two-dimensional thin layer chromatography. *J. Biol. Chem.* 257, 9759–9769.

Bogan, J. A., and Helmstetter, C. E. (1997). DNA sequestration and transcription in the *oriC* region of *Escherichia coli*. *Mol. Microbiol.* 26, 889–896. doi: 10.1046/j.1365-2958.1997.6221989.x

Bramhill, D., and Kornberg, A. (1988). A model for initiation at origins of DNA replication. *Cell* 54, 915–918. doi: 10.1016/0092-8674(88)90102-X

Cagliero, C., Grand, R. S., Jones, M. B., Jin, D. J., and O'Sullivan, J. M. (2013). Genome conformation capture reveals that the *Escherichia coli* chromosome is organized by replication and transcription. *Nucleic Acids Res.* 41, 6058–6071. doi: 10.1093/nar/gkt325

Campbell, J. L., and Kleckner, N. (1990). *E. coli oriC* and the *dnaA* gene promoter are sequestered from dam methyltransferase following the passage of the chromosomal replication fork. *Cell* 62, 967–979. doi: 10.1016/0092-8674(90)90271-F

Charbon, G., Bjørn, L., Mendoza-Chamizo, B., Frimodt-Møller, J., and Løbner-Olesen, A. (2014). Oxidative DNA damage is instrumental in hyperreplication stress-induced inviability of *Escherichia coli*. *Nucleic Acids Res.* 42, 13228–13241. doi: 10.1093/nar/gku1149

Charbon, G., Campion, C., Chan, S. H. J., Bjørn, L., Weimann, A., da Silva, L. C. N., et al. (2017). Rewiring of energy metabolism promotes viability during hyperreplication stress in *E. coli*. *PLOS Genet.* 13:e1006590. doi: 10.1371/journal.pgen.1006590

Chodavarapu, S., Felczak, M. M., and Kaguni, J. M. (2011). Two forms of ribosomal protein L2 of *Escherichia coli* that inhibit DnaA in DNA replication. *Nucleic Acids Res.* 39, 4180–4191. doi: 10.1093/nar/gkq120

Chodavarapu, S., Felczak, M. M., Rouvière-Yaniv, J., and Kaguni, J. M. (2008a). *Escherichia coli* DnaA interacts with HU in initiation at the *E. coli* replication origin. *Mol. Microbiol.* 67, 781–792. doi: 10.1111/j.1365-2958.2007.06094.x

Chodavarapu, S., Gomez, R., Vicente, M., and Kaguni, J. M. (2008b). *Escherichia coli* Dps interacts with DnaA protein to impede initiation: a model of adaptive mutation. *Mol. Microbiol.* 67, 1331–1346. doi: 10.1111/j.1365-2958.2008.06127.x

Dillon, S. C., and Dorman, C. J. (2010). Bacterial nucleoid-associated proteins, nucleoid structure and gene expression. *Nat. Rev. Microbiol.* 8, 185–195. doi: 10.1038/nrmicro2261

Duderstadt, K. E., Chuang, K., and Berger, J. M. (2011). DNA stretching by bacterial initiators promotes replication origin opening. *Nature* 478, 209–213. doi: 10.1038/nature10455

Dueber, E. L. C., Corn, J. E., Bell, S. D., and Berger, J. M. (2007). Replication origin recognition and deformation by a heterodimeric archaeal Orc1 complex. *Science* 317, 1210–1213. doi: 10.1126/science.1143690

Erzberger, J. P., Pirruccello, M. M., and Berger, J. M. (2002). The structure of bacterial DnaA: implications for general mechanisms underlying DNA replication initiation. *EMBO J.* 21, 4763–4773. doi: 10.1093/emboj/cdf496

Felczak, M. M., and Kaguni, J. M. (2004). The box VII motif of *Escherichia coli* DnaA protein is required for DnaA oligomerization at the *E. coli* replication origin. *J. Biol. Chem.* 279, 51156–51162. doi: 10.1074/jbc.M409695200

Felczak, M. M., Simmons, L. A., and Kaguni, J. M. (2005). An essential tryptophan of *Escherichia coli* DnaA protein functions in oligomerization at the *E. coli* replication origin. *J. Biol. Chem.* 280, 24627–24633. doi: 10.1074/jbc.M503684200

Fingland, N., Flåtten, I., Downey, C. D., Fossum-Raunehaug, S., Skarstad, K., and Crooke, E. (2012). Depletion of acidic phospholipids influences chromosomal replication in *Escherichia coli*. *Microbiology* 1, 450–466. doi: 10.1002/mbo3.46

Flåtten, I., Fossum-Raunehaug, S., Taipale, R., Martinsen, S., and Skarstad, K. (2015). The DnaA protein is not the limiting factor for initiation of replication in *Escherichia coli*. *PLOS Genet.* 11:e1005276. doi: 10.1371/journal.pgen.1005276

Frimodt-Møller, J., Charbon, G., Krogfelt, K. A., and Løbner-Olesen, A. (2015). Control regions for chromosome replication are conserved with respect to sequence and location among *Escherichia coli* strains. *Front. Microbiol.* 6:1011. doi: 10.3389/fmicb.2015.01011

Frimodt-Møller, J., Charbon, G., Krogfelt, K. A., and Løbner-Olesen, A. (2016). DNA replication control is linked to genomic positioning of control regions in *Escherichia coli*. *PLOS Genet.* 12:e1006286. doi: 10.1371/journal.pgen.1006286

Fujikawa, N., Kurumizaka, H., Nureki, O., Terada, T., Shirouzu, M., Katayama, T., et al. (2003). Structural basis of replication origin recognition by the DnaA protein. *Nucleic Acids Res.* 31, 2077–2086. doi: 10.1093/nar/gkg309

Fujimitsu, K., Senriuchi, T., and Katayama, T. (2009). Specific genomic sequences of *E. coli* promote replicational initiation by directly reactivating ADP-DnaA. *Genes Dev.* 23, 1221–1233. doi: 10.1101/gad.1775809

Fujimitsu, K., Su'etsugu, M., Yamaguchi, Y., Mazda, K., Fu, N., Kawakami, H., et al. (2008). Modes of overinitiation, *dnaA* gene expression, and inhibition of cell division in a novel cold-sensitive *hda* mutant of *Escherichia coli*. *J. Bacteriol.* 190, 5368–5381. doi: 10.1128/JB.00044-08

Garner, J., and Crooke, E. (1996). Membrane regulation of the chromosomal replication activity of *E. coli* DnaA requires a discrete site on the protein. *EMBO J.* 15, 2313–2321.

Grimwade, J. E., Ryan, V. T., and Leonard, A. C. (2000). IHF redistributes bound initiator protein, DnaA, on supercoiled *oriC* of *Escherichia coli*. *Mol. Microbiol.* 35, 835–844. doi: 10.1046/j.1365-2958.2000.01755.x

Hansen, F. G., Christensen, B. B., and Atlung, T. (2007). Sequence characteristics required for cooperative binding and efficient *in vivo* titration of the replication initiator protein DnaA in *E. coli*. *J. Mol. Biol.* 367, 942–952. doi: 10.1016/j.jmb.2007.01.056

Higgins, C. F., Dorman, C. J., Stirling, D. A., Waddell, L., Booth, I. R., May, G., et al. (1988). A physiological role for DNA supercoiling in the osmotic regulation of gene expression in *S. typhimurium* and *E. coli*. *Cell* 52, 569–584.

Hwang, D. S., and Kornberg, A. (1992). Opening of the replication origin of *Escherichia coli* by DnaA protein with protein HU or IHF. *J. Biol. Chem.* 267, 23083–23086.

Inoue, Y., Tanaka, H., Kasho, K., Fujimitsu, K., Oshima, T., and Katayama, T. (2016). Chromosomal location of the DnaA-reactivating sequence *DARS2* is important to regulate timely initiation of DNA replication in *Escherichia coli*. *Genes Cells* 21, 1015–1023. doi: 10.1111/gtc.12395

Ishida, T., Akimitsu, N., Kashioka, T., Hatano, M., Kubota, T., Ogata, Y., et al. (2004). DiaA, a novel DnaA-binding protein, ensures the initiation timing of *E. coli* chromosome replication. *J. Biol. Chem.* 279, 45546–45555. doi: 10.1074/jbc.M402762200

Iyer, L. M., Leipe, D. D., Koonin, E. V., and Aravind, L. (2004). Evolutionary history and higher order classification of AAA+ ATPases. *J. Struct. Biol.* 146, 11–31. doi: 10.1016/j.jsb.2003.10.010

Kaguni, J. M. (2011). Replication initiation at the *Escherichia coli* chromosomal origin. *Curr. Opin. Chem. Biol.* 15, 606–613. doi: 10.1016/j.cbpa.2011.07.016

Kano, Y., and Imamoto, F. (1990). Requirement of integration host factor (IHF) for growth of *Escherichia coli* deficient in HU protein. *Gene* 89, 133–137. doi: 10.1016/0378-1119(90)90216-E

Kasho, K., Fujimitsu, K., Matoba, T., Oshima, T., and Katayama, T. (2014). Timely binding of IHF and Fis to *DARS2* regulates ATP-DnaA production and replication initiation. *Nucleic Acids Res.* 42, 13134–13149. doi: 10.1093/nar/gku1051

Kasho, K., and Katayama, T. (2013). DnaA binding locus *datA* promotes DnaA-ATP hydrolysis to enable cell cycle-coordinated replication initiation. *Proc. Natl. Acad. Sci. U.S.A.* 110, 936–941. doi: 10.1073/pnas.1212070110

Kasho, K., Tanaka, H., Sakai, R., and Katayama, T. (2017). Cooperative DnaA binding to the negatively supercoiled *datA* locus stimulates DnaA-ATP hydrolysis. *J. Biol. Chem.* 292, 1251–1266. doi: 10.1074/jbc.M116.762815

Katayama, T., Kubota, T., Kurokawa, K., Crooke, E., and Sekimizu, K. (1998). The initiator function of DnaA protein is negatively regulated by the sliding clamp of the *E. coli* chromosomal replicase. *Cell* 94, 61–71.

Katayama, T., Ozaki, S., Keyamura, K., and Fujimitsu, K. (2010). Regulation of the replication cycle: conserved and diverse regulatory systems for DnaA and *oriC*. *Nat. Rev. Microbiol.* 8, 163–170. doi: 10.1038/nrmicro2314

Kato, J., and Katayama, T. (2001). Hda, a novel DnaA-related protein, regulates the replication cycle in *Escherichia coli*. *EMBO J.* 20, 4253–4262. doi: 10.1093/emboj/20.15.4253

Kaur, G., Vora, M. P., Czerwonka, C. A., Rozgaja, T. A., Grimwade, J. E., and Leonard, A. C. (2014). Building the bacterial orisome: high-affinity DnaA recognition plays a role in setting the conformation of *oriC* DNA. *Mol. Microbiol.* 91, 1148–1163. doi: 10.1111/mmi.12525

Kawakami, H., Keyamura, K., and Katayama, T. (2005). Formation of an ATP-DnaA-specific initiation complex requires DnaA Arginine 285, a conserved motif in the AAA+ protein family. *J. Biol. Chem.* 280, 27420–27430. doi: 10.1074/jbc.M502764200

Kawakami, H., Su'etsugu, M., and Katayama, T. (2006). An isolated Hda-clamp complex is functional in the regulatory inactivation of DnaA and DNA replication. *J. Struct. Biol.* 156, 220–229. doi: 10.1016/j.jsb.2006.02.007

Keyamura, K., Abe, Y., Higashi, M., Ueda, T., and Katayama, T. (2009). DiaA dynamics are coupled with changes in initial origin complexes leading to helicase loading. *J. Biol. Chem.* 284, 25038–25050. doi: 10.1074/jbc.M109.002717

Keyamura, K., Fujikawa, N., Ishida, T., Ozaki, S., Su'etsugu, M., Fujimitsu, K., et al. (2007). The interaction of DiaA and DnaA regulates the replication cycle in *E. coli* by directly promoting ATP-DnaA-specific initiation complexes. *Genes Dev.* 21, 2083–2099. doi: 10.1101/gad.1561207

Keyamura, K., and Katayama, T. (2011). DnaA protein DNA-binding domain binds to Hda protein to promote inter-AAA+ domain interaction involved in regulatory inactivation of DnaA. *J. Biol. Chem.* 286, 29336–29346. doi: 10.1074/jbc.M111.233403

Kim, J. S., Nanfara, M. T., Chodavarapu, S., Jin, K. S., Babu, V. M. P., Ghazy, M. A., et al. (2017). Dynamic assembly of Hda and the sliding clamp in the regulation of replication licensing. *Nucleic Acids Res.* 45, 3888–3905. doi: 10.1093/nar/gkx081

Kitagawa, R., Mitsuki, H., Okazaki, T., and Ogawa, T. (1996). A novel DnaA protein-binding site at 94.7 min on the *Escherichia coli* chromosome. *Mol. Microbiol.* 19, 1137–1147. doi: 10.1046/j.1365-2958.1996.453983.x

Kitagawa, R., Ozaki, T., Moriya, S., and Ogawa, T. (1998). Negative control of replication initiation by a novel chromosomal locus exhibiting exceptional affinity for *Escherichia coli* DnaA protein. *Genes Dev.* 12, 3032–3043. doi: 10.1101/gad.12.19.3032

Kurokawa, K., Nishida, S., Emoto, A., Sekimizu, K., and Katayama, T. (1999) Replication cycle-coordinated change of the adenine nucleotide-bound forms of DnaA protein in *Escherichia coli*. *EMBO J.* 18, 6642–6652. doi: 10.1093/emboj/18.23.6642

Leonard, A. C., and Grimwade, J. E. (2015). The orisome: structure and function. *Front. Microbiol.* 6:545. doi: 10.3389/fmicb.2015.00545

Li, S., Zhang, Q., Xu, Z., and Yao, Y. (2017). Acetylation of lysine 243 inhibits the *oriC* binding ability of DnaA in *Escherichia coli*. *Front. Microbiol.* 8:699. doi: 10.3389/fmicb.2017.00699

Lu, M., Campbell, J. L., Boye, E., and Kleckner, N. (1994). SeqA: a negative modulator of replication initiation in *E. coli*. *Cell* 77, 413–426. doi: 10.1016/0092-8674(94)90156-2

Margulies, C., and Kaguni, J. M. (1998). The FIS protein fails to block the binding of DnaA protein to *oriC*, the *Escherichia coli* chromosomal origin. *Nucleic Acids Res.* 26, 5170–5175. doi: 10.1093/nar/26.22.5170

McGarry, K. C., Ryan, V. T., Grimwade, J. E., and Leonard, A. C. (2004). Two discriminatory binding sites in the *Escherichia coli* replication origin are required for DNA strand opening by initiator DnaA-ATP. *Proc. Natl. Acad. Sci. U.S.A.* 101, 2811–2816. doi: 10.1073/pnas.0400340101

Mercier, R., Petit, M. A., Schbath, S., Robin, S., El Karoui, M., Boccard, F., et al. (2008). The MatP/*matS* site-specific system organizes the terminus region of the *E. coli* chromosome into a macrodomain. *Cell* 135, 475–485. doi: 10.1016/j.cell.2008.08.031

Messer, W. (2002). The bacterial replication initiator DnaA. DnaA and oriC, the bacterial mode to initiate DNA replication. *FEMS Microbiol. Rev.* 26, 355–374.

Messer, W., and Weigel, C. (1997). DnaA initiator–also a transcription factor. *Mol. Microbiol.* 24, 1–6. doi: 10.1046/j.1365-2958.1997.3171678.x

Miller, D. T., Grimwade, J. E., Betteridge, T., Rozgaja, T., Torgue, J. J., and Leonard, A. C. (2009). Bacterial origin recognition complexes direct assembly of higher-order DnaA oligomeric structures. *Proc. Natl. Acad. Sci. U.S.A.* 106, 18479–18484. doi: 10.1073/pnas.0909472106

Morigen, Løbner-Olesen, A., and Skarstad, K. (2003). Titration of the *Escherichia coli* DnaA protein to excess *datA* sites causes destabilization of replication forks, delayed replication initiation and delayed cell division. *Mol. Microbiol.* 50, 349–362. doi: 10.1046/j.1365-2958.2003.03695.x

Morigen, Skarstad, K., and Molina, F. (2005). Deletion of the *datA* site does not affect once-per-cell-cycle timing but induces rifampin-resistant replication. *J. Bacteriol.* 187, 3913–3920. doi: 10.1128/JB.187.12.3913-3920.2005

Morigen, M., Flåtten, I., and Skarstad, K. (2014). The *Escherichia coli datA* site promotes proper regulation of cell division. *Microbiology* 160, 703–710. doi: 10.1099/mic.0.074898-0

Mott, M. L., Erzberger, J. P., Coons, M. M., and Berger, J. M. (2008). Structural synergy and molecular crosstalk between bacterial helicase loaders and replication initiators. *Cell* 135, 623–634. doi: 10.1016/j.cell.2008.09.058

Nishida, S., Fujimitsu, K., Sekimizu, K., Ohmura, T., Ueda, T., and Katayama, T. (2002). A nucleotide switch in the *Escherichia coli* DnaA protein initiates chromosomal replication: evidence from a mutant DnaA protein defective in regulatory ATP hydrolysis *in vitro* and *in vivo*. *J. Biol. Chem.* 277, 14986–14995. doi: 10.1074/jbc.M108303200

Noguchi, Y., and Katayama, T. (2016). The *Escherichia coli* cryptic prophage protein YfdR binds to DnaA and initiation of chromosomal replication is inhibited by overexpression of the gene cluster *yfdQ-yfdR-yfdS-yfdT*. *Front. Microbiol.* 7:239. doi: 10.3389/fmicb.2016.00239

Noguchi, Y., Sakiyama, Y., Kawakami, H., and Katayama, T. (2015). The Arg fingers of key DnaA protomers are oriented inward within the replication origin *oriC* and stimulate DnaA subcomplexes in the initiation complex. *J. Biol. Chem.* 290, 20295–20312. doi: 10.1074/jbc.M115.662601

Nozaki, S., and Ogawa, T. (2008). Determination of the minimum domain II size of *Escherichia coli* DnaA protein essential for cell viability. *Microbiology* 154, 3379–3384. doi: 10.1099/mic.0.2008/019745-0

Nozaki, S., Yamada, Y., and Ogawa, T. (2009). Initiator titration complex formed at *datA* with the aid of IHF regulates replication timing in *Escherichia coli*. *Genes Cells* 14, 329–341. doi: 10.1111/j.1365-2443.2008.01269.x

Obita, T., Iwura, T., Su'etsugu, M., Yoshida, Y., Tanaka, Y., Katayama, T., et al. (2002). Determination of the secondary structure in solution of the *Escherichia coli* DnaA DNA-binding domain. *Biochem. Biophys. Res. Commun.* 299, 42–48. doi: 10.1016/S0006-291X(02)02590-1

Ogawa, T., Yamada, Y., Kuroda, T., Kishi, T., and Moriya, S. (2002). The *datA* locus predominantly contributes to the initiator titration mechanism in the control of replication initiation in *Escherichia coli*. *Mol. Microbiol.* 44, 1367–1375. doi: 10.1046/j.1365-2958.2002.02969.x

Okumura, H., Yoshimura, M., Ueki, M., Oshima, T., Ogasawara, N., and Ishikawa, S. (2012). Regulation of chromosomal replication initiation by *oriC*-proximal DnaA-box clusters in *Bacillus subtilis*. *Nucleic Acids Res.* 40, 220–234. doi: 10.1093/nar/gkr716

Olliver, A., Saggioro, C., Herrick, J., and Sclavi, B. (2010). DnaA-ATP acts as a molecular switch to control levels of ribonucleotide reductase expression in *Escherichia coli*. *Mol. Microbiol.* 76, 1555–1571. doi: 10.1111/j.1365-2958.2010.07185.x

Ozaki, S., and Katayama, T. (2009). DnaA structure, function, and dynamics in the initiation at the chromosomal origin. *Plasmid* 62, 71–82. doi: 10.1016/j.plasmid.2009.06.003

Ozaki, S., and Katayama, T. (2012). Highly organized DnaA-*oriC* complexes recruit the single-stranded DNA for replication initiation. *Nucleic Acids Res.* 40, 1648–1665. doi: 10.1093/nar/gkr832

Ozaki, S., Kawakami, H., Nakamura, K., Fujikawa, N., Kagawa, W., Park, S.-Y., et al. (2008). A common mechanism for the ATP-DnaA-dependent formation of open complexes at the replication origin. *J. Biol. Chem.* 283, 8351–8362. doi: 10.1074/jbc.M708684200

Ozaki, S., Noguchi, Y., Hayashi, Y., Miyazaki, E., and Katayama, T. (2012a). Differentiation of the DnaA-*oriC* subcomplex for DNA unwinding in a replication initiation complex. *J. Biol. Chem.* 287, 37458–37471. doi: 10.1074/jbc.M112.372052

Ozaki, S., Noguchi, Y., Nishimura, M., and Katayama, T. (2012b). Stable nucleotide binding to DnaA requires a specific glutamic acid residue within the AAA+ box II motif. *J. Struct. Biol.* 179, 242–250. doi: 10.1016/j.jsb.2012.05.001

Riber, L., Frimodt-Møller, J., Charbon, G., and Løbner-Olesen, A. (2016). Multiple DNA binding proteins contribute to timing of chromosome replication in *E. coli*. *Front. Mol. Biosci.* 3:29. doi: 10.3389/fmolb.2016.00029

Riber, L., and Løbner-Olesen, A. (2005). Coordinated replication and sequestration of oriC and dnaA are required for maintaining controlled once-per-cell-cycle initiation in *Escherichia coli*. *J. Bacteriol.* 187, 5605–5613. doi: 10.1128/JB.187.16.5605-5613.2005

Richardson, T. T., Harran, O., and Murray, H. (2016). The bacterial DnaA-trio replication origin element specifies single-stranded DNA initiator binding. *Nature* 534, 412–416. doi: 10.1038/nature17962

Roth, A., and Messer, W. (1998). High-affinity binding sites for the initiator protein DnaA on the chromosome of *Escherichia coli*. *Mol. Microbiol.* 28, 395–401. doi: 10.1046/j.1365-2958.1998.00813.x

Rozgaja, T. A., Grimwade, J. E., Iqbal, M., Czerwonka, C., Vora, M., and Leonard, A. C. (2011). Two oppositely oriented arrays of low-affinity recognition sites in *oriC* guide progressive binding of DnaA during *Escherichia coli* pre-RC assembly. *Mol. Microbiol.* 82, 475–488. doi: 10.1111/j.1365-2958.2011.07827.x

Sakiyama, Y., Kasho, K., Noguchi, Y., Kawakami, H., and Katayama, T. (2017). Regulatory dynamics in the ternary DnaA complex for initiation of chromosomal replication in *Escherichia coli*. *Nucleic Acids Res.* 45, 12354–12373. doi: 10.1093/nar/gkx914

Samitt, C. E., Hansen, F. G., Miller, J. F., and Schaechter, M. (1989). *In vivo* studies of DnaA binding to the origin of replication of *Escherichia coli*. *EMBO J.* 8, 989–993.

Saxena, R., Fingland, N., Patil, D., Sharma, A. K., and Crooke, E. (2013). Crosstalk between DnaA protein, the initiator of *Escherichia coli* chromosomal replication, and acidic phospholipids present in bacterial membranes. *Int. J. Mol. Sci.* 14, 8517–8537. doi: 10.3390/ijms14048517

Saxena, R., Rozgaja, T., Grimwade, J., and Crooke, E. (2011). Remodeling of nucleoprotein complexes is independent of the nucleotide state of a mutant AAA+ protein. *J. Biol. Chem.* 286, 33770–33777. doi: 10.1074/jbc.M111.223495

Saxena, R., Vasudevan, S., Patil, D., Ashoura, N., Grimwade, J. E., and Crooke, E. (2015). Nucleotide-induced conformational changes in *Escherichia coli* DnaA protein are required for bacterial ORC to pre-RC conversion at the chromosomal origin. *Int. J. Mol. Sci.* 16, 27897–27911. doi: 10.3390/ijms161126064

Schenk, K., Hervás, A. B., Rösch, T. C., Eisemann, M., Schmitt, B. A., Dahlke, S., et al. (2017). Rapid turnover of DnaA at replication origin regions contributes to initiation control of DNA replication. *PLOS Genet.* 13:e1006561. doi: 10.1371/journal.pgen.1006561

Sekimizu, K., Bramhill, D., and Kornberg, A. (1987). ATP activates dnaA protein in initiating replication of plasmids bearing the origin of the *E. coli* chromosome. *Cell* 50, 259–265. doi: 10.1016/0092-8674(87)90221-2

Sekimizu, K., Bramhill, D., and Kornberg, A. (1988). Sequential early stages in the in vitro initiation of replication at the origin of the *Escherichia coli* chromosome. *J. Biol. Chem.* 263, 7124–7130.

Shimizu, M., Noguchi, Y., Sakiyama, Y., Kawakami, H., Katayama, T., and Takada, S. (2016). Near-atomic structural model for bacterial DNA replication initiation complex and its functional insights. *Proc. Natl. Acad. Sci. U.S.A.* 113, E8021–E8030. doi: 10.1073/pnas.1609649113

Simmons, L. A., Felczak, M., and Kaguni, J. M. (2003). DnaA Protein of *Escherichia coli*: oligomerization at the *E. coli* chromosomal origin is required for initiation and involves specific N-terminal amino acids. *Mol. Microbiol.* 49, 849–858. doi: 10.1046/j.1365-2958.2003.03603.x

Skarstad, K., and Katayama, T. (2013). Regulating DNA replication in bacteria. *Cold Spring Harb. Perspect. Biol.* 5:a012922. doi: 10.1101/cshperspect.a012922

Smulczyk-Krawczyszyn, A., Jakimowicz, D., Ruban-Osmialowska, B., Zawilak-Pawlik, A., Majka, J., Chater, K., et al. (2006). Cluster of DnaA boxes involved in regulation of *Streptomyces* chromosome replication: from *in silico* to *in vivo* studies. *J. Bacteriol.* 188, 6184–6194. doi: 10.1128/JB.00528-06

Speck, C., Weigel, C., and Messer, W. (1999). ATP- and ADP-dnaA protein, a molecular switch in gene regulation. *EMBO J.* 18, 6169–6176. doi: 10.1093/emboj/18.21.6169

Stauffer, M. E., and Chazin, W. J. (2004). Structural mechanisms of DNA replication, repair, and recombination. *J. Biol. Chem.* 279, 30915–30918. doi: 10.1074/jbc.R400015200

Su'etsugu, M., Harada, Y., Keyamura, K., Matsunaga, C., Kasho, K., Abe, Y., et al. (2013). The DnaA N-terminal domain interacts with Hda to facilitate replicase clamp-mediated inactivation of DnaA. *Environ. Microbiol.* 15, 3183–3195. doi: 10.1111/1462-2920.12147

Su'etsugu, M., Nakamura, K., Keyamura, K., Kudo, Y., and Katayama, T. (2008). Hda monomerization by ADP binding promotes replicase clamp-mediated DnaA-ATP hydrolysis. *J. Biol. Chem.* 283, 36118–36131. doi: 10.1074/jbc.M803158200

Sutton, M. D., Carr, K. M., Vicente, M., and Kaguni, J. M. (1998). *Escherichia coli* DnaA protein. The N-terminal domain and loading of DnaB helicase at the *E. coli* chromosomal origin. *J. Biol. Chem.* 273, 34255–34262. doi: 10.1074/jbc.273.51.34255

Sutton, M. D., and Kaguni, J. M. (1997). Threonine 435 of *Escherichia coli* DnaA protein confers sequence-specific DNA binding activity. *J. Biol. Chem.* 272, 23017–23024. doi: 10.1074/jbc.272.37.23017

Swinger, K. K., and Rice, P. A. (2004). IHF and HU: flexible architects of bent DNA. *Curr. Opin. Struct. Biol.* 14, 28–35. doi: 10.1016/j.sbi.2003.12.003

Tesfa-Selase, F., and Drabble, W. T. (1992). Regulation of the *gua* operon of *Escherichia coli* by the DnaA protein. *Mol. Gen. Genet.* 231, 256–264.

Travers, A., and Muskhelishvili, G. (2005). DNA supercoiling - a global transcriptional regulator for enterobacterial growth? *Nat. Rev. Microbiol.* 3, 157–169.

von Freiesleben, U., Rasmussen, K. V., Atlung, T., and Hansen, F. G. (2000). Rifampicin-resistant initiation of chromosome replication from *oriC* in *ihf* mutants. *Mol. Microbiol.* 37, 1087–1093. doi: 10.1046/j.1365-2958.2000.02060.x

Waldminghaus, T., and Skarstad, K. (2009). The *Escherichia coli* SeqA protein. *Plasmid* 61, 141–150. doi: 10.1016/j.plasmid.2009.02.004

Weigel, C., Messer, W., Preiss, S., Welzeck, M., Morigen, and Boye, E. (2001). The sequence requirements for a functional *Escherichia coli* replication origin are different for the chromosome and a minichromosome. *Mol. Microbiol.* 40, 498–507. doi: 10.1046/j.1365-2958.2001.02409.x

Wolański, M., Donczew, R., Zawilak-Pawlik, A., and Zakrzewska-Czerwińska, J. (2015). *oriC*-encoded instructions for the initiation of bacterial chromosome replication. *Front. Microbiol.* 5:735. doi: 10.3389/fmicb.2014.00735

Yoshida, Y., Obita, T., Kokusho, Y., Ohmura, T., Katayama, T., Ueda, T., et al. (2003). Identification of the region in *Escherichia coli* DnaA protein required for specific recognition of the DnaA box. *Cell. Mol. Life Sci.* 60, 1998–2008. doi: 10.1007/s00018-003-3176-7

Zhang, Q., Zhou, A., Li, S., Ni, J., Tao, J., Lu, J., et al. (2016). Reversible lysine acetylation is involved in DNA replication initiation by regulating activities of initiator DnaA in *Escherichia coli*. *Sci. Rep.* 6:30837. doi: 10.1038/srep30837

Zhou, H. X. (2001). The affinity-enhancing roles of flexible linkers in two-domain DNA-binding proteins. *Biochemistry* 40, 15069–15073. doi: 10.1021/bi015795g

Conflict of Interest Statement: The authors declare that the research was conducted in the absence of any commercial or financial relationships that could be construed as a potential conflict of interest.

frontiers in Microbiology

ORIGINAL RESEARCH
published: 26 July 2018
doi: 10.3389/fmicb.2018.01673

Low Affinity DnaA-ATP Recognition Sites in *E. coli oriC* Make Non-equivalent and Growth Rate-Dependent Contributions to the Regulated Timing of Chromosome Replication

*Prassanna Rao[1], Tania A. Rozgaja[2], Abdulaziz Alqahtani[1], Julia E. Grimwade[1] and Alan C. Leonard[1]**

[1] Department of Biological Sciences, Florida Institute of Technology, Melbourne, FL, United States, [2] AREVA Med, Plano, TX, United States

OPEN ACCESS

Edited by:
Arieh Zaritsky, Ben-Gurion University of the Negev, Israel

Reviewed by:
Flemming Gotfred Hansen, Technical University of Denmark, Denmark
Dhruba Chattoraj, National Institutes of Health (NIH), United States

***Correspondence:**
Alan C. Leonard
aleonard@fit.edu

Specialty section:
This article was submitted to Microbial Physiology and Metabolism, a section of the journal Frontiers in Microbiology

Received: *05 February 2018*
Accepted: *04 July 2018*
Published: *26 July 2018*

Citation:
Rao P, Rozgaja TA, Alqahtani A, Grimwade JE and Leonard AC (2018) Low Affinity DnaA-ATP Recognition Sites in E. coli oriC Make Non-equivalent and Growth Rate-Dependent Contributions to the Regulated Timing of Chromosome Replication. Front. Microbiol. 9:1673. doi: 10.3389/fmicb.2018.01673

Although the mechanisms that precisely time initiation of chromosome replication in bacteria remain unclear, most clock models are based on accumulation of the active initiator protein, DnaA-ATP. During each cell division cycle, sufficient DnaA-ATP must become available to interact with a distinct set of low affinity recognition sites in the unique chromosomal replication origin, *oriC*, and assemble the pre-replicative complex (orisome) that unwinds origin DNA and helps load the replicative helicase. The low affinity *oriC*-DnaA-ATP interactions are required for the orisome's mechanical functions, and may also play a role in timing of new rounds of DNA synthesis. To further examine this possibility, we constructed chromosomal *oriC*s with equal preference for DnaA-ADP or DnaA-ATP at one or more low affinity recognition sites, thereby lowering the DnaA-ATP requirement for orisome assembly, and measured the effect of the mutations on cell cycle timing of DNA synthesis. Under slow growth conditions, mutation of any one of the six low affinity DnaA-ATP sites in chromosomal *oriC* resulted in initiation earlier in the cell cycle, but the shift was not equivalent for every recognition site. Mutation of τ2 caused a greater change in initiation age, suggesting its occupation by DnaA-ATP is a temporal bottleneck during orisome assembly. In contrast, during rapid growth, all origins with a single mutated site displayed wild-type initiation timing. Based on these observations, we propose that *E. coli* uses two different, DnaA-ATP-dependent initiation timing mechanisms; a slow growth timer that is directly coupled to individual site occupation, and a fast growth timer comprising DnaA-ATP and additional factors that regulate DnaA access to *oriC*. Analysis of origins with paired mutated sites suggests that Fis is an important component of the fast growth timing mechanism.

Keywords: *oriC*, DnaA, DNA replication, replication origin, orisomes, pre-replicative complexes, DNA binding proteins, cell cycle

INTRODUCTION

All cells must initiate new rounds of chromosomal DNA synthesis with temporal precision and only once per cell cycle to avoid genome instability. Bacteria accomplish this by using a triggering mechanism that requires the AAA+ (ATPases Associated with various cellular Activities) initiator protein, DnaA. In cells, DnaA is bound to either ATP or ADP, and DnaA-ATP is considered to be the active form of the initiator based on *in vitro* unwinding and replication assays (Sekimizu et al., 1987). Multiple DnaA molecules interact with distinct high and low affinity recognition sites in the unique chromosomal replication origin (*oriC*) to assemble a pre-replicative complex (orisome) that unwinds origin DNA and then assists with loading the replicative helicase onto the single strands (reviewed in Bell and Kaguni, 2013; Leonard and Grimwade, 2015; Chodavarapu and Kaguni, 2016).

In *E. coli oriC*, there are 11 DnaA binding sites within the 190 base pairs that are adjacent to the DNA Unwinding Element (DUE) (**Figure 1A**; Bramhill and Kornberg, 1988; Kowalski and Eddy, 1989; Rozgaja et al., 2011). Three of these sites (R1, R2, and R4), with consensus sequence, 5′-TTA/TTNCACA-3′, bind DnaA with high affinity. The remaining eight sites deviate at two or more positions and bind DnaA with low affinity (**Figure 1A**), reviewed in Leonard and Grimwade (2011), Leonard and Méchali (2013), and Wolański et al. (2014). These weak binding sites lie in the gap regions between R1 and R2, and R2 and R4, with each gap containing a cluster of four sites separated by 2 bp (**Figure 1A**). All low affinity DnaA recognition sites in *oriC* are incapable of binding DnaA directly (Schaper and Messer, 1995); instead, their occupation requires the DnaA occupying high affinity sites (usually R1 and R4) to recruit and donate DnaA to the nearest low affinity site (usually R5M and C1), followed by cooperative DnaA binding between the arrayed low affinity sites, so that DnaA occupation progresses toward the center of *oriC* (Simmons et al., 2003; Miller et al., 2009; Rozgaja et al., 2011).

Two DNA bending proteins, IHF and Fis, modulate the low affinity DnaA interactions in *oriC*. IHF-catalyzed bending of the DNA between R1 and R5M places these two sites into proximity, facilitating cooperative binding in *trans,* and thus beginning the progressive DnaA occupation of the left half of *oriC* (Grimwade et al., 2000; Rozgaja et al., 2011). However, IHF binding to its recognition site is prohibited as long as Fis

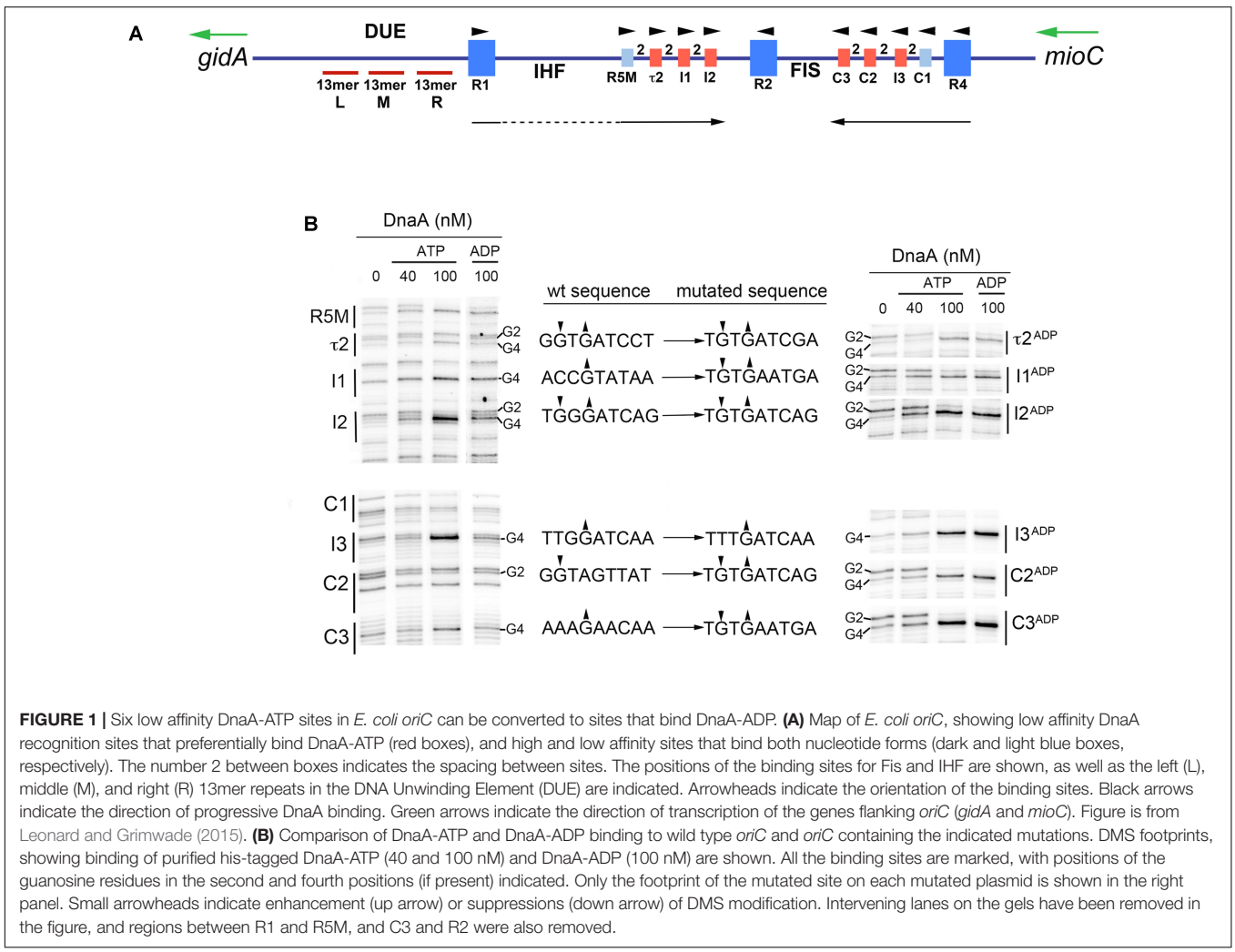

FIGURE 1 | Six low affinity DnaA-ATP sites in *E. coli oriC* can be converted to sites that bind DnaA-ADP. **(A)** Map of *E. coli oriC*, showing low affinity DnaA recognition sites that preferentially bind DnaA-ATP (red boxes), and high and low affinity sites that bind both nucleotide forms (dark and light blue boxes, respectively). The number 2 between boxes indicates the spacing between sites. The positions of the binding sites for Fis and IHF are shown, as well as the left (L), middle (M), and right (R) 13mer repeats in the DNA Unwinding Element (DUE) are indicated. Arrowheads indicate the orientation of the binding sites. Black arrows indicate the direction of progressive DnaA binding. Green arrows indicate the direction of transcription of the genes flanking *oriC* (*gidA* and *mioC*). Figure is from Leonard and Grimwade (2015). **(B)** Comparison of DnaA-ATP and DnaA-ADP binding to wild type *oriC* and *oriC* containing the indicated mutations. DMS footprints, showing binding of purified his-tagged DnaA-ATP (40 and 100 nM) and DnaA-ADP (100 nM) are shown. All the binding sites are marked, with positions of the guanosine residues in the second and fourth positions (if present) indicated. Only the footprint of the mutated site on each mutated plasmid is shown in the right panel. Small arrowheads indicate enhancement (up arrow) or suppressions (down arrow) of DMS modification. Intervening lanes on the gels have been removed in the figure, and regions between R1 and R5M, and C3 and R2 were also removed.

occupies its recognition site between R2 and C3, and higher levels of DnaA are required for orisome assembly if the *oriC* template is occupied by Fis (Ryan et al., 2004). Fis is bound to *oriC* throughout most of the cell cycle, but is displaced by the progressive DnaA binding extending from R4 (Ryan et al., 2004); loss of Fis relieves the repression of IHF binding and allows rapid DnaA occupation of any unbound low affinity sites. This dynamic interplay among DnaA, Fis, and IHF ensures synchronous initiations from the multiple *oriC* copies that exist during rapid growth (Weigel et al., 2001; Ryan et al., 2004). However, because Fis is a growth rate-regulated protein (Nilsson et al., 1992; Mallik et al., 2006) it is not likely to be an orisome component in slowly growing cells, and without Fis-mediated inhibition, IHF is likely to be bound thought the cell cycle.

Despite our ever-increasing understanding of orisome assembly and regulation (Leonard and Grimwade, 2011; Skarstad and Katayama, 2013; Katayama et al., 2017; Schenk et al., 2017), it remains unclear how replication initiation is precisely coupled to the bacterial cell division cycle. Most models for initiation timing (Mahaffy and Zyskind, 1989; Hansen et al., 1991b; Browning et al., 2004; Grant et al., 2011; Zhang and Shi, 2012) are based on accumulation of DnaA-ATP, whose levels fluctuate during the cell cycle, peaking near the time of initiation (Kurokawa et al., 1999). There is extensive experimental evidence in support of these models (Atlung et al., 1987; Pierucci et al., 1987; Løbner-Olesen et al., 1989; Skarstad et al., 1989; Atlung and Hansen, 1993), but some controversy remains (Xu and Bremer, 1988; Flåtten et al., 2015). In addition, most models have yet to take into account the manner in which DnaA-ATP interacts with *oriC*. The three high affinity sites bind DnaA-ATP and DnaA-ADP equivalently (McGarry et al., 2004), and remain occupied throughout the cell cycle (Samitt et al., 1989; Nievera et al., 2006). For this reason, occupation of these sites is unlikely to be the rate-limiting step in triggering chromosome replication. Instead, it is more probable that initiation timing is determined by the filling of the low affinity DnaA recognition sites because occupation of these sites is transient and takes place immediately before initiation (Nievera et al., 2006; Rozgaja et al., 2011). Further, although sites C1 and R5M have equal preference for DnaA-ATP and DnaA–ADP, all remaining low affinity sites (τ2, I1, I2, and C3, C2, and I3) exhibit a 4-fold binding preference for DnaA-ATP (McGarry et al., 2004; Grimwade et al., 2018), suggesting that occupation of the sites with DnaA-ATP could couple initiation to levels of available DnaA-ATP.

Site preference or non-preference for DnaA-ATP is determined by nucleotide sequence, and previous work demonstrates that *oriC* remains functional when some or all low affinity sites are altered by mutagenesis to allow both DnaA-ATP and -ADP forms to bind equivalently without changing overall site affinity (McGarry et al., 2004; Grimwade et al., 2018). DnaA is not normally degraded after bound ATP is hydrolyzed, and DnaA-ADP is prevalent in cells, fluctuating between 30 and 70% of total DnaA (Kurokawa et al., 1999). Since mixed complexes of DnaA-ATP and DnaA-ADP can activate *oriC* (Yung et al., 1990; Grimwade et al., 2007, 2018), if DnaA-ADP can access *oriC* at mutated sites, this binding should reduce the requirement for DnaA-ATP in orisome formation, and shift the timing of initiation earlier in the cell cycle. Previous studies support this idea. For example, although cloned wild-type *oriC*, initiates synchronously with the wild-type chromosomal copy (Helmstetter and Leonard, 1987; Koppes, 1987; Løbner-Olesen, 1999), *oriC* plasmids carrying loss of preference mutations at I2 and I3 rapidly integrate and replace chromosomal *oriC*, consistent with the cloned origin initiating earlier and out-competing the chromosomal origin (Grimwade et al., 2007). Further, changing all the DnaA-ATP sites in chromosomal *oriC* into sites that bind both DnaA-ATP and DnaA-ADP causes over-initiation and loss of initiation synchrony (Grimwade et al., 2018), similar to the phenotype of cells in which there is a 3–4-fold excess of DnaA (Atlung and Hansen, 1993). However, it remains unclear whether all DnaA-ATP sites play equivalent timing roles (i.e., each site requiring a fixed amount of time to become occupied as newly synthesized DnaA-ATP becomes available) or if additional factors might contribute to how DnaA accesses the origin sites.

To better understand the relationship between low affinity site occupation and the initiation clock, we measured the timing of DNA synthesis in cells whose only chromosomal *oriC* copy carried mutations resulting in loss of DnaA-ATP preference at individual or pairs of low affinity recognition sites. We observed that during slow growth, the onset of chromosomal DNA replication was shifted to earlier cell cycle times for all single site mutations, but the shift was greater in cells carrying mutations at the τ2 site, revealing a possible bottleneck step during orisome assembly. Initiation timing in cells where pairs of sites were mutated was consistent with this idea. However, altering DnaA-ATP preference at single sites did not affect timing when assays were performed under rapid growth conditions. These observations are consistent with the existence of two distinct, growth-rate dependent timing mechanisms in *E. coli*, and we propose that the occupation of *oriC* low affinity DnaA-ATP recognition sites directly regulates initiation timing only during slow growth. In rapidly growing cells, although initiation is not triggered until all the low affinity sites are occupied, other factors modulate binding of DnaA-ATP to these sites. Examination of double site mutations during fast-growth suggests that one of these factors is the growth rate-regulated protein Fis, making this architectural protein an important component of the initiation timing mechanism.

MATERIALS AND METHODS

Chemicals, Proteins, Enzymes, and Oligonucleotides

Reagent grade chemicals were purchased from IBI, ThermoFisher, or Sigma. Media components were from IBI or Difco. All enzymes were from New England Biolabs. Oligonucleotides were purchased from ThermoFisher. His-tagged DnaA was isolated as described (Li and Crooke, 1999), including a urea wash step to remove bound nucleotide and lipids.

Construction of *oriC*s With Loss of DnaA-ATP Preference

The positions of mutated DnaA recognition sites are shown in **Figure 1A**. Specific changes in nucleotide sequence are listed in **Figure 1B**. Site-directed mutagenesis was performed as described in McGarry et al. (2004). The starting template for all *oriC* mutations was pOC170 (3,852 bp) (Langer et al., 1996), which carries both the pBR322 replication origin and *oriC*. Overlapping 30–35 bp primers carrying the base alterations were flanked by 10 bp of DNA homologous to the template. To make mutations in multiple DnaA binding sites in *oriC*, a single site was mutated per reaction, and the resulting plasmid used as template to make additional mutations. Supercoiled plasmid was isolated using a plasmid preparation kit (IBI). Mutations in *oriC* were confirmed by sequence analysis (sequencing primer was 5′-CTCAACTTTGTCGGCTTGAG) and plasmids were introduced into DH5α by transformation selecting for ampicillin resistance.

Recombineering

PCR fragments carrying the mutant *oriC* were amplified from plasmids using primers near *gidA* (5′-CACGGCCA CCGCTGTAATTAT) and *mioC* (5′-ATCCCATACTTTT CCACAGG). The fragments were introduced by electroporation into ACL402 (*asnB32, relA1, spoT1, thi-1, fuc-1, lysA, ilv-192, zia*::pKN500, Δ*dnaA, mad-1*, λcI857Δ(*cro-bioA*), *nad*::Tn10, Δ*oriC*::*cat-sacB*) following induction of RED gene expression, as described in Kaur et al. (2014). ACL402 was constructed by inserting the cat-*sacB* cassette from pK03 (Link et al., 1997) into ACL401 (Kaur et al., 2014). Transformed cells were grown in LB overnight at 32°C without selection, and then diluted and plated onto LB agar plates containing 5% sucrose and incubated at 32°C overnight. Replacement of the Δ*oriC*::*cat sac* with the mutated *oriC* was verified in sucrose resistant cells by testing for loss of chloramphenicol resistance, and nucleotide sequence analysis. The *oriC* region from verified mutant cells was transduced using P1 phage into an JEG22, an MG1655 derivative which is *asnA*::cat and *asnB*::Tn10 and transductants were selected for growth in the absence of asparagine on minimal salts agar (Helmstetter and Krajewski, 1982), supplemented with 0.1% glucose as described in Kaur et al. (2014).

Dimethyl Sulfate Footprinting

DMS modification of DNA (0.75 μg) *in vitro* was performed as described (Ryan et al., 2004). DnaA was pre-incubated in reaction buffer with 5 mM ATP or ADP for 5 min before addition to reactions at the concentrations indicated in **Figure 1B**. DMS-treated samples were extended with radiolabeled primer as described (Ryan et al., 2004). Primer sequences were 5′-GTATACAGATCGTGCGATC, for revealing R1-I2, and 5′-GGATCATTAACTGTGAATG, for revealing R4-R2. Extension products were resolved on 6% polyacrylamide sequencing gels, and dried gels were scanned on a Bio-Rad Molecular Imager FX PhosphorImager. Representative scans are shown in **Figure 1B**.

Western Blots

MG1655 was grown for at least five generations in exponential growth, in minimal media containing 0.1% uracil supplemented with 0.1% glucose plus 0.1% casamino acids; 0.1% glucose; 0.2% glycerol; or 0.4% succinate. Samples were removed from the cultures, pelleted, and flash frozen in liquid nitrogen three times to lyse the cells. Protein concentrations in each sample were quantified using the MicroBCA assay (Pierce) and then equal amounts of protein (5 mg) were resolved on 12% PAGE/SDS gels. The proteins were transferred to nitrocellulose, and DnaA and Fis on the blots were revealed using anti-DnaA and anti-Fis antibodies with detection by chemiluminescence (Bio-Rad ImunoStar kit). Assays were done in triplicate, with representative scans shown in Supplementary Figure S1.

Flow Cytometry

Wild-type or mutant *oriC* strains (MG1655 derivatives) were grown in minimal salts media (Helmstetter and Krajewski, 1982; Løbner-Olesen et al., 1989) supplemented with 20 μg/ml uracil and either 0.4% succinate or 0.1% glucose, 0.1% casamino acids, and 0.1% uracil, and liquid cultures were grown to exponential phase at 37°C with vigorous shaking. Cells were then treated with 300 μg/ml rifampicin and 15 μg/ml cephalexin (Skarstad et al., 1986; Løbner-Olesen et al., 1989), and incubation was continued at 37°C for at least 4 h. After drug treatment, 1 ml of cells was fixed with 9 ml of 70% ethanol and stored at 4°C. Prior to flow cytometric analysis, 1 ml of the fixed cell suspension was pelleted, washed with 50 mM Tris-Cl, pH 7.5, 150 mM NaCl (TBS), and resuspended in 1 ml of TBS containing 0.5 μl/ml Vybrant DyeCycle Green (ThermoFisher) (final concentration of dye is 2.5 μM). Stained cells (3,000–5,000 cells/ml) were analyzed using an Accuri C6 personal flow cytometer, and data from 10,000 cells were collected. Forward scatter was used for cell mass measurement. CFlow software was used to calculate the percentage of cells in each chromosomal DNA peak.

RESULTS

Conversion of a DnaA-ATP Site Into One That Binds DnaA-ADP Alters Initiation Timing in Slowly Growing *E. coli* Cells

DnaA-ADP is produced in bacterial cells by hydrolysis of DnaA-ATP, which, in *E. coli*, is stimulated by the Hda protein associated with replication forks, as well as by the *datA* locus, reviewed in Katayama et al. (2017). Since *E. coli* cells do not degrade DnaA-ADP, this form is generally available for *oriC* interactions at any recognition sites capable of binding it. Therefore, mutation of a low affinity DnaA-ATP recognition site to allow interaction with DnaA-ADP should decrease the amount of DnaA-ATP required for orisome formation, and, if the mutation is carried in chromosomal *oriC*, it should shift initiation timing to earlier in the cell cycle. To examine this possibility, we first expanded our collection of site mutants (McGarry et al., 2004; Grimwade et al., 2007, 2018) by altering each of the six individual DnaA-ATP recognition sites (see **Figures 1A,B**), as well as pairs of sites

in *oriC* specifically chosen for their location (two sites on the right, two on the left, and one in each half). Since we wished to retain the low affinity attribute while allowing DnaA-ADP binding, the I3, C2, C3, I2 I1, and τ2 sites were each individually mutated to sequences identical or similar to R5M. The sequence of the mutated sites is shown in **Figure 1B**. To verify that the mutations relieved the DnaA-ATP preference, but did not alter overall site affinity, binding of DnaA-ATP or DnaA-ADP to each site was evaluated using dimethyl sulfate (DMS) footprinting (**Figure 1B**). DnaA was pre-incubated with nucleotide, and then bound to supercoiled *oriC* plasmid prior to DMS treatment and primer extension. Sites that are occupied by DnaA are revealed by distinctive changes to the DMS modification pattern resolved on sequencing gels. Specifically, the G4 of the 9 mer consensus 5′-TGTGGATAA (or variations of this sequence) becomes hypersensitive, and the G2 less sensitive to DMS (**Figure 1B**), causing darker and lighter bands, respectively. The changes in band intensity increase as all of the plasmid molecules in the treatment population become occupied. It should be noted that not all binding sites have guanosines at both positions. For evaluation of site affinity, two concentrations of DnaA-ATP were used: 40 nM, which is insufficient for full occupation of all low affinity sites, and 100 nM, which previous studies have shown to be a saturating concentration, resulting in complete DnaA-ATP binding to all *oriC* copies in the reaction mix (McGarry et al., 2004; Grimwade et al., 2007). In wild type *oriC* (**Figure 1B**, left panel), the pattern of DnaA-ATP binding is consistent with previous studies showing R1, R2, and R4 as higher affinity sites fully occupied at 40 nM DnaA, and the remaining sites being fully occupied only at the higher concentration. The DnaA-ATP binding pattern is similar for origins containing the mutated sites, indicating that the mutations do not alter any sites' affinity for DnaA-ATP. However, when DnaA-ADP is used in the reaction, only the mutant origin is fully occupied by 100 nM DnaA-ADP (**Figure 1B**); in contrast, binding of 100 nM DnaA-ADP binding to I3, C2, C3, I2 I1, and τ2 in wild type *oriC* gives a DMS modification pattern similar to that seen with 40 nM DnaA-ATP (McGarry et al., 2004).

We next evaluated the effect of single site mutations on initiation timing. A previous study reported that mutations may affect chromosomal *oriC* differently than *oriC*'s harbored on a plasmid (Weigel et al., 2001). Therefore, recombineering (homologous recombination-mediated genetic engineering) was used to delete wild-type *oriC* on the chromosome (Court et al., 2002), and replace it at the native location with one of the mutant *oriC*s carrying an altered low affinity site. After verifying successful origin transplantation by sequence analysis, P1 phage was then used to transfer the mutated origin from the recombineering strain into MG1655 for analysis of cell cycle timing. In the initial experiments, *E. coli* containing wild type or mutant *oriC* were grown in minimal media supplemented with succinate as a carbon source (generation time 101–103 min). This growth rate allows us to examine the simplest initiation scenario, in which only one *oriC* copy per cell must be activated, since the generation time of *E. coli* growing in this media should be greater than the time needed to complete chromosome replication and divide (∼60 min), so exponentially growing cells will contain only one copy of *oriC* prior to the time of initiation (Cooper and Helmstetter, 1968). Further, since previous studies by our lab revealed that Fis, when bound to *oriC*, reduces binding of DnaA to low affinity sites, and because Fis is a growth-rate regulated protein, orisome assembly in cells growing in succinate media should take place without Fis inhibition. To confirm this, equal amounts of total protein from cells with wild type *oriC*, growing exponentially at four different growth rates were separated on denaturing polyacrylamide gels, transferred to nitrocellulose, and the blots were incubated with both anti-DnaA and anti-Fis antibodies (Supplementary Figure S1). The blots confirm that Fis levels decrease as a function of growth rate (Flåtten and Skarstad, 2013), and are nearly undetectable in cells using succinate as a carbon source, while DnaA concentrations remain constant among the growth rates tested, as has been reported previously (Hansen et al., 1991a).

To evaluate initiation timing, cells carrying the mutated *oriC*s were grown to mid-exponential phase in minimal media supplemented with succinate. Then, cells were treated with rifampicin to inhibit new rounds of chromosome replication, and cephalexin, which prevents cell division, followed by incubation to allow completion of ongoing rounds of replication. After staining cellular DNA with a fluorescent dye, the number of chromosomes in the cell, which reflects the number of *oriC* copies present at the time of drug addition, was detected by flow cytometry. The origin number doubles at the time of initiation, and at all growth rates, only 2^n origins should be in these cells. Accordingly, cultures of MG1655 cells contained 1 or 2 origins (**Figure 2A**), and initiated ∼36 min after cell division (**Table 1**). Although previous studies report that cells growing slowly with acetate as the carbon source display rifampicin resistant initiations (Flåtten et al., 2009), we do not see evidence of this in cells growing in succinate media, since the percentage of cells that have not yet started chromosome replication (1 chromosome peak) does not decrease after addition of rifampicin (Supplementary Figure S2). Interestingly, converting a single DnaA-ATP site into one that binds both of DnaA's nucleotide forms changed initiation timing in all the mutant cells, resulting in an increased number of origins per cell, and an earlier initiation time in the cell cycle (**Figures 2B–G** and **Table 1**). The conversion of the τ2 site to $\tau2^{ADP}$ caused a greater change in timing (**Table 1**), suggesting that filling this site might represent a rate-limiting step in slow growth orisome formation.

The change in initiation time caused by converting one DnaA-ATP site to the non-discriminatory form raised the possibility that changing more than one site might have an additive effect. To evaluate this, we examined the effect of mutation pairs on initiation during slow growth. Mutation pairs chosen for study were located either in *oriC*'s right half (I3/C3), left half (τ2/I2) or each half (τ2/I3; I2/I3), because there is evidence that DnaA assembled onto the left and right halves of *oriC* play different roles in initiation (Ozaki et al., 2012), and we wished to examine if the two sub-assemblies made equivalent contributions to setting the time of initiation. Accordingly, cells carrying the double mutations were grown in minimal media supplemented with succinate, treated with rifampicin and cephalexin, and the number of chromosome equivalents, corresponding the number

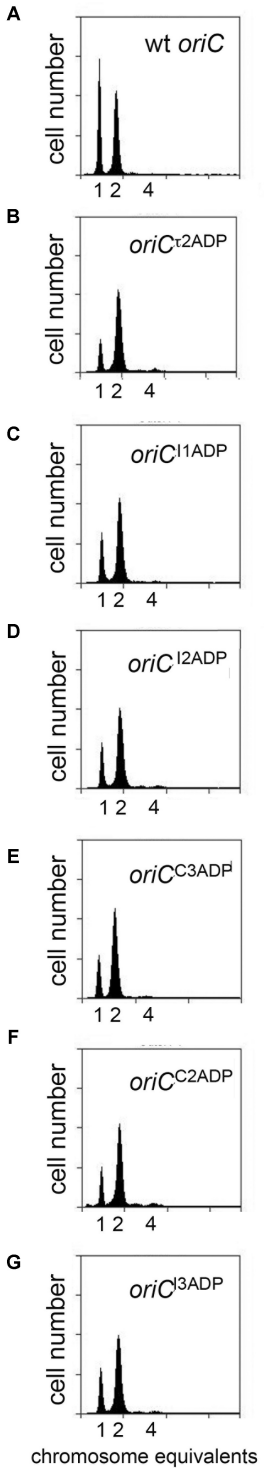

FIGURE 2 | Mutation of individual DnaA-ATP sites into sequences that equivalently bind DnaA-ADP causes a shift in initiation timing in slowly growing *E. coli* cells. **(A–G)** DNA histograms of cells with wild type *oriC* or with *oriC*s carrying the indicated single site mutations, growing in minimal media using succinate as the carbon source were treated with cephalexin and rifampicin, and analyzed by flow cytometry. The number of chromosome equivalents, corresponding to the number of origins at the time of drug treatment, is shown.

of origins at the time of drug treatment, was determined by flow cytometry (**Figure 3**). The effect of mutating two sites in the right sub-assembly ($I3^{ADP}$ and $C3^{ADP}$) did not change timing appreciably from that obtained for cells containing these mutations individually (**Figure 3D** and **Table 1**). In contrast, placing two mutations ($\tau2^{ADP}$ and $I2^{ADP}$) in the left sub-assembly shifted the time of initiation much more than either of the single mutations (**Figure 3B** and **Table 1**). Initiation timing in cells harboring a mutated site in both left and right assemblies appeared to be determined largely by the left half mutation, with the $\tau2^{ADP}/I3^{ADP}$ mutant cells initiating slightly earlier that the $I2^{ADP}/I3^{ADP}$ cells (**Figures 3C,E** and **Table 1**), consistent with the idea that τ2 plays a greater timing role than I2. These results remain consistent with models suggesting that the right and left sub-assemblies are not equivalent (Ozaki et al., 2012).

Individual Low Affinity DnaA-ATP Sites Do Not Play an Initiation Timing Role in Rapidly Growing Cells

Although the studies described above show that mutations causing loss of preference for DnaA-ATP shift initiations to earlier cell cycle times in slow growing cells, Riber et al. previously reported that the same mutations in I2 or I3 had no effect on initiation timing in rapidly growing cells (Riber et al., 2009), suggesting that the timing role of individual DnaA-ATP sites might be dependent on growth rate. To examine this possibility, we evaluated initiation timing of the six single DnaA-ATP site mutations in cells growing in minimal media supplemented with glucose and Casamino acids, with doubling times of ∼33 min. Exponentially growing cells were treated with rifampicin and cephalexin, and DNA content was measured by flow cytometry after incubation to allow completion of ongoing rounds of DNA replication. Under these growth conditions, the *E. coli* generation time is less than the time needed to complete chromosome replication, and exponentially growing cells normally contain more than one copy of *oriC*, and all origin copies initiate chromosome replication synchronously, once per cell cycle, on partially duplicated chromosomes (Cooper and Helmstetter, 1968; Skarstad et al., 1986). Accordingly, cultures of MG1655 cells contained 2, 4, or 8 origins (**Figure 4A**), and initiated ∼3 min after division. When cells containing origins carrying single site mutations were examined, we found that initiation timing was identical to that observed in cells with wild type *oriC* (**Figures 4B–G** and **Table 2**), in contrast to the shift in timing seen at the slower growth rate. These results confirm previous reports (Riber et al., 2009) and suggest that another factor may contribute to initiation timing regulation in rapidly growing cells.

We also used flow cytometry to examine DNA content in cells containing two site mutations to determine if this might alter timing (**Figure 5**). As was done in the studies of slow growing cells, the double mutants were selected to allow examination of left and right sub-assemblies (e.g., τ2/I2, I3/C3, τ2/I3, and I2/I3). Interestingly, changing both τ2 and I2 in the left half of *oriC* was sufficient to perturb initiation (**Figure 5B**), but the alteration in timing was more complex than the simple shift to earlier

TABLE 1 | Doubling times, number of origins, and cell mass of strains carrying mutated sites growing in minimal media supplemented with succinate.

Site mutated	Doubling time (min)	Number of origins/cell	Relative cell mass[a]	Origins/cell mass	Ai[b]
None	102	1.57	1.0	1.57	0.35 (36 min)
$\tau2^{ADP}$	101	2.00	1.0	2.00	0.13 (13 min)
$I1^{ADP}$	102	1.81	1.0	1.81	0.18 (18 min)
$I2^{ADP}$	103	1.82	1.0	1.82	0.17 (18 min)
$C2^{ADP}$	102	1.81	1.0	1.81	0.18 (18 min)
$C3^{ADP}$	102	1.84	1.0	1.84	0.18 (18 min)
$I3^{ADP}$	103	1.80	1.0	1.80	0.18 (18 min)
$\tau2/I2^{ADP}$	102	2.70	1.0	2.70	0.05 (5 min)
$\tau2/I3^{ADP}$	101	2.05	1.0	2.05	0.11 (11 min)
$I3/C3^{ADP}$	102	1.83	1.0	1.83	0.18 (18 min)
$I2/I3^{ADP}$	102	2.00	1.0	2.00	0.13 (13 min)

[a] *Relative cell mass was measured by flow cytometry, using forward scattered light of mutant strain relative to the wild type strain.*
[b] *Ai (age at initiation), as a fraction of the cell cycle generation time, was calculated using the formula Ai = -ln(1-F/2)/ln2 where F is the fraction of cells in a population that have not initiated chromosome replication, measured from flow cytometric histograms of cells treated with rifampicin and cephalexin (**Figures 2**, **3**). The calculated Ai was multiplied by the generation time to give age of initiation in minutes.*

TABLE 2 | Doubling times, number of origins, and cell mass of strains carrying mutated sites growing in minimal media supplemented with glucose and casamino acids.

Site mutated	Doubling time (min)	Number of origins/cell	Relative cell mass[a]	Origins/cell mass	Ai[b]
None	33	4.20	1.0	4.20	0.1 (3 min)
$\tau2^{ADP}$	33	4.23	1.0	4.23	0.1 (3 min)
$I1^{ADP}$	34	4.21	1.0	4.21	0.1 (3 min)
$I2^{ADP}$	33	4.20	1.0	4.20	0.1 (3 min)
$C2^{ADP}$	34	4.19	1.0	4.19	0.1 (3 min)
$C3^{ADP}$	32	4.20	1.0	4.20	0.1 (3 min)
$I3^{ADP}$	33	4.20	1.0	4.20	0.1 (3 min)
$\tau2/I2^{ADP}$	34	4.68	1.0	4.68	—
$\tau2/I3^{ADP}$	34	4.55	1.0	4.55	—
$I3/C3^{ADP}$	33	3.40	1.0	3.40	—
$I2/I3^{ADP}$	33	4.20	1.0	4.20	0.1 (3 min)

[a] *Relative cell mass was measured by flow cytometry, using forward scattered light of mutant strain relative to the wild type strain*
[b] *Ai (age at initiation), as a fraction of the cell cycle generation time, was calculated from cultures with synchronous initiations using the formula Ai = -ln(1-F/2)/ln2 where F is the fraction of cells in a population that have not initiated chromosome replication, measured from flow cytometric histograms of cells treated with rifampicin and cephalexin (**Figures 4**, **5**). The calculated Ai was multiplied by the generation time to give age of initiation in minutes.*

times seen in slower growing cells. While most of the cells in the population had 4 origins, odd numbers of origins were also detected, indicating that initiations in these cells were no longer synchronous (**Figure 5B**). The number of origins per cell was also slightly increased (**Table 2**). A similar pattern of asynchronous initiations was seen when τ2 was mutated in the left sub-assembly and I3 was mutated in the right sub-assembly (**Figure 5C** and **Table 2**). However, origins carrying both the $I2^{ADP}$ (left) and $I3^{ADP}$ (right) mutations showed essentially normal initiation timing (**Figure 5E**), as was previously reported (Riber et al., 2009). These results support idea that τ2 plays a greater role in initiation timing than the other sites.

Unlike the slight over-initiation seen in cells with origins carrying $\tau2^{ADP}/I2^{ADP}$ and $\tau2^{ADP}/I3^{ADP}$ mutations, cells with $oriC^{I3ADP/C3ADP}$ contained fewer origin copies per cell, with a larger percentage of cells containing 2 or 3 origins, and a lower number of cells containing 8 origins (**Figure 5D** and **Table 2**). These results reveal a clear difference in the response to changes in the left and right halves of *oriC*. One possible cause of this difference is the role of the right DnaA sub-assembly in displacing Fis (Ryan et al., 2004). While further studies are needed to verify this idea, it is intriguing to note that the pattern of initiation in cells lacking Fis is similar to the $I3^{ADP}/C3^{ADP}$ mutant (**Figure 5F**).

DISCUSSION

An important question about the regulation of DNA replication during the *E. coli* cell cycle is whether low affinity DnaA recognition sites in *oriC* are components of the timing mechanism. There are several possible roles for recognition sites in a clock model based on the availability of DnaA-ATP. In one simple scenario, each low affinity recognition site would require an equivalent amount of time to become occupied. Alternatively, the timer might be based on site occupation, but sites could play a non-equivalent role, i.e., some sites would require more or less time to become occupied than others. A third possibility is that despite a requirement to fill sites with DnaA-ATP during orisome assembly, some other factor acts as the initiation timer by

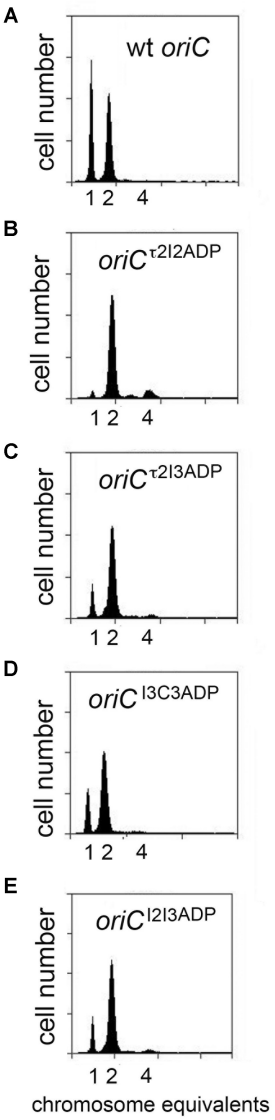

FIGURE 3 | Initiation timing of slowly growing *E. coli* cells carrying two DnaA-ATP site mutations in *oriC*. **(A–E)** DNA histograms of cells with wild type *oriC* or with *oriC*s carrying the indicated two site mutations, growing in minimal media supplemented with succinate, were treated with cephalexin and rifampicin, and analyzed by flow cytometry. The number of chromosome equivalents, corresponding to the number of origins at the time of drug treatment, is shown.

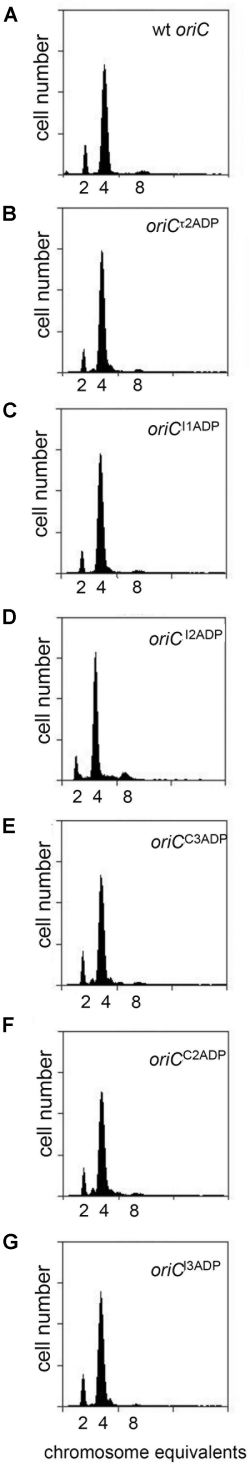

FIGURE 4 | Mutation of individual DnaA-ATP sites into sequences that bind DnaA-ADP equivalently does not change initiation timing in rapidly growing *E. coli* cells. **(A–G)** DNA histograms of cells with wild type *oriC* or with *oriC*s carrying the indicated single site mutations, growing in minimal media supplemented with glucose and casamino acids were treated with cephalexin and rifampicin, and analyzed by flow cytometry. The number of chromosome equivalents, corresponding to the number of origins at the time of drug treatment, is shown.

restricting or facilitating DnaA-ATP access to *oriC*, thus setting the DnaA-ATP level for site occupation and origin activation. Since previous DnaA over-expression studies both support and oppose DnaA's role in initiation timing (Churchward et al., 1983; Atlung et al., 1987; Pierucci et al., 1987; Xu and Bremer, 1988; Løbner-Olesen et al., 1989; Skarstad et al., 1989; Atlung and Hansen, 1993; Flåtten et al., 2015), our approach was to examine minimally disturbed cells with altered chromosomal *oriC* low affinity DnaA recognition sites that bind to DnaA-ATP or DnaA-ADP equivalently. Any differences in DNA replication during

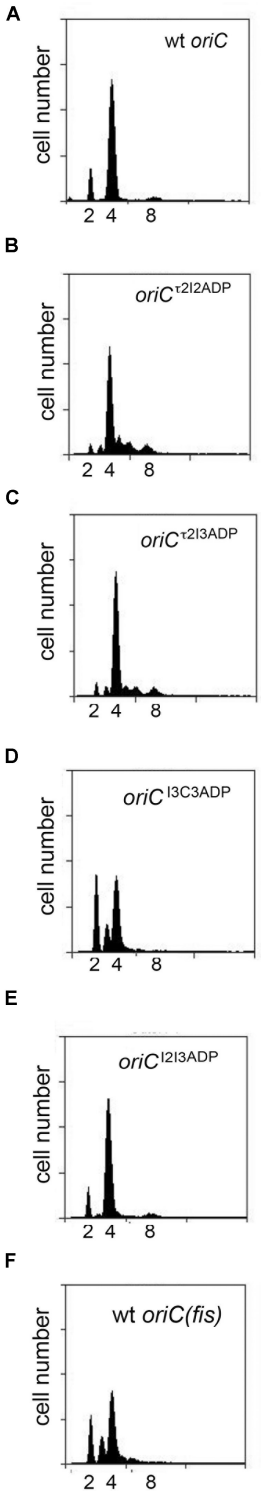

FIGURE 5 | Initiation timing of rapidly growing *E. coli* cells carrying two DnaA-ATP site mutations in *oriC*. **(A–E)** DNA histograms of cells with wild type *oriC* or with *oriC*s carrying the two indicated site mutations **(F)** growing in minimal media supplemented with glucose and casamino acids were treated with cephalexin and rifampicin, and analyzed by flow cytometry. The number of chromosome equivalents, corresponding to the number origins at the time of drug treatment, is shown.

the cell cycle compared to the wild-type version of *oriC* should implicate the altered site as a timing component.

We obtained evidence that loss of DnaA-ATP preference at *oriC* low affinity recognition sites can shift initiation timing during the cell cycle. However, the timing role for recognition sites was more complex than expected, and we identify a dependence on both recognition site location and cellular growth rate. During slow growth in minimal medium with a succinate carbon source, we found that removing DnaA-ATP preference at any of the low affinity recognition sites caused a shift in initiation timing, supporting a site filling-dependent clock mechanism where sites fill when a molecule of DnaA-ATP becomes available to them. But, the unexpectedly larger change in initiation time caused by mutations at τ2 suggests that occupation of this site acts as a bottleneck step during orisome assembly. Although we can only speculate about the mechanism responsible, we note that filling the arrayed low affinity sites in *oriC*'s left half requires IHF-stabilized DNA bending to position the DnaA occupying R1 close enough to R5(M) and τ2 to allow cross-strand DnaA donation (Rozgaja et al., 2011; Ozaki and Katayama, 2012; Kaur et al., 2014; Shimizu et al., 2016; **Figure 6**). It is possible that some structural aspect of this orisome assembly step could impede DnaA-ATP access to τ2. It is also possible that cross-strand interactions between DnaA-ATP bound to τ2 and R1 are required to stabilize an origin configuration that promotes DnaA binding to the unwound DUE (Ozaki and Katayama, 2012; Sakiyama et al., 2017), and achieving this configuration may be more time consuming than lateral cooperative DnaA-ATP binding between arrayed sites.

Any bottleneck in orisome assembly functioning during slow growth would also be expected to function during the synchronous initiations of multiple *oriC* copies during rapid growth. However, none of the single site loss of preference mutations changed initiation timing in fast growing *E. coli*, suggesting that there could be a fast growth-specific mechanism that controls DnaA-ATP availability or its access to *oriC*. One likely component of this mechanism is the growth rate-regulated protein, Fis. We previously reported that binding of purified Fis protein to *oriC* increases the amount of DnaA-ATP required to assemble orisomes *in vitro* (Ryan et al., 2004), with displacement of Fis allowing IHF binding and immediate filling of unoccupied recognition sites by the excess DnaA (Ryan et al., 2004; Leonard and Grimwade, 2011). It is reasonable to expect an analogous situation exists *in vivo*. If the level of DnaA-ATP required to displace Fis from *oriC* over-shoots the amount needed to fill all remaining low affinity DnaA-ATP recognition sites, initiation timing would be determined by how long it takes to accumulate enough DnaA-ATP to displace Fis (see **Figure 6**). In this model, Fis serves as both a negative and positive regulator during orisome assembly, negatively regulating IHF-dependent orisome assembly steps, but positively regulating synchronous initiation by ensuring enough DnaA-ATP accumulates to fire all *oriC* copies (Ryan et al., 2004; Flåtten and Skarstad, 2013). In support of this model, we observed that mutations allowing DnaA-ADP binding at two low affinity recognition sites in the right half of *oriC* caused under-initiation as well as initiation asynchrony (**Figure 5D**). This is the expected result if the mutations resulted in Fis

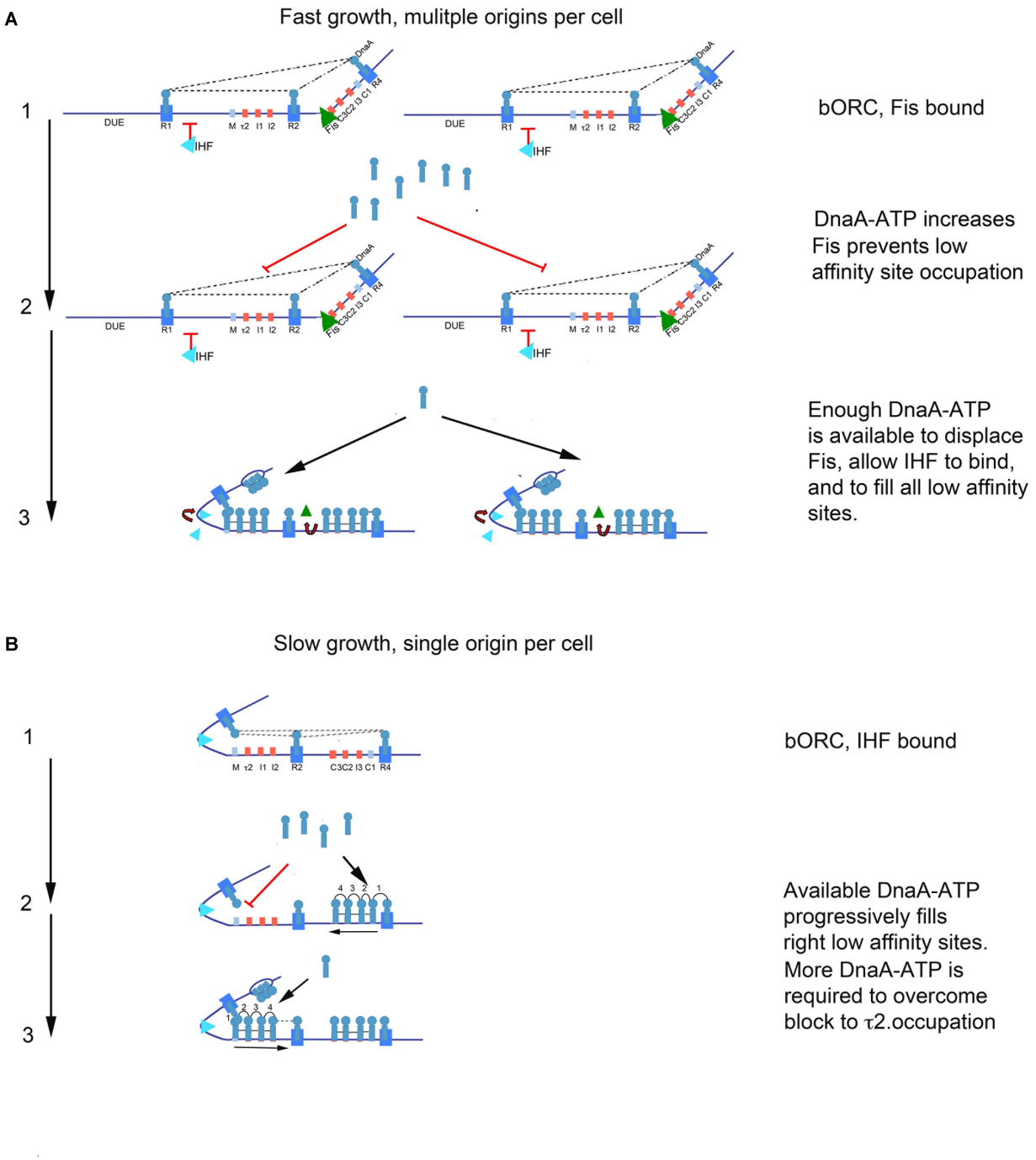

FIGURE 6 | Model of growth-rate dependent regulation of DnaA-ATP site occupation during orisome assembly in *E. coli*. **(A)** In rapidly growing cells, DnaA-ATP site occupation is regulated by Fis. Stage 1 (bacterial Origin Recognition Complex; bORC): Cells contain more than one copy of *oriC*, and DnaA is bound to high affinity R1, R2, and R4 sites throughout most of the cell cycle. Fis is also bound at this stage, and inhibits IHF from occupying its site. Dotted lines indicate putative interactions between R1, R2, and R4. Low affinity sites are unoccupied. Stage 2: Bound Fis prevents accumulating DnaA-ATP from occupying low affinity sites. Stage 3: When enough DnaA-ATP accumulates and becomes available, Fis is displaced. Loss of Fis allows IHF to bind to *oriC*, and also allows all low affinity sites on all *oriC* copies in the cell to become occupied by DnaA. The sharp bend induced by IHF binding allows DnaA bound to R1 to assist loading of R5M and the left array of DnaA-ATP sites. In this configuration, *oriC* DNA is unwound in the DUE, and DnaA-ATP in the form of a compact filament binds to the ssDNA. **(B)** In slowly growing cells, DnaA-ATP site occupation is determined by the availability of DnaA-ATP, and the ability to occupy the τ2 site. Stage 1: Cells contain only one copy of *oriC*, and DnaA is bound to high affinity sites throughout most of the cell cycle. IHF is also bound at this stage. Dotted lines indicate possible interaction between DnaA bound at R1, R2, and R4. Stage 2:As DnaA-ATP become available, it progressively binds right-side low affinity sites, nucleated by DnaA bound to R4. Occupation of the low affinity sites in the left half of *oriC* is delayed by a bottleneck in filling the τ2 site. When enough DnaA-ATP has accumulated to overcome this bottleneck, *oriC* DNA is unwound in the DUE, and DnaA-ATP in the form of a compact filament binds to the ssDNA.

displacement at lower DnaA-ATP levels than would be required for synchronous initiations at all *oriC* copies. Interestingly, there is more than one Fis recognition site in the right half of *oriC* (Filutowicz et al., 1992; Hengen et al., 2003), and it is possible that the amount of accumulated DnaA needed to displace Fis might change over a range of growth rates. There may also be additional mechanisms, such as DnaA acetylation (Zhang et al., 2016; Li et al., 2017), that regulate DnaA access to *oriC* and initiation timing at very slow growth rates, where Fis is absent. Support for this idea comes from reports that *E. coli* cells using acetate as the sole carbon source have higher DnaA/*oriC* ratios than expected (Flåtten et al., 2009). It should also be noted that other DNA binding proteins can contribute to initiation timing by blocking DNA access, changing topology, or changing the availability of DnaA-ATP, reviewed in Riber et al. (2016), and it is possible that some of these could also be growth rate-dependent.

Taken together, our results suggest that *E. coli* may not use a single initiation timing mechanism at all growth rates. Instead, it appears that there are multiple timing mechanisms, each optimized for particular growth conditions, with the ability to shift between them if nutrient availability changes. Timing mechanisms might also vary among bacterial types, depending on their particular lifestyles, and this may be one reason for the large variety in the number and positioning of DnaA recognition sites seen in different bacterial replication origins (Leonard and Méchali, 2013). Although it remains to be determined whether low affinity recognition sites with DnaA-ATP preference are ubiquitous among *oriC*s (Charbon and Lobner-Olesen, 2011), variations in high affinity recognition site number and position may also result in bottlenecks and/or growth rate regulators similar to those that we suggest for *E. coli*.

Finally, it is worth noting that the change in initiation age that we observe for our mutant *oriC*s during slow growth suggests that while there must be free DnaA-ADP available to interact with recognition sites during the majority of the cell cycle, supporting previous findings for rapidly growing cells (Kurokawa et al., 1999; Grimwade et al., 2018), the availability of DnaA-ATP must be stringently restricted even near the time of initiation, such that each low affinity DnaA-ATP site fills only when a DnaA-ATP molecule becomes available. Our ability to remove the preference for DnaA-ATP from low affinity recognition sites in *oriC* and retain orisome activity also demonstrates the functional equivalence of the active and inactive (DnaA-ADP) form of the initiator for most of the steps required for orisome assembly, as long as DnaA-ADP can access the appropriate recognition sites.

AUTHOR CONTRIBUTIONS

PR, JG, and AL planned the experiments. PR, JG, AA, and TR performed the experiments. PR, JG, and AL analyzed data. JG and AL wrote the manuscript.

FUNDING

The work in our laboratories was supported by Public Health Service grant GM54042. Publication of this article was funded in part by the Open Access Subvention Fund and the Florida Tech Libraries.

ACKNOWLEDGMENTS

We thank Charlotte Chen and Jessica Blanco for technical assistance, and Reid Johnson and Elliot Crooke for gifts of anti-Fis and anti-DnaA antibodies, respectively.

SUPPLEMENTARY MATERIAL

The Supplementary Material for this article can be found online at: https://www.frontiersin.org/articles/10.3389/fmicb.2018.01673/full#supplementary-material

REFERENCES

Atlung, T., and Hansen, F. G. (1993). Three distinct chromosome replication states are induced by increasing concentrations of DnaA protein in *Escherichia coli*. *J. Bacteriol.* 175, 6537–6545. doi: 10.1128/jb.175.20.6537-6545.1993

Atlung, T., Løbner-Olesen, A., and Hansen, F. G. (1987). Overproduction of DnaA protein stimulates initiation of chromosome and minichromosome replication in *Escherichia coli*. *Mol. Gen. Genet.* 206, 51–59. doi: 10.1007/BF00326535

Bell, S. P., and Kaguni, J. M. (2013). Helicase loading at chromosomal origins of replication. *Cold Spring Harb. Perspect. Biol.* 5:a010124. doi: 10.1101/cshperspect.a010124

Bramhill, D., and Kornberg, A. (1988). Duplex opening by dnaA protein at novel sequences in initiation of replication at the origin of the *E. coli* chromosome. *Cell* 52, 743–755. doi: 10.1016/0092-8674(88)90412-6

Browning, S. T., Castellanos, M., and Shuler, M. L. (2004). Robust control of initiation of prokaryotic chromosome replication: essential considerations for a minimal cell. *Biotechnol. Bioeng.* 88, 575–584. doi: 10.1002/bit.20223

Charbon, G., and Lobner-Olesen, A. (2011). A role for the weak DnaA binding sites in bacterial replication origins. *Mol. Microbiol.* 82, 272–274. doi: 10.1111/j.1365-2958.2011.07840.x

Chodavarapu, S., and Kaguni, J. M. (2016). Replication initiation in bacteria. *Enzymes* 39, 1–30. doi: 10.1016/bs.enz.2016.03.001

Churchward, G., Holmans, P., and Bremer, H. (1983). Increased expression of the dnaA gene has no effect on DNA replication in a dnaA+ strain of *Escherichia coli*. *Mol. Gen. Genet.* 192, 506–508. doi: 10.1007/BF00392197

Cooper, S., and Helmstetter, C. E. (1968). Chromosome replication and the division cycle of *Escherichia coli* B/r. *J. Mol. Biol.* 31, 519–540. doi: 10.1016/0022-2836(68)90425-7

Court, D. L., Sawitzke, J. A., and Thomason, L. C. (2002). Genetic engineering using homologous recombination. *Annu. Rev. Genet.* 36, 361–388. doi: 10.1146/annurev.genet.36.061102.093104

Filutowicz, M., Ross, W., Wild, J., and Gourse, R. L. (1992). Involvement of Fis protein in replication of the *Escherichia coli* chromosome. *J. Bacteriol.* 174, 398–407. doi: 10.1128/jb.174.2.398-407.1992

Flåtten, I., Fossum-Raunehaug, S., Taipale, R., Martinsen, S., and Skarstad, K. (2015). The DnaA protein is not the limiting factor for initiation of replication in *Escherichia coli*. *PLoS Genet.* 11:e1005276. doi: 10.1371/journal.pgen.1005276

Flåtten, I., Morigen, and Skarstad, K. (2009). DnaA protein interacts with RNA polymerase and partially protects it from the effect of rifampicin. *Mol. Microbiol.* 71, 1018–1030. doi: 10.1111/j.1365-2958.2008.06585.x

Flåtten, I., and Skarstad, K. (2013). The Fis protein has a stimulating role in initiation of replication in *Escherichia coli* in vivo. *PLoS One* 8:e83562. doi: 10.1371/journal.pone.0083562

Grant, M. A., Saggioro, C., Ferrari, U., Bassetti, B., Sclavi, B., and Cosentino Lagomarsino, M. (2011). DnaA and the timing of chromosome replication in *Escherichia coli* as a function of growth rate. *BMC Syst. Biol.* 5:201. doi: 10.1186/1752-0509-5-201

Grimwade, J. E., Rozgaja, T. A., Gupta, R., Dyson, K., Rao, P., and Leonard, A. C. (2018). Origin recognition is the predominant role for DnaA-ATP in initiation of chromosome replication. *Nucleic Acids Res.* 46, 6140–6151. doi: 10.1093/nar/gky457

Grimwade, J. E., Ryan, V. T., and Leonard, A. C. (2000). IHF redistributes bound initiator protein, DnaA, on supercoiled *oriC* of *Escherichia coli*. *Mol. Microbiol.* 35, 835–844. doi: 10.1046/j.1365-2958.2000.01755.x

Grimwade, J. E., Torgue, J. J., McGarry, K. C., Rozgaja, T., Enloe, S. T., and Leonard, A. C. (2007). Mutational analysis reveals *Escherichia coli oriC* interacts with both DnaA-ATP and DnaA-ADP during pre-RC assembly. *Mol. Microbiol.* 66, 428–439. doi: 10.1111/j.1365-2958.2007.05930.x

Hansen, F. G., Atlung, T., Braun, R. E., Wright, A., Hughes, P., and Kohiyama, M. (1991a). Initiator (DnaA) protein concentration as a function of growth rate in *Escherichia coli* and *Salmonella typhimurium*. *J. Bacteriol.* 173, 5194–5199.

Hansen, F. G., Christensen, B. B., and Atlung, T. (1991b). The initiator titration model: computer simulation of chromosome and minichromosome control. *Res. Microbiol.* 142, 161–167.

Helmstetter, C. E., and Krajewski, C. A. (1982). Initiation of chromosome replication in dnaA and dnaC mutants of *Escherichia coli* B/r F. *J. Bacteriol.* 149, 685–693.

Helmstetter, C. E., and Leonard, A. C. (1987). Coordinate initiation of chromosome and minichromosome replication in *Escherichia coli*. *J. Bacteriol.* 169, 3489–3494. doi: 10.1128/jb.169.8.3489-3494.1987

Hengen, P. N., Lyakhov, I. G., Stewart, L. E., and Schneider, T. D. (2003). Molecular flip-flops formed by overlapping Fis sites. *Nucleic Acids Res.* 31, 6663–6673. doi: 10.1093/nar/gkg877

Katayama, T., Kasho, K., and Kawakami, H. (2017) . The DnaA Cycle in *Escherichia coli*: activation, function and inactivation of the initiator protein. *Front. Microbiol.* 8:2496. doi: 10.3389/fmicb.2017.02496

Kaur, G., Vora, M. P., Czerwonka, C. A., Rozgaja, T. A., Grimwade, J. E., and Leonard, A. C. (2014). Building the bacterial orisome: high-affinity DnaA recognition plays a role in setting the conformation of *oriC* DNA. *Mol. Microbiol.* 91, 1148–1163. doi: 10.1111/mmi.12525

Koppes, L. J. (1987). *OriC* plasmids do not affect timing of chromosome replication in *Escherichia coli* K12. *Mol. Gen. Genet.* 209, 188–192. doi: 10.1007/BF00329857

Kowalski, D., and Eddy, M. J. (1989). The DNA unwinding element: a novel, cis-acting component that facilitates opening of the *Escherichia coli* replication origin. *EMBO J.* 8, 4335–4344.

Kurokawa, K., Nishida, S., Emoto, A., Sekimizu, K., and Katayama, T. (1999). Replication cycle-coordinated change of the adenine nucleotide-bound forms of DnaA protein in *Escherichia coli*. *EMBO J.* 18, 6642–6652. doi: 10.1093/emboj/18.23.6642

Langer, U., Richter, S., Roth, A., Weigel, C., and Messer, W. (1996). A comprehensive set of DnaA-box mutations in the replication origin, *oriC*, of *Escherichia coli*. *Mol. Microbiol.* 21, 301–311. doi: 10.1046/j.1365-2958.1996.6481362.x

Leonard, A. C., and Grimwade, J. E. (2011). Regulation of DnaA assembly and activity: taking directions from the genome. *Annu. Rev. Microbiol.* 65, 19–35. doi: 10.1146/annurev-micro-090110-102934

Leonard, A. C., and Grimwade, J. E. (2015). The orisome: structure and function. *Front. Microbiol.* 6:545. doi: 10.3389/fmicb.2015.00545

Leonard, A. C., and Méchali, M. (2013). DNA replication origins. *Cold Spring Harb. Perspect. Biol.* 5:a010116. doi: 10.1101/cshperspect.a010116

Li, S., Zhang, Q., Xu, Z., and Yao, Y. F. (2017). Acetylation of lysine 243 inhibits the *oriC* binding ability of DnaA in *Escherichia coli*. *Front. Microbiol.* 8:699. doi: 10.3389/fmicb.2017.00699

Li, Z., and Crooke, E. (1999). Functional analysis of affinity-purified polyhistidine-tagged DnaA protein. *Protein Expr. Purif.* 17, 41–48. doi: 10.1006/prep.1999.1094

Link, A. J., Phillips, D., and Church, G. M. (1997). Methods for generating precise deletions and insertions in the genome of wild-type *Escherichia coli*: application to open reading frame characterization. *J. Bacteriol.* 179, 6228–6237. doi: 10.1128/jb.179.20.6228-6237.1997

Løbner-Olesen, A. (1999). Distribution of minichromosomes in individual *Escherichia coli* cells: implications for replication control. *EMBO J.* 18, 1712–1721. doi: 10.1093/emboj/18.6.1712

Løbner-Olesen, A., Skarstad, K., Hansen, F. G., von Meyenburg, K., and Boye, E. (1989). The DnaA protein determines the initiation mass of *Escherichia coli* K-12. *Cell* 57, 881–889. doi: 10.1016/0092-8674(89)90802-7

Mahaffy, J. M., and Zyskind, J. W. (1989). A model for the initiation of replication in *Escherichia coli*. *J. Theor. Biol.* 140, 453–477. doi: 10.1016/S0022-5193(89)80109-2

Mallik, P., Paul, B. J., Rutherford, S. T., Gourse, R. L., and Osuna, R. (2006). DksA is required for growth phase-dependent regulation, growth rate-dependent control, and stringent control of fis expression in *Escherichia coli*. *J. Bacteriol.* 188, 5775–5782. doi: 10.1128/JB.00276-06

McGarry, K. C., Ryan, V. T., Grimwade, J. E., and Leonard, A. C. (2004). Two discriminatory binding sites in the *Escherichia coli* replication origin are required for DNA strand opening by initiator DnaA-ATP. *Proc. Natl. Acad. Sci. U.S.A.* 101, 2811–2816. doi: 10.1073/pnas.0400340101

Miller, D. T., Grimwade, J. E., Betteridge, T., Rozgaja, T., Torgue, J. J., and Leonard, A. C. (2009). Bacterial origin recognition complexes direct assembly of higher-order DnaA oligomeric structures. *Proc. Natl. Acad. Sci. U.S.A.* 106, 18479–18484. doi: 10.1073/pnas.0909472106

Nievera, C., Torgue, J. J., Grimwade, J. E., and Leonard, A. C. (2006). SeqA blocking of DnaA-*oriC* interactions ensures staged assembly of the *E. coli* pre-RC. *Mol. Cell* 24, 581–592. doi: 10.1016/j.molcel.2006.09.016

Nilsson, L., Verbeek, H., Vijgenboom, E., van Drunen, C., Vanet, A., and Bosch, L. (1992). FIS-dependent trans activation of stable RNA operons of *Escherichia coli* under various growth conditions. *J. Bacteriol.* 174, 921–929. doi: 10.1128/jb.174.3.921-929.1992

Ozaki, S., and Katayama, T. (2012). Highly organized DnaA-*oriC* complexes recruit the single-stranded DNA for replication initiation. *Nucleic Acids Res.* 40, 1648–1665. doi: 10.1093/nar/gkr832

Ozaki, S., Noguchi, Y., Hayashi, Y., Miyazaki, E., and Katayama, T. (2012). Differentiation of the DnaA-*oriC* subcomplex for DNA unwinding in a replication initiation complex. *J. Biol. Chem.* 287, 37458–37471. doi: 10.1074/jbc.M112.372052

Pierucci, O., Helmstetter, C. E., Rickert, M., Weinberger, M., and Leonard, A. C. (1987). Overexpression of the dnaA gene in *Escherichia coli* B/r: chromosome and minichromosome replication in the presence of rifampin. *J. Bacteriol.* 169, 1871–1877. doi: 10.1128/jb.169.5.1871-1877.1987

Riber, L., Frimodt-Møller, J., Charbon, G., and Løbner-Olesen, A. (2016). Multiple DNA binding proteins contribute to timing of chromosome replication in *E. coli*. *Front. Mol. Biosci.* 3:29. doi: 10.3389/fmolb.2016.00029

Riber, L., Fujimitsu, K., Katayama, T., and Løbner-Olesen, A. (2009). Loss of Hda activity stimulates replication initiation from I-box, but not R4 mutant origins in *Escherichia coli*. *Mol. Microbiol.* 71, 107–122. doi: 10.1111/j.1365-2958.2008.06516.x

Rozgaja, T. A., Grimwade, J. E., Iqbal, M., Czerwonka, C., Vora, M., and Leonard, A. C. (2011). Two oppositely oriented arrays of low-affinity recognition sites in *oriC* guide progressive binding of DnaA during *Escherichia coli* pre-RC assembly. *Mol. Microbiol.* 82, 475–488. doi: 10.1111/j.1365-2958.2011.07827.x

Ryan, V. T., Grimwade, J. E., Camara, J. E., Crooke, E., and Leonard, A. C. (2004). *Escherichia coli* prereplication complex assembly is regulated by dynamic interplay among Fis, IHF and DnaA. *Mol. Microbiol.* 51, 1347–1359. doi: 10.1046/j.1365-2958.2003.03906.x

Sakiyama, Y., Kasho, K., Noguchi, Y., Kawakami, H., and Katayama, T. (2017). Regulatory dynamics in the ternary DnaA complex for initiation of chromosomal replication in *Escherichia coli*. *Nucleic Acids Res.* 45, 12354–12373. doi: 10.1093/nar/gkx914

Samitt, C. E., Hansen, F. G., Miller, J. F., and Schaechter, M. (1989). In vivo studies of DnaA binding to the origin of replication of *Escherichia coli*. *EMBO J.* 8, 989–993.

Schaper, S., and Messer, W. (1995). Interaction of the initiator protein DnaA of *Escherichia coli* with its DNA target. *J. Biol. Chem.* 270, 17622–17626. doi: 10.1074/jbc.270.29.17622

Schenk, K., Hervás, A. B., Rösch, T. C., Eisemann, M., Schmitt, B. A., Dahlke, S., et al. (2017). Rapid turnover of DnaA at replication origin regions contributes to initiation control of DNA replication. *PLoS Genet.* 13:e1006561. doi: 10.1371/journal.pgen.1006561

Sekimizu, K., Bramhill, D., and Kornberg, A. (1987). ATP activates dnaA protein in initiating replication of plasmids bearing the origin of the *E. coli* chromosome. *Cell* 50, 259–265. doi: 10.1016/0092-8674(87)90221-2

Shimizu, M., Noguchi, Y., Sakiyama, Y., Kawakami, H., Katayama, T., and Takada, S. (2016). Near-atomic structural model for bacterial DNA replication initiation complex and its functional insights. *Proc. Natl. Acad. Sci. U.S.A.* 113, E8021–E8030. doi: 10.1073/pnas.1609649113

Simmons, L. A., Felczak, M., and Kaguni, J. M. (2003). DnaA protein of *Escherichia coli*: oligomerization at the *E. coli* chromosomal origin is required for initiation and involves specific N-terminal amino acids. *Mol. Microbiol.* 49, 849–858. doi: 10.1046/j.1365-2958.2003.03603.x

Skarstad, K., Boye, E., and Steen, H. B. (1986). Timing of initiation of chromosome replication in individual *Escherichia coli* cells. *EMBO J.* 5, 1711–1717.

Skarstad, K., and Katayama, T. (2013). Regulating DNA replication in bacteria. *Cold Spring Harb. Perspect. Biol.* 5:a012922. doi: 10.1101/cshperspect.a012922

Skarstad, K., Løbner-Olesen, A., Atlung, T., von Meyenburg, K., and Boye, E. (1989). Initiation of DNA replication in *Escherichia coli* after overproduction of the DnaA protein. *Mol. Gen. Genet.* 218, 50–56. doi: 10.1007/BF0033 0564

Weigel, C., Messer, W., Preiss, S., Welzeck, M., and Morigenand Boye, E. (2001). The sequence requirements for a functional *Escherichia coli* replication origin are different for the chromosome and a minichromosome. *Mol. Microbiol.* 40, 498–507. doi: 10.1046/j.1365-2958.2001.02409.x

Wolański, M., Donczew, R., Zawilak-Pawlik, A., and Zakrzewska-Czerwińska, J. (2014). *oriC*-encoded instructions for the initiation of bacterial chromosome replication. *Front. Microbiol.* 5:735. doi: 10.3389/fmicb.2014.00735

Xu, Y. C., and Bremer, H. (1988). Chromosome replication in *Escherichia coli* induced by oversupply of DnaA. *Mol. Gen. Genet.* 211, 138–142. doi: 10.1007/BF00338404

Yung, B. Y., Crooke, E., and Kornberg, A. (1990). Fate of the DnaA initiator protein in replication at the origin of the *Escherichia coli* chromosome in vitro. *J. Biol. Chem.* 265, 1282–1285.

Zhang, Q., and Shi, H. (2012). Coupling chromosomal replication to cell growth by the initiator protein DnaA in *Escherichia coli*. *J. Theor. Biol.* 314, 164–172. doi: 10.1016/j.jtbi.2012.08.045

Zhang, Q., Zhou, A., Li, S., Ni, J., Tao, J., Lu, J., et al. (2016). Reversible lysine acetylation is involved in DNA replication initiation by regulating activities of initiator DnaA in *Escherichia coli*. *Sci. Rep.* 6:30837. doi: 10.1038/srep30837

Conflict of Interest Statement: The authors declare that the research was conducted in the absence of any commercial or financial relationships that could be construed as a potential conflict of interest.

frontiers in Microbiology

REVIEW
published: 28 February 2018
doi: 10.3389/fmicb.2018.00319

The DnaA Tale

Flemming G. Hansen[1]* *and Tove Atlung*[2]

[1] Department of Bioengineering, Technical University of Denmark, Lyngby, Denmark, [2] Department of Science and Environment, Roskilde University, Roskilde, Denmark

More than 50 years have passed since the presentation of the Replicon Model which states that a positively acting initiator interacts with a specific site on a circular chromosome molecule to initiate DNA replication. Since then, the origin of chromosome replication, *oriC*, has been determined as a specific region that carries sequences required for binding of positively acting initiator proteins, DnaA-boxes and DnaA proteins, respectively. In this review we will give a historical overview of significant findings which have led to the very detailed knowledge we now possess about the initiation process in bacteria using *Escherichia coli* as the model organism, but emphasizing that virtually all bacteria have DnaA proteins that interacts with DnaA boxes to initiate chromosome replication. We will discuss the *dnaA* gene regulation, the special features of the *dnaA* gene expression, promoter strength, and translation efficiency, as well as, the DnaA protein, its concentration, its binding to DnaA-boxes, and its binding of ATP or ADP. Furthermore, we will discuss the different models for regulation of initiation which have been proposed over the years, with particular emphasis on the Initiator Titration Model.

Keywords: DnaA protein, DnaA box, *dnaA* gene, DnaA ADP/ATP, *oriC*, initiation control models, initiator titration, cell cycle

OPEN ACCESS

Edited by:
Arieh Zaritsky,
Ben-Gurion University of the Negev, Israel

Reviewed by:
Charles Edward Helmstetter, Florida Institute of Technology, United States
Judith Weaver Zyskind, San Diego State University, United States

***Correspondence:**
Flemming G. Hansen
fgha@dtu.dk

Specialty section:
This article was submitted to Microbial Physiology and Metabolism, a section of the journal Frontiers in Microbiology

Received: *04 January 2018*
Accepted: *09 February 2018*
Published: *28 February 2018*

Citation:
Hansen FG and Atlung T (2018) The DnaA Tale. Front. Microbiol. 9:319. doi: 10.3389/fmicb.2018.00319

INTRODUCTION

The Replicon Model hypothesizes that to initiate DNA replication a positively acting initiator molecule interacts with a specific site, the replicator, on a circular chromosome (**Figure 1**; Jacob et al., 1963). The model was probably designed based on two main findings: (1) that the bacterial chromosome was circular (Cairns, 1963); and (2) that arrest of protein and/or RNA synthesis led to inhibition of initiation but allowed termination of ongoing rounds of replication (Maaløe and Hanawalt, 1961).

Since then, several models, to be addressed later, have been designed to explain some of the characteristics of the coupling between the cell cycle and the growth of *Escherichia coli* and possibly also several other bacteria. *Escherichia coli* can grow at very different growth rates depending on the carbon source and other nutrients present in the growth medium. The generation time in rich media, such as LB medium, is ∼20 min at 37°C whereas generation times in minimal media with poor carbon sources can be several hours. At all these generation times it is characteristic for *E. coli* (and most other bacteria) that fast growing cells are big and slowly growing cells are small, but the size of a baby cell will always be very close to half the size of the mother cell independent of the growth rate (Schaechter et al., 1958; Maaløe and Kjeldgaard, 1966).

It should be emphasized that the present review is the story about DnaA and *oriC*. For more detailed reviews see e.g., Messer (2002), Skarstad and Katayama (2013), or Leonard and Grimwade (2015).

FIGURE 1 | The replicon model. A drawing in the sand (provided by M. Mechali to an EMBO meeting report by Skarstad et al. (2003, Copyright, John Wiley and Sons) to celebrate the 40th anniversary of the model.

THE CELL CYCLE

A very important early input to characterization of the bacterial cell cycle was obtained in the work with the baby cell machine; a membrane elution technique (Helmstetter and Cummings, 1963, 1964). In this method the cells of an exponentially growing culture are attached to a membrane filter, the filter holder is inverted and growth medium is passed through the filter. The bacteria grow on the filter and one daughter cell detaches upon cell division and is collected. The main findings were that if cells grew with generation times shorter than 60 min the time it took to replicate the chromosome was close to 40 min, this was termed the C-period, and that the time it took from termination of chromosome replication to cell division was close to 20 min, termed the D-period (Helmstetter, 1967; Helmstetter and Cooper, 1968; Helmstetter et al., 1968). These primary studies were carried out using the *Escherichia coli* B/r strain that behaved very well in the baby cell machine, i.e., the mother cells were firmly attached to the filter (Helmstetter and Cummings, 1963, 1964). Two different approaches have been used in baby cell experiments. One where DNA was labeled with radioactivity before the cells were attached to the filter and radioactivity was determined in the effluent at different times, the other (and conceptually simpler) where newborn cells were collected on ice to stop growth and an experiment was started with bacterial babies transferred to the desired growth temperature getting synchronized cell division (Clark and Maaløe, 1967). This has been the preferred method for later experiments addressing cell cycle parameters. Cells with generation times longer than 60 min very often have a period with only one non-replicating chromosome, this period was termed the B-period (Helmstetter and Pierucci, 1976). Cells growing with generation times longer than 60 min have longer C- and D-periods than given above, and the B-, C-, and D-period show some variation in different strains of *E. coli* (Helmstetter, 1996; Michelsen et al., 2003).

THE INITIATION MASS

The determination of the cell cycle parameters (see above) and the very careful measurements of DNA and cell mass in a study of macromolecular concentrations at different growth rates of *Salmonella typhimurium* (Schaechter et al., 1958) led to the suggestion that bacteria like *E. coli* and to *S. typhimurium*, initiate replication when a certain mass (or volume) is present per origin of replication, the initiation mass (Donachie, 1968) or the critical volume (Pritchard et al., 1969).There has been some dispute whether the initiation mass is the same at all growth rates (Wold et al., 1994). However, it is generally accepted that the initiation mass does not vary very much in *E. coli* K-12 growing at different growth rates (Herrick et al., 1996).

PHENOMENOLOGY OF CONTROL OF CHROMOSOME REPLICATION

The results obtained with the baby cell machine can only be explained if all chromosomal origins in a cell are initiated once and only once per cell cycle. The length of the C and D periods for fast growing bacteria implies that these cells contain several origins and have several ongoing replication forks. That this is the case was demonstrated clearly by flow cytometry of cultures treated with rifampicin that inhibits initiation of chromosome replication but allows ongoing replication forks to terminate (Skarstad et al., 1986). To determine origins per cell at the time of drug addition it is necessary also to stop cell division (Løbner-Olesen et al., 1989) by simultaneous addition of cephalexin (Begg and Donachie, 1985). In the fast growing cells which carried more than one origin at the time of initiation (and rifampicin addition) flow cytometry showed in addition that all origins were initiated synchronously, i.e., cells had either 2^n or $2^{(n+1)}$ replicated chromosomes (Skarstad et al., 1986) which (with simultaneous cephalexin addition) will be equal to the number of origins per cell (Skarstad et al., 1986; Løbner-Olesen et al., 1989). Thus, a model for control of chromosome replication should satisfy what we know about the cell cycle and the behavior of chromosomes and origins. However, before going into the modeling mode we will give a relatively detailed description of the *dnaA* gene and its gene product, which is a positively acting initiator, and the origin of replication, which is the replicator. In Francois Jacob's laboratory, Masamichi Kohiyama isolated temperature sensitive DNA replication mutants some of which continued to replicate at a non-permissive growth temperature until they terminated replication, presumably at the terminus of replication (Jacob et al., 1963; Kohiyama et al., 1963). Some of these mutants were *dnaA* mutants. This historical tale is about the initiator, the DnaA protein and its interaction with the replicator, the origin of replication - *oriC*, and will focus on details about the *dnaA* gene encoding the DnaA protein as well as the requirements for the interaction of the DnaA protein with *oriC*.

THE *dnaA* MUTANTS

The temperature sensitive K-12 strains CRT46 and CRT83, were the first strains carrying mutations in the *dnaA* gene, *dnaA46,* and *dnaA83*, respectively. These mutations were genetically mapped and found to be located in the vicinity of the *ilv* locus (Hirota et al., 1968). In the following years several strains carrying mutations in the *dnaA* gene (see **Figure 5** below) were isolated in different laboratories (Kuempel, 1969; Carl, 1970; Wechsler and Gross, 1971; Beyersmann et al., 1974; Sevastopoulos et al., 1977). The PC2 strain (Carl, 1970) exhibits a slow stop phenotype similar to that of *dnaA* mutants, but carries a mutation in the *dnaC* gene that encodes the loading factor for DnaB, the DNA helicase.

FINE MAPPING OF THE *dnaA GENE*

The genetic structure of the *dnaA* region of the chromosome was characterized using specialized transducing λ bacteriophages, λ*tna* (Hansen and von Meyenburg, 1979; Ream et al., 1980). The chromosomal genes carried on the phages were identified by recombinational rescue of mutations known to be located close to the *ilv* locus, and mapped relative to an *Eco*RI restriction enzyme map constructed from cleavage of different transducing phages. In this study the size of gene products, the proteins, were also characterized by introducing the λ*tna* phages into UV-killed bacteria which had degraded all chromosomal DNA (Murialdo and Siminovitch, 1972). The *dnaA* and *dnaN* genes were also characterized by a Japanese group (Sakakibara and Mizukami, 1980). Several recombinant plasmids were constructed using restriction enzymes and DNA from different specialized transducing λ*tna* phages. These plasmids were used to determine the precise position of more genes by complementation of mutants and characterization of gene products in the maxicell system (Sancar et al., 1979; Hansen F. G. et al., 1982; Hansen et al., 1985). The *dnaA* region as characterized by λ*tna* phages and plasmids derived from the phages is shown in **Figure 2**.

THE ORIGIN OF REPLICATION—*oriC*

The origin of replication was found to be located close to the *ilv* genes in several studies during the 1970s (e.g., Bird et al., 1972; Marsh and Worcel, 1977). The *oriC* symbol was introduced for the origin of replication (Hiraga, 1976). A minichromosome, pSY211, carrying *oriC* was constructed by combining an ∼9.5 kb *Eco*RI fragment with a non-replicating fragment conferring ampicillin resistance (Yasuda and Hirota, 1977). It was also obtained on specialized transducing λ*asn* phages (von Meyenburg et al., 1979) which could be established as minichromosomes when transduced into a recombination deficient *recA* strain lysogenic for λ and requiring asparagine. Such strains are heat-sensitive due to the presence of the λcI_{857} gene on the λ-minichromosome. Small minichromosomes, e.g., pCM959 (von Meyenburg et al., 1979; Buhk and Messer, 1983) carrying exclusively chromosomal DNA, were isolated by selecting heat-resistant Asn^+ clones (von Meyenburg et al., 1979). Further characterization of *oriC* was carried out by deletion analysis of a plasmid carrying a fragment with a selectable marker and the 9.5 kb *Eco*RI fragment from λ*asn132* (Messer et al., 1978, 1979). In this way *oriC* could be located between a *Bam*HI and a *Xho*I site and this 422 bp region was sequenced (Meijer et al., 1979; Messer et al., 1979; Sugimoto et al., 1979)[1]. Further deletion analysis limited the *oriC* region to 245 bp (Tabata et al., 1983).

THE DnaA-BOXES

The sequence of the *E. coli oriC* was the first origin of replication to be reported for a cellular organism. The next origin to be sequenced was that of *Salmonella typhimurium* (Zyskind and Smith, 1980). Similarly to the *E. coli oriC* the *Salmonella* sequence carried an unexpected high density of GATC sites (**Figure 3**), where the position of most were conserved when compared to *E. coli*.

Sequencing other origins of the *Enterobacteriacea* family (Zyskind et al., 1981; Cleary et al., 1982) revealed a ***r***epeated sequence (R-box) which was later renamed the DnaA-box. Since these early days hundreds of bacteria have been sequenced. Virtually all bacteria carry a *dnaA* gene. The approximate position of the origin of replication can in many cases be determined by the Base-Skew-Method (McLean et al., 1998) and in most cases the precise location of the origin can be identified by the presence of DnaA-boxes which are also present in virtually all bacteria.

DnaA SETS THE INITIATION MASS—IS THE MASTER REGULATOR OF INITIATION

The first evidence that DnaA was not just essential for the initiation process but could be the initiator regulating initiation came from the studies of *dnaA*(Ts) mutants at permissive temperature which showed that initiation mass increased with increasing growth temperature (Hansen and Rasmussen, 1977; Tippe-Schindler et al., 1979). Further support for DnaA as the initiator was provided by the *dnaA*cos mutant (a pseudorevertant of *dnaA46*) which has a decreased initiation mass at low temperature (Kellenberger-Gujer et al., 1978). The hypothesis that DnaA was the initiator was disputed after the first studies of strains carrying DnaA overproducing plasmids since they did not show an increase in DNA per mass as expected

[1] At the Cold Spring Harbor meeting in 1978 where the 422 bp sequence carrying *oriC* was presented (Messer et al., 1979), Hirota's group presented the complete sequence of a 2.1 kb BamHI fragment. After the meeting K. von Meyenburg and F. G. Hansen went to Arthur Kornberg's laboratory at Stanford University where we after comparing the sequences could see that the small 91 bp BamHI fragment was missing from the original presentation of the Japanese group. Therefore minichromosome pSY211, which was available at Stanford University, was restricted with *Bam*HI and analyzed on non-denaturing poly-acrylamide gels that allowed the separation of very small fragments. F.G.Hansen found that minichromosome pSY211 also contained 2 two small BamHI fragment. The sequence of the 91 bp BamHI fragments was added to the final report from the Japanese group (Hirota et al., 1979) and referred to as "Hausen and Schaller, personal communication."

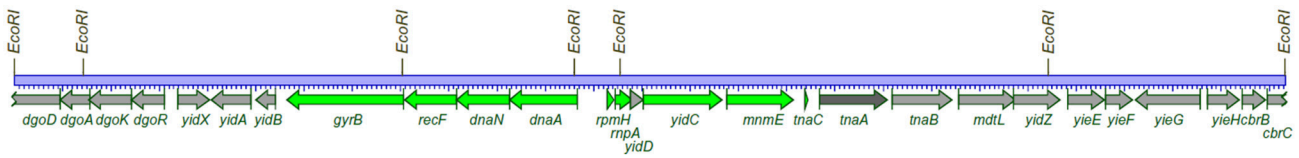

FIGURE 2 | The *dnaA* region of the *E. coli* chromosome. 26,332 bp between the outmost *Eco*RI sites is the chromosomal DNA present on two λ*tna* phages (λ*tna* 552 and λ *tna* 530). The drawing is based on the published complete *E. coli* sequence version (acc.no. U00096.2). The genes (proteins) stained green are those that could be identified on SDS-polyacrylamide gels. The light gray proteins and the dark gray protein encoded by the *tnaA* gene were not visible (Hansen and von Meyenburg, 1979; Ream et al., 1980).

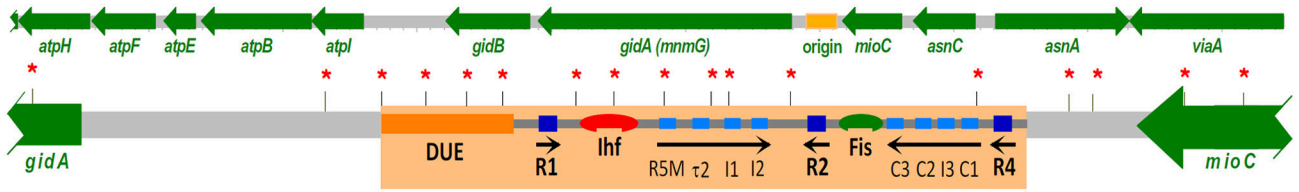

FIGURE 3 | The region of the *E. coli* chromosome carrying *oriC*, the origin of replication, and neighboring genes. A recent review presents a detailed walkthrough of the various binding sites in *oriC* and the interactions with the DnaA protein and other factors in forming the orisome that is required to initiate replication (Leonard and Grimwade, 2015). DnaA boxes with high (dark blue boxes) and low (light blue boxes) affinity, respectively; positions of GATC sites (*). However, in an exponentially growing culture containing cells of all ages only the R1, R2, and R4 are bound by DnaA protein (Samitt et al., 1989).

from a decreased initiation mass (Churchward et al., 1983). An analysis measuring also the actual concentration of *oriC* DNA per mass (Atlung et al., 1987) revealed that initiation was stimulated in cells overproducing DnaA protein, but the replication speed was decreased so much that there was virtually no increase in DNA per mass. A later analysis where we used p*lac* controlled expression to increase the DnaA protein concentration from 1.2- to 4-fold the normal (Atlung and Hansen, 1993) showed that within a limited range the origins per mass responded to the DnaA protein concentration (see **Figure 4**) showing that DnaA protein is indeed the limiting factor for initiation. Also in these experiments replication speed is decreased inversely with the higher DnaA protein concentration. Supporting this finding are the following experiments: (1) where wild type DnaA protein was induced to different subnormal levels in a *dnaA46* mutant at 42°C which showed low DNA per mass (Løbner-Olesen et al., 1989); (2) lowering the expression in a *dnaA*$^+$ strain by interfering with the expression of the messenger of the chromosomal *dnaA* gene using the tCRISPRi system (Si et al., 2017); and 3. using a slowly growing *dnaA204* mutant where the DnaA protein concentration was significantly reduced, due to instability of the protein, causing an increase in the initiation mass and thus a decrease in origin to mass ratio (Torheim et al., 2000).

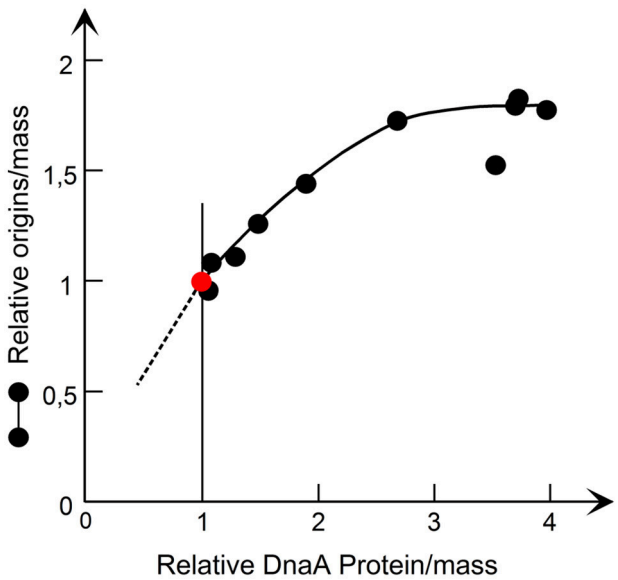

FIGURE 4 | The origin/mass responds to an increase in DnaA protein. The DnaA protein was synthesized from a *lacP* controlled *dnaA* gene and origins/mass was determined by flow cytometry. The data are redrawn from Figure 4 in Atlung and Hansen (1993, Copyright, American Society for Microbiology).

THE DnaA PROTEIN STRUCTURE

The DnaA protein has four domains (Messer et al., 1999). The domain structure was first suggested by the comparison of the *E. coli* and *B. subtilis* proteins (Ogasawara et al., 1985) which showed that there is a moderately conserved N-terminal region and a more highly conserved large C-terminal region separated by a region of highly variable sequence and length. More closely related proteins show a high conservation of the N- and C-terminal domains—e.g., the Enterobacterial proteins

have virtually identical sequences in these domains—but many amino acid substitutions, deletions and insertions in the variable region (Skovgaard and Hansen, 1987; Skovgaard, 1990). The C-terminal region contains domains III and IV, with an AAA+ family ATPase motif and the DNA binding domain respectively (Messer et al., 1999). It took a long time after the initial purification of the DnaA protein (Chakraborty et al., 1982; Fuller and Kornberg, 1983) before the first physical structures of DnaA were obtained and as yet no structure of the full length protein has been reported. The structure of domain IV from *E. coli* was determined by NMR and (Obita et al., 2002) and a year later the crystal structure of domain IV in complex with a DnaA-box was obtained (Fujikawa et al., 2003). This confirmed that the DNA binding is mediated by a combination of a basic loop and a helix-turn-helix motif. The structure of domain III has only been obtained from *Aquifex aeolicus* (Erzberger et al., 2002). When bound to ATP, but not to ADP, DnaA forms a super-helical structure with four monomers per turn (Erzberger et al., 2006; see Mott and Berger, 2007; for review and for the best figure). The structure of domain I has been determined for *E. coli* by NMR (Abe et al., 2007) and from three other bacterial species (see Zawilak-Pawlik et al., 2017 for review).

FUNCTION OF THE DIFFERENT DOMAINS

The first indication that each of the domains is essential for the activity of the DnaA protein came from the mapping and sequencing of the classical *dnaA*Ts mutants (Hansen et al., 1984, 1992), see **Figure 5** for position of the mutations and their amino acid changes. Since then many other *dnaA* mutants have been isolated both by different selections and by screening of *in vitro* generated mutants (e.g., reviewed in Erzberger et al., 2002; and additional mutants described in the following citations: Felczak and Kaguni, 2004; Asklund and Atlung, 2005; Felczak et al., 2005; Chodavarapu et al., 2013).

The C-terminal domain IV is alone responsible for sequence specific binding to double stranded DNA and the classical *dnaA*Ts mutations mapping here reduce the binding (Roth and Messer, 1995).

Domain III contains the AAA+ ATPase motif and is responsible for nucleotide binding (Sekimizu et al., 1987). DnaA binds both ATP and ADP with similar affinities, K_D 10–30 nM and 60–100 nM respectively (Sekimizu et al., 1987; Kawakami et al., 2006; Keyamura and Katayama, 2011), and the ATP form is required for the normal control of initiation of replication (Sekimizu et al., 1987). The ATP form facilitates cooperative binding to weak DnaA boxes (Margulies and Kaguni, 1996; Speck et al., 1999; McGarry et al., 2004), is necessary for unwinding of the DUE (Duplex Unwinding Element) in *oriC* (Sekimizu et al., 1987), and for binding to single stranded (ss) DNA in the DUE (Speck and Messer, 2001; Ozaki and Katayama, 2012). Domain III binds the ss DNA directly through specific amino acids, e.g., V211 and R245 (Ozaki et al., 2008; Duderstadt et al., 2011). The terminal part of Domain III also contains a sequence patch for interaction with the membrane (Garner and Crooke, 1996) which stimulates release of the nucleotide from DnaA (Sekimizu and Kornberg, 1988). Except for *dnaA167*, and possibly also *dnaA517*, all the other classical Ts *dnaA* mutants that map in domain III carry the same mutation, i.e., the A184V change close to the P-loop of the Walker A ATP binding motif and four different secondary mutations (**Figure 3**), and the DnaA46 protein has been shown to be defective in nucleotide binding (Hwang and Kaguni, 1988; Carr and Kaguni, 1996).

Domain II is thought to be a flexible linker connecting domains I and III. All parts of domain II (between residues 78 and 136) can be deleted without major effects on function as long as the linker is 21–27 amino acids long (Nozaki and Ogawa, 2008) and the entire YFP sequence can be inserted without any effect on function (Nozaki et al., 2009a).

Domain I has several functions in relation to protein-protein interactions (see Zawilak-Pawlik et al., 2017 for review). Domain I is responsible for dimerization of DnaA protein (Weigel et al.,

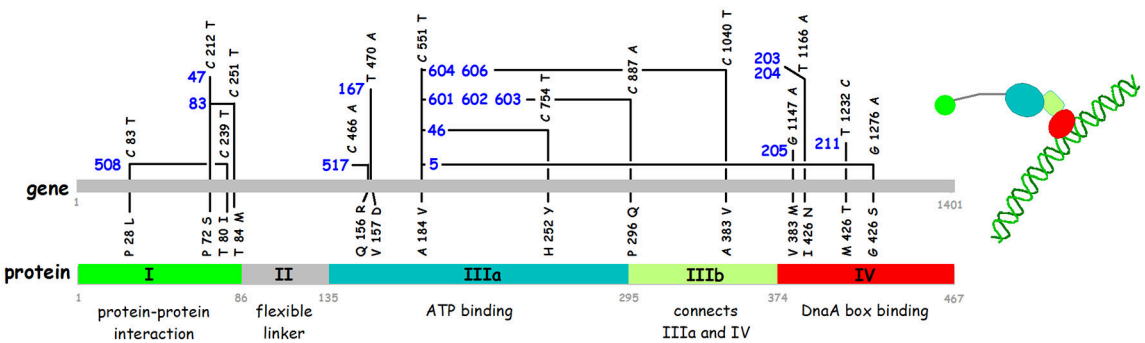

FIGURE 5 | Nucleotide and amino acid alterations in the *dnaA* gene of sixteen temperature sensitive mutants. The mutant numbers are in blue. References for the isolation of the different mutants are: *dnaA508*, *dnaA517* (Wechsler and Gross, 1971); *dnaA47* (Kuempel, 1969); *dnaA46*, *dnaA83* (Kohiyama et al., 1966); *dnaA167* (Abe and Tomizawa, 1971); *dnaA601*, *dnaA602*, *dnaA603*, *dnaA604*, *dnaA606* (Sevastopoulos et al., 1977); *dnaA203*, *dnaA204*, *dnaA205*, *dnaA211* (Beyersmann et al., 1974). The sequences of 12 of these mutants are described by Hansen et al. (1992). The four mutations *dnaA47*, *dnaA83*, *dnaA517*, and *dnaA603* were sequenced using PCR fragments obtained from the original mutant strains (this work). The domains in the DnaA protein and the borders between them are shown in the lower part of the figure.

1999). The dimerization is essential for the function of the protein in initiation of replication as deletion of the first 24 amino acids renders the protein inactive in complementation of the *dnaA46* mutant (Weigel et al., 1999). Residues 24–86 are essential for interaction with DnaB, but recruitment of DnaB at *oriC* also requires the first 23 amino acids (Seitz et al., 2000). The DiaA (*D*naA *i*nitiator *a*ssociating protein) also interacts with domain I. The *diaA* gene was identified in a selection for suppressors of the *dnaAcos* mutant that over initiates (Ishida et al., 2004). The DiaA protein is not essential, but stimulates initiation of replication *in vitro*, and a *diaA* null mutant is slightly impaired in initiation and shows moderate asynchrony (Ishida et al., 2004). The DiaA protein is a tetramer (Keyamura et al., 2007, 2009). The amino acids in DnaA involved in dimerization and in DiaA/DnaB interaction are located on opposite faces of the 3 D structure of domain I, therefore the DiaA tetramer protein can act as a connector for more distantly located DnaA dimers and monomers.

AUTOREGULATION OF DnaA PROTEIN SYNTHESIS

The first indication that the *dnaA* gene is autoregulated came from the studies of *dnaA*(Ts) mutants. DnaA protein continues to be synthesized at non-permissive temperatures where it is inactive, but in some mutants it can be reactivated when brought back to a permissive growth temperature (Hanna and Carl, 1975; Messer et al., 1975). This reversible initiation capacity, which could be observed in the absence of protein synthesis at the permissive temperature, was higher than expected from the mass increase of the culture and suggested that the DnaA protein synthesis was derepressed at the high growth temperature. These findings led to a detailed study of the *dnaA46* mutant at permissive, intermediate, and non-permissive growth temperatures (Hansen and Rasmussen, 1977). The results obtained in this study suggested that the DnaA46 protein became less and less active—the higher the growth temperature—resulting in gradually lower DNA and origin concentrations at the intermediate temperatures. In parallel with the decrease in DnaA protein activity an increase in initiation capacity was observed. Based on these findings Hansen and Rasmussen (1977) proposed that the DnaA protein had a positive role in initiation of replication and a negative role in its own synthesis.

The *dnaA* promoter region and the *dnaA* gene was sequenced (Hansen E. B. et al., 1982; Hansen F. G. et al., 1982) and two promoters giving transcripts entering the *dnaA* gene were identified. The DnaA promoter region carries 9 GATC sites within 225 bp and between the two promoters a sequence homologous to repeats (DnaA-boxes) in the *oriC* region was identified (box 1 in **Figure 6**). Both promoters are negatively regulated by DnaA protein (Atlung et al., 1984, 1985; Braun et al., 1985; Kücherer et al., 1986). In these studies the *dnaA* transcription was found to be increased up to 5-fold in *dnaA*Ts mutants at non-permissive temperature and to be repressed 4- to 5-fold by overproduction of DnaA protein. The DnaA-box is essential for the autoregulation of the *dnaA* gene (Atlung et al., 1984, 1985; Braun et al., 1985). A closer look at the sequence of the *dnaA2p* promoter region reveals interesting features. Two GATC sites are present in this promoter, one in the−10 sequence and the other in the −35 sequence, and methylation enhances transcription 2-fold from this promoter both *in vivo* and *in vitro* (Braun and Wright, 1986). Furthermore, DnaA protein binds with high affinity to sequences upstream of the *dnaA2p* promoter (Speck et al., 1999). This *in vitro* study showed that DnaA-ATP as well as DnaA-ADP binds to what they call DnaA box 1 and DnaA box 2, whereas a box they call "DnaA box a" that has two misfits to the consensus sequence (see below) only binds DnaA-ATP. From a comparison of the *dnaA2p* promoter region with the *mioC* promoter region (see below) as well as from a closer look at the *in vitro* binding data (Speck et al., 1999) we suggest that the region act as having four closely spaced DnaA boxes upstream of the *dnaA2p* promoter region one of which requires DnaA-ATP for binding (**Figure 6**) and two sites, box b and box c with no homology to DnaA boxes, which also requires DnaA-ATP. The DnaA-ATP form is required for repression of both promoters *in vitro* (Speck et al., 1999) in accordance with the location of the different kinds of DnaA-boxes.

OTHER FEATURES OF *dnaA* GENE EXPRESSION

Transcription

The *dnaA* promoter region is fairly strong, giving transcription corresponding to 50% of the *tet* promoter in pBR322 (Atlung et al., 1984). The *dnaA* gene proximal promoter p2 is approximately 3-fold stronger than the p1 promoter (Atlung

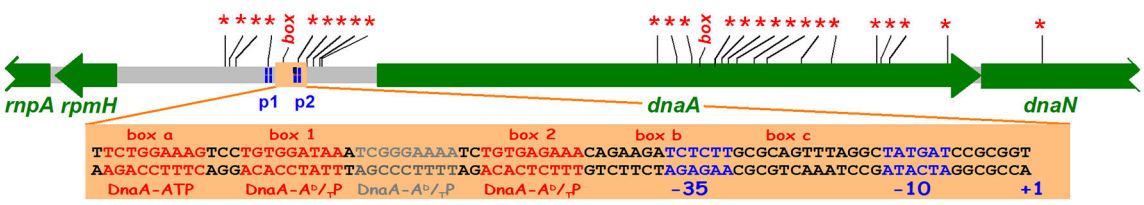

FIGURE 6 | The *dnaA* region with GATC sites (*) and consensus DnaA boxes (box). The position of *dnaA* promoters p1 and p2 are indicated (Hansen F. G. et al., 1982). The light orange rectangle shows the p2 promoter and potential DnaA boxes upstream of and overlapping the promoter. box1, box2 and the region in between are protected both by DnaA-ADP and DnaA-ATP, the boxes a, b, and c require DnaA-ATP (Speck et al., 1999). The CCGCGG sequence upstream of the +1 position is a Travers box (Travers, 1980).

et al., 1985; Kücherer et al., 1986; Chiaramello and Zyskind, 1990). *dnaA* transcription has been reported to be growth rate regulated decreasing with decreasing growth rate (Chiaramello and Zyskind, 1990; Polaczek and Wright, 1990). The p2 promoter carries a discriminator "Travers box" (Travers, 1980) downstream of the −10 sequence and transcription is, like that of the growth rate regulated *rrnP1* promoter, almost completely inhibited by high ppGpp levels.

Translation and mRNA Stability

The coding sequence of *dnaA* has a GUG start codon and a rather poor ribosome binding site (GGAG). The efficiency of translation initiation in mRNA with a SD sequence is 2- to 3-fold lower with a GUG start codon relative to an AUG start codon (Reddy et al., 1985; Donnell and Janssen, 2001). That this is similar for the *dnaA* mRNA is supported by the finding that the *dnaA508cos* mutant carrying a GUG to AUG mutation has an increased DnaA protein level sufficient to give auto-suppression of the temperature sensitivity (Eberle et al., 1989). This is similar to suppression of the temperature sensitivity obtained by having a *dnaA*(Ts) gene on pBR322 derived plasmids and on the chromosome (Hansen et al., 1992; Nyborg et al., 2000).

In addition to the low translation frequency the production of DnaA protein from the mRNA is limited by a short mRNA half-life. The chemical half-life is in the low range, in minimal medium it was amongst the shortest 1% of all mRNAs (1/3 of the mean half-life, Bernstein et al., 2002).

The wild type DnaA protein is stable (Atlung and Hansen, 1999) and is present in K-12 at ∼200 monomeric molecules per *oriC* (Hansen et al., 1991b). Therefore, the cell has to produce 100 new molecules per *dnaA* gene per generation. The above characteristics of DnaA expression, moderately high transcription rate, low translation initiation frequency and highly unstable mRNA we estimate to give on the average one protein molecule per transcript. These are the features needed to ensure a well-regulated production of protein over the cell cycle that responds smoothly to regulatory changes in transcription initiation (see **Figure 8**).

DnaA PROTEIN AT DIFFERENT GROWTH RATES

DnaA protein concentration in several different *E. coli* K-12 strains and in S*almonella typhimurium* was determined by immunoblot analysis and found to be very similar in all these strains (Hansen et al., 1991b). This study furthermore showed that the concentration of DnaA protein in all the strains was the same at all growth rates (doubling times between 150 and 22 min). Similar studies using four different primary DnaA antibodies gave the same results (Herrick et al., 1996). The constant DnaA protein concentration might intuitively be in conflict with increasing levels of mRNA with increasing growth rate. But you have to consider two factors: (1) the time available for protein synthesis, i.e., the generation time, (2) the translation efficiency, i.e., the number of proteins produced per mRNA at the different growth rates (see **Table 1**). If the translation efficiency is the same at 30 and 60 min doubling times, you will need twice as many mRNAs/mass to produce the same number of protein molecules/mass in the faster growing cells. It has been calculated that the average mRNAs are translated more efficiently in faster growing cultures, close to proportionality between number of translations and growth rate (Bremer and Dennis, 1996). The *dnaA* mRNA is, however, very different from the average mRNA in translation efficiency, we estimated it to be one translation per mRNA (see above) compared to the 30–90 translations for the average mRNA. It is therefore likely that *dnaA* mRNA efficiency might be more similar at different growth rates.

TABLE 1 | DnaA protein production at different growth rates.

Row	Entity	Generation time (min)			Reference/derivation
		100	60	30	
1	Relative total RNA/mass	0,6	0,74	1	Bremer and Dennis, 1996
2	% mRNA of total RNA	2	2	2	Bremer and Dennis, 1996
3	Relative total mRNA/mass	0,6	0,75	1	From rows 1 and 2
4	Average no of translations per mRNA	27	33	71	Bremer and Dennis, 1996
5	Relative *dnaA* mRNA/total RNA	0,27	0,37	1	Chiaramello and Zyskind, 1990
6	Relative *dnaA* mRNA/mass	0,45	0,5	1	from rows 1 and 5
7	Relative DnaA per mass	1	1	1	Hansen et al., 1991b

INITIATOR TITRATION

The first studies on titration of DnaA protein by DnaA boxes *in vivo* were conducted looking at derepression of the *dnaA* gene by DnaA boxes from *oriC—mioC* and the *dnaA* promoter region using a single copy *dnaA-lacZ* fusion (Hansen et al., 1987) and lead to the formulation of the initiator-titration model for control of initiation of replication (see below, Hansen et al., 1991a).

This was followed by two studies aimed at identifying other high affinity DnaA binding sites on the chromosome. In the first only one fragment was obtained and analyzed (Kitagawa et al., 1996). It carried what was later named the *datA* (DnaA titration) locus. The *datA* locus contains two consensus DnaA boxes and four 1-misfit boxes (see **Figure 14**) but was found to titrate much more DnaA protein than the *oriC mioC* region (Kitagawa et al., 1996). The other study, using a fishing method to isolate high affinity DNA fragments, identified five loci (in addition to *oriC*) including *datA* and the *mutH* promoter (Roth and Messer, 1998) that was later found in the search for DARSs (DnaA Reactivating Sequences, see below; Fujimitsu and Katayama, 2004). The *in vivo* titration ability—effect on

dnaA transcription—of these other four loci has not been studied.

The consensus DnaA box TTWTNCACA was suggested by Schaper and Messer (1995) based on binding of purified DnaA protein to 21 bp oligonucleotides. There are 307 of these consensus DnaA boxes on the *E. coli* chromosome. The DnaA box quality depends on the base in the fifth position and on the neighboring base sequence. Oligonucleotides which carried a DnaA box of the R1-R4 type (TTATCCACA) and had the neighboring bases as present in *oriC* were very efficient in binding the protein (K_D 10^{-9} M). Similar experiments were carried out using 17 bp double stranded oligonucleotides with 6 bp upstream and 2 bp downstream of the four consensus boxes starting with TTAT and the *mioC* (R5) box TTTTCCACA as well as with 104 bp PCR fragments with identical sequences except for the 8 different consensus boxes in the middle of the PCR fragment (Hansen et al., 2006). In the boxes starting with TTAT a C in the fifth position (R1-R4 type) is better than A (R2) or G which is better than T. In the boxes of the *mioC* type starting with TTTT, C in the fifth position is much better than the other possibilities, which show very weak or unspecific binding. Plasmids carrying the *mioC* promoter with the 8 different consensus boxes gave varying degrees of titration of DnaA protein that was in good accordance with the *in vitro* determined relative binding affinities, and the degree of repression of transcription from the *mioC* promoter also varied as expected from the binding affinities.

As noted above the *mioC* promoter region carries one consensus DnaA box and the *oriC* region carries three boxes, which in the gel shift assays were found to be very efficient binders. Nevertheless, the plasmid carrying the *mioC* promoter region is as efficient in titrating DnaA protein as a plasmid carrying an inactivated *oriC* region (Hansen et al., 2006). This study also demonstrated that sequences ∼100 bp upstream of the promoter contributed to efficient titration and thus derepression of the *dnaA-lacZ* promoter. An even more detailed study (Hansen et al., 2007) led to definition of DnaA boxes in the *mioC* region with several misfits (**Figure 7**). The number of DnaA proteins per origin has been determined to be ∼200 monomers in several different *E. coli* K-12 derivatives growing at different growth rates (Hansen et al., 1991b). The plasmid with the *mioC* promoter region increases *dnaA* gene expression 1.4-fold corresponding to 80 DnaA monomers and as the pBR322 derived plasmid carrying the *mioC* promoter region is present in ∼10 copies/*oriC* (Atlung et al., 1999) it follows that each *mioC* promoter region titrates approximately eight DnaA monomers. Similar calculations for the titration caused by the *dnaA* promoter region (Hansen et al., 1987) suggest that the *dnaA* promoter region titrates 3–4 DnaA proteins.

The presence of plasmids carrying DnaA boxes affects initiation of replication leading to increased initiation mass in parallel with the increased *dnaA* gene expression (Christensen et al., 1999; Morigen et al., 2003).

As mentioned above the *datA* region that carries two consensus DnaA boxes surrounded by closely spaced boxes with up to several misfits (see **Figure 14**) titrates large amounts of DnaA protein and plasmids carrying these boxes are difficult to handle in wild type cells.

GATC SITES, SeqA PROTEIN, AND THE ECLIPSE PERIOD

The average density of the GATC sequence in a DNA sequence containing equal amounts of the four bases is one in 256 bp. The density of GATC sites in the *oriC* sequence and the *dnaA* promoter sequence is approx. ten times higher (**Figures 3**, **6**). Unmethylated plasmids carrying the *oriC* or the pBR322 origin cannot transform Dam^+ strains, and fully methylated plasmids cannot transform a Dam^- strain. In both of these cases the plasmids will become hemimethylated upon replication in the recipient cell, therefore it was concluded that full methylation was essential for the establishment of the plasmids (Russell and Zinder, 1987). The *oriC* and the *dnaA* regions become hemimethylated after initiation of replication and stays hemimethylated (are sequestered) for a considerable time period (1/3 and 1/5 of a doubling time, respectively) while regions with few GATC-sites become methylated within 1–2 min (Lark, 1968; Campbell and Kleckner, 1990).

The SeqA protein binds to closely spaced hemi-methylated GATC sites (Brendler et al., 2000) and the *oriC* and *dnaA* promoter regions contains several closely spaced GATC sites (see **Figures 3**, **6**). These regions were "sequestered" in much shorter periods when the *seqA* gene was mutated or absent (Lu et al., 1994; von Freiesleben et al., 1994). A flow cytometric study of the re-initiation kinetics in several *dnaA*(Ts) mutants

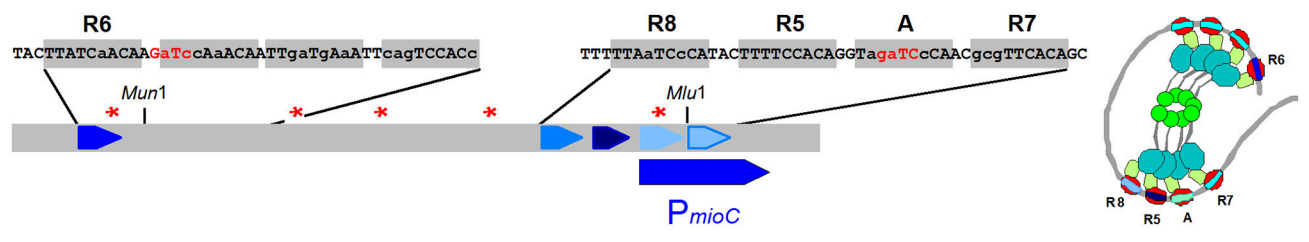

FIGURE 7 | The five experimentally verified DnaA boxes in the *mioC* region are named above the sequence boxes (Hansen et al., 2007) but also potential box sequences to the right of the R6 box are indicated. GATC sites are indicated with red stars (or red letters). To the right is a speculative view of DnaA protein bound to the DnaA-boxes in the *mioC* region (see **Figure 5** for domain colors).

which had been initiation aligned at high temperatures showed that after the immediate initiation of one round of replication at the permissive temperature there was a constant number of origins until a second initiation took place (Hansen, 1995). This period, the eclipse, was studied in more detail in strains producing normal, less than normal, and higher than normal Dam-methylase (von Freiesleben et al., 2000a). These experiments showed clearly that the length of the eclipse (sequestration) period was inversely related to the cellular level of Dam-methylase.

THE INITIATION CASCADE

Flow cytometry studies of wild type and *dam* mutant cells using synchronous cultures obtained by the baby cell machine (Løbner-Olesen et al., 1994) gave the experimental evidence for the initiation cascade as a model for how *E. coli* containing multiple origins initiates all of these once and only once per cell cycle (Hansen et al., 1991a). The cascade states that in wild type cells initiation of one origin will lead to release of DnaA protein bound to that origin, these DnaA molecules cannot bind to the two new *oriC* sequences due to the sequestration of the hemimethylated DNA by the SeqA protein. Therefore, the level of unbound DnaA protein is raised and will promote initiation at another "old" fully methylated origin. Thus, initiation will continue until all origins have initiated. To prevent reinitiation in the same cell cycle the availability of unbound initiation competent DnaA protein must be lowered before the end of the eclipse period.

The initiation cascade also explains the lack of incompatibility between minichromosomes and the chromosome despite the fairly high copy number of the minichromosomes (average 8–10 copies per chromosomal *oriC*; Løbner-Olesen et al., 1987). Before the isolation and characterization of the first minichromosomes it was expected, based on the observations with plasmids, that there would be incompatibility between the chromosomal and minichromosomal *oriC*s, i.e., that the presence of minichromosomes would inhibit initiation of chromosomal replication. Baby cell experiments showed that the minichromosomes initiate at the same time in the cell cycle as the chromosome (Leonard and Helmstetter, 1986), and flow cytometric analysis showed that the presence of a minichromosome only has a very small effect on the synchronous initiation of 4 or 8 chromosomal origins in fast growing cells (Løbner-Olesen and von Freiesleben, 1996; Skarstad and Løbner-Olesen, 2003). In contrast DnaA boxes carried on plasmids like pBR322 that replicate randomly during the cell cycle disturbs the initiation cascade leading to asynchrony (Christensen et al., 1999; Morigen et al., 2003).

SYNTHESIS OF DnaA PROTEIN DURING THE CELL CYCLE

Transcript analysis using an initiation aligned *dnaC2* mutant showed that after 30 min at 40°C transcription of the *mioC* gene was completely shut down, *dnaA* transcription was halved and *gidA* transcription was virtually unaffected (Theisen et al., 1993). This suggests that DnaA protein synthesized during the incubation of the culture at 40°C will be filling the DnaA boxes in the *mioC* promoter region effectively repressing all transcription, while the *dnaA* promoter will be less affected since it can only be partially repressed. The *gidA* promoter, that has no DnaA boxes, is not affected at the high temperature. Soon after initiation at the permissive temperature, there was virtually no transcription from the *dnaA* promoter and only a little from the *gidA* promoter whereas *mioC* transcription was restored after a few minutes. One minute after initiation the *dnaA* gene is replicated and the *dnaA* promoter region will become hemimethylated and sequestered by SeqA for a considerable period (~10 min; Campbell and Kleckner, 1990; Lu et al., 1994) inactivating the two promoters. The *gidA* promoter is located close to the sequestered *oriC* and is probably partially co-sequestered with the *oriC* region for some time. The *mioC* promoter is not sequestered and repression will be reduced by decreased DnaA activity due to titration and RIDA as replication proceeds. The findings obtained with the *dnaC* aligned system was confirmed using synchronous cultures obtained with the baby cell machine (Theisen et al., 1993). A considerable number of non-sequestered genes was also analyzed using these two synchronization techniques (Zhou et al., 1997) but no dramatic changes during the cell cycle were observed.

The *dnaA* transcription data presented above (Theisen et al., 1993) allow us to speculate about the relative numbers of DnaA protein and DnaA boxes during the cell cycle in the simple situation of a slowly growing culture. Assuming that DnaA protein is synthesized in proportion to the DnaA messenger we can predict how the number of DnaA proteins increases during a cell cycle (**Figure 8**). There is a period before initiation where *dnaA* messenger and thus protein is accumulated slowly due to autorepression. Soon after initiation the *dnaA* promoter region is sequestered and both *dnaA* promoters are inactivated. When the *dnaA* promoters are released from sequestration following methylation, the DnaA protein synthesis rate will be high, due to

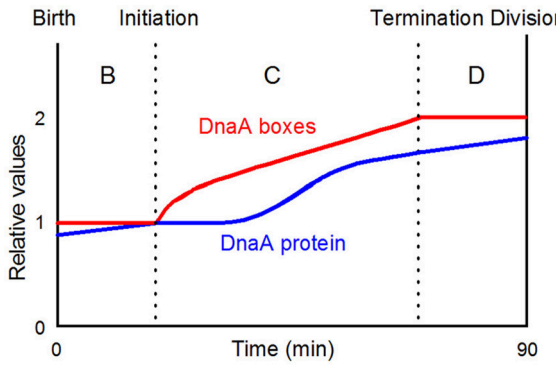

FIGURE 8 | A simplistic view of when initiation takes place in the cell cycle of slowly growing bacteria. The DnaA protein curve is drawn on the basis of the data presented by Theisen et al. (1993). DnaA-boxes with any distribution will be doubled during the C-period; the actual distribution of all consensus DnaA-boxes and selected groups of consensus boxes are presented in **Figure 10**; the figure is redrawn from Figure 2A in Herrick et al. (1996, Copyright, John Wiley and Sons).

a low concentration of DnaA protein relative to titrating DnaA boxes. The level of DnaA-ATP, that is the active form repressing the *dnaA* promoter, will also be low, due to RIDA and DDAH (see later).

MODELS FOR CONTROL OF INITIATION OF CHROMOSOME REPLICATION

The Replicon Model (Jacob et al., 1963) states that an initiator structure has to be build to interact with the origin to initiate replication. At initiation new origins are synthesized and the initiator structure is destroyed or at least prevented from reinitiating at newly synthesized origins. New initiator structures have to be constructed/reformed before initiation can take place in the following cell cycle. Basically such a model is valid but at the time it was presented the molecular basis for the initiator structure could not be addressed.

A model which attracted a lot of attention at these early times was the Inhibitor Dilution Model (Pritchard et al., 1969). It postulates that a fixed amount of messengers coding for inhibitor molecules are synthesized in a burst soon after initiation. These inhibitors would be diluted during growth of the cell and when the concentration reaches a threshold allow initiation to take place followed by the burst of new inhibitors. The molecular mechanism for how to synthesize a "fixed" amount of inhibitor after initiation was not discussed. This model inspired formulation of new models for how initiation in *E. coli* could be controlled. The inhibitor dilution model has later been formally rejected by Margalit and Grover (1987).

The autorepressor model (Sompayrac and Maaløe, 1973) hypothesizes the existence of an operon with two genes, one coding for a repressor protein, the other for an initiator protein (**Figure 9**). The repressor interacts with an operator in the promoter and represses its own synthesis to keep the repressor concentration constant and thus the production of initiator molecules constant. The model proposes that the initiator molecules build an initiator structure which will be ready to initiate when the cell reaches its initiation mass and will be destroyed at initiation. After initiation the cell can start building a new initiator structure which can be used to initiate the following replication cycle. An analysis of the model using a stochastic approach suggested that the synthesis of 250 initiator molecules shows the best fit to the experimental observations in a culture synchronized with the baby cell machine (Clark and Maaløe, 1967). This number is surprisingly close to the number of DnaA proteins per *oriC* found in several *E. coli* strains (Hansen et al., 1991b). The autorepressor model has been tested in a very detailed theoretical study by Margalit et al. (1984) in which it was concluded that the model could be valid provided that the location of the operon is close to *oriC*, that the promoter is moderate to strong, translation efficiency is low, and that the repressor binds with a moderate affinity ($K_D \sim 10^{-9}$ M); the *dnaA* gene and DnaA protein fulfills all of these requirements.

The model published by Mahaffy and Zyskind (1989) was based on data stating that the DnaA protein concentration increases at increasing growth rates (Chiaramello and Zyskind, 1989). This is at variance with the now generally accepted invariance of DnaA protein concentration in K-12. It should be noted that Mahaffy and Zyskind (1989) had to use different nucleotide bound forms of DnaA to get the model to fit with the different DnaA concentrations at different growth rates.

The Initiator Titration Model, which we will cover in some detail, was first presented at the EMBO workshop in Segovia, Spain in 1987 and it did not change before it was published (Hansen et al., 1991a).

The model hypothesizes that:

1. *The initiator—DnaA protein—has a high affinity for specific sites—DnaA boxes on the chromosome.*
2. *The initiator—DnaA protein—has a lower affinity for sites involved in the formation of the initiation complex.*
3. *DnaA protein bound to DnaA boxes is released (pushed off) by replication.*
4. *A newly replicated origin is refractory to initiation for the period it takes to regain a normal topology.*

The model was analyzed by computer simulations using a stochastic approach. A main goal was to find ONE set of parameters to put into *in silico* experiments which could be compared to different *in vivo* experimental data. To this end the comprehensive theoretical study which concluded that the autorepressor model might be a possible model (Margalit et al., 1984) was very helpful. Some of the parameters we have used are presented in **Table 2**. When we designed parameters for the model we hypothesized that the active form of DnaA protein was a tetramer and most often we used 75 DnaA-boxes distributed on the chromosome, usually with a higher occurrence of DnaA-boxes close to the origin. The actual consensus DnaA box distribution on the chromosome is presented in **Figure 10**.

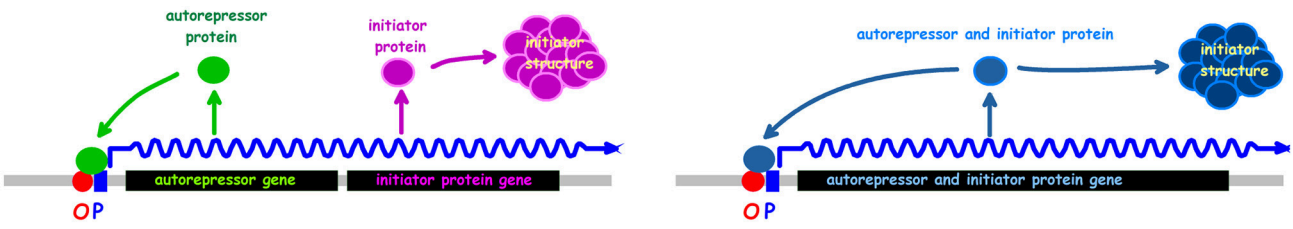

FIGURE 9 | The autorepressor model. The left drawing presents the model in its original formulation (Sompayrac and Maaløe, 1973). The right drawing shows an alternative where the autorepressor and initiator is the same protein.

TABLE 2 | Selected parameters used in the Initiator Titration Model.

Input variables		Calculated numbers	
τ	Doubling time	V	Cell volume
C	Replication time	T	Age of cells
D	Time from termination to cell division	T_n's	Replication fork positions
A_i	Number of DnaA molecules required for initiation	n	DnaA boxes per growing cell
K_D	Dissociation constant for DnaA-DnaA box interaction	G	Genome equivalents per cell
k_{dnaA1p}	Promoter constant *dnaA1p* (3)[a]	g	*dnaA* genes per cell
k_{dnaA2p}	Promoter constant *dnaA2p* (15)[a]	A	DnaA proteins per cell
k_{dnaAcp}	Promoter constant *dnaA* constitutive component (3)[a]	m	*dam* genes per cell
k_{dam}	Promoter constant *damP* (0.5)[a]	δ	Fraction of time the *dnaA* promoters are open (calculated using K_D, A, n, V)

[a] *The numbers in parentheses are relative promoter activities.*

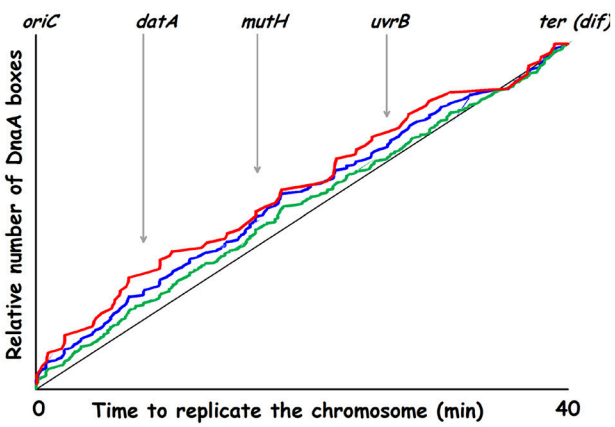

FIGURE 10 | Replication time for DnaA boxes on the K-12 chromosome. Green curve: 307 consensus DnaA boxes (TTWTNCACA); blue curve: 164 DnaA boxes (TTATNCACA + TTTTCCACA); red curve: 78 DnaA boxes (TTATNCACA where N is either C, A, or G). Genes in or lying close to chromosomal regions involved in nucleotide conversions are indicated.

In the computer experiments we started with one predefined unit baby cell that was allowed to run through 50 generations where one randomly chosen daughter was discarded. After 50 generations randomly selected daughters (baby cells) were saved in an array until arriving at a chosen cell number (e.g., 1,000 cells). These computer cells can be used directly as a perfectly synchronized culture, or they can be randomized to obtain an exponential culture by starting the baby cells one by one at different times. The computer culture grows and accumulates cells, until the cell number has doubled, then the computer culture is diluted 2-fold.

The *in silico* experiment shown in **Figure 11B** was first carried out with the assumption that the mother cell divided into two equally sized baby cells. To our surprise these simulations resulted in a computer culture behaving incredibly synchronous and that kept the synchrony for a much longer time than should be expected (data not shown). This *in silico* result was the reason why we changed the cell division mode to have a stochastic positioning of the division septum. To illustrate our stochastic approach we present an example where we use experimental data from the literature to address cell size variation after cell division. The cell length of mothers and daughters of slowly growing *E. coli* B/r cells were analyzed (Schaechter et al., 1962; Koppes et al., 1978) and found to exhibit some variation (coefficient of variation, CV, of 8–10%) in the positioning of the septum. **Figure 12** demonstrates how we handle every single cell at division.

Consequences of Asymmetric Divisions

The synthesis of DnaA protein can be described by the formulas:

$$\frac{dDnaA}{dt} = C_{cell} * C_{promoter} \quad (1)$$

C_{cell} is a component describing the general status of the cell at a given time point:

$$C_{cell} = \frac{PSS * g}{G} \quad (2)$$

where PSS is the amount of ribosomes, RNA polymerase, and other proteins, as well as nucleotides, amino acids and other small molecules needed to synthesize proteins, RNA, and DNA. The PSS will be proportional to the cell size. The g is the actual number of *dnaA* genes in the cell at any given time in the cell cycle, and G is the actual number of genome equivalents in the cell which will be proportional to all the other genes. And the promoter component:

$$C_{promoter} = k_\mu \times \alpha \left(\delta(k_{dnaA1p} + k_{dnaA2p}) + k_{dnaAc}\right) \quad (3)$$

that is growth rate dependent (k_μ), α is 0 if the promoter region is sequestered or 1 if the region is accessible, the k_{dnaA1} and k_{dnaA2} are promoter constants, k_{dnaAc} describes the DnaA protein synthesis that cannot be repressed. For each cell in the computer at each time step as the cell grows the degree of promoter openness (δ) will be calculated from K_D, the number of DnaA proteins, and the number of DnaA boxes.

Thus if a cell divides asymmetrically one of the babies will become bigger and will therefore contain more PSS, but each baby will be born with the same number of number of *dnaA* genes (g) and the same amount of genome equivalents (G). The net result of the asymmetric division will be that the big daughter synthesizes DnaA protein a little faster than the smaller and therefore will be ready for the next initiation a little faster than the other. The overall result of this is that the two cells have about the same size (but not the same age) at the next initiation.

Today we know much more than we did in 1987, and we have to include the different nucleotide bound forms of DnaA protein (see later). However, the model with its original parameter setting can simulate several experiments as published earlier (Hansen et al., 1991a) and the one shown in **Figure 11**.

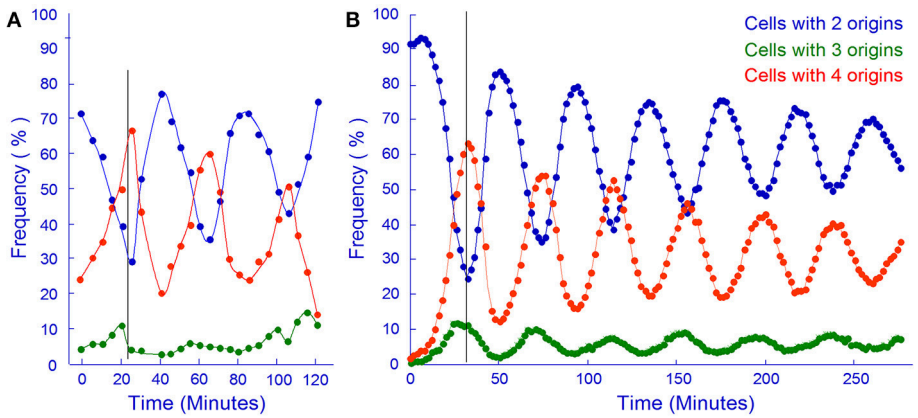

FIGURE 11 | *In vivo* and *in silico* synchronized cultures. **(A)** Samples from a synchronous culture obtained using the baby cell machine were incubated with rifampicin and the frequency of cells containing different numbers of origins were determined by flow cytometry (redrawn from Figure 4A in Løbner-Olesen et al., 1994, Copyright, John Wiley and Sons). **(B)** Same as A but using computer simulation of the Initiator Titration Model to obtain baby cells. The cell size variation in this simulation had a CV of 6.3.

```
c->volum_start=c->volum_start*pow(2.0,(double)c->tim[0]/(double)con.gen_time);

for(i=0;i<No_of_random_no;++i){
   rnd=(double)rand();
   rnd/=(double)RAND_MAX;
   rnd1+=rnd;
}
rnd1/=No_of_random_no;
rnd1*=0.4;
z->volum_start=c->volum_start*(0.3+rnd1);
c->volum_start-=z->volum_start;
```

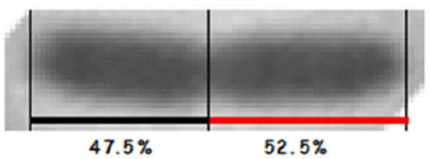

FIGURE 12 | The picture shows a constricted cell of *E. coli* which will divide asymmetrically. The cell length and the position of the constriction was found using a macro written for the Image-Pro Plus software (Nielsen and Hansen, 2010). To the left is C-code showing how we handle cell division in our simulation. c is the starting cell that increases exponentially in size with a constant generation time. At division a sum of random numbers are generated and divided with the number of random numbers. For this calculation we assume that the division take place in the central 40% of the cell (~the multiplication by 0.4), thus one of new cells will inherit 30% of the size of the old cell plus what came out of the random number considerations. If the No_of_random_no is 8 or 13 it will give CVs of 8.3 or 6.3, respectively.

RECENT ADDITIONAL FEATURES OF REGULATION OF INITIATION BY DnaA

The initiator titration model was formulated based on the concept that the concentration of DnaA protein determines the initiation mass and the findings of titration of DnaA protein by plasmids carrying DnaA boxes. The model incorporated detailed knowledge about regulation of *dnaA* gene expression, the eclipse period and the role of Dam, and the initiation synchrony of multiple origins in fast growing cells. In these last sections we will review the newer findings about the role of the *datA* locus as well as the DARS1 and DARS2 loci and the interconversion of the two nucleotide forms of DnaA (**Figure 13**) and evaluate their respective contributions to initiation control before concluding remarks about revision of the model for control of initiation to include these aspects.

DnaA-ATP HYDROLYSIS—Hda AND *datA*

Replicative inactivation of DnaA (RIDA) through hydrolysis of DnaA-ATP to DnaA-ADP was first discovered *in vitro* and shown to be dependent on replication and to require the "IdaB" (now Hda) protein and the β-clamp (DnaN; Katayama et al., 1998). A large increase in the DnaA-ATP form is found at high temperature in the *dnaN59*(Ts) and several other temperature sensitive replication mutants (Katayama et al., 1998; Kurokawa et al., 1999), showing that RIDA is also working *in vivo*. The *hda* gene was found in a search for clones that complemented (new) mutants defective in F plasmid maintenance at permissive temperature and were Ts for growth (Kato and Katayama, 2001). The gene was named *hda* (homologous to DnaA) and the Hda protein has extensive homology to domain III of DnaA. The Hda protein was shown to be identical to the IdaB protein through *in vitro* complementation, and an *hda* null mutant was shown to have a high percentage of DnaA-ATP (Kato and Katayama, 2001). In this study the *hda*(Ts) strain was also characterized *in vivo* and found to have increased *oriC* DNA per mass and increased *oriC*/*terC* indicating "abortive replication."

Until recently, there has been some controversy regarding the essentiality of the *hda* gene. In the initial identification of *hda* (Kato and Katayama, 2001) it was found that the gene could not

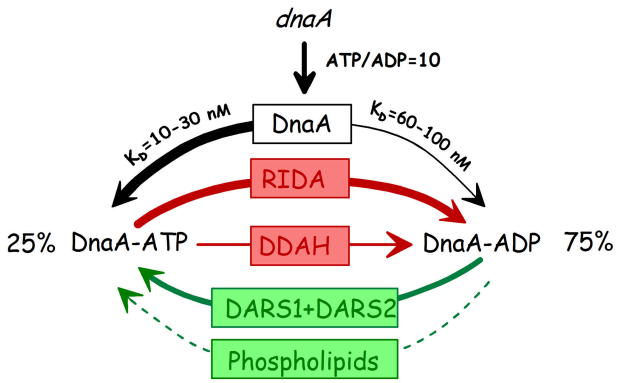

FIGURE 13 | The three states of the DnaA protein. The thickness of the arrows indicate the approximate relative contributions of the different elements to the interconversion of the different forms. Stipled arrow: the relative contribution of phospholipid mediated nucleotide exchange (Sekimizu and Kornberg, 1988; Aranovich et al., 2006, 2015) is unknown. RIDA: Replicative inactivation of DnaA (Katayama et al., 1998; Kato and Katayama, 2001); DDAH: *datA* dependent ATP hydrolysis (Kasho and Katayama, 2013); DARS: DnaA Reactivating sequence (Fujimitsu et al., 2009).

be deleted and only conditional mutants could be obtained. A little later isolation of an *hda* null mutant was reported (Camara et al., 2003). The *hda* null mutants are, however, slowly growing under standard conditions (aerobically on rich medium at 37°C) and genetically very unstable and quickly acquire suppressor mutations of many different types (Riber et al., 2006; Charbon et al., 2011). The growth defects are due to replication fork collapse caused by oxidative DNA damage so *hda* mutants have virtually no growth defects when grown anaerobically (Charbon et al., 2014) and also grow well in minimal media (Charbon et al., 2017). When grown under either of these permissive conditions the *hda* mutants still exhibit a decreased initiation mass (0.70–0.75) and moderate asynchrony.

The *datA* locus was originally believed to exert its effect on regulation of initiation through titration of DnaA protein, similar to, but much stronger than, the titration by plasmids with the *mioC* or *dnaA* promoters (Kitagawa et al., 1998; Morigen et al., 2005). Later it was found that *datA* mediates DnaA-ATP hydrolysis of DNA bound protein, a process named DDAH (Kasho and Katayama, 2013). Only two of the five original DnaA-boxes (box 2 and 3) were absolutely required together with the IHF binding site (IBS) located between them. Further studies showed that a 2-misfit box next to box 2 (box 7, see **Figure 14**) was also essential for the DDAH activity (Kasho et al., 2017). The contribution of DDAH to DnaA-ATP hydrolysis is fairly small, in an otherwise wt strain deletion of *datA* increased DnaA-ATP a few % (Katayama et al., 2001) and when the *datA* deletion was introduced into the *rnhA* Δ*oriC*- Δ*hda* strain the percentage of DnaA-ATP was increased from 72 to ∼90% (Kasho and Katayama, 2013).

Deletion of the *datA* locus has no effect on the growth rate of the bacteria but does affect the initiation control, leading to a decrease in the initiation mass (Kitagawa et al., 1998; Morigen et al., 2005; Frimodt-Møller et al., 2016). There is some controversy as to the degree of asynchrony conferred by deletion of *datA*. The first study which found a rather pronounced asynchrony in Δ*datA* cells (Kitagawa et al., 1998) also showed that such cells have close to the same DNA content and the same cell size distribution as wild type cells. Morigen et al. (2005) showed that much of the apparent asynchrony was due to rifampicin resistant initiations. It should be noted (emphasized) that rifampicin resistant initiations lead to overestimation of the effect on initiation mass. Rifampicin resistant initiation of chromosome replication has also been observed in *ihf* mutants, however, such initiations did not take place in strains carrying *ihf* and *dnaA46* mutations (von Freiesleben et al., 2000b) suggesting that the rifampicin resistant initiation phenotype of *ihf* mutants might be due to reduced function of *datA* in DDAH.

The phenotype of the Δ*datA* strain must primarily be due to the lack of DDAH activity since different point mutations inactivating the DDHA activity—mutation of the IBS, or inactivation of box 2 or box 7 have the same phenotype (Ogawa et al., 2002; Nozaki et al., 2009b; Kasho et al., 2017). The apparent very high titration activity of plasmids with the intact *datA* locus can largely be explained by the DDAH activity which lowers the DnaA-ATP level and gives increased expression from promoters which require this form of DnaA for repression. It is, however, clear that the *datA* locus also directly titrates DnaA protein by binding to the boxes, both from the initial deletion analysis of the *datA* plasmids where deletions outside the box 1–4 region gave reduced titration (Kitagawa et al., 1996) and from the analysis of plasmids with a box 2 or an IBS point mutation that only reduced titration (Nozaki et al., 2009b).

DnaA-ADP REJUVENATION

The first DARS DnaA-reactivating sequence, which is present in the ColE1 plasmid origin, was found somewhat fortuitously in a search for factors mediating *in vitro* DnaA-ADP to ATP exchange (Fujimitsu and Katayama, 2004). The full ColE1 DARS was delimited to a 70 bp sequence with three DnaA boxes, where two of the boxes in correct orientation were essential for activity. Subsequently two chromosomal DARSs were identified in the genome sequence amongst 52 pairs of similarly arranged DnaA boxes with 0 or 1 misfit to the sequence TTATNCACA (Fujimitsu et al., 2009). The DARS1 sequence is located in the *uvrB* promoter region and DARS2 in the *mutH* promoter (**Figures 10**, **15**), both previously identified as sequences that interact with DnaA (van den Berg et al., 1985; Roth and Messer, 1998). The presence of extra DARS1 or DARS2 sequences on low copy number plasmids leads to decreased initiation mass (Fujimitsu et al., 2009; Charbon et al., 2011) and introduction of higher copy number plasmids with DARS1 or DARS2 is deleterious to the cells (van den Berg et al., 1985; Fujimitsu et al., 2009). Deletion of either DARS1 or DARS2 from the chromosome increases initiation mass by ∼20% (Fujimitsu et al., 2009; Frimodt-Møller et al., 2016) and the two DARS sequences act synergistically since deletion of both increase initiation mass to close to 150% of the normal (Fujimitsu et al., 2009). Deletion of either DARS sequence reduce the DnaA-ATP percentage in the *rnhA* Δ*oriC*-Δ*hda* strain, and deletion of both DARS's almost returns the DnaA-ATP level to that of the *hda*$^+$ strain (Fujimitsu et al., 2009). The effect of the DARS deletions, especially DARS2, is sufficient to give suppression of

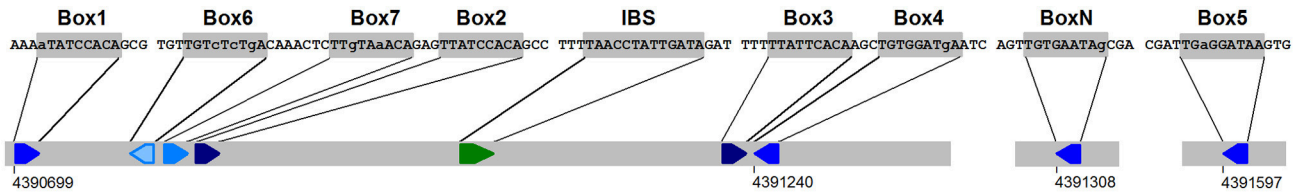

FIGURE 14 | The *datA* region responsible for DDAH (*datA* dependent ATP hydrolysis, Kitagawa et al., 1998; Morigen et al., 2005). The DnaA boxes 2, 7, 3, and IBS are absolutely required for DDAH activity (Kasho et al., 2017). The coordinates are from *E. coli* K12 (acc.no. U00096.2). IBS: IHF binding site. The color code of the boxes is the same as in **Figure 7**. An additional one-misfit box (BoxN) is also indicated.

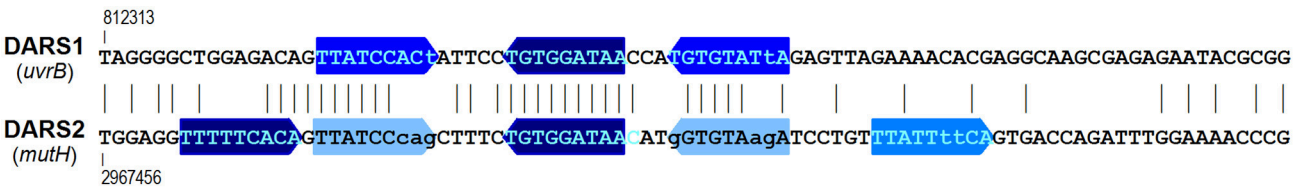

FIGURE 15 | The DARSs (DnaA reactivating sequences). The coordinates given above and below the DARS sequences (Fujimitsu et al., 2009) are from *E. coli* K12 (acc.no. U00096.2). Vertical lines between the sequences indicate identical bases. See **Figure 7** for color code for the boxes.

the lethality associated with lack of Hda mediated ATP hydrolysis (Fujimitsu et al., 2009; Charbon et al., 2011).

Intriguingly, it is only plasmids with DARS2, not with DARS1, that give asynchrony (Fujimitsu et al., 2009; Charbon et al., 2011), and only the DARS2 deletion that leads to asynchrony (Fujimitsu et al., 2009; Frimodt-Møller et al., 2016). This might be due to a higher efficiency of DARS2 in DnaA rejuvenation giving a stronger effect on DnaA-ATP % (Fujimitsu et al., 2009). It should be noted that all the data concerning initiation mass and asynchrony referred to above are from cells grown in minimal glucose casamino acids supplemented medium at 37°C. No systematic studies of the effect of DARS have been published for other growth media—i.e., slow growing cells.

We have summarized the effects of the different elements, de novo synthesis, RIDA, DDAH, and DARS on the interconversion of the two nucleotide bound forms of DnaA in **Figure 13**.

INITIATOR TITRATION REVISITED

A fundamental feature of the initiator titration model is that at the end of the eclipse (*oriC* sequestration) period the replication process has increased the number of DnaA boxes sufficiently to titrate so many DnaA proteins that there is not enough available for the low affinity binding at *oriC*. The additional feature with the two nucleotide forms of the DnaA protein and their interconversion does not essentially change this concept, in this case the amount of DnaA-ATP protein has to be reduced below a threshold during the eclipse period. Let us first consider a relatively slowly growing cell, e.g., 60 min doubling with a C time of 40 min. As soon as replication starts RIDA begins to work due to the presence of β-clamps remaining on the DNA after passage of the replisome, and when the *datA* locus is duplicated (8 min after initiation) the DDAH process will increase the hydrolysis rate a little. During these first approx. 10 min there is no DnaA protein synthesis and only one copy of the DARS sequences, and therefore the DnaA-ATP level will fall quickly. When the *dnaA* gene is no longer sequestered the DnaA-ATP dependent autorepression, will be low, and the DnaA-ATP level will start to increase due to synthesis of new proteins. At 16 min DARS2 is duplicated. In this relatively slow growing cell DARS2 might, however, be inefficient in nucleotide release since it requires Fis for this activity (Kasho et al., 2014) and Fis concentration is low in slow growing cells (Ball et al., 1992). At 26 min also DARS1 is duplicated and this will increase the building up of DnaA-ATP levels. At 40 min replication terminates and soon after RIDA will cease due to unloading of the β-clamps from the DNA which only takes a few minutes (Leu et al., 2000)[2]. In faster growing cells with overlapping replication cycles RIDA will be active throughout the cell cycle, but will vary with the number of replication forks, e.g., in a cell growing with 25 min doubling time the old forks will terminate 15 min after initiation, reducing the RIDA activity to two thirds, thus accelerating the buildup of DnaA-ATP. Unfortunately the variation in DnaA-ATP levels over the cell cycle has not been investigated using baby cells, it has only been measured in *dnaC* initiation synchronized cells (Kurokawa et al., 1999), which is an artificial situation probably with an unnaturally high DnaA-ATP starting level.

It will be interesting to incorporate the DnaA-ATP/ADP conversion systems into the initiator titration model and see how that behaves compared to the original initiator titration model,

[2]The calculated average residence time for the β-clamps (3.5–7 min) is based on a very careful determination of the number of molecules of different polymerase subunits per cell, giving a number of 350 β-clamp dimers/cell in an exponentially growing culture of C600 in LB medium. However, the final calculation uses only 2–4,000 Okazaki fragments produced per cell in 40 min, corresponding to only one replicating chromosome per cell, but C600 growing in LB medium has mostly 8 origins per cell, and thus 4 pairs of replisomes, so the average residence time therefore has to be 3- to 4-fold shorter.

and to a version of the model where we insert the actual high affinity DnaA-box distribution.

It is clear that the original initiator titration model can to a large extent simulate the behavior of *E. coli* during exponential growth. And the *dnaA46* mutant with a protein that does not bind ATP (*in vitro*) is quite fit at low temperature, growing with an almost normal growth rate and having a reasonably uniform cell size distribution despite the asynchrony of initiation (and increased initiation mass). This raises the question why has *E. coli* (and other bacteria) evolved an additional level of regulation with the DnaA-ATP/DnaA-ADP interconversion systems? It will be interesting to see if these systems are necessary and under which growth conditions—how does an *E. coli* strain that is deleted for *hda*, *datA*, and the two DARSs behave? It will probably be necessary to simultaneously reduce the *dnaA* gene expression to get a cell with a normal initiation mass avoiding the side effects of over initiation.

AUTHOR CONTRIBUTIONS

All authors listed have made a substantial, direct and intellectual contribution to the work, and approved it for publication.

ACKNOWLEDGMENTS

The authors are particularly grateful to Knud V. Rasmussen who as a Master project supervisor started our scientific entry into the field of initiation of chromosome replication and to Kaspar von Meyenburg who took part in much of the early work on the subject. We are also grateful to deceased Walter Messer who has participated in a number of open discussions of what his group did at the Max Planck Institute in Berlin and what we did in Copenhagen. At different periods we have also had close collaboration with Anders Løbner-Olesen, Ole Skovgaard, and Bjarke Bak Christensen.

REFERENCES

Abe, M., and Tomizawa, J. (1971). Chromosome replication in *E. coli* K12 mutant affected in DNA initiation. *Genetics* 69, 1–15.

Abe, Y., Jo, T., Matsuda, Y., Matsunaga, C., Katayama, T., and Ueda, T. (2007). Structure and function of DnaA N-terminal domains: specific sites and mechanisms in inter-DnaA interaction and in DnaB helicase loading on oriC. *J. Biol. Chem.* 282, 17816–17827. doi: 10.1074/jbc.M701841200

Aranovich, A., Braier-Marcovitz, S., Ansbacher, E., Granek, R., Parola, A. H., and Fishov, I. (2015). N-terminal-mediated oligomerization of DnaA drives the occupancy-dependent rejuvenation of the protein on the membrane. *Biosci. Rep.* 35:e00250. doi: 10.1042/BSR20150175

Aranovich, A., Gdalevsky, G. Y., Cohen-Luria, R., Fishov, I., and Parola, A. H. (2006). Membrane-catalyzed nucleotide exchange on DnaA. Effect of surface molecular crowding. *J. Biol. Chem.* 281, 12526–12534. doi: 10.1074/jbc.M510266200

Asklund, M., and Atlung, T. (2005). New non-detrimental DNA-binding mutants of the *Escherichia coli* initiator protein DnaA. *J. Mol. Biol.* 345, 717–730. doi: 10.1016/j.jmb.2004.10.092

Atlung, T., Christensen, B. B., and Hansen, F. G. (1999). Role of the Rom protein in copy number control of plasmid pBR322 at different growth rates in *Escherichia coli* K-12. *Plasmid* 41, 110–119. doi: 10.1006/plas.1998.1386

Atlung, T., Clausen, E., and Hansen, F. G. (1984). "Autorepression of the *dnaA* gene of *Escherichia coli*," in *Proteins Involved in DNA Replication*, eds U. Huebscher and S. Spadari (New York, NY; London: Plenum Press), 199–207.

Atlung, T., Clausen, E. S., and Hansen, F. G. (1985). Autoregulation of the *dnaA* gene of *Escherichia coli*. *Mol. Gen. Genet.* 200, 442–450. doi: 10.1007/BF00425729

Atlung, T., and Hansen, F. G. (1993). Three distinct chromosome replication states are induced by increasing concentrations of DnaA protein in *Escherichia coli*. *J. Bacteriol.* 175, 6537–6545. doi: 10.1128/jb.175.20.6537-6545.1993

Atlung, T., and Hansen, F. G. (1999). Low-temperature-induced dnaa protein synthesis does not change initiation mass in *Escherichia coli* K-12 low-temperature-induced dnaa protein synthesis does not change initiation mass in *Escherichia coli* K-12. *J. Bacteriol.* 181, 5557–5562.

Atlung, T., Løbner-Olesen, A., and Hansen, F. G. (1987). Overproduction of DnaA protein stimulates initiation of chromosome and minichromosome replication in *E. coli*. *Mol. Gen. Genet.* 206, 51–59. doi: 10.1007/BF00326535

Ball, C. A., Osuna, R., Ferguson, K. C., and Johnson, R. C. (1992). Dramatic change of fis level upon nutrient upshift in *Escherichia coli*. *J. Bacteriol.* 174, 8043–8056. doi: 10.1128/jb.174.24.8043-8056.1992

Begg, K. J., and Donachie, W. D. (1985). Cell shape and division in *Escherichia coli*: experiments with shape and division mutants. *J. Bacteriol.* 163, 615–622.

Bernstein, J. A., Khodursky, A. B., Lin, P. H., Lin-Chao, S., and Cohen, S. N. (2002). Global analysis of mRNA decay and abundance in *Escherichia coli* at single-gene resolution using two-color fluorescent DNA microarrays. *Proc. Natl. Acad. Sci. U.S.A.* 99, 9697–9702. doi: 10.1073/pnas.112318199

Beyersmann, D., Messer, W., and Schlicht, M. (1974). Mutants of *Escherichia coli* B/r defective in DNA initiation: dnaI, a new gene for replication. *J. Bacteriol.* 118, 783–789.

Bird, R. E., Louarn, J., Maruscelli, J., and Caro, L. (1972). Origin and sequence of chromosome replication in *Escherichia coli*. *J.Mol.Biol.* 70, 549–566. doi: 10.1016/0022-2836(72)90559-1

Braun, R. E., O'Day, K., and Wright, A. (1985). Autoregulation of the DNA replication gene *dnaA* in *E. coli*. *Cell* 40, 159–169.

Braun, R. E., and Wright, A. (1986). DNA methylation differentially enhances the expression of one of the two *E. coli dnaA* promoters *in vivo* and *in vitro*. *Mol. Gen. Genet.* 202, 246–250. doi: 10.1007/BF00331644

Bremer, H., and Dennis, P. P. (1996). "Modulation of chemical composition and other parameters of the cell by growth rate," in *Escherichia coli* and *Salmonella: Cellular and Molecular Biology*, eds F. C. Neidhardt, R. I. Curtiss, J. L. Ingraham, E. C. C. Lin, K. Brooks Low, B. Magasanik et al. (Washington, DC: American Society for Microbiology), 1553–1569.

Brendler, T., Sawitzke, J., Sergueev, K., and Austin, S. (2000). A case for sliding SeqA tracts at anchored replication forks during *Escherichia coli* chromosome replication and segregation. *EMBO J.* 19, 6249–6258. doi: 10.1093/emboj/19.22.6249

Buhk, H.-J., and Messer, W. (1983). The replication origin region of *Escherichia coli:* nucleotide sequence and functional units. *Gene* 24, 265–279. doi: 10.1016/0378-1119(83)90087-2

Cairns, J. (1963). The chromosome of *Escherichia coli*. *Cold Spring Harb. Symp. Quant. Biol.* 28, 43–46. doi: 10.1101/SQB.1963.028.01.011

Camara, J. E., Skarstad, K., and Crooke, E. (2003). Controlled initiation of chromosomal replication in *Escherichia coli* requires functional Hda protein. *J. Bacteriol.* 185, 3244–3248. doi: 10.1128/JB.185.10.3244-3248.2003

Campbell, J. L., and Kleckner, N. (1990). *E. coli oriC* and the *dnaA* gene promoter are sequestered from dam methyltransferase following the passage of the chromosomal replication fork. *Cell* 62, 967–979. doi: 10.1016/0092-8674(90)90271-F

Carl, P. L. (1970). *E. coli* mutants with temperature sensitive synthesis of DNA. *Mol. Gen. Genet.* 109, 107–122. doi: 10.1007/BF00269647

Carr, K. M., and Kaguni, J. M. (1996). The A184V missense mutation of the *dnaA5* and *dnaA46* alleles confers a defect in ATP binding and thermolability in initiation of *Escherichia coli* DNA replication. *Mol. Microbiol.* 20, 1307–1318. doi: 10.1111/j.1365-2958.1996.tb02649.x

Chakraborty, T., Yoshinaga, K., Lother, H., and Messer, W. (1982). Purification of the *E. coli dnaA* gene product. *EMBO J.* 1, 1545–1549.

Charbon, G., Bjørn, L., Mendoza-Chamizo, B., Frimodt-Møller, J., and Løbner-Olesen, A. (2014). Oxidative DNA damage is instrumental in

hyperreplication stress-induced inviability of *Escherichia coli*. *Nucleic Acids Res.* 42, 13228–13241. doi: 10.1093/nar/gku1149

Charbon, G., Campion, C., Chan, S. H. J., Bjørn, L., Weimann, A., da Silva, L., et al. (2017). Re-wiring of energy metabolism promotes viability during hyperreplication stress in *E. coli*. *PLoS Genet.* 13:e1006590. doi: 10.1371/journal.pgen.1006590

Charbon, G., Riber, L., Cohen, M., Skovgaard, O., Fujimitsu, K., Katayama, T., et al. (2011). Suppressors of DnaA(ATP) imposed overinitiation in *Escherichia coli*. *Mol. Microbiol.* 79, 914–928. doi: 10.1111/j.1365-2958.2010.07493.x

Chiaramello, A. E., and Zyskind, J. W. (1989). Expression of *Escherichia coli dnaA* and *mioC* genes as function of growth rate. *J. Bacteriol.* 171, 4272–4280. doi: 10.1128/jb.171.8.4272-4280.1989

Chiaramello, A. E., and Zyskind, J. W. (1990). Coupling of DNA replication to growth rate in *Escherichia coli*: a possible role for guanosine tetraphosphate. *J. Bacteriol.* 172, 2013–2019. doi: 10.1128/jb.172.4.2013-2019.1990

Chodavarapu, S., Felczak, M. M., Simmons, L. A., Murillo, A., and Kaguni, J. M. (2013). Mutant DnaAs of *Escherichia coli* that are refractory to negative control. *Nucleic Acids Res.* 41, 10254–10267. doi: 10.1093/nar/gkt774

Christensen, B. B., Atlung, T., and Hansen, F. G. (1999). DnaA boxes are important elements in setting the initiation mass of *Escherichia coli*. *J. Bacteriol.* 181, 2683–2688.

Churchward, G., Holmans, P., and Bremer, H. (1983). Increased expression of the *dnaA* gene has no effect on DNA replication in a *dnaA*+ strain of *Escherichia coli*. *Mol. Gen. Genet.* 192, 506–508. doi: 10.1007/BF00392197

Clark, D. J., and Maaløe, O. (1967). DNA replication and the division cycle in *Escherichia coli*. *J. Mol. Biol.* 23, 99–112. doi: 10.1016/S0022-2836(67)80070-6

Cleary, J. M., Smith, D. W., Harding, N. E., and Zyskind, J. W. (1982). Primary structure of the chromosomal origins (*oriC*) of *Enterobacter aerogenes* and *Klebsiella pneumoniae*: comparisons and evolutionary relationships. *J. Bacteriol.* 150, 1467–1471.

Donachie, W. D. (1968). Relationship between cell size and time of initiation of DNA replication. *Nature* 219, 1077–1079. doi: 10.1038/2191077a0

Donnell, S. M. O., and Janssen, G. R. (2001). The initiation codon affects ribosome binding and translational efficiency in *Escherichia coli* of *c*I mRNA with or without the 5′ untranslated leader. *J. Bacteriol.* 183, 1277–1283. doi: 10.1128/JB.183.4.1277-1283.2001

Duderstadt, K. E., Chuang, K., and Berger, J. M. (2011). DNA stretching by bacterial initiators promotes replication origin opening. *Nature* 478, 209–213. doi: 10.1038/nature10455

Eberle, H., van de Merwe, W., Madden, K., Kampo, G., Wright, L., and Donlon, K. (1989). The nature of an intragenic suppressor of the *Escherichia coli dnaA508* temperature-sensitive mutation. *Gene* 84, 237–245. doi: 10.1016/0378-1119(89)90497-6

Erzberger, J. P., Mott, M. L., and Berger, J. M. (2006). Structural basis for ATP-dependent DnaA assembly and replication-origin remodeling. *Nat. Struct. Mol. Biol.* 13, 676–683. doi: 10.1038/nsmb1115

Erzberger, J. P., Pirruccello, M. M., and Berger, J. M. (2002). The structure of bacterial DnaA: implications for general mechanisms underlying DNA replication initiation. *EMBO J.* 21, 4763–4773. doi: 10.1093/emboj/cdf496

Felczak, M. M., and Kaguni, J. M. (2004). The box VII motif of *Escherichia coli* DnaA protein is required for DnaA oligomerization at the *E. coli* replication origin. *J. Biol. Chem.* 279, 51156–51162. doi: 10.1074/jbc.M409695200

Felczak, M. M., Simmons, L. A., and Kaguni, J. M. (2005). An essential tryptophan of *Escherichia coli* DnaA protein functions in oligomerization at the *E. coli* replication origin. *J. Biol. Chem.* 280, 24627–24633. doi: 10.1074/jbc.M503684200

Frimodt-Møller, J., Charbon, G., Krogfelt, K. A., and Løbner-Olesen, A. (2016). DNA replication control is linked to genomic positioning of control regions in *Escherichia coli*. *PLoS Genet.* 12:e1006286. doi: 10.1371/journal.pgen.1006286

Fujikawa, N., Kurumizaka, H., Nureki, O., Terada, T., Shirouzu, M., Katayama, T., et al. (2003). Structural basis of replication origin recognition by the DnaA protein. *Nucleic Acids Res.* 31, 2077–2086. doi: 10.1093/nar/gkg309

Fujimitsu, K., and Katayama, T. (2004). Reactivation of DnaA by DNA sequence-specific nucleotide exchange *in vitro*. *Biochem. Biophys. Res. Commun.* 322, 411–419. doi: 10.1016/j.bbrc.2004.07.141

Fujimitsu, K., Senriuchi, T., and Katayama, T. (2009). Specific genomic sequences of *E. coli* promote replicational initiation by directly reactivating ADP-DnaA. *Genes Dev.* 23, 1221–1233. doi: 10.1101/gad.1775809

Fuller, R. S., and Kornberg, A. (1983). Purified *dnaA* protein in initiation of replication at the *Escherichia coli* chromosomal origin of replication. *Proc. Natl. Acad. Sci. U.S.A.* 80, 5817–5821. doi: 10.1073/pnas.80.19.5817

Garner, J., and Crooke, E. (1996). Membrane regulation of the chromosomal replication activity of *E. coli* DnaA requires a discrete site on the protein. *EMBO J.* 15, 3477–3485.

Hanna, M. H., and Carl, P. L. (1975). Reinitiation of deoxyribonucleic acid synthesis by deoxyribonucleic acid initiation mutants of *E. coli*: role of ribonucleic acid synthesis, protein synthesis, and cell division. *J. Bacteriol.* 121, 219–226.

Hansen, E. B., Atlung, T., Hansen, F. G., Skovgaard, O., and von Meyenburg, K. (1984). Fine structure genetic map and complementation analysis of mutations in the *dnaA* gene of *Escherichia coli*. *Mol. Gen. Genet.* 196, 387–396. doi: 10.1007/BF00436184

Hansen, E. B., Hansen, F. G., and von Meyenburg, K. (1982). The nucleotide sequence of the *dnaA* gene and the first part of the *dnaN* gene of *Escherichia coli* K12. *Nucleic Acids Res.* 10, 7373–7385. doi: 10.1093/nar/10.22.7373

Hansen, F. G. (1995). Reinitiation kinetics in eight *dnaA*(Ts) mutants of *Escherichia coli*: rifampicin resistant initiation of chromosome replication. *Mol. Microbiol.* 15, 133–140. doi: 10.1111/j.1365-2958.1995.tb02227.x

Hansen, F. G., Atlung, T., Braun, R. E., Wright, A., Hughes, P., and Kohiyama, M. (1991b). Initiator (DnaA) protein concentration as a function of growth rate in *Escherichia coli* and *Salmonella typhimurium*. *J. Bacteriol.* 173, 5194–5199. doi: 10.1128/jb.173.16.5194-5199.1991

Hansen, F. G., Christensen, B. B., and Atlung, T. (1991a). The initiator titration model: computer simulation of chromosome and minichromosome control. *Res. Microbiol.* 142, 161–167. doi: 10.1016/0923-2508(91)90025-6

Hansen, F. G., Christensen, B. B., and Atlung, T. (2007). Sequence characteristics required for cooperative binding and efficient *in vivo* titration of the replication initiator protein DnaA in *E. coli*. *J. Mol. Biol.* 367, 942–952. doi: 10.1016/j.jmb.2007.01.056

Hansen, F. G., Christensen, B. B., Nielsen, C. B., and Atlung, T. (2006). Insights into the quality of DnaA boxes and their cooperativity. *J. Mol. Biol.* 355, 85–95. doi: 10.1016/j.jmb.2005.10.036

Hansen, F. G., Hansen, E. B., and Atlung, T. (1982). The nucleotide sequence of the *dnaA* gene promoter and of the adjacent *rpmH* gene, coding for the ribosomal protein L34, of *Escherichia coli*. *EMBO J.* 1, 1043–1048.

Hansen, F. G., Hansen, E. B., and Atlung, T. (1985). Physical mapping and DNA sequence of the gene *rnpA*, that encodes the protein component of ribonuclease P in *Escherichia coli*. *Gene* 38, 85–93. doi: 10.1016/0378-1119(85)90206-9

Hansen, F. G., Koefoed, S., and Atlung, T. (1992). Cloning and nucleotide sequence determination of twelve mutant *dnaA* genes of *Escherichia coli*. *Mol. Gen. Genet.* 234, 14–21.

Hansen, F. G., Koefoed, S., Sørensen, L., and Atlung, T. (1987). Titration of DnaA protein by *oriC* DnaA-boxes increases *dnaA* gene expression in *Escherichia coli*. *EMBO J.* 6, 255–258.

Hansen, F. G., and Rasmussen, K. V. (1977). Regulation of the *dnaA* product in *E. coli*. *Mol. Gen. Genet.* 155, 219–225. doi: 10.1007/BF00393163

Hansen, F. G., and von Meyenburg, K. (1979). Characterization of the *dnaA*, *gyrB* and other genes in the *dnaA* region of the *Escherichia coli* chromosome on specialized transducing phages lambda-*tna*. *Mol. Gen. Genet.* 175, 135–144. doi: 10.1007/BF00425529

Helmstetter, C. E. (1967). Rate of DNA synthesis during the division cycle of *E. coli* B/r. *J. Mol. Biol.* 24, 417–427. doi: 10.1016/0022-2836(67)90228-8

Helmstetter, C. E. (1996). "Timing of synthetic activities in the cell cycle," in *Escherichia coli and Salmonella Cellular and Molecular Biology*, eds F. C. Neidhardt, J. L. Ingraham, E. C. C. Lin, K. B. Low, B. Magasanik, W. S. Reznikoff et al. (Washington, DC: ASM Press), 1627–1639.

Helmstetter, C. E., and Cooper, S. (1968). DNA synthesis during the division cycle of rapidly growing *Escherichia coli* B/r. *J. Mol. Biol.* 31, 507–518. doi: 10.1016/0022-2836(68)90424-5

Helmstetter, C. E., Cooper, S., Pierucci, D., and Revelas, E. (1968). The bacterial life cycle. *Cold Spring Harb. Symp. Quant. Biol.* 33, 809–822. doi: 10.1101/SQB.1968.033.01.093

Helmstetter, C. E., and Cummings, D. J. (1963). Bacterial synchronization by selection of cells at division. *Proc. Natl. Acad. Sci. U.S.A.* 50, 767–774. doi: 10.1073/pnas.50.4.767

Helmstetter, C. E., and Cummings, D. J. (1964). An improved method for the selection of bacterial cells at division. *Biochim. Biophys. Acta* 82, 608–610. doi: 10.1016/0304-4165(64)90453-2

Helmstetter, C. E., and Pierucci, O. (1976). DNA synthesis during the division cycle of three substrains of *Escherichia coli* B/r. *J. Mol. Biol.* 102, 477–486. doi: 10.1016/0022-2836(76)90329-6

Herrick, J., Kohiyama, M., Atlung, T., and Hansen, F. G. (1996). The initiation mess? *Mol. Microbiol.* 19, 659–666. doi: 10.1046/j.1365-2958.1996.432956.x

Hiraga, S. (1976). Novel F prime factors able to replicate in *E. coli* Hfr strains. *Proc. Natl. Acad. Sci. U.S.A.* 73, 198–202. doi: 10.1073/pnas.73.1.198

Hirota, Y., Ryter, A., and Jacob, F. (1968). Thermosensitive mutants of *E. coli* affected in the process of DNA synthesis and cellular division. *Cold Spring Harb. Symp. Quant. Biol.* 33, 677–693. doi: 10.1101/SQB.1968.033.01.077

Hirota, Y., Yasuda, S., Yamada, M., Nishimura, A., Sugimoto, K., Sugisaki, H., et al. (1979). Structural and functional properties of the *Escherichia coli* origin of DNA replication. *Cold Spring Harb. Symp. Quant. Biol.* 43, 129–138. doi: 10.1101/SQB.1979.043.01.019

Hwang, D. S., and Kaguni, J. M. (1988). Interaction of dnaA46 protein with a stimulatory protein in replication from the *Escherichia coli* chromosomal origin. *J. Biol. Chem.* 263, 10633–10640.

Ishida, T., Akimitsu, N., Kashioka, T., Hatano, M., Kubota, T., Ogata , Y., et al. (2004). DiaA, a novel DnaA-binding protein, ensures the timely initiation of *Escherichia coli* chromosome replication. *J. Biol. Chem.* 279, 45546–45555. doi: 10.1074/jbc.M402762200

Jacob, F., Brenner, S., and Cuzin, F. (1963). On the regulation of DNA replication in bacteria. *Cold Spring Harb. Symp. Quant. Biol.* 28, 329–348. doi: 10.1101/SQB.1963.028.01.048

Kasho, K., Fujimitsu, K., Matoba, T., Oshima, T., and Katayama, T. (2014). Timely binding of IHF and Fis to DARS2 regulates ATP-DnaA production and replication initiation. *Nucleic Acids Res.* 42, 13134–13149. doi: 10.1093/nar/gku1051

Kasho, K., and Katayama, T. (2013). DnaA binding locus datA promotes DnaA-ATP hydrolysis to enable cell cycle-coordinated replication initiation. *Proc. Natl. Acad. Sci. U.S.A.* 110, 936–941. doi: 10.1073/pnas.1212070110

Kasho, K., Tanaka, H., Sakai, R., and Katayama, T. (2017). Cooperative DnaA binding to the negatively supercoiled datA locus stimulates DnaA-ATP hydrolysis. *J. Biol. Chem.* 292, 1251–1266. doi: 10.1074/jbc.M116.762815

Katayama, T., Fujimitsu, K., and Ogawa, T. (2001). Multiple pathways regulating DnaA function in *Escherichia coli*: distinct roles for DnaA titration by the datA locus and the regulatory inactivation of DnaA. *Biochimie* 83, 13–17. doi: 10.1016/S0300-9084(00)01206-2

Katayama, T., Kubota, T., Kurokawa, K., Crooke, E., and Sekimizu, K. (1998). The initiator function of DnaA protein is negatively regulated by the sliding clamp of the *E. coli* Chromosomal replicase. *Cell* 94, 61–71. doi: 10.1016/S0092-8674(00)81222-2

Kato, J., and Katayama, T. (2001). Hda, a novel DnaA-related protein, regulates the replication cycle in *Escherichia coli*. *EMBO J.* 20, 4253–4262. doi: 10.1093/emboj/2

Kawakami, H., Ozaki S., Suzuki,S., Nakamura, K., Senriuchi, T., Su'etsugu, M., et al. (2006). The exceptionally tight affinity of DnaA for ATP/ADP requires a unique aspartic acid residue in the AAA+ sensor 1 motif. *Mol. Microbiol.* 62, 1310–1324. doi: 10.1111/j.1365-2958.2006.05450.x

Kellenberger-Gujer, G., Podhajska, A. J., and Caro, L. (1978). A cold sensitive *dnaA* mutant of *E. coli* which overinitiates chromosome replication at low temperature. *Mol. Gen. Genet.* 162, 9–16. doi: 10.1007/BF00333845

Keyamura, K., Abe, Y., Higashi, M., Ueda, T., and Katayama, T. (2009). DiaA dynamics are coupled with changes in initial origin complexes leading to helicase loading. *J. Biol. Chem.* 284, 25038–25050. doi: 10.1074/jbc.M109.002717

Keyamura, K., Fujikawa, N., Ishida, T., Ozaki, S., Su'etsugu, M., Fujimitsu K., et al. (2007). The interaction of DiaA and DnaA regulates the replication cycle in *E. coli* by directly promoting ATP-DnaA-specific initiation complexes. *Genes Dev.* 21, 2083–2099. doi: 10.1101/gad.1561207

Keyamura, K., and Katayama, T. (2011). DnaA protein DNA-binding domain binds to Hda protein to promote inter-AAA+ domain interaction involved in regulatory inactivation of DnaA. *J. Biol. Chem.* 286, 29336–29346. doi: 10.1074/jbc.M111.233403

Kitagawa, R., Mitsuki, H., Okazaki, T., and Ogawa, T. (1996). A novel DnaA protein-binding site at 94.7 min on the *Escherichia coli* chromosome. *Mol. Microbiol.* 19, 1137–1147. doi: 10.1046/j.1365-2958.1996.453983.x

Kitagawa, R., Ozaki, T., Moriya, S., and Ogawa, T. (1998). Negative control of replication initiation by a novel chromosomal locus exhibiting exceptional affinity for *Escherichia coli* DnaA protein. *Genes Dev.* 12, 3032–3043. doi: 10.1101/gad.12.19.3032

Kohiyama, M., Cousin, D., Ryter, A., and Jacob, F. (1966). Mutants thermosensibles d'E. coli K-12. I. Isolement et characterisation rapide. *Ann. Inst. Pasteur* 110, 465–486.

Kohiyama, M., Lanfrom, H., Brenner, S., and Jacob, F. (1963). Modifications de fonctions indispensables chez des mutants thermosensibles *D'escherichia Coli*. sur une mutation emp echant la r'eplication du chromosome bact'erien. *C. R. Hebd. Seances Acad. Sci.* 257, 1979–1981.

Koppes, L. J. H., Woldringh, C. L., and Nanninga, N. (1978). Size variation and correlation of different cell cycle events in slow-growing *Escherichia coli*. *J. Bacteriol.* 134, 423–433.

Kücherer, C., Lother, H., Kölling, R., Schauzu, M. A., and Messer, W. (1986). Regulation of transcription of the chromosomal *dnaA* gene of *Escherichia coli*. *Mol. Gen. Genet.* 205, 115–121. doi: 10.1007/BF02428040

Kuempel, P. L. (1969). Temperature-sensitive initiation of chromosome replication in a mutant of *Escherichia coli*. *J. Bacteriol.* 100, 1302–1310.

Kurokawa, K., Nishida, S., Emoto, A., Sekimizu, K., and Katayama, T. (1999). Replication cycle-coordinated change of the adenine nucleotide-bound forms of DnaA protein in *Escherichia coli*. *EMBO J.* 18, 6642–6652. doi: 10.1093/emboj/18.23.6642

Lark, C. (1968). Studies on the *in vivo* methylation of DNA in *Escherichia coli* 15T-. *J. Mol. Biol.* 31, 389–399. doi: 10.1016/0022-2836(68)90416-6

Leonard, A. C., and Grimwade, J. E. (2015). The orisome: structure and function. *Front. Microbiol.* 6:545. doi: 10.3389/fmicb.2015.00545

Leonard, A. C., and Helmstetter, C. E. (1986). Cell cycle-specific replication of *E. coli* minichromosomes. *Proc. Natl Acad. Sci. U.S.A.* 83, 5101–5105. doi: 10.1073/pnas.83.14.5101

Leu, F. P., Hingorani, M. M., Turner, J., and O'donnell, M. (2000). The delta subunit of DNA polymerase III holoenzyme serves as a sliding clamp unloader in *Escherichia coli*. *J. Biol. Chem.* 275, 34609–34618. doi: 10.1074/jbc.M005495200

Løbner-Olesen, A., Atlung, T., and Rasmussen, K. V. (1987). Stability and replication control of *E. coli* minichromosomes. *J. Bacteriol.* 169, 2835–2842. doi: 10.1128/jb.169.6.2835-2842.1987

Løbner-Olesen, A., Hansen, F. G., Rasmussen, K. V., Martin, B., and Kuempel, P. L. (1994). The initiation cascade for chromosome replication in wild-type and Dam methyltransferase deficient *Escherichia coli* cells. *EMBO J.* 13, 1856–1862.

Løbner-Olesen, A., Skarstad, K., Hansen, F. G., von Meyenburg, K., and Boye, E. (1989). The DnaA protein determines the initiation mass of *Escherichia coli* K-12. *Cell* 57, 881–889. doi: 10.1016/0092-8674(89)90802-7

Løbner-Olesen, A., and von Freiesleben, U. (1996). Chromosomal replication incompatibility in Dam methyltransferase deficient *Escherichia coli* cells. *EMBO J.* 15, 5999–6008.

Lu, M., Campbell, J. L., Boye, E., and Kleckner, N. (1994). SeqA: a negative modulator of replication initiation in *E. coli*. *Cell* 77, 413–426. doi: 10.1016/0092-8674(94)90156-2

Maaløe, O., and Hanawalt, P. C. (1961). Thymine deficiency and the normal DNA replication cycle I. *J. Mol. Biol.* 3, 144–155. doi: 10.1016/S0022-2836(61)80041-7

Maaløe, O., and Kjeldgaard, N. O. (1966). *Control of Macromolecular Synthesis*. New York, NY: Amsterdam;Benjamin.

Mahaffy, J. M., and Zyskind, J. W. (1989). A model for the initiation of replication in *Escherichia coli*. *J. Theor. Biol.* 140, 453–477. doi: 10.1016/S0022-5193(89)80109-2

Margalit, H., and Grover, N. B. (1987). Initiation of chromosome replication in bacteria: analysis of an inhibitor control model. *J. Bacteriol.* 169, 5231–5240. doi: 10.1128/jb.169.11.5231-5240.1987

Margalit, H., Rosenberger, R. F., and Grover, N. B. (1984). Initiation of DNA replication in bacteria: analysis of an autorepressor model. *J. Theor. Biol.* 111, 183–199. doi: 10.1016/S0022-5193(84)80204-0

Margulies, C., and Kaguni, J. M. (1996). Ordered and sequential binding of DnaA protein to *oriC*, the chromosomal origin of *Escherichia coli*. *J. Biol. Chem.* 271, 17035–17040. doi: 10.1074/jbc.271.29.17035

Marsh, R. C., and Worcel, A. (1977). A DNA fragment containing the origin of replication of the *E. coli* chromosome. *Proc. Natl. Acad. Sci. U.S.A.* 74, 2720–2724. doi: 10.1073/pnas.74.7.2720

McGarry, K. C., Ryan, V. T., Grimwade, J. E., and Leonard, A. C. (2004). Two discriminatory binding sites in the *Escherichia coli* replication origin are required for DNA strand opening by initiator DnaA-ATP. *Proc. Natl. Acad. Sci. U.S.A.* 101, 2811–2816. doi: 10.1073/pnas.0400340101

McLean, M. J., Wolfe, K. H., and Devine, K. M. (1998). Base composition skews, replication orientation, and gene orientation in 12 prokaryote genomes. *J. Mol. Evol.* 47, 691–696. doi: 10.1007/PL00006428

Meijer, M., Beck, E., Hansen, F. G., Bergmans, H. E., Messer, W., von Meyenburg, K., et al. (1979). Nucleotide sequence of the origin of replication of the *E. coli* K-12 chromosome. *Proc. Natl. Acad. Sci. U.S.A.* 76, 580–584. doi: 10.1073/pnas.76.2.580

Messer, W. (2002). The bacterial replication initiator DnaA. DnaA and oriC, the bacterial mode to initiate DNA replication. *FEMS Microbiol. Rev.* 26, 355–374. doi: 10.1016/S0168-6445(02)00127-4

Messer, W., Bergmans, H. E., Meijer, M., Womack, J. E., Hansen, F. G., and von Meyenburg, K. (1978). Minichromosomes: plasmids which carry the *E. coli* replication origin. *Mol. Gen. Genet.* 162, 269–275. doi: 10.1007/BF00268852

Messer, W., Blaesing, F., Majka, J., Nardmann, J., Schaper, S., Schmidt, A., et al. (1999). Functional domains of DnaA proteins. *Biochimie* 81, 819–825. doi: 10.1016/S0300-9084(99)00215-1

Messer, W., Dankwarth, L., Tippe-Schindler, R., Womack, J. E., and Zahn, G. (1975). Regulation of the initiation of DNA replication in *E. coli*. Isolation of iRNA and the control of iRNA synthesis. *ICN-UCLA Symp. Mol. Cell. Biol.* 3, 602–617.

Messer, W., Meijer, M., Bergmans, H. E., Hansen, F. G., von Meyenburg, K., Beck, E., et al. (1979). Origin of replication, *oriC*, of the *Escherichia coli* K- 12 chromosome: nucleotide sequence. *Cold Spring Harb. Symp. Quant. Biol.* 43, 139–145. doi: 10.1101/SQB.1979.043.01.020

Michelsen, O., Teixeira de Mattos, M. J., Jensen, P. R., and Hansen, F. G. (2003). Precise determinations of C and D periods by flow cytometry in *Escherichia coli* K-12 and B/r. *Microbiology* 149, 1001–1010. doi: 10.1099/mic.0.26058-0

Morigen, Løbner-Olesen, A., and Skarstad, K. (2003). Titration of the *Escherichia coli* DnaA protein to excess *datA* sites causes destabilization of replication forks, delayed replication initiation and delayed cell division. *Mol. Microbiol.* 50, 349–362. doi: 10.1046/j.1365-2958.2003.03695.x

Morigen, Molina, F., and Skarstad, K. (2005). Deletion of the *datA* site does not affect once-per-cell-cycle timing but induces rifampin-resistant replication. *J. Bacteriol.* 187, 3913–3920. doi: 10.1128/JB.187.12.3913-3920.2005

Mott, M. L., and Berger, J. M. (2007). DNA replication initiation: mechanisms and regulation in bacteria. *Nat. Rev. Microbiol.* 5, 343–354. doi: 10.1038/nrmicro1640

Murialdo, H., and Siminovitch, L. (1972). The morphogenesis of bacteriophage lambda. IV. Identification of gene products and control of the expression of the morphogenetic information. *Virology* 48, 785–823. doi: 10.1016/0042-6822(72)90162-6

Nielsen, H. J., and Hansen, F. G. (2010). An automated and highly efficient method for counting and measuring fluorescent foci in rod-shaped bacteria. *J. Microsc.* 239, 194–199. doi: 10.1111/j.1365-2818.2010.03374.x

Nozaki, S., Niki, H., and Ogawa, T. (2009a). Replication initiator DnaA of *Escherichia coli* changes its assembly form on the replication origin during the cell cycle. *J. Bacteriol.* 191, 4807–4814. doi: 10.1128/JB.00435-09

Nozaki, S., and Ogawa, T. (2008). Determination of the minimum domain II size of *Escherichia coli* DnaA protein essential for cell viability. *Microbiology* 154, 3379–3384. doi: 10.1099/mic.0.2008/019745-0

Nozaki, S., Yamada, Y., and Ogawa, T. (2009b). Initiator titration complex formed at *datA* with the aid of IHF regulates replication timing in *Escherichia coli*. *Genes Cells* 14, 329–341. doi: 10.1111/j.1365-2443.2008.01269.x

Nyborg, M., Atlung, T., Skovgaard, O., and Hansen, F. G. (2000). Two types of cold sensitivity associated with the A184V change in the DnaA protein. *Mol. Microbiol.* 35, 1202–1210. doi: 10.1046/j.1365-2958.2000.01790.x

Obita, T., Iwura, T., Su'etsugu, M., Yoshida, Y., Tanaka, Y., Katayama, T., et al. (2002). Determination of the secondary structure in solution of the *Escherichia coli* DnaA DNA-binding domain. *Biochem. Biophys. Res. Commun.* 299, 42–48. doi: 10.1016/S0006-291X(02)02590-1

Ogasawara, N., Moriya, S., von Meyenburg, K., Hansen, F. G., and Yoshikawa, H. (1985). Conservation of genes and their organization in the chromosomal replication origin region of *Bacillus subtilis* and *Escherichia coli*. *EMBO J.* 4, 3345–3350.

Ogawa, T., Yamada, Y., Kuroda, T., Kishi, T., and Moriya, S. (2002). The *datA* locus predominantly contributes to the initiator titration mechanism in the control of replication initiation in *Escherichia coli*. *Mol. Microbiol.* 44, 1367–1375. doi: 10.1046/j.1365-2958.2002.02969.x

Ozaki, S., and Katayama, T. (2012). Highly organized DnaA-oriC complexes recruit the single-stranded DNA for replication initiation. *Nucleic Acids Res.* 40, 1648–1665. doi: 10.1093/nar/gkr832

Ozaki, S., Kawakami, H., Nakamura, K., Fujikawa, N., Kagawa, W., Park, S. Y., et al. (2008). A common mechanism for the ATP-DnaA-dependent formation of open complexes at the replication origin. *J. Biol. Chem.* 283, 8351–8362. doi: 10.1074/jbc.M708684200

Polaczek, P., and Wright, A. (1990). Regulation of expression of the *dnaA* gene in *Escherichia coli*: role of the two promoters and the DnaA box. *New Biol.* 2, 564–582.

Pritchard, R. H., Barth, P. T., and Collins, J. (1969). Control of DNA synthesis in bacteria. *Symp. Soc. Gen. Microbiol.* 19, 263–297.

Ream, L. W., Margossian, L., Clark, A. J., Hansen, F. G., and von Meyenburg, K. (1980). Genetic and physical mapping of *recF* in *Escherichia coli* K- 12. *Mol. Gen. Genet.* 180, 115–121. doi: 10.1007/BF00267359

Reddy, P., Peterkofsky, A., and McKenney, K. (1985). Translational efficiency of the *Escherichia coli* adenylate cyclase gene: mutating the UUG initiation codon to GUG or AUG results in increased gene expression. *Proc. Natl. Acad. Sci. U.S.A.* 82, 5656–5660. doi: 10.1073/pnas.82.17.5656

Riber, L., Olsson, J. A., Jensen, R. B., Skovgaard, O., Dasgupta, S., and Marinus, M. G. (2006). Hda-mediated inactivation of the DnaA protein and *dnaA* gene autoregulation act in concert to ensure homeostatic maintenance of the *Escherichia coli* chromosome. *Genes Dev.* 20, 2121–2134. doi: 10.1101/gad.379506

Roth, A., and Messer, W. (1995). The DNA binding domain of the initiator protein DnaA. *EMBO J.* 14, 2106–2111.

Roth, A., and Messer, W. (1998). High-affinity binding sites for the initiator protein DnaA on the chromosome of *Escherichia coli*. *Mol. Microbiol.* 28, 395–401. doi: 10.1046/j.1365-2958.1998.00813.x

Russell, D. W., and Zinder, N. D. (1987). Hemimethylation prevents DNA replication in *E. coli*. *Cell* 50, 1071–1079. doi: 10.1016/0092-8674(87)90173-5

Sakakibara, Y., and Mizukami, T. (1980). A temperature sensitive *Escherichia coli* mutant defective in DNA replication: *dnaN*, a new gene adjacent to the *dnaA* gene. *Mol. Gen. Genet.* 178, 541–553. doi: 10.1007/BF00337859

Samitt, C. E., Hansen, F. G., Miller, J. F., and Schaechter, M. (1989). *In vivo* studies of DnaA binding to the origin of replication of *Escherichia coli*. *EMBO J.* 8, 989–993.

Sancar, A., Hack, A. M., and Rupp, W. D. (1979). Simple method for identification of plasmid-coded proteins. *J. Bacteriol.* 137, 692–693.

Schaechter, M., Maaløe, O., and Kjeldgaard, N. O. (1958). Dependency on medium and temperature of cell size chemical composition during balanced growth of *Salmonella typhimurium*. *J. Gen. Microbiol.* 19, 592–606. doi: 10.1099/00221287-19-3-592

Schaechter, M., Williamson, J. P., Hood, J. R., and Koch, A. L. (1962). Growth, cell and nuclear divisions in some bacteria. *J. Gen. Microbiol.* 29, 421–434. doi: 10.1099/00221287-29-3-421

Schaper, S., and Messer, W. (1995). Interaction of the initiator protein DnaA of *Escherichia coli* with its DNA target. *J. Biol. Chem.* 270, 17622–17626. doi: 10.1074/jbc.270.29.17622

Seitz, H., Weigel, C., and Messer, W. (2000). The interaction domains of the DnaA and DnaB replication proteins of *Escherichia coli*. *Mol. Microbiol.* 37, 1270–1279. doi: 10.1046/j.1365-2958.2000.02096.x

Sekimizu, K., Bramhill, D., and Kornberg, A. (1987). ATP activates dnaA protein in initiating replication of plasmids bearing the origin of the *E. coli* chromosome. *Cell* 50, 259–265. doi: 10.1016/0092-8674(87)90221-2

Sekimizu, K., and Kornberg, A. (1988). Cardiolipin activation of dnaA protein, the initiation protein of replication in *Escherichia coli*. *J. Biol. Chem.* 263, 7131–7135.

Sevastopoulos, C. G., Wehr, C. T., and Glaser, D. A. (1977). Largescale automated isolation of *Escherichia coli* mutants with thermosensitive DNA replication. *Proc. Natl. Acad. Sci. U.S.A.* 74, 3485–3489. doi: 10.1073/pnas.74.8.3485

Si, F., Li, D., Cox, S. E., Sauls, J. T., Azizi, O., Sou, C., et al. (2017). Invariance of initiation mass and predictability of cell size in *Escherichia coli*. *Curr. Biol.* 27, 1278–1287. doi: 10.1016/j.cub.2017.03.022

Skarstad, K., Boye, E., and Fanning, E. (2003). Circles in the sand. *EMBO Rep.* 4, 661–665. doi: 10.1038/sj.embor.embor888

Skarstad, K., Boye, E., and Steen, H. B. (1986). Timing of initiation of chromosome replication in individual *E. coli* cells. *EMBO J.* 5, 1711–1717.

Skarstad, K., and Katayama, T. (2013). Regulating DNA replication in bacteria. *Cold Spring Harb. Perspect. Biol.* 5, 1–17. doi: 10.1101/cshperspect.a0 12922

Skarstad, K., and Løbner-Olesen, A. (2003). Stable co-existence of separate replicons in *Escherichia coli* is dependent on once-per-cell-cycle initiation. *EMBO J.* 22, 140–150. doi: 10.1093/emboj/cdg003

Skovgaard, O. (1990). Nucleotide sequence of a *Proteus mirabilis* fragment homologous to the *60K-rnpA-rpmH-dnaA-dnaN-recF-gyrB* region of *Escherichia coli*. *Gene* 93, 27–34. doi: 10.1016/0378-1119(90)90131-A

Skovgaard, O., and Hansen, F. G. (1987). Comparison of *dnaA* nucleotide sequences of *Escherichia coli*, *Salmonella typhimurium*, and *Serratia Marcescens*. *J. Bacteriol.* 169, 3976–3981. doi: 10.1128/jb.169.9.3976-3981.1987

Sompayrac, L., and Maaloe, O. (1973). Autorepressor model for control of DNA replication. *Nat. New Biol.* 241, 133–135. doi: 10.1038/newbio241 133a0

Speck, C., and Messer, W. (2001). Mechanism of origin unwinding: sequential binding of DnaA to double- and single-stranded DNA. *EMBO J.* 20, 1469–1476. doi: 10.1093/emboj/20.6.1469

Speck, C., Weigel, C., and Messer, W. (1999). ATP- and ADP-DnaA protein, a molecular switch in gene regulation. *EMBO J.* 18, 6169–6176. doi: 10.1093/emboj/18.21.6169

Sugimoto, K., Oka, A., Sugisaki, H., Takanami, M., Nishimura, A., Yasuda, Y., et al. (1979). Nucleotide sequence of *Escherichia coli* replication origin. *Proc. Natl. Acad. Sci. U.S.A.* 76, 575–579. doi: 10.1073/pnas.76.2.575

Tabata, S., Oka, A., Sugimoto, K., Takanami, M., Yasuda, S., and Hirota, Y. (1983). The 245 bp *oriC* sequence of the *E. coli* chromosome directs bidirectional replication at an adjacent region. *Nucleic Acids Res.* 11, 2617–2626. doi: 10.1093/nar/11.9.2617

Theisen, P. W., Grimwade, J. E., Leonard, A. C., Bogan, J. A., and Helmstetter, C. E. (1993). Correlation of gene transcription with the time of initiation of chromosome replication in *Escherichia coli*. *Mol. Microbiol.* 10, 575–584. doi: 10.1111/j.1365-2958.1993.tb00929.x

Tippe-Schindler, R., Zahn, G., and Messer, W. (1979). Control of the initiation of DNA replication in *E. coli*. I. Negative control of initiation. *Mol. Gen. Genet.* 168, 185–195. doi: 10.1007/BF00431444

Torheim, N. K., Boye, E., Løbner-Olesen, A., Stokke, T., and Skarstad, K. (2000). The *Escherichia coli* SeqA protein destabilizes mutant DnaA204 protein. *Mol. Microbiol.* 37, 629–638. doi: 10.1046/j.1365-2958.2000. 02031.x

Travers, A. A. (1980). Promoter sequence for stringent control of bacterial ribonucleic acid synthesis. *J. Bacteriol.* 141, 973–976.

van den Berg, E. A., Geerse, R. H., Memelink, J., Bovenberg, R. A. L., Magnée, F. A., and van de Putte, P. (1985). Analysis of regulatory sequences upstream of the *E. coli* uvrB gene; involvement of the DnaA protein. *Nucleic Acids Res.* 13, 1829–1840. doi: 10.1093/nar/13.6.1829

von Freiesleben, U., Krekling, M. A., Hansen, F. G., and Løbner-Olesen, A. (2000a). The eclipse period of *Escherichia coli*. *EMBO J.* 19, 6240–6248. doi: 10.1093/emboj/19.22.6240

von Freiesleben, U., Rasmussen, K. V., Atlung, T., and Hansen, F. G. (2000b). Rifampicin resistant initiation of chromosome replication from *oriC* in *ihf* mutants. *Mol. Microbiol.* 37, 1087–1093. doi: 10.1046/j.1365-2958.2000.02060.x

von Freiesleben, U., Rasmussen, K. V., and Schaechter, M. (1994). SeqA limits DnaA activity in replication from *oriC* in *Escherichia coli*. *Mol. Microbiol.* 14, 763–772. doi: 10.1111/j.1365-2958.1994.tb01313.x

von Meyenburg, K., Hansen, F. G., Riise, E., Bergmans, H. E., Meijer, M., and Messer, W. (1979). Origin of replication, *oriC*, of the *E. coli* K-12 chromosome: genetic mapping and minichromosome replication. *Cold Spring Harb. Symp. Quant. Biol.* 43, 121–128. doi: 10.1101/SQB.1979.043.01.018

Wechsler, J. A., and Gross, J. D. (1971). *Escherichia coli* mutants temperature sensitive for DNA synthesis. *Mol. Gen. Genet.* 113, 273–284. doi: 10.1007/BF00339547

Weigel, C., Schmidt, A., Seitz, H., Tüngler, D., Welzeck, M., and Messer, W. (1999). The N-terminus promotes oligomerization of the *Escherichia coli* initiator protein DnaA. *Mol. Microbiol.* 34, 53–66. doi: 10.1046/j.1365-2958.1999.01568.x

Wold, S., Skarstad, K., Steen, H. B., Stokke, T., and Boye, E. (1994). The initiation mass for DNA replication in *Escherichia coli* K-12 is dependent on growth rate. *EMBO J.* 13, 2097–2102.

Yasuda, S., and Hirota, Y. (1977). Cloning and mapping of the replication origin of *Escherichia coli*. *Proc. Natl. Acad. Sci. U.S.A.* 74, 5458–5462. doi: 10.1073/pnas.74.12.5458

Zawilak-Pawlik, A., Nowaczyk, M., and Zakrzewska-Czerwinska, J. (2017). The role of the N-terminal domains of bacterial initiator DnaA in the assembly and regulation of the bacterial replication initiation complex. *Genes* 8, 1–18. doi: 10.3390/genes8050136

Zhou, P., Bogan, J. A., Welch, K., Pickett, S. R., Wang, H. J., Zaritsky, A., et al. (1997). Gene transcription and chromosome replication in *Escherichia coli*. *J. Bacteriol.* 179, 163–169. doi: 10.1128/jb.179.1.163-169.1997

Zyskind, J. W., Harding, N. E., Takeda, Y., Cleary, J. M., and Smith, D. W. (1981). The DNA replication origin region of the *Enterobacteriaceae*. *ICN-UCLA Symp. Mol. Cell. Biol.* 22, 13–25. doi: 10.1016/B978-0-12-583580-0.50007-8

Zyskind, J. W., and Smith, D. W. (1980). Nucleotide sequence of the *Salmonella typhimurium*_ origin of DNA replication. *Proc. Natl. Acad. Sci. U.S.A.* 77, 2460–2464. doi: 10.1073/pnas.77.5.2460

Conflict of Interest Statement: The authors declare that the research was conducted in the absence of any commercial or financial relationships that could be construed as a potential conflict of interest.

frontiers in Microbiology

ORIGINAL RESEARCH
published: 05 April 2018
doi: 10.3389/fmicb.2018.00664

Different Amounts of DNA in Newborn Cells of *Escherichia coli* Preclude a Role for the Chromosome in Size Control According to the "Adder" Model

Peter G. Huls[1], *Norbert O. E. Vischer*[2] *and Conrad L. Woldringh*[2]*

[1] Faculty of Science, Swammerdam Institute for Life Sciences, University of Amsterdam, Amsterdam, Netherlands,
[2] Bacterial Cell Biology, Swammerdam Institute for Life Sciences, University of Amsterdam, Amsterdam, Netherlands

According to the recently-revived adder model for cell size control, newborn cells of *Escherichia coli* will grow and divide after having added a constant size or length, ΔL, irrespective of their size at birth. Assuming exponential elongation, this implies that large newborns will divide earlier than small ones. The molecular basis for the constant size increment is still unknown. As DNA replication and cell growth are coordinated, the constant ΔL could be based on duplication of an equal amount of DNA, ΔG, present in newborn cells. To test this idea, we measured amounts of DNA and lengths of nucleoids in DAPI-stained cells growing in batch culture at slow and fast rates. Deeply-constricted cells were divided in two subpopulations of longer and shorter lengths than average; these were considered to represent large and small prospective daughter cells, respectively. While at slow growth, large and small prospective daughter cells contained similar amounts of DNA, fast growing cells with multiforked replicating chromosomes, showed a significantly higher amount of DNA (20%) in the larger cells. This observation precludes the hypothesis that ΔL is based on the synthesis of a constant ΔG. Growth curves were constructed for siblings generated by asymmetric division and growing according to the adder model. Under the assumption that all cells at the same growth rate exhibit the same time between initiation of DNA replication and cell division (i.e., constant $C+D$-period), the constructions predict that initiation occurs at different sizes (Li) and that, at fast growth, large newborn cells transiently contain more DNA than small newborns, in accordance with the observations. Because the state of segregation, measured as the distance between separated nucleoids, was found to be more advanced in larger deeply-constricted cells, we propose that in larger newborns nucleoid separation occurs faster and at a shorter length, allowing them to divide earlier. We propose a composite model in which both differential initiation and segregation leads to an adder-like behavior of large and small newborn cells.

Keywords: *Escherichia coli*, deeply-constricted cells, newborn cells, DAPI-stained nucleoid, DNA segregation, adder growth model, ObjectJ

OPEN ACCESS

Edited by:
Marc Bramkamp,
Ludwig-Maximilians-Universität München, Germany

Reviewed by:
Johannes Geiselmann,
Université Grenoble Alpes, France
Dennis Claessen,
Leiden University, Netherlands

***Correspondence:**
Conrad L. Woldringh
c.woldringh@gmail.com

Specialty section:
This article was submitted to Microbial Physiology and Metabolism, a section of the journal Frontiers in Microbiology

Received: *04 December 2017*
Accepted: *21 March 2018*
Published: *05 April 2018*

Citation:
Huls PG, Vischer NOE and Woldringh CL (2018) Different Amounts of DNA in Newborn Cells of Escherichia coli Preclude a Role for the Chromosome in Size Control According to the "Adder" Model. Front. Microbiol. 9:664. doi: 10.3389/fmicb.2018.00664

INTRODUCTION

The early ideas of Koppes et al. (1978a,b) and Voorn et al. (1993) that *Escherichia coli* cells grow by adding a constant length between divisions, were based on measurements of cell lengths and the rate of DNA replication in pulse-labeled cells grown in batch culture and prepared for electron microscopic autoradiography. This view has recently been revived in several studies (Amir, 2014; Campos et al., 2014; Jun and Taheri-Araghi, 2014); in the new experiments on cell size homeostasis (Campos et al., 2014; Taheri-Araghi et al., 2015; Wallden et al., 2016), the bacteria are grown in microfluidic chambers and observed by fluorescence light microscopy.

Whereas Koppes et al. (1978a,b) were able to measure only the length increment between initiation of DNA replication and the start of cell constriction, the extensive measurements of Jun and co-workers on large numbers of individual *E. coli* cells growing in a microfluidic "mother machine" (Wang et al., 2010) under a wide range of growth conditions covered the entire cell cycle (Taheri-Araghi et al., 2015). They confirm that at the population level, average cell size depends on growth rate exponentially (Schaechter et al., 1958); more importantly, they also show at the single cell level, that all cells in a particular growth medium grow in size at the same exponential rate and increase in size by the same amount (ΔL) between birth and division irrespective of their newborn size. Consequently, a large newborn cell will synthesize ΔL faster and will divide at a slightly earlier age than a small newborn cell, thus contributing to homeostasis (Figure 3 in Taheri-Araghi et al., 2015).

In several recent studies it has been discussed that the chromosome could play a role in establishing the constant size increment inherent to the adder model (Campos et al., 2014; Robert, 2015). Such constancy could be based on the chromosome serving as a "measuring stick" if newborn cells contain the same amount of DNA independent of their size at birth. For signaling cell division after duplicating this amount of DNA, a tight relation would have to exist between nucleoid replication/segregation and the peptidoglycan synthesizing machinery for cell division (Woldringh et al., 1991; Typas et al., 2012). This could be established via the so-called transertion process that involves transcription–translation and translocation of membrane proteins (Norris, 1995; Woldringh, 2002; Rabinovitch et al., 2003) and has been proposed to interfere with the assembly of the FtsZ-ring through nucleoid occlusion (Woldringh et al., 1991; Wu and Errington, 2012).

To detect whether newborn cells indeed contain equal amounts of DNA irrespective of their birth size, we have measured the DNA in nucleoids of large and small prospective daughter cells that can be assumed to give rise to large and small newborn cells. Cells were obtained from populations grown in batch cultures under steady state conditions at two different growth rates. As to be expected, only a small difference in DNA content (6%) was observed in newborn cells at slow growth. However, at fast growth and in the presence of multifork replication, large and small prospective daughter cells contained significantly different amounts of DNA (20%). This observation makes it unlikely that newborn cells base their constant length increment, ΔL, on the synthesis of equal amounts of DNA.

Graphical constructions of the adder cell cycle were made under the assumption that large and small newborn cells, generated by asymmetric division, have the same $C+D$-period. The constructions of length growth and genome content of single cells show that at fast growth large newborn cells exhibit a transient increase in the amount of DNA compared to small newborns, in agreement with the measurements. This lends support to the assumption that all individual newborns in a population have the same $C+D$-period and that large and small newborn cells initiate DNA replication at different sizes. Moreover, the advanced state of segregation, measured as the distance between separated nucleoids, found in the larger deeply-constricted cells, allows for differential segregation and earlier division in the larger cells, as required by the adder model and for obtaining homeostasis.

MATERIALS AND METHODS

Cells and Growth Medium

Escherichia coli strain PJ4271 (strain MC1000 transformed with pBR322) was grown at 37°C in MOPS-buffered minimal medium (Neidhardt et al., 1974) with 100 mg/ml ampicillin according to Jensen et al. (1999), except that NaCl was added (about 27 ml of 2 M NaCl to 500 ml of MOPS-medium) to increase the osmolality to 300 mOsm. For slow growth the medium was supplemented with succinate (4 g per l), giving a doubling time *Td* of 122 min. For rapid growth glucose (5 g per l) and 20 amino acids (at millimolar concentrations according to Neidhardt et al., 1974) were added, giving a *Td* of 29 min. Exponentially growing cultures with constant OD450/cell (determined with a Coulter counter) were grown to OD450 of 0.1 to 0.2 and processed for microscopy (cf. Stuger et al., 2002).

Fluorescence Microscopy and Image Analysis

DNA was labeled by addition of DAPI (4′,6-diamino-2-phenylindole dihydrochloride, Molecular Probes) at a final concentration of 0.05 mg/ml to cells fixed with OsO_4 (0.1% w/v). After at least 15 min the cells were concentrated by centrifugation (1 min at 13000 rpm) and attached to microscopy slides coated with a thin layer of 1% agarose in culture medium. Pictures were taken with an Olympus BX60 fluorescence microscope equipped with a 100W mercury lamp and a Princeton RTE 1317-k-1 cooled CCD-camera. To limit photobleaching and DNA damage by ultraviolet light we focused the cells in phase contrast mode before photography. In this way all cells were exposed to the same (limited) amount of UV light.

DNA content per cell (expressed in chromosome equivalents) was measured after mixing the fixed *E. coli* PJ4271 cells with fixed *E. coli pbpA*(Ts) cells that contain one, or two fully replicated chromosomes when grown into stationary phase at the permissive temperature (30°C) for at least 48 h (Vischer et al., 1999) and after staining the mixture with DAPI. The *pbpA* mutant cells used for calibration could be distinguished from the

PJ4271 cells because of their larger diameter and spherical shape. Cells were measured using the program "Coli-Inspector"[1]. This is a specialized software package developed for the analysis of shape and fluorescence related properties of bacterial cells. The program runs in combination with ImageJ with plug-in ObjectJ (see Figure 1 in Vischer et al., 2015). Amounts of DNA were calculated by assuming that the value of integrated fluorescence per cell of the left peak of the DNA distribution of *pbpA* cells equals 1 chromosome equivalent (Supplementary Figures S1A,B; cf. Huls et al., 1999).

To calculate integrated fluorescence (see Vischer et al., 1999), the modal value of the entire image was considered as background and was subtracted before subsequent image analysis.

Determination of *C* and *C*+*D*-Periods

For the construction of the cell cycles at the two growth rates (succinate with Td = 122 min and glucose plus amino acids with Td = 29 min), the *C*- and *D*-periods have to be known. These were determined by image-cytometric measurement of the amount of DNA per cell during run-off DNA synthesis after inhibiting initiations with 300 μg/ml rifampicin, as previously described (see Figure 3 in Huls et al., 1999). In similar experiments the accumulation of DNA per cell (and per nucleoid) reached a plateau value after about 70 or 53 min in succinate or glucose plus amino acids medium, respectively. With these population values of the *C*-periods, the *D*-periods were subsequently calculated from the values of average chromosome equivalents per cell G_c, using the expression $G_c = \{T_d/C.\ln 2\}\{2^{(C+D)/Td}-2^{D/Td}\}$ (Cooper and Helmstetter, 1968; Bremer and Churchward, 1977). It should be emphasized that this formula is only applicable to cell populations in steady-state growth. In our experiments this was verified by a constancy of average cell mass (OD450/cell counts) during the 5 h preceding cell sampling.

From the experimental values for G_c of 1.5 and 3.7 chromosome equivalents per cell in the slowly (Td = 122 min) and rapidly (Td = 29 min) growing populations, the *D*-periods were calculated to be 40 and 25 min (cf. **Figures 2B,D** below). The values are comparable with those reported by Huls et al. (1999); note that the growth temperature in those experiments was 28°C, whereas it is 37°C in the present study. Variations in the values for *C*- and *D*-periods have also been reported for *E. coli* K-12 strains grown at 30°C (Michelsen et al., 2003).

[1]https://sils.fnwi.uva.nl/bcb/objectj/examples/Coli-Inspector/Coli-Inspector-MD/coli-inspector.html

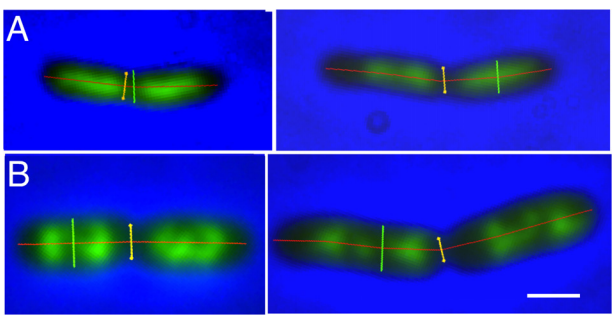

FIGURE 1 | Examples of deeply-constricted *Escherichia coli* MC1000 cells, fixed with osmium tetroxide and stained with DAPI. Fluorescence images are overlaid with phase-contrast images and with markers, transiently displayed upon the images, for cell length (red), cell diameter (green) and the diameter at the constriction site (yellow), as measured by "Coli-Inspector" with ImageJ plugin ObjectJ. **(A)** Slow growing cells in succinate medium (Td = 122 min). Left and right panel, cell shorter and longer than 3.7 μm, respectively. **(B)** Fast growing cells in glucose plus amino acids medium (Td = 29 min). Left and right panel, cell shorter and longer than 4.3 μm, respectively. See mean lengths in **Table 1**, column 10. DAPI fluorescence is seen in green. Scale bar equals 1 μm.

RESULTS

Measurement of DAPI-Stained Nucleoids in Prospective Daughter Cells

To determine the amount of DNA in large and small prospective daughter cells, we stained fixed cells with DAPI and measured the fluorescence of the nucleoids and the size of the cells in fast- and slow-growing populations. From the subpopulations of constricting cells we sampled the deeply-constricted cells, defined as those having a diameter at the constriction site that is smaller than the mean constriction diameter (**Table 1**, column 9). These deeply-constricted cells that were just about to divide, were assumed to represent prospective newborn cells (see Grover and Woldringh, 2001, for a similar analysis). Although the average length of the deeply-constricted cells with respect to all constricting cells had slightly increased (by 1–4%; see **Table 1**, compare columns 7 and 10), they largely covered the range of all constricting cells (Supplementary Figure S2), indicating a limited elongation during the constriction process.

Figures 1A,B show examples of deeply-constricted cells with their nucleoids from slow (Td = 122 min) and fast (Td = 29 min) growing cultures. The separated nucleoids can be seen to have a more extended shape in the longer constricted cells (right panels). As will be discussed below the distances between the segregated daughter nucleoids are larger in these cells.

In **Figures 2A,C**, the cell boundaries (magenta) and DNA fluorescence (green) of all individual cells in the two populations are arranged in so-called maps of cell profiles according to length, using the ImageJ plugin ObjectJ with software "Coli-Inspector" (see section "Materials and Methods"). In **Figures 2B,D**, histograms of all cells and of constricting cells (gray and red distributions, respectively) are shown together with a plot of the amount of DNA per cell (in chromosome equivalents) as a function of cell length. The plots indicate that in slow-growing cells (**Figure 2B**), DNA synthesis starts after a short *B*-period and slows down at the end, indicative of termination and a *D*-period. Because of overlapping DNA replication cycles (multifork replication) in the fast growing cells, such decreases in the rate of DNA synthesis are absent in **Figure 2D**.

The maps of DNA profiles in **Figures 2A,C** illustrate the gradual elongation of both cells (magenta) and nucleoids (green).

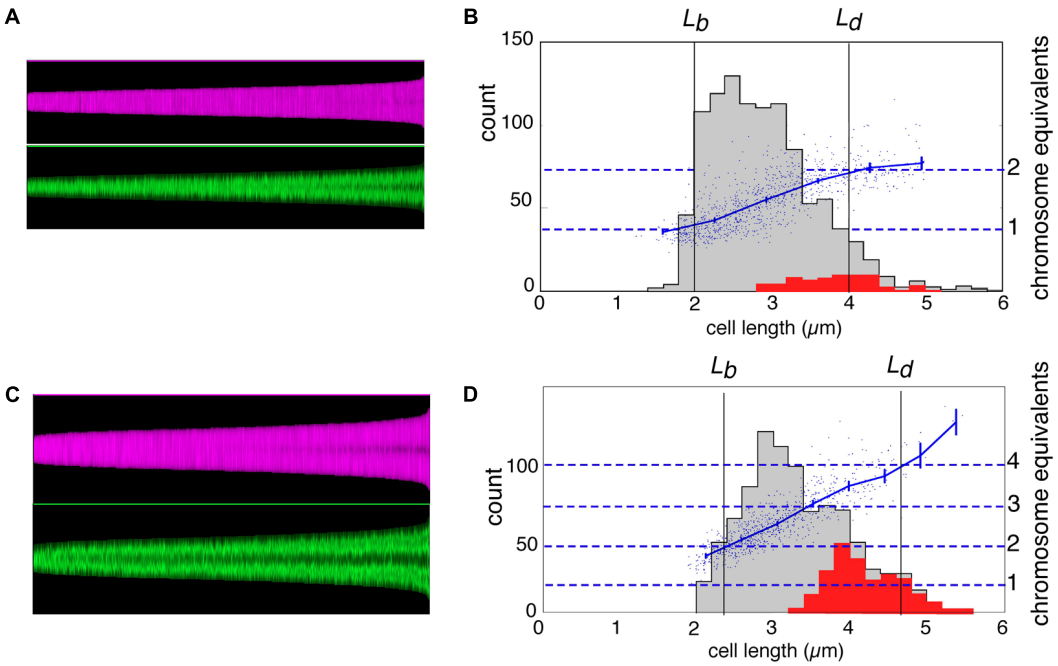

FIGURE 2 | Maps of cell profiles and distributions of cell lengths. **(A,C)** Map of cell profiles, sorted according to ascending cell length. Each cell is visualized as a 1-pixel-wide column with a height corresponding to the cell length (in pixels) and showing local diameter (magenta) or the local fluorescence (green). The profile map visualizes the development of the constriction before cell division (magenta band becomes darker in the center due to the smaller diameter at the constriction site) and the change in fluorescence distribution of the (segregating) nucleoids along the cell length (green) (see Vischer et al., 2015). **(B,D)** Distribution of cell length of the total population (gray) and of constricting cells (red) with the lengths of newborn (*Lb*) and dividing cells (*Ld*) indicated. *Lb* was calculated from $Lb = < L > /2ln2$, in which $< L >$ is the mean length of all cells, under the assumption of exponential elongation. In addition, the total DAPI-fluorescence per cell is shown by a scatter plot, with a line through the averages of binned data with vertical 95% confidence error bars in blue (in chromosome equivalents, right-hand ordinate). **(A,B)** Slow growing cells in succinate medium (Td = 122 min). **(C,D)** Fast growing cells in glucose plus amino acids medium (Td = 29 min).

At fast growth a second segregation event can be seen to occur in the largest deeply-constricted cells (**Figures 3C,D**, right panels), indicative of re-initiation of DNA replication (see below).

To determine the amount of DNA in large and small newborn cells, we measured the integrated fluorescence per nucleoid and the cellular positions and lengths of the nucleoids for cells smaller and larger than the mean length of deeply-constricted cells, all of which contained two separated daughter nucleoids. The results are presented in **Figure 3** and **Table 1**. Because the nucleoids in the fast growing cells show rather irregular, lobular shapes characteristic of multifork replication (cf. **Figure 1B**), we also measured from the same cell populations nucleoid lengths manually (**Table 1**, columns 13 and 14).

Both the integrated fluorescence intensities, which represent the amount of DNA per nucleoid (**Figures 3B,D** and **Table 1**, columns 11 and 12), and the measurements of nucleoid lengths (**Table 1**, columns 13 and 14) indicate that the difference in DNA between small and large deeply-constricted cells at the fast growth rate is highly significant ($p < 10^{-8}$, as determined by a two-tail *t*-test); at the slow growth rate, the difference remains significant, but just barely ($p = 0.035$). These differences are difficult to reconcile with a fixed amount of DNA (ΔG) serving as a constant in both large and small newborn cells, on which the constant length increment (ΔL) of the adder model could be based.

The State of Nucleoid Segregation

The measurements of the amount of DNA in small and large constricting cells also give information on the state of segregation in deeply constricted cells, defined as the distance between their segregated nucleoids. The distances between nucleoids in deeply-constricted cells have been measured manually (**Table 2**, columns 4 and 5). Nucleoid separation was evaluated by eye for each individual cell. If some DAPI fluorescence could still be seen between nucleoids (usually after contrast enhancement) they were considered not to have segregated. In addition, distances between the centers of mass of segregated nucleoids have been calculated from the DNA profile plots as shown in **Figures 3B,D** (**Table 2**, columns 6 and 7).

The results in **Table 2** (columns 4 and 5) indicate that the difference between the distances measured manually in the large and those in the small deeply-constricted cells at the fast growth rate, is very highly significant ($p < 10^{-8}$). At the slow growth rate, the difference is still statistically significant but much less so ($p = 0.0006$). The same holds for the differences between the centers of mass (**Table 2**, columns 6 and 7) calculated from the profile plots for slow ($p < 10^{-6}$) and fast growth ($p < 10^{-20}$).

The present experimental set-up cannot provide information about the segregation-period of individual cells, *S* (the time during which two separated nucleoids exist or, in other words, the time between visible separation of daughter nucleoids and cell

TABLE 1 | Properties of small and large newborn cells as estimated from deeply-constricted cells assumed to represent prospective daughter cells.

Growth medium (Td)	Total population			Constricted cells[1]				Deeply-constricted cells (diameter at constriction site < mean diameter at constriction site[2])					
	Cell count	Mean length, μm	Mean diameter, μm	% Constricted cells (count)	Constriction period *T*, min	Mean cell length, μm (CV^3)	Mean cell diameter, μm	Mean diameter at constriction site, μm	Mean length, μm (count)	Amount of DNA[4] arbitrary units ± SD (count)		Nucleoid length[5] μm ± *SD* (count)	
										Small[6] (count)	Large[6] (count)	Small[6] (count)	Large[6] (count)
1	**2**	**3**	**4**	**5**	**6**	**7**	**8**	**9**	**10**	**11**	**12**	**13**	**14**
Succinate (122 min)	1022	2.78	0.63	9 (95)	15	3.67 (10%)	0.6 (8%)	0.5	3.7 (51)	0.36 ± 0.03 (24)	0.38 ± 0.03 (27)	0.98 ± 0.09 (24)	1.06 ± 0.11 (26)
Glucose+aa (29 min)	772	3.24	0.88	26 (198)	10	4.12 (13%)	0.9 (6%)	0.7	4.3 (119)	0.62 ± 0.08 (63)	0.75 ± 0.12 (56)	1.19 ± 0.14 (62)	1.45 ± 0.19 (55)

Parameters are shown of length distributions of constricted cells for two populations of E. coli MC4100, with values of fluorescence of DAPI-stained nucleoids and of nucleoid lengths. [1]Automatically measured by the ImageJ plug-in ObjectJ using the program "Coli-Inspector." The constriction period, T, was calculated from T = Td.ln(1+F)/ln2, in which F is the fraction of constricted cells (based on Bremer and Churchward, 1977). [2]Constricting cells with a diameter at the constriction site smaller than the mean diameter at the constriction site are considered to be deeply-constricted cells and assumed to represent prospective daughter cells. [3]CV, coefficient of variation. [4]Amount of DNA, automatically measured by ObjectJ using "Coli-Inspector," and expressed as fluorescence brightness in arbitrary units. See profile plots in ***Figures 3B,D****. [5]Measured manually with ObjectJ. CV of nucleoid lengths varied between 9 and 14%. [6]Small and large cells are, respectively, smaller or larger than mean length of deeply-constricted cells.*

division). We can, however, determine the average *S*-period, on a population level, from the percentage of cells containing two nucleoids (**Table 2**, column 2, just as the duration of constriction, *T*, was calculated from the percentage of constricting cells (**Table 1**, column 6). Whether large and small newborn cells exhibit the same *S*- and *T*-periods can only be estimated from time-lapse studies (e.g., Wallden et al., 2016). In the Discussion we will argue that the more advanced state of segregation at the end of the cell cycle of large, deeply-constricted cells could result from the larger space available to the nucleoids when being pushed apart in the long cell axis by the invaginating envelope during the constriction process (Supplementary Figure S3).

Generation of Large and Small Newborn Cells

Different newborn cell sizes can be assumed to originate either from stochastically postponed or premature symmetric divisions, or from asymmetric cell divisions. We do not know what their relative contributions are to the length distributions in the present populations. However, the coefficients of variation of the so-called *K(L)* distributions (length of prospective daughter cell/length constricting cell; Trueba, 1982), indicative of the degree of asymmetry, were found to be 9.5 and 4.9% for the succinate and glucose+amino acids populations, respectively. This suggests that asymmetric divisions do contribute to the subpopulations of large and small prospective daughter cells that we consider here.

Siblings generated by asymmetric division will have the same DNA content (*G*) present in a larger or smaller cell volume (see shaded insert in **Figures 4A,B**). To understand their behavior in subsequent cell cycles, we constructed for slow and fast growing cells their growth curves assuming exponential elongation. Consequently, after adding a constant length (gray upward arrows, ΔL, in **Figure 4**), the large newborns divide at a younger age than the small newborns, thus decreasing the difference in the size at division and leading to homeostasis (Taheri-Araghi et al., 2015). In the graphs of the cell cycles of single slow and fast growing newborn cells, we also depict the time of initiation of DNA replication by subtracting the *C*+*D*-period from the time of division under the assumption that all newborn cells have the same *C*+*D*-period. The graphs show that the size differences at birth induced by the asymmetric division, become less at division, reaching steady state after about four cycles (**Figure 4B**), as predicted by the adder model (cf. **Figure 3** in Taheri-Araghi et al., 2015). The adder principle and the constant *C*+*D*-period cause initiations to occur at different lengths (*Li*, open red circles in **Figure 4**). These differences also return to the steady state of initiation length *Li* after about four cycles.

In the slow growing population with *C*+*D* = 110 min (**Figure 4A**), both large and small newborn cells can be seen to exhibit a short *B*-period and a relatively long *D*-period (cf. **Figure 2B**). In the fast growing population with *C*+*D* = 78 min (**Figure 4B**), large newborn cells will initiate very early in their cycle. This means that some newborn cells could have already initiated prior to their birth (i.e., in the previous generation), in

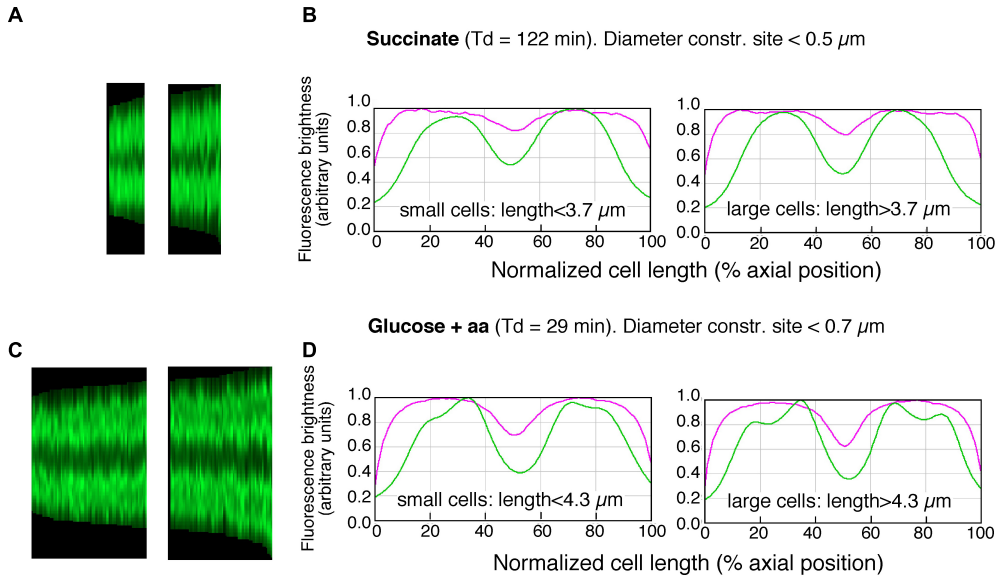

FIGURE 3 | Maps of profiles and collective plots. **(A,C)** Maps of profiles of DAPI-fluorescence (cf. lower panels in **Figures 2A,C**) of deeply-constricted cells in slow **(A)** and fast **(C)** growing populations; subpopulations of small and large deeply-constricted cells are shown in left and right panels, respectively. **(B,D)** Collective profiles created from all cell profiles in the maps **(A,C)** by resampling to a normalized cell length of 100 data points and averaging to a single plot. Mean diameter- (magenta) and DAPI-fluorescence (green) are plotted in arbitrary units of brightness as a function of normalized cell length for slow **(B)** and fast **(D)** growing cells; subpopulations of small and large deeply-constricted cells are shown in left and right panels, respectively.

accordance with the observation of a second segregation event in **Figures 3C,D** (right panels) and with the theoretical predictions of Taheri-Araghi (2015).

The average values of C and D measured for the two populations (see section "Materials and Methods") were used to calculate the genome contents (G) of the dividing cells indicated in **Figure 4B**. It can be seen that after asymmetric division siblings with identical chromosomes and the same multifork chromosome structure, acquire different genome contents at their subsequent divisions (during about three cycles). It follows that the adder model together with the assumed constant C+D-period predict a transient increase of the amount of DNA in the progeny of large newborn cells (see red G-numbers in **Figure 4**), in qualitative agreement with the present observations (**Table 1**). The same behavior is obtained when constructing the cycles of large and small newborn cells after stochastically premature or postponed divisions, for instance, due to variations in the C+D-period.

DISCUSSION

According to the adder model (Amir, 2014; Campos et al., 2014; Osella et al., 2014; Taheri-Araghi et al., 2015), individual cells sense neither time nor absolute size but "measure" a fixed increase in length between divisions. The differences in size at division predicted by the three models, sizer, timer, and adder are rather small (Figure 5 in Zaritsky and Woldringh, 2015), but the observed positive correlation between sizes at division and at birth falsifies the sizer model, while the timer model is falsified by the negative correlation between generation time and size at birth (Figure 1D in Taheri-Araghi et al., 2015).

The adder mechanism requires that an individual cell monitor a property that is equal in all newborn cells. A constant total number of proteins per cell in different newborns and growth conditions were proposed to trigger cell division after reaching a threshold in each generation (Taheri-Araghi et al., 2015; Sauls et al., 2016). Alternatively, the absolute constant amount of DNA per nucleoid could serve as the signal. If equal in all newborn cells, the duplicating nucleoid could function as a "molecular ruler" to monitor a constant size increment (Campos et al., 2014; Zaritsky, 2015; Zaritsky and Woldringh, 2015). The present results, however, have shown that large newborn cells in a fast growing population, contain significantly more DNA (20%; **Table 1**) than small newborns, precluding the possibility that the adder model is based on duplication of a fixed amount of DNA in all newborn cells.

We based our observations of the amount of DNA in prospective daughters on the evaluation of the degree of constriction in fixed cells visualized by phase contrast microscopy using the software package of ObjectJ (see section "Materials and Methods"; for an elaborate analysis of constricting *E. coli* cells see Reshes et al., 2008). Classification of the degree of constriction has been performed previously on *E. coli* cells prepared by agar filtration and visualized by electron microscopy (Koppes and Nanninga, 1980; Grover et al., 1987; Vardi and Grover, 1993; Grover and Woldringh, 2001). However, subtle shape changes like the degree of constriction and the variation in cell width during cell elongation (Trueba and Woldringh, 1980) can also be observed using light microscopy of living or fixed

TABLE 2 | Distances between segregated nucleoids in deeply-constricted cells from slow and fast growing populations of *E. coli* MC1000.

Growth medium (Td min)	Cells with two nucleoids		Distances (μm) between nucleoids in deeply-constricted cells (diameter at constriction site < mean diameter at constriction site; see Table 1, columns 11 to 14)					
	% (cell count)	S-period[(1)], min	Measured manually[(2)]		Distance between centers of mass measured from profile plots[(3)]			
			Small cells mean ± *SD* (cell count)	Large cells mean ± *SD* (cell count)	Small cells mean ± *SD* (cell count)		Large cells mean ± *SD* (cell count)	
1	2	3	4	5	6		7	
Succinate (122 min)	17 (1017)	24	0.56 ± 0.11 (24)	0.70 ± 0.14 (26)	1.26 ± 0.33 (25)		1.72 ± 0.21 (26)	
Glucose+aa (29 min)	74 (747)	23	0.74 ± 0.12 (63)	0.89 ± 0.14 (56)	1.79 ± 0.15 (63)		2.21 ± 0.22 (56)	

*[(1)]The period, S, during which cells contain two separated nucleoids, was calculated from S = Td.ln(1+F)/ln2, in which F is the fraction of cells with two nucleoids (based on Bremer and Churchward, 1977). [(2)]Measured manually with ObjectJ program "Coli-Inspector." [(3)]For each cell the fluorescence profile along the cell axis (see **Figures 3A,C**) was subdivided in two parts left and right of the central minimum value (cf. **Figures 3B,D**). From either part, the center of mass was calculated from the region that exceeded the central minimum, and the distance between both was calculated.*

(Supplementary Figure S5) cells. Such studies could prove very informative with large populations growing in a microfluidics device (Taheri-Araghi et al., 2015; Wallden et al., 2016).

To understand better how differences in the amount of DNA in large and small newborn cells could arise, we constructed length growth curves according to the adder model and calculated the genome contents (*G*) of large and small siblings that initiate DNA replication *C+D* min before division (**Figure 4**). Large newborn cells initiate earlier and at a larger length (*Li*) than small newborns (red open circles), and at fast growth they also develop transiently a higher genome content during the first three cycles (*G* and red numbers in **Figure 4B**). This qualitative agreement with the measurements of DNA contents (**Table 1**) supports the assumption of an equal *C+D*-period in all individual cells, consistent with the observations of Wallden et al. (2016). A mathematical framework for these graphical constructions has been presented before (Amir, 2014; Ho and Amir, 2015; Taheri-Araghi, 2015; Taheri-Araghi et al., 2015). The implied differential initiation could be explained by assuming that the differently-sized siblings, although born with identical chromosomes, have a different balance between the amount of their DNA and cytoplasmic initiators such as DnaA or other regulators (Hansen et al., 1991; Katayama et al., 2010; Skarstad and Katayama, 2013). The chromosome in the sibling with a larger volume could consequently initiate earlier than that in the smaller sibling if the cell contained more initiators. The open circles at Cycle 1 in **Figure 4** indicate that large and small siblings initiate at different lengths, deviating from the average length for initiation as indicated by *Li* (dashed horizontal red line in **Figure 4**). Here, cell length represents cell volume if diameter remains constant during the cell cycle. It should be noted that to our knowledge the earlier division in the larger sibling has not directly been observed in, for instance, time-lapse studies with cells growing in microfluidic channels (Taheri-Araghi et al., 2015; Wallden et al., 2016).

The question remains as to what the dominant mechanism is behind the adder phenomenon of cell growth. Do large and small newborn cells monitor their size (ΔL) from birth on, dividing after a fixed size increment that is based on some constant property other than the amount of DNA (cf. "birth-centric" view; Amir, 2016)? Or do different newborns initiate DNA replication at different sizes and divide after a constant *C+D*-period, causing large newborns to have shorter and small newborns longer generation times as though growing according to the adder principle? This "initiation-centric" or "adder-per-origin" model has been described by Ho and Amir (2015) and Zheng et al. (2016). The model is based on sensing the activity of initiation proteins (cf. Hansen et al., 1991) rather than on the need for cells to "measure" a size increment that depends on the synthesis of many macromolecules. However, the model still requires an additional timing mechanism for triggering cell division at the end of the *C+D*-period. As previously suggested (Campos et al., 2014; Zaritsky and Woldringh, 2015), this could be established by the sequence of events occurring in elongating cells starting with replication and the concomitant segregation of chromosome arms (Wiggins et al., 2010; Youngren et al., 2014; Woldringh et al., 2015; Männik et al., 2016) during the *C*-period.

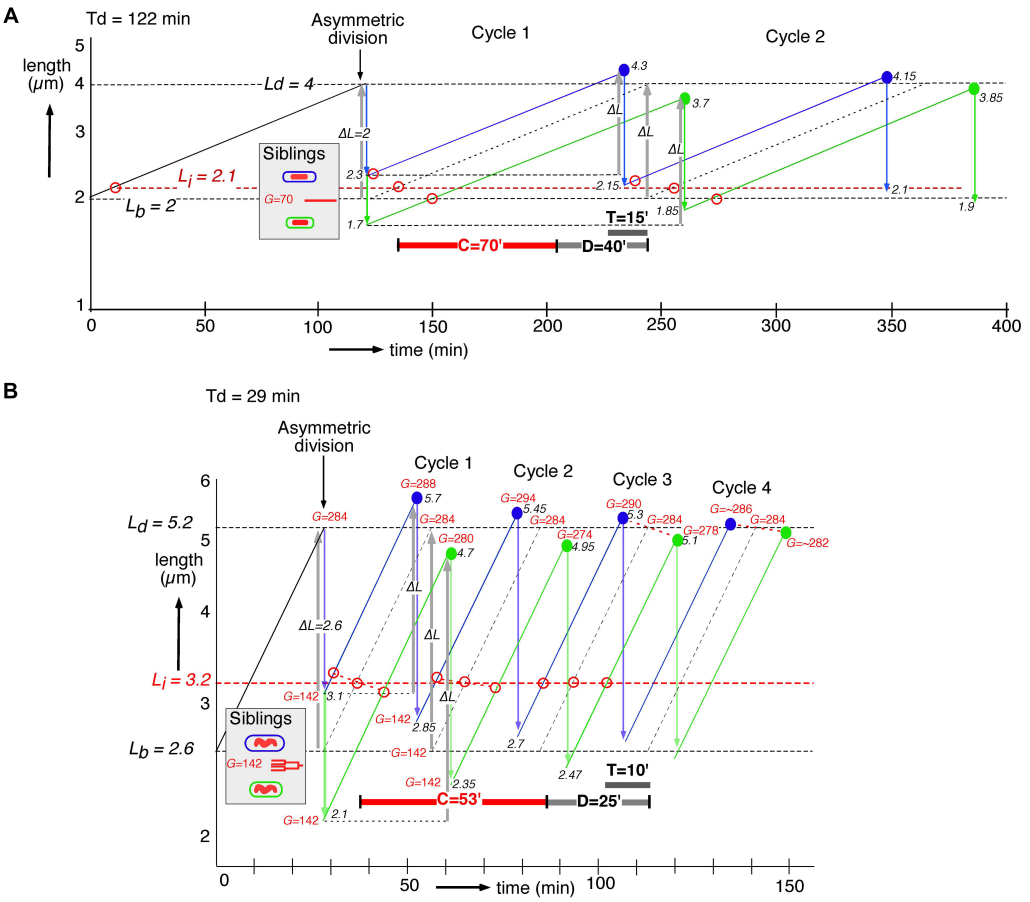

FIGURE 4 | Construction of length growth curves of large (blue lines) and small (green lines) siblings, generated by asymmetric division. Cells elongate exponentially (elongation rate proportional to length); note log scale of the ordinate. Cell lengths can be considered to represent cell volumes if cell diameter is assumed to remain constant during the cell cycle. The graphs are inspired by, but different from Figure 6 in Koppes et al. (1978b), where the constant length increment was assumed to occur between initiation of DNA replication and initiation of constriction. Average lengths at birth (*Lb*) and division (*Ld*) are indicated by dashed horizontal black lines. The first division of an average cell is assumed to occur asymmetrically producing a large (*Lb + 1 SD*) and a small (*Lb – 1 SD*) newborn cell. Each newborn cell is constrained to add a fixed length, Δ*L* (gray upward arrows) before division. Lengths at division for large and small newborn cells are indicated by solid blue and green circles, respectively; their subsequent symmetrical divisions are indicated by blue and green downward arrows. Black numbers refer to cell lengths *L* (μm) at division or birth. The time of initiation of DNA replication (open red circles) is determined by subtracting the *C+D*-period from the time of division dictated by the adder model. The original length at initiation (*Li*) is indicated by a dashed horizontal red line. Red numbers refer to genome content, *G*, expressed in minutes; division by *C* = 70 or 53 min gives *G* in genome equivalents. **(A)** An individual cell from a slow growing succinate population (Td = 122 min) with a length at birth of *Lb* = 2 μm, equal to the average length of newborn cells (CV = 15%), dividing after a size increment of Δ*L* = 2 μm. **(B)** Similar construction of an individual cell growing in glucose plus amino acids medium (Td = 29 min) with a length at birth *Lb* = 2.6 (CV = 15%) and a size increment of Δ*L* = 2.6 μm.

After termination and relief of nucleoid occlusion (Woldringh et al., 1991; Wu and Errington, 2012; Cambridge et al., 2014), the *D*-period starts by assembling the FtsZ-ring (den Blaauwen et al., 1999; Aarsman et al., 2005), followed by divisome maturation (van der Ploeg et al., 2013; Vischer et al., 2015) and visible cell constriction (*T*-period; Reshes et al., 2008; Tsukanov et al., 2011).

These latter processes, occurring during the *D*-period, can all be expected to proceed in a growth-rate dependent way. But because at higher growth rate cell width will increase, the duration of the joint processes of FtsZ-ring assembly, divisome maturation and polar-cap peptidoglycan synthesis, may remain the same. The effect of a higher growth rate is thus compensated by the increased surface of the polar cap to be synthesized, causing a constant *D*-period. Such phenomenon is supported by the observation that the *T*-period is more or less constant for doubling times shorter than 60 min (Woldringh et al., 1977; Zaritsky et al., 2006). Under conditions of thymine limitation, when cell width increases without a compensating change in growth rate (Zaritsky and Pritchard, 1973), the *D*-period has been found to increase (Zaritsky et al., 1999).

At slow growth (**Figure 4A**), the earlier initiation in the larger sibling and the constant *C+D*-period enable it to divide earlier in the first cycle than the average newborn cell. At fast growth (**Figure 4B**), the earlier initiation in the larger sibling will trigger a division event also after *C+D* min, but occurring in the *third* cycle. How then can the large sibling already divide earlier than the average newborn cell in the *first* cycle, as dictated by the adder model and how does chromosome segregation

accord with this adder principle? The unexpected observation of an increased distance (∼20%) between segregated nucleoids in large, deeply-constricted cells (**Table 2**) could explain the necessary acceleration of the cell cycle in large siblings. We envisage that a faster segregation of the nucleoid in the larger sibling could transiently occur because of the larger space along the length axis, accelerating the onset of constriction and division already in the first cycle. That the constriction process itself can enhance nucleoid separation has been demonstrated previously (Huls et al., 1999; Aarsman et al., 2005). It is also suggested here by the gradual increase in the distance between nucleoids during advancing constriction in both slow and fast growing cells (Supplementary Figure S3) and by the increased distance between separated nucleoids in constricting cells as a function of their length (Supplementary Figure S4). Whether the separation of daughter nucleoids also occurs faster in large elongating cells before the onset of constriction can only be ascertained by direct observation of live cells growing in microfluidics channels.

That cell volume regulates initiation of DNA replication seems well-established (Si et al., 2016; Zheng et al., 2016). That cell length regulates initiation of constriction has been proposed previously (Grover and Woldringh, 2001). This length model predicts the decrease observed in cell diameter during elongation (Trueba and Woldringh, 1980), and the correlations between cell dimensions and the coefficients of variation of cell length and volume at specific events like the onset of constriction. The proposal here thus comes down to a composite model in which both cell volume (for initiation of DNA replication) and cell length (for initiation of Z-ring assembly) play roles in determining cell division. Just as in the case of the larger sibling where the greater volume enables the chromosome to initiate earlier than average, its longer length enables faster segregation and earlier division, as dictated by the adder principle. Visualizing and measuring nucleoids at the single-cell level *in vivo* would establish whether or not differently-sized siblings indeed initiate DNA replication at different cell volumes and segregate nucleoids and initiate cell constrictions at different cell lengths. Such information could well be obtained using quantitative time-lapse imaging of mutants with enhanced asymmetric division (Männik et al., 2017).

AUTHOR CONTRIBUTIONS

PH performed the research and reviewed the manuscript. NV analyzed the data and reviewed the manuscript. CW wrote the paper.

FUNDING

This work was inspired by the observations of L. J. H. Koppes, who developed the constant length increment model long before the others. However, he lacked the opportunity to continue his experimental work. His theoretical work was greatly supported by N. B. Grover, resulting in a paper the abstract of which reads: "Two statistical hypotheses for the occurrence of cell division were tested by observed distributions of cell size during steady-state growth. The 30 year old so-called sloppy-size model could be rejected, whereas the newly-developed incremental-size model was accepted (by lack of alternatives)" (see Voorn et al., 1993). Revival of the incremental model occurred in 2014 in Boston (see Amir, 2014) and San Diego (see Jun and Taheri-Araghi, 2014).

ACKNOWLEDGMENTS

We thank Arieh Zaritsky for his continuous support and stimulation and N. B. Grover for the critical remarks that greatly improved the manuscript and for the statistical tests. Nanne Nanninga, Charles Helmstetter, Suckjoon Jun, Jim Walker, Ariel Amir, Frank Trueba, and Vic Norris are thanked for the stimulating discussions and suggestions. We are indebted to Rogier Stuger for the *E. coli* strain and to Tanneke den Blaauwen for the comments and laboratory facilities.

SUPPLEMENTARY MATERIAL

The Supplementary Material for this article can be found online at: https://www.frontiersin.org/articles/10.3389/fmicb.2018.00664/full#supplementary-material

REFERENCES

Aarsman, M. E. G., Piette, A., Fraipont, C., Vinkenvleugel, T. M. F., Nguyen-Disteche, M., and den Blaauwen, T. (2005). Maturation of *Escherichia coli* divisome occurs in two steps. *Mol. Microbiol.* 55, 1631–1645. doi: 10.1111/j.1365-2958.2005.04502.x

Amir, A. (2014). Cell size regulation in bacteria. *Phys. Rev. Lett.* 112:208102. doi: 10.1103/PhysRevLett.112.208102

Amir, A. (2016). Is cell size a spandrel? *eLife* 6:e22186. doi: 10.7554/eLife.22186

Bremer, H., and Churchward, G. (1977). An examination of the Cooper-Helmstetter theory of DNA replication in bacteria and its underlying assumptions. *J. Bacteriol.* 69, 645–654. doi: 10.1016/0022-5193(77)90373-3

Cambridge, J., Blinkova, A., Magnan, D., Bates, D., and Walker, J. R. (2014). A replication-inhibited unsegregated nucleoid at mid-cell blocks Z-ring formation and cell division independently of SOS and the SlmA nucleoid occlusion protein in *Escherichia coli*. *J. Bacteriol.* 196, 36–49. doi: 10.1128/JB.01230-12

Campos, M., Surovtsev, I. V., Kato, S., Paintdakhi, A., Beltran, B., Ebmeier, S. E., et al. (2014). A constant size extension drives bacterial cell size homeostasis. *Cell* 159, 1433–1446. doi: 10.1016/j.cell.2014.11.022

Cooper, S., and Helmstetter, C. E. (1968). Chromosome replication and the division cycle of *Escherichia coli* B/r. *J. Mol. Biol.* 31, 519–540. doi: 10.1016/0022-2836(68)90425-7

den Blaauwen, T., Buddelmeijer, N., Aarsman, M. E. G., Hameete, C. M., and Nanninga, N. (1999). Timing of FtsZ assembly in *Escherichia coli*. *J. Bacteriol.* 181, 5167–5175.

Grover, N. B., and Woldringh, C. L. (2001). Dimensional regulation of cell-cycle events in *Escherichia coli* during steady-state growth. *Microbiology* 147, 171–181. doi: 10.1099/00221287-147-1-171

Grover, N. B., Woldringh, C. L., and Koppes, L. J. (1987). Elongation and surface extension of individual cells of *Escherichia coli* B/r: comparison of theoretical and experimental size distributions. *J. Theor. Biol.* 129, 337–348. doi: 10.1016/S0022-5193(87)80006-1

Hansen, F. G., Christensen, B. B., and Atlung, T. (1991). The initiator titration model: computer simulation of chromosome and minichromosome

control. *Res. Microbiol.* 142, 161–167. doi: 10.1016/0923-2508(91)90025-6

Ho, P. Y., and Amir, A. (2015). Simultaneous regulation of cell size and chromosome replication in bacteria. *Front. Microbiol.* 6:662. doi: 10.3389/fmicb.2015.00662

Huls, P. G., Vischer, N. O. E., and Woldringh, C. L. (1999). Delayed nucleoid segregation in *Escherichia coli*. *Mol. Microbiol.* 33, 959–970. doi: 10.1046/j.1365-2958.1999.01535.x

Jensen, P. R., Van Der Weijden, C. C., Jensen, L. B., Westerhoff, H. V., and Snoep, J. L. (1999). Extensive regulation compromises the extent to which DNA gyrase controls DNA supercoiling and growth rate of *Escherichia coli*. *Eur. J. Biochem.* 266, 865–877. doi: 10.1046/j.1432-1327.1999.00921.x

Jun, S., and Taheri-Araghi, S. (2014). Cell-size maintenance: universal strategy revealed. *Trends Microbiol.* 23, 4–6. doi: 10.1016/j.tim.2014.12.001

Katayama, T., Ozaki, S., Keyamura, K., and Fujimitsu, K. (2010). Regulation of the replication cycle: conserved and diverse regulatory systems for DnaA and oriC. *Nat. Rev. Microbiol.* 60, 351–375. doi: 10.1038/nrmicro2314

Koppes, L. J. H., and Nanninga, N. (1980). Positive correlation between size at initiation of chromosome replication in *Escherichia coli* and size at initiation of cell constriction. *J. Bacteriol.* 143, 89–99.

Koppes, L. J. H., Overbeeke, N., and Nanninga, N. (1978a). DNA replication patterns and cell wall growth in *Escherichia coli* PAT84. *J. Bacteriol.* 133, 1053–1061.

Koppes, L. J. H., Woldringh, C. L., and Nanninga, N. (1978b). Size variations and correlation of different cell cycle events in slow-growing *Escherichia coli*. *J. Bacteriol.* 134, 423–433.

Männik, J., Bailey, M. W., O'Neill, J. C., and Männik, J. (2017). Kinetics of large-scale chromosomal movement during asymmetric division in *Escherichia coli*. *PLoS Genet.* 13:e1006638. doi: 10.1371/journal.pgen.1006638

Männik, J., Castillo, D. E., Yang, D., Siopsis, G., and Männik, J. (2016). The role of MatP, ZapA and ZapB in chromosomal organization and dynamics in *Escherichia coli*. *Nucleic Acids Res.* 44, 2016–2026. doi: 10.1093/nar/gkv1484

Michelsen, O., Teixeira de Mattos, M. J., Jensen, P. R., and Hansen, F. G. (2003). Precise determinations of C and D periods by flow cytometry in *Escherichia coli* K-12 and B/r. *Microbiology* 149, 1001–1010. doi: 10.1099/mic.0.26058-0

Neidhardt, F. C., Bloch, P. L., and Smith, D. F. (1974). Culture medium for enterobacteria. *J. Bacteriol.* 119, 736–747.

Norris, V. (1995). Hypothesis: chromosome separation in *Escherichia coli* involves autocatalytic gene expression, translation and membrane-domain formation. *Mol. Microbiol.* 16, 1051–1057. doi: 10.1111/j.1365-2958.1995.tb02330.x

Osella, M., Nugent, E., and Cosentino Lagomarsino, M. (2014). Concerted control of *Escherichia coli* cell division. *Proc. Natl. Acad. Sci. U.S.A.* 111, 3431–3435. doi: 10.1073/pnas.1313715111

Rabinovitch, A., Zaritsky, A., and Feingold, M. (2003). DNA-membrane interactions can localize bacterial cell center. *J. Theor. Biol.* 225, 393–396. doi: 10.1016/S0022-5193(03)00292-3

Reshes, G., Vanounou, S., Fishov, I., and Feingold, M. (2008). Timing the start of division in *E. coli*: a single-cell study. *Phys. Biol.* 5:046001. doi: 10.1088/1478-3975/5/5/4/046001

Robert, L. (2015). Size sensors in bacteria, cell cycle control, and size control. *Front. Microbiol.* 6:515. doi: 10.3389/fmicb.2015.00515

Sauls, J., Li, D., and Jun, S. (2016). Adder and a coarse-grained approach to cell size homeostasis in bacteria. *Curr. Opin. Cell Biol.* 38, 38–44. doi: 10.1016/j.ceb.2016.02.004

Schaechter, M., Maaløe, O., and Kjeldgaard, N. O. (1958). Dependency on medium and temperature of cell size and chemical composition during balanced growth of *Salmonella typhimurium*. *J. Gen. Microbiol.* 19, 592–606. doi: 10.1099/00221287-19-3-592

Si, F., Li, D., Cox, S. E., Sauls, J. T., Azizi, O., Sou, C., et al. (2016). Invariance of initiation mass and predictability of cell size in *Escherichia coli*. *Curr. Biol.* 27, 1278–1287. doi: 10.1016/j.cub.2017.03.022

Skarstad, K., and Katayama, T. (2013). Regulating DNA replication in bacteria. *Cold Spring Harb. Perspect. Biol.* 5:a012922. doi: 10.1101/cshperspect.a012922

Stuger, R., Woldringh, C. L., van der Weijden, C. C., Vischer, N. O. E., Bakker, B. M., van Spanning, R. J. M., et al. (2002). DNA supercoiling by gyrase is linked to nucleoid compaction. *Mol. Biol. Rep.* 29, 79–82. doi: 10.1023/A:1020318705894

Taheri-Araghi, S. (2015). Self-consistent examination of Donachie's constant initiation size at the single-cell level. *Front. Microbiol.* 6:1349. doi: 10.3389/fmicb.2015.01349

Taheri-Araghi, S., Bradda, S., Sauls, J. T., Hill, N. S., Levin, P. A., Paulsson, J., et al. (2015). Cell-size control and homeostasis. *Curr. Biol.* 25, 1–7. doi: 10.1016/j.cub.2014.12.009

Trueba, F. J. (1982). On the precision and accuracy achieved by *Escherichia coli* cells at fission about their middle. *Arch. Microbiol.* 131, 55–59. doi: 10.1007/BF00451499

Trueba, F. J., and Woldringh, C. L. (1980). Changes in cell diameter during the division cycle of *Escherichia coli*. *J. Bacteriol.* 142, 869–878.

Tsukanov, R., Reshes, G., Carmon, G., Fischer-Friedrich, E., Gov, N. S., Fishov, I., et al. (2011). Timing of Z-ring localization in *Escherichia coli*. *Phys. Biol.* 8:066003. doi: 10.1088/1478-3975/8/6/066003

Typas, A., Banzhaf, M., Gross, C. A., and Vollmer, W. (2012). From the regulation of peptidoglycan synthesis to bacterial growth and morphology. *Nat. Rev. Microbiol.* 10, 123–135. doi: 10.1038/nrmicro2677

van der Ploeg, R., Verheul, J., Vischer, N. O. E., Alexeeva, S., Hoogendoorn, E., Postma, M., et al. (2013). Colocalization and interaction between elongasome and divisome during a preparative cell division phase in *Escherichia coli*. *Mol. Microbiol.* 87, 1074–1087. doi: 10.1111/mmi.12150

Vardi, E., and Grover, N. B. (1993). Shape changes in *Escherichia coli* B/rA during agar filtration. *Cytometry* 14, 173–178. doi: 10.1002/cyto.990140209

Vischer, N. O. E., Huls, P. G., Ghauharali, R. I., Brakenhoff, G. J., Nanninga, N., and Woldringh, C. L. (1999). Image cytometric method for quantifying the relative amount of DNA in bacterial nucleoids using *Escherichia coli*. *J. Microsc.* 196, 61–68. doi: 10.1046/j.1365-2818.1999.00597.x

Vischer, N. O. E., Verheul, J., Postma, M., van den Berg van Saparoea, B., Galli, E., Natale, P., et al. (2015). Cell age dependent concentration of *Escherichia coli* divisome proteins analyzed with ImageJ and ObjectJ. *Front. Microbiol.* 6:586. doi: 10.3389/fmicb.2015.00586

Voorn, W. J., Koppes, L. J. H., and Grover, N. B. (1993). Mathematics of cell division in *Escherichia coli*: comparison between sloppy-size and incremental-size kinetics. *Curr. Top. Mol. Gen.* 1, 187–194.

Wallden, M., Fange, D., Lundius, E. G., Baltekin, O., and Elf, J. (2016). The synchronization of replication and division cycles in individual *E. coli* cells. *Cell* 166, 729–739. doi: 10.1016/j.cell.2016.06.052

Wang, P., Robert, L., Pelletier, J., Dang, W. L., Taddei, F., Wright, A., et al. (2010). Robust growth of *Escherichia coli*. *Curr. Biol.* 20, 1099–1103. doi: 10.1016/j.cub.2010.04.045

Wiggins, P. A., Cheveralls, K. C., Martin, J. S., Lintner, R., and Kondev, J. (2010). Strong intranucleoid interactions organize the *Escherichia coli* chromosome into a nucleoid filament. *Proc. Natl. Acad. Sci. U.S.A.* 107, 4991–4995. doi: 10.1073/pnas.0912062107

Woldringh, C. L. (2002). The role of co-transcriptional translation and protein translocation (transertion) in bacterial chromosome segregation. *Mol. Microbiol.* 45, 17–29. doi: 10.1046/j.1365-2958.2002.02993.x

Woldringh, C. L., de Jong, M. A., van den Berg, W., and Koppes, L. (1977). Morphological analysis of the division cycle of two *Escherichia coli* substrains during slow growth. *J. Bacteriol.* 131, 270–279.

Woldringh, C. L., Hansen, F. G., Vischer, N. O. E., and Atlung, T. (2015). Segregation of chromosome arms in growing and non-growing *Escherichia coli* cells. *Front. Microbiol.* 6:448. doi: 10.3389/fmicb.2015.00448

Woldringh, C. L., Mulder, E., Huls, P. G., and Vischer, N. (1991). Toporegulation of bacterial division according to the nucleoid occlusion model. *Res. Microbiol.* 142, 309–320. doi: 10.1016/0923-2508(91)90046-D

Wu, L. J., and Errington, J. (2012). Nucleoid occlusion and bacterial cell division. *Nat. Rev. Microbiol.* 10, 8–12. doi: 10.1038/nrmicro2671

Youngren, B., Nielsen, H. J., Jun, S., and Austin, S. (2014). The multifork *Escherichia coli* chromosome is a self-duplicating and self-segregating thermodynamic ring polymer. *Genes Dev.* 28, 71–84. doi: 10.1101/gad.231050.113

Zaritsky, A. (2015). Cell-shape homeostasis in *Escherichia coli* is driven by growth, division, and nucleoid complexity. *Biophys. J.* 109, 178–181. doi: 10.1016/j.bpj.2015.06.026

Zaritsky, A., and Pritchard, R. H. (1973). Changes in cell size and shape associated with changes in the replication time of the chromosome of *Escherichia coli*. *J. Bacteriol.* 114, 824–837.

Zaritsky, A., van Geel, A., Fishov, I., Pas, E., Einav, M., and Woldringh, C. L. (1999). Visualizing multiple constrictions in spheroidal *Escherichia coli* cells. *Biochimie* 81, 897–900. doi: 10.1016/S0300-9084(99)00206-0

Zaritsky, A., and Woldringh, C. L. (2015). Chromosome replication, cell growth, division and shape: a personal perspective. *Front. Microbiol.* 6:756. doi: 10.3389/fmicb.2015.00756

Zaritsky, A., Woldringh, C. L., Einav, M., and Alexeeva, S. (2006). Use of thymine limitation and thymine starvation to study bacterial physiology and cytology. *J. Bacteriol.* 188, 1667–1679. doi: 10.1128/JB.188.5.1667-1679.2006

Zheng, H., Ho, P.-Y., Jiang, M., Tang, B., Liu, W., Li, D., et al. (2016). Interrogating the *Escherichia coli* cell cycle by cell dimension perturbations. *Proc. Natl. Acad. Sci. U.S.A.* 113, 15000–15005. doi: 10.1073/pnas.1617932114

Conflict of Interest Statement: The authors declare that the research was conducted in the absence of any commercial or financial relationships that could be construed as a potential conflict of interest.

Advantages of publishing in Frontiers

OPEN ACCESS
Articles are free to read for greatest visibility and readership

FAST PUBLICATION
Around 90 days from submission to decision

HIGH QUALITY PEER-REVIEW
Rigorous, collaborative, and constructive peer-review

TRANSPARENT PEER-REVIEW
Editors and reviewers acknowledged by name on published articles

Frontiers
Avenue du Tribunal-Fédéral 34
1005 Lausanne | Switzerland

Visit us: www.frontiersin.org
Contact us: info@frontiersin.org | +41 21 510 17 00

REPRODUCIBILITY OF RESEARCH
Support open data and methods to enhance research reproducibility

DIGITAL PUBLISHING
Articles designed for optimal readership across devices

FOLLOW US
@frontiersin

IMPACT METRICS
Advanced article metrics track visibility across digital media

EXTENSIVE PROMOTION
Marketing and promotion of impactful research

LOOP RESEARCH NETWORK
Our network increases your article's readership